WARSAW UNIVERSITY OF TECHNOLOGY

Ph.D. Thesis

Discipline of Science – Mechanical Engineering
Field of Science – Engineering and Technology

Jan Michna, M.Sc.

Modelling of laminar-to-turbulent transition and laminar separation bubbles using Computational Fluid Dynamics methods in the case of aerodynamic analysis of a laboratory-scale Vertical-Axis Wind Turbine

Supervisor
dr hab. inż., prof. uczelni, **Krzysztof Rogowski**

Warsaw 2026

To my beloved parents,
Alicja and Andrzej,
with endless gratitude and love.

Acknowledgments

When I started this work almost six years ago, I could hardly imagine how challenging, yet rewarding, this journey would be. At that time, I was absolutely certain about that I would meet extraordinary people who would support, inspire, and guide me along the way.

First and foremost, I would like to express my deepest gratitude to my beloved parents, Alicja and Andrzej. You raised me with patience, love, and curiosity about the world. Your unwavering support, encouragement, and faith in me have been the foundation on which everything else has been built. Everything I have achieved is, in many ways, a reflection of what you have given me.

I owe my sincere appreciation to my supervisor, Professor Krzysztof Rogowski, for his guidance, trust, and partnership throughout this research. Your scientific insight, openness to discussion, and constant encouragement have been invaluable. I am deeply grateful that you treated me not only as a student, but as a collaborator. The experience of working together has profoundly shaped my way of thinking about research, and I am confident that the results of our cooperation have left a lasting mark on my academic path.

I am grateful to my PhD student colleagues for your continuous support. I am very pleased to thank all the members of the Division of Mechanics, and the academic community who contributed, directly or indirectly, to this thesis. Your helpful feedback, stimulating discussions, and inspiring atmosphere made this work feasible.

I would also like to thank my family and all my friends who accompanied me along the way. Your questions, humor, and persistent "How's the thesis going?" kept me motivated when I sometimes lacked it. Thank you for helping me keep perspective when the finish line seemed distant. Also, your patience, understanding, and belief in me carried me through this PhD expedition.

Looking back, this work represents not just an academic achievement, but a journey defined by learning, collaboration, and growth — both scientific and personal.

Warsaw, February 6, 2026 Jan Michna

Abstract

As Horizontal-Axis Wind Turbines (HAWTs) have developed rapidly over recent decades, wind energy has grown rapidly in many parts of the world. This development was preceded by the efforts of scientists and inventors worldwide. This has resulted in HAWTs becoming a mature invention from the perspective of aerodynamics, aeroelasticity, durability, control, and power engineering.

Competitors to these classical solutions are Vertical-Axis Wind Turbines (VAWTs). The most well-known example is the Darrieus turbine, patented in 1926, which shows that this is by no means a new concept for harvesting wind energy. From the offshore application perspective, this type of turbine offers several significant advantages. These include a low-lying center of gravity, accessibility of a massive generator at the waterline, independence from wind direction, a shorter aerodynamic wake enabling denser turbine placement within a wind farm, and a subjectively lower visual impact on the landscape. However, their maximum power coefficient is lower compared to Horizontal-Axis Wind Turbines. In this context, due to still-imperfect modelling approaches for VAWTs, there remains considerable potential to improve their efficiency and generated power.

This dissertation focuses on the analysis of phenomena occurring in the blade boundary layer of Vertical-Axis Wind Turbines and their impact on aerodynamic loads, wake characteristics, and the turbine power coefficient.

The influence of the laminar–turbulent transition location and laminar separation bubbles on the aerodynamic characteristics of turbine blades was investigated. The study was conducted under wind-tunnel conditions representative of the TU Delft facility, characterized by low Reynolds numbers (up to 200,000) and low turbulence intensity levels (up to 0.5%). Aerodynamic forces obtained under such laboratory-scale conditions differ significantly from those occurring in real flow conditions around full-scale turbine blades. The effect of zigzag tapes is also considered, as their use is common in wind-turbine experiments due to their ability to control flow separation and suppress laminar separation bubbles.

To analyze boundary-layer phenomena on turbine blades at low Reynolds numbers, computational fluid mechanics methods were employed, in particular the Un-

steady Reynolds-Averaged Navier–Stokes (URANS) approach. The study focused on the $\gamma - Re_\theta$ turbulence model for simulating laminar–turbulent transition in the boundary layer. The obtained results were compared with wind-tunnel measurements available in the literature, as well as with experimental data generated within the framework of the journal publications.

The results obtained during this doctoral thesis provide a foundation for the development of numerous simulation methods for Vertical-Axis Wind Turbines. They provide insight into turbine behavior at low Reynolds numbers and under varying turbulence levels, reflecting conditions encountered in experimental wind tunnel studies.

The dissertation is constituted by a series of publications, of which the author of the doctoral thesis is a co-author.

Keywords:
Vertical-Axis Wind Turbine, Computation Fluid Dynamics, aerodynamics, laminar-to-turbulent transition, laminar separation bubble

Streszczenie

W wyniku gwałtownego rozwoju turbin wiatrowych o poziomej osi obrotu (Horizontal-Axis Wind Turbines – HAWT) w ciągu ostatnich dekad, energetyka wiatrowa doznała szybkiego wzrostu w wielu miejscach na świecie. Ten rozwój poprzedził wysiłek naukowców i wynalazców na całym świecie. Wskutek tego siłownie wiatrowe o poziomej osi obrotu stały się dojrzałym wynalazkiem z punktu widzenia aerodynamiki, aeroelastyczności, wytrzymałości, sterowania czy elektroenergetyki.

Konkurentami dla tych klasycznych rozwiązań są siłownie o pionowej osi obrotu (Vertical-Axis Wind Turbines – VAWT). Najbardziej znanym przykładem jest wiatrak typu Darrieusa opatentowany w 1926 roku – nie jest to zatem nowy pomysł na pozyskiwanie energii wiatrowej. Z punktu widzenia zastosowań offshore, ten typ turbin ma wiele istotnych zalet. Charakteryzuje się on nisko położonym środkiem ciężkości, dostępnością masywnego generatora z poziomu lustra wody, niezależnością od kierunku wiatru, krótszym śladem aerodynamicznym pozwalającym na gęstsze usytuowanie turbin na farmie czy subiektywnie mniejszym wpływem na krajobraz. Jednak, ich maksymalny współczynnik mocy jest niższy w porównaniu z turbinami o poziomej osi obrotu. Tutaj, ze względu na wciąż niedoskonałe metody modelowania tych turbin, jest nadal przestrzeń do poprawy ich sprawności i generowanych mocy.

Poniższa praca skupia się na analizie zjawisk występujących w warstwie przyściennej łopat turbin wiatrowych o pionowej osi obrotu oraz ich wpływu na obciążenia aerodynamiczne, ślad aerodynamiczny oraz współczynnik mocy turbin.

Przeanalizowano wpływ położenia przejścia laminarno-turbulentnego oraz bąbla laminarnego na charakterystykę aerodynamiczną łopat turbin. Badania przeprowadzono dla warunków występujących w tunelu aerodynamicznym w TU Delft, takich jak niska liczba Reynoldsa (do 200 000) oraz niskie wartości intensywności turbulencji (do 0,5%). Siły aerodynamiczne uzyskiwane w takich warunkach, tj. w skali laboratoryjnej, różnią się znacząco w porównaniu z rzeczywistymi warunkami przepływu wokół łopat pełnoskalowych urządzeń. Rozważany jest również wpływ taśm turbulizacyjnych (zigzag), których stosowanie jest popularne we wszystkich eksperymentach badających pracę turbin wiatrowych ze względu na możliwość kontroli oderwania i redukcji bąbli laminarnych.

Do analizy zjawisk w warstwie przyściennej łopaty w zakresie niskich liczb Re wykorzystano metody numeryczne mechaniki płynów, w szczególności metodę Unsteady Reynolds-Averaged Navier-Stokes (URANS). Skupiono się na modelu turbulencji $\gamma - Re_\theta$ modelującego zjawisko przejścia w warstwie przyściennej. Otrzymane wyniki porównano z wynikami badań tunelowych dostępnych w literaturze i przeprowadzonych w ramach prac nad artykułami.

Wyniki otrzymane w toku pracy doktorskiej są fundamentem do rozwoju wielu metod symulacji turbin wiatrowych o pionowej osi obrotu. Dają obraz zachowania się turbin w zakresach niskich liczb Reynoldsa oraz przy różnych poziomach turbulencji, co odpowiada warunkom spotykanym w tunelach aerodynamicznych.

Praca składa się z cyklu artykułów, którego autor pracy doktorskiej jest współautorem.

Słowa kluczowe:
turbina wiatrowa o pionowej osi obrotu, obliczeniowa mechanika płynów, aerodynamika, przejście laminarno-turbulentne, bąbel laminarny

Contents

1 Introduction

1.1 Problem background and motivation

In 2024, wind energy plays a significant role in global electricity generation, contributing 8% of the global power mix (*Global Energy Review 2025*, 2025). The combined share of solar PV and wind generation in the European Union surpassed that of coal and gas for the first time, indicating an upward trend in wind energy growth.

The global transition towards renewable energy sources has underscored the critical need for innovative and efficient technologies in harnessing wind energy (Kumar et al., 2018).

Veers et al. (2019) differentiate three grand challenges in wind energy research. In addition to improving the understanding of atmospheric flow physics and the integration of wind power plants into the future electricity grid, they demonstrate that the aerodynamics of wind turbines still have to be addressed.

While traditional Horizontal-Axis Wind Turbines (HAWTs) are recognized for their high-quality wind harnessing capabilities, they often present significant challenges related to installation, maintenance, and scalability in certain environments (Shires, 2013).

Due to these challenges, Vertical-Axis Wind Turbines (VAWTs) have garnered significant attention for their unique advantages, including omnidirectional wind capture and a lower center of gravity, which enhance stability and reduce structural stress. Next to operation without a yaw system, VAWTs have a smaller physical footprint and lower noise emissions. However, their broader adoption is often hindered by challenges, including limited self-starting capabilities and reduced aerodynamic efficiency at lower Re numbers (Abdolahifar & Zanj, 2024).

Different types of VAWTs can be distinguished. The basic solution is a Darrieus turbine, invented by Georges Darrieus in 1926 (Darrieus, 1926) with bent blades.

However, this thesis focuses generally on Darrieus turbine subtype — Darrieus H-Shape (or H-Darrieus) wind turbines, lift-driven ones with straight vertical blades

(Figure 1.1). This kind of turbine has been tested various times in wind tunnel conditions (Tescione et al., 2014, Castelein et al., 2015).

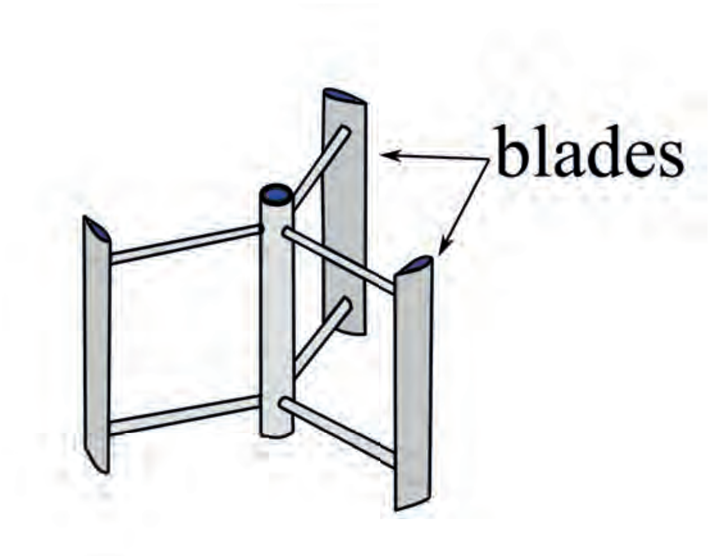

Figure 1.1: Silhouette of the H-type Darrieus wind turbine. Source: Figure 1 (Michna & Rogowski, 2022)

The second most common Vertical-Axis Wind Turbine is the Savonius turbine, invented in 1924 (Savonius, 1929). The simple construction and high torque have to be put to the advantage of these devices. Nevertheless, they are drag-driven turbines, which makes their power coefficient low (Michna & Rogowski, 2023).

Other combined solutions of vertical-axis wind turbines, like X-Rotor (Giri Ajay et al., 2024), exist with potential that has to be investigated. The VAWTs also have the potential to be used in offshore applications as floating devices. The detailed review is prepared by Ghigo et al. (2024).

VAWTs present a compelling alternative, particularly for offshore applications where harsh environmental conditions and complex logistics can hinder the deployment of traditional HAWTs. Their design enables easier maintenance and lower operational costs, making them ideal for offshore wind farms.

Also, the small VAWTs are suitable for urban environments and applications along highways, where tight space constraints and low wind conditions present unique challenges.

The motivation for this doctoral thesis stems from the necessity to bridge the existing knowledge gap regarding the performance under various conditions, optimization, and primarily scalability of VAWTs. The next section will provide a detailed description of this gap.

1.2 Research gaps

The thesis motivation can be described by defining the research gaps, defined as areas within existing knowledge that have not yet been fully explored. These gaps represent missing pieces in the scientific literature, underscoring the novelty of this work.

Below is listed all the research gaps for this thesis, followed by detailed descriptions.

A The aerodynamic performance of thick airfoils in the low Reynolds number range has not been investigated experimentally and numerically sufficiently.

Low Reynolds number flows are a critical area of study due to their relevance in various modern aerodynamic applications. These flows are typically observed in devices such as micro air vehicles (MAVs) and small-scale wind turbines, including Vertical-Axis Wind Turbines (VAWTs). MAVs operate in environments requiring low-speed cruising and are characterized by low weight and small size, leading to Reynolds numbers typically ranging from tens of thousands to several hundred thousand (Mueller & DeLaurier, 2003). In the case of VAWTs, low Reynolds numbers are encountered in the wind tunnel experiments as the turbines are scaled to laboratory size.

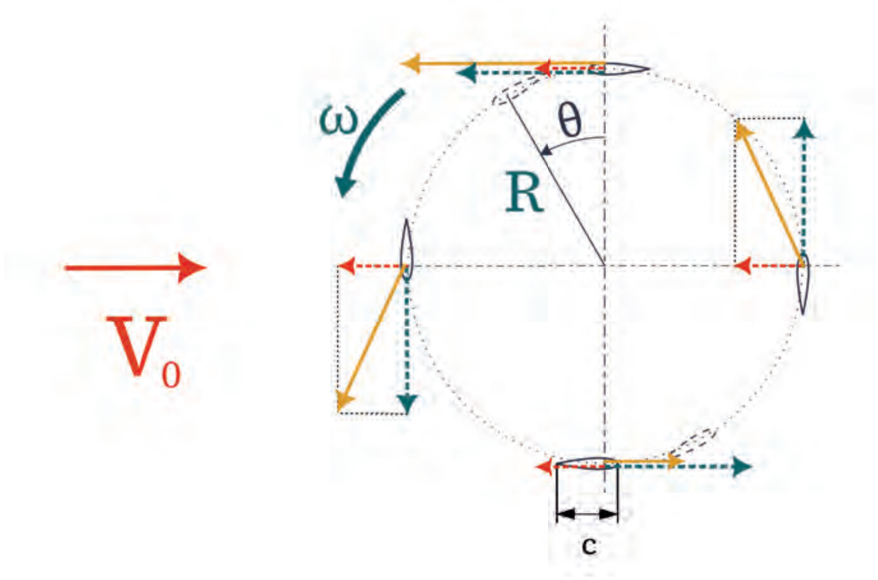

Figure 1.2: Relative velocity (orange) can be estimated using vector calculation from turbine rotation (green) and free-stream velocity (red).

For VAWTs, the Re is defined by the chord-based Reynolds number:

$$Re_c = V_{rel} c \rho / \mu \tag{1.1}$$

where V_{rel} is the relative velocity of the blade to the wind, ρ is the air density, and μ is the dynamic viscosity of air. For the VAWT model used in the Tescione et al. (2014) experiment, the chord-based Reynolds number varies from 1.3×10^5 to 2.1×10^5 during rotation. This is due to the variation in relative velocity. In the case of an undisturbed and uniform flow, the relative velocity can be estimated using simple geometry and vector analysis (see Figure 1.2).

Based on turbine rotation and free-stream velocity, the relative blade velocity can be defined as a function of blade azimuth θ:

$$V_{rel}^2(\theta) = \omega^2 R^2 + V_0^2 + 2\omega R V_0 \cos\theta \tag{1.2}$$

The average value of V_{rel} of one rotation is equal:

$$\overline{V_{rel}} = \frac{1}{2\pi} \int_0^{2\pi} V_{rel}(\theta)\, d\theta = \sqrt{\omega^2 R^2 + V_0^2} \tag{1.3}$$

Based on these calculations, the mean chord-based Reynolds number is approximately 1.6×10^5 in the case of Tescione et al. (2014) experiment.

In a different case with a turbine with a 1 m diameter investigated by Bianchini et al. (2017), the range of Reynolds number is smaller than 1×10^6 and even drops to 3×10^4 for the lowest tip speed ratio. It is important to highlight that the Reynolds numbers are typically much lower for small turbines than those for larger wind turbines (Giri Ajay et al., 2024).

It is crucial to underscore that these conditions are not typically encountered in traditional aviation (Castelein et al., 2015, Rogowski et al., 2020). This is because the low Reynolds number flows are characterized by unique aerodynamic phenomena that differ significantly from conventional high Reynolds number flows.

As articulated by Winslow et al. (2018), under conditions of low Reynolds numbers, the boundary layer exhibits a laminar state over a larger area of the airfoil surface, thereby increasing its vulnerability to separation induced by an adverse pressure gradient. This separated shear layer has significant potential to evolve into a turbulent one and subsequently reattach, forming a laminar separation bubble (LSB).

There are a few experimental aerodynamic force measurements of the NACA 0018 airfoil used in the Tescione et al. (2014) experiment. However, Timmer (2008) reported significant differences in lift characteristics between the experiments performed over time for Reynolds numbers below 300,000, partly due to the sensitivity to flow conditions in the wind tunnel. The author suggested that the difference between his newer and historical data in the Jacobs and Sherman (1937) report might stem from high turbulence levels in the wind tunnel in 1937, affecting transition characteristics.

The problem is understanding the airfoil behaviour under this Reynolds number regime based on accurate experimental data. From a numerical simulation perspective, RANS models do not perform well in this range, and LES and DNS approaches require large mesh sizes and substantial computational resources. This makes a numerical calculation for laboratory-scale VAWT demanding. In the end, it makes numerical validation of the experimental results hard to perform.

In conclusion, the low Reynolds number regime is highly relevant to the design and operation of VAWTs and MAVs, presenting unique aerodynamic challenges not seen in traditional aviation.

B Lack of knowledge about the turbulence intensity's impact on the airfoil parameters.

Turbulence intensity (TI) is a crucial factor in determining the operating conditions of devices operating in the low Reynolds number regime. It is defined as the ratio of the root-mean-square of velocity fluctuations to the average flow velocity. In modern low-turbulence wind tunnels, the turbulence intensity of undisturbed flow can be as low as 0.05 % (Timmer, 2008). However, in the atmosphere, it typically ranges from a few to several dozen percent (Ren et al., 2018).

For Darrieus wind turbines, the rotor blades operate under variable turbulence intensities due to the slowdown and disturbance of airflow caused by a blade moving in the upwind part of the rotor, leading to highly disturbed flow in the downwind part (Rogowski et al., 2016). It is worth noting that Reynolds number and angle of attack also vary during rotation. This makes the accurate modeling of vertical-axis wind turbines complex and demanding.

Also, the turbulence intensity plays a vital role in the Darrieus turbine wind tunnel measurements. Belabes and Paraschivoiu (2021) demonstrate that the effect of the turbulence intensity on the power coefficient is typically observed for the small wind turbines. This is because the influence of TI on the airfoil's aerodynamic characteristics is noticeable in the low chord-based Reynolds number regime. In wind tunnel experiments, wind turbines are scaled down to small dimensions and tested in a very low-turbulence environment. Because of that, the turbulence intensity must be taken into account during the experiment's design process. The comprehensive experimental work confirming the positive influence of higher intensities on the VAWT's outcome was conducted by Carbó Molina et al. (2019).

The literature still lacks comprehensive airfoil characteristics measured with different turbulence intensity levels. Understanding the airfoil's behavior under various intensities is crucial for modeling and designing wind turbines.

This lack of experimental data also makes it hard to properly validate RANS turbulence models for VAWT modeling. This validation is necessary to perform an accurate simulation and design an efficient solution for vertical-axis wind turbines.

C The VAWT modeling needs more accurate methods to be developed due to the flow and performance complexity.

Vertical-Axis Wind Turbines (VAWTs) offer several benefits compared to Horizontal Axis Wind Turbines (HAWTs). These advantages include the absence of yaw mechanisms, a smaller wake area behind the rotor, and reduced installation and maintenance costs due to the generator's location on the ground (Du et al., 2019).

Despite their advantages, VAWTs present challenges such as complex turbine aerodynamics, a demanding self-starting process (low self-start torque), and generally lower power coefficients than HAWTs. A critical challenge involves accurately estimating rotor aerodynamic performance, which is complicated by phenomena such as dynamic stall and blade-wake interaction (Amet et al., 2009).

Modeling the aerodynamic performance of Vertical-Axis Wind Turbines is a complex task. Unlike other wind energy devices, VAWTs are inherently subjected to oscillating loads (Rogowski, 2019). The airflow around the blades of a working wind turbine rotor is complex and highly unsteady, arising from the continuous shift in the tangential velocity direction of the blade, which leads to constant changes in the angle of attack and relative velocity. Angles of attack can even exceed the static stall angle throughout their operation (Castelein et al., 2015). Blades also interact with the rotor's aerodynamic wake and operate in conditions of varying turbulence intensity (Belabes & Paraschivoiu, 2021). These properties make their aerodynamic behavior distinct from other devices.

Various operational parameters influence the power performance of VAWTs. These include the airfoil's shape and chord length, blade pitch angle, turbine solidity, Reynolds numbers, tip speed ratio, shaft diameter, and turbulence intensity (Rezaeiha et al., 2018). For example, research has shown that a 'toe-in' fixed pitch angle can significantly improve VAWT performance (Fiedler & Tullis, 2009).

These complexities make computational fluid dynamics (CFD) methods, particularly those using Reynolds-averaged Navier-Stokes (RANS) equations with various turbulence models, essential for analyzing aerodynamic characteristics.

The second approach for VAWT modeling is the three-dimensional Actuator Line Model (ALM). It combines classical blade element theory with Navier-Stokes-based flow models. This integration, developed by Sørensen and Shen (1999), enables comprehensive simulation of the turbine's interaction with the fluid. In the ALM, wind turbine blades are represented as lines of actuator elements, positioned at their quarter-chord. Blade forces are calculated using local velocities, the angle of attack, and relative velocity for each blade element. These forces are then reintroduced into the Navier-Stokes solver as momentum equation terms. This approach can significantly reduce the numerical resources necessary.

Thus, VAWT modeling is challenging. It demands many computational resources (3D CFD simulations) or accurate experimental data to calibrate models (ALM approach). The issue is more difficult to address when the low-Reynolds number regime and turbulence intensity are taken into account, as is the case in modeling wind turbines used in wind tunnel experiments.

Understanding the aerodynamic behavior of VAWTs is essential for optimizing their design and performance. This is crucial for building efficient numerical models of the airfoil's pitching motion. It can also contribute to the development of methods based on blade element theory, such as blade element momentum (BEM), lifting-line, actuator line, and actuator cylinder methods. Advanced turbulence models and their comparison with experimental data are key to addressing the complexities of these systems.

In summary, while VAWTs offer distinct advantages, their complex aerodynamics, particularly concerning wake characteristics and blade interactions, pose significant challenges to performance optimization. Understanding these factors is crucial for bridging the aerodynamic performance gap between VAWTs and HAWTs.

D The impact of laminar separation bubbles and transition phenomena on VAWTs' performance has to be investigated in depth.

A key characteristic of low Reynolds number flows is the occurrence of laminar boundary layer separation, which leads to the formation of laminar separation bubbles (LSB). These bubbles can vary in size depending on the angle of attack and Reynolds number, influencing flow separation characteristics. For example, Istvan and Yarusevych (2018) show that as the Reynolds number decreases, the reattachment point moves further downstream, increasing bubble size and drag while reducing lift efficiency. Also, Nakano et al. (2007) demonstrate using the NACA 0018 airfoil that the LSB on the suction side decreases and moves to the leading edge with the angle of attack increasing.

LSBs are associated with the laminar-to-turbulent transition phenomenon, which is also characteristic of the low-Re regime. Transition effects are crucial for pressure distributions, and their accurate modeling is essential for obtaining reliable aerodynamic forces. Developing a robust transition model for general-purpose CFD codes is complex due to the varied mechanisms of transition processes and the limitations of conventional Reynolds-averaged Navier-Stokes (RANS) procedures in describing transient flow (Langtry & Menter, 2009).

Some methods, like the e^N method implemented in the XFOIL code, are capable of detecting the location of transition and accounting for phenomena such as limited trailing edge separation and laminar separation bubbles (Youngren & Drela, 1991).

Unfortunately, they are not compatible with common general-purpose CFD codes. This highlights a gap that correlation-based transition turbulence models, like the $\gamma - Re_\theta$ model, aim to fill.

Studying deeply laminar separation bubbles is computationally intensive, often requiring advanced numerical approaches like Direct Numerical Simulation (DNS) or Large-Eddy Simulation (LES), which are typically performed on supercomputers (Kawai et al., 2023). Due to high computational costs, previous studies using these methods have primarily focused on thin airfoils only.

Due to these constraints, the understanding of the impact of laminar separation and transition on vertical-axis wind turbines needs to be filled.

E Effects of zigzag tape on Vertical-Axis Wind Turbines should be investigated.

In the TU Delft VAWT experiment (Tescione et al., 2014), zigzag tape was applied on the blades to mitigate laminar separation bubbles, a common issue affecting airfoil performance at low Reynolds numbers. They also used tape to avoid the laminar boundary layer, which does not exist in full-scale wind turbines due to significant differences in Re.

The zigzag tape can also be used to represent surface contamination effects, which are essential for evaluating VAWT performance and wake behavior in real applications, providing valuable insights for wind turbine design and optimization. Kruse et al. (2018) studied the aerodynamic characteristics of the NACA 63_3-418 airfoil, demonstrating the significance of surface roughness and transition modeling. This suggests that real-world conditions, where blade surfaces may not always be perfectly clean, can significantly alter turbine efficiency.

Zigzag tapes significantly influence the aerodynamic forces and wake characteristics of Vertical-Axis Wind Turbines (VAWTs) by changing boundary layer behaviour. This impact has to be investigated in depth.

F **Angle of attack estimation methods should be developed.**

Estimating blade loads is crucial for the design of Darrieus-type wind turbines. However, it is challenging because the variable angle of attack encountered during blade rotation often exceeds the static stall angle. The ability to estimate the angle of attack during rotation allows a better understanding of the influence of airfoil shape on the final turbine power coefficient. This knowledge can give crucial insight into the dependency between static and dynamic airfoil characteristics.

The simple geometrical angle of attack can be computed from the relative velocity of the blade obtained by vector calculation, as demonstrated in Figure 1.2. This angle can be defined as the angle between the relative velocity of the blade and the chord (see Figure 3.8a). The issue is that the relative velocity computed from the velocity vector calculation can differ from the actual results due to virtual camber effects or vortices induced on the preceding blade.

Thus, extracting the exact angle of attack from the velocity field around the blade is complicated, especially in the case of the high chord to turbine radius ratio (Balduzzi et al., 2015). The amplitude of angle of attack variations can be substantial, depending on the tip-speed ratio, number of blades, and pitch angle. There are a few propositions of angle of attack extraction methods.

Balduzzi et al. (2015) proposed a solution based on an averaging technique and inverse BEM method to estimate the angle of attack in Darrieus turbines, yielding promising results for flow curvature effects, though its application is limited to attached flow and its accuracy is constrained by inherent limitations.

Bianchini et al. (2016) proposed a new CFD-based method for determining the angle of attack on a rotating airfoil, incorporating a ”virtual camber” effect to treat the real airfoil as a virtual straight-flow equivalent. This method enhances robustness by eliminating user-selected variables and shows potential for analyzing complex flow phenomena, including dynamic stall.

Melani et al. (2020) mentioned three additional methods: the 3-Points method, the Trajectory method, and the Line Average method. The 3-Points method uses three sampling points, the Trajectory method uses a single point, and Line Average analyzes the velocity field around the turbine to capture induced flow more precisely.

Various numerical and experimental methods have been developed to address this, each with its own strengths and limitations, particularly in capturing dynamic effects and adapting to different flow conditions. The gap is investigating the accuracy and stability of these methods, which is necessary to deepen the understanding of vertical-axis wind turbine performance.

G The applicability limits of the Transition SST model in the case of VAWT modeling are unknown.

Computational Fluid Dynamics (CFD) models face significant challenges in accurately simulating transitional boundary layer flows, especially for airfoils with high relative thickness and complex geometries, or for those operating under unsteady conditions. Traditional one- or two-equation turbulence models often yield inaccurate aerodynamic forces (Rogowski et al., 2021), as they may over-predict separation at high angles of attack (Zhong et al., 2018).

A general-purpose transition turbulence model should be locally formulated, allow for calibration, and consider different transition mechanisms. The unique correlation-based transition turbulence model, also known as the $\gamma - Re_\theta$ or Transition SST model, is based strictly on local variables and was developed to be compatible with modern CFD codes using unstructured meshes (Langtry & Menter, 2009). It is important to note that this model primarily provides a framework for transition correlations rather than physically modeling the transition process itself, which makes this model inaccurate. However, while it has shown effectiveness at low Reynolds numbers, accurately estimating the dynamic characteristics of pitching airfoils under very low Reynolds number conditions remains a significant challenge for this model. Discrepancies between the Transition SST model's predictions and experimental data persist, especially at higher angles of attack, due to its correlation-based formulation.

The Choudhry et al. (2015) highlights that the $\gamma - Re_\theta$ model relies heavily on empiricism and lacks universality. They postulated that the $k - k_l - \omega$ model is more suitable in the case of laminar separation bubbles on thick airfoils in the low Reynolds regime.

Developing a robust transition model for general-purpose CFD codes is challenging because conventional Reynolds-averaged Navier-Stokes (RANS) procedures are not well-suited to describe transient flow processes, where both linear and nonlinear effects are crucial.

Traditional turbulence models, such as the $k-\omega$ or $k-\varepsilon$ families, struggle to accurately predict the nonlinear behavior of the lift coefficient below the critical angle of attack because they treat the entire boundary layer as fully turbulent and neglect crucial transition effects.

Transition effects significantly influence pressure distributions and are essential for accurate aerodynamic force calculations. A review of the literature indicates that the two-equation turbulence model $k-\omega$ SST is frequently used in analyses, partly because transition models are not yet adequately validated, and the $k-\omega$ SST model is stable and less computationally expensive (Kątski & Rogowski, 2020). However, research has shown that even in the linear range of the lift coefficient, a transition model is necessary for RANS approaches to obtain more accurate drag coefficient results compared to fully turbulent models (Zhang, Sun, et al., 2017).

However, the $k-\omega$ SST model, which assumes a fully turbulent flow, can approximate the effect of zigzag tape or profile contamination by enforcing early transition (Zhang, Van Zuijlen, & Van Bussel, 2017). This model provides robust and reliable predictions, especially in regions with strong adverse pressure gradients. In contrast, the $\gamma-Re_\theta$ model is more suitable for capturing transitional effects, such as laminar separation bubbles, as it explicitly accounts for laminar-to-turbulent transition in the boundary layer.

There are non-RANS techniques, such as Large Eddy Simulation (LES) and Direct Numerical Simulation (DNS), which, while capable of providing reliable data, are too computationally expensive to use across a wide range of angles of attack and flow conditions.

The challenge is calibrating a correlation-based model to use in a low Reynolds regime or with angles of attack exceeding the stall angle. This approach can be a solution for the VAWT modeling issue. The other challenge is to determine the applicability limits of the Transition SST model in terms of Reynolds number. Also, a better turbulence model for these operational conditions would be groundbreaking.

H More research is needed to bridge the gap between 2-D and 3-D CFD modeling approaches.

A 2-D CFD analysis using the $k-\omega$ SST and $\gamma - Re_\theta$ models is a standard procedure for verifying aerodynamic characterization and understanding the impact of transition phenomena, such as laminar separation bubbles. These models are known to accurately predict rotor loads (Rogowski, 2019, Rezaeiha et al., 2019). Unfortunately, they can be imprecise, especially under certain operating conditions (low tip speed ratio, high turbulence).

While 3-D CFD, particularly URANS, provides valuable insights into complex flow phenomena like tip vortices, dynamic stall, wake characteristics, and blade interactions, its high computational cost remains a limitation (Mendoza et al., 2019, Lam and Peng, 2016).

Experimental measurements, like those obtained using Particle Image Velocimetry (PIV), often show significant differences in the aerodynamic wake when compared to 2D model predictions, highlighting the impact of these uncaptured 3D phenomena.

Therefore, lower-order models such as the blade element momentum (BEM) and Actuator Line Model (ALM) remain popular alternatives. These methods rely on airfoil aerodynamic characteristics and additional corrections (e.g., flow curvature, dynamic stall models) and can incorporate finite blade and added mass effects.

The challenge is to develop computationally less expensive methods, such as 2D URANS, that can also provide accurate flow visualization necessary to understand vertical-axis wind turbine performance.

I Limited wind tunnel experimental data of airfoil characteristics for Vertical-Axis Wind Turbines design and validation.

Historically, the wind energy sector has primarily concentrated on horizontal-axis wind turbines (HAWTs). However, increasing attention is now being directed towards improving the aerodynamic performance of VAWTs to bridge the efficiency gap between these two types of turbines (Kumar et al., 2018). To achieve this goal, obtaining static and dynamic airfoil characteristics across different Re regimes is essential because of the different conditions in the case of the experiment-scale and full-scale turbines. The most popular airfoils used in VAWTs are from the NACA series, such as NACA 0018. Unfortunately, experimental studies on the NACA 0018 airfoil for a wide range of flow parameters were not widely available until recently.

For over 70 years, since 1933, there have been almost no new experimental studies on the NACA 0018 profile to investigate its performance in the regime of low and medium Reynolds numbers. This lack of data includes various turbulence parameters and becomes a challenge because the conditions in modern wind tunnels differ vastly from those in Earth's atmosphere (Rogowski et al., 2021).

Historical data, such as the famous Report No. 460 from 1933 (Jacobs et al., 1933), which provided NACA 0018 profile characteristics for a Reynolds number of 3,200,000, are not helpful as input for engineering models developed for Darrieus wind turbines due to their much lower blade Reynolds numbers. While more valuable characteristics were found in Report No. 568 (Jacobs & Sherman, 1937), these too had limitations.

Before 2011, the primary available airfoil database was from Sheldahl and Klimas (1981), which mainly contained characteristics of four-digit NACA series airfoils. The results presented in this study for low Reynolds numbers significantly differ from more recent findings.

Melani et al. (2019) published a significant paper summarizing experimental and numerical studies for low and medium Reynolds numbers.

Among others, some of the experiments are worth highlighting. Study of Timmer (2008) on wind turbines at a laboratory scale has shown chord-based Reynolds numbers in the range of 150,000–1,000,000, often using four-digit NACA series airfoils despite their poor performance under these flow conditions.

Nakano et al. (2007) conducted unique studies using Particle Image Velocimetry (PIV) to investigate flow and noise characteristics of the NACA 0018 airfoil at a moderate Reynolds number of 160,000, revealing the connection between flow separation, reattachment, and tonal noise.

The University of Waterloo made significant advancements in measurement techniques for NACA 0018 and other four-digit NACA series airfoils, exemplified by Gerakopulos et al. (2010) publication. Their study analyzed the NACA 0018 airfoil at low Reynolds numbers (80,000 to 200,000), characterizing its lift and separation bubble behavior and how the separation bubble's position and length change with Reynolds number and angle of attack.

Imperial College conducted measurements in a low-turbulence wind tunnel, using pressure distribution measurements to capture aerodynamic characteristics of airfoils at Reynolds numbers from 60,000 to 300,000 and angles of attack from 0° to 180°. These results validated the hypothesis of virtual camber effects Bianchini et al. (2015).

Du (2016) study involved in-depth experimental and numerical analysis of the NACA 0018 airfoil at low Reynolds numbers (60,000 to 140,000), utilizing sophisticated measurement techniques like PIV and pressure distribution analysis to explore flow separation and reattachment.

In summary, experimental work in low Reynolds number aerodynamics, especially for NACA 0018 airfoils, has been crucial for understanding unique flow behaviors like laminar separation and hysteresis. Despite advancements, challenges remain in model calibration due to differences between wind tunnel and atmospheric conditions, and a continued need for more comprehensive experimental data to improve numerical predictions.

All research gaps identified above are presented below as a list:

- **A** Low Reynolds number range aerodynamic performance.
- **B** Turbulence intensity's impact on the airfoil aerodynamics.
- **C** The VAWT modeling needs more accurate methods to be developed.
- **D** The boundary layer phenomena's impact on VAWT performance.
- **E** Effects of zigzag tape on VAWTs should be investigated.
- **F** Angle of attack estimation methods should be developed.
- **G** The applicability limits of the Transition SST model.
- **H** Bridge the gap between 2-D and 3-D modeling approaches.
- **I** Limited airfoil characteristics experimental data.

1.3 Formulating hypoteses

To address the gaps outlined, three general hypotheses are presented.

1 This thesis generally focuses on the numerical modeling of a laboratory-scale Vertical-Axis Wind Turbine based on experimental research conducted at Delft University of Technology (Tescione et al., 2014). The turbine investigated during this research was validated by various numerical simulations (e.g., Rezaeiha et al., 2019), but without modeling the tape. The authors of the experiments use zigzag tape placed at 8 percent of the chord from the leading edge on both sides. The effect of this turbulization tape on laboratory-scale VAWT has never been investigated in depth.

Hypothesis ① Missing zigzag tape effect understanding

The zigzag tape modifies airfoil characteristics by eliminating the laminar separation bubble, thereby changing the aerodynamic blade loads and wake geometry of a VAWT.

This thesis shows the zigzag impact on VAWT torque, aerodynamic loads on the blades, and wake behind the rotor. Also, the influence of laminar separation bubble formation on boundary layer characteristics and loads is investigated.

2 The Vertical-Axis Wind Turbine design process consists of, among others, a wind tunnel validation stage. Unfortunately, when the H-Darrieus wind turbine scale shrinks to a size moveable into a wind tunnel, the chord-based Reynolds number drops according to the chord length decreasing.

This scalability issue has to be addressed during the wind tunnel tests design stage, and any numerical validation performed. The blade loading and boundary-layer characteristics can differ between full-scale and laboratory-scale conditions due to differences in the chord-based Reynolds number. Moreover, slight changes in the oncoming wind velocity can lead to noticeable differences in aerodynamic loads for laboratory-scale VAWTs. This is due to the higher aerodynamic sensitivity of airfoils in the low-Re regime. Also, in this regime, the influence of the turbulence intensity (TI) on the airfoils' aerodynamic characteristics is greater. These issues are not observable in the full-scale wind turbines.

This thesis focuses on the investigation of Re and TI impacts using URANS methods, validated with experimental data obtained during the work and with results from the literature. The outcome provides a foundation for subsequent research focused on proposing improved validation procedures and more accurate models of VAWTs.

Hypothesis ② Reynolds number and turbulence intensity influence on laboratory-scaled VAWTs

In the low-Re regime, the Reynolds number has a substantial impact on the airfoil characteristics, thereby affecting the power coefficient of the VAWT. The influence of TI is visible but smaller than that of Re. This influence is not observable for the high and moderate Re.

This thesis investigates the impact of Re and TI on aerodynamic force coefficients. For $Re < 200{,}000$, this influence is noticeable. Also, this work addresses the lack of experimental data on airfoils at low Reynolds numbers.

3 To accurately estimate the power coefficient of the VAWT, a deep understanding of the static and especially dynamic behavior of the airfoils is obligatory. These characteristics can be obtained using numerical and experimental methods.

The aerodynamics and flow around the VAWT rotor are complicated. Consequently, the dynamic behaviour of the airfoil differs significantly from the static one. A deep understanding of this difference is crucial for accurately determining aerodynamic forces and, consequently, the device's efficiency. This also allows for acquiring knowledge for improvement methods, such as the Actuator Line Model, or for developing a pitching motion model.

Hypothesis ③ Static and dynamic characteristics of airfoils in the low-Re regime

The static and dynamic loads characteristic of the VAWT blade are strongly dependent on the laminar separation bubble and the laminar-to-turbulent transition occurring in the boundary layer of the blades. These phenomena are typical of low Reynolds number flow around thick airfoils.

The work focuses on the aerodynamic characteristics of the DU-91-W2-250 and NACA 0018 airfoils. Also, this dissertation analyzes the influence of VAWT operational parameters and fixed-pitch on force results using URANS modeling. The methods for estimating the angle of attack are tested and discussed. The dynamic behaviour of the turbine's blades is investigated as a foundation for the pitching motion model.

1.4 New testable predictions

To test the hypothesis, a detailed list of new testable predictions is prepared. The scope of this thesis is wide. Thus, all issues must be carefully classified and addressed. A new testable prediction is the way to order these issues. Each paper constituting this dissertation tests some of the predictions listed below.

Hypothesis 1 Missing zigzag tape effect understanding

I Effect of zigzag tape on lift coefficient

Zigzag tape linearizes the lift coefficient characteristic. This can be tested by comparing the lift coefficient (C_L) versus angle of attack (α) curves for a clean airfoil and a zigzag-taped airfoil.

II Impact of zigzag tape on aerodynamic efficiency

Zigzag tape leads to a reduction in aerodynamic efficiency due to increased drag and decreased lift below the critical angle of attack. This can be tested by measuring the lift and drag forces and calculating the lift-to-drag ratio for airfoils with and without zigzag tape.

III Wake recovery distance prediction of VAWT

Wake recovery occurs later for the zigzag tape profile. Measuring the velocity profiles at different distances downstream can test this.

IV Wake asymmetry prediction of VAWT

Zigzag tape promotes asymmetry in the aerodynamic wake behind the rotor. This can be tested using PIV (Particle Image Velocimetry) measurements to compare the wake symmetry behind rotors with and without zigzag tape. Also, this prediction can be validated with Computational Fluid Dynamics and Actuator Line Model methods.

Hypothesis 2 Reynolds number and turbulence intensity influence on laboratory-scaled VAWTs

V Reynolds number and turbulence intensity influence on airfoil performance

The aerodynamic performance of the NACA 0018 airfoil is largely dependent on the Reynolds number and less dependent on turbulence intensity. To test this, one could vary the Reynolds number and turbulence intensity in experiments or simulations and measure the lift and drag coefficients to quantify their respective impacts.

VI Aerodynamic characteristics prediction at low-Reynolds numbers

For a NACA 0018 airfoil at a low Reynolds number, the drag coefficient at low angles of attack decreases significantly as the Reynolds number increases from 30,000 to 160,000. This can be tested by measuring the drag coefficient at different Reynolds numbers in the specified range. The results can be compared with CFD outcomes to evaluate these methods at low Reynolds numbers.

VII Reynolds number influence on C_L^{max} of airfoil

The Reynolds number significantly affects C_L^{max}, with the differences becoming more pronounced as the Reynolds number decreases. Experimental tests at various Reynolds numbers can validate this.

VIII Impact of pitch angle on wake deflection of VAWT

The pitch angle configuration influences wake deflection and deformation in vertical-axis wind turbines. The PIV measurements proving this from the literature can be tested and validated using CFD wind turbine models with a wide scope of configurations.

IX Thrust and lateral forces validation of VAWT

Using a 2-D numerical rotor model, thrust and lateral forces can be validated against experimental measurements. Comparing experimental measurements of thrust and lateral forces with simulations from a 2-D numerical rotor model can test this.

X **Turbulence intensity decay rate influence limits**

The decay rate of turbulence intensity depends on the turbulence intensity at the inlet. A testable hypothesis is that RANS models predict high turbulence intensity decays, and whether this makes keeping high intensities around Darrieus rotors possible to simulate. During simulations, the turbulence intensity on the domain inlet can be raised to 20 %–30 % to find the highest reachable intensity values near the rotor.

Hypothesis 3 **Static and dynamic characteristics of airfoils in the low-Re regime**

XI **Stall hysteresis prediction**

The post-stall hysteresis loops move to the higher angles of attack with rising Reynolds numbers for NACA 0018 airfoils. Experimental measurements at varying Reynolds numbers could validate this prediction.

XII **Dynamic and static lift coefficient slopes prediction**

The slope of the static C_L (lift coefficient) curve corresponds closely to that of the dynamic curve, despite the dynamic curve not passing through zero angle of attack, due to the "virtual camber" effect. This can be tested by comparing the static and dynamic C_L curves in different flow conditions.

XIII **Influence of laminar separation bubbles on aerodynamic hysteresis and oscillations**

It was hypothesized that laminar separation bubbles would significantly cause hysteresis in the lift coefficient at low angles of attack and lead to notable oscillations in the aerodynamic forces.

XIV **$\gamma - Re_\theta$ model accuracy prediction**

The $\gamma - Re_\theta$ model (also known as Transition SST) can predict the aerodynamic performance of an airfoil more accurately for moderate Reynolds numbers. Comparing experimental force measurements with 2-D CFD simulations using the Transition SST model could validate this.

XV Limitations of the $k - \omega$ SST turbulence model in capturing laminar flow effects

The work tested the prediction that the classical two-equation $k - \omega$ SST turbulence model, which assumes a fully turbulent boundary layer, would fail to capture nonlinearities in lift force characteristics and the effects of laminar separation bubbles.

1.5 Thesis structure

This work opens with an introductory subsection that describes the research background. All research gaps that this thesis tries to fill are listed. Then, based on these gaps, the hypotheses are formulated. All new testable predictions are described in detail, which concludes Section 1.

The Section 2 describes three scientific papers that were the first stage of work. They focus on airfoil aerodynamics and boundary layer behaviour in the case of vertical-axis wind turbine applications.

Next Section 3 contains an overview of the four papers constituting the dissertation. This part focuses on VAWT modeling using different numerical methods and under different conditions. The results are validated against various experiments from the literature.

All general conclusions and future work recommendations are collected in the summary Section 4. In the Appendix, all copies of publications constituting this dissertation are included.

2 Low-Re flow and turbulence model influence on airfoil aerodynamics

2.1 Reynolds number influence on laminar-to-turbulent transition and aerodynamic characteristics in the case of DU 91-W2-250

Michna et al. (2021)

Title: "Accuracy of the Gamma Re-Theta Transition Model for Simulating the DU-91-W2-250 Airfoil at High Reynolds Numbers"

Authors: Jan Michna, Krzysztof Rogowski, Galih Bangga, Martin O. L. Hansen

Journal: Energies **Date:** December 2021 **MNiSW Points:** 140 pts

Contribution: methodology, software, validation, numerical analysis, writing - review and editing, visualization

New Testable Predictions:

XIV $\gamma - Re_\theta$ model accuracy prediction

XV Limitations of the $k - \omega$ SST turbulence model in capturing laminar flow effects

Research Gaps:

D The boundary layer phenomena's impact on VAWT performance.

G The applicability limits of the Transition SST model.

As a first step, the thesis focused on the DU 91-W2-250 airfoil designed for wind turbine applications (Figure 2.1a). The results are collected in the scientific paper (Michna et al., 2021). From the thesis perspective, it was a proper introduction to testing and familiarizing with the numerical airfoil investigation methodologies, and a general understanding of airfoil behaviour below the critical angle.

This study focuses on point of transition estimation using URANS (Unsteady Reynolds-Averaged Navier-Stokes) method with the four-equation Transition SST ($\gamma - Re_\theta$) turbulence model in aerodynamic numerical simulations of the airfoil at moderate Reynolds numbers and angles of attack below the critical angle. The second aim was to verify whether this numerical approach is suitable for modeling the flow around this thick kind of airfoil (25 % of chord thickness) used in wind turbines. The turbulence model incorporates modeling of the laminar-to-turbulent transition. This unique property of the Transition SST turbulence model allows presenting the predicted transition point alongside the analysis of aerodynamic force results.

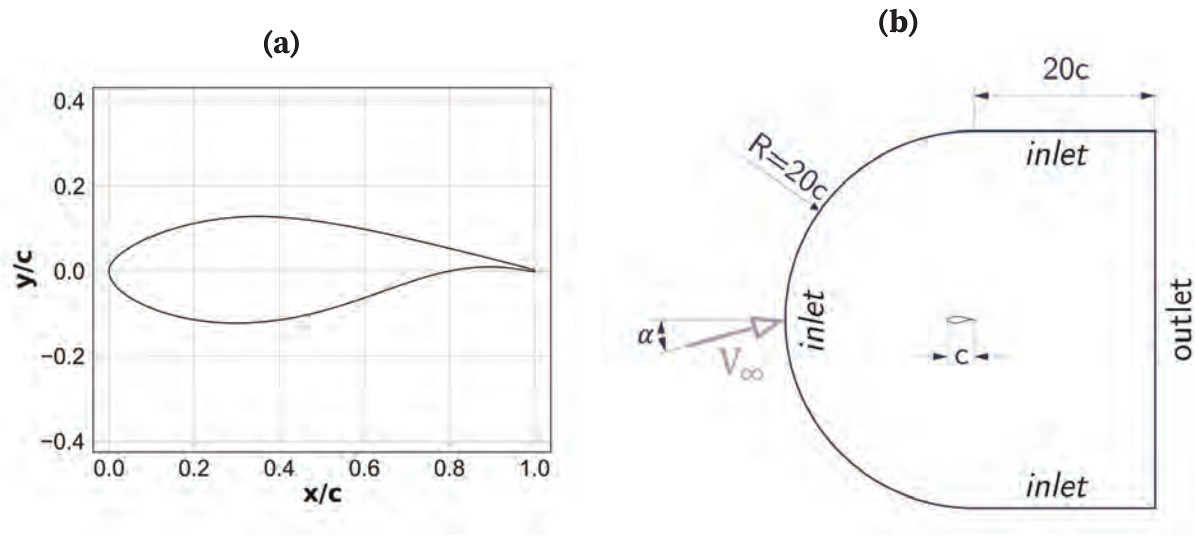

Figure 2.1: DU 91-W2-250 airfoil (a); computational domain and boundary conditions (b). Source: Figure 1 (Michna et al., 2021)

A two-dimensional numerical model of the DU 91-W2-250 airfoil was introduced (Figure 2.1b). The simulations use URANS and the Transition SST model in ANSYS Fluent 19.0. The aerodynamic characteristics of the airfoil were studied at Reynolds numbers of 3×10^6 and 6×10^6, compared against results from a data source from wind tunnel experiments and those obtained using other turbulence models ($k-\omega$ SST and $k-\varepsilon$ RNG). The turbulence conditions were kept similar to those of the typical wind tunnel. The XFOIL results with the e^N method implemented are also included. The N value was set to 9, corresponding to a smooth wing surface with a low free-stream turbulence level.

In addition to aerodynamic forces, the study examined the location of the transition point as a function of angle of attack and Reynolds number. Also, the plots of static pressure and skin friction coefficient distributions were prepared.

The lift coefficient C_L and drag coefficient C_D values were extracted from the simulation (Figure 2.2). To verify results and measure turbulence model accuracy, the slope of the lift coefficient $\mathrm{d}C_L/\mathrm{d}\alpha$ was compared. For URANS and experimental results, the aerodynamic derivative $dC_L/d\alpha$ values are calculated from 0 to 8.1 degrees. The difference observed was negligibly slight, as seen in the Figure 2.2.

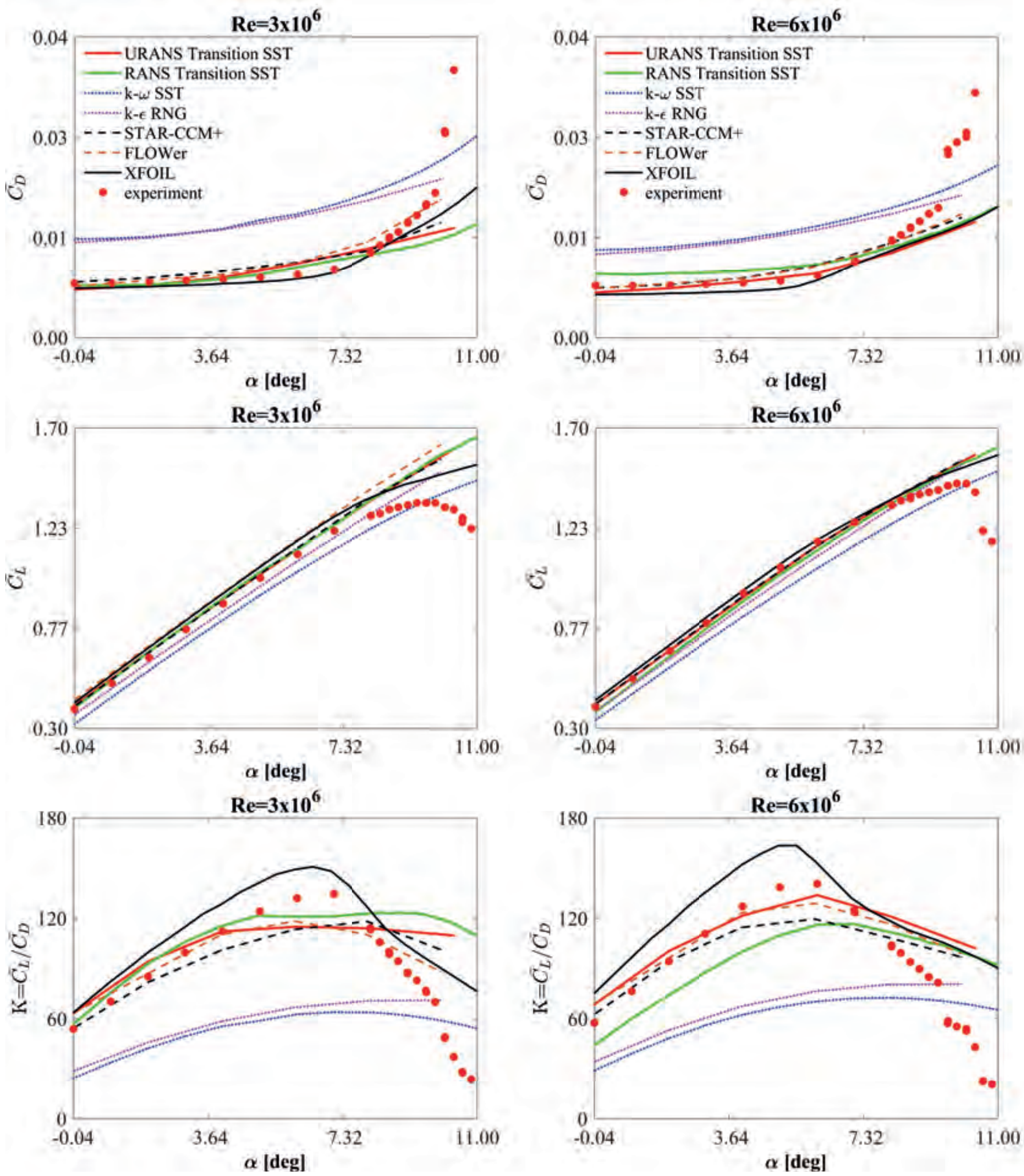

Figure 2.2: DU 91-W2-250 airfoil performance for two Reynolds numbers of 3×10^6 and 6×10^6. Source: Figure 5 (Michna et al., 2021)

The results showed that the static pressure distribution depends mainly on the angle of attack and, to a lesser extent, on the Reynolds number. Figure 2.3 presents the standard deviations of this pressure distribution. Looking at Figure 2.3(b), the maximum values can be observed in a narrow strip around the position $x/c = 0.4$. This location is not coincidental; it is where the laminar-to-turbulent transition occurs.

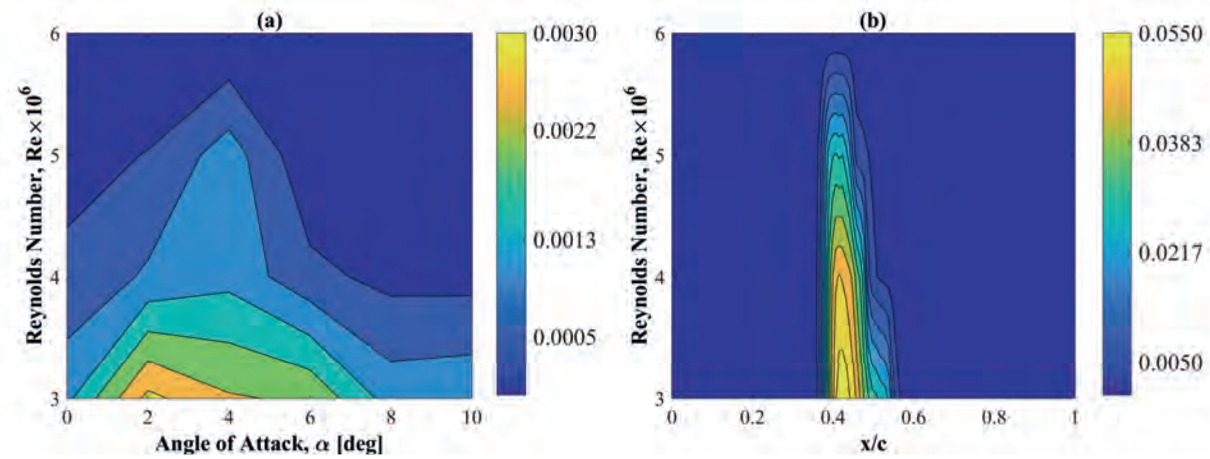

Figure 2.3: Standard deviation of the static pressure coefficient for the suction side of the airfoil and the angle of attack of 4 degrees. Subfigure (a) shows standard deviations as a function of the angle of attack and Reynolds number, whereas (b) shows standard deviations as a function of position and Reynolds number. Source: Figure 11 (Michna et al., 2021)

In contrast to the pressure distribution, the skin friction coefficient distribution $C_f(x/c)$ depends strongly on the Reynolds number (Figure 2.4). It should be noted that the influence of Re is visible on the suction side of the airfoil (Figure 2.4(b)). There, it can be observed that as the Reynolds number increases, the skin friction changes as the transition shifts toward the leading edge.

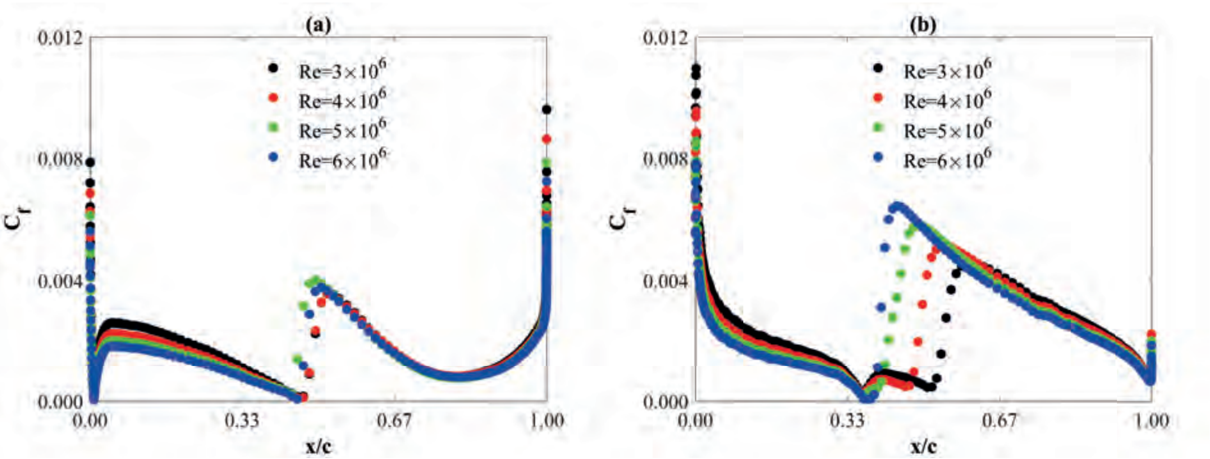

Figure 2.4: Skin friction coefficient distribution at the angle of attack of 4° with different Reynolds numbers for (a) the suction side and (b) the pressure side. These results are given for the Transition SST turbulence model. Source: Figure 13 (Michna et al., 2021)

Points of transition x_{tr} were predicted based on the skin friction coefficient distribution C_f. This point is associated with a derivative of C_f – rapid growth of skin friction shows the position of the limit between laminar and turbulent boundary conditions, i.e., the point of transition x_{tr}. Two different derivatives of $x_{tr}(\alpha)$ for the suction side can be distinguished from the Figure 2.5: the first one in the range of angles from $0°$ to $6°$ and the second one from $6°$ to $10°$. However, for the pressure side, the distribution of points of transitions is almost linear over the entire range considered.

The paper confirms that the Transition SST model can be successfully used for aerodynamic analysis of this class of airfoils in the below-critical angle of attack range. The results of aerodynamic force coefficients were compared with other implementations of the Transition SST model in different CFD codes. The significant difference was not found.

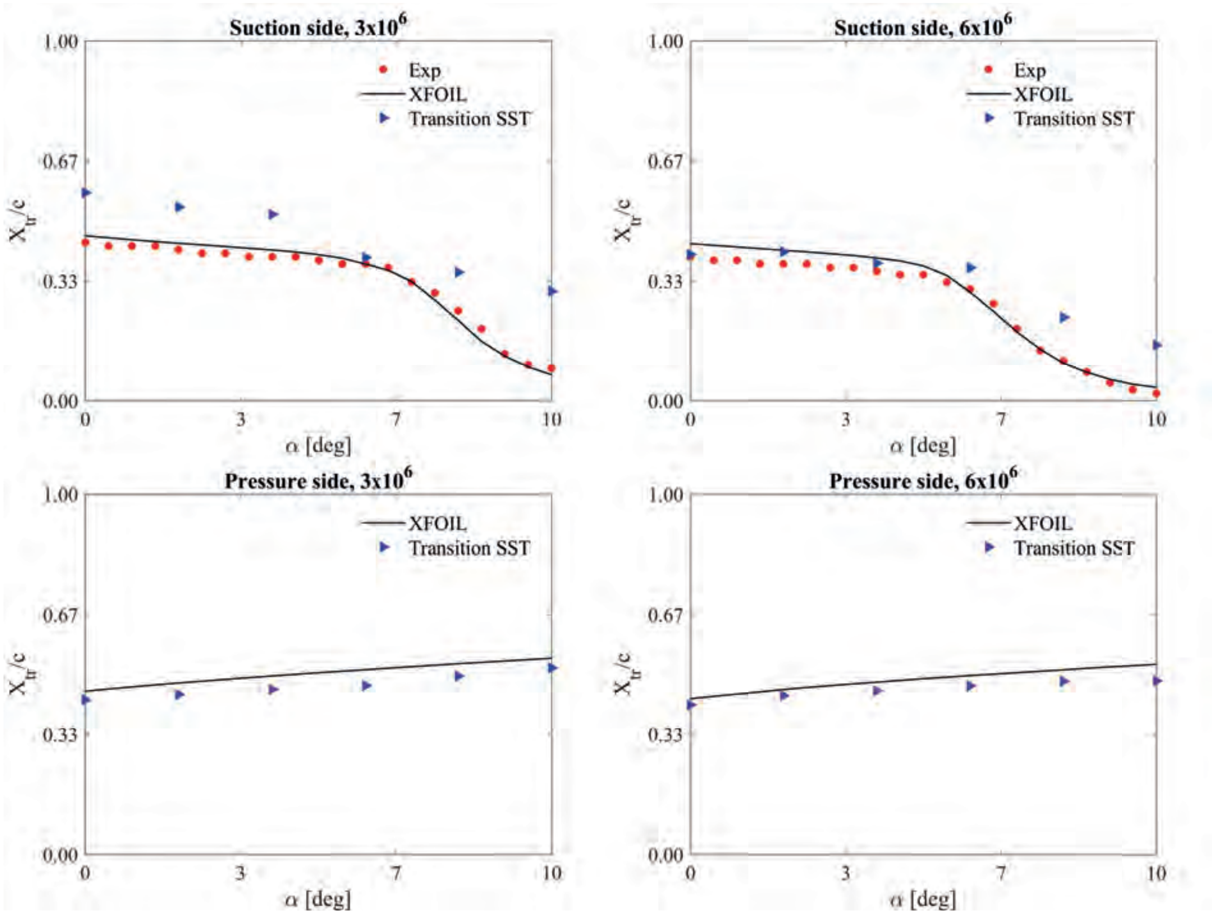

Figure 2.5: Variation of transition location with the angle of attack for two Reynolds numbers. The Transition SST results are compared with XFOIL simulation and experimental tunnel data. Source: Figure 16 (Michna et al., 2021)

The results show that this model provides better results than the $k - \varepsilon$ and $k - \omega$ turbulence models. This conclusion shows that modeling the transition phenomenon plays a key role in aerodynamic simulations and gives more accurate results. However, the error in the transition location estimation was noticeable. That shows room for turbulence modeling improvement and/or recalibration of the Transition SST model itself.

2.2 NACA 0018 performance under different turbulence conditions

Michna and Rogowski (2022)

Title: "Numerical Study of the Effect of the Reynolds Number and the Turbulence Intensity on the Performance of the NACA 0018 Airfoil at the Low Reynolds Number Regime"

Authors: Jan Michna, Krzysztof Rogowski

Journal: Processes **Date:** May 2022 **MNiSW Points:** 100 pts

Contribution: methodology, software, validation, numerical analysis, writing—review and editing, visualization

New Testable Predictions:

- **V** Reynolds number and turbulence intensity influence on airfoil performance
- **X** Turbulence intensity decay rate influence limits

Research Gaps:

- **A** Low Reynolds number range aerodynamic performance.
- **B** Turbulence intensity's impact on the airfoil aerodynamics.

The following study focuses on the impact of low Reynolds number and turbulence intensity on the characteristics of the NACA 0018 airfoil (Michna & Rogowski, 2022). The novelty of this work is the numerical examination of the airfoil against different turbulence intensities. The objective was to identify how these parameters affect the airfoil's performance, which is crucial for designing vertical-axis wind turbine (VAWT) blades. The airfoil used is a well-investigated geometry and was implemented in the investigated laboratory-scale Darrieus Wind Turbine at Delft University of Technology.

The methodology is similar to before and involves numerical simulations using the URANS (Unsteady Reynolds-Averaged Navier-Stokes) approach with the Transition SST $\gamma - Re_\theta$ turbulence model. This model was chosen based on previous work (Michna et al., 2021). The study was conducted for Reynolds numbers ranging from 50,000 to 200,000 and turbulence intensities from 0.01 % to 0.5 %. Aerodynamic force coefficients of the NACA 0018 airfoil were analyzed for angles of attack between

0 and 10 degrees, far below the critical angle. The numerical model was validated by comparing it with wind tunnel experimental data from DUT (Timmer, 2008).

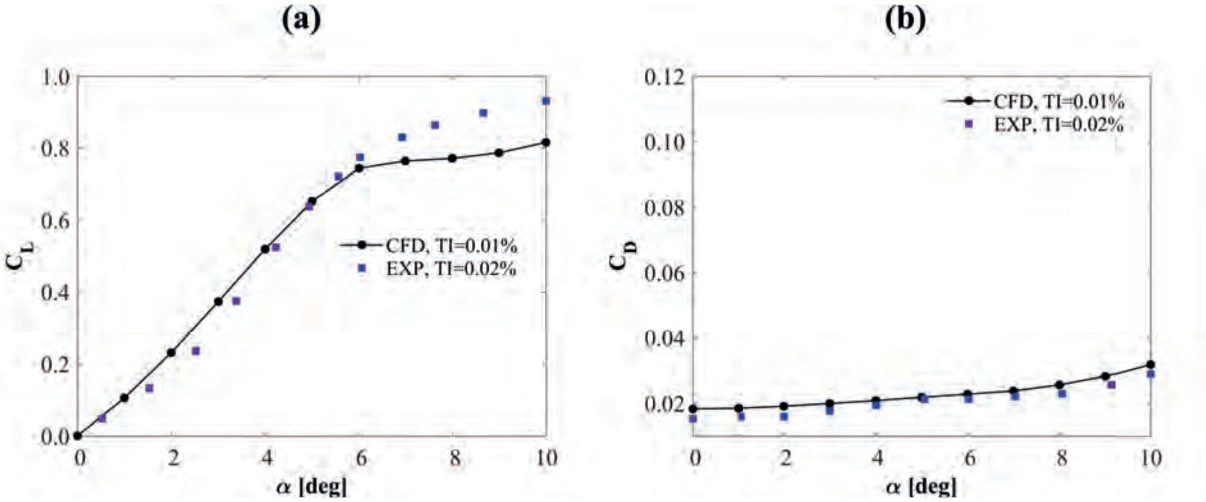

Figure 2.6: Aerodynamic characteristics of the NACA 0018 profile. Lift coefficient (a) and drag coefficient (b) as a function of the angle of attack. Source: Figure 5 (Michna & Rogowski, 2022)

This validation is presented in Figure 2.6. As the plot shows, in the case of the lift coefficient (Figure 2.6a), both series of results are sufficiently consistent in the range of angles of attack up to 6 degrees. Slightly more significant coefficient differences are visible above this angle of attack. One of the possible causes of differences is that the 3D effects were not considered in these studies. The second reason is that the turbulence model is not calibrated enough through the model constants that control the characteristics of the separation bubble.

The results highlight the significant influence of Reynolds number and turbulence intensity on the behavior of the NACA 0018 airfoil at low Reynolds numbers. As observed, the effect of the turbulence intensity on the lift coefficient is much lower than the Reynolds number effect. Although at a low Reynolds number regime, even relatively small differences in these quantities can significantly change the lift and drag airfoil characteristics. This shows that turbulence intensity significantly affects the aerodynamic characteristics of the airfoil, specifically in the laboratory-scale VAWT Reynolds number operational range.

Although turbulence decay was observed upstream of the airfoil in URANS simulations, the decay rate depends primarily on the inlet intensity. Higher turbulence intensity at the inlet leads to faster decay, while near the airfoil's leading edge, turbulence remains low regardless of inlet conditions. During the preparation of the simulation stage, it was observed that under specified conditions, in the URANS simulation, the turbulence intensity just before the airfoil higher than 0.5 % is hard to reach.

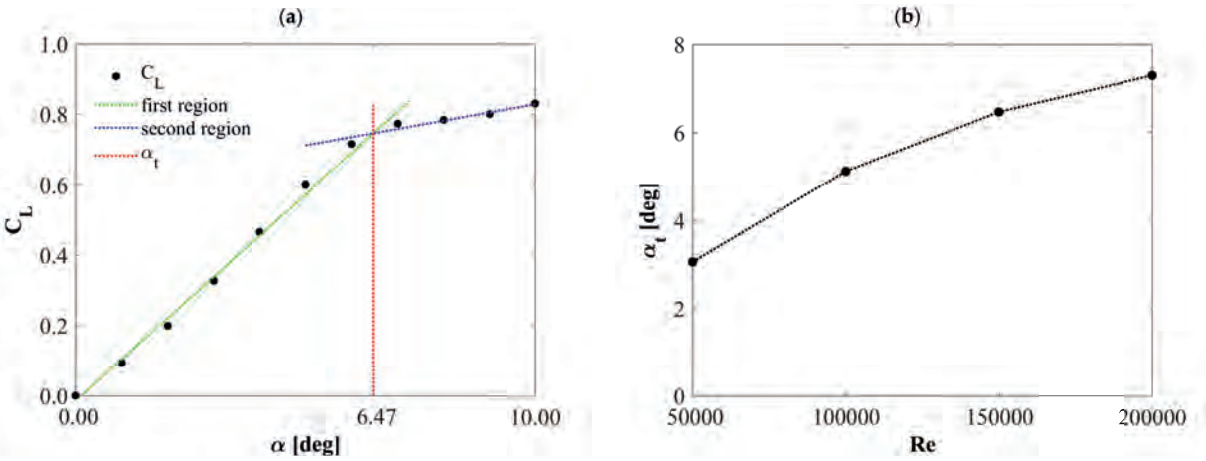

Figure 2.7: The approach for determining the transition angle α_t. Subfigure (a) shows the lift coefficient against angle of attack for Re = 150,000 and TI = 0.25 %. Subfigure (b) shows the transition angle against Reynolds number for TI = 0.25 %. Source: Figure 9 (Michna & Rogowski, 2022)

The lift coefficient result (Figure 2.7) shows that the lift is not linear at low Reynolds numbers. Moreover, two specific regions can be distinguished in the plot. For each region, the lift coefficient slope is different. The transition angle α_t, the border between regions, was found during the investigation for each Reynolds number used. As shown, this angle increases with increasing Reynolds number.

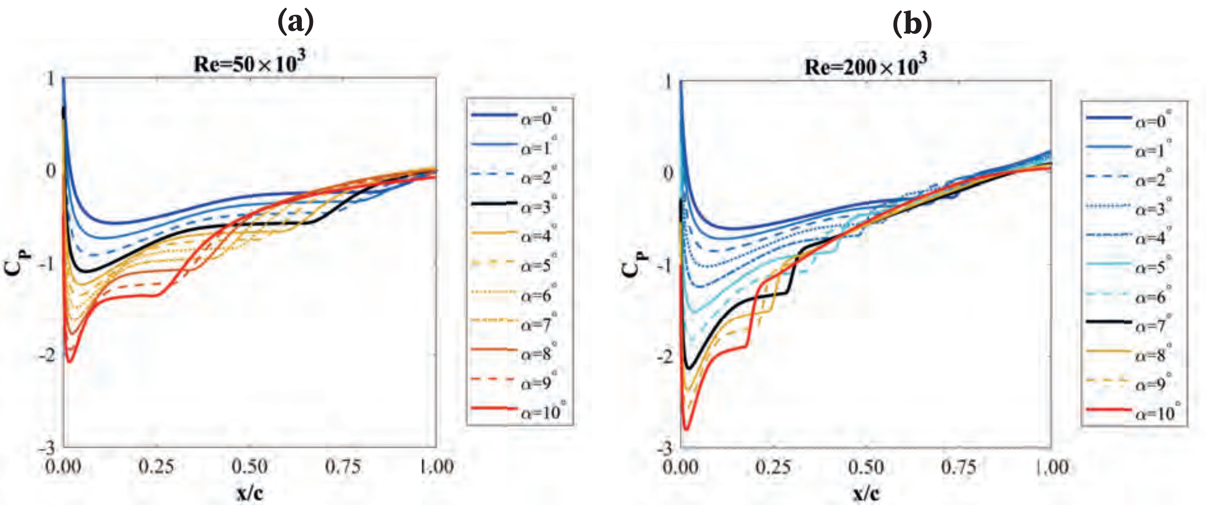

Figure 2.8: Static pressure coefficient on the pressure side at Re = 50,000 (a) and Re = 200,000 (b). Source: Figure 17 (Michna & Rogowski, 2022)

The results of pressure coefficient distributions show that for angles of attack larger than α_t, there is no longer a laminar-separation bubble on the pressure surface of the airfoil (Figure 2.8). Also, pressure noticeably depends on the Reynolds number, quantitatively and qualitatively.

In summary, the results demonstrate that turbulence intensity significantly affects the aerodynamic performance of the NACA 0018 airfoil at low Reynolds numbers. Specifically, increasing turbulence intensity reduces the aerodynamic derivative $\mathrm{d}C_L/\mathrm{d}\alpha$ in the first region and increases it in the subsequent region. It also delays the transition angle α_t. This trend is consistent across all Re numbers investigated.

The formation of a wide laminar separation bubble in the boundary layer leads to the presence of two distinct lift curve slopes prior to stall. While increasing the Reynolds number causes a nearly linear rise $\mathrm{d}C_L/\mathrm{d}\alpha$ within the first region, the slope in the second region remains largely unaffected.

This paper highlights the necessity of a deeper investigation of the airfoil's aerodynamic performance at low and very low Reynolds numbers. In this range, the slight change in turbulence levels has a crucial effect on lift due to the laminar separation bubble and the laminar-to-turbulent transition occurred in the boundary layer.

2.3 Airfoil performance at low Reynolds numbers - experiment

Rogowski, Mikkelsen, et al. (2025)

Title: "Aerodynamic performance analysis of NACA 0018 airfoil at low Reynolds numbers in a low-turbulence wind tunnel"

Authors: Krzysztof Rogowski, Robert Flemming Mikkelsen, **Jan Michna**, Jan Wiśniewski

Journal: *ASTRJ* **Date:** January 2025 **MNiSW Points:** 100 pts

Contribution: methodology, software, CFD simulation, numerical analysis, validation, writing - original draft preparation, writing - review and editing

New Testable Predictions:		Research Gaps:	
VI	Aerodynamic characteristics prediction at low-Reynolds numbers	**A**	Low Reynolds number range aerodynamic performance.
VII	Reynolds number influence on C_L^{max} of airfoil	**G**	The applicability limits of the Transition SST model.
XI	Stall hysteresis prediction	**I**	Limited airfoil characteristics experimental data.

Based on the previous work recommendation, the next step was to investigate the lowest range of Reynolds numbers (Rogowski, Mikkelsen, et al., 2025). The goal was to measure the aerodynamic characteristics of the NACA 0018 airfoil across a range of low Reynolds numbers, emphasizing unique behaviors observed in this regime. The study specifically aimed to acquire experimental data at a Reynolds number of 30,000, where lift behavior significantly deviates from that at higher Reynolds numbers. This research contributes to filling the scientific gap of limited experimental data at low Reynolds numbers. This data is crucial for calibrating and validating CFD models needed for the VAWT simulations because of typical chord-based Reynolds numbers common for laboratory-scale Vertical-Axis Wind Turbines.

The methodology employed aerodynamic measurements at a low-turbulence wind tunnel at the Technical University of Denmark (DTU). The authors utilized the wall pressure taps technique, a pressure rake, and a force gauge to assess aerodynamic loads. Two rectangular foils, one made of aluminum and the other 3D printed using PLA, were tested. Aerodynamic measurements were taken at Reynolds numbers ranging from 30,000 to 160,000 and angles of attack from −190 to 20 degrees (Figure 2.9). Two independent techniques were used to measure lift force, and the drag coefficient was determined based on wake velocity measurements. The experimental results were compared with XFOIL and 2-D URANS CFD simulations.

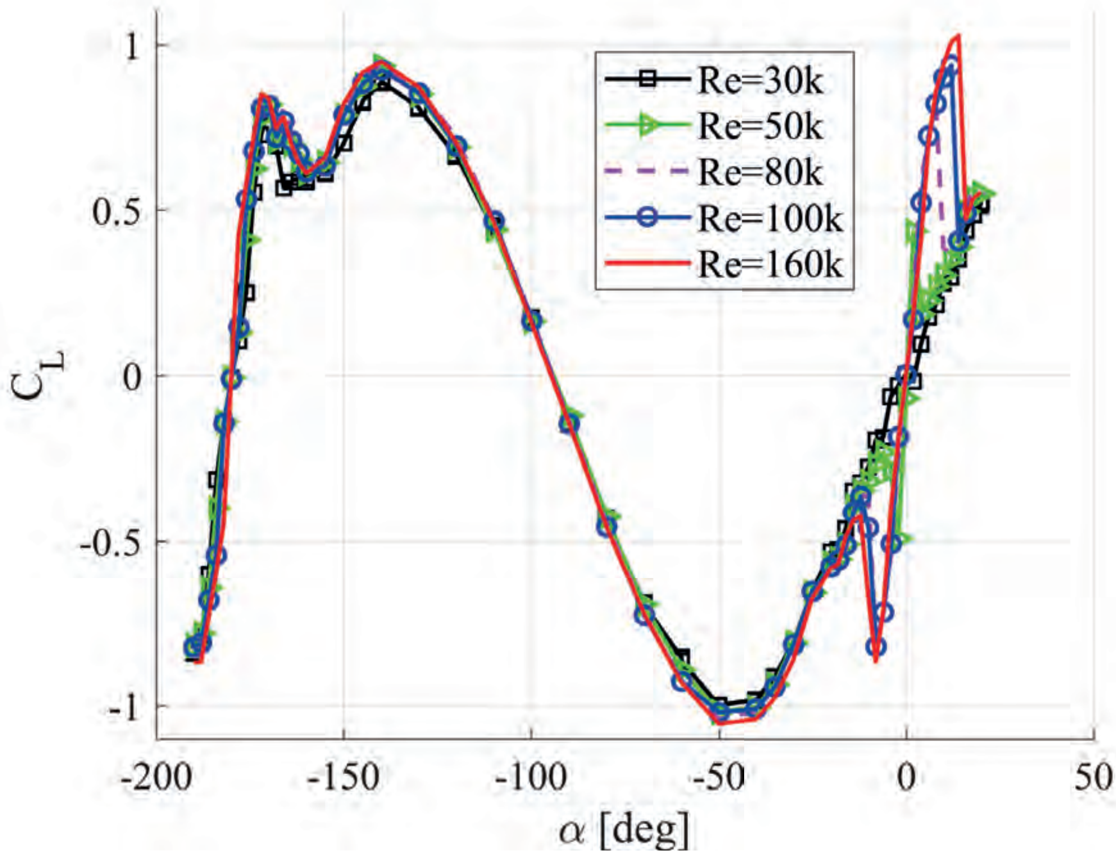

Figure 2.9: The lift coefficient C_L as a function of angle of attack α ($-190°$–$20°$) for different Reynolds numbers shows the crucial impact of Re on the airfoil's aerodynamic characteristic. Source: Figure 6 (Rogowski, Mikkelsen, et al., 2025)

At first, the comparison of the two measurement techniques (pressure taps and force gauge) was made. For the lift force at $Re = 100{,}000$, it shows strong agreement across most of the tested angle of attack range, despite some discrepancies in specific regions, confirming the reliability of both methods under varying conditions.

The study's outcomes demonstrated a strong dependence of aerodynamic characteristics on the Reynolds number. The results for the angle of attack in the ($-20°$–$20°$)

range show linear behaviour of the lift coefficient for Reynolds numbers above 50,000 (Figure 2.10).

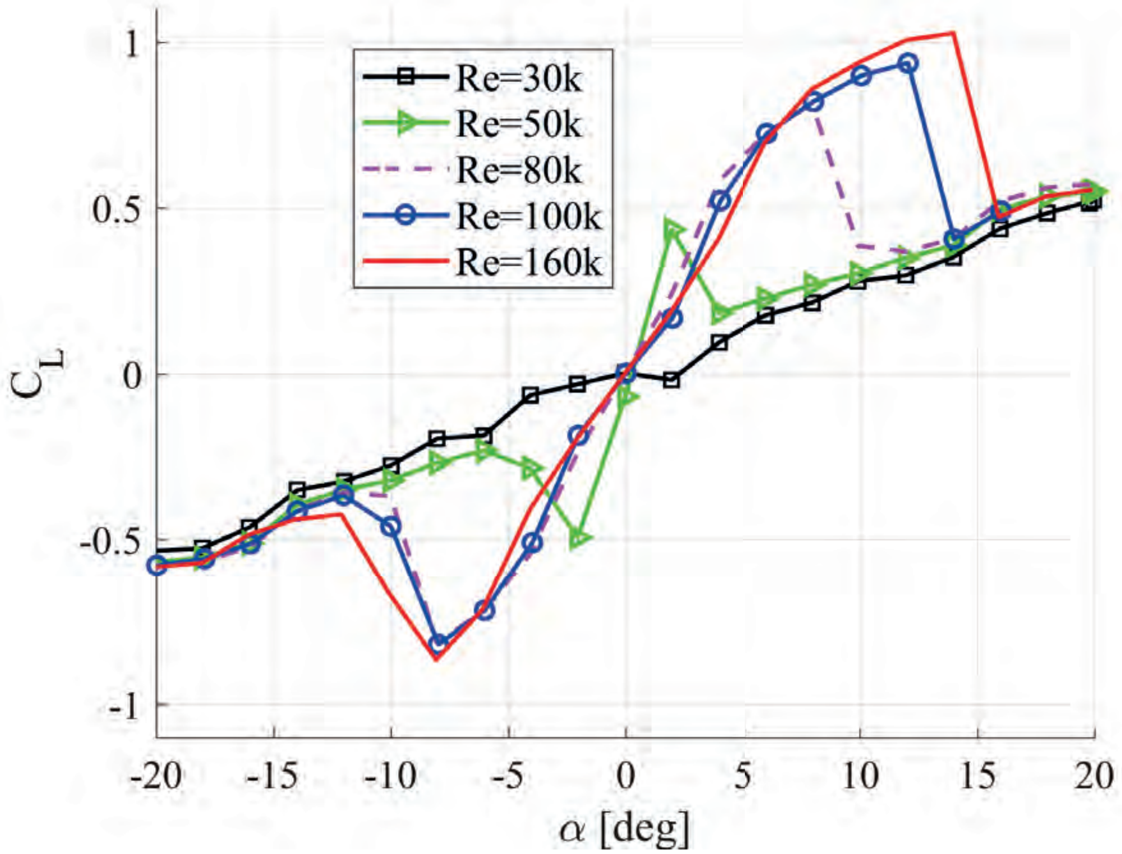

Figure 2.10: The lift coefficient as a function of angle of attack ($-20°$–$20°$) for different Reynolds numbers. Source: Figure 7 (Rogowski, Mikkelsen, et al., 2025)

The formation of laminar separation bubbles leads to considerable nonlinearities in lift force behaviour, with a significant loss of lift – around 58.4 % at $Re = 100{,}000$ – occurring after surpassing the critical angle of attack.

The critical angle for each Re can be distinguished from the plot, and it shows that this angle increases with the Reynolds number. The lift coefficient exhibited different behavior at the lowest Reynolds number tested (30,000) compared to higher Reynolds numbers. The lift coefficient is non-linear and can have non-zero values at zero angle of attack. For a tiny positive angle of attack, the negative values were measured.

The study also highlighted challenges in measuring around the zero angle of attack due to aerodynamic noise and vortex shedding. While passing through this region, noticeable aerodynamic noise was observed, resulting from the shedding of vortex structures from both the suction and pressure sides.

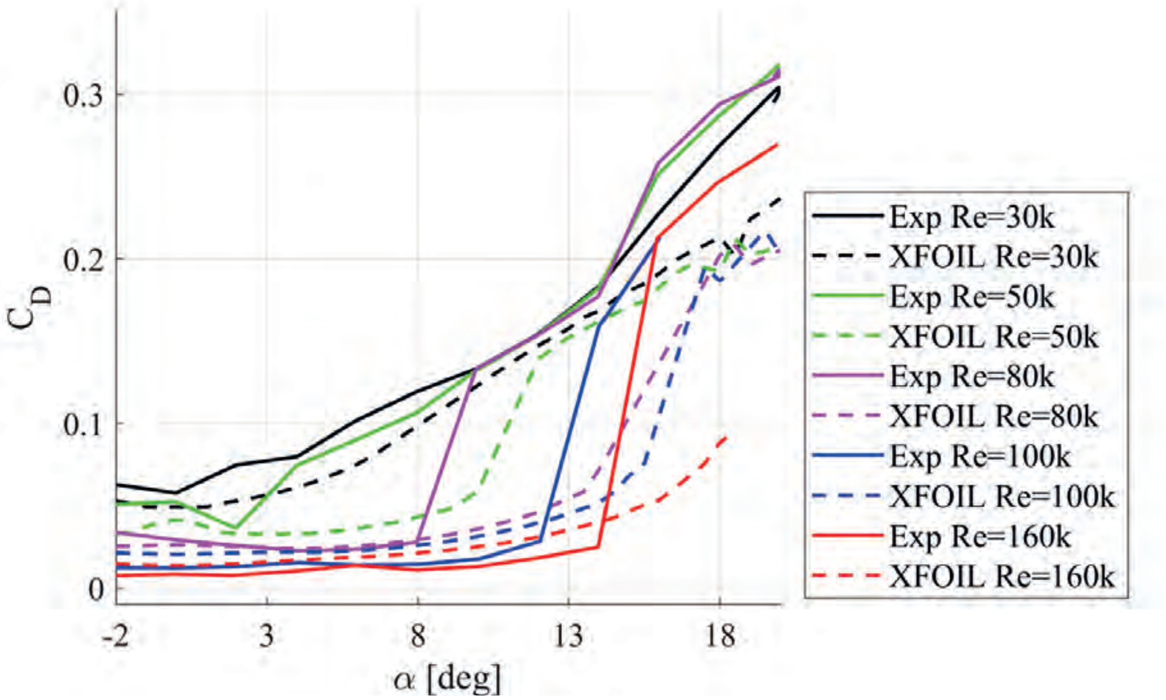

Figure 2.11: Drag coefficient as a function of the angle of attack. Comparison of experimental results with XFOIL. Source: Figure 14 (Rogowski, Mikkelsen, et al., 2025)

The drag coefficient at a zero angle of attack decreased significantly (over 700 percent) when the Reynolds number increased from 30,000 to 160,000. The experimental results confirm XFOIL calculations (Figure 2.11). This shows how drag values are influenced by the Reynolds number, especially for the lowest examined Re values.

The experimental results were consistent with both XFOIL and 2-D CFD simulations, although the numerical models had limitations in accurately predicting the maximum lift coefficient and stall angle value (Figure 2.12). While XFOIL tends to overestimate the maximum lift coefficient, it accurately captures the overall trends, including the linear lift behaviour at the lowest Reynolds number and the significant drag increase at higher Reynolds numbers. These findings validate the reliability of XFOIL as a predictive tool for aerodynamic analysis within the tested parameter range.

The 2-D CFD approach, utilizing the Transition SST model, provides a more accurate prediction of drag increase compared to XFOIL but tends to underestimate lift values.

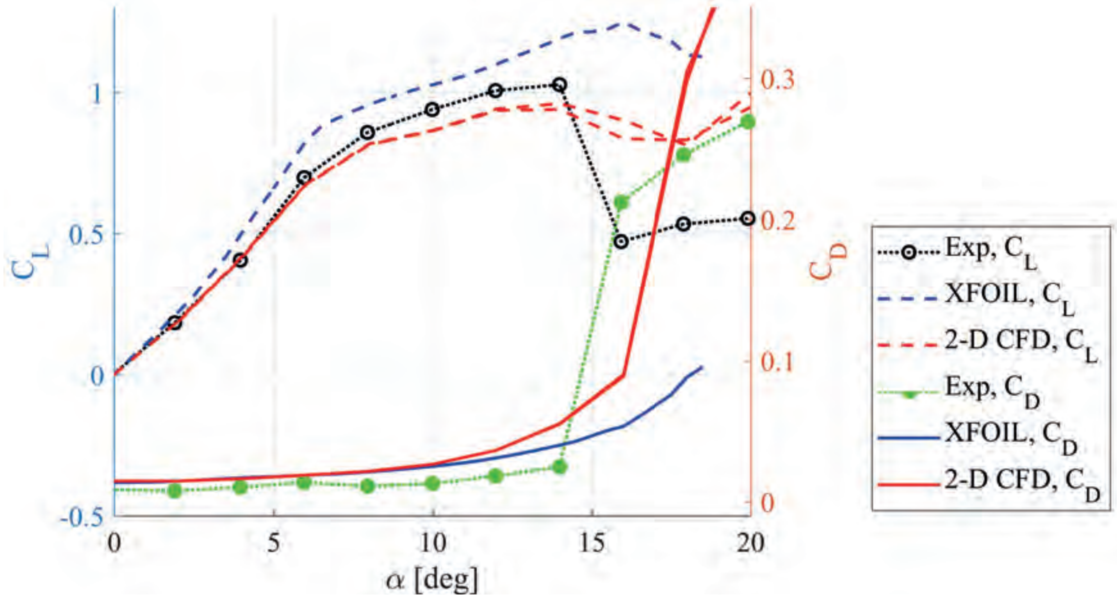

Figure 2.12: Comparison of airfoil characteristics at $Re = 160{,}000$ obtained from experiments and 2-D CFD using the Transition SST model. Source: Figure 15 (Rogowski, Mikkelsen, et al., 2025)

The effect of this paper is data needed for the validation of CFD techniques and gives an understanding of NACA 0018 behaviour at the low Reynolds regime. The paper's findings emphasize the importance of considering Reynolds number effects when designing airfoils for low-speed applications and provide a foundation for future research on surface contamination and three-dimensional flow effects.

Airfoils from the four-digit NACA series are quite often used for wind turbines at a laboratory scale, where the chord-based Reynolds number reaches values in the range of 20,000–30,000 However, these airfoils perform poorly under such flow conditions, which can be observed for the lift coefficient results — e.g., very low C_{Lmax} values (Figure 2.10) and high C_D values (Figure 2.11).

3 Vertical-Axis Wind Turbine modeling

3.1 Harmonic pitching airfoil model

Michna et al. (2025)

Title: "The Harmonic Pitching NACA 0018 Airfoil in Low Reynolds Number Flow"

Authors: Jan Michna, Maciej Śledziewski, Krzysztof Rogowski

Journal: Energies **Date:** May 2025 **MNiSW Points:** 140 pts

Contribution: conceptualization, methodology, software, validation, formal analysis, writing - review and editing, visualization, supervision

New Testable Predictions:

- **XIII** Influence of laminar separation bubbles on aerodynamic hysteresis and oscillations
- **XV** Limitations of the $k-\omega$ SST turbulence model in capturing laminar flow effects

Research Gaps:

- **A** Low Reynolds number range aerodynamic performance.
- **C** The VAWT modeling needs more accurate methods to be developed.
- **D** The boundary layer phenomena's impact on VAWT performance.

The harmonic pitching airfoil model was employed to address the critical area of aerodynamic performance for airfoils operating under low Reynolds number conditions, a regime particularly relevant to modern aerial (e.g., MAVs) and wind energy systems (e.g., VAWTs). The research aims to bridge existing knowledge gaps and provide deeper insights into complex flow phenomena (Michna et al., 2025).

Even with the use of 2-D models, numerical simulations of the vertical-axis wind turbines still have a high computational cost. As a consequence, many simplified methods have been developed, like Actuator Line, Cylinder, or Blade Element methods. These approaches demand high-quality airfoil characteristics as an input. What is crucial, even static characteristics are sensitive to varying Reynolds number and turbulence intensity (Michna & Rogowski, 2022). Moreover, static results are not enough.

An understanding of dynamic airfoil behavior is necessary to simulate the VAWTs accurately. This work employed 2-D CFD URANS modeling to simulate an airfoil with pitching motion to investigate aerodynamic force hysteresis. These results can be a foundation to improve dynamic models used in the numerical methods mentioned above.

The primary objective of this research is to enhance the understanding of the aerodynamic performance of thick airfoils, specifically the NACA 0018, when subjected to harmonic pitching motions under low Reynolds number conditions. This particular airfoil and motion type are relevant to applications like H-Darrieus VAWTs.

By comparing numerical predictions with experimental data, the research seeks to unravel the intricate dynamics of hysteresis loops, the formation and behavior of laminar separation bubbles, and various turbulence effects that significantly influence aerodynamic forces.

All numerical simulations were conducted using the Unsteady Reynolds-Averaged Navier-Stokes (URANS) approach. This method is necessary due to the high temporal variability of physical phenomena within the boundary layer near the airfoil surface, even for steady (no pitch) cases. To achieve the paper's objectives, the study employs two different turbulence modeling techniques, the $\gamma - Re_\theta$ transition model and the $k - \omega$ SST model.

The computational domain with a hybrid mesh was prepared based on the working section of the Red Wind Tunnel at TU Delft (details in Rogowski, Mikkelsen, et al., 2025). The sliding mesh working section technique with a circular subdomain around the airfoil was used to simulate pitching motion.

Three different motion frequencies were investigated: 1 Hz, 2 Hz, and 13.3 Hz. The choice of the last frequency value was motivated by the rotational speed characteristics of Darrieus vertical-axis wind turbines (Tescione et al., 2014).

The Figure 3.1 presents the time histories for the lift and drag coefficients from $\gamma - Re_\theta$ model used with a 1 Hz frequency motion case. For an amplitude of $A = 4^\circ$, the drag coefficient corresponding to a Reynolds number of $Re = 80{,}000$ was found to be approximately 67 % greater than that observed at $Re = 160{,}000$. Conversely, for $A = 8^\circ$, the drag coefficient was approximately 51 % higher in the same comparative analysis.

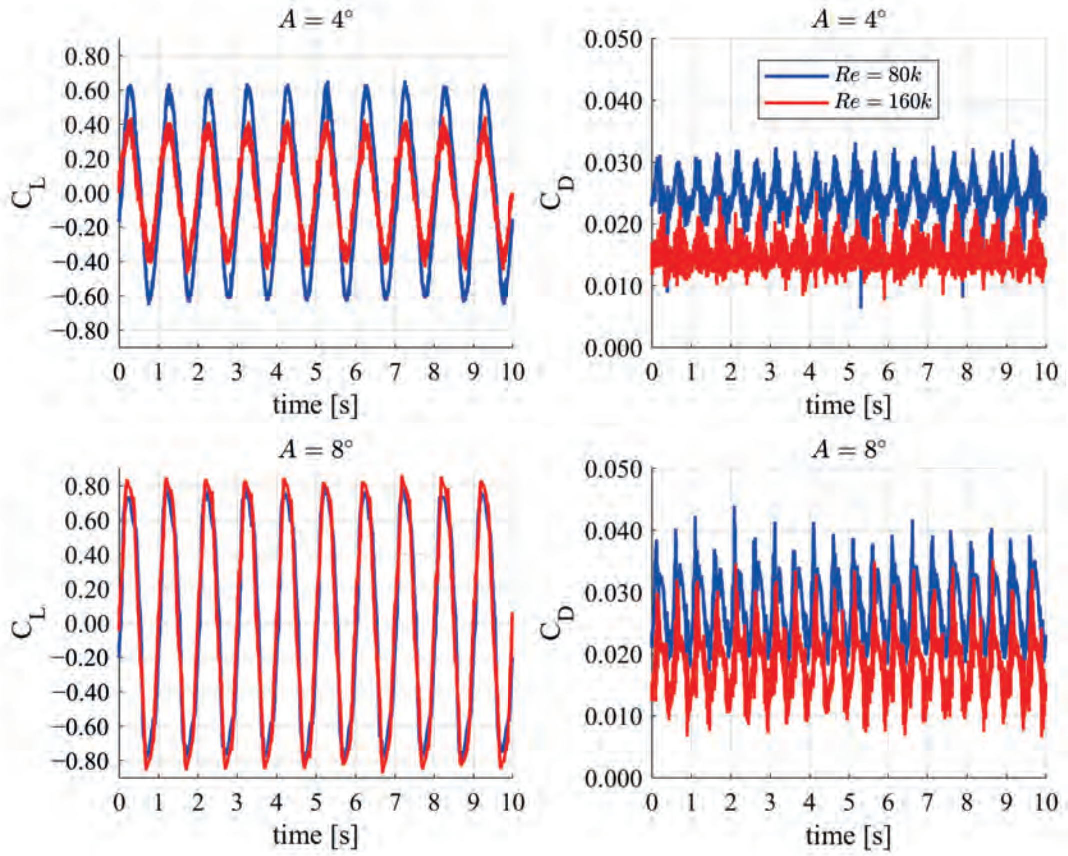

Figure 3.1: Time histories of the lift coefficient (C_L) and drag coefficient (C_D) for pitching amplitudes $A = 4°$ and $A = 8°$ at Reynolds numbers $Re = 80{,}000$ and $Re = 160{,}000$ — $\gamma - Re_\theta$ model used with 1 Hz frequency motion. The top row corresponds to $A = 4°$, while the bottom row corresponds to $A = 8°$. Source: Figure 7 (Michna et al., 2025)

Our findings further indicated that the peak values of the lift coefficient for the amplitude $A = 4°$ were greater at reduced Reynolds numbers. This apparent discrepancy in lift coefficient trends between $A = 4°$ and $A = 8°$ can be elucidated by the nonlinear dynamics associated with the laminar-to-turbulent transition and their heightened sensitivity to variations in the Reynolds number.

At diminished amplitudes ($A = 4°$), the airfoil predominantly functions within a regime characterized by a delayed transition location, particularly at lower Reynolds numbers, resulting in a more pronounced laminar flow and an elevated lift coefficient. Conversely, at increased amplitudes ($A = 8°$), the pitching motion transitions into a more turbulent regime marked by intensified flow separation. In this scenario, a higher Reynolds number ($Re = 160{,}000$) facilitates an earlier transition and subsequent reattachment, ultimately leading to an increased maximum lift coefficient.

Further analysis indicates a markedly reduced effect of the Reynolds number on aerodynamic efficiency, particularly for the lesser amplitude of 4 degrees (Figure 3.2). This suggests that the increased drag linked to the lower Reynolds number counterbalances the prospective advantages of higher lift coefficient values. For the larger amplitude being examined, a higher Reynolds number yields enhanced values of the C_L/C_D ratio, especially at increased angles of attack.

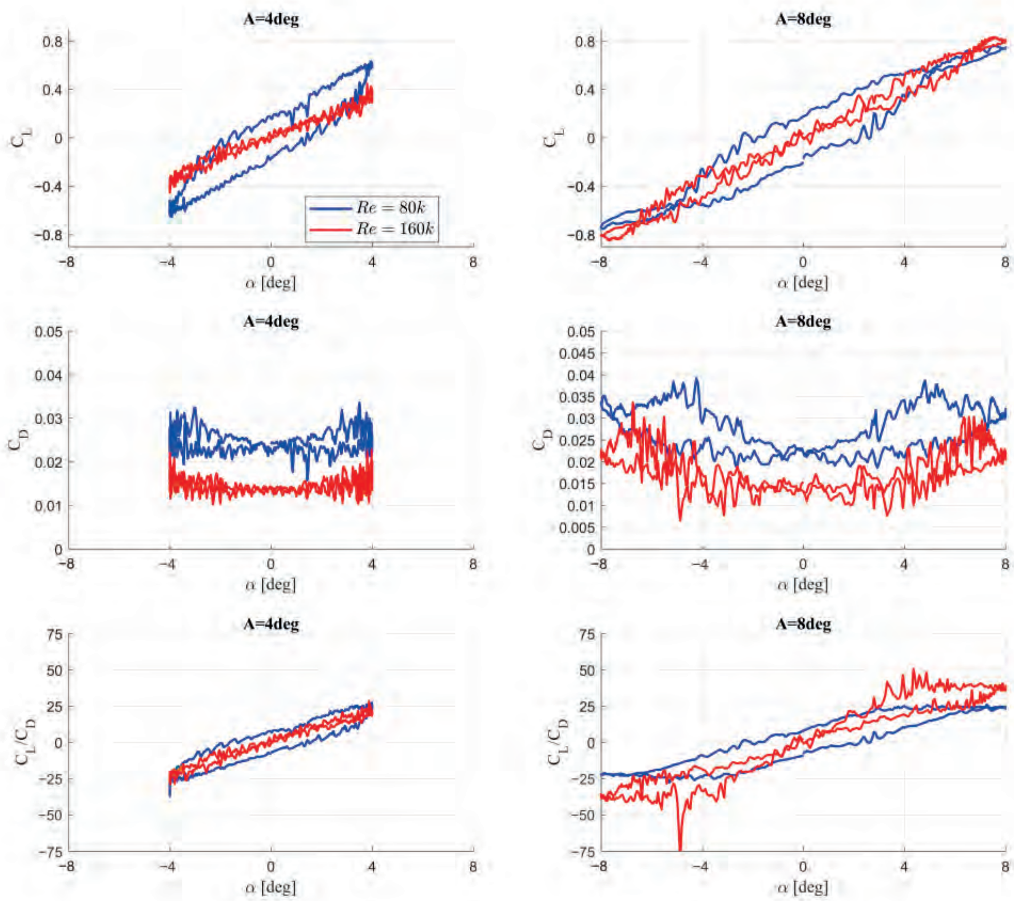

Figure 3.2: Hysteresis loops of the lift coefficient (C_L), drag coefficient (C_D), and lift-to-drag ratio (C_L/C_D) as a function of the angle of attack (α) for pitching amplitudes $A = 4^\circ$ and $A = 8^\circ$ at Reynolds numbers $Re = 80{,}000$ and $Re = 160{,}000$ — $\gamma - Re_\theta$ model used with 1 Hz frequency motion. The left column corresponds to $A = 4^\circ$, and the right column corresponds to $A = 8^\circ$. Source: Figure 8 (Michna et al., 2025)

In juxtaposition to the $\gamma - Re_\theta$ model, the $k - \omega$ SST turbulence model demonstrated that the maximum lift coefficient values computed for case $A = 4^\circ$ and $Re = 160{,}000$ were marginally elevated compared to those for $Re = 80{,}000$. No irregularities are visible in the airfoil characteristics in the case of the $k - \omega$ SST turbulence model.

This $k - \omega$ SST results also elucidate an unexpected outcome noted in Section 3.4, where both models forecasted comparable rotor loads despite fundamentally differing methodologies in addressing the transition. The current simplified model accentuates the inherent differences more distinctly.

Also, it is essential to note that the time histories of the aerodynamic force coefficients show qualitatively similar results for 1 Hz and 2 Hz pitching motion.

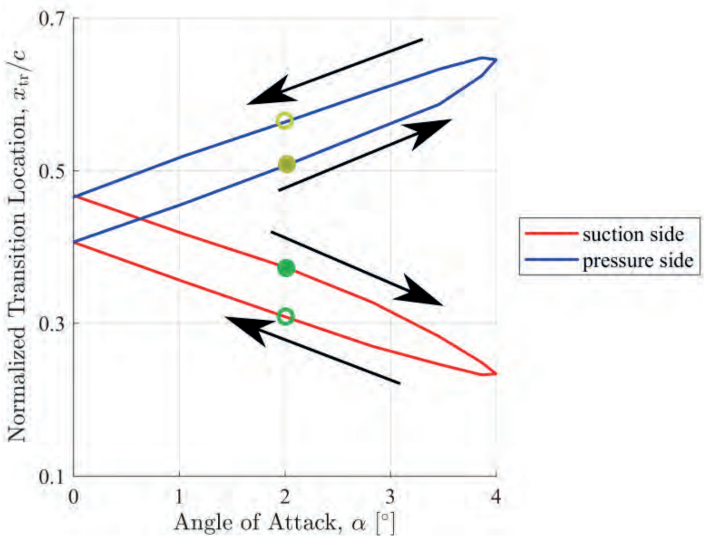

Figure 3.3: Normalized transition location during motion, x_{tr}/c. Source: Figure 16c (Michna et al., 2025)

Figure 3.3 illustrates the ”migration” of the transition point, x_{tr}/c, scaled by the airfoil chord c. Various colors signify the transition properties of both the suction and pressure sides of the airfoil. The illustration indicates that with an increase in pitch angle, the onset of separation is delayed on the suction side while occurring sooner on the pressure side of the airfoil.

The 13.3 Hz frequency oscillation, mirrored with typical VAWT motion, was modeled as part of research. As can be seen in the Figure 3.4, the results of the $k - \omega$ SST model match more accurately with the $\gamma - Re_\theta$ model for Reynolds number 160,000. It should be noted that the drag coefficient at higher Re is exceptionally consistent. Moreover, there is an absence of aerodynamic forces oscillations with the $\gamma - Re_\theta$ model for this frequency. This shows the reduced impact of laminar separation bubbles on the characteristics.

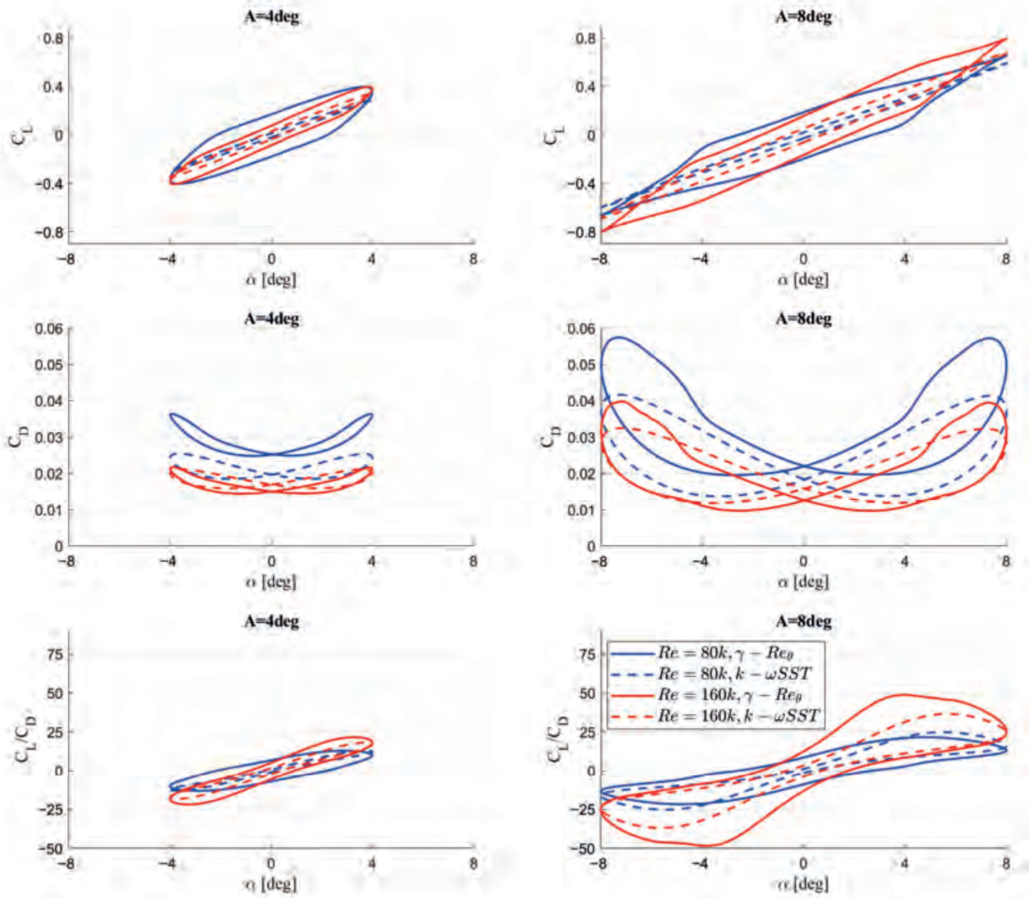

Figure 3.4: Hysteresis loops of the lift coefficient (C_L), drag coefficient (C_D), and lift-to-drag ratio (C_L/C_D) as a function of the angle of attack (α) for pitching amplitudes $A = 4^\circ$ and $A = 8^\circ$ at Reynolds numbers $Re = 80{,}000$ and $Re = 160{,}000$ — 13.3 Hz frequency motion. The left column corresponds to $A = 4^\circ$, and the right column corresponds to $A = 8^\circ$. Source: Figure 17 (Michna et al., 2025)

This investigation enhances understanding of airfoil aerodynamics at low Reynolds numbers, accounting for the complexities introduced by the distinct operational conditions of Micro Air Vehicles (MAVs) and Vertical-Axis Wind Turbines (VAWTs) through comprehensive computational assessments of harmonic pitching dynamics and intricate flow phenomena.

This research underscores that the four-equation $\gamma - Re_\theta$ turbulence model demonstrated markedly superior performance in forecasting the steady aerodynamic properties at elevated Reynolds numbers. Conversely, at lower Reynolds numbers, as the flow transitions to laminar conditions, the model encounters challenges in accurately portraying the lift coefficient curve, even at minimal angles of attack. Nevertheless, the outcomes derived from the Transition SST model exhibit greater physical fidelity compared to those produced by simpler turbulence modeling approaches.

Moreover, the results prove that laminar separation bubbles induce considerable hysteresis in the lift coefficient at low angles of attack, resulting in pronounced fluctuations in the aerodynamic forces.

These revelations elucidate the aerodynamic efficacy of thick airfoils at low Reynolds numbers and underscore the critical role of turbulence modeling in effectively capturing the intricacies of flow physics.

3.2 VAWT performance with fixed-pitched blades

Rogowski et al. (2024)

Title: "Numerical Analysis of Aerodynamic Performance of a Fixed-Pitch Vertical Axis Wind Turbine Rotor"

Authors: Krzysztof Rogowski, **Jan Michna**, Carlos Simao Ferreira

Journal: *ASTRJ* **Date:** September 2024 **MNiSW Points:** 100 pts

Contribution: conceptualization, methodology, software, validation, numerical analysis, writing—review and editing, visualization

New Testable Predictions:

VIII Impact of pitch angle on wake deflection of VAWT

IX Thrust and lateral forces validation of VAWT

Research Gaps:

C The VAWT modeling needs more accurate methods to be developed.

H Bridge the gap between 2-D and 3-D modeling approaches.

The next stage of the thesis was to assess the accuracy of CFD methods in predicting aerodynamic loads and investigate the aerodynamic wake characteristics of a laboratory-scale vertical-axis wind turbine (VAWT) rotor (Rogowski et al., 2024). This was achieved using a simplified two-dimensional numerical rotor model and an advanced numerical approach – the Scale Adaptive Simulation (SAS) coupled with the four-equation $\gamma - Re_\theta$ turbulence model. The study also focused on the challenge posed by the rotor's operating conditions, blade pitch angles, and very small geometric dimensions. The rotor, with a diameter of 0.3 m, operates at a low tip speed ratio of 2.5 and a very low chord-based Reynolds number of approximately 22,000. Performance settings and rotor geometry are based on an already experimentally tested vertical-axis wind turbine at Delft University of Technology (DUT). The main takeaway was to examine the turbine performance with different pitch angles (β): -10, 0, and 10 degrees. These operating conditions make typical turbine performance at low Reynolds numbers and very large angles of attack.

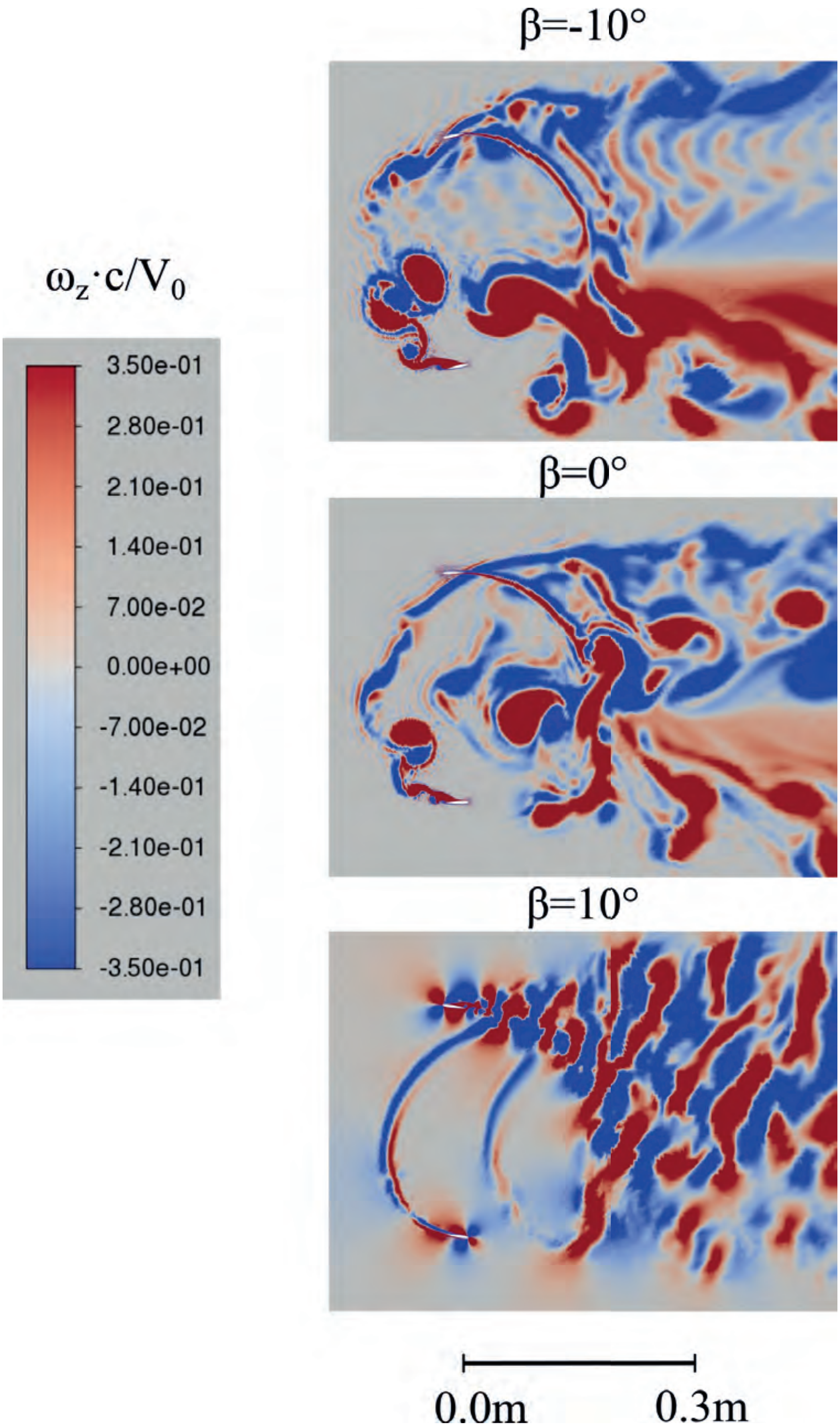

Figure 3.5: Countours of normalized z-vorticity in the rotor area at three pitch angles. Source: Figure 7 (Rogowski et al., 2024)

The methodology involved a two-dimensional URANS approach using the 4-equation $\gamma - Re_\theta$ model, also known as the Transition SST turbulence model in ANSYS Fluent. The Scale Adaptive Simulation (SAS) approach was utilized to represent the velocity field more accurately in the rotor region and the rotor aerodynamic wake. The two-bladed wind turbine rotor was surrounded by a rectangular domain, and the sliding mesh technique was employed to simulate the rotor's movement. The computational model was validated against high-fidelity measurements obtained using the PIV technique at DUT. Also, lateral and longitudinal forces were measured during the PIV experiment. These results were also included in the validation process. The accuracy of the 2-D URANS method used was compared with the Actuator Line Model with RANS technique (ALM).

The URANS results presented in the work are the average of 10 full rotations. It should be mentioned that the averaging window of 5 full rotations came out to be sufficient.

The study's outcomes showed that the rotor loads and velocity profiles are surprisingly reliable for $\beta = 0^\circ$ and $\beta = -10^\circ$. It was observed that the rotor aerodynamic loads gained numerically are slightly overestimated compared to the experimental values.

However, the 2-D model was found to be too imprecise to estimate both aerodynamic loads and velocity fields accurately, especially for the case of $\beta = 10^\circ$.

The observed flow in the rotor region (Figure 3.5) was highly complex because of the extreme operating conditions (low tip speed ratio, angles of attack far above the critical angle). The numerous vortices created on the blade's trailing edges due to dynamic detachment can be distinguished. The results demonstrate a similar flow character for $\beta = 0^\circ$ and $\beta = -10^\circ$, and a visible difference character for the $\beta = 10^\circ$ case.

Flow character and observed differences have a crucial impact on normal and tangential forces, as can be seen in Figure 3.6.

The result of velocity deficit profiles (Figure 3.7) shows that the ALM technique provides higher fidelity compared with URANS used in this work. This can be caused by the fact that ALM is a 3-D model.

The results of rotor loads and velocity profiles showed good reliability for cases with blade pitch angles of 0° and -10°. However, the work highlights the limitations of 2-D models and the need for advanced turbulence modeling techniques that can capture three-dimensional effects. This 2-D CFD approach fails in the case of the most heavily loaded rotor.

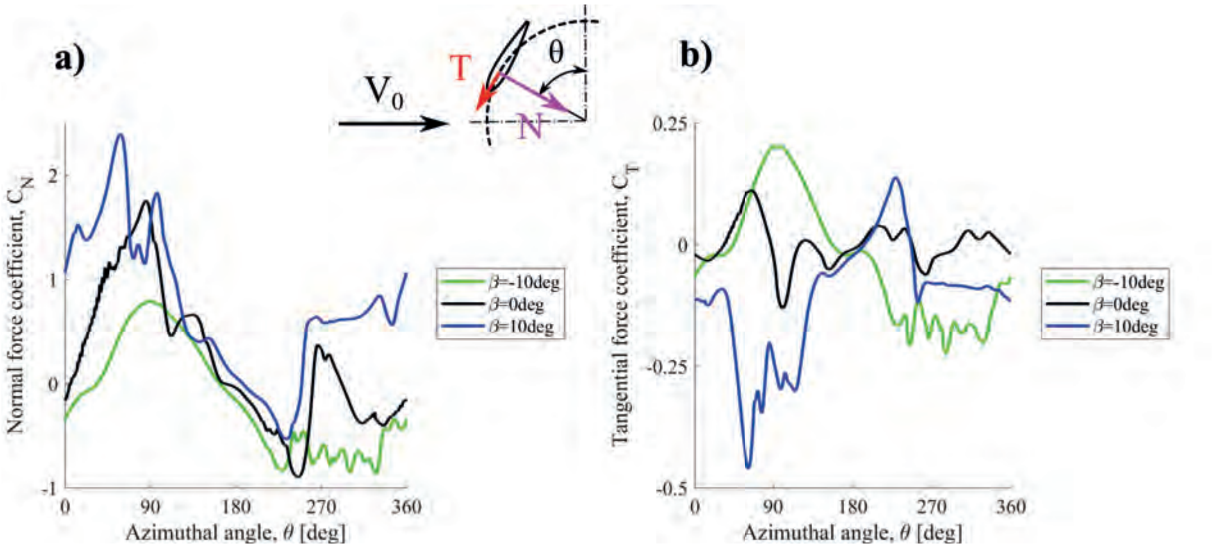

Figure 3.6: Aerodynamic blade load coefficients at three pitch angles: normal component (a) and tangential component (b). Source: Figure 5 (Rogowski et al., 2024)

Implementing a positive pitch angle leads to substantial blade performance amidst significant detachment occurrences, concurrently inducing considerable alterations in the rotor wake's flow patterns. This phenomenon holds potential for application in wind farm design utilizing such rotors, enabling passive manipulation of wake geometry.

The study underscores the importance of high-resolution experimental data for model validation, particularly at low Reynolds numbers. The findings suggest that accurately predicting the aerodynamic performance and wake characteristics of VAWTs requires a comprehensive approach that integrates experimental data with advanced CFD simulations. Further numerical and experimental research on the impact of the rotor aspect ratio on wake geometry, especially in cases with significant pitch angles, is undoubtedly needed.

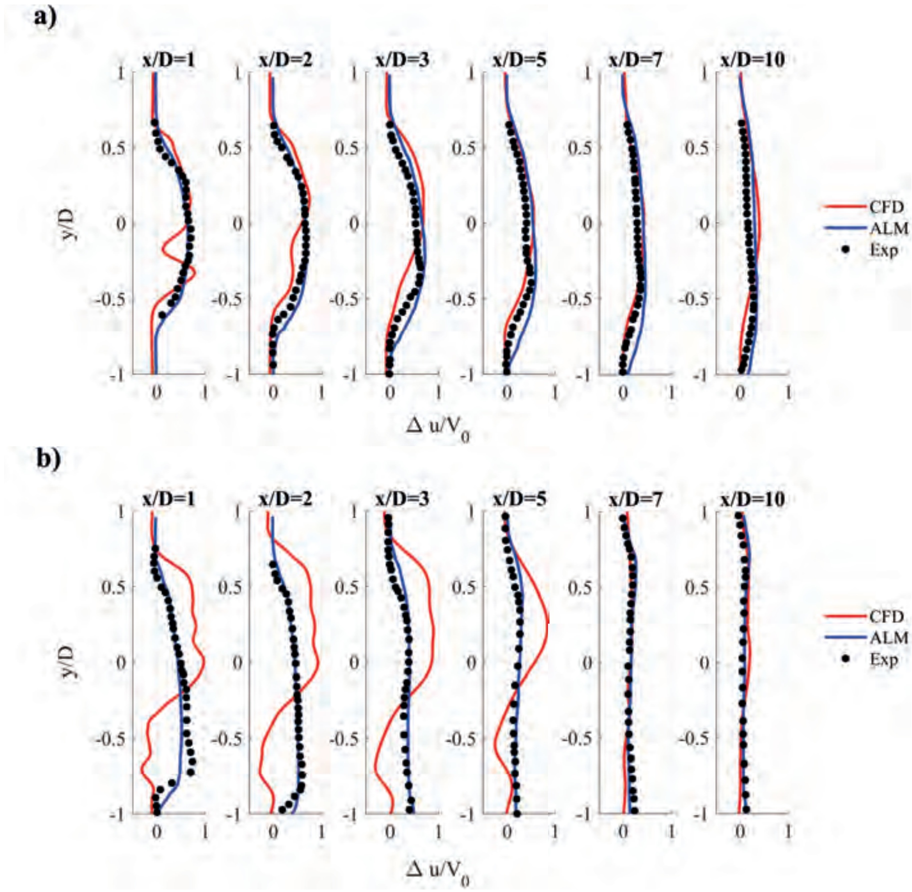

Figure 3.7: Velocity deficit profiles for (a) $\beta = 0°$, (b) $\beta = 10°$. Source: Figure 6 (Rogowski et al., 2024)

3.3 VAWT angle of attack estimation procedure

Michna and Rogowski (2024)

Title: "A Refined Approach for Angle of Attack Estimation and Dynamic Force Hysteresis in H-Type Darrieus Wind Turbines"

Authors: Jan Michna, Krzysztof Rogowski

Journal: Energies **Date:** December 2024 **MNiSW Points:** 140 pts

Contribution: conceptualization, methodology, software, validation, formal analysis, numerical analysis, investigation, writing-orginal draft, writing—review and editing, visualization

New Testable Predictions:

XII Dynamic and static lift coefficient slopes prediction

Research Gaps:

C The VAWT modeling needs more accurate methods to be developed.

F Angle of attack estimation methods should be developed.

The next study investigates the aerodynamic performance with angle of attack analysis and intricate flow dynamics characteristic of H-type Darrieus vertical-axis wind turbines, employing a comprehensive approach that combines numerical simulations with experimental validation (Michna & Rogowski, 2024).

A primary objective of this research was to meticulously analyze the impact of key operational parameters, such as rotor solidity and pitch angle, on the aerodynamic loads and flow characteristics of these turbines. A crucial aspect involved enhancing the accuracy of turbulence modeling, especially at low Reynolds numbers, to improve the overall performance and expand the applicability of VAWTs across diverse operational conditions. The issue that makes efforts hard is the complexity and the unsteadiness of the flow around VAWT.

A key focus of this work lies in refining methods for estimating the local angle of attack, a critical parameter essential for a profound understanding of the intricate flow phenomena associated with this turbine type. During rotation, the angle of attack often exceeds the static stall angle, which makes dynamic analysis demanding. Furthermore, the blades interact with vortices produced on the trailing edge in the rotor's wake, especially in the downwind section. In this case, the turbulence intensity varies in addition to the velocity vector.

The numerical calculations for this study are fundamentally based on previous experimental investigations by Tescione et al. (2014) and leverage the established vertical-axis wind turbine model developed at Delft University of Technology. Consistent with prior research, the methodology employs a 2-D Unsteady Reynolds-Averaged Navier-Stokes simulation, utilizing the Transition SST ($\gamma - Re_\theta$) model to accurately capture transient effects within the flow. To further enhance turbulence model performance, particularly in scenarios involving unstable flow separations, the scale-adaptive simulation approach was additionally applied.

The local angle of attack, a critical parameter for understanding flow phenomena, was determined using the improved LineAverage method described by Melani et al. (2020). In the case of this paper, the 200 points around the blade were set in a circular pattern with homogeneous spacing as shown in Figure 3.8b. In the next step, the mean of the velocity vectors read at these points was calculated (shown as yellow vectors in Figure 3.8a). Using basic vector calculations, taking into account blade motion, the relative velocity vector with an angle of attack was estimated.

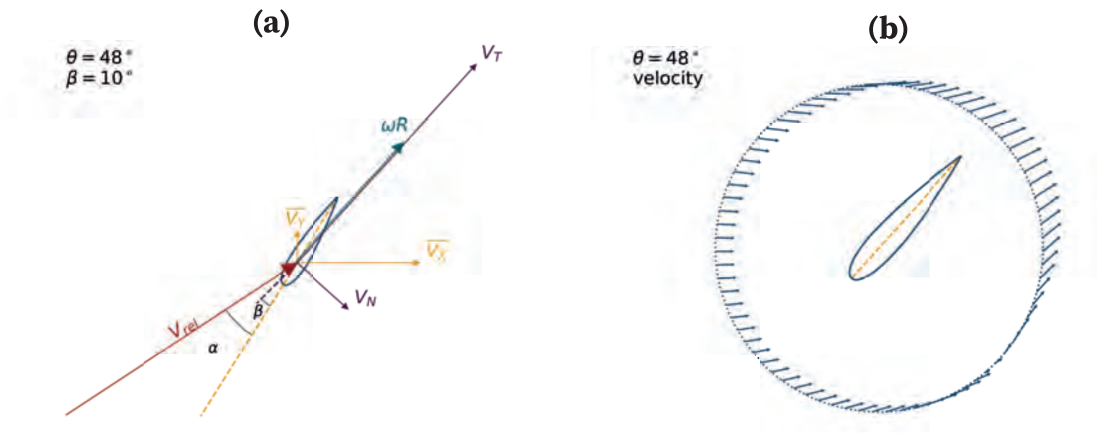

Figure 3.8: On the left (a), illustration of the angle of attack (α) and relative velocity (V_{rel}) for a blade in a vertical-axis wind turbine. The pitch angle ($\beta = 10°$) and the azimuthal position angle ($\theta = 48°$) are indicated. On the right (b), the velocity distribution around the airfoil at an azimuthal angle $\theta = 48°$ showing a circular sampling line. Source: Figure 9 & 10 (Michna & Rogowski, 2024)

Several rotor configurations were systematically analyzed to assess their influence on aerodynamic loads and flow characteristics. This included variations in the number of rotor blades (1, 2, 3, and 4) and the application of fixed pitch angles at -10°, 0°, and 10°. While this work does not specifically delve into the impact of the Reynolds number on turbine performance, it is noted that the Reynolds number, based on the blade chord length, was approximately 160,000.

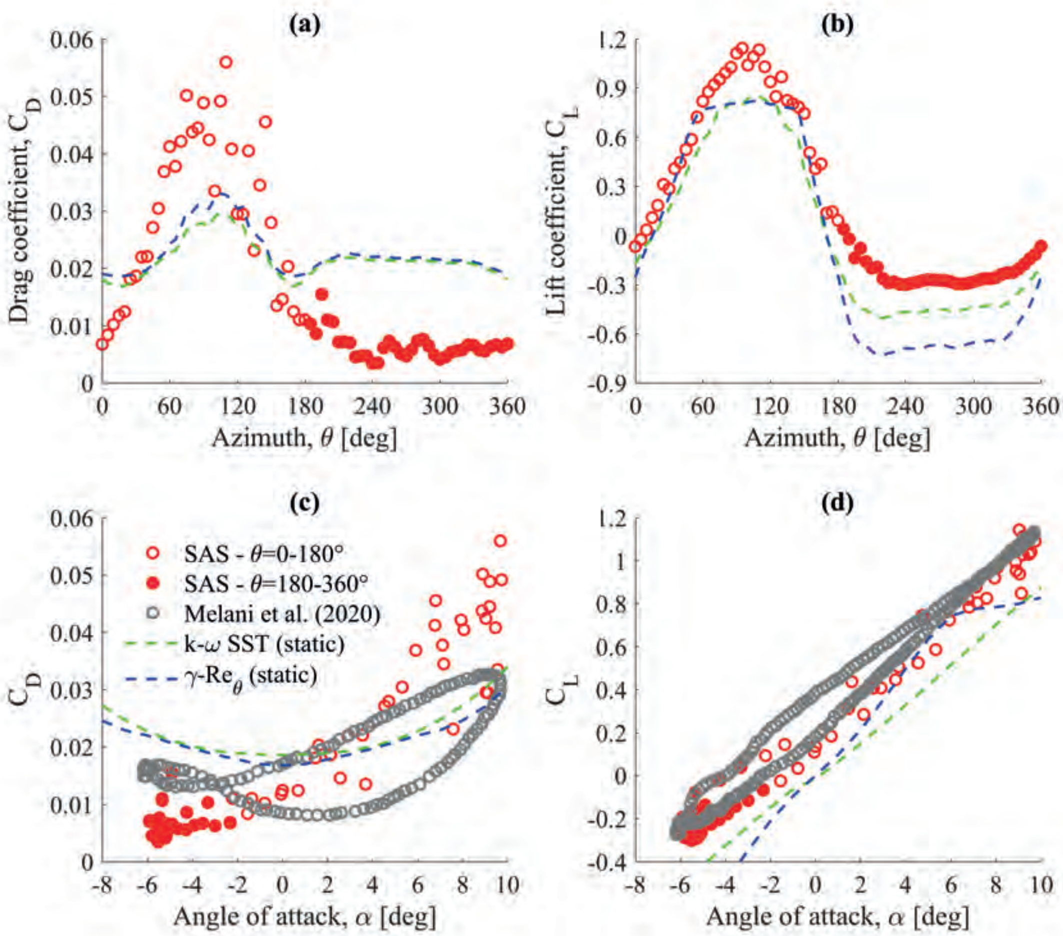

Figure 3.9: The upper subfigures illustrate the drag coefficient C_D (a) and lift coefficient C_L (b) as functions of the azimuthal angle θ. The lower subfigures depict the same coefficients—drag (c) and lift (d)—analyzed for varying angles of attack α. The presented data include SAS approach results, static results from Rogowski et al. (2021), and experimental reference data from Melani et al. (2020). Source: Figure 14 (Michna & Rogowski, 2024)

The study's findings reveal significant insights into the aerodynamic performance of H-type Darrieus VAWTs, particularly highlighting the strong correlations between rotor configuration and aerodynamic loads. A key observation was the close correspondence between the slope of the static and dynamic lift coefficient curves, despite the dynamic curve not passing through a zero angle of attack. This phenomenon is attributed to the ”virtual camber” effect, as previously noted by Bianchini et al. (2016), which influences the dynamic angle of attack.

Further analysis indicated that the choice of turbulence model significantly impacts the accuracy of aerodynamic calculations (see Figure 3.9). The $k - \omega$ SST model, used in the study by Melani et al. (2020), demonstrated superior performance in more turbulent regions of the flow, whereas the Transition SST model proved more suitable for areas with lower turbulence intensity, such as the upwind section of the rotor. Presenting both dynamic and static results provided valuable insight into how these different models affect calculations across various phases of the turbine's operational cycle.

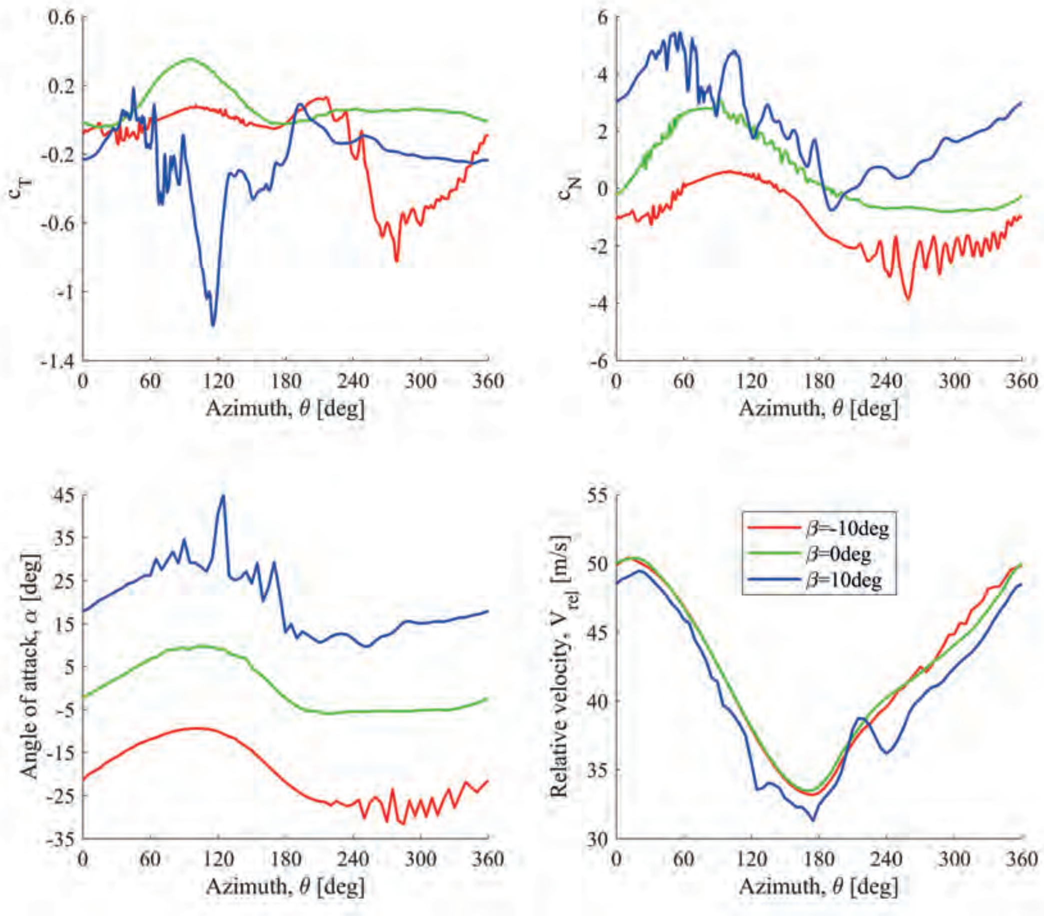

Figure 3.10: Effect of the pitch angle on the normal and tangential force coefficients, as well as on the local angle of attack and relative velocity, as a function of azimuth θ for a 2-bladed rotor configuration at a tip-speed ratio of 4.5. Source: Figure 17 (Michna & Rogowski, 2024)

The LineAverage method, employed for determining the angle of attack, was validated for its high accuracy and its capacity to account for circulation effects and flow distortions. This method showed strong correlations between rotor configuration and load variations, specifically underscoring the influence of the number of blades and the pitch angle on aerodynamic efficiency.

Fewer blades consistently led to higher aerodynamic loads, especially tangential loads in the downwind region. Single-bladed configurations, in particular, often exhibited minimal or even negative contributions to energy production. Similarly, adjustments to the pitch angle also had considerable effects on rotor performance. Large positive and negative pitch angles were found to significantly deteriorate the rotor's aerodynamic performance, primarily by increasing loads on the normal force component. Dynamic effects, including vortex formations, were observed to cause pronounced oscillations, particularly at a 10-degree pitch angle (Figure 3.10).

During the validation process, the velocity profiles within the rotor wake were compared against experimental measurements. While the computed velocities were slightly higher than experimental data, particularly on the "upwind" side of the rotor, the numerical results accurately captured the correct trend. Moreover, the aerodynamic loads derived from the simulations were successfully validated against experimental studies (Castelein et al., 2015).

The research illustrates that the Line Average method serves as a proficient strategy for the accurate determination of the local angle of attack, as it accounts for the influences of shed and trailing vorticity surrounding the airfoil. Investigation reveals that utilizing 200 sampling points provides a dependable resolution, effectively capturing critical flow characteristics while reducing sensitivity to variations in the azimuthal angle, particularly in areas susceptible to significant fluctuations. This methodology was corroborated across various rotor configurations, and the trends observed in the resultant values appear to maintain consistency and accuracy across different configurations, thereby reinforcing the reliability of this approach.

The findings underscore that the judicious selection of the turbulence model in the context of (U)RANS is vital for obtaining precise results, particularly within the low Reynolds number regime.

The significant contributions of this research include an in-depth analysis of both the angle of attack and dynamic aerodynamic loads, providing crucial insights into the complex physics of VAWT operation. These findings are instrumental in advancing engineering aerodynamic models for VAWTs, thereby enhancing their performance and broadening their applicability in diverse operational settings.

3.4 VAWT with zigzag tape performance

Rogowski, Michna, et al. (2025)

Title: "Impact of zigzag tape on blade loads and aerodynamic wake in a vertical axis wind turbine"

Authors: Krzysztof Rogowski, **Jan Michna**, Robert Flemming Mikkelsen, Carlos Simao Ferreira

Journal: *Energy* **Date:** March 2025 **MNiSW Points:** 200 pts

Contribution: writing – review and editing, writing – original draft, visualization, validation, software, methodology, formal analysis, data curation, conceptualization

New Testable Predictions:

- **I** Effect of zigzag tape on lift coefficient
- **II** Impact of zigzag tape on aerodynamic efficiency
- **III** Wake recovery distance prediction of VAWT
- **IV** Wake asymmetry prediction of VAWT

Research Gaps:

- **C** The VAWT modeling needs more accurate methods to be developed.
- **E** Effects of zigzag tape on VAWTs should be investigated.
- **H** Bridge the gap between 2-D and 3-D modeling approaches.

In the following thesis stage, the effects of zigzag tape on the aerodynamic performance and wake characteristics of the Delft Vertical-Axis Wind Turbine were investigated (Rogowski, Michna, et al., 2025). The primary goal is to understand how zigzag tape influences blade loads and the resulting aerodynamic wake, particularly focusing on aspects not previously addressed in relation to VAWTs, such as the impact of contaminated blades on wake morphology.

The study builds upon extensive experimental investigations conducted by Tescione et al. (2014), which involved Particle Image Velocimetry (PIV) in the investigation of a two-bladed H-shaped VAWT at Delft University of Technology (DUT).

The current study's VAWT model was based on the geometric framework of this turbine, simplifying it by excluding struts and support towers.

Zigzag tape is an effective method for influencing the behavior of the boundary layer in experimental aerodynamics. This study highlights its role in modifying the aerodynamic characteristics of an airfoil and reducing the influence of laminar separation bubbles. The research also identifies critical factors for understanding the relationship between airfoil aerodynamic properties and rotor wake dynamics.

The study emphasizes that zigzag tape significantly impacts the wake downstream of the rotor. This effect, which has not been previously explored for VAWTs, is crucial for assessing how surface contamination, such as that simulated by zigzag tape, affects wake behavior and overall VAWT performance and optimization.

The primary methodology employed in this investigation to assess the influence of zigzag tape on the aerodynamics of Vertical-Axis Wind Turbines (VAWTs) is the Actuator Line Model (ALM). This approach offers a substantial reduction in computational expenses when contrasted with Reynolds-Averaged Navier-Stokes (RANS) simulations that utilize three-dimensional blades. In this study, dynamic influences on lift and drag forces are incorporated via the Dynamic Stall Model (DSM), thereby ensuring accurate aerodynamic representation across varying operational scenarios. The ALM approach utilizes airfoil characteristics obtained from wind tunnel experiments at the Technical University of Denmark (DTU) and also data obtained from the literature Bianchini et al., 2015, Sheldahl and Klimas, 1981).

To further substantiate these findings and gain insights into the effects of transitional phenomena, such as laminar separation bubbles, a two-dimensional URANS analysis was conducted. This 2-D CFD analysis utilized the $k - \omega$ SST and $\gamma - Re_\theta$ turbulence models, specifically to assess the impact of transition phenomena on rotor performance.

Figure 3.11 illustrates the experimental lift coefficient (C_L) and drag coefficient (C_D) variation with the angle of attack (α) for the NACA 0018 airfoil equipped with zigzag tape. The measurements were conducted at a Reynolds number of 1.6×10^5. The lift coefficient is shown to grow almost linearly for angles of attack up to a critical angle. A significant hysteresis loop is evident in the lift coefficient, particularly during the "downward" measurement.

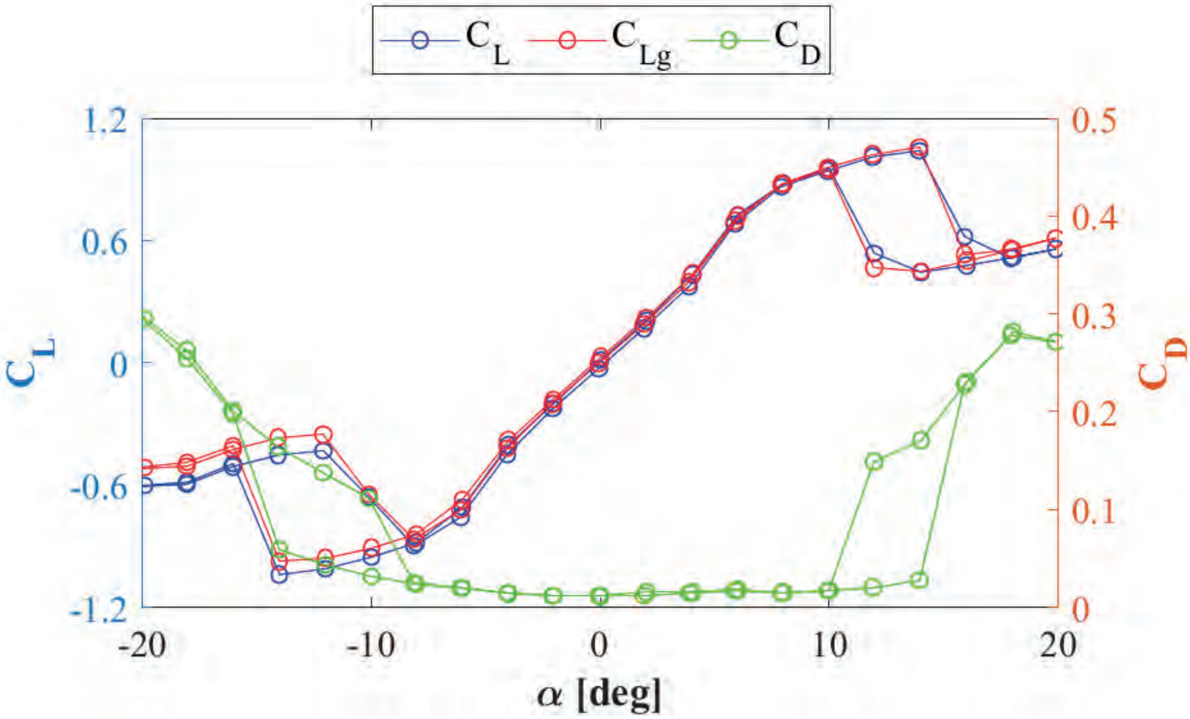

Figure 3.11: Experimental Lift Coefficient (C_L) using wall pressure taps and a force gauge (C_{Lg}) as well as Drag Coefficient (C_D) variation with Angle of Attack (α) for zigzag configuration. Source: Figure 3 (Rogowski, Michna, et al., 2025)

Figure 3.12 provides a comparative analysis of the aerodynamic performance of the NACA 0018 airfoil in both clean and zigzag tape configurations. The zigzag tape linearizes the C_L characteristics, resulting in very similar $\mathrm{d}C_L/\mathrm{d}\alpha$ derivatives for both Reynolds numbers. However, the presence of the tape significantly increases the minimum drag by approximately 73.4 %.

While the hysteresis loops for both clean and zigzag configurations remain quite similar in terms of value and shape, the nonlinearity of the $C_L(\alpha)$ curve in the clean airfoil (due to laminar bubbles) leads to a significant improvement in aerodynamic efficiency. The results also show that the Reynolds number plays a critical role, particularly in the clean airfoil's performance and its sensitivity to flow separation.

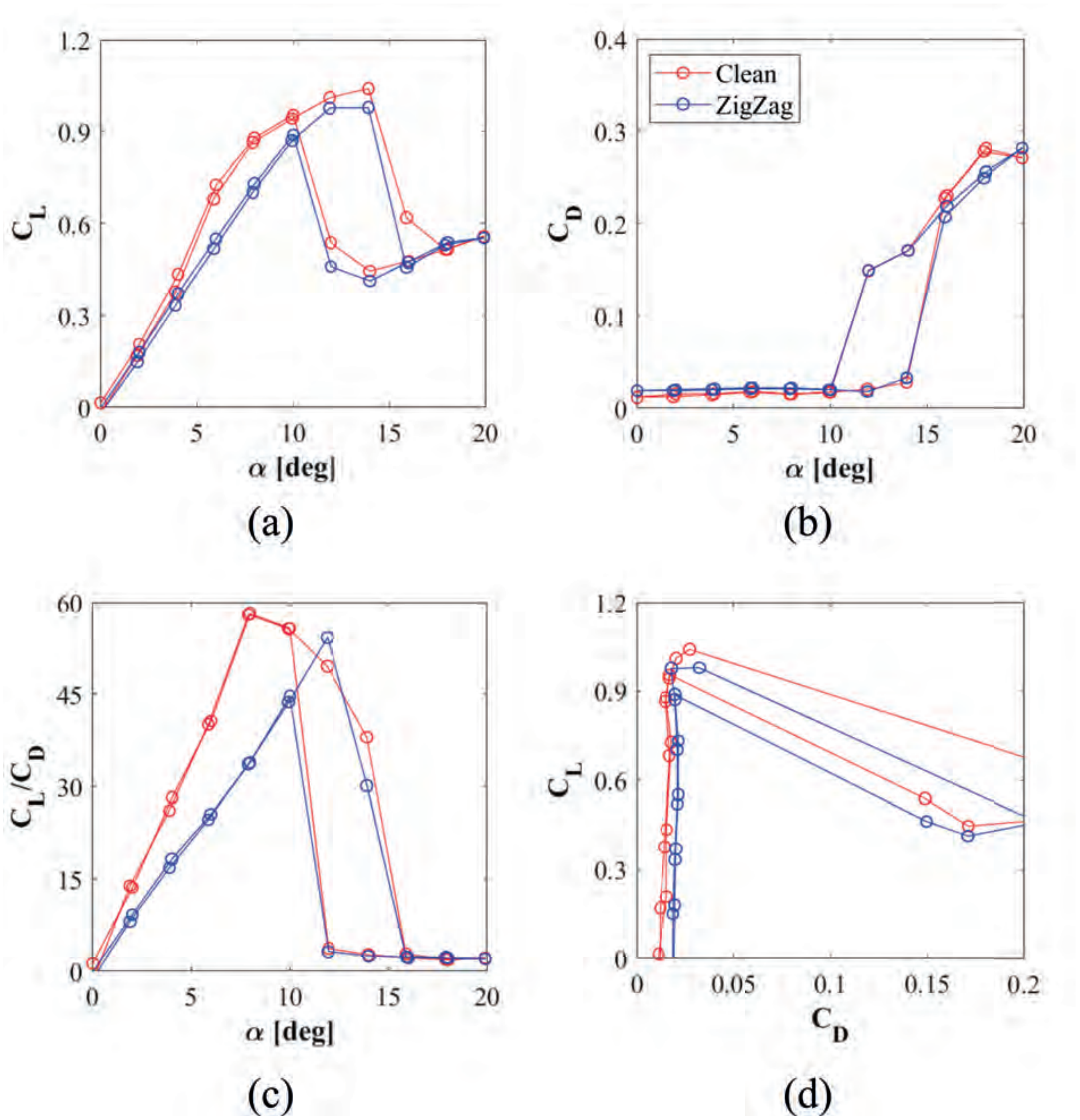

Figure 3.12: Comparison of aerodynamic performance for the NACA 0018 airfoil: (a) lift coefficient C_L vs. angle of attack α, (b) drag coefficient C_D, (c) lift-to-drag ratio C_L/C_D, and (d) C_L vs. C_D. Results are shown for both clean (Rogowski, Mikkelsen, et al., 2025) and zigzag tape configurations. Source: Figure 4 (Rogowski, Michna, et al., 2025)

Figure 3.13 illustrates the comparison of the tangential force characteristics for the TU Delft VAWT when using the ALM method with different airfoil polars and a 2-D CFD approach. This figure is crucial for understanding how various airfoil properties and simulation methods influence the tangential forces acting on the turbine blades. The results highlight the significant impact of zigzag tape on reducing tangential forces and the role of different turbulence models in capturing aerodynamic characteristics, particularly with the presence of laminar separation bubbles.

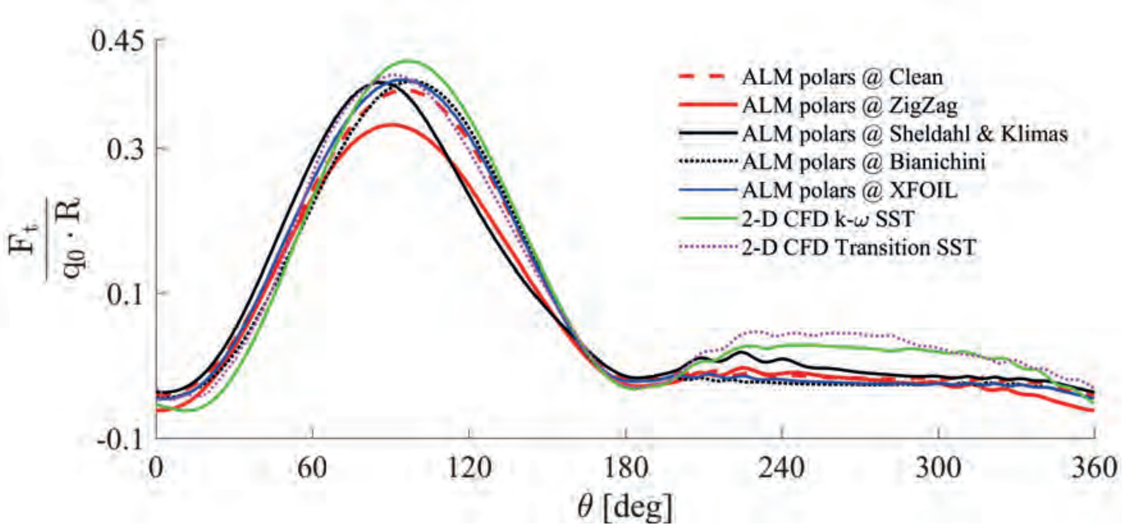

Figure 3.13: Comparison of the tangential force characteristics for the TU Delft VAWT using different airfoil polars and a 2-D CFD approach. Source: Figure 13 (Rogowski, Michna, et al., 2025)

It is important to acknowledge that the discrepancies in the two-dimensional computational fluid dynamics outcomes produced by the two turbulence models, namely the $k - \omega$ SST and the $\gamma - Re_\theta$, are relatively insignificant. This observation holds true despite the pronounced variations observed in the static $C_L(\alpha)$ and $C_D(\alpha)$ characteristics exhibited by both models, as documented in prior research (Michna & Rogowski, 2022).

Figures 3.14 and 3.15 present graphical illustrations of the velocity fields in the wake of the TU Delft VAWT, elucidating the effects of various airfoil configurations (clean versus zigzag tape) and simulation models on the characteristics of the wake.

The velocity data indicate an asymmetrical distribution of u_x profiles around $y/D = 0$ for the Sheldahl and Klimas (1981) polars and zigzag tape, in contrast to the clean profile, which can be attributed to the vortex structures induced by the profile with free transition.

The velocity field posterior to the clean airfoil exhibits greater disturbance due to the formation of laminar separation bubbles on the airfoil surfaces, which generate shed vortices that evolve within the wake. The presence of zigzag tape amplifies wake asymmetry, further accentuated by the lack of laminar bubbles. In the case of the clean profile, a broader and more symmetrical region of low velocity is discernible in comparison to the results obtained with the zigzag tape.

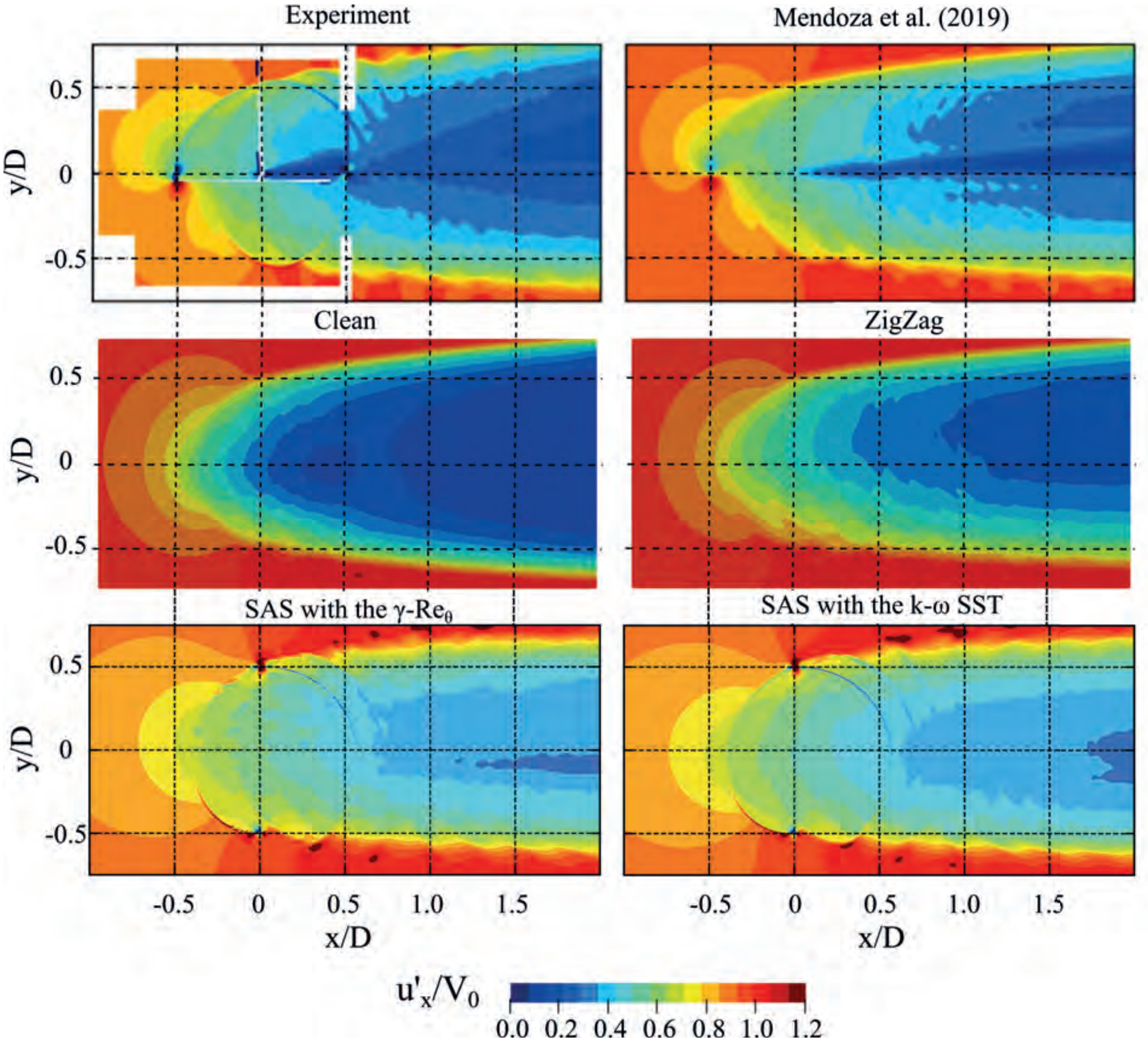

Figure 3.14: Contour plots of the normalized instantaneous u'_x/V_0 velocity component in the turbine wake for clean and zigzag tape configurations. The top row compares PIV measurements with the ALM model from Mendoza et al. (2019), the middle row shows velocity distributions for both configurations, and the bottom row presents 2-D CFD results. Source: Figure 17 (Rogowski, Michna, et al., 2025)

From this analysis, two salient features emerge: the aerodynamic wake is more extensive for the clean profile, and the recovery of the wake occurs later for the zigzag tape profile.

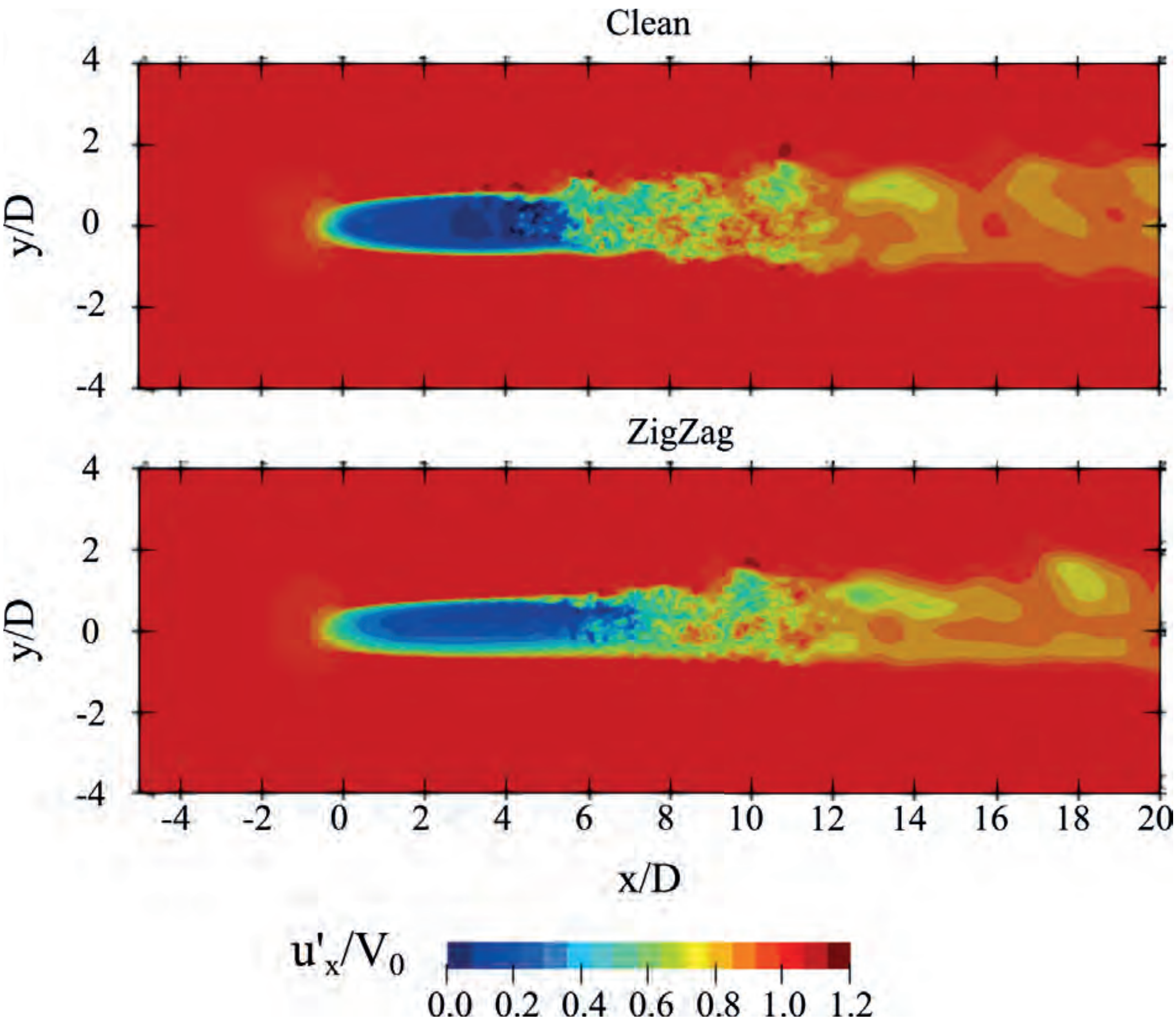

Figure 3.15: Contour plots of the normalized instantaneous u'_x/V_0 velocity component in the far wake downstream behind the rotor. Source: Figure 18 (Rogowski, Michna, et al., 2025)

The investigation closely examines the notable impact of zigzag tape on the loads experienced by VAWT blades and the associated aerodynamic wake, building upon prior experimental findings and underscoring the necessity of accounting for the effects of surface contamination in the design of wind turbines.

The observed aerodynamic properties of a rectangular wing featuring a NACA 0018 airfoil, devoid of any turbulators, exhibit pronounced nonlinearity in the $C_L(\alpha)$ response, attributable to the development of laminar bubbles on both the suction and pressure surfaces of the airfoil. This observation suggests that the chosen airfoil performs suboptimally under these flow conditions, particularly at low Reynolds numbers.

The implementation of zigzag tape, while effectively ”linearizing” the static lift coefficient response without diminishing the maximum lift, markedly reduces the aerodynamic loads on the rotor blades operating at a tip-speed ratio where one would anticipate elevated aerodynamic efficiency, exemplified by a high power coefficient. Additionally, it produces a significant alteration in the wake velocity field downstream of the rotor.

4 Conclusions and future work

The following general conclusions are composed below based on the formulated new testable predictions. The issues are grouped by related hypotheses. At the end, future research directions are proposed.

Hypothesis ① Missing zigzag tape effect understanding

The zigzag tape modifies airfoil characteristics by eliminating the laminar separation bubble, thereby changing the aerodynamic blade loads and wake geometry of a VAWT.

I [Section 3.4] The results of experiments Rogowski, Michna, et al. (2025) confirm that zigzag tape linearizes the lift coefficient characteristic by modifying the boundary layer. The lift coefficient at angles just below the stall angle is evidently higher for clean airfoil cases than for zigzag-taped cases.

II [Section 3.4] Zigzag tape, while linearizing the lift characteristic, generally impairs aerodynamic efficiency by increasing drag and reducing lift at subcritical angles of attack (Rogowski, Michna, et al., 2025). This impact can be quantified through experimental measurements of lift and drag coefficients using various tools.

III [Section 3.4] Zigzag tape leads to a delayed wake recovery for VAWTs. This characteristic can be effectively measured and analyzed by comparing normalized velocity profiles at increasing distances downstream from the turbine (Rogowski, Michna, et al., 2025).

IV [Section 3.4] The CFD and ALM results (Rogowski, Michna, et al., 2025) confirm the prediction that zigzag has a visible influence on the wake, and it can significantly deflect the wake, making the flow asymmetrical.

This dissertation investigates the zigzag impact, which has not yet been thoroughly researched. It brings a crucial understanding of the zigzag tapes' behavior in the laboratory-scale Vertical-Axis Wind Turbines case. The next steps should focus on the CFD model of the tape on the airfoil, with the tape's complete geometry implemented. Also, the pitching airfoil model with tape should be investigated in the experimental wind tunnel.

Hypothesis ② Reynolds number and turbulence intensity influence on laboratory-scaled VAWTs

In the low-Re regime, the Reynolds number has a substantial impact on the airfoil characteristics, thereby affecting the power coefficient of the VAWT. The influence of TI is visible but smaller than that of Re. This influence is not observable for the high and moderate Re.

V [Section 2.2] The results from Michna and Rogowski (2022) verify that the aerodynamic characteristic of the NACA 0018 airfoil in the low-Re regime depends on Reynolds number (mainly) and turbulence intensity (less). With increased turbulence intensity, the lift coefficient decreases in the 0-6 degrees region (below "transition angle"). Lower Re gives a higher increase in drag value with a rising angle of attack.

VI [Section 2.3] The lift and drag coefficients strongly depend on the Reynolds number in the low-Re regime. Moreover, the experimental studies Rogowski, Mikkelsen, et al. (2025) confirmed that the drag coefficient rises significantly with lowering Re number.

VII [Section 2.3] The experimental results from Rogowski, Mikkelsen, et al. (2025) shows that with Reynolds number growth, the C_L^{max} values rises. This phenomenon is stronger in the low Reynolds regime.

VIII [Section 3.2] The numerical results Rogowski et al. (2024) confirm that pitch angle configuration can control wake deflection and deformation. The contour plots show different lengths, vortex sizes, and flow structures. The flow character for cases of 0 degrees pitch angle and -10 degrees pitch angle has a distinct character from the case of 10 degrees pitch angle.

X [Section 3.2] Comparison between the 2-D CFD numerical rotor model and experimental measurement of thrust and lateral forces shows some reliability for certain conditions (Rogowski et al., 2024). However, these numerical models have significant limitations due to their inability to capture crucial 3D phenomena.

X [Section 2.2] The publication Michna and Rogowski (2022) shows that URANS models have a high decay rate of turbulence intensity. With a low length scale value, typical for the wind tunnel, achieving a turbulence intensity higher than 0.5% just before the airfoil is hard, even with a 10% intensity level at the input.

RANS numerical methods yield corrected results in high-Re regimes. However, for Re around 1×10^5, when boundary layer phenomena take the leading role in aerodynamic force results, the outcome from RANS approaches is visibly less accurate. There is room for improvement in the turbulence modeling.

Although it seems that using the Large Eddy Simulation (LES) or Direct Navier-Stokes (DNS) approaches is the way to achieve evidently better results. Unfortunately, for complex geometries, such as an entire vertical-axis wind turbine, the demand for computational resources is enormous and sometimes exceeds what is achievable. Future work can follow both RANS and non-RANS approaches to accurately model laboratory-scale VAWTs.

Moreover, the scientific focus should be on the specifications for wind tunnel turbulence levels. It seems that precise knowledge of turbulence intensities, typical turbulence length scales, or even the entire turbulence energy spectrum is key to achieving accurate numerical results in the low Reynolds number regime.

Hypothesis ③ Static and dynamic characteristics of airfoils in the low-Re regime

The static and dynamic loads characteristic of the VAWT blade are strongly dependent on the laminar separation bubble and the laminar-to-turbulent transition occurring in the boundary layer of the blades. These phenomena are typical of low Reynolds number flow around thick airfoils.

XI [Section 2.3] The experimental results from Rogowski, Mikkelsen, et al. (2025) verified that post-stall hysteresis loop moves to the higher angle of attack with Reynolds number growth.

XII [Section 3.3] The paper Michna and Rogowski (2024) confirms that the dynamic curve of the lift coefficient does not pass through zero at zero angle of attack. The comparison between static and dynamic force coefficients clearly shows the "virtual camber" effect.

XIII [Section 3.1] The results of harmonic pitching model simulations (Michna et al., 2025) show that with the use of the Transition SST turbulence model, significant lift coefficient hysteresis and visible oscillations are shown up during motion. This outcome confirms that laminar separation bubbles can cause hysteresis and oscillations. However, additional experiments are necessary to validate this conclusion.

XIV [Section 2.1] The Michna et al. (2021) paper corroborated that the Transition SST turbulence model can bring more accurate force characteristics results for moderate Reynolds numbers by considering laminar-to-turbulent transition.

XV [Section 2.1 and 3.1] The work Michna et al. (2021) and Michna et al. (2025) confirmed that classical two-equation turbulence models are inadequate for accurately predicting nonlinearities in lift force characteristics and fail to capture the critical effects of laminar separation bubbles, necessitating the use of transition-sensitive models like the Transition SST approach.

The static and dynamic load characteristics were investigated, showing dependence on boundary-layer phenomena. Based on these high-fidelity outcomes, the next step is to develop the airfoil's pitching motion model. This model may serve as a simplified representation of a vertical-axis wind turbine's blade during rotation. Using this approach to estimate Vertical-Axis Wind Turbine forces is a promising way to follow.

Bibliography

Abdolahifar, A., & Zanj, A. (2024). Addressing VAWT aerodynamic challenges as the key to unlocking their potential in the wind energy sector. *Energies*, *17*(20), 5052. https://doi.org/10.3390/en17205052

Amet, E., Maître, T., Pellone, C., & Achard, J.-L. (2009). 2D numerical simulations of blade-vortex interaction in a Darrieus turbine. *Journal of Fluids Engineering*, *131*(111103). https://doi.org/10.1115/1.4000258

Balduzzi, F., Bianchini, A., Maleci, R., Ferrara, G., & Ferrari, L. (2015). Blade design criteria to compensate the flow curvature effects in H-Darrieus wind turbines. *Journal of Turbomachinery*, *137*(1), 011006. https://doi.org/10.1115/1.4028245

Belabes, B., & Paraschivoiu, M. (2021). Numerical study of the effect of turbulence intensity on VAWT performance. *Energy*, *233*, 121139. https://doi.org/10.1016/j.energy.2021.121139

Bianchini, A., Balduzzi, F., Bachant, P., Ferrara, G., & Ferrari, L. (2017). Effectiveness of two-dimensional CFD simulations for darrieus VAWTs: A combined numerical and experimental assessment. *Energy Conversion and Management*, *136*, 318–328. https://doi.org/10.1016/j.enconman.2017.01.026

Bianchini, A., Balduzzi, F., Ferrara, G., & Ferrari, L. (2016). A computational procedure to define the incidence angle on airfoils rotating around an axis orthogonal to flow direction. *Energy Conversion and Management*, *126*, 790–798. https://doi.org/10.1016/j.enconman.2016.08.010

Bianchini, A., Balduzzi, F., Rainbird, J. M., Peiro, J., Graham, J. M. R., Ferrara, G., & Ferrari, L. (2015). An experimental and numerical assessment of airfoil polars for use in darrieus wind turbines—part I: Flow curvature effects. *Journal of Engineering for Gas Turbines and Power*, *138*(3), 032602. https://doi.org/10.1115/1.4031269

Carbó Molina, A., De Troyer, T., Massai, T., Vergaerde, A., Runacres, M. C., & Bartoli, G. (2019). Effect of turbulence on the performance of VAWTs: An experimental study in two different wind tunnels. *Journal of Wind Engineering and Industrial Aerodynamics*, *193*, 103969. https://doi.org/10.1016/j.jweia.2019.103969

Castelein, D., Tescione, G., Ragni, D., Simao Ferreira, C., & Gaunaa, M. (2015). Creating a benchmark of vertical axis wind turbines in dynamic stall for validating numerical models. *33rd Wind Energy Symposium*. https://doi.org/10.2514/6.2015-0723

Choudhry, A., Arjomandi, M., & Kelso, R. (2015). A study of long separation bubble on thick airfoils and its consequent effects. *International Journal of Heat and Fluid Flow*, *52*, 84–96. https://doi.org/10.1016/j.ijheatfluidflow.2014.12.001

Darrieus, G. J.-M. (1926, May 3). *Turbine à axe de rotation transversal à la direction du courant* (French pat. No. 604390A).

Du, L. (2016). *Numerical and experimental investigations of darrieus wind turbine start-up and operation* [Doctoral Thesis]. Durham University. Retrieved April 15, 2022, from http://etheses.dur.ac.uk/11384/

Du, L., Ingram, G., & Dominy, R. G. (2019). A review of H-Darrieus wind turbine aerodynamic research. *Proceedings of the Institution of Mechanical Engineers, Part C: Journal of Mechanical Engineering Science*, *233*(23), 7590–7616. https://doi.org/10.1177/0954406219885962

Fiedler, A. J., & Tullis, S. (2009). Blade offset and pitch effects on a high solidity vertical axis wind turbine. *Wind Engineering*, *33*(3), 237–246. https://doi.org/10.1260/030952409789140955

Gerakopulos, R., Boutilier, M., & Yarusevych, S. (2010). Aerodynamic characterization of a NACA 0018 airfoil at low reynolds numbers. *40th Fluid Dynamics Conference and Exhibit*. https://doi.org/10.2514/6.2010-4629

Ghigo, A., Faraggiana, E., Giorgi, G., Mattiazzo, G., & Bracco, G. (2024). Floating vertical axis wind turbines for offshore applications among potentialities and challenges: A review. *Renewable and Sustainable Energy Reviews*, *193*, 114302. https://doi.org/10.1016/j.rser.2024.114302

Giri Ajay, A., Morgan, L., Wu, Y., Bretos, D., Cascales, A., Pires, O., & Ferreira, C. (2024). Aerodynamic model comparison for an x-shaped vertical-axis wind turbine. *Wind Energy Science*, *9*(2), 453–470. https://doi.org/10.5194/wes-9-453-2024

Global energy review 2025. (2025, March 24). IEA. Paris. Retrieved September 11, 2025, from https://www.iea.org/reports/global-energy-review-2025

Istvan, M. S., & Yarusevych, S. (2018). Effects of free-stream turbulence intensity on transition in a laminar separation bubble formed over an airfoil. *Experiments in Fluids*, *59*(3), 52. https://doi.org/10.1007/s00348-018-2511-6

Jacobs, E. N., & Sherman, A. (1937). *Airfoil section characteristics as affected by variations of the reynolds number* (Technical Report No. NACA-TR-586). National Advisory Committee for Aeronautics. Langley Field, VA, USA. https://ntrs.nasa.gov/api/citations/19930091662/downloads/19930091662.pdf

Jacobs, E. N., Ward, K. E., & Pinkerton, R. M. (1933, January 1). *The characteristics of 78 related airfoil sections from tests in the variable-density wind tunnel* (Technical Report No. NACA-TR-460). National Advisory Committee for Aeronautics. Retrieved April 14, 2022, from https://ntrs.nasa.gov/api/citations/19930091108/downloads/19930091108.pdf

Kątski, B., & Rogowski, K. (2020). Analiza własności aerodynamicznych profilu NACA 0018 w zakresie małych liczb Reynodsa. *ML-XIX 2020*, 57–65. https://doi.org/10.15632/ML2020/57-65

Kawai, S., Asada, K., & Oyama, A. (2023). Freestream turbulence effects in Large-Eddy Simulations of laminar separation bubble. *Journal of Aircraft*, *60*(5), 1721–1727. https://doi.org/10.2514/1.C037058

Kruse, E. K., Sørensen, N. N., & Bak, C. (2018). Predicting the influence of surface protuberance on the aerodynamic characteristics of a NACA 63_3-418. *Journal of Physics: Conference Series*, *1037*, 022008. https://doi.org/10.1088/1742-6596/1037/2/022008

Kumar, R., Raahemifar, K., & Fung, A. S. (2018). A critical review of vertical axis wind turbines for urban applications. *Renewable and Sustainable Energy Reviews*, *89*, 281–291. https://doi.org/10.1016/j.rser.2018.03.033

Lam, H., & Peng, H. (2016). Study of wake characteristics of a vertical axis wind turbine by two- and three-dimensional computational fluid dynamics simulations. *Renewable Energy*, *90*, 386–398. https://doi.org/10.1016/j.renene.2016.01.011

Langtry, R. B., & Menter, F. R. (2009). Correlation-based transition modeling for unstructured parallelized computational fluid dynamics codes. *AIAA Journal*, *47*(12), 2894–2906. https://doi.org/10.2514/1.42362

Melani, P. F., Balduzzi, F., Ferrara, G., & Bianchini, A. (2019). An annotated database of low reynolds aerodynamic coefficients for the NACA0018 airfoil. *AIP Conference Proceedings*, *2191*, 020110. https://doi.org/10.1063/1.5138843

Melani, P. F., Balduzzi, F., Ferrara, G., & Bianchini, A. (2020). How to extract the angle attack on airfoils in cycloidal motion from a flow field solved with computational fluid dynamics? Development and verification of a robust computational procedure. *Energy Conversion and Management, 223,* 113284. https://doi.org/10.1016/j.enconman.2020.113284

Mendoza, V., Bachant, P., Ferreira, C., & Goude, A. (2019). Near-wake flow simulation of a vertical axis turbine using an actuator line model. *Wind Energy*, *22*(2), 171–188. https://doi.org/10.1002/we.2277

Michna, J., & Rogowski, K. (2023). CFD calculations of average flow parameters around the rotor of a Savonius wind turbine. *Energies*, *16*(1), 281. https://doi.org/10.3390/en16010281

Michna, J., Rogowski, K., & Kubacki, S. (2024). Investigation of aerodynamic performance of the NACA 0018 airfoil at low reynolds numbers: A comparative study of 2-D and 3-D models using Transition SST and K- ω SST approaches. https://psaa.meil.pw.edu.pl/READ2024/Papers/paperID80.pdf

Mueller, T. J., & DeLaurier, J. D. (2003). Aerodynamics of small vehicles. *Annual Review of Fluid Mechanics, 35,* 89–111. https://doi.org/10.1146/annurev.fluid.35.101101.161102

Nakano, T., Fujisawa, N., Oguma, Y., Takagi, Y., & Lee, S. (2007). Experimental study on flow and noise characteristics of NACA0018 airfoil. *Journal of Wind Engineering and Industrial Aerodynamics, 95*(7), 511–531. https://doi.org/10.1016/j.jweia.2006.11.002

Ren, G., Liu, J., Wan, J., Li, F., Guo, Y., & Yu, D. (2018). The analysis of turbulence intensity based on wind speed data in onshore wind farms. *Renewable Energy*, *123*, 756–766. https://doi.org/10.1016/j.renene.2018.02.080

Rezaeiha, A., Montazeri, H., & Blocken, B. (2018). Characterization of aerodynamic performance of vertical axis wind turbines: Impact of operational parameters. *Energy Conversion and Management, 169,* 45–77. https://doi.org/10.1016/j.enconman.2018.05.042

Rezaeiha, A., Montazeri, H., & Blocken, B. (2019). On the accuracy of turbulence models for CFD simulations of vertical axis wind turbines. *Energy, 180,* 838–857. https://doi.org/10.1016/j.energy.2019.05.053

Rogowski, K., Hansen, M. O. L., Maroński, R., & Lichota, P. (2016). Scale adaptive simulation model for the darrieus wind turbine. *Journal of Physics: Conference Series, 753*, 022050. https://doi.org/10.1088/1742-6596/753/2/022050

Rogowski, K. (2019). CFD computation of the h-darrieus wind turbine—the impact of the rotating shaft on the rotor performance. *Energies, 12*(13), 2506. https://doi.org/10.3390/en12132506

Rogowski, K., Hansen, M. O. L., & Bangga, G. (2020). Performance analysis of a H-Darrieus wind turbine for a series of 4-digit NACA airfoils. *Energies, 13*(12), 3196. https://doi.org/10.3390/en13123196

Rogowski, K., Królak, G., & Bangga, G. (2021). Numerical study on the aerodynamic characteristics of the NACA 0018 airfoil at low reynolds number for darrieus wind turbines using the transition SST model. *Processes, 9*(3), 477. https://doi.org/10.3390/pr9030477

Rogowski, K., Kubacki, S., & Michna, J. (2026). DNS dataset of a thick symmetric airfoil at low reynolds number: NACA 0018 with LES comparison. *Journal of Applied Fluid Mechanics, 19*(2), 29–44. https://doi.org/10.47176/jafm.19.2.3738

Savonius, J. S. (1929, January 1). *Rotor adapted to be driven by wind or flowing water* (U.S. pat. No. 1697574A).

Sheldahl, R. E., & Klimas, P. C. (1981, March 1). *Aerodynamic characteristics of seven symmetrical airfoil sections through 180-degree angle of attack for use in aerodynamic analysis of vertical axis wind turbines* (SAND-80-2114). Sandia National Labs., Albuquerque, NM (USA). https://doi.org/10.2172/6548367

Shires, A. (2013). Development and evaluation of an aerodynamic model for a novel vertical axis wind turbine concept. *Energies, 6*(5), 2501–2520. https://doi.org/10.3390/en6052501

Sørensen, J. N., & Shen, W. Z. (1999). Computation of wind turbine wakes using combined Navier-Stokes Actuator-Line methodology. In *1999 european wind energy conference*. Routledge.

Tescione, G., Ragni, D., He, C., Simão Ferreira, C., & van Bussel, G. (2014). Near wake flow analysis of a vertical axis wind turbine by stereoscopic particle image velocimetry. *Renewable Energy, 70*, 47–61. https://doi.org/10.1016/j.renene.2014.02.042

Timmer, W. (2008). Two-dimensional low-Reynolds number wind tunnel results for airfoil NACA 0018. *Wind Engineering*, *32*(6), 525–537. https://doi.org/10.1260/030952408787548848

Veers, P., Dykes, K., Lantz, E., Barth, S., Bottasso, C. L., Carlson, O., Clifton, A., Green, J., Green, P., Holttinen, H., Laird, D., Lehtomäki, V., Lundquist, J. K., Manwell, J., Marquis, M., Meneveau, C., Moriarty, P., Munduate, X., Muskulus, M., … Wiser, R. (2019). Grand challenges in the science of wind energy. *Science*, *366*(6464), eaau2027. https://doi.org/10.1126/science.aau2027

Winslow, J., Otsuka, H., Govindarajan, B., & Chopra, I. (2018). Basic understanding of airfoil characteristics at low Reynolds numbers. *Journal of Aircraft*, *55*(3), 1050–1061. https://doi.org/10.2514/1.C034415

Youngren, H., & Drela, M. (1991, June 24). Viscous/inviscid method for preliminary design of transonic cascades. In *27th joint propulsion conference*. American Institute of Aeronautics; Astronautics. https://doi.org/10.2514/6.1991-2364

Zhang, Y., Sun, Z., van Zuijlen, A., & van Bussel, G. (2017). Numerical simulation of transitional flow on a wind turbine airfoil with RANS-based transition model. *Journal of Turbulence*, *18*(9), 879–898. https://doi.org/10.1080/14685248.2017.1334908

Zhang, Y., Van Zuijlen, A., & Van Bussel, G. (2017). The MEXICO rotor aerodynamic loads prediction: ZigZag tape effects and laminar-turbulent transition modeling in CFD. *Journal of Wind Engineering and Industrial Aerodynamics*, *168*, 152–163. https://doi.org/10.1016/j.jweia.2017.06.002

Zhong, W., Tang, H., Wang, T., & Zhu, C. (2018). Accurate RANS simulation of wind turbine stall by turbulence coefficient calibration. *Applied Sciences*, *8*(9), 1444. https://doi.org/10.3390/app8091444

The bibliography list of the publications constituting the thesis

Michna, J., & Rogowski, K. (2022). Numerical Study of the Effect of the Reynolds Number and the Turbulence Intensity on the Performance of the NACA 0018 Airfoil at the Low Reynolds Number Regime. *Processes*, *10*(5), 1004. https://doi.org/10.3390/pr10051004

Michna, J., & Rogowski, K. (2024). A Refined Approach for Angle of Attack Estimation and Dynamic Force Hysteresis in H-Type Darrieus Wind Turbines. *Energies*, *17*(24), 6264. https://doi.org/10.3390/en17246264

Michna, J., Rogowski, K., Bangga, G., & Hansen, M. O. L. (2021). Accuracy of the Gamma Re-Theta Transition Model for Simulating the DU-91-W2-250 Airfoil at High Reynolds Numbers. *Energies*, *14*(24), 8224. https://doi.org/10.3390/en14248224

Michna, J., Śledziewski, M., & Rogowski, K. (2025). The Harmonic Pitching NACA 0018 Airfoil in Low Reynolds Number Flow. *Energies*, *18*(11), 2884. https://doi.org/10.3390/en18112884

Rogowski, K., Michna, J., & Ferreira, C. S. (2024). Numerical Analysis of Aerodynamic Performance of a Fixed-Pitch Vertical Axis Wind Turbine Rotor. *Advances in Science and Technology Research Journal*, *18*(6), 97–109. https://doi.org/10.12913/22998624/191128

Rogowski, K., Michna, J., Mikkelsen, R. F., & Ferreira, C. S. (2025). Impact of zigzag tape on blade loads and aerodynamic wake in a vertical axis wind turbine: A Delft VAWT case study. *Energy*, *321*, 135344. https://doi.org/10.1016/j.energy.2025.135344

Rogowski, K., Mikkelsen, R. F., Michna, J., & Wiśniewski, J. (2025). Aerodynamic performance analysis of NACA 0018 airfoil at low Reynolds numbers in a low-turbulence wind tunnel. *Advances in Science and Technology. Research Journal*, *19*(2), 136–150. https://doi.org/10.12913/22998624/195556

List of Figures

A Copies of the publications constituting the dissertation

This thesis is constituted on the publications which thesis' author is a co-author. The copies of these publications are attached here.

Michna et al. (2021)

Title: "Accuracy of the Gamma Re-Theta Transition Model for Simulating the DU-91-W2-250 Airfoil at High Reynolds Numbers"

Authors: **Jan Michna**, Krzysztof Rogowski, Galih Bangga, Martin O. L. Hansen

Journal: Energies *14*,8224 **Date:** December 2021 **MNiSW:** 140 pts

DOI: https://doi.org/10.3390/en14248224

Michna and Rogowski (2022)

Title: "Numerical Study of the Effect of the Reynolds Number and the Turbulence Intensity on the Performance of the NACA 0018 Airfoil at the Low Reynolds Number Regime"

Authors: **Jan Michna**, Krzysztof Rogowski

Journal: Processes *10*,1004 **Date:** May 2022 **MNiSW:** 100 pts

DOI: https://doi.org/10.3390/pr10051004

Rogowski, Mikkelsen, et al. (2025)

Title: "Aerodynamic performance analysis of NACA 0018 airfoil at low Reynolds numbers in a low-turbulence wind tunnel"

Authors: Krzysztof Rogowski, Robert Flemming Mikkelsen, **Jan Michna**, Jan Wiśniewski

Journal: *ASTRJ 19*,136–150 **Date:** January 2025 **MNiSW:** 100 pts

DOI: https://doi.org/10.12913/22998624/195556

Michna et al. (2025)

Title: "The Harmonic Pitching NACA 0018 Airfoil in Low Reynolds Number Flow"

Authors: **Jan Michna**, Maciej Śledziewski, Krzysztof Rogowski

Journal: Energies *18*,2884 **Date:** May 2025 **MNiSW:** 140 pts

DOI: https://doi.org/10.3390/en18112884

Rogowski et al. (2024)

Title: "Numerical Analysis of Aerodynamic Performance of a Fixed-Pitch Vertical Axis Wind Turbine Rotor"

Authors: Krzysztof Rogowski, **Jan Michna**, Carlos Simao Ferreira

Journal: *ASTRJ 18*,97–109 **Date:** September 2024 **MNiSW:** 100 pts

DOI: https://doi.org/10.12913/22998624/191128

Michna and Rogowski (2024)

Title: "A Refined Approach for Angle of Attack Estimation and Dynamic Force Hysteresis in H-Type Darrieus Wind Turbines"

Authors: **Jan Michna**, Krzysztof Rogowski

Journal: Energies *17*,6264 **Date:** December 2024 **MNiSW:** 140 pts

DOI: https://doi.org/10.3390/en17246264

Rogowski, Michna, et al. (2025)

Title: "Impact of zigzag tape on blade loads and aerodynamic wake in a vertical axis wind turbine"

Authors: Krzysztof Rogowski, **Jan Michna**, Robert Flemming Mikkelsen, Carlos Simao Ferreira

Journal: *Energy 321*,135344 **Date:** March 2025 **MNiSW:** 200 pts

DOI: https://doi.org/10.1016/j.energy.2025.135344

energies

Article

Accuracy of the Gamma Re-Theta Transition Model for Simulating the DU-91-W2-250 Airfoil at High Reynolds Numbers

Jan Michna [1], Krzysztof Rogowski [1,*], Galih Bangga [2] and Martin O. L. Hansen [3]

1 Institute of Aeronautics and Applied Mechanics, Warsaw University of Technology, 00-665 Warsaw, Poland; jan.michna.dokt@pw.edu.pl
2 Institute of Aerodynamics and Gas Dynamics, University of Stuttgart, 70569 Stuttgart, Germany; bangga@iag.uni-stuttgart.de
3 Department of Wind Energy, Technical University of Denmark, DK2800 Lyngby, Denmark; molh@dtu.dk
* Correspondence: krogowski@meil.pw.edu.pl; Tel.: +48-506-193-919

Abstract: Accurate computation of the performance of a horizontal-axis wind turbine (HAWT) using Blade Element Momentum (BEM) based codes requires good quality aerodynamic characteristics of airfoils. This paper shows a numerical investigation of transitional flow over the DU 91-W2-250 airfoil with chord-based Reynolds number ranging from 3×10^6 to 6×10^6. The primary goal of the present paper is to validate the unsteady Reynolds averaged Navier-Stokes (URANS) approach together with the four-equation transition SST turbulence model with experimental data from a wind tunnel. The main computational fluid dynamics (CFD) code used in this work was ANSYS Fluent. For comparison, two more CFD codes with the Transition SST model were used: FLOWer and STAR-CCM +. The obtained airfoil characteristics were also compared with the results of fully turbulent models published in other works. The XFOIL approach was also used in this work for comparison. The aerodynamic force coefficients obtained with the Transition SST model implemented in different CFD codes do not differ significantly from each other despite the different mesh distributions used. The drag coefficients obtained with fully turbulent models are too high. With the lowest Reynolds numbers analyzed in this work, the error in estimating the location of the transition was significant. This error decreases as the Reynolds number increases. The applicability of the uncalibrated transition SST approach for a two-dimensional thick airfoil is up to the critical angle of attack.

Keywords: CFD; RANS modeling; airfoil; wind turbine; boundary layer; transition

Citation: Michna, J.; Rogowski, K.; Bangga, G.; Hansen, M.O.L. Accuracy of the Gamma Re-Theta Transition Model for Simulating the DU-91-W2-250 Airfoil at High Reynolds Numbers. *Energies* **2021**, *14*, 8224. https://doi.org/10.3390/en14248224

Academic Editor: Davide Astolfi

Received: 30 October 2021
Accepted: 29 November 2021
Published: 7 December 2021

1. Introduction

During the last two decades many countries all over the world have invested in wind energy technology in view of renewable energy targets and carbon emissions reduction [1,2]. Recent trends in the wind energy industry present the development of large wind turbines in offshore wind farms. The European Wind Energy Association reported that the latest generation of wind turbines had a rated capacity of up to 7 MW and rotor diameters up to 170 m. In addition, 10–20 MW turbines are currently under development. Offshore wind turbines development tends towards larger wind farms built in deeper waters and further from the coast. Extending the current water depth limit of 50 m for the fixed substructure concepts will significantly expand the potential of the deeper seas for offshore wind farms [3–6]. The development of big floating wind farms of multi-MW machines entails new challenges for engineers. One of the main challenges is the verification of numeric codes, both Computational Fluid Dynamics (CFD) and Blade Element Momentum (BEM) codes, for determining the aerodynamic performance of wind turbines at different flow velocity regimes than before.

The reliability of the airfoil polars is an essential factor for the prediction accuracy of aerodynamic blade loads using BEM approaches [7–11]. These polars can be obtained in various ways, e.g., from wind tunnel measurements [12,13], from CFD analyzes [14–16], using the XFOIL code [17–19], or also from flight tests [20,21]. In order to improve the accuracy of the characteristics predicted by CFD, numerical methods have been developed for boundary layer flows in recent years. However, the use of classical two-equation turbulence models such as, for example, the k-ε family models, may yield overly optimistic results when they predict the separation on an airfoil at large angles of attack [22–24].

Transitional boundary layer flows are especially significant in many CFD applications of engineering interest such as airfoils, wind turbines, vehicles, or turbomachinery blade rows [25–27]. In many cases, the transition effects are so important for pressure distributions that classic one or two-equation turbulence models give inaccurate aerodynamic forces results [9]. Various mechanisms of the transition formation, depending on the flow regime, the free-stream turbulence intensity, and the geometry of the flowing objects, make it extremely difficult for 2D CFD models. Particularly problematic are also airfoils with a high relative thickness and complex geometry, as well as objects operating at unsteady flow conditions, e.g., Darrieus-type wind turbines [28].

There has been significant progress towards developing reliable turbulence models that can simulate a wide range of engineering flows in recent years. The effort of many researchers has resulted in models of the laminar-turbulent transition. Developing a reliable transition model for general-purpose CFD codes is not an easy task for several reasons. First of all, there is no single mechanism for the transition process [29–34]. The second reason is related to conventional Reynolds averaged Navier-Stokes (RANS) procedures, which are not suitable for describing transient flow processes, where both linear and non-linear effects are crucial [35]. Of course, some methods do not have such a limitation, such as, for example, the e^N method [36–38] implemented in the XFOIL code [39]. However, they are not compatible with common general-purpose CFD codes [40].

A general-purpose transition turbulence model should enable the user to calibrate, it should consider different transition mechanisms, and above all, it should be formulated locally. A unique correlation-based transition turbulence model, also known as the $\gamma - Re_\theta$ model, is based strictly on local variables [35,41,42]. The purpose of the inventors was to develop a general-purpose turbulence model that would be compatible with modern CFD codes that can use unstructured meshes. It, however, should be remembered that the $\gamma - Re_\theta$ model does not model the physics of the transition process. It only forms a framework for the use of transition correlations. This article discusses the problem of flow through a very thick airfoil in the large Reynolds number range.

The DU 91-W2-250 airfoil is a wind turbine dedicated profile developed at Delft University of Technology (DUT) [43,44]. The design assumptions for the DU series were to keep the sensitivity as low as possible due to imperfections of the nose contour and contamination of the leading edge. The maximum lift capacity was kept at moderate levels to limit the loss of lift due to surface contamination. Thicker NACA airfoils used in the root area had inferior performance due to premature transition. In order to avoid early separation, the airfoils had a limited thickness of the upper surface. Therefore, the S-shape of the pressure side, typical for the DU airfoil family, has been developed. This compensated for the loss of lift [45,46]. The general designation of this airfoil is as follows: DU yy-W-xxx, where DU stands for Delft University, yy is the year the airfoil was designed, W means that the airfoil was designed for wind turbines. The last three digits of this designation, xxx, define 10 times the airfoil's maximum thickness as a percentage of the chord. In the case of the DU 91-W2-250 airfoil, an additional number 2 next to the symbol W means that more than one airfoil has been designed in a given year. The DU-airfoils are commonly used in blades for wind turbines with diameters ranging from 29 m to over 100 m. Such machines reach a maximum power of 350 kW to 3.5 MW [43]. In recent years, a lot of research into these airfoils has focused on improving their performance through the use of vortex generators [47,48].

Despite the significant development of CFD techniques in recent years and despite numerous numerical analyzes of thick airfoils, there is still a lack of comprehensive analysis results validating current general-purpose transition turbulence models over a wide range of Reynolds numbers, angles of attack and undisturbed turbulence intensity. A large number of citations of these two papers [43,44] proves the great interest of the wind energy community in the DU airfoil series. Despite this interest, there is still little validation of the aerodynamic performance of these profiles. This is because the DU airfoil series are still young compared to, for example, the well-known NACA airfoil families [49–51] or with the popular the S809 airfoil [52]. So far, several works have been devoted to the validation of the aerodynamic performance of DU series profiles using advanced CFD tools [15,53–60]. All of these articles, except papers [57,59,60], take into account CFD investigation of the DU 91-W2-250 airfoil.

A review of the literature in terms of CFD calculations of the DU airfoil family proves that the two-equation turbulence model k-ω SST is still very often used in analyzes [54,56,57,59]. This is due to the fact that the transition models are not yet adequately validated and that the k-ω SST model is quite stable and less expensive.

Xu et al. analyzed the aerodynamic performance of blunt trailing edge airfoils at a chord Reynolds number of 3×10^6 based on the DU 91-W2-250, DU 97-W-300 and DU 96-W-350 airfoils by enlarging the thickness of the trailing edge. The aerodynamic performance of blunt trailing edge airfoils was obtained using the fully turbulent k-ω SST, the transitional k-ω SST model and the RFOIL code. These authors concluded that the transient calculations over-predict the drag at all angles of attack and the lift at large angles of attack in comparison with steady calculations [53]. Zhang et al. analyzed the DU-91-W2-250 profile using the RANS approach together with the $k - k_L - \omega$ three-equation turbulence model [55]. However, the research of these authors focused on only one Reynolds number equal to 1×10^6. However, these investigations prove that even in the linear range of the lift coefficient, a transition model is necessary. First of all, it allows obtaining more accurate results of the drag coefficient compared to a fully turbulent model. The four equations $\gamma - Re_\theta$ model and three-dimensional Reynolds-averaged Navier-Stokes equations were used by Campobasso et al. to analyze the aerodynamic performance of the DU 96-W-180 airfoil with large and sparse erosion cavities. The obtained results correspond relatively well with the experimental values in the linear range of the lift coefficient, even for the eroded variant of the profile [61]. It seems that the use of the three-dimensional RANS CFD may slightly improve the calculated characteristics at higher angles of attack. However, it should be remembered that despite the development of computer infrastructure, 3D calculations are still numerically expensive; therefore, there are still too few 3D analysis results [58]. As long as the full numerical analysis of the 2D model in the unsteady state is not carried out, simple analytical tools such as RFOIL will continue to lead the way in transition prediction [51]. Therefore, it is necessary to accurately estimate all flow parameters related to the laminar-turbulent transition phenomenon for a wide range of angles of attack as well as Reynolds numbers so that the model can be calibrated in the future.

The main aim of this work is to study the suitability, in terms of accuracy, of the Unsteady Reynolds-Averaged Navier–Stokes (URANS) with the Transition SST turbulence model for simulations of the DU-91-W2-250 airfoil at high Reynolds numbers and in the range of angles of attack below the critical angle of attack.

2. The DU 91-W2-250 Airfoil and the Flow Regime

This work developed a two-dimensional numerical model of the DU 91-W2-250 airfoil then analyzed using the URANS approach and the Transition SST turbulence model implemented in the commercial CFD code—ANSYS Fluent 19.0. The main goal of this work is to validate the applied numerical methods based on good quality experimental data. Figure 1a shows the shape of the DU 91-W2-250 airfoil [43]. Chord length c of the airfoil is kept as 1000 mm. The airfoil's relative thickness as a percent of its chord length is 25%.

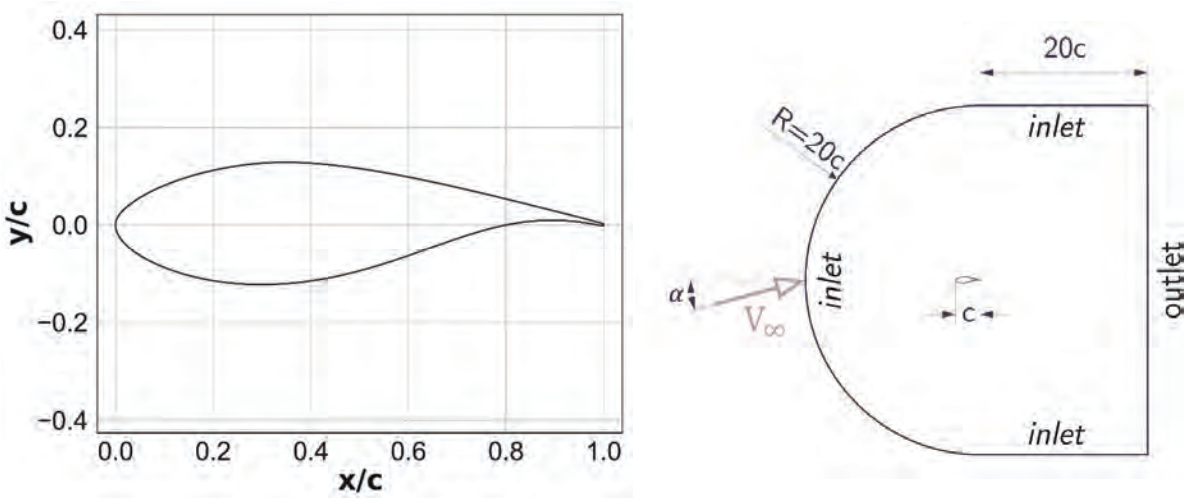

(**a**) (**b**)

Figure 1. Numerical model: (**a**) DU-91-W2-250 airfoil; (**b**) computational domain and boundary conditions.

In this paper the comparison of the aerodynamic performance of the DU 91-W2-250 airfoil is presented at four different Reynolds numbers: 3×10^6, 4×10^6, 5×10^6 and 6×10^6. The lift and drag performance of the airfoil are analyzed for six different angles of attack, α: $-0.04°$, $2°$, $4.03°$, $6.07°$, $8.1°$, $10.38°$. Such a high accuracy of the angles of attack, two decimal places, was chosen so that the simulation conditions corresponded as closely as possible to the conditions in the experiment. The experimental data of the aerodynamic characteristics of the airfoil correspond to two Reynolds numbers: 3×10^6 and 6×10^6. The Mach number was 0.15 for the Reynolds number of 3×10^6 and 0.3 for the Reynolds number of 6×10^6. In this work, this range was extended by two additional Reynolds numbers, 4×10^6 and 5×10^6 in order to obtain the dependence of airfoil characteristics on this quantity. In these studies, only six angles of attack were selected because the analyzes were very detailed and, as a result, very time-consuming and numerically expensive.

In this work, the turbulence intensity is set to 0.05%, equal to the experimental value [15,58]. The turbulence length scale is set at 0.0001 m and it was not investigated in this work. Cao [61] and Butler et al. [62] reported that the variation of the turbulence length scale does not have a significant effect. The turbulence intensity has a much greater effect on the transition process and turbulent structures.

The good quality data was provided by the LM Low Speed Wind Tunnel (LSWT), which is of a closed-loop type. The fan has a power of 1 MW and can deliver up to 105 m/s in the 2.7 m $\times$ 1.35 m $\times$ 7 m (H $\times$ W $\times$ L) test section. The constant temperature was kept in the wind tunnel by using a cooling system. The test section has a turbulence intensity of less than 0.05%. In order to measure lift coefficients, 62 pressure taps were integrated into the airfoil across the entire chord. The measurements were performed in May 2015. More information on these wind tunnel tests can be found in earlier papers [15,58].

3. Numerical Procedure

In this work, the transition shear stress transport (SST) turbulence model with the unsteady Reynolds-averaged Navier–Stokes (URANS) implemented in the ANSYS Fluent package was thoroughly assessed for the DU-91-W2-250 airfoil. This approach has been investigated in great detail, both in terms of the sensitivity analysis of the method as well as the obtained results of the aerodynamic characteristics of the airfoil.

Additionally, this work uses the same Transition SST approach implemented in the FLOWer and STAR-CCM + packages. In this study, no sensitivity analysis was performed for these methods.

3.1. Computational Domain, Mesh and Boundary Conditions

A C-type mesh is very popular for the simulation of transitional flow over airfoils [63]. This is due to the ability to adjust the computing domain to the simulated flow, for example, the ability to simulate a longer aerodynamic wake without enlarging the entire computational domain [64,65], as in the case of O-type mesh [66]. Figure 1b presents the C-type computational domain that was adopted in the present simulations. As shown in Figure 1a, the origin of the coordinate system is located at the leading edge of the airfoil. The radius R of the semicircle is selected as 20 c, and the height and length of the rectangle are selected as 40 c and 20 c, respectively (Figure 1b). Two types of boundary conditions were selected in these numerical analyses: *velocity inlet* and *pressure outlet*, as shown in Figure 1b. The velocity inlet condition was given on three edges of the computational domain: on the front semicircular edge and on the top and bottom edges. The pressure outlet boundary condition is assumed only on the rear vertical edge of the computational domain.

In this work, the velocity inlet boundary condition is used to define the velocity of the flow at inlet boundaries. However, the use of this boundary condition requires that it is located far enough from the obstacle [67]. There is no unanimity in the literature when it comes to choosing the right size of the computing domain. Lu et al. [68] investigated the impact of mesh properties on RANS simulations for rudder hydrodynamics. These authors showed that too small size of a C-type mesh generates a larger error, mainly in the drag coefficient. In order to avoid the effects of too small size of the domain, Thomas and Salas conducted research for the mesh size L/c = 500, where L is the distance from the airfoil to the domain boundary [69]. There are also works where a domain with a much smaller size is used. Wang et al. [70] adopted C-H where the flow domain in the flow field was 12.5 times the chord length of the airfoil. Wang et al. showed that even in such a case, results consistent with the experiment can be obtained. Fully turbulent and transitional computations of the 2D S809 airfoil were performed by Langtry et al. (initiators of the transition SST model) [71]. In their study, the far-field boundary was located 10 chord-lengths away from the airfoil. Many published works show that the L/c size in the range between 10 and 20 is sufficient to obtain sufficiently accurate results of the aerodynamic force coefficients [72,73]. This applies to both airfoils with a small relative thickness [72,73] and thick profiles [71]. Moreover, this also applies to airfoils operating at low Reynolds number regimes [72] as well as high ones, similar to those analyzed in this paper [71,73,74]. Therefore, in this work the domain shown in Figure 1b was used, in which the distance between the airfoil and the edge of the domain is 20 c.

Moreover, by comparing the results of the aerodynamic force coefficients obtained with the ANSYS Fluent code with the results obtained with the FLOWer code, where the domain size L/c is 100, no significant differences were noticed.

During the simulation, the orientation of the airfoil with respect to the computing domain was not changed. Therefore, in order to obtain the aerodynamic forces for different angles of attack, the following mathematical formulas are used:

$$L = Y \cos \alpha - X \sin \alpha, \tag{1}$$

$$D = Y \sin \alpha + X \cos \alpha, \tag{2}$$

where L and D are lift and drag forces, respectively, whereas Y and X represent the aerodynamic force components based on the coordinate system of ANSYS Fluent.

In order to simulate the airfoil, a completely structured mesh was performed. The grid has 300 cells along the pressure side of the airfoil and 320 cells along the suction side. The total number of grids is 152,720. The typical distribution of the wall y^+ parameter along the airfoil surfaces is equal to 0.1 for all simulations presented in this paper. A literature review shows that this wall mesh spacing should be considered enough to capture the boundary layer separation [75]. A growth rate of quadrilateral boundary layer elements was 1.1 in the wall-normal direction. Figure 2a shows the distribution of the mesh elements throughout the computing domain whereas Figure 2b presents the mesh around the airfoil.

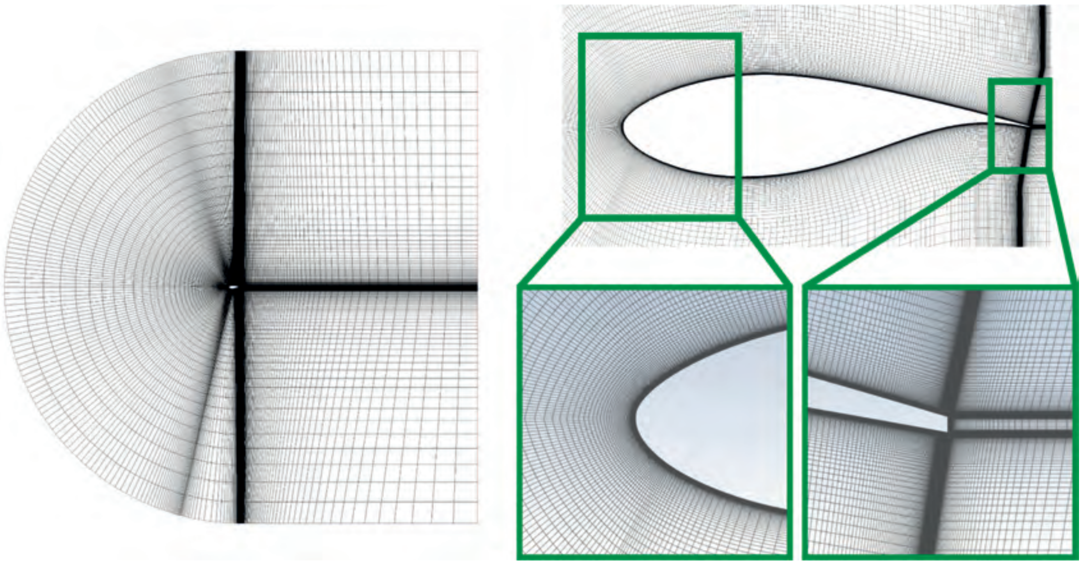

(**a**) (**b**)

Figure 2. Mesh: (**a**) The mesh in the entire computing domain; (**b**) The distribution of the mesh around the airfoil.

3.2. CFD Procedure and the Turbulence Model

In this study, the coupled pressure-velocity coupling algorithm was adopted with the second-order upwind scheme for the spatial discretization of the momentum equation as well as the turbulence quantities and a second-order scheme for the pressure equation.

In ANSYS Fluent CFD code, there are two different algorithms for the pressure-based solver: pressure-based segregated and pressure-based coupled. In the segregated algorithm, the solution variables are calculated separately in each iteration. In contrast, in the coupled algorithm, the momentum equations and pressure-based continuity equation is calculated simultaneously in each iteration. Therefore, the required memory capacity is larger for the coupled algorithm in comparison with the segregated algorithm. However, the coupled algorithm gives faster convergence as compared to the segregated algorithm [76]. Therefore, the coupled solver was used in this work on this account.

This paper discusses the issues concerning the unsteady flow over the DU 91-W2-250 airfoil. Such issues require that the numerical calculations be continued until the effect of homogeneous initial conditions does not affect the aerodynamic characteristics of the airfoil. In this work, the calculations were performed for a time period of 0.7 s. with a very small time step size Δt equal to 6×10^{-6} s. The Courant number was specified to be 200 and the Explicit Relaxation Factors for Momentum and Pressure were set at 0.75 by default [77]. All residuals were set to the same convergence level equal to 10^{-6}.

In this study, for turbulence closure, the transition SST turbulence model, also known as $\gamma - Re_\theta$ model developed by Langtry et al. [78] and Menter et al. [79] is used to predict the occurrence of transition in the turbulent boundary layer. This transition turbulence model was developed for implementation in modern, unstructured, parallel CFD codes. The model implemented in the ANSYS Fluent 19.0 code is a four-equation formulation based on the popular two-equation k-ω SST model. In order to provide a more accurate prediction of laminar to turbulent transition, this model solves two additional transport equations for momentum-thickness Reynolds number Re_θ and for intermittency γ. More details of the Transition SST turbulence model are given by Menter et al. [57] and Langtry et al. [79].

3.3. Verification to Grid Sensitivity

A mesh sensitivity study has been conducted to establish the optimum number of nodes on the airfoil surface. The mesh shown in Figure 2 has N = 620 nodes on the airfoil surface. This mesh is identified as Case 1. The grid was varied considering N/4 (Case 2), N/2 (Case 3) and 2N (Case 4) nodes. The studies were performed for one angle of attack equal to 4 deg. and for one Reynolds number of 4×10^6. Table 1 shows the results of the averaged drag coefficient for each test case. As the number of nodes increases, the value of the drag coefficient decreases. The mean value of the drag coefficient for Case 4 is 2.6% lower compared to the drag coefficient for Case 1. The drag coefficient for the coarsest mesh (Case 2) is 19.8% higher than that for Case 1. The 620-node mesh finally provided an accurate numerical solution.

Table 1. Mesh convergence study. The drag coefficient for a different number of nodes on the airfoil surface for the Reynolds number of 4×10^6.

Test Case (No. of Nodes on Airfoil Surface)	Drag Coefficient, C_D	Percentage Difference of Drag Coefficient to Case 1
Case 2 (N/4 = 155)	0.009173	19.77%
Case 3 (N/2 = 310)	0.008326	8.71%
Case 1 (N = 620)	**0.007659**	**0.00%**
Case 4 (2N = 1240)	0.007459	−2.60%

3.4. Verification of the Length of the Simulation Time

As was mentioned above, the numerical calculations should be continued until the effect of homogeneous initial conditions does not affect the aerodynamic characteristics of the airfoil. Moreover, vortex structures may appear in the unsteady flow around the analyzed object. The presence of these vortex structures is manifested by oscillations in the components of the aerodynamic force exerted on the body by the air. The components of the aerodynamic force calculated employing classical turbulence models, e.g., the SST model, resemble a sinusoid [80]. The longer the simulation time, the less successive oscillation of the aerodynamic force representing the periodic appearance of specific vortex structures around the flowing object differs from the previous one. The aerodynamic characteristics of the Darrieus rotor blades for a non-rotating shaft rotor configuration, calculated using classical turbulence models, behave similarly [19].

In this work, the calculations were made for a time period of 0.7 s. This analysis aims to verify the length of the simulation time period to avoid the effect of homogeneous initial conditions. Therefore, an additional goal of this test is to check whether the aerodynamic forces will have an oscillating course. Figure 3 shows the averaged drag and lift coefficients, $\overline{C}_D$ and $\overline{C}_L$ respectively, as a function of simulation time. The aerodynamic force components were averaged every 0.1 s. In this work, the standard deviation was used to evaluate the oscillation of the aerodynamic forces. A standard deviation was also calculated for each time interval. The results presented in the graphs show that the period of the simulation time should be at least 0.4 s to avoid the effects of the initial conditions. Obviously, this minimum simulation time period is determined by a given undisturbed flow velocity and the geometry of the computing domain presented in Figure 1b. The larger the computational domain surrounding the airfoil, the longer simulation time period should be taken into account [19]. The results shown in Figure 3a,b also prove that although the time step size assumed in this test was very small ($\Delta t = 6 \times 10^{-6}$), oscillation of the aerodynamic force components practically did not occur. An almost constant course of aerodynamic characteristics was obtained for all angles of attack investigated in this paper and for all analyzed Reynolds numbers. A similar trend in the aerodynamic force characteristics was also observed in the URANS simulations of the symmetrical NACA 0018 airfoil at low Reynolds numbers [9].

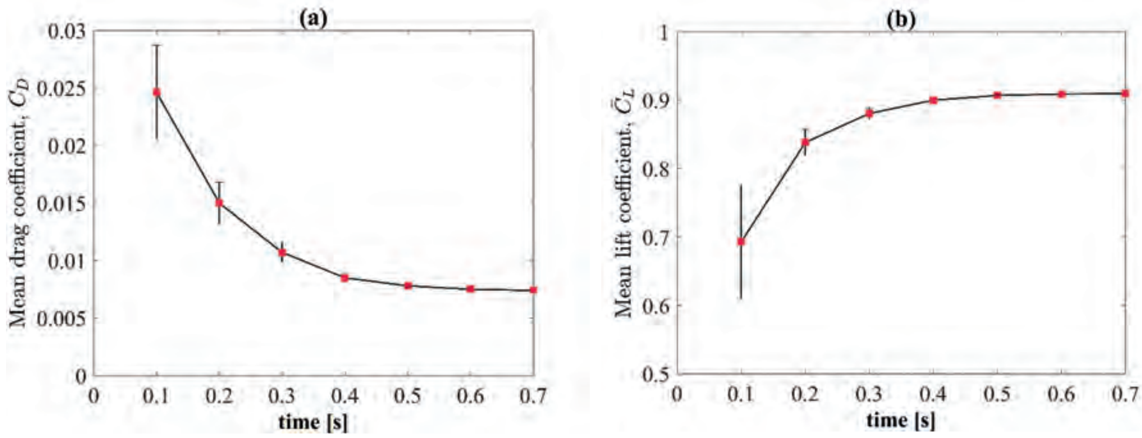

Figure 3. The averaged aerodynamic force coefficients and their standard deviation at the angle of attack of 4°: (**a**) lift coefficient; (**b**) drag coefficient.

3.5. Verification of the Length of Time Step

In all performed numerical calculations presented in this paper, the time step size Δt equal to 6×10^{-6} s was selected. The Courant number was specified to be 200 by default and the Explicit Relaxation Factors for Momentum and Pressure were set at 0.75 by default [66]. In these studies, the size of the time step was examined. The calculations have been performed for the Reynolds number of 4×10^6 and an angle of attack of 4 degrees. Three different time step sizes have been used for comparison: 3×10^{-6} s ($\Delta t/2$), 6×10^{-6} s (Δt) and 1.2×10^{-5} s ($2{\cdot}\Delta t$). For each specified time step size, the convergence was reached within 5–20 iteration per time-step. All residuals were set to the same convergence level equal to 10^{-6}. The mean values of the drag coefficient are 0.007654, 0.007659 and 0.007666, respectively. For the smallest time step used ($\Delta t/2$), the drag coefficient is lower by 0.06% compared to the case of Δt whereas for case $2{\cdot}\Delta t$, the drag coefficient is 0.09% larger in comparison with the case Δt. This analysis shows that reducing the time step size below $\Delta t = 6 \times 10^{-6}$ does not significantly affect the drag force coefficient, but the calculation time increases.

3.6. Other CFD Procedures

In this work, the primary tool to determine the aerodynamic performance of the DU 91-W2-250 airfoil was the transition SST turbulence model implemented in the ANSYS Fluent code. In order to verify the results of numerical calculations obtained by this procedure, the FLOWer and STAR-CCM + codes were also used, in which the $\gamma - Re_\theta$ The transition turbulence model was implemented according to Menter. In the case of the analysis with these two numerical codes, the sensitivity analysis of the numerical solution to changes of computational parameters and mesh distribution was not performed. The numerical grids used in these analyzes were prepared on the basis of the authors' previous experiences [54,56,57]. The numerical grid for the FLOWer code is shown in Figure 4a. The O-type mesh generated in this simulation had a total number of cells equal to 104,448. The number of cells on the airfoil edges was 256×2, whereas on the trailing edge it was 32. The far-field distance was 100 chords. The analysis was performed for unsteady flow assuming time step size of $\Delta t = c/(100{\cdot}V_\infty)$.

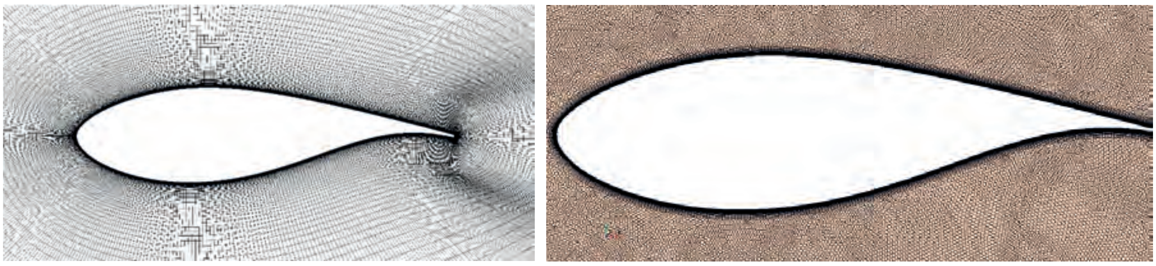

(**a**) (**b**)

Figure 4. Mesh: (**a**) FLOWer; (**b**) STAR-CCM +.

The STAR-CMM+ simulations were made using an unstructured polyhedral grid and in 3D, but with a very thin spanwise dimension of 0.05 c and with only few cells in this direction. To ensure a fine mesh resolution around the airfoil, an extra block was created around it and prescribing a small base size of 5 mm. This should be compared to the overall computational domain, where a base size of 1 m was used. Note that the specified base sizes are not the actual size of the cells, but some target values used by the unstructured grid solver. To resolve the boundary layer, an inflation layer of 40 points was specified with a total thickness of 15 mm and with a stretching of 1.15 giving a total number of cells of 1.28 mill. A steady-state RANS using SST (Menter) k-ω turbulence model, low y+ wall treatment, constant density and Gamma-Re theta transition model was applied. For the angle of attack of 4 degrees the maximum y+ was 1.4.

3.7. XFOIL Procedure

Due to its formulation, the XFOIL code enables rapid computation of the aerodynamic characteristics of different airfoils. The formulation of this approach is a combination of the potential flow panel method and the integral boundary layer formulation. This numerical approach was developed to predict aerodynamic characteristics of airfoil under the low Reynolds number regime. XFOIL takes into account the effect of limited trailing edge separation and a laminar separation bubble. Additionally, it uses the e^N method to detect the location of transition. In this paper, the N value is set to 9. This value corresponds to a smooth wing surface in a flow with a low free-stream turbulence level [81,82].

4. Results

4.1. Lift and Drag Airfoil Characteristics

Figure 5 shows the aerodynamic characteristics of the DU-91 W2-250 airfoil for two Reynolds numbers 3×10^6 and 6×10^6. These characteristics were calculated using the numerical procedures described in Section 3 of this paper. Additionally, the characteristics obtained with full-turbulence models (the k-ω SST and the k-ε RNG) published in [83,84] were used for comparison. These numerical predictions were compared with the experimental measurements [15,58].

For the qualitative assessment of numerical approaches, the relative error, δ, was calculated from the formula:

$$\delta = \left| C_{D_{exp}} - \overline{C}_D \right| / C_{D_{exp}} \times 100\%. \quad (3)$$

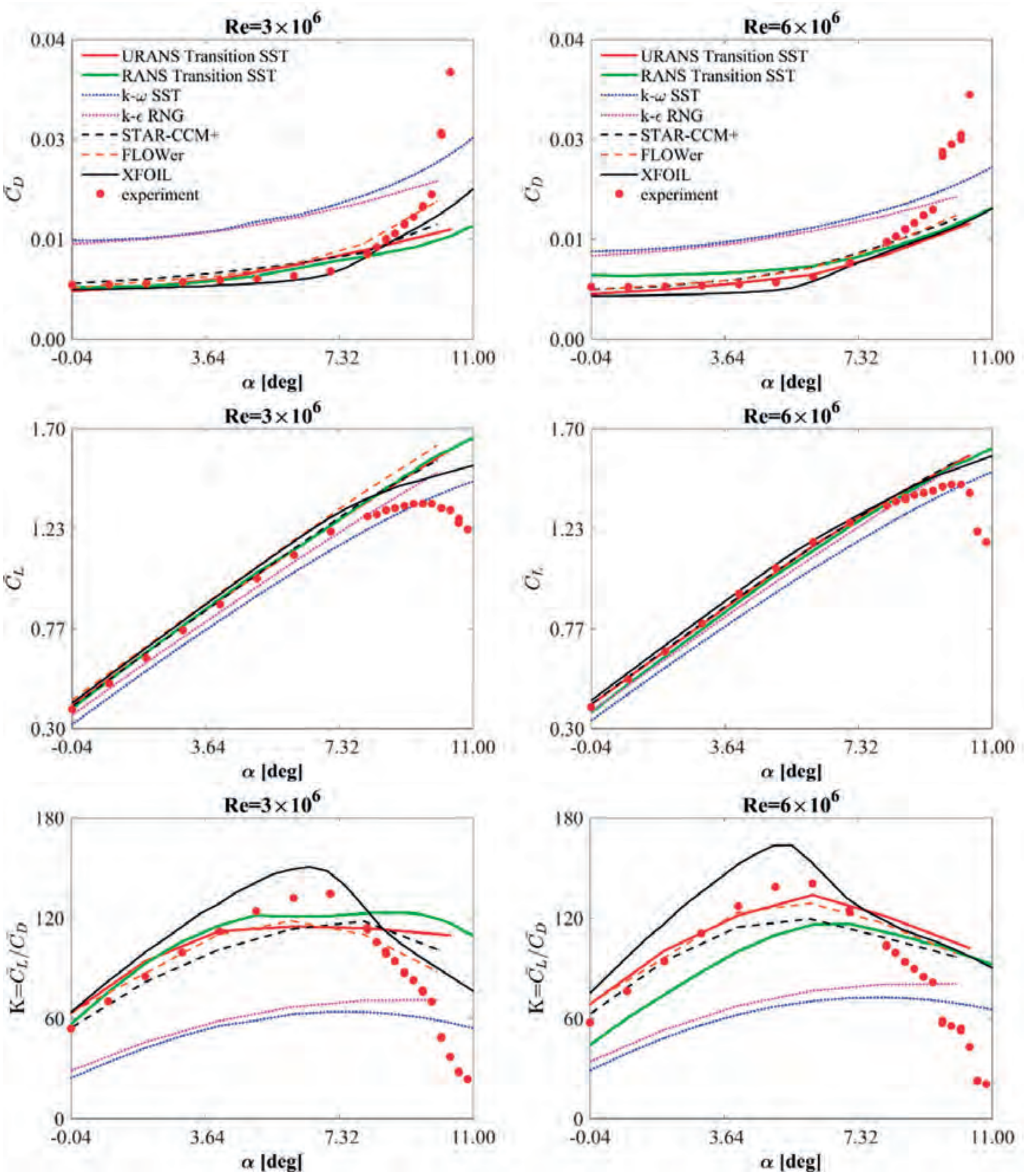

Figure 5. DU-91-W2-250 airfoil performance for two Reynolds numbers of 3×10^6 and 6×10^6.

For the zero angle of attack, the values of the drag coefficients measured in the wind tunnel are 0.0072 for a Reynolds number of 3×10^6 and 0.0069 for a Reynolds number of 6×10^6. For both analyzed Reynolds numbers, the relative error of all numerical approaches used, except for the k-ω SST and k-ε RNG models, was less than 12%. The lowest relative error was obtained for the STAR-CCM + code; it was 3% for Reynolds number of 3×10^6 and 4% for Reynolds number of 6×10^6. The obtained results showed that the relative error increases with the increase of the Reynolds number for all the used transition models, including the XFOIL code. The reverse tendency was observed for full-turbulence models. However, for these models the relative error of 60–70% for a Reynolds number of 6×10^6 is quite large.

For experimental data, the aerodynamic derivative $a = dC_L/d\alpha$ was 6.88 for a Reynolds number of 3×10^6 and 7.08 for a Reynold numbers of 6×10^6. These derivatives are estimated for angles of attack in the range from 0° to 8.1°. For the same angles of attack range, the RANS approach together with the Transition SST turbulence model provided the aerodynamic derivatives of 7.03 and 6.95 for Reynolds numbers of 3×10^6 and 6×10^6, respectively. Values of the relative error of the aerodynamic derivative are 2.25% for $Re = 3 \times 10^6$ and 1.9% for $Re = 6 \times 10^6$. In the case of the URANS approach with the Transition SST model, the numerical results of the lift force coefficients are obtained for angles of attack in the range from $-0.04°$ to 10.4°. Since, for the angle of attack equal to 10.4°, the calculated value of the $\overline{C}_L$ coefficient differs significantly from the experimental one (as can be seen with the naked eye in Figure 5), the qualitative assessment of the lift coefficient characteristics by using the aerodynamic derivative is limited to the range of angles of attack from 0° to 8.1°. For the URANS approach, the relative error of the aerodynamic derivative is 6.1% for the Reynolds number of 3×10^6 and 1.5% for the Reynolds number of 6×10^6. In comparison with the experiment, only for the angle of attack of 10.4°, the relative error is 21.5% for the Reynolds number of 3×10^6 and 12.4% for a Reynolds number of 6×10^6. Although the largest differences between the experimental and numerical values are observed for the angle of attack equal to 10.4°, with the increase of the Reynolds number, the value of the relative error decreases. The increasing relative error of both components of the aerodynamic force starting from the angle of attack equal to 8.1° for both analyzed Reynolds numbers results from the simplifying assumptions used. Using the DES technique, Rogowski et al. proved that even at a small angle of attack, significant velocity fluctuations in spanwise direction are observed [58]. These fluctuations increase with the angle of attack; however, their quantitative analysis using the DES technique is extremely computationally expensive.

The lift-to-drag ratio is the amount of lift generated by a wing divided by the aerodynamic drag:

$$K = \frac{\overline{C}_L}{\overline{C}_D}. \tag{4}$$

Figure 5 shows the lift-to-drag ratio, K, as a function of the angle of attack, α, for the Reynolds numbers of 3×10^6 and 6×10^6. The results shown in this figure clearly favor the Transition SST approach. The characteristics of the lift-to-drag ratio calculated using the classical two-equation turbulence models (the RNG k-ε and the SST k-ω models) that are widely used to simulate the flow field in engineering applications, differ significantly from predictions given by the experiment and the Transition SST models. It can be observed that for both analyzed Reynolds numbers the two-equation turbulence models underestimate the values of the lift-to-drag ratio whereas the XFOIL method overestimates the characteristics. Table 2 summarizes the derivative of the lift-to-drag ratio with respect to the angle of attack, $dK/d\alpha$ for the various aerodynamic methods and for the linear range of the lift-to-drag ratio characteristics up to $\alpha = 4°$. The results shown in this table confirm the similar compliance of all CFD codes with the implemented Transition SST turbulence model. Moreover, the aerodynamic characteristics obtained by means of classical turbulence models prove the critical role of transition phenomena in the boundary layer.

Table 2. The derivative of the lift-to-drag ratio $dK/d\alpha$ for the range of angles of attack from 0° to 4° and for different aerodynamic methods.

Aerodynamic Method	$dK/d\alpha$ (Re = 3×10³)	Relative Error (Re = 3×10³)	$dK/d\alpha$ (Re = 6×10³)	Relative Error (Re = 6×10³)
Experiment	819.74	0.00	978.81	0.00
URANS with the Transition SST	688.39	16.02	748.22	23.56
RANS with the Transition SST	822.90	0.39	789.68	19.32
k-ω SST	439.08	46.44	470.90	51.89
k-ε	414.39	49.45	471.11	51.87
RNG k-ε	420.98	48.64	451.06	53.92
STAR-CCM +	660.36	19.44	735.75	29.65
FLOWer	665.11	18.86	771.97	25.23
XFOIL	917.16	11.88	1088.33	11.19

Figure 6 shows characteristics of the aerodynamic force coefficients, $\overline{C}_D$ and $\overline{C}_L$ and the torque coefficient $\overline{C}_M$, as a function of the Reynolds number for the six angles of attack. Numerical calculations are made for four Reynolds numbers: 3×10^6, 4×10^6, 5×10^6, and 6×10^6. These investigations were only conducted using the ANSYS Fluent CFD code and URANS approach together with the Transition SST turbulence model. As it can be seen from this figure, the lift coefficients are practically constant over the entire investigated range of both Reynolds numbers and angles of attack (Figure 6c,d). The largest differences in the results are seen for the drag coefficient (Figure 6a,b). The drag coefficient is a function of both the Reynolds number and the angle of attack. Charts illustrated in Figure 6a,b show that up to an angle of attack equal to 6 degrees the drag decreases with increasing the Reynolds number. For angles of attack of 8 and 10 degrees the $\overline{C}_D$ characteristics follow a slightly different trend: at first, the drag decreases, and then it begins to increase. Munson et al. provided a typical character of the drag coefficient of an airfoil [85]. The airfoil drag coefficient decreases as the Reynolds number increases. At first, the drag decreases faster and then its changes are not very important. According to Munson et al., a faster decrease in drag is seen in the range of Reynolds numbers from $\sim 10^4$ to $\sim 10^6$ [85]. Then, up to the value of $Re \approx 10^7$, the drag coefficient changes little. It has been proven in these studies that starting from a Reynolds number of 4×10^6, the drag becomes almost constant at zero angle of attack. As the angles of attack increase, the airfoil begins to behave like a blunt body and pressure drag plays a more significant role. This explains the increase in drag for angles of attack of 8 and 10 degrees. Figure 6e,f show the torque coefficients for different angles of attack and as a function of the Reynolds number. The torque coefficient increases with the angle of attack, however, it is independent of the Reynolds number up to the angle of attack of 10 degrees.

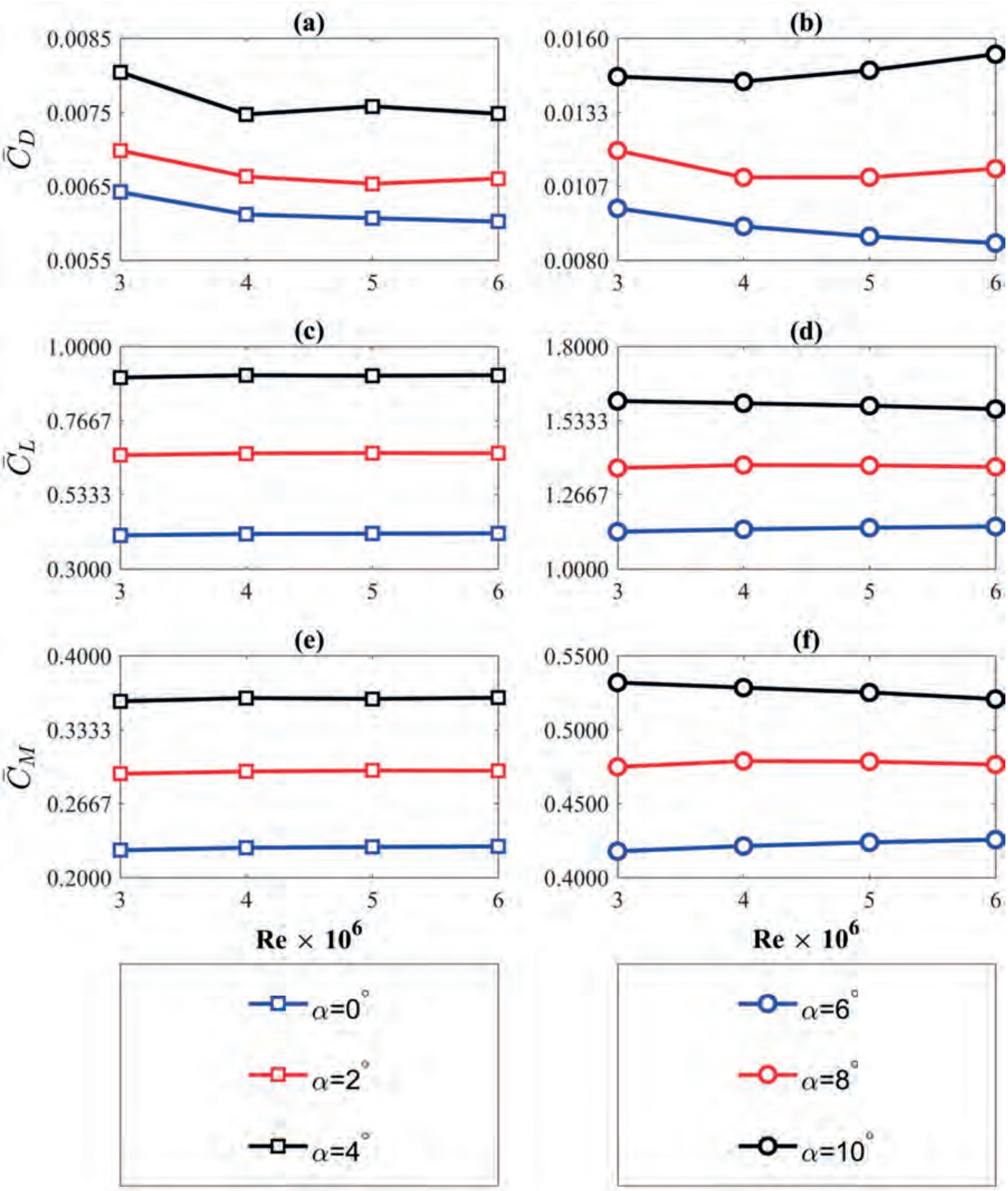

Figure 6. The drag and lift coefficients as a function of the Reynolds number for six angles of attack: (**a**,**b**) drag coefficients; (**c**,**d**) lift coefficients; (**e**,**f**) torque coefficients. The results are given only for URANS with the Transition SST turbulence model.

4.2. Static Pressure Coefficients

When an airfoil moves through the air, an interaction between the airfoil and the air occurs. In the previous subsection of this paper, this effect is described in terms of the aerodynamic forces. This subsection discusses this effect using the static pressure coefficient distributions along the airfoil. Static pressure coefficient is defined as:

$$C_P = \frac{P - P_{ref}}{q_{ref}}, \tag{5}$$

where P is the static pressure, P_{ref} is the reference pressure, and q_{ref} is the dynamic reference pressure defined as:

$$q_{ref} = \frac{1}{2}\rho_\infty V_\infty, \tag{6}$$

where ρ_∞ is the free stream density and V_∞ is the free stream velocity.

The distribution of static pressure along an airfoil depends on many factors. These are both the shape of the airfoil itself and the flow parameters. This paper compares the pressure distributions obtained by different analytical approaches. Moreover, the influence of the Reynolds number and the angle of attack on the pressure distributions is shown here. In Section 2 of this paper, it was proved that the oscillations of the aerodynamic forces obtained using the transient momentum equations and the Transition SST turbulence model are not large (Figure 3). This Section also shows the effect of transient flow conditions on pressure distributions.

Figure 7 shows the validation of various numerical approaches based on experimental data. For clarity, the first four plots in Figure 7 show the results obtained with the Transition SST approach implemented in various CFD codes, while the following four graphs in the same figure illustrate the results obtained with the two fully turbulent models. Figure 7 also compares the results for the XFOIL code. The validation of all analytical approaches has been shown for one angle of attack of 4 degrees and for two Reynolds numbers of 3×10^6 and 6×10^6. A similar tendency in the difference between the experimental and numerical results was observed for the remaining angles of attack taken into account in this paper; therefore, they are not presented in this paper. The pressure distributions calculated using the Transition SST model and ANSYS Fluent CFD code shown in Figure 7 are averaged over the same time interval as the aerodynamic forces discussed in the previous Section 3. Due to the fact that practically no oscillations of the components of the aerodynamic forces appear, the instantaneous pressure distributions differ slightly from the instantaneous values. The obtained results show clearly greater accuracy of the Transition SST model with the k-ω SST and k-ε RNG models. The obtained results also show a much greater discrepancy with the experimental results and with each other for the largest Reynolds number studied in this paper. In particular, these differences are visible on the suction side of the airfoil for x/c ranging from 0.12 to 0.5. Rogowski and Hansen showed that for this case, which corresponded to a Mach number of 0.3, the local Mach number in the vicinity of the blade edge reaches the value of 0.5 [58]. With the increase of the angle of attack on the suction edge of the airfoil, the area of the large Mach number field also increases. However, numerical calculations taking into account the compressibility of a continuous medium are definitely more expensive [58].

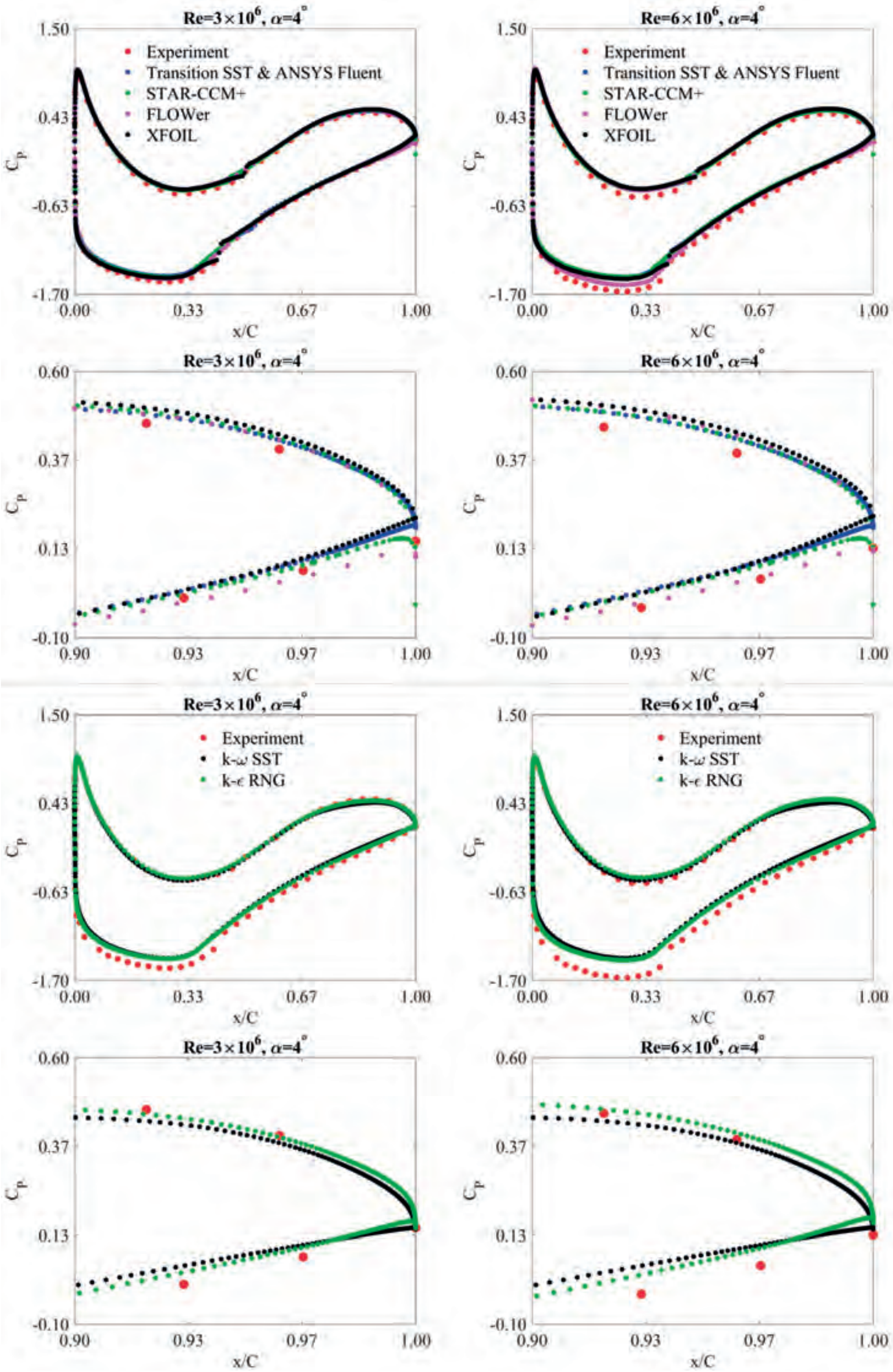

Figure 7. Static pressure distributions calculated for different numerical approaches. The results are presented for one angle of attack equal to 4 degrees.

Validation of the Transition SST approach more broadly is shown in Figure 8. In this case, for better clarity of the graphs, the results are given only obtained with the ANSYS Fluent CFD code. These plots clearly show that the effects of compressibility can affect the accuracy of static pressure distributions.

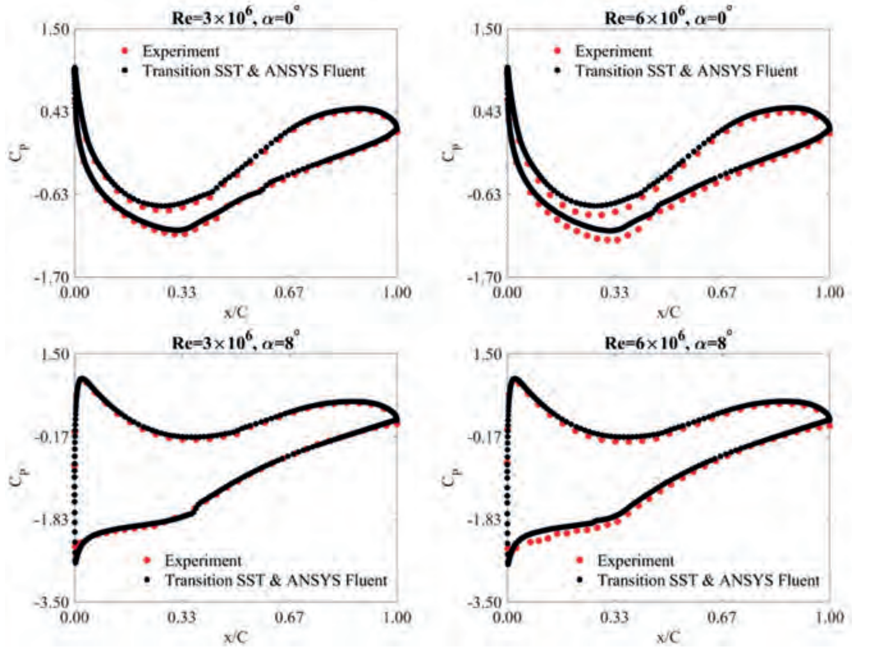

Figure 8. Static pressure distributions calculated for different angles of attack and for different Reynolds numbers.

As already mentioned above, the static pressure distributions obtained using the in ANSYS Fluent CFD code together with the URANS approach and the Transition SST turbulence model show a high agreement with the experimental results. In particular, very good agreement with the experimental results is obtained for the lower Reynolds number of 3×10^6. In order to qualitatively compare both data sets, experimental and numerical, a quantitative analysis was performed using the definition of relative error:

$$\delta = \left| C_{p_{exp}} - C_{p_{CFD}} \right| / C_{P_{exp}} \tag{7}$$

where C_{Pexp} is the measured static pressure coefficient, whereas C_{PCFD} is the static pressure coefficient calculated using CFD. Since, as already mentioned, the experimental and numerical results behave in a similar manner for both analyzed Reynolds numbers (for a lower Reynolds number the better agreement of the numerical results with the experimental ones, and for a larger Reynolds number the agreement is smaller), an angle of attack equal to 4 degrees was selected for the quantitative analysis. To perform such a quantitative comparative analysis, the C_P results obtained in the CFD analysis are interpolated into the coordinates for which the pressures were measured during the experiment. The relative error obtained from this analysis, averaged over the entire airfoil, is 9.8% for the Reynolds number of 3×10^6 and 17.8% for the Reynolds number of 6×10^6. The relative error was calculated separately for the suction side of the airfoil and for the pressure side to make this analysis even more useful. This analysis showed that for the lower analyzed Reynolds number, the relative error is 8.6% for the suction side of the airfoil and 11.3% for the pressure side. For the Reynolds number equal to 6×10^6, the following results are obtained: 17% for the suction side of the profile and 18.8% for the pressure side. Based on this quantitative analysis, we can clearly see that as the Reynolds number increases, the relative error increases, especially for the pressure side. There are two possible reasons for this increase. One of the reasons may be the high Mach number locally present on the profile surface. In the numerical calculations performed in this work, the Mach number of undisturbed flow was 0.15 for a Reynolds number equal to 3×10^6 and 0.3 for $Re = 6 \times 10^6$ [58]. The second reason that may cause a larger error on the pressure surface of the airfoil is the neglect of the effects that occur in the spanwise direction [15].

Figures 7 and 8 illustrate the validation of the numerical results of static pressure distributions with the experiment. However, due to the very high similarity, these figures do not show the effect of the Reynolds number on the static pressure coefficient characteristics. Figure 9 presents a comparison of C_P characteristics as a function of x/c for four Reynolds numbers: 3×10^6, 4×10^6, 5×10^6, and 6×10^6. As the differences in pressure distributions for the analyzed Reynolds number values are practically invisible at the suction side of the airfoil, only pressure distributions on the pressure side were considered in this analysis. Additionally, since the nature of these functions is similar for all analyzed angles of attack, only the results for one angle of attack equal to 4° are compared. Figure 9 shows the Reynolds number effect at only two locations on the profile. These locations are marked with dashed lines for which other colors have been selected: detail one (magenta) and two (blue). Figure 9c,d show zooms of these details. As shown in Figure 9d, as the Reynolds number increased, a slight pressure increase is observed over the aft part of the airfoil, for $x/c = 0.88$.

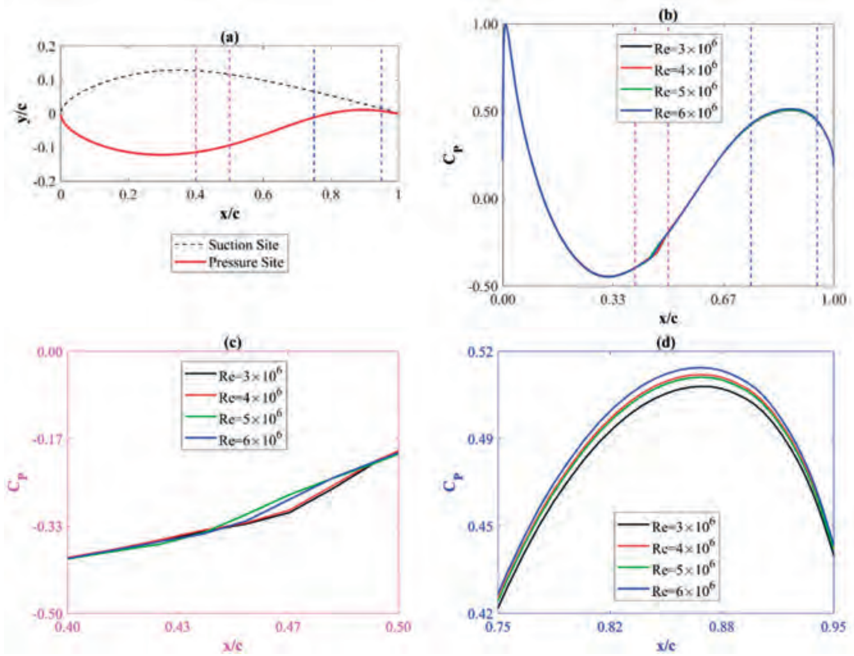

Figure 9. Effect of the Reynolds number on static pressure coefficient characteristics: (**a**) airfoil shape; (**b**) distribution of the static pressure coefficients on the pressure side of the airfoil; (**c**,**d**) details of the static pressure distributions on the pressure side of the airfoil—the details are marked in these figures with the appropriate colors.

From Figures 7 and 8 it can be seen that the static pressure distribution depends primarily on the angle of attack. This was also proved above by analyzing the effect of the Reynolds number on static pressure distributions. Therefore, in this work, the effect of the angle of attack on the static pressure distribution was investigated for only one Reynolds number. Figure 10 presents the static pressure distributions on the airfoil depending on the angle of attack for $Re = 6 \times 10^6$. The obtained results are compared for six different angles of attack ranging from 0 to 10 degrees. The analysis of these curves showed that in the case of the pressure side of the airfoil, the local peak of the $C_P(\mathrm{x/c})$ curve near the leading edge of the profile is observed. This peak has a very similar value equal to approximately 1 for all investigated angles of attack, however, as the angle of attack increases, the peak moves towards the back of the airfoil. The analysis of the location of this peak as a function of the angle of attack showed that this change is not linear but is a second-degree quadratic function with the equation: $(\mathrm{x/c})_{max} = 0.00020{\cdot}\alpha^2 + 0.00118{\cdot}\alpha + 0.0004$.

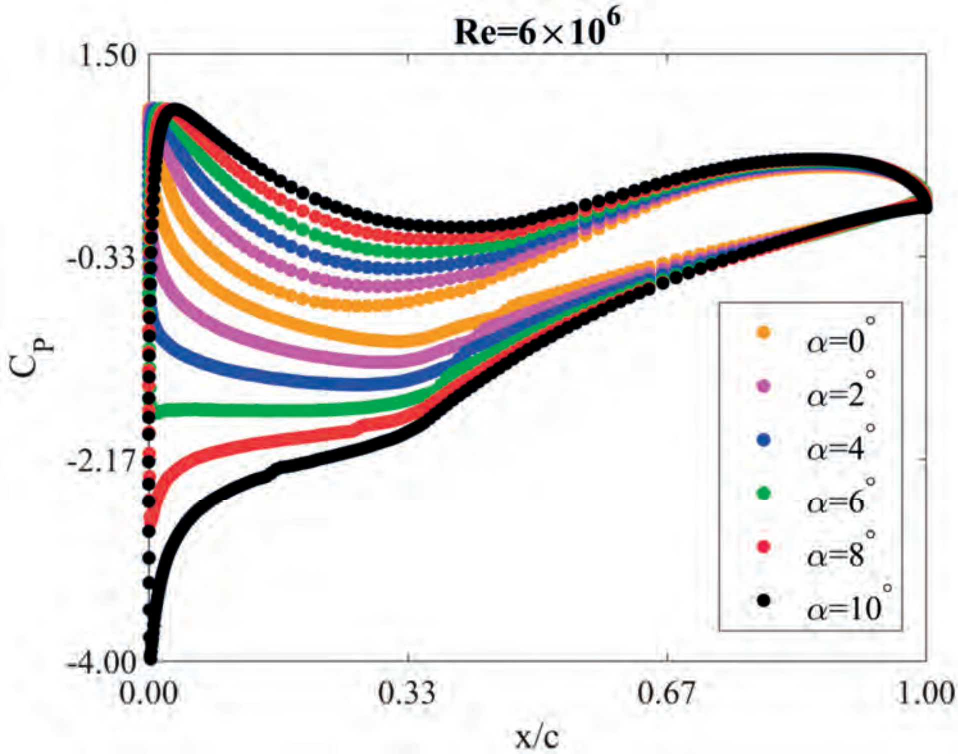

Figure 10. Static pressure coefficient for Reynolds number of 6×10^6. The influence of the angle of attack.

In the case of the suction side of the airfoil, the shape of the $C_P(\mathrm{x/c})$ curve has a slightly different course in two ranges of the angle of attack: up to an angle equal to 6 degrees and above it. Starting at an angle of attack of 6 degrees, a characteristic peak near the leading edge of the airfoil becomes visible on the C_P curve. This peak increases as the angle of attack increases from the value of 1.76 for an angle of attack of 6 degrees to the value of 4 for an angle of attack of 10 degrees. The location of this peak slightly shifts towards the leading edge from the value of $\mathrm{x/c} = 0.0056$ for the angle of attack equal to 6 degrees to the value of 0.0025 for the angle of 10 degrees.

As mentioned at the beginning of this subsection, the nature of the transient flow parameters was also studied in this paper. Since, as already discussed in Section 3 of this paper, the nature of the $\overline{C}_L$ and $\overline{C}_D$ curves is almost constant, therefore the instantaneous static pressure distributions differ very slightly from the averaged distributions illustrated above. In order to study quantitatively the dispersion of the instantaneous distributions from the mean value, the standard deviation (STD) distributions of the pressure coefficients have been calculated. Standard deviation is a parameter that is used much more often to evaluate the scatter of measurement results. However, since the obtained results of C_P

differed very little, it was decided to use this classic measure of variation. The following definition was used to calculate the standard deviation:

$$STD = \sqrt{\frac{1}{N_p} \sum_{i=1}^{N_p} (C_{Pi} - C_P)^2}, \quad (8)$$

where N_p is the number of population samples (in these simulations, the values of $N_p = 33,334$), C_{Pi} is the instantaneous pressure coefficient, and C_P is the averaged pressure coefficient.

As is mentioned in Section 3 of this paper, the mesh that provides an independent numerical solution has 620 nodes on the airfoil surface. In this work, the standard deviation was calculated separately for each node on the airfoil surface and separately for the suction and pressure sides of the airfoil. Standard deviation analysis was performed for two cases: (a) constant Reynolds number and variable angle of attack and (b) constant angle of attack and variable Reynolds number. The investigation showed that the standard deviation is a function of both these quantities. The performed simulations also proved that the obtained values of the standard deviation of the static pressure coefficient are much higher for the suction side of the airfoil compared to the pressure side. Therefore, only the STD distributions for the suction side of the airfoil are discussed in the further part of this paper.

Figure 11a shows a contour map of the standard deviation of the static pressure depending on the Reynolds number and the angle of attack of the airfoil. This figure shows that with the increase in the angle of attack, an increase in the value of STD is observed up to the angle of attack from 2° to 4°, then, the decrease in the value of STD with the angle of attack is observed. The angle at which the STD reaches its maximum depends on the Reynolds number; as the Reynolds number increases, the peak values of the STD function move towards higher angles of attack.

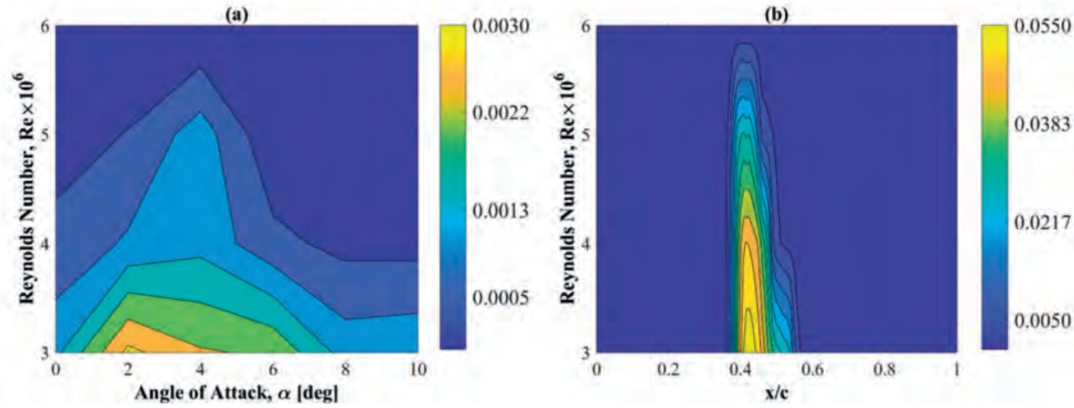

Figure 11. Standard deviation of the static pressure coefficient for the suction side of the airfoil and for the angle of attack of 4 degrees: (**a**) as a function of the angle of attack and Reynolds number; (**b**) as a function of x/c and Reynolds number.

As already mentioned above, the standard deviation of the static pressure coefficients also has a distribution along the airfoil surfaces. Since the character of the STD is the same for all Reynolds numbers taken into account in this paper, case b (constant angle of attack and variable Re value) is considered for one angle of attack. An angle of attack equal to 4 degrees is selected for the analysis, for which the standard deviations reach maximum values. Figure 11b shows a contour map of the standard deviation of the static pressure coefficients in terms of Reynolds number and x/c. The results shown in this figure apply only to the suction side of the airfoil since, as highlighted above, the largest changes in the STD values are observed on this surface. The contour map clearly shows that the maximum values of STD are concentrated in a narrow strip around the position x/c = 0.4. Additionally, it was observed that the width of this strip decreased with increasing Reynolds number. The location of the maximum values of STD is not accidental. It is related to the location of the laminar-turbulent transition.

In general, the values of the standard deviation obtained in all analyzes are minimal. The obtained minimum value of this parameter was 1.9×10^{-5} and the maximum value was 0.003. Low standard deviation values indicate that the values tend to be close to the mean static pressure coefficients.

4.3. Skin Friction Coefficient

The time-averaged skin friction depends on the same factors as static pressure. The formulation of the transition SST approach makes it possible to obtain such a distribution of the skin friction that it is possible to study the laminar-turbulent transition.

In this work, various numerical approaches were used to determine the aerodynamic performance of the DU 91-W2-250 profile. Basically, for three different numeric codes, the same turbulence model was used—the Transition SST approach developed by Langtry and Menter [78]. The other tools were two fully turbulent models and XFOIL code. As the results of both forces, pressures and skin friction distributions obtained by various implementations of the Transition SST approach were very similar, this subsection of the paper was limited only to the analysis of the results obtained using the ANSYS Fluent code together with the URANS method.

In the first part of this subsection, the distributions of the skin friction coefficient for the angle of attack equal to 4 degrees and for two Reynolds numbers 3×10^6 and 6×10^6 obtained with this method were compared only with the results of the XFOIL code and the k-ε RNG turbulence model (Figure 12). As expected, the results obtained with the k-ε RNG turbulence model are of a completely different nature compared to the transition models. This is due to a different formulation of this turbulence model, whereby the entire boundary layer is taken into account as turbulent. Such an assumption, however, causes that the distribution of the skin friction coefficient differs significantly from the real one [35]. The C_f characteristics obtained by the two approaches that take into account the transition effect are similar; in particular, it concerns the Reynolds number equal to 6×10^6. For the Reynolds number of 3×10^6, an overestimated value of the C_f coefficient, computed using the XFOIL code, was observed in comparison with the numerical results obtained using the Transition SST approach. The results of the e^N transition method based on linear stability and implemented in the XFOIL code are dependent on the N-factor, which should be determined by wind tunnel or flight test calibration [35].

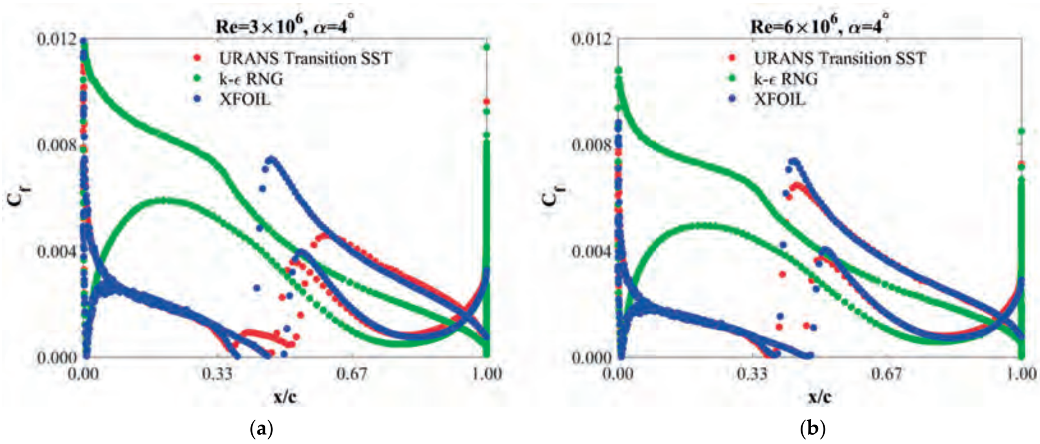

Figure 12. Skin friction coefficient at the angle of attack of 4° for two Reynolds number of 3×10^6 (**a**) and 6×10^6 (**b**). The results are given for three numerical approaches: ANSYS Fluent code together with the URANS method; the k-ε RNG turbulence model; the XFOIL code.

Figure 12 shows the results for both the suction side and the pressure side of the airfoil. As it can be seen from this figure, the values of the C_f coefficient also depend on the airfoil side; this effect will be discussed in detail below.

In this part of the paper, the effects of the Reynolds number and angle of attack on the distributions of the C_f coefficient will be discussed. As mentioned above, the C_f distributions are different on both the suction and the pressure side of the airfoil. In this paper, the obtained results are illustrated separately for both sides of the profile to make these effects more visible.

Characteristics of the C_f coefficient separately for the pressure and the suction side of the airfoil are shown in Figure 13. Since the nature of the graphs obtained in this work is similar for all angles of attack analyzed here, the figure only illustrates the results for the angle of attack of 4 degrees. The characteristics shown in this figure are given for four Reynolds numbers: 3×10^6, 4×10^6, 5×10^6, and 6×10^6. Contrary to the static pressure coefficients (Figure 9), the skin friction coefficient distributions significantly depend on the Reynolds number. However, it should be emphasized that the influence of the Reynolds number is mainly visible on the suction side of the airfoil (Figure 13b). As the Reynolds number increases, the maximum value of the C_f coefficient increases in the middle part of the airfoil, where the laminar-turbulent transition occurs. Moreover, as the Reynolds number increases, the jump in C_f shifts to the leading edge. For the suction side of the airfoil and for the Reynolds number of 6×10^6, the maximum value of the skin friction coefficient C_{fmax} increased by 40.8% compared to the C_{fmax} for $Re = 3 \times 10^6$. At the same time, the maximum value of the C_f coefficient for $Re = 3 \times 10^6$ was located at $x/c = 0.60$ whereas for the $Re = 6 \times 10^6$, the C_{fmax} has shifted towards the leading edge to the value $x/c = 0.44$. For a Reynolds number of 3×10^6, the maximum value of the C_f coefficient for the suction side of the airfoil is 28.1% larger compared to the C_{fmax} for the pressure side. However, for the Reynolds number of 6×10^6, this value increases to 71.1%. The increase of the C_{fmax} with the increase of the Reynolds number is linear on the suction surface of the airfoil.

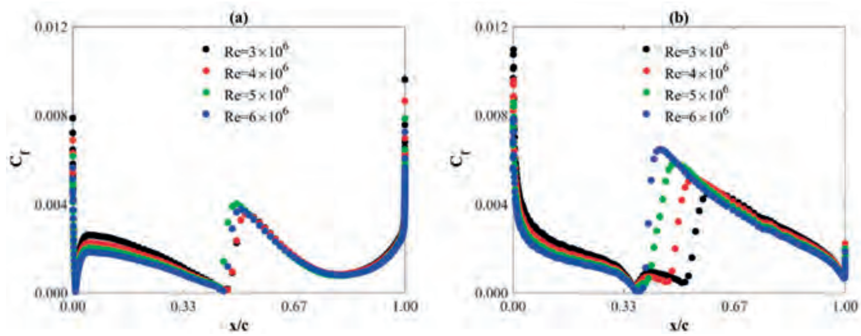

Figure 13. Skin friction coefficient at the angle of attack of 4°—Reynolds number effect for (**a**) the pressure side of the airfoil and (**b**) the suction side of the airfoil. These results are given for URANS with the Transition SST model.

The effect of the Reynolds number on the distribution of the skin friction coefficient is discussed above. The second important factor influencing this physical quantity is the angle of attack. Figure 14 discusses the C_f distributions for two Reynolds numbers and for six angles of attack ranging from 0 to 10 degrees. Additionally, as already stated above, the C_f distributions are different on the suction and pressure side of the airfoil, therefore Figure 14 compares the C_f distributions for both sides of the airfoil separately.

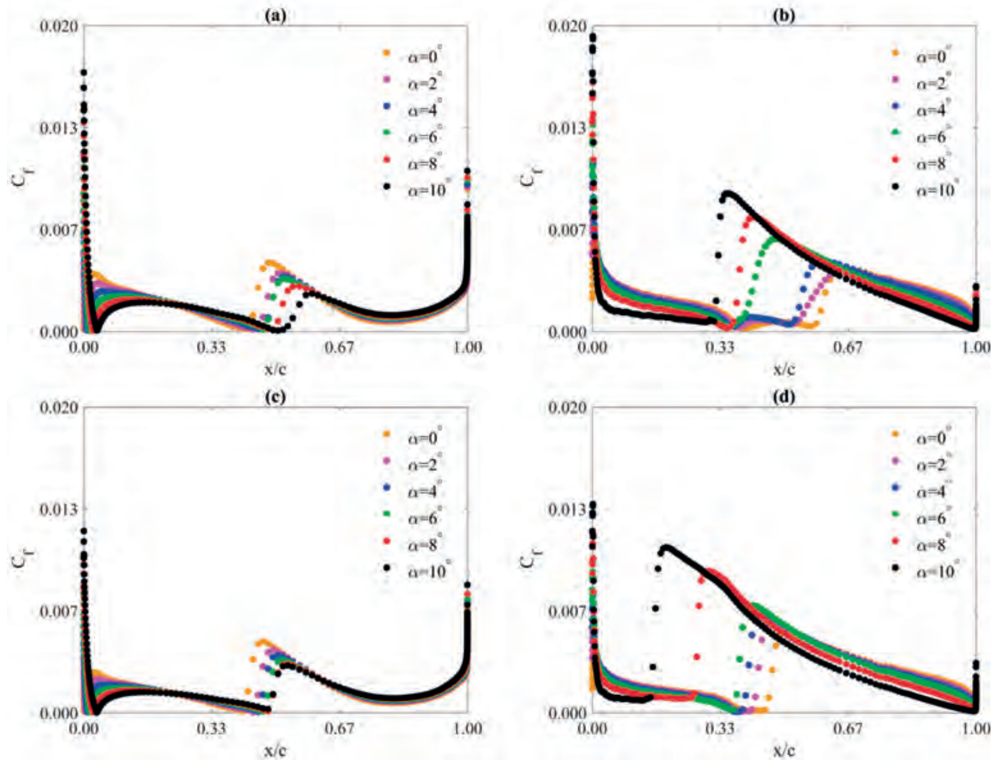

Figure 14. Skin friction coefficient—the effect of the angle of attack for (**a**,**b**) $Re = 3 \times 10^6$ and (**c**,**d**) $Re = 6 \times 10^6$. Moreover, C_f for the pressure side of the airfoil are given in (**a**,**c**), whereas for the suction side of the airfoil are given in (**b**,**d**). These results are given for URANS with the Transition SST model.

As mentioned above and shown in Figure 13, the Reynolds number effect is more visible on the suction side of the airfoil. As shown in Figure 14, this conclusion applies to all Reynolds numbers analyzed in this work. Moreover, as documented in Figure 14, the effect of the angle of attack is also larger on the suction side of the airfoil as compared to the pressure side. The C_f coefficient for both sides of the airfoil differs both in its maximum value and in its x/c location. As the angle of attack increases on the suction side of the airfoil, the maximum value of the C_f coefficient moves towards the leading edge and towards the trailing edge on the pressure side of the airfoil. Moreover, as the angle of attack increases, the C_{fmax} increases on the suction side of the airfoil and decreases on the pressure side. For a Reynolds number equal to 3×10^6, with an angle of attack increment equal to 10 degrees ($\Delta\alpha = 10°$), the absolute value of the $\Delta x/c$ increment corresponding to the C_{fmax} is 0.3126 on the suction surface and 0.1148 on the pressure surface. For a Reynolds number of 6×10^6, the same values are respectively 0.3166 for the suction side and 0.0647 for the pressure side. It can be concluded from this analysis that with the increase of the Reynolds number, the value of the $\Delta x/c$ on the suction side is almost constant and it has been shortened by half on the pressure side. For all the angles of attack analyzed in this paper, on the pressure side of the airfoil, the decrease in the maximum value of the C_f coefficient with the increase in the angle of attack is approximately linear whereas on the suction side of the airfoil, the increase in the maximum value of the C_f coefficient with the increase in the angle of attack is an exponential function.

As in the case of static pressure distributions (Section 4.2 and Figure 11), this work also examined the deviations of the instantaneous values of the skin friction coefficient from the average value (Figure 15). This paper also uses the standard deviation formula

(Equation (8)) to evaluate this deviation. As with the static pressure distributions, the values of the standard deviation for the suction side of the airfoil are much larger than for the pressure side (please see Section 4.2). In the case of the C_f coefficient, the STD results for the suction side of the airfoil are on average 11 times higher compared to the pressure side. The values of the standard deviation of the skin friction coefficient turned out to be small of the higher order and almost 99 times lower compared to the values of the standard deviation calculated for the static pressure coefficients.

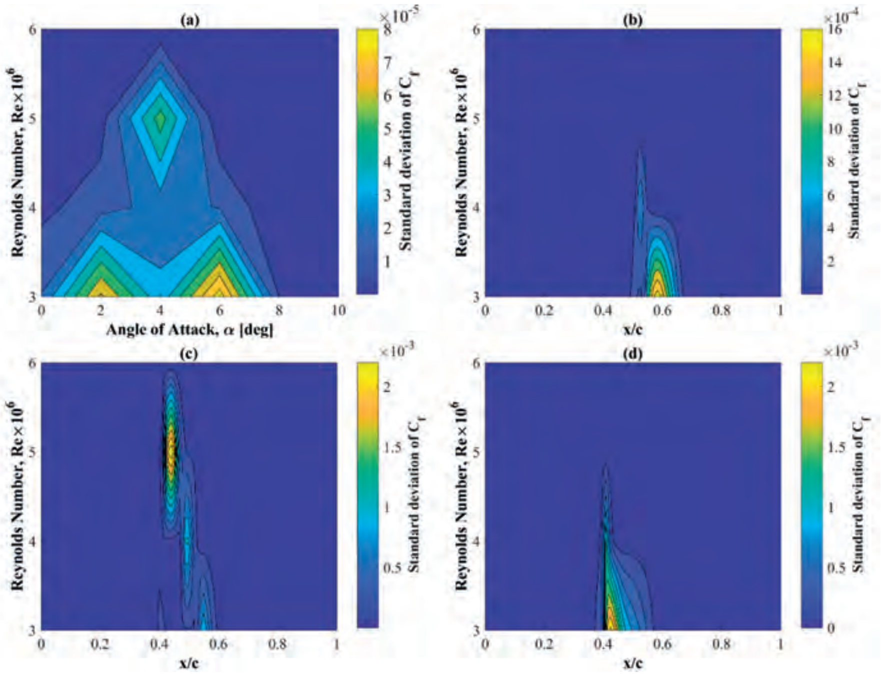

Figure 15. Standard deviation of the skin friction coefficient for the suction side of the airfoil—the effect of the angle of attack and the Reynolds number (**a**); the effect of the Reynolds number and x/c for: $\alpha = 2°$ (**b**); $\alpha = 4°$ (**c**); and $\alpha = 6°$ (**d**).

4.4. Variation of Transition Location with the Angle of Attack

The location of the transition is a very important engineering issue in modern fluid mechanics; however, it is not easy to determine. For the XFOIL code, this position is one of the simulation results. In the case of CFD analyzes, this location can be found on the basis of intermittency, γ. In our CFD studies, however, this position was estimated from the distribution of the skin friction coefficient C_f, discussed in the previous subsection. In order to estimate the transition location X_{tr} the point where the skin friction increases sharply, e.g., as shown in Figure 14, was chosen. This is more consistent with the way the transition is determined experimentally where the intermittency is not known, e.g., using hot film sensors to directly measure the skin friction or a take thermal image of the airfoil surface and see when the heat flux often changes very sharply. Therefore, in this work, to determine this value, a criterion was used, which was established on the basis of the C_f results obtained from the XFOIL approach. It was found that the position of X_{tr} corresponds to an increase of the C_f coefficient by 80% compared to the minimum value.

Figure 16 compares the location X_{tr} of the laminar-turbulent transition predicted by the two analytical approaches and with the experiment. In this work, the analytical approaches used for the comparison are the Transition SST turbulence model implemented in the ANSYS Fluent CFD code and the XFOIL code. All simulations were carried out for the range of angles of attack in the range from 0 to 10 degrees. The authors of this work had only experimental data for the suction side of the airfoil.

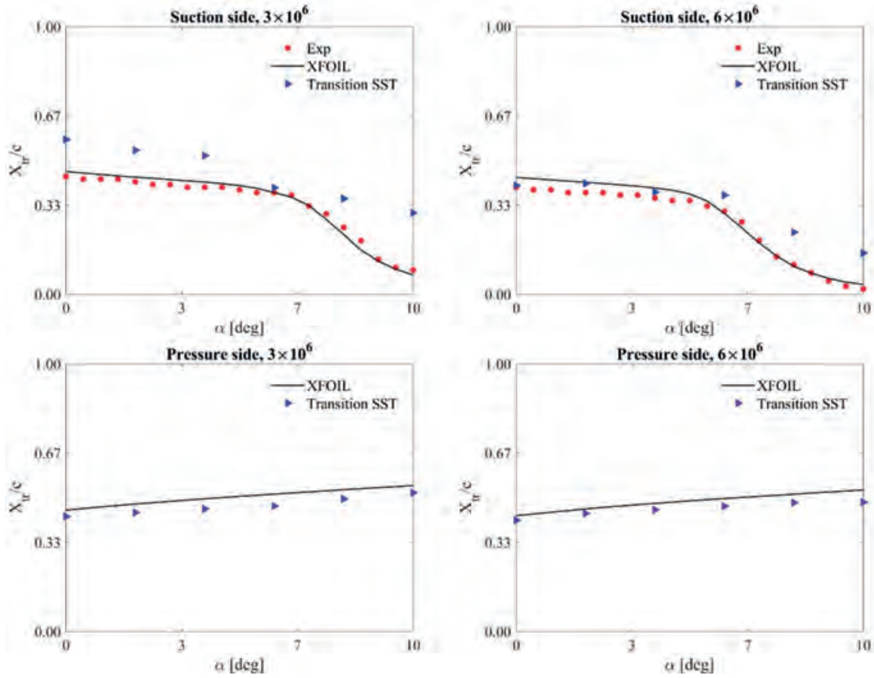

Figure 16. Variation of transition location with the angle of attack for two Reynolds numbers. For the suction side of the airfoil: validation of the Transition SST turbulence model and the XFOIL code using the experimental data; for the pressure side: comparison of the results obtained from CFD and XFOIL simulations.

In Figure 16, it can be seen that two distinct areas are visible on the suction side of the airfoil. The $X_{tr}(\alpha)$ curves shown in this figure have two derivatives: in the range of angles of attack from 0 to 6 degrees for the first area, and in the range of angles of about 6 to 10 degrees for the second area. On the other hand, the relationship of the X_{tr}-coordinate for the pressure side of the profile is almost linear over the entire range of angles of attack taken into account in this paper.

5. Conclusions

The main purpose of the present study is to validate the unsteady Reynolds averaged Navier-Stokes (URANS) approach together with the four-equation transition SST turbulence model with experimental data from a wind tunnel. The main computational fluid dynamics (CFD) code used in this work was ANSYS Fluent v 19.0. For comparison, two more CFD codes with the Transition SST model were used: FLOWer and STAR-CCM +. The obtained airfoil characteristics were also compared with the results of fully turbulent models published in other papers. The XFOIL approach was also used in this work for comparison. Based on the obtained results, it was determined that:

- The aerodynamic characteristics obtained by means of classical turbulence models prove the important role of transition phenomena in the boundary layer.
- For the studied range of Reynolds numbers, the static pressure distributions do not significantly depend on the Reynolds number.
- The angle of attack has a much more significant influence on the pressure around the airfoil.

- Contrary to static pressure distributions, the skin friction coefficient distributions depend on both the angle of attack and the Reynolds number. However, the Reynolds number effect is mainly seen on the suction side of the airfoil. An increase in the Reynolds number causes an increase in the value of this coefficient on the suction edge and its shift towards the leading edge.
- For all the angles of attack analyzed in this study, on the pressure side of the profile, the decrease in the maximum value of the skin friction coefficient with the increase in the angle of attack is almost linear.
- On the suction side of the profile, the increase in the maximum value of the skin friction coefficient with the increase in the angle of attack is an exponential function.
- As with static pressure, the angle of attack has a larger effect on the distribution of the skin friction coefficient than the Reynolds number, but mainly for the suction side of the airfoil.
- With the increase of the angle of attack, the maximum value of the skin friction coefficient increases on the suction side and decreases on the pressure side.
- For the angle of attack range investigated, the maximum values of the skin friction coefficient are larger on the suction side of the airfoil compared to the pressure side. As the Reynolds number increases, the difference is larger.
- The deviations of the instantaneous pressure values from the average value are minimal.
- The maximum values of the standard deviation of the static pressure coefficients are concentrated around the areas of the laminar-turbulent transition.
- The deviations of the instantaneous values of the skin friction coefficients from the averaged values are almost constant in time and close to zero.

Author Contributions: Conceptualization, K.R.; methodology, J.M., K.R., G.B. and M.O.L.H.; software, J.M., K.R., G.B. and M.O.L.H.; validation K.R. and J.M.; numerical analysis, J.M., K.R., G.B. and M.O.L.H.; writing—original draft preparation, K.R.; writing—review and editing, J.M., K.R., G.B. and M.O.L.H.; visualization, J.M. and K.R., supervision, G.B. and M.O.L.H. All authors have read and agreed to the published version of the manuscript.

Funding: This research was carried out with the support of the Interdisciplinary Centre for Mathematical and Computational Modelling ICM) University of Warsaw under computational allocation no GB83-33.

Institutional Review Board Statement: Not applicable.

Informed Consent Statement: Not applicable.

Data Availability Statement: Data sharing not applicable.

Conflicts of Interest: The authors declare no conflict of interest.

Nomenclature

Symbol	
c	chord length
α	angle of attack
L	lift force
D	drag force
$\overline{C}_L$	mean lift coefficient
$\overline{C}_D$	mean drag coefficient
Δt	time step size
V_∞	undisturbed flow velocity
K	lift-to-drag ratio
P	static pressure
P_{ref}	reference static pressure

q_{ref}	reference dynamic pressure
ρ_∞	free stream density
V_∞	free stream velocity
STD	standard deviation
C_f	skin friction coefficient
C_{fmax}	maximum skin friction coefficient
C_P	static pressure coefficient
X_{tr}	location of the laminar-turbulent transition

References

1. Kaldellis, J.K.; Apostolou, D.; Kapsali, M.; Kondili, E. Environmental and social footprint of offshore wind energy. Comparison with onshore counterpart. *Renew. Energy* **2016**, *92*, 543–556. [CrossRef]
2. Loukogeorgaki, E.; Vagiona, D.G.; Vasileiou, M. Site Selection of Hybrid Offshore Wind and Wave Energy Systems in Greece Incorporating Environmental Impact Assessment. *Energies* **2018**, *11*, 2095. [CrossRef]
3. Tescione, G.; Sim~ao Ferreira, C.J.; van Bussel, G.J.W. Analysis of a free vortex wake model for the study of the rotor and near wake flow of a vertical axis wind turbine. *Renew. Energy* **2016**, *87*, 552–563. [CrossRef]
4. *Wind in Our Sails. The Coming of Europe's Offshore Wind Energy Industry*; Technical Report; European Wind Energy Association (EWEA), 2011. Available online: https://tethys.pnnl.gov/publications/wind-our-sails-coming-europes-offshore-wind-energy-industry (accessed on 1 December 2021).
5. Hu, Y.; Yang, J.; Baniotopoulos, C. Study of the Bearing Capacity of Stiffened Tall Offshore Wind Turbine Towers during the Erection Phase. *Energies* **2020**, *13*, 5102. [CrossRef]
6. Castro-Santos, L.; Filgueira-Vizoso, A.; Álvarez-Feal, C.; Carral, L. Influence of Size on the Economic Feasibility of Floating Offshore Wind Farms. *Sustainability* **2018**, *10*, 4484. [CrossRef]
7. Yang, H.; Shen, W.Z.; Xu, H.; Hong, Z.; Liu, C. Prediction of the wind turbine performance by using BEM with airfoil data extracted from CFD. *Renew. Energy* **2014**, *70*, 107–115. [CrossRef]
8. Zidane, I.F.; Swadener, G.; Ma, X.; Shehadeh, M.F.; Salem, M.H.; Saqr, K.M. Performance of a Wind Turbine Blade in Sandstorms Using a CFD-BEM Based Neural Network. *J. Renew. Sustain. Energy* **2020**, *12*, 053310. [CrossRef]
9. Rogowski, K.; Królak, G.; Bangga, G. Numerical Study on the Aerodynamic Characteristics of the NACA 0018 Airfoil at Low Reynolds Number for Darrieus Wind Turbines Using the Transition SST Model. *Processes* **2021**, *9*, 477. [CrossRef]
10. Monteiro, J.P.; Silvestre, M.R.; Piggott, H.; Andre, J.C. Wind tunnel testing of a horizontal axis wind turbine rotor and comparison with simulations from two blade element momentum codes. *J. Wind Eng. Ind. Aerod.* **2013**, *123*, 99–106. [CrossRef]
11. Bai, C.-J.; Wang, W.-C. Review of computational and experimental approaches to analysis of aerodynamic performance in horizontal-axis wind turbines (HAWTs). *Renew. Sustain. Energy Rev.* **2016**, *63*, 506–519. [CrossRef]
12. Rogowski, K.; Maroński, R.; Hansen, M.O.L. Steady and unsteady analysis of NACA 0018 airfoil in vertical-axis wind turbine. *J. Theor. Appl. Mech.* **2018**, *51*, 203–212. [CrossRef]
13. Timmer, W.A. Two-Dimensional Low-Reynolds Number Wind Tunnel Results for Airfoil NACA 0018. *Wind. Eng.* **2008**, *32*, 525–537. [CrossRef]
14. Sanei, M.; Razaghi, R. Numerical investigation of three turbulence simulation models for S809 wind turbine airfoil. *Proc. Inst. Mech. Eng. Part A J. Power Energy* **2018**, *232*, 1037–1048. [CrossRef]
15. Rogowski, K.; Hansen, M.O.L. RANS Simulations of Flow Past an DU-91-W2-250 Airfoil at High Reynolds Number. In Proceedings of the 10th Conference on Interdisciplinary Problems in Environmental Protection and Engineering EKO-DOK, Polanica-Zdrój, Poland, 16–18 April 2018. [CrossRef]
16. Bak, C.; Zahle, F.; Bitsche, R.; Kim, T.; Yde, A.; Henriksen, L.C.; Natarajan, A.; Hansen, M.H. Description of the DTU 10 MW Reference Wind Turbine. DTU Wind Energy Report-I-0092. 2013. Available online: https://orbit.dtu.dk/en/publications/the-dtu-10-mw-reference-wind-turbine (accessed on 1 December 2021).
17. Drela, M. *XFOIL: An Analysis and Design System for Low Reynolds Number Airfoils*; Low Reynolds Number Aerodynamics. Lecture Notes in Engineering; Mueller, T.J., Ed.; Springer: Berlin/Heidelberg, Germany, 1989; Volume 54. [CrossRef]
18. Fontecha, R.; Kemper, F.; Feldmann, M. On the Determination of the Aerodynamic Damping of Wind Turbines Using the Forced Oscillations Method in Wind Tunnel Experiments. *Energies* **2019**, *12*, 2452. [CrossRef]
19. Rogowski, K.; Hansen, M.O.L.; Bangga, G. Performance Analysis of a H-Darrieus Wind Turbine for a Series of 4-Digit NACA Airfoils. *Energies* **2020**, *13*, 3196. [CrossRef]
20. Lichota, P. Multi-Axis Inputs for Identification of a Reconfigurable Fixed-Wing UAV. *Aerospace* **2020**, *7*, 113. [CrossRef]
21. Lichota, P.; Noreña, D.A. A Priori Model Inclusion in the Multisine Maneuver Design. In Proceedings of the 17th International Carpathian Control Conference, High Tatras, Slovakia, 29 May–1 June 2016; pp. 440–445. [CrossRef]
22. Wolfe, W.P.; Ochs, S.S. CFD Calculations of S809 Aerodynamic Characteristics. In Proceedings of the 35th Aerospace Sciences Meeting and Exhibit, AIAA, Reno, NV, USA, 6–9 January 1997.
23. Rogowski, K.; Hansen, M.O.L.; Maroński, R.; Lichota, P. Scale Adaptive Simulation Model for the Darrieus Wind Turbine. *J. Phys. Conf. Ser.* **2016**, *753*, 022050. [CrossRef]

24. Zhong, W.; Tang, H.; Wang, T.; Zhu, C. Accurate RANS Simulation of Wind Turbine Stall by Turbulence Coefficient Calibration. *Appl. Sci.* **2018**, *8*, 1444. [CrossRef]
25. Mo, J.-o.; Rho, B.-s. Characteristics and Effects of Laminar Separation Bubbles on NREL S809 Airfoil Using the γ—R e θ Transition Model. *Appl. Sci.* **2020**, *10*, 6095. [CrossRef]
26. D'Alessandro, V.; Montelpare, S.; Ricci, R. Assessment of a Spalart–Allmaras Model Coupled with Local Correlation Based Transition Approaches for Wind Turbine Airfoils. *Appl. Sci.* **2021**, *11*, 1872. [CrossRef]
27. Kubacki, S.; Simoni, D.; Lengani, D.; Dellacasagrande, M.; Dick, E. Extension of an algebraic intermittency model for better prediction of transition in separated layers under strong free-stream turbulence. *Int. J. Heat Fluid Flow* **2021**, *92*, 108860. [CrossRef]
28. Rezaeiha, A.; Montazeri, H.; Blocken, B. Towards accurate CFD simulations of vertical axis wind turbines at different tip speed ratios and solidities: Guidelines for azimuthal increment, domain size and convergence. *Energy Convers. Manag.* **2018**, *156*, 301–316. [CrossRef]
29. Schlichting, H. *Boundary Layer Theory*, 7th ed.; McGraw-Hill: New York, NY, USA, 1979.
30. Morkovin, M.V. *On the Many Faces of Transition*; Viscous Drag Reduction; Wells, C.S., Ed.; Plenum Press: New York, NY, USA, 1969; pp. 1–31.
31. Mayle, R.E. The role of laminar-turbulent transition in gas turbine engines. *J. Turbomach.* **1991**, *113*, 509–537. [CrossRef]
32. Dick, E.; Kubacki, S. Transition Models for Turbomachinery Boundary Layer Flows: A Review. *Int. J. Turbomach. Propuls. Power* **2017**, *2*, 4. [CrossRef]
33. Liu, G.; Sun, S.; Liang, K.; Yang, X.; An, D.; Wen, Q.; Ren, X. Simulation Study on the Effect of Flue Gas on Flow Field and Rotor Stress in Gas Turbines. *Energies* **2021**, *14*, 6135. [CrossRef]
34. Engelmann, D.; Sinkwitz, M.; di Mare, F.; Koppe, B.; Mailach, R.; Ventosa-Molina, J.; Fröhlich, J.; Schubert, T.; Niehuis, R. Near-Wall Flow in Turbomachinery Cascades—Results of a German Collaborative Project. *Int. J. Turbomach. Propuls. Power* **2021**, *6*, 9. [CrossRef]
35. Langtry, R.B. A Correlation-Based Transition Model Using Local Variables for Unstructured Parallelized CFD Codes. Ph.D. Thesis, University of Stuttgart, Stuttgart, Germany, 2006. [CrossRef]
36. Smith, A.M.O.; Gamberoni, N. *Transition, Pressure Gradient and Stability Theory*; Douglas Aircraft Company, El Segundo Division: Los Angeles, CA, USA, 1956.
37. Van Ingen, J.L. *A Suggested Semi-Empirical Method for the Calculation of the Boundary Layer Transition Region*; Report VTH-74; Department of Aerospace Engineering, Delft University of Technology: Delft, The Netherlands, 1956.
38. Themistokleous, C.; Markatos, N.-G.; Prospathopoulos, J.; Riziotis, V.; Sieros, G.; Papadakis, G. A High-Lift Optimization Methodology for the Design of Leading and Trailing Edges on Morphing Wings. *Appl. Sci.* **2021**, *11*, 2822. [CrossRef]
39. Youngren, H.; Drela, M. Viscous/Inviscid method for preliminary design of transonic cascades. In Proceedings of the 27th Joint Propulsion Conference, Sacramento, CA, USA, 24–26 June 1991.
40. Stock, H.W. e^N Transition prediction in three-dimensional boundary layers on inclined prolate spheroids. *AIAA J.* **2006**, *44*, 108–118. [CrossRef]
41. Menter, F.R.; Langtry, R.B. Transition Modelling for Turbomachinery Flows. In *Low Reynolds Number Aerodynamics and Transition*; Genc, M.S., Ed.; InTech: London, UK, 2012. Available online: http://www.intechopen.com/books/low-reynolds-number-aerodynamics-and-transition/transitionmodelling-for-turbomachinery-flows (accessed on 21 October 2021). ISBN 978-953-51-0492-6.
42. Vlahostergios, Z. Performance Assessment of Reynolds Stress and Eddy Viscosity Models on a Transitional DCA Compressor Blade. *Aerospace* **2018**, *5*, 102. [CrossRef]
43. Timmer, W.A.; van Rooij, R.P.J.O.M. Summary of the Delft University Wind Turbine Dedicated Airfoils. *J. Sol. Energy Eng.* **2003**, *125*, 488–496. [CrossRef]
44. van Rooij, R.P.J.O.M.; Timmer, W.A. Roughness Sensitivity Considerations for Thick Rotor Blade Airfoils. *J. Sol. Energy Eng.* **2003**, *125*, 468–478. [CrossRef]
45. Ahmed, R.M. Blade sections for wind turbine and tidal current turbine applications—Current status and future challenges. *Int. J. Energy Res.* **2012**, *36*, 829–844. [CrossRef]
46. Schubel, P.J.; Crossley, R.J. Wind Turbine Blade Design. *Energies* **2012**, *5*, 3425–3449. [CrossRef]
47. Baldacchino, D.; Manolesos, M.; Ferreira, C.; González Salcedo, Á.; Aparicio, M.; Chaviaropoulos, T.; Diakakis, K.; Florentie, L.; García, N.G.; Papadakis, G.; et al. Experimental benchmark and code validation for airfoils equipped with passive vortex generators. *J. Phys. Conf. Ser.* **2016**, *753*, 022002. [CrossRef]
48. Velte, C.M.; Hansen, M.O.L.; Meyer, K.E. Evaluation of the Performance of Vortex Generators on the DU 91-W2-250 Profile using Stereoscopic PIV. In Proceedings of the WMSCI 2008: 12th World Multi-Conference on Systemics, Cybernetics and Informatics, Orlando, FL, USA, 29 June–2 July 2008; Volume 2, pp. 263–267.
49. Bak, C.; Gaunaa, M.; Olsen, A.S.; Kruse, E.K. What is the critical height of leading edge roughness for aerodynamics? *J. Phys. Conf. Ser.* **2016**, *753*, 022023. [CrossRef]
50. Langel, C.M. A Transport Equation Approach to Modeling the Influence of Surface Roughness on Boundary Layer Transition. Master's Thesis, University of California, Albuquerque, NM, USA, 2014.
51. Ren, N.; Ou, J. Numerical Simulation of Surface Roughness Effect on Wind Turbine Thick Airfoils. In Proceedings of the 2009 Asia-Pacific Power and Energy Engineering Conference, Wuhan, China, 27–31 March 2009; pp. 1–4. [CrossRef]

52. Langtry, R.B.; Gola, J.; Menter, F.R. Predicting 2D Airfoil and 3D Wind Turbine Rotor Performance using a Transition Model for General CFD Codes. In Proceedings of the 44th AIAA Aerospace Sciences Meeting and Exhibit, Reno, NV, USA, 9–12 January 2006; AIAA 2006-395.
53. Xu, H.; Shen, W.; Zhu, W.; Yang, H.; Liu, C. Aerodynamic Analysis of Trailing Edge Enlarged Wind Turbine Airfoils. *J. Phys. Conf. Ser.* **2014**, *524*, 012010. [CrossRef]
54. Bangga, G.; Lutz, T.; Schwarz, E.; Krämer, E. CFD studies on rotational augmentation at the inboard sections of a 10 MW wind turbine rotor. *Renew. Sust. Energ. Rev.* **2017**, *9*, 023304. [CrossRef]
55. Zhang, Y.; Sun, Z.; van Zuijlen, A.; van Bussel, G. Numerical simulation of transitional flow on a wind turbine airfoil with RANS-based transition model. *J. Turbul.* **2017**, *18*, 879–898. [CrossRef]
56. Bangga, G.; Kusumadewi, T.; Hutomo, G.; Sabila, A.; Syawitri, T.; Setiadi, H.; Faisa, M.; Wiranegara, R.; Hendranata, Y.; Lastomo, D.; et al. Improving a two-equation eddy-viscosity turbulence model to predict the aerodynamic performance of thick wind turbine airfoils. *J. Phys. Conf. Ser.* **2018**, *974*, 012019. [CrossRef]
57. Bangga, G.; Lutz, T.; Krämer, E. Active separation control on a very thick wind turbine airfoil—A URANS and DDES perspective. *J. Phys. Conf. Ser.* **2018**, *1037*, 022025. [CrossRef]
58. Rogowski, K.; Hansen, M.O.L.; Hansen, R.; Piechna, J.; Lichota, P. Detached Eddy Simulation Model for the DU-91-W2-250 Airfoil. *J. Phys. Conf. Ser.* **2018**, *1037*, 022019. [CrossRef]
59. Chillon, S.; Uriarte-Uriarte, A.; Aramendia, I.; Martínez-Filgueira, P.; Fernandez-Gamiz, U.; Ibarra-Udaeta, I. jBAY Modeling of Vane-Type Vortex Generators and Study on Airfoil Aerodynamic Performance. *Energies* **2020**, *13*, 2423. [CrossRef]
60. Campobasso, M.S.; Castorrini, A.; Cappugi, L.; Bonfiglioli, A. Experimentally validated three-dimensional computational aerodynamics of wind turbine blade sections featuring leading edge erosion cavities. *Wind. Energy* **2021**, 1–22. [CrossRef]
61. Cao, N. Effects of Turbulence Intensity and Integral Length Scale on an Asymmetric Airfoil at Low Reynolds Numbers. Master's Thesis, University of Windsor, Windsor, ON, USA, 2010.
62. Butler, R.J.; Byerley, A.R.; VanTreuren, K.; Baughn, J.W. The effect of turbulence intensity and length scale on low-pressure turbine blade aerodynamics. *Int. J. Heat Fluid Flow* **2001**, *22*, 123–133. [CrossRef]
63. Menter, F.R.; Smirnov, P.E.; Liu, T.A. One-Equation Local Correlation-Based Transition Model. *Flow Turbul. Combust.* **2015**, *95*, 583–619. [CrossRef]
64. Wang, H.; Ding, J.; Ma, G.; Li, S. Aerodynamic simulation of wind turbine blade airfoil with different turbulence models. *J. Vibroeng.* **2014**, *16*, 2474–2483.
65. Gupta, M.K.; Subbarao, P.M.V. Development of a semi-analytical model to select a suitable airfoil section for blades of horizontal axis hydrokinetic turbine. In Proceedings of the 6th International Conference on Energy and Environment Research, ICEER 2019, Aveiro, Portugal, 22–25 July 2019; Energy Reports 6, 2020; University of Aveiro: Aveiro, Portugal, 2019; pp. 32–37. [CrossRef]
66. Kruse, E.K.; Sorensen, N.N.; Bak, C. A twodimensional quantitative parametric investigation of simplified surface imperfections on the aerodynamic characteristics of a NACA 633 418 airfoil. *Wind. Energy* **2021**, *24*, 310–322. [CrossRef]
67. ANSYS Fluent Theory Guide Version 19. Available online: https://www.ansys.com/products/fluids/ansys-fluent (accessed on 1 December 2021).
68. Thomas, J.L.; Salas, M.D. Far-field boundary conditions for transonic lifting solutions to the Euler equations. *AIAA J.* **1986**, *24*, 1074–1080. [CrossRef]
69. Wang, H.; Zhang, B.; Qiu, Q.; Xu, X. Flow control on the NREL S809 wind turbine airfoil using vortex generators. *Energy* **2017**, *118*, 1210–1221. [CrossRef]
70. Lu, S.; Liu, J.; Hekkenberg, R. Mesh Properties for RANS Simulations of Airfoil-Shaped Profiles: A Case Study of Rudder Hydrodynamics. *J. Mar. Sci. Eng.* **2021**, *9*, 1062. [CrossRef]
71. Menter, F.R.; Langtry, R.; Völker, S. Transition Modelling for General Purpose CFD Codes. *Flow Turbul. Combust.* **2006**, *77*, 277–303. [CrossRef]
72. Şahin, I.; Acir, A. Numerical and Experimental Investigations of Lift and Drag Performances of NACA 0015 Wind Turbine Airfoil. *Int. J. Mater. Mech. Manuf.* **2015**, *3*, 22–25. [CrossRef]
73. Xiao, S.; Chen, Z. Investigation of Flow over the Airfoil NACA 0010-35 with Various Angle of Attack. In Proceedings of the MATEC Web of Conferences 179, 03020, Wuhan, China, 10–13 May 2018. [CrossRef]
74. Ockfen, A.E.; Matveev, K.I. Aerodynamic characteristics of NACA 4412 airfoil section with flap in extreme ground effect. *Int. J. Nav. Archit* **2009**, *1*, 1–12. [CrossRef]
75. Aftab, S.M.A.; Mohd Rafie, A.S.; Razak, N.A.; Ahmad, K.A. Turbulence Model Selection for Low Reynolds Number Flows. *PLoS ONE* **2016**, *11*, e0153755. [CrossRef] [PubMed]
76. Abdul Hamid, M.; Toufique Hasan, A.B.M.; Alimuzzaman, S.M.; Matsuo, S.; Setoguchi, T. Compressible flow characteristics around a biconvex arc airfoil in a channel. *Propuls. Power Res.* **2014**, *3*, 29–40. [CrossRef]
77. Jansson, L.; Lövmark, J. An Investigation of the Dynamic Characteristics of a Tilting Disc Check Valve Using CFD Analyses. Master's Thesis, Chalmers University of Technology, Göteborg, Sweden, 2013.
78. Menter, F.R.; Langtry, R.B.; Likki, S.R.; Suzen, Y.B.; Huang, P.G.; Völker, S. A correlationbased transition model using local variables—part I: Model formulation. *J. Turbomach.* **2006**, *128*, 413–422. [CrossRef]
79. Langtry, R.B.; Menter, F.R.; Likki, S.R.; Suzen, Y.B.; Huang, P.G.; Völker, S. A correlation based transition model using local variables—part II: Test cases and industrial applications. *J. Turbomach.* **2006**, *128*, 423–434. [CrossRef]

80. Wang, S.; Ingham, D.B.; Ma, L.; Pourkashanian, M.; Tao, Z. Turbulence modeling of deep dynamic stall at relatively low Reynolds number. *J. Fluids Struct.* **2012**, *33*, 191–209. [CrossRef]
81. Morgado, J.; Vizinho, R.; Silvestre, M.A.R.; Páscoa, J.C. XFOIL vs. CFD performance predictions for high lift low Reynoldsnumber airfoils. *Aerosp. Sci. Technol.* **2016**, *52*, 207–214. [CrossRef]
82. Drela, M.; Giles, M. Viscous-Inviscid Analysis of Transonic and Low Reynolds Number Airfoils. *AIAA J.* **1987**, *25*, 1347–1355. [CrossRef]
83. Nieroba, W. Application of the k-ε Turbulence Model in the Analysis of the Flow over DU 91-W2-250 Airfoil. Bachelor's Thesis, Warsaw University of Technology, Faculty of Power and Aeronautical Engineering, Warsaw, Poland, 2019.
84. Królak, G. k-ω Turbulence Model for the DU 91-W2-250 Airfoil at High Reynolds Number. Bachelor's Thesis, Warsaw University of Technology, Faculty of Power and Aeronautical Engineering, Warsaw, Poland, 2019.
85. Munson, B.R.; Young, D.F.; Okiishi, T.H. *Introduction to Fluid Mechanics*, 5th ed.; John Wiley & Sons: Hoboken, NJ, USA, 2005.

processes

Article

Numerical Study of the Effect of the Reynolds Number and the Turbulence Intensity on the Performance of the NACA 0018 Airfoil at the Low Reynolds Number Regime

Jan Michna and **Krzysztof Rogowski** *

Institute of Aeronautics and Applied Mechanics, Warsaw University of Technology, 00-665 Warsaw, Poland; jan.michna.dokt@pw.edu.pl

* Correspondence: krogowski@meil.pw.edu.pl; Tel.: +48-506-193-919

Abstract: In recent years, there has been an increased interest in the old NACA four-digit series when designing wind turbines or small aircraft. One of the airfoils frequently used for this purpose is the NACA 0018 profile. However, since 1933, for over 70 years, almost no new experimental studies of this profile have been carried out to investigate its performance in the regime of small and medium Reynolds numbers as well as for various turbulence parameters. This paper discusses the effect of the Reynolds number and the turbulence intensity on the lift and drag coefficients of the NACA 0018 airfoil under the low Reynolds number regime. The research was carried out for the range of Reynolds numbers from 50,000 to 200,000 and for the range of turbulence intensity on the airfoil from 0.01% to 0.5%. Moreover, the tests were carried out for the range of angles of attack from 0 to 10 degrees. The uncalibrated $\gamma - Re_\theta$ transition turbulence model was used for the analysis. Our research has shown that airfoil performance is largely dependent on the Reynolds number and less on the turbulence intensity. For this range of Reynolds numbers, the characteristic of the lift coefficient is not linear and cannot be analyzed using a single aerodynamic derivative as for large Reynolds numbers. The largest differences in both aerodynamic coefficients are observed for the Reynolds number of 50,000.

Keywords: computational fluid dynamics; Reynolds-averaged Navier–Stokes; unsteady; turbulent; aerodynamic; airfoil; NACA 0018; lift force; drag force; vertical axis wind turbine

Citation: Michna, J.; Rogowski, K. Numerical Study of the Effect of the Reynolds Number and the Turbulence Intensity on the Performance of the NACA 0018 Airfoil at the Low Reynolds Number Regime. *Processes* **2022**, *10*, 1004. https://doi.org/10.3390/pr10051004

Academic Editor: Li Xi

Received: 6 May 2022
Accepted: 16 May 2022
Published: 18 May 2022

1. Introduction

Nowadays, computational fluid dynamics (CFD) methods are still not fast enough and sufficiently precise in terms of large angles of attack to completely replace simplified engineering methods based on the principle of conservation of momentum used to simulate the movement of micro-air vehicles, high-altitude unmanned air vehicles, or rotors of wind turbines [1–5]. The accuracy of the results of the aerodynamic characteristics of both aircraft and rotors obtained by these engineering methods depends largely on the airfoil characteristics [6]. These airfoil characteristics, in the form of the coefficients of the aerodynamic forces as a function of the angle of attack, constitute the input data for the engineering methods [7–11]. In recent years, there has been an increased interest in small aircraft and small wind turbines [12–17]. From the point of view of simplified approaches, a significant problem is the working conditions in which these devices must operate. One of the key quantities determining these working conditions is the Reynolds number and turbulence. The Reynolds number experienced by the airfoils of small wind turbines or UAVs can range from tens of thousands to several hundred thousand [18–22]. Therefore, these are not conditions encountered in traditional aviation. However, in the case of turbulence, the problem is the different turbulence intensity values found in wind tunnels and real operating conditions. Generally, a value of less than 1% is considered to be of low turbulence intensity, while a value of more than 10% is considered to be of high turbulence intensity. In the case of modern low turbulence wind tunnels, the turbulence intensity of undisturbed flow can be even less than 0.05% [23,24]. The turbulence intensity measured in the atmosphere is usually from a few to several dozen percent [25,26]. The aerodynamics of a vertical axis wind turbine rotor (Figure 1) is even more complicated as its blades constantly operate under varying flow conditions. As the rotor rotates, the angle of attack of the airfoil changes, and thus the local Reynolds number also changes constantly [27–31]. During the operation of the rotor of the Darrieus wind turbine, the rotor blade works with variable turbulence intensities [32]. This is due to the slowdown and disturbance of the airflow by a blade moving in the upwind part of the rotor. In the downwind part of the rotor, the blade already works in a sometimes highly disturbed flow.

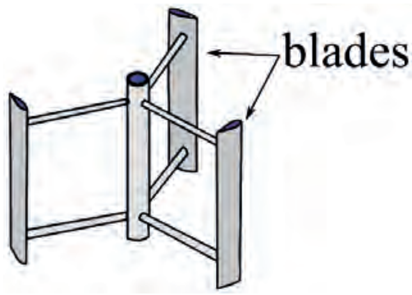

Figure 1. Silhouette of the H-type Darrieus wind turbine.

In the previous work, Rogowski et al. [6] studied the aerodynamic characteristics of the NACA0018 airfoil operating at the low Reynolds number regime ($Re = 160 \times 10^3$) and at very low inlet turbulence intensity corresponding to a very clean flow. These authors used the uncalibrated Transition SST approach implemented in the ANSYS Fluent CFD solver. This paper discusses the performance of this profile considering Reynolds numbers from 50,000 to 200,000 and turbulence intensities at the airfoil ranging from 0.01% to 0.5%. The numerical results of the aerodynamic force coefficients of the symmetrical NACA 0018 airfoil shown in this paper are primarily intended to serve as input data for analytical approaches dedicated to Darrieus wind turbine rotors [7,33].

The result of the work of the American agency NACA (National Advisory Committee for Aeronautics) was the preparation of Technical Report No. 460 "The Characteristics of 78 Related Airfoil Sections from Tests in the Variable-Density Wind Tunnel" [34]. It presents a new family of four-digit airfoils intended to operate in the high Reynolds number regime. Researchers found that the airfoil performance is most influenced by three parameters: the maximum camber, the location of the maximum camber, and the maximum thickness of the airfoil. The *NACA abcd* profile designation contains information on these three parameters: the first digit *a* denotes the maximum camber as a percentage of the chord, the second digit *b* indicates the distance from the leading edge to the maximum camber in tenths of the chord, whereas the last two digits *cd* describe the maximum thickness of the profile as a percent of the chord [35]. For example, in the case of the NACA 0018 profile, the maximum camber is 0%, and the maximum thickness is 18%. The airfoil's maximum thickness is located at 30% of the chord length from the leading edge. The airfoil shape is described using a mathematical formula available in many scientific publications, e.g., [36,37]. Even though the NACA 0018 airfoil was designed relatively long ago, it is still prevalent in VAWT design because of the balance between structural integrity and aerodynamic efficiency [24,38].

The famous Report No. 460 from 1933 published the NACA 0018 profile characteristics for a Reynolds number of 3,200,000 [34]. However, these results by the American agency NACA are not helpful as inputs for engineering models developed to find the aerodynamic characteristics of Darrieus wind turbines because the blade Reynolds numbers of even the largest wind turbines of this type are much lower [39,40]. More valuable characteristics can be found in Report No. 568 published in 1937, which presents the NACA 0018 airfoil performance measured for the Reynolds number regime from 40,000 to 3,000,000 [41]. The characteristics of the lift coefficients presented in this report show some, though slight, dependence on the Reynolds number. A much more significant effect of the Reynolds number was observed for the drag coefficient. In the case of the largest Reynolds numbers analyzed by these authors (2.97×10^6 and 2.36×10^6), an almost independence of the lift coefficients from the Reynolds number in the linear part of the $C_L(\alpha)$ curve is observed, and a slight influence of the Reynolds number on the drag coefficient [41]. A similar trend of the C_L characteristics for the NACA 0009 airfoil for Reynolds numbers in the range of 3×10^6 to 6×10^6 can be found in the well-known report "Summary of Airfoil Data" from 1945 [42]. Even though the Jacobs and Sherman results are more useful for VAWTs because of the low Reynolds numbers [41]. Unfortunately, the range of angles of attack considered in this experiment is insufficient to calculate the performance of a Darrieus rotor operating at low tip speed ratios. For this reason, as part of the program on the Darrieus vertical axis wind turbine (VAWT) at Sandia National Laboratories, a series of measurements in the wind tunnel for four airfoil sections: NACA-0009, -0012, -0012H, and -0015 were carried out at low Reynolds numbers. These obtained experimental data of the airfoil sections were then extrapolated for the Reynolds number range from 10^4 to 10^7, and for the NACA-0018, -0021 and -0025 airfoil sections [7,43]. For many years, researchers and engineers have used this database to analyze and design vertical axis wind turbines [44–48]. However, since these NACA 0018 airfoil characteristics obtained by Sheldahl and Klimas were extrapolated (not measured directly), until the beginning of this century, only measurement data published by Jacobs and Sherman in 1937 were available. Of course, there are sometimes individual studies, e.g., [27], of this airfoil in the literature, but they are not carried out for a wide range of flow parameters. Only in the last two decades, as a result of increased interest in vertical-axis wind turbines, several experimental studies of the NACA 0018 profile were carried out [24,49–56]. The relatively late appearance of a new measurement series for the NACA 0018 airfoil for a long time retained the possibility of validating the aerodynamic characteristics calculated using modern analytical tools offering the possibility of capturing transition phenomena. In 2019, Melani et al. [57] published an important paper summarizing the collected results of experimental and numerical studies of this airfoil for low and medium Reynolds numbers. A juxtaposition of the results of various researchers shows significant differences in the lift characteristics for Reynolds numbers below 300,000. This is due to, among other things, the sensitivity to the flow conditions in the wind tunnel. Timmer concluded that the characteristics published in 1937 by Jacobs and Sherman might be affected by errors resulting from the high level of turbulence in the wind tunnel, which may significantly affect the transition characteristics [24,41]. Research by Melani et al. [57] also shows that the $\gamma - Re_\theta$ turbulence model provides sufficiently accurate aerodynamic characteristics for the NACA 0018 airfoil. As mentioned above, in the case of medium and high Reynolds numbers, its influence on the airfoil performance is not so significant, which is also confirmed by the observations of Melani et al. [57], and sufficient accuracy of the results may also be ensured by, e.g., the popular two-equation k-ω SST turbulence model [20]. In addition to the dependence of the airfoil characteristics on the angle of attack and the Reynolds number, a dependence on the freestream turbulence intensity is also necessary to find the reliable aerodynamic performance of the VAWTs [58]. This is evidenced by some recent precise experimental and numerical studies [53,59]. However, the literature still lacks the NACA 0018 airfoil characteristics calculated with the uncalibrated $\gamma - Re_\theta$ model for a wide range of different flow parameters to serve as a benchmark for further investigations.

As discussed in the first paragraph of this section, the accuracy of engineering approaches for vertical axis wind turbines depends, inter alia, on the accuracy of the input data of the airfoil characteristics. In aerospace engineering and wind energy, numerical techniques are very often used in parametric studies of airfoils. It is believed that solving the Navier–Stokes (NS) equations will provide information on all turbulence scales in the flow, making it possible to study all the aerodynamic phenomena in a given flow. The

Direct Numerical Simulation (DNS) method used, among other things, by Marxen et al. [60] to study the flow over a flat plate allowed a more detailed analysis of the separation-induced transition phenomenon. Another slightly less numerically expensive technique is an approach called large eddy simulation (LES). In the 1960s, this method was proposed to simulate atmospheric flows. With the increase in computing power of supercomputers, this approach has become very attractive and promising for simulating turbulent flows [61–63]. From an engineering point of view, both of these methods, DNS and LES, are still numerically too expensive to simulate the wall-bounded flows. In aerospace engineering, Reynolds-averaged Navier–Stokes (RANS) techniques together with one- or two-equation turbulence models are still common [64]. However, numerous studies have shown that classical turbulence models fail for small Reynolds numbers [28,57]. In order to avoid these shortcomings, in recent years, RANS techniques have been developed to capture the separation-induced transition. The $\kappa - \kappa_L - \omega$ [65,66] and $\gamma - Re_\theta$ [67] models are some of the better-known turbulence models available in many modern CFD codes, e.g., [23]. These turbulence models have been successfully validated against standard test cases [65,68]. Suluksna and Juntasaro showed that the predictive reliability of the $\gamma - Re_\theta$ model was better compared to other correlation-based models [69]. Choudhry and Arjomandi compared these transition models for the NACA 0021 airfoil operating in the small Reynolds number regime [70]. In the conclusions, these authors indicated a slightly higher accuracy of the $\kappa - \kappa_L - \omega$ turbulence model in comparison with the $\gamma - Re_\theta$ model. In recent years, a comparison of five turbulence models has also been made by Aftab et al. [71] for the flow around the NACA 4415 airfoil at a Reynolds number of 120,000. They compared the following approaches: the one-equation Spalart–Allmaras, the two-equation SST k-ω, the SST k-ω with the intermittency equation, the $\kappa - \kappa_L - \omega$, and the $\gamma - Re_\theta$. In the conclusions, the authors indicated reliable results of the aerodynamic force coefficients of both transition models. However, they reported problems with the computation time for the $\kappa - \kappa_L - \omega$ model and problems with the accurate capture of the reattachment of the flow for a moderate angle of attack equal to 6 degrees [71]. The CFD-based transition modeling approaches mentioned in this section are not the only ones available on the market. It is also worth mentioning that there are relatively fast analytical tools, such as XFOIL developed by Drela or RFOIL [24], modified versions of the well-known XFOIL code, which are relatively good at determining aerodynamic profile characteristics, taking into account the phenomena related to laminar-turbulent transition. However, these approaches are challenging to implement in modern CFD codes [67]. It should be added that they can be an additional comparative tool for profile performance studies [6,72].

Given the differing opinions on the robustness of the $\kappa - \kappa_L - \omega$ approach, the authors of this paper aim to thoroughly investigate the $\gamma - Re_\theta$ turbulence model available in the ANSYS Fluent CFD code called Transition SST without correcting the default constants of the model [23]. The intention of the authors is, among other things, to provide guidelines for users of this commonly used CFD code as well as for users of other CFD codes with an implementation of the $\gamma - Re_\theta$ turbulence model and, in addition, to obtain a database for further comparisons.

2. Numerical Model and Its Validation

Rogowski et al. [6] analyzed the well-known NACA 0018 airfoil for only a Reynolds number of 160,000. This was a direct result of the operating conditions of the vertical-axis wind turbine analyzed at TU Delft [73]. Moreover, in the previous work, the two-dimensional airfoil section with chord length c of 1 m was analyzed in a very clean flow—the turbulence intensity was assumed to be 0.05%, which corresponded to the flow conditions in the experiment of Timmer at TU Delft [24]. This paper aims to estimate the aerodynamic performance of the NACA 0018 airfoil at different values of turbulence intensity in undisturbed flow and at different Reynolds numbers.

2.1. Numerical Domain and CFD Solver Settings

As shown in Figure 2, simulations were performed using a C-mesh surrounding the NACA 0018 profile and extending 7.5 c from the semicircular edge of the domain and 15 c from the vertical edge of the domain. The size of the computational domain is vital for the results of the aerodynamic forces. Therefore, this effect will be discussed in Section 2.2 of this paper. The "pressure outlet" boundary condition was assumed on the vertical edge of the domain and the "velocity inlet" boundary condition on the remaining outer edges of the computational domain. The airfoil surfaces are treated as no-slip walls—zero velocity was ensured on the airfoil surfaces.

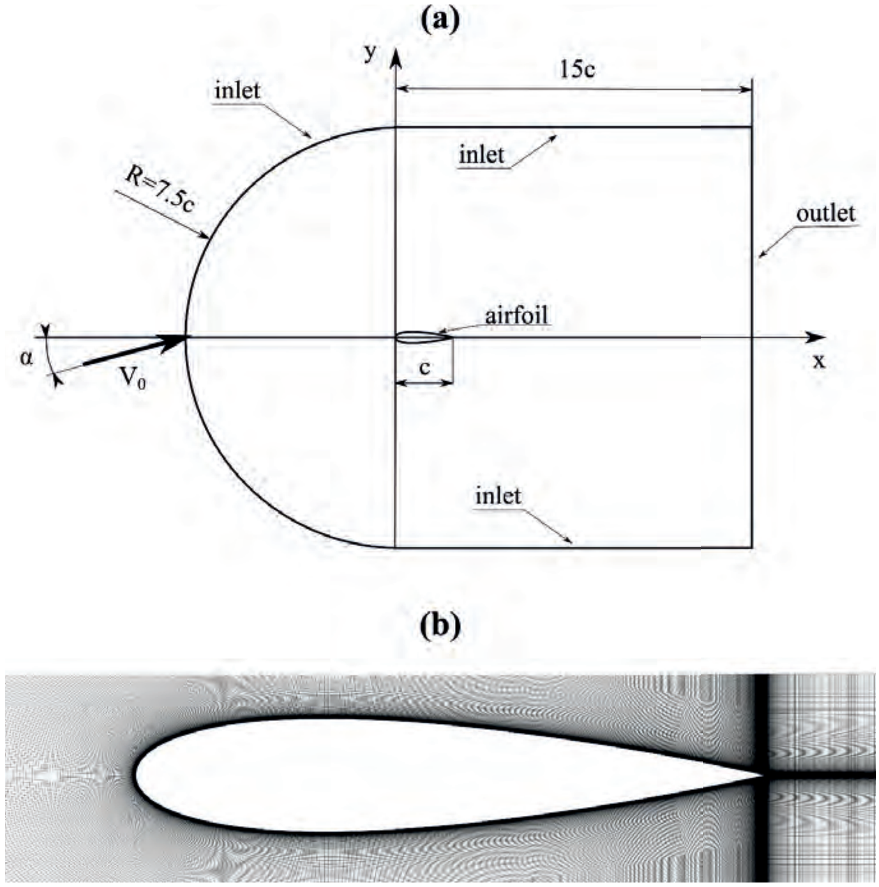

Figure 2. Computational domain (**a**) and mesh around the airfoil (**b**).

The two-dimensional, incompressible governing equations are considered in all analyzes presented in this paper. The unsteady Reynolds-averaged Navier–Stokes (URANS) approach with the SIMPLE pressure velocity coupling scheme and second-order discretization for all variables were employed. Moreover, in all simulations presented herein, the Green–Gauss node-based method was employed [74]. The flow over the NACA 0018 profile was investigated using the commercial computational fluid dynamics (CFD) code ANSYS Fluent 19.1 [23].

In this work, the transient flow around a symmetrical airfoil is discussed. The effect of such simulations are, among others, oscillations of aerodynamic forces that result from pressure changes around the airfoil. Observing these transient changes in the airfoil's aerodynamic characteristics is possible if the time step size is sufficiently small, adapted to the observed physical phenomena occurring during the flow around the airfoil. As shown in the previous research [6], setting even a very small time step size does not give significant changes in the characteristics of the aerodynamic force coefficients. Of course, the oscillation size depends on the angle of attack. As the angle grows, the oscillations become larger and larger. However, even in the case of the largest analyzed angle of attack, equal to 10 degrees, the deviation of the instantaneous values of the aerodynamic force components from the average was not too large. This means that the flow is almost without separation for angles of attack up to 10 degrees. It also means that the instantaneous pressure coefficient distributions resemble those calculated with the Reynolds-averaged Navier–Stokes (RANS) technique. Based on the previous research, in all of the results presented in this paper, the time step size was assumed to be 0.0001 s. For the transient solution using the implicit formulation, ANSYS Fluent CFD code requires multiple iterations to be specified at each time step. In this work, the convergence of every time step solution was usually achieved at approximately 10–15 iterations, with a declaration of 20 maximum iterations per time step. The level of residuals of 10^{-6} was used for all computed variables.

An important problem in time-dependent analysis is the effect of initial conditions. In the initial phase of the simulation, the oscillations of the aerodynamic forces are significant, and the values of these forces differ significantly from the final ones. In this work, uniform velocity in all finite volumes of the numerical mesh was assumed as initial conditions. The initial conditions for velocity and turbulence were taken from the boundary conditions at the inlet. Simulations of ten seconds of air movement showed that this effect disappears after approximately 5–6 s. The aerodynamic force coefficients were averaged every second. The aerodynamic characteristics shown in the graphs in the result section of this paper (Section 3) correspond to the last tenth second of motion.

2.2. Computing Domain Size Effect

As mentioned above, the size of the computing domain is an essential aspect of CFD calculations. Some authors pointed out that the influence of the domain size on the accuracy of the calculated airfoil characteristics depends, inter alia, on the type of mesh (e.g., C-mesh, O-mesh, etc.), its density, and physical parameters of the flow. A review of the literature shows that there is no consensus on the size of the computational domain concerning the length of the chord. This applies to both airfoils operating at low and high Reynolds numbers [75–78]. Some researchers employ small computing domain sizes. In this case, the distance from the obstacle to the domain's boundary is from several to dozen airfoil chords. Conventionally, the domain area in the wake region is longer than the distance from the inlet to the obstacle. Some researchers create computing domains of huge sizes. Sometimes the distance from the leading edge of the airfoil to the boundary of the computational domain is even several hundred times larger than the airfoil chord length.

Paper [6] discusses the effect of three domain widths, 3.75 c, 7.5 c, and 15 c, on the characteristics of the lift and drag coefficients. Those authors concluded that the domain width does not significantly affect the airfoil aerodynamic characteristics. However, the drag coefficient is more sensitive to changing the domain width than the lift coefficient. A numerical domain with a width of 15 c gives acceptable results for the aerodynamic components. At the same time, the number of mesh nodes is half as compared to the mesh for a domain twice as wide. Therefore, a nominal 15 c-wide domain was used in these studies (the radius of the semicircular outer edge of the domain is 7.5 c).

The length of the computational domain in the wake area behind the obstacle is also an important aspect of CFD calculations. This effect was not discussed in previous studies by Rogowski et al. [6]. Therefore, the authors of this paper decided to verify the numerical model for several different lengths of the computational domain. For this purpose, four computational domains of different lengths were developed. The variable in these analyzes is the length L, measured from the airfoil's trailing edge to the domain's outlet boundary, as shown in Figure 3a. The distance from the leading edge of the airfoil to the inlet was the same for all analyzed test cases. Since the range of angles of attack from 0 to 10 degrees is discussed in this paper, the numerical model was verified for two angles of attack: 4 and 10 degrees. Thus, the analysis of the effect of length L on the aerodynamic characteristics of the NACA 0018 airfoil was carried out based on eight test cases. The change in the length of the computational domain results in a change in the number of finite volume elements of the model (the size of the computational grid). For the lowest domain considered in this paper, the number of mesh elements was 797,000, while for the largest domain it was 871,000. Twenty seconds of air movement was simulated for each test case. In addition, a Reynolds number of 150,000 and a turbulence intensity of 0.25% were used to verify the numerical model. Taking into account both the range of Reynolds numbers as well as the range of turbulence intensity analyzed in this paper, the values of *Re* and *TI* used for this verification are more or less average values.

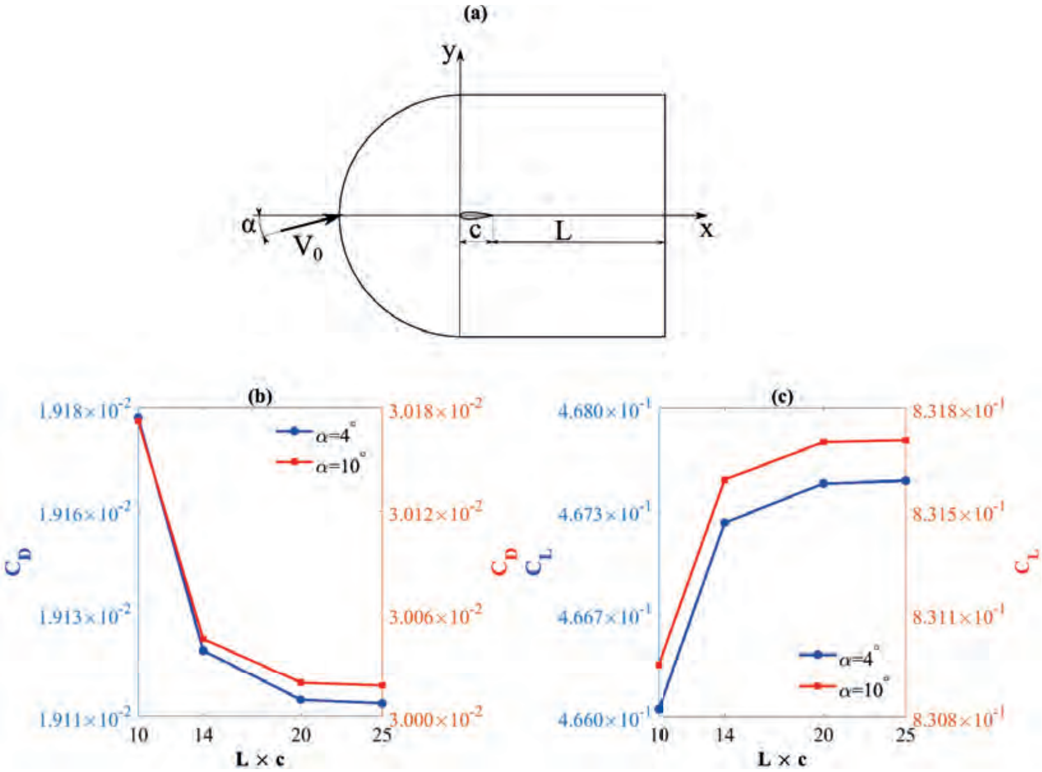

Figure 3. The computing domain and the distance from the trailing edge to the outlet, L (**a**). The influence of the domain length on the drag coefficient (**b**) and the lift coefficient (**c**).

The results of the numerical calculations of the lift and drag coefficients are presented in Figure 3b,c, respectively. These charts were made in such a way that it was possible to compare the coefficients both qualitatively and quantitatively. Therefore, the results for the angle of attack equal to 4 degrees are presented on the ordinate axis, whereas the results for the angle of 10 degrees are plotted on the auxiliary *y*-axis. The results compiled in this way show that the numerical values of the coefficients differ very little for a given angle of attack. For an angle of attack of 4 degrees and a length L of 14 c, the drag coefficient is 0.28% less than the drag coefficient for the case L = 10 c. Figure 3c shows that, in contrast to the drag coefficient, as the length of the computational domain in the wake region increases, the lift coefficient increases. However, this increase is also slight. For an angle of attack of 4 degrees and a length L of 14 c, it is only 0.26% compared to the case of L = 10 c. For the angle of attack of 4 degrees, the increase in the C_L/C_D ratio for the case of L = 14 c is also only 0.54% in relation to the case of L = 10 c, a further increase in the parameter L from

14 c to 20 c causes an increase in the C_L/C_D ratio by only 0.11%. The conducted analyzes confirm that for the L of 14 c, the characteristics of the aerodynamic force coefficients can be treated as largely independent of the domain length in the wake area.

This study also investigated the effect of the computational domain length on the wall Y + parameter and the decrease in turbulence intensity in the area from the inlet to the obstacle. However, the conducted analysis showed that the influence of the computational domain length on both parameters was so negligible that the discussion was limited only to this comment. Both of these parameters are affected, as in the case of aerodynamic forces, only by the angle of attack.

2.3. Turbulence Intensity Effect and Mesh Sensitivity Studies

One of the key achievements of this paper is the analysis of the aerodynamic performance of the symmetrical NACA 0018 airfoil in relation to the turbulence intensity. As a result of numerical dissipation, the turbulence intensity just before the airfoil is sometimes completely different from the turbulence intensity assumed for the boundary conditions. This analysis aims to find a correlation between the turbulence intensity at an inlet and just before the airfoil (at the point located close to the airfoil nose). The different types of boundary conditions available in CFD codes require different flow parameters to be specified. In this work, the *velocity inlet* boundary condition is employed as shown in Figure 2a. In the current investigations, two turbulence quantities were specified at the inlet: the turbulence intensity, TI_0, and the turbulence length scale, l. The turbulence intensity is determined as the ratio of the root-mean-square of the velocity fluctuations to the average flow velocity. The turbulence length scale is the quantity that is appropriate to the size of large eddies which contain energy in turbulent flow [23]. Many reports from experimental measurements in wind tunnels only provide information about turbulence intensity at the location of the analyzed obstacle. It is very often the only turbulence parameter measured during experiments. Following the guidelines available in the ANSYS Fluent documentation [23], in the case of wall-bounded flows, it is recommended to calculate the turbulence scale from the following formula: $l = 0.4\,\delta_{99}$, where δ_{99} is the boundary-layer thickness. In the current research, the turbulence length scale, l, was estimated on the airfoil for the coordinate x/c = 0.3, and it is equal to 0.003845 m. This paper does not analyze the sensitivity of the airfoil performance due to this parameter.

A numerical experiment was carried out to investigate the rate of decay of turbulence intensity and determine the correlation between the turbulence intensity at the domain inlet and just before the airfoil. The analysis was performed for the following flow parameters: the Reynolds number was assumed to be 150,000, the undisturbed flow velocity was 2.1911 m/s, and the angle of attack was 6 degrees. In this study, eight values of the turbulence inlet intensity were used: 0.1%, 0.5%, 1%, 2%, 4%, 6%, 8%, and 10%. Unsteady calculations were performed for ten seconds of air movement, assuming a time step length of 0.0001 s. Figure 4b,c illustrates the dependence of the turbulence intensity on the x coordinate, starting from the boundary of the computational domain up to the checkpoint located just at the airfoil nose. Both points representing the start and end of the control segment are shown in Figure 4a. The decay rate of this quantity is strongly dependent on the turbulence intensity that was set for the boundary condition TI_0. The higher the TI_0, the higher the decay rate. As shown in Figure 4b, in the case of the lowest turbulence intensity analyzed in this work, equal to 0.1%, the decay rate is represented by an almost constant function slightly dependent on the x coordinate. In the case of turbulence intensity higher than 0.5%, the characteristic inflection of the TI curve is visible. This inflection occurs approximately 0.5 c from the first control point located at the domain entrance. Before this inflection, the turbulence intensity decay is much higher than after it. Near the nose of the airfoil, the turbulence intensity is very low for each test case. Therefore, to compare the differences in the turbulence intensity values in the vicinity of the airfoil, an additional chart was prepared in which the x coordinate was limited to the last meter before the airfoil (Figure 4c). In this figure, it can be seen that the TI just before the airfoil varies from 0.0484% for $TI_0 = 0.1\%$ to $TI_0 = 10\%$. In the first case, it gives a decrease of 51.6%, in the second case by 95.3%. This data can be used to interpolate the TI_0 value to obtain the expected TI

value on the profile. This data shown in Figure 4b,c can be used for interpolation of TI_0 to obtain a specific TI on the airfoil.

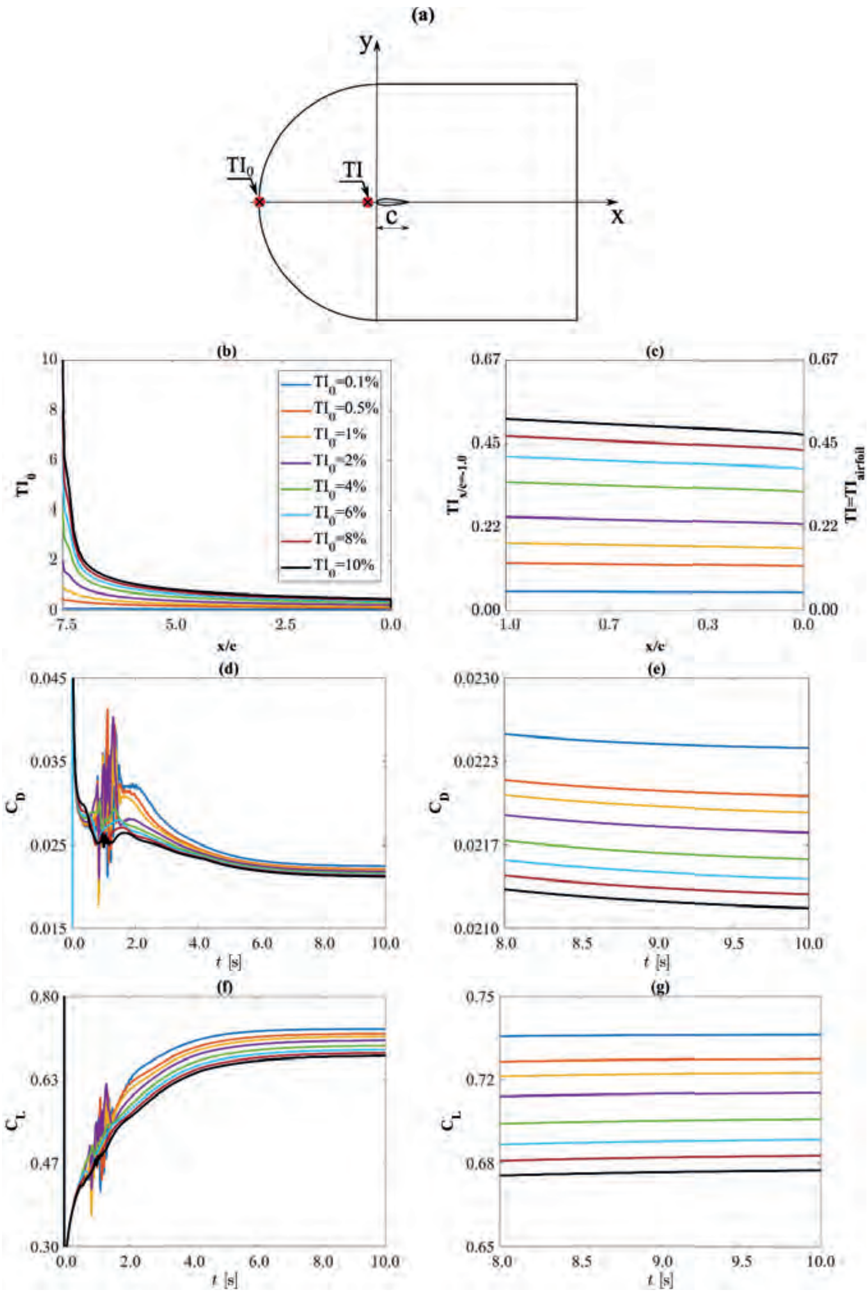

Figure 4. Segment definition for calculating the dependence $TI(x)$, where TI_0—segment start point and TI—segment endpoint (**a**), turbulence intensity as a function of distance from the airfoil nose (**b**,**c**), coefficients of aerodynamic forces as a function of time for different values of turbulence intensity (**d**–**g**).

Moreover, a mesh density influence on turbulence decay was examined. Four additional meshes were prepared, from extra coarse to extra fine. Cases with typical settings, Reynolds number, 150,000, and inlet TI_0 equals 0.25%, were prepared. Studies were performed for two angles of attack: 4 degrees and 10 degrees. All results presented in Table 1 show that differences from the "Medium" case are tiny. Therefore, it can be claimed that mesh density influence on turbulence decay is negligible.

Table 1. Turbulence intensity results for mesh sensitivity studies.

Mesh	Number of Mesh Elements	TI on the Airfoil [%] [1]	
		AoA = 4°	AoA = 10°
Extra coarse	600,000	−0.00041	−0.00041
Coarse	700,000	−0.00016	−0.00016
Medium	800,000	0.24916	0.25065
Fine	900,000	0.00011	0.00011
Extra fine	1,000,000	0.00020	0.00020

[1] Only absolute values for the "Medium" case are presented. For others, differences from the "Medium" case.

In addition to the rate of turbulence intensity decay with distance from the nose of the airfoil, this paper also discusses the effect of turbulence intensity on the aerodynamic characteristics of the airfoil. These characteristics are discussed in detail in the Results section of this paper. However, Figure 4d–g shows the time dependence of the components of the aerodynamic forces. These graphs show that the coefficients become time independent after 8–9 s. However, the lift coefficient becomes time independent faster than the drag coefficient.

2.4. Validation of the Numerical Model

Figure 5 shows a comparison of the aerodynamic force characteristics of the NACA 0018 airfoil obtained using the $\gamma - Re_\theta$ approach with the aerodynamic airfoil characteristics measured in the Delft University Low-speed Wind Tunnel by Timmer [24]. The lowest Reynolds number published in the paper [24], equal to 0.15×10^6, was used to compare the numerical results. With this Reynolds number, the turbulence intensity in the test section was 0.02%. This turbulence intensity value is very close to the lowest one considered in these investigations. The graphs shown in Figure 5 have the same scales as those in Figures 12 and 14 in the Results section of this paper. As shown in Figure 5b, the drag coefficient results agree with the experiment both qualitatively and quantitatively. The absolute error of the minimum drag coefficient compared to the experiment is only 0.00282. In the case of the lift coefficient (Figure 5a), both series of results are sufficiently consistent in the range of angles of attack up to 6 degrees. Slightly more significant differences in the coefficients are visible above this angle of attack. This effect is shown in the earlier work of Rogowski et al. [6] as well as in the studies by Melani et al. [57]. One of the possible causes of differences is the 3D effects not considered in these studies. The second reason is that the turbulence model is not calibrated through the model constants that control the characteristics of the separation bubble [70].

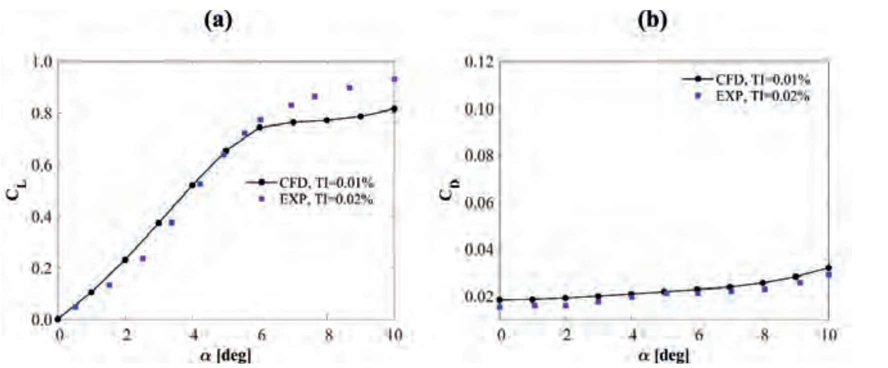

Figure 5. Aerodynamic characteristics of the NACA 0018 profile: lift force coefficient as a function of the angle of attack (**a**) and drag coefficient (**b**). Comparison of CFD results with the experiment [24].

3. Results

3.1. Reynolds Number Effect on Lift and Drag Coefficients

At a low Reynolds number regime, relatively small differences in this quantity can significantly change lift and drag airfoil characteristics. This section details the effect of the Reynolds number on the shape of the $C_L(\alpha)$ and $C_D(\alpha)$ curves. It was decided to discuss both components separately in this section.

3.1.1. Lift Force Coefficient

All simulations carried out in this paper, regardless of the Reynolds number and the turbulent intensity showed a zero-lift coefficient at a zero angle of attack. The characteristics of the lift coefficient as a function of the angle of attack at the low Reynolds number regime are slightly different from the characteristics at much higher velocities [41]. As the Reynolds number increases, the influence of the laminar separation bubble on the lift coefficient C_L characteristics decrease, as can be seen in Figure 6.

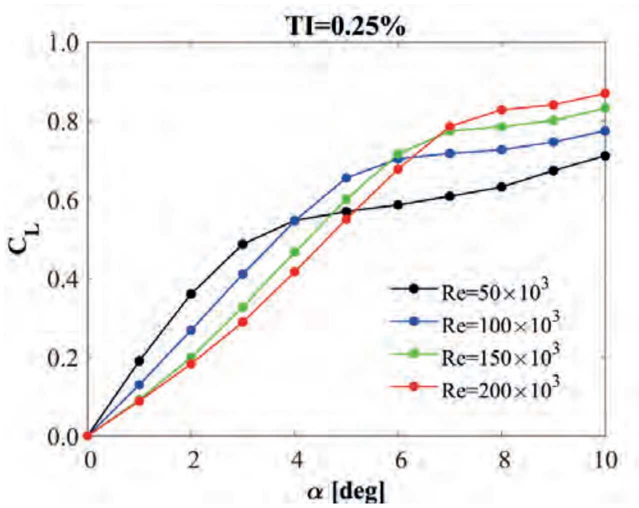

Figure 6. Lift coefficient vs. angle of attack. Reynolds number effect.

Analyzing these lift force coefficient characteristics (Figure 6), the characteristic "bend" of the C_L curve can be observed. The lift force characteristics are not linear in the whole range of the angles of attack up to the critical angle. In other words, the derivative $dC_L/d\alpha$ is not constant over this range of angles of attack. On both sides of this bend, the C_L characteristics can be analyzed by considering two derivatives $dC_L/d\alpha$ that can be regarded to a large extent as constant. Both Gerakopulos et al. [79] and Rogowski et al. [6] used such derivatives to define the two regions. In both of these regions, the increase in the lift coefficient with the angle of attack is largely linear. The region in the range of the angles of attack from zero to the location of the bend is called the "first region", whereas the region above this bend is called the "second region". The approach for determining the aerodynamic derivative of $dC_L/d\alpha$ used in this work was taken from publication [79]. Figure 7 shows an example of determining these two derivatives of the C_L curve for the Reynolds number of 150×10^3 and for the turbulence intensity, TI, of 0.25%.

As mentioned above, Figures 6 and 7 only show the lift coefficient results obtained for one value of turbulence intensity of 0.25%. This is due to two reasons. First, this is the average turbulence intensity value for the turbulence intensity range considered in this work. Secondly, the C_L results for the remaining turbulence intensities considered in this paper are very similar. Thirdly, we found the experimental data of the aerodynamic derivatives developed for similar flow conditions. According to Gerakopulos et al. [79], the turbulence intensity measured during the experiment was less than 0.3%. Therefore, there was a possibility of further validation of our results. Figure 8 shows a comparison of the experimental and numerical results of the $dC_L/d\alpha$ derivatives separately for two regions. According to the authors of this paper, the accuracy of the numerical series is satisfactory. For the Reynolds number of 100,000, the most significant differences in the results of the $dC_L/d\alpha$ derivatives are visible. However, they may result from both the dispersion of the values of the lift coefficients used to calculate the derivatives based on the linear approximation and the range of angles of attack used to calculate individual derivatives.

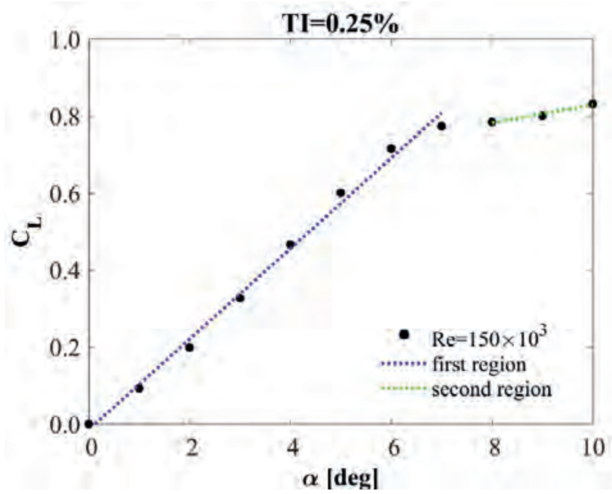

Figure 7. Two regions of linear growth of lift coefficient curve.

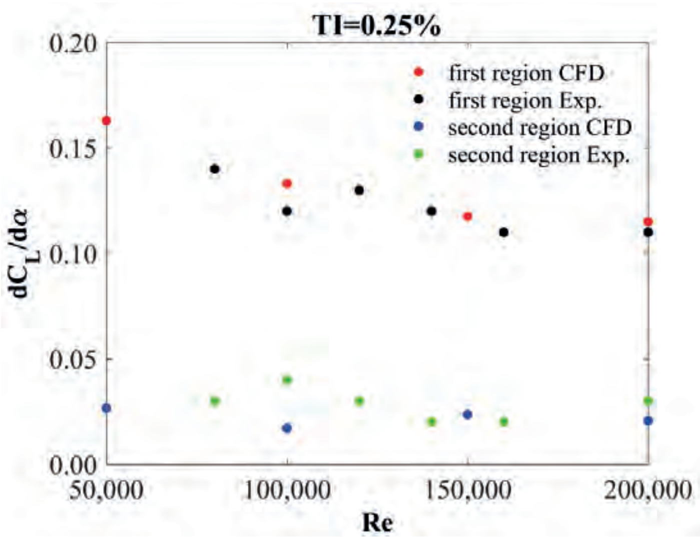

Figure 8. $dC_L/d\alpha$ derivatives for two regions. The comparison between present results and data available in the literature [79].

From the observation of the data shown in Figure 8, the derivatives in the first region tend to decrease as the Reynolds number increases, while the derivatives in the second region are not as dependent on the Reynolds number. As seen "with the naked eye" in this figure, an increase in the Reynolds number causes an increase in the first region. However, a more detailed analysis of this effect requires the location of the transition point between the first and second regions to be specified. As mentioned above, the $C_L(\alpha)$ is a continuous function around the bend. This publication proposes another way to find the transition location. For this paper, the transition angle of attack was defined and marked with the symbol α_t. This angle was found analytically by solving a simple system of equations composed of trend line equations approximating both regions. In other words, it is the angle at the intersection of the trend lines for the first and second regions (Figure 9a). Figure 9b quantitatively documents the nearly linear growth of the first region as the Reynolds number increases.

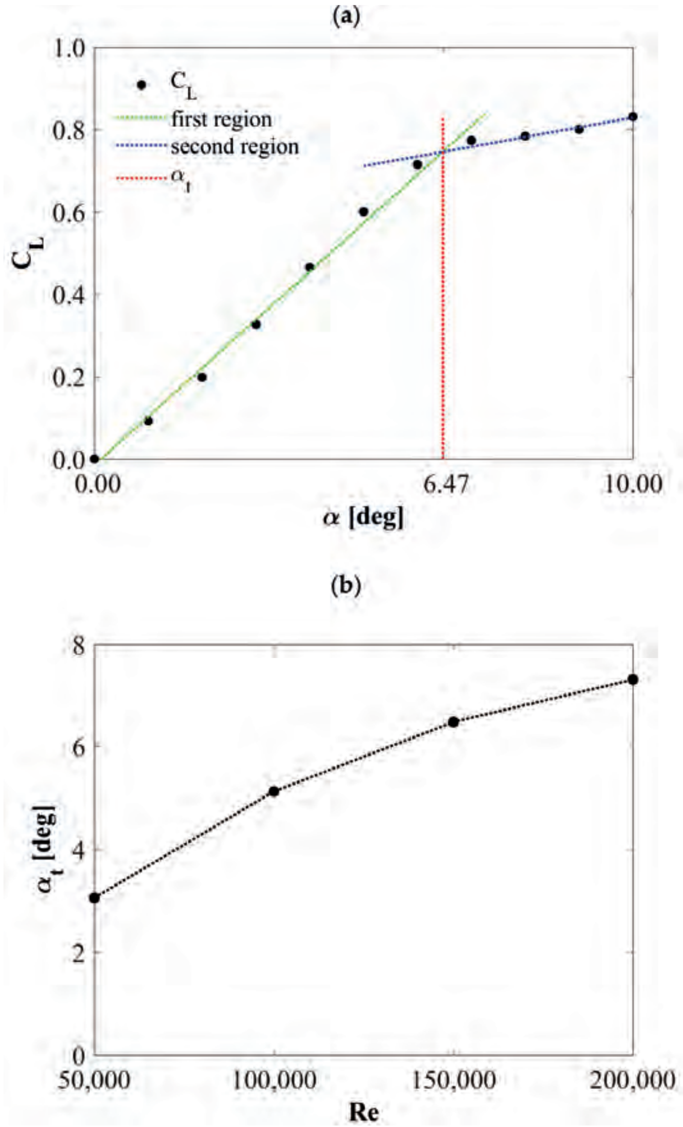

Figure 9. Lift coefficient vs. angle of attack for $Re = 150 \times 10^3$ and $TI = 0.25\%$. An approach for determining the transition angle, α_t (**a**). The transition angle vs. Reynolds number for $TI = 0.25\%$ (**b**).

3.1.2. Drag Force Coefficient

Figure 10 shows the dependence of the drag coefficient on the angle of attack and the Reynolds number. These results are also discussed for one turbulence intensity of 0.25%.

The largest drag coefficients are calculated for the lowest Reynolds number taken into account in this study, of 50,000. At this Reynolds number, a faster increase in drag is also observed starting from an angle of attack of 6 deg. In the case of Reynolds numbers larger than 50,000, the increase in drag as a function of the angle of attack is much smoother.

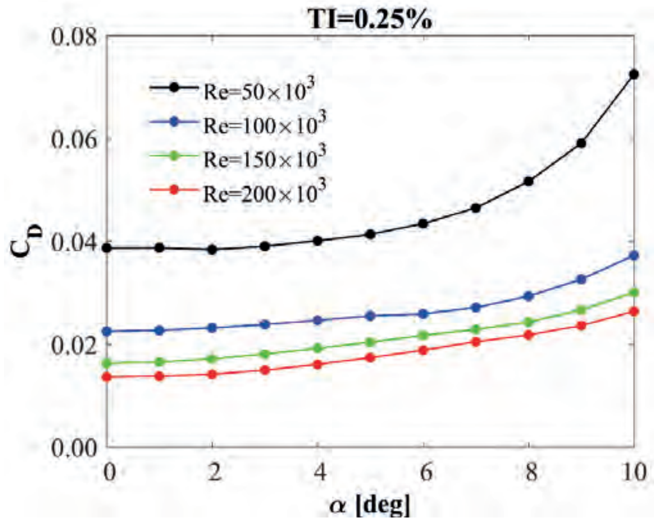

Figure 10. Drag coefficient vs. angle of attack. Reynolds number effect.

In this work, the qualitative dependence of the drag coefficient as a function of the Reynolds number for individual angles of attack was also examined. Figure 11 shows the dependence of the drag coefficient on the Reynolds number separately for different angles of attack considered in this work. The results shown in this graph are for a turbulence intensity of 0.25%. As can be seen from this figure, the drag coefficients differ very little for small angles of attack and Reynolds numbers larger than 100,000. Moreover, $C_D(Re)$ dependencies are not linear functions. The functions that best approximate these calculated coefficient values are third-degree polynomials.

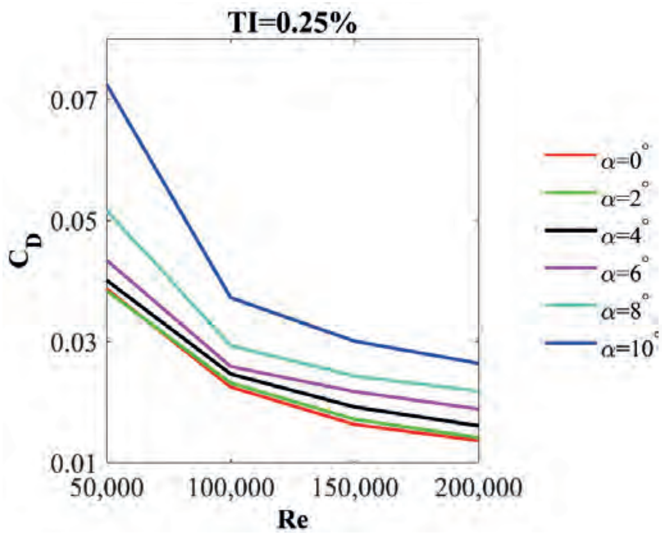

Figure 11. Drag coefficient as a function of Reynolds number.

3.2. Turbulence Intensity Effect on Lift and Drag Coefficients

As was reported in Section 3.1, relatively small differences in the Reynolds number result in significant variations in the aerodynamic loads of the airfoil. The effect of turbulence intensity on the aerodynamic characteristics (aerodynamic force coefficients as a function of the angle of attack) of the NACA 0018 airfoil, is much smaller compared to the Reynolds number effect. Nevertheless, the influence of turbulence intensity is particularly important with the lowest value of Re, investigated in this paper, equal to 50,000. Therefore, although the effect of the Reynolds number has been discussed in detail above, this subsection also takes this effect into account. The primary purpose of this subsection is to analyze the effects of turbulence intensity on airfoil performance.

3.2.1. Lift Force Coefficient

Figure 12 shows the characteristics of the lift coefficient, C_L, as a function of angle of attack, α. These results are compared for the different turbulence intensities considered in this work. Additionally, these results are presented separately for each Reynolds number used in these investigations. The same scale is used in all the graphs in this figure so that the obtained C_L results can be better compared.

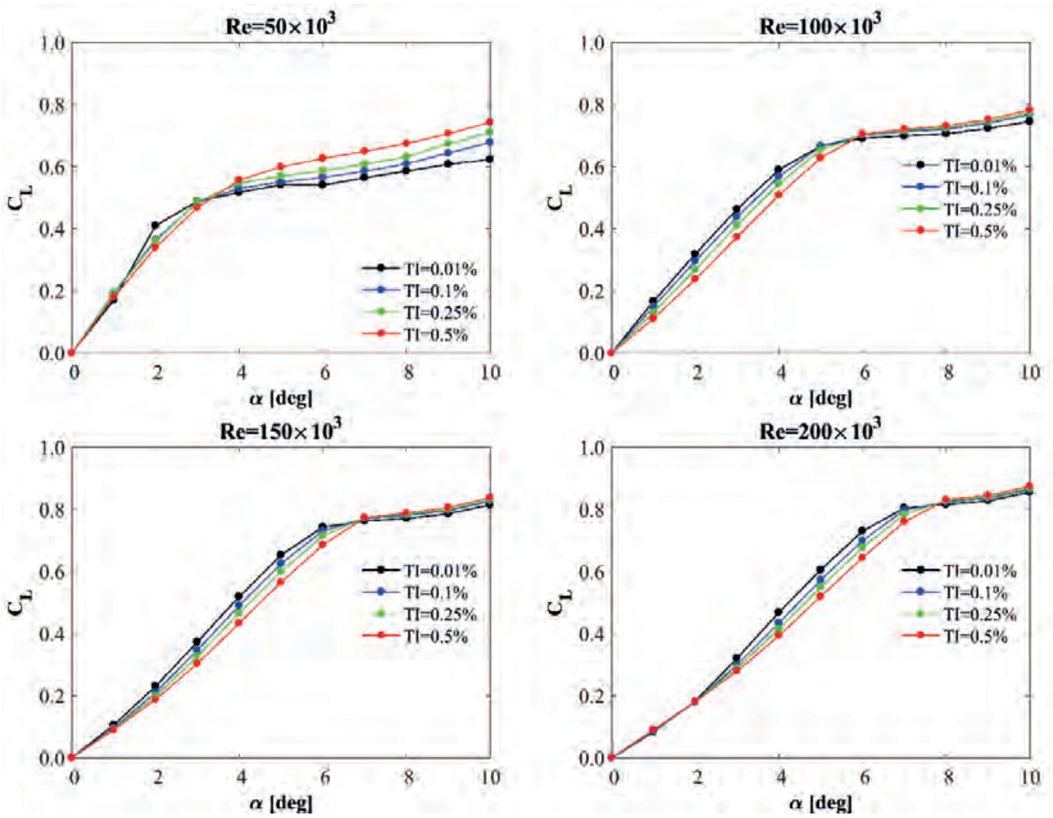

Figure 12. Lift coefficient vs. angle of attack. Turbulence intensity effect.

It can be seen comparing Figures 6 and 12 that the influence of the turbulence intensity on the lift coefficient is much smaller than the Reynolds number effect. All the C_L characteristics show that the increase in turbulence intensity causes the lift coefficient to decrease in the first region and increase in the second region. In the case of Reynolds numbers larger than 50,000, the significant differences in the C_L values are observed approximately in the middle of the analyzed range of angles of attack. Moreover, as the Reynolds number increases, the differences in C_L results decrease significantly in the second region.

As mentioned in Section 3.1, all simulations carried out in these investigations, regardless of the Reynolds number and the turbulent intensity, showed a zero-lift coefficient at a zero angle of attack.

As discussed above, the turbulence intensity affects the values of the lift coefficients differently in both the first and second regions. The graphs shown in Figure 12 show a common trend for all the calculated series. The turbulence intensity significantly influences the $dC_L/d\alpha$ derivative in both regions. This subsection also presents a qualitative analysis of the $dC_L/d\alpha$ derivatives for both of these regions. The derivatives of $dC_L/d\alpha$ as a function of Reynolds number and for different turbulence intensity values for the first and second regions are shown in Figure 13a,b, respectively. Additionally, Figure 13c also illustrates the transition angle, α_t, as a function of Reynolds number. The method of determining this angle for this work is also discussed in the previous subsection and Figure 9a. The graphs shown in Figure 13 quantitatively prove three things:

1. An increase in *TI* causes a decrease in the $dC_L/d\alpha$ derivative in the first area, an increase in the $dC_L/d\alpha$ derivative in the second area, and an increase in α_t.
2. An increase in *Re* causes a decrease in the $dC_L/d\alpha$ derivative in the first region and an almost linear increase in the α_t angle.
3. Figure 13c does not show a clear trend of the $dC_L/d\alpha$ derivative as a function of *Re* in the second area, both downward and upward. A similar trend of this derivative for the second region is also seen in the experimental studies taken from the literature [79], and is shown in Figure 8.

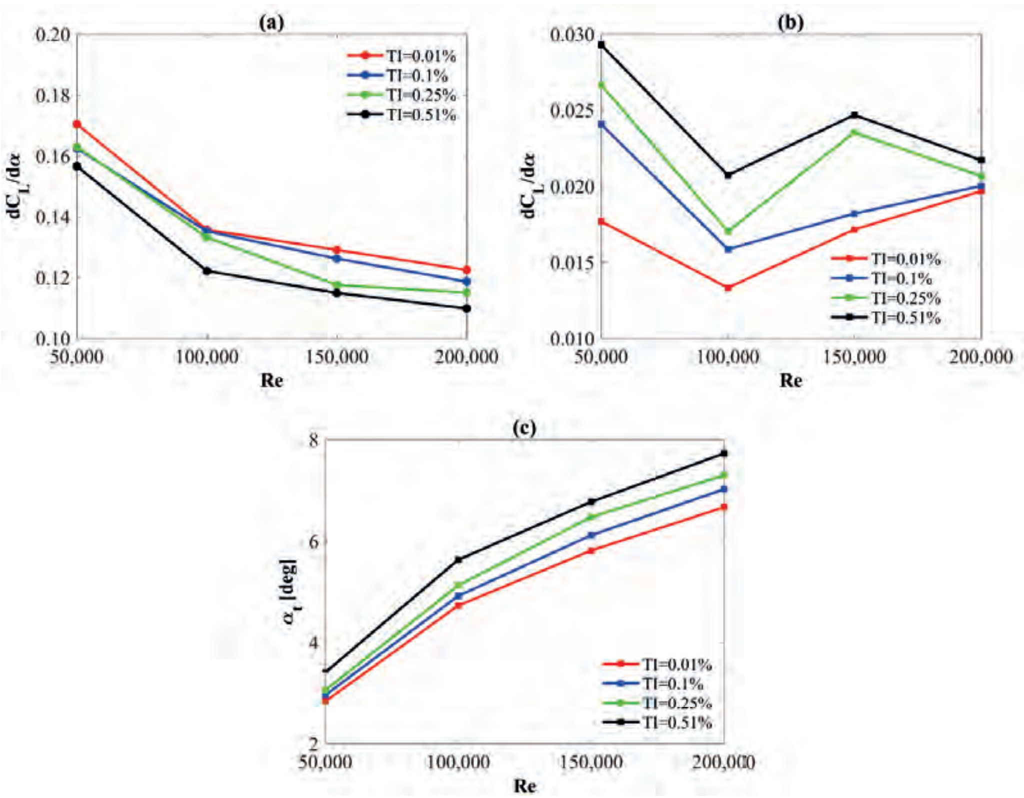

Figure 13. The aerodynamic derivatives $dC_L/d\alpha$ as a function of Reynolds number for the first region (**a**) and for the second region (**b**). Transition angle of attack as a function of Reynolds number (**c**).

3.2.2. Drag Force

The results of the drag coefficient, C_D, seem to be even less sensitive to the turbulence intensity than the lift coefficients, except for the case of Re = 50,000 (Figure 14). At this Reynolds number, the drag coefficient in the entire range of the angles of attack significantly depends on both the intensity of turbulence and the angle of attack. However, in the case of Re = 200,000, the differences in the drag coefficient results are minimal. In general, an increase in the angle of attack causes an increase in drag. However, as shown in Figure 14, the drag increase is very large at Re = 50,000. In order to compare the results, all the graphs shown in this figure have the same scale.

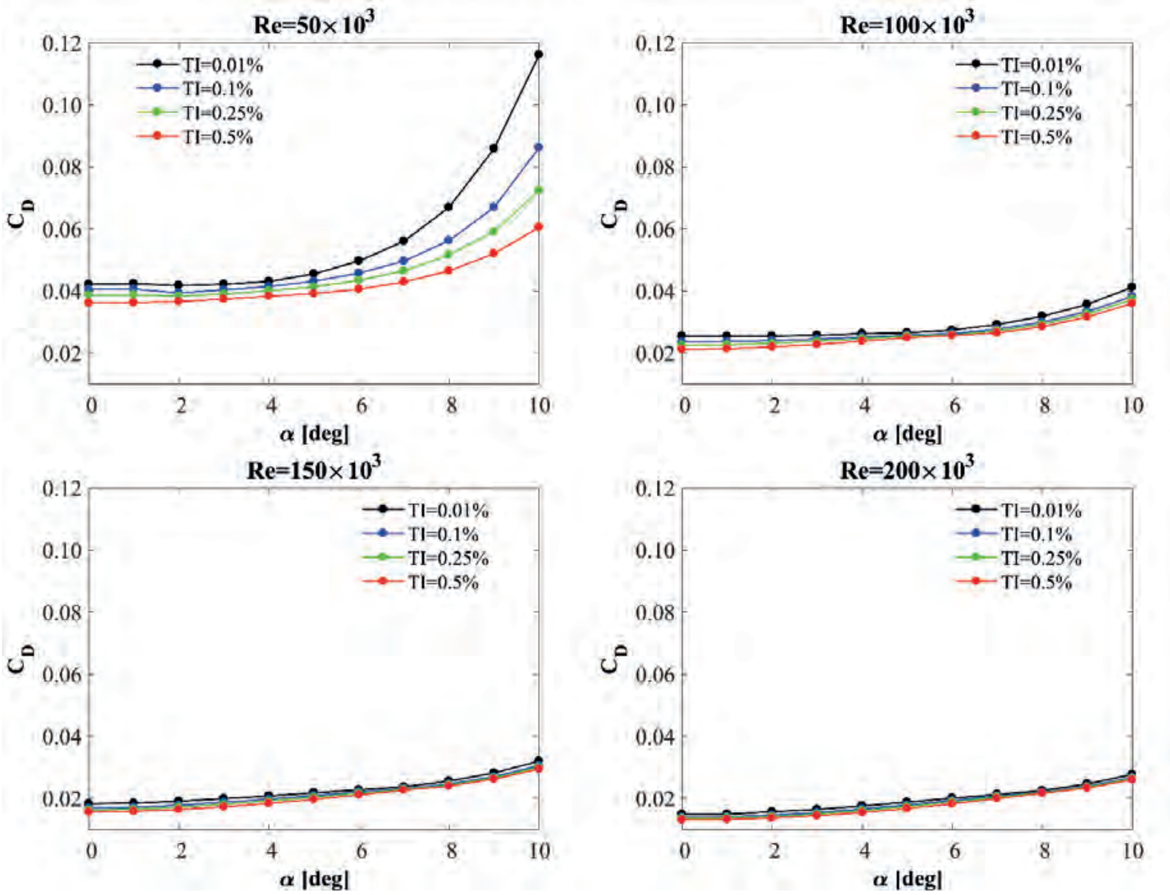

Figure 14. Drag coefficient vs. angle of attack. Turbulence intensity effect.

As mentioned above, the drag coefficient is dependent not only on the Reynolds number and the turbulence intensity but also on the angle of attack. For Reynolds numbers in the range of 100,000 to 200,000, this effect is relatively small. Therefore, Figure 15b only shows the values of the drag coefficient as a function of turbulence intensity for an exemplary Reynolds number of 150,000 because, in the case of Re numbers of 100,000 and 200,000, both the values of the coefficients and their decreases as a function of *TI* are very similar. Only the results of the C_D coefficient calculated for Re = 50,000 differ significantly from the others. Therefore, these results are shown in a separate figure (Figure 15a). The results shown in Figure 15 show a non-linear relationship of the drag coefficient with the turbulence intensity. Although it is worth noting that it is non-linear, mostly close to

TI = 0.1%. In the rest of the TI values taken into account in this paper, an almost constant decrease in the C_D ratio can be observed.

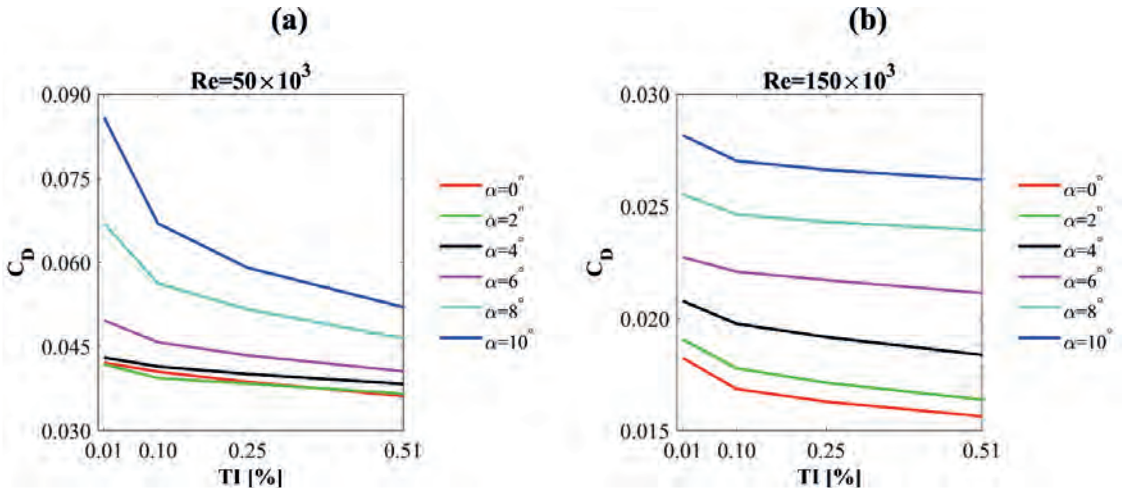

Figure 15. Effect of turbulence intensity on drag coefficient: (**a**) for Reynolds number of 50,000 and (**b**) for Reynolds number of 150,000.

3.3. Static Pressure

The characteristics of the aerodynamic forces discussed in the subsections above result from the pressure distributions around the airfoil. The phenomena occurring in the boundary layer have a significant influence on these distributions. This subsection discusses the effect of the Reynolds number and the turbulence intensity on the static pressure characteristics. In order to better visualize the cause of the occurrence of two regions visible in the lift force coefficient characteristics, the authors of this paper decided to analyze the pressure distributions for both sides of the airfoil separately. Therefore, Figures 16 and 17 show the static pressure coefficients for the suction and pressure sides, respectively. These charts compare the pressure coefficient distributions for different angles of attack and fixed Reynolds numbers. The distributions of the C_P coefficient for the angles of attack closest to the transition angles of attack are shown in black on each of these graphs. The shades of blue represent the angles of attack lower than the transition angle of attack, while the other colors represent the higher angles. It can be seen from Figure 17 that for angles of attack larger than α_t, there is no longer a laminar-separation bubble on the pressure surface of the airfoil. Moreover, above this angle of attack, the distributions C_P on this side of the profile are already much less dependent on the angle of attack. Figures 16 and 17 show that the largest differences in the C_P coefficients, both on the suction and pressure side of the profile, occur for the smallest Reynolds number of 50,000 analyzed in this study. This explains such significant differences in both the drag coefficient (Figure 10) and the lift coefficient (Figure 6).

Figures 16 and 17 show the effect of the angle of attack for given Reynolds number values. As a result, a qualitative difference was found in the characteristics of the $C_P(x/c)$ coefficient for the first and second regions (the method of determining the regions is discussed in Section 3.1 of this paper). Figure 18 compares the static pressure coefficients for two angles of attack, one ($\alpha = 2°$) for the first region and one ($\alpha = 10°$) for the second region. The top two plots shown in this figure compare the C_P relationships for one turbulence intensity value of 0.25%, and the bottom two for one Reynolds number value of 150,000. These characteristics clearly show that the Reynolds number has a much greater effect on the pressure distributions than the turbulence intensity. The effect of both quantities, Reynolds number and turbulence intensity, is much greater on the suction side of the airfoil.

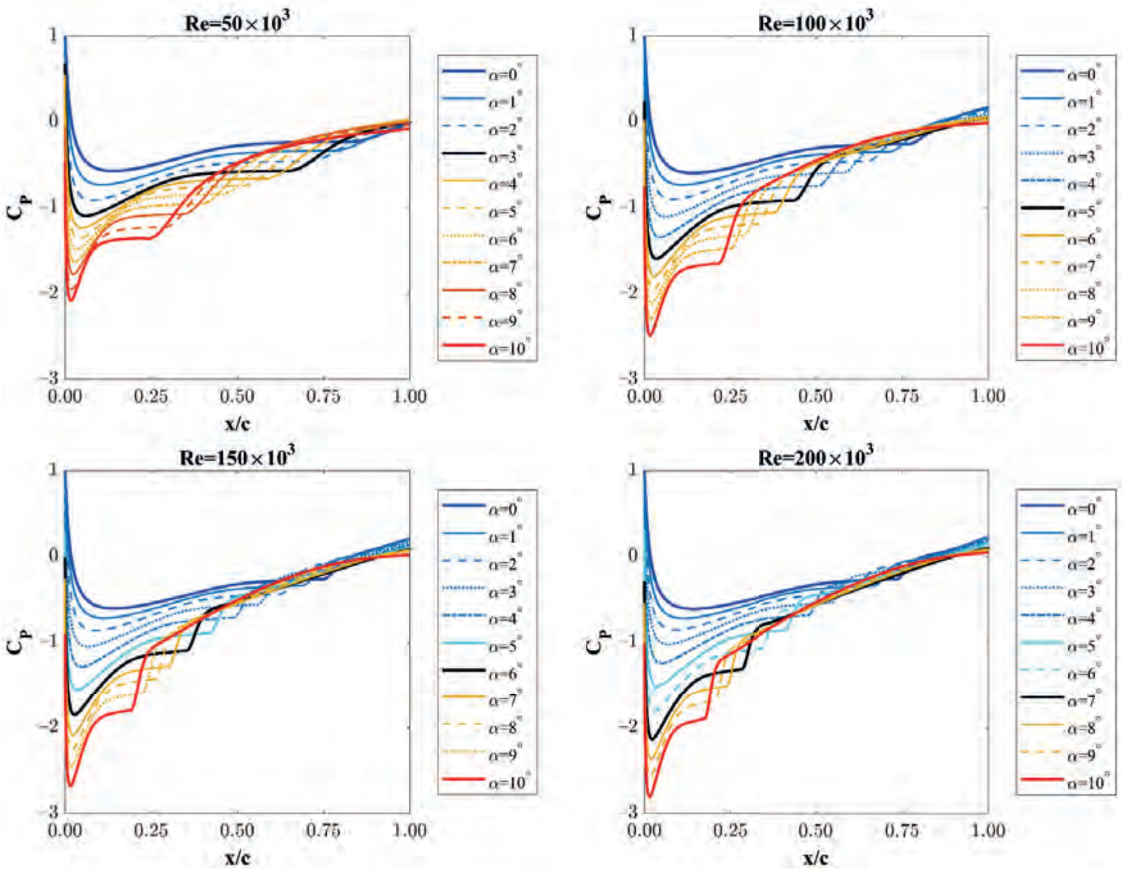

Figure 16. Static pressure coefficient on the suction side at different Reynolds numbers; angle of attack effect.

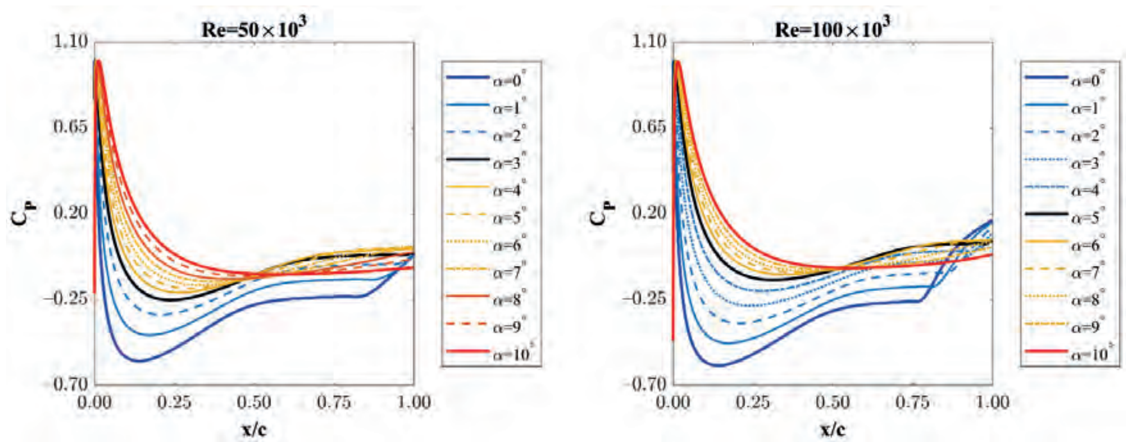

Figure 17. *Cont.*

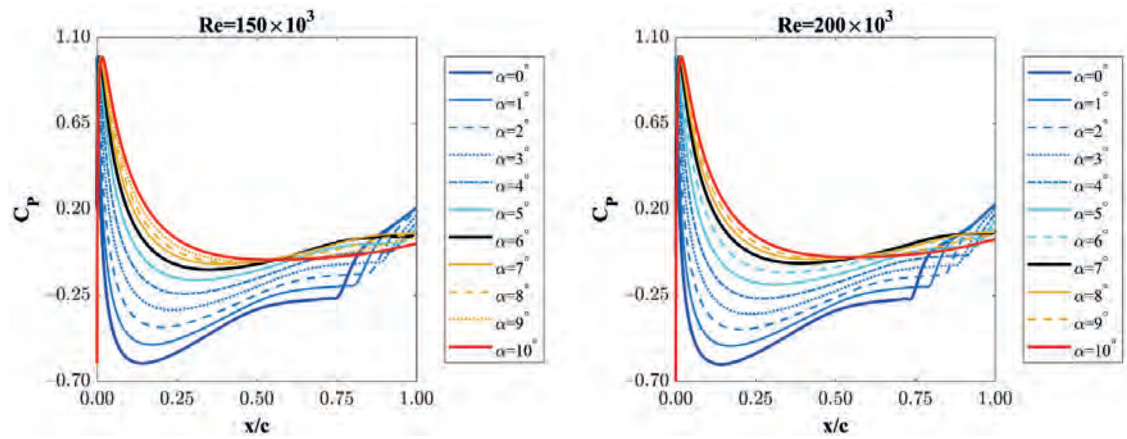

Figure 17. Static pressure coefficient on pressure side at different Reynolds numbers; angle of attack effect.

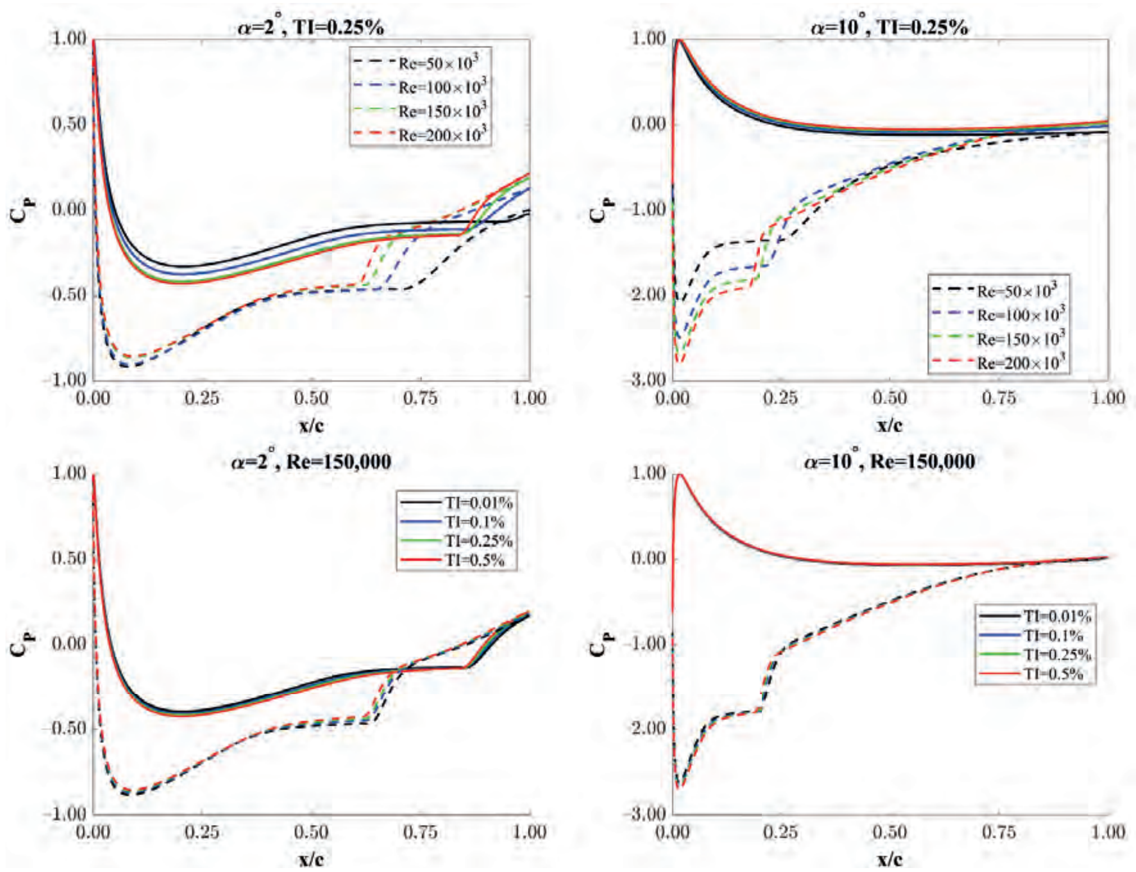

Figure 18. Static pressure coefficient on the pressure side (solid lines) and the suction side (dashed lines). Reynolds number effect (upper plots); turbulence intensity effect (lower plots).

4. Conclusions

This paper discusses the effect of the Reynolds number and the turbulence intensity on the performance of the NACA 0018 profile under the low Reynolds numbers. The research was carried out for the range of Reynolds numbers from 50,000 to 200,000 and for the range of turbulence intensity on the airfoil from 0.01% to 0.5%. Moreover, the investigations were realized for the range of angles of attack from 0 to 10 degrees. Numerical analyzes were performed utilizing the URANS approach with the uncalibrated transition turbulence model $\gamma - Re_\theta$. Based on the numerical investigations of the airfoil, the following conclusions are drawn:

- One of the key achievements of this paper is the analysis of the aerodynamic characteristics of the NACA 0018 airfoil in relation to the turbulence intensity. The decay rate of turbulence intensity strongly depends on the turbulence intensity at the inlet. The higher the turbulence intensity at the inlet, the higher the decay rate. For the lowest turbulence intensity analyzed in this work, equal to 0.1%, the decay rate is almost constant. In the vicinity of the nose of the profile, the turbulence intensity is very low regardless of the inlet's turbulence intensity. The results shown in Figure 4b,c have practical applications when using the mesh described in the paper [6]. The data shown in these graphs can be used to interpolate the turbulence intensity at the inlet in order to obtain a specific value of the turbulence intensity on the airfoil.
- All calculations carried out in this paper, regardless of the Reynolds number and the turbulent intensity, showed a zero-lift coefficient at a zero angle of attack.
- The presence of a wide laminar-separation bubble in the boundary layer results in the occurrence of two aerodynamic derivatives of the lift coefficient in the range of angles of attack before stall. The increase in Reynolds number primarily causes a linear increase in the first region. On the other hand, the aerodynamic derivative in the second region is almost independent of the Reynolds number.
- At a Reynolds number of 50,000, a faster increase in drag is observed starting from an angle of attack of 6 deg. For higher Reynolds numbers, the increase in drag coefficient as a function of the angle of attack is much smoother. The drag coefficients differ very little for low angles of attack and Reynolds numbers higher than 100,000.
- Generally, the effect of the turbulence intensity on the lift coefficient is much lower than the Reynolds number effect. The increase in turbulence intensity causes the lift coefficient to decrease in the first region and increase in the second region. Differences in lift coefficients for high angles of attack decrease with increasing the Reynolds number and the turbulence intensity.
- The increase in turbulence intensity causes a decrease in the aerodynamic derivative $dC_L/d\alpha$ in the first region and its increase in the second region. Increasing turbulence intensity also increases the transition angle of attack. This trend is visible for all the Reynolds numbers studied in this work.
- For angles of attack higher than the transition angle of attack, there is no longer a laminar-separation bubble on the pressure surface of the airfoil.
- Drag coefficients are less sensitive to the turbulence intensity than the lift coefficients, except for the lowest investigated Reynolds number of 50,000. In general, an increase in the angle of attack causes an increase in the drag coefficient.
- The Reynolds number has a much greater effect on the pressure distributions than the turbulence intensity. The effect of Reynolds number and turbulence intensity is much greater on the suction side of the profile.
- The performed numerical analyzes showed clear differences in the characteristics of the drag coefficient for a Reynolds number of 50,000. For the other considered Reynolds numbers in the range of 100,000 to 200,000, the changes in the drag coefficients are rather linear as a function of both the turbulence intensity and the Reynolds number.

Author Contributions: Conceptualization, K.R.; methodology, J.M. and K.R.; software, J.M. and K.R.; validation J.M. and K.R.; numerical analysis, J.M.; writing—Original draft preparation, K.R.; writing—review and editing, J.M. and K.R.; visualization, J.M. and K.R., supervision, K.R. All authors have read and agreed to the published version of the manuscript.

Funding: This research was carried out with the support of the Interdisciplinary Centre for Mathematical and Computational Modelling (ICM) University of Warsaw under computational allocation no GB83-33. Research was funded by POB Energy of Warsaw University of Technology within the Excellence Initiative: Research University (IDUB) programme. Grant No. 1820/355/Z01/POB7/2021.

Institutional Review Board Statement: Not applicable.

Informed Consent Statement: Not applicable.

Data Availability Statement: Not applicable.

Conflicts of Interest: The authors declare no conflict of interest.

Nomenclature

c	chord length
C_D	drag coefficient
C_L	lift coefficient
C_P	static pressure coefficient
$dC_L/d\alpha$	rate of change of lift coefficient with angle of attack
l	turbulence length scale
L	length from the airfoil's trailing edge to the domain's outlet boundary
Re	chord-based Reynolds number
TI	turbulence intensity on the airfoil
TI_0	inlet turbulence intensity
V_0	free stream wind velocity [m/s]
α	angle of attack
α_t	transition angle of attack (the angle between the first and the second region)
δ_{99}	boundary-layer thickness

References

1. Lin, J.M.; Pauley, L.L. Low-Reynolds-number separation on an airfoil. *AIAA J.* **1996**, *34*, 1570–1577. [CrossRef]
2. Bangga, G.; Dessoky, A.; Wu, Z.; Rogowski, K.; Hansen, M.O.L. Accuracy and consistency of CFD and engineering models for simulating vertical axis wind turbine loads. *Energy* **2020**, *206*, 118087. [CrossRef]
3. Ramírez, J.M.; Saravia, M. Assessment of Reynolds-averaged Navier–Stokes method for modeling the startup regime of a Darrieus rotor. *Phys. Fluids* **2021**, *33*, 037125. [CrossRef]
4. Branlard, E.; Brownstein, I.; Strom, B.; Jonkman, J.; Dana, S.; Baring-Gould, E.I. A multipurpose lifting-line flow solver for arbitrary wind energy concepts. *Wind Energ. Sci.* **2022**, *7*, 455–467. [CrossRef]
5. Silva, J.E.; Danao, L.A.M. Varying VAWT Cluster Configuration and the Effect on Individual Rotor and Overall Cluster Performance. *Energies* **2021**, *14*, 1567. [CrossRef]
6. Rogowski, K.; Królak, G.; Bangga, G. Numerical Study on the Aerodynamic Characteristics of the NACA 0018 Airfoil at Low Reynolds Number for Darrieus Wind Turbines Using the Transition SST Model. *Processes* **2021**, *9*, 477. [CrossRef]
7. Paraschivoiu, I. *Wind Turbine Design: With Emphasis on Darrieus Concept*; Polytechnic International Press: Montreal, QC, Canada, 2002.
8. Martinez, J.; Bernabini, L.; Probst, O.; Rodriguez, C. An improved BEM model for the power curve prediction of stall-regulated wind turbines. *Wind Energy* **2005**, *8*, 385–402. [CrossRef]
9. Hansen, M.O.L. *Aerodynamics of Wind Turbines*; Earthscan Publications Ltd.: London, UK, 2008.
10. Zhang, Z.; Nielsen, S.R.K.; Blaabjerg, F.; Zhou, D. Dynamics and Control of Lateral Tower Vibrations in Offshore Wind Turbines by Means of Active Generator Torque. *Energies* **2014**, *7*, 7746–7772. [CrossRef]
11. Fernandez-Gamiz, U.; Zulueta, E.; Boyano, A.; Ansoategui, I.; Uriarte, I. Five Megawatt Wind Turbine Power Output Improvements by Passive Flow Control Devices. *Energies* **2017**, *10*, 742. [CrossRef]
12. Żugaj, M.; Bibik, P.; Jacewicz, M. UAV aircraft model for control system failures analysis. *J. Theor. Appl. Mech.* **2016**, *54*, 1405–1415. [CrossRef]
13. Jimenez, P.; Lichota, P.; Agudelo, D.; Rogowski, K. Experimental Validation of Total Energy Control System for UAVs. *Energies* **2020**, *13*, 14. [CrossRef]
14. Sheng, H.; Zhang, C.; Xiang, Y. Mathematical Modeling and Stability Analysis of Tiltrotor Aircraft. *Drones* **2022**, *6*, 92. [CrossRef]
15. El-Fahham, I.; Abdelshahid, G.; Mokhiamar, O. Pitch Angle Modulation of the Horizontal and Vertical Axes Wind Turbine Using Fuzzy Logic Control. *Processes* **2021**, *9*, 1337. [CrossRef]
16. Sakamoto, L.; Fukui, T.; Morinishi, K. Blade Dimension Optimization and Performance Analysis of the 2-D Ugrinsky Wind Turbine. *Energies* **2022**, *15*, 2478. [CrossRef]

17. Ghiasi, P.; Najafi, G.; Ghobadian, B.; Jafari, A.; Mazlan, M. Analytical Study of the Impact of Solidity, Chord Length, Number of Blades, Aspect Ratio and Airfoil Type on H-Rotor Darrieus Wind Turbine Performance at Low Reynolds Number. *Sustainability* **2022**, *14*, 2623. [CrossRef]
18. Ferreira, C.S.; Madsen, H.A.; Barone, M.; Roscher, B.; Deglaire, P.; Arduin, I. Comparison of aerodynamic models for Vertical Axis Wind Turbines. *J. Phys. Conf. Ser.* **2014**, *524*, 012125. [CrossRef]
19. Castelein, D.; Ragni, D.; Tescione, G.; Ferreira, C.J.S.; Gaunaa, M. Creating a benchmark of Vertical Axis Wind Turbines in Dynamic Stall for validating numerical models. In Proceedings of the 33rd Wind Energy Symposium, AIAA SciTech, AIAA 2015-0723, Kissimmee, FL, USA, 5–9 January 2015. [CrossRef]
20. Rogowski, K.; Hansen, M.O.L.; Bangga, G. Performance Analysis of a H-Darrieus Wind Turbine for a Series of 4-Digit NACA Airfoils. *Energies* **2020**, *13*, 3196. [CrossRef]
21. Lichota, P. Multi-Axis Inputs for Identification of a Reconfigurable Fixed-Wing UAV. *Aerospace* **2020**, *7*, 113. [CrossRef]
22. Lichota, P.; Norena, D.A. A Priori Model Inclusion in the Multisine Maneuver Design. In Proceedings of the 17th International Carpathian Control Conference, High Tatras, Slovakia, 29 May–1 June 2016; Petras, I., Podlubny, I., Kacur, J., Eds.; IEEE: Tatranská Lomnica, Slovakia, 2016; pp. 440–445. [CrossRef]
23. ANSYS, Inc. *ANSYS Fluent Theory Guide, Release 19.1.*; ANSYS, Inc.: Canonsburg, PA, USA, 2019.
24. Timmer, W.A. Two-Dimensional Low-Reynolds Number Wind Tunnel Results for Airfoil NACA 0018. *Wind. Eng.* **2008**, *32*, 525–537. [CrossRef]
25. Dul, F.; Lichota, P.; Rusowicz, A. Generalized Linear Quadratic Control for a Full Tracking Problem in Aviation. *Sensors* **2020**, *20*, 2955. [CrossRef]
26. Ren, G.; Liu, J.; Wan, J.; Li, F.; Guo, Y.; Yu, D. The analysis of turbulence intensity based on wind speed data in onshore wind farms. *Renew. Energy* **2018**, *123*, 756–766. [CrossRef]
27. Laneville, A.; Vittecoq, P. Dynamic stall: The case of the vertical axis wind turbine. *J. Sol. Energy Eng.* **1986**, *108*, 140–145. [CrossRef]
28. Rogowski, K.; Maroński, R.; Hansen, M.O.L. Steady and unsteady analysis of NACA 0018 airfoil in vertical-axis wind turbine. *J. Theor. Appl. Mech.* **2018**, *51*, 203–212. [CrossRef]
29. Yang, Y.; Guo, Z.; Zhang, Y.; Jinyama, H.; Li, Q. Numerical Investigation of the Tip Vortex of a Straight-Bladed Vertical Axis Wind Turbine with Double-Blades. *Energies* **2017**, *10*, 1721. [CrossRef]
30. Mohan Kumar, P.; Sivalingam, K.; Lim, T.-C.; Ramakrishna, S.; Wei, H. Strategies for Enhancing the Low Wind Speed Performance of H-Darrieus Wind Turbine—Part 1. *Clean Technol.* **2019**, *1*, 185–204. [CrossRef]
31. Rogowski, K. CFD Computation of the H-Darrieus Wind Turbine—The Impact of the Rotating Shaft on the Rotor Performance. *Energies* **2019**, *12*, 2506. [CrossRef]
32. Rogowski, K.; Hansen, M.O.L.; Maroński, R.; Lichota, P. Scale Adaptive Simulation Model for the Darrieus Wind Turbine. *J. Phys. Conf. Ser.* **2016**, *753*, 022050. [CrossRef]
33. Alaimo, A.; Esposito, A.; Messineo, A.; Orlando, C.; Tumino, D. 3D CFD Analysis of a Vertical Axis Wind Turbine. *Energies* **2015**, *8*, 3013–3033. [CrossRef]
34. Jacobs, N.E.; Ward, K.E.; Pinkerton, R.M. The Characteristics of 78 Related Airfoil Sections from Tests in the Variable-Density Wind Tunnel. In *NACA Report 460*; Langley Memorial Aeronautical Laboratory: Hampton, VA, USA, 1933; ISBN NACA-460. Available online: https://ntrs.nasa.gov/api/citations/19930091108/downloads/19930091108.pdf (accessed on 15 April 2022).
35. Anderson, J.D., Jr. *Fundamentals of Aerodynamics*, 5th ed.; McGraw-Hill: New York, NY, USA, 2011.
36. Moran, J. *An Introduction to Theoretical and Computational Aerodynamics*, 1st ed.; John Wiley & Sons: New York, NY, USA, 1984.
37. Królak, G. Numerical Analysis of Aerodynamic Characteristics of the NACA 0018 Airfoil Used in the Darrieus wind Turbines. Master's Thesis, The Faculty of Power and Aeronautical Engineering, Warsaw University of Technology, Warsaw, Poland, 2020.
38. Ferreira, C.S.; Barone, M.; Zanon, A.; Giannattasio, P. Airfoil optimization for stall regulated vertical axis wind turbines. In Proceedings of the AIAA SciTech—33rd Wind Energy Symposium, Kissimmee, FL, USA, 5–9 January 2015; pp. 1–16. [CrossRef]
39. Ashwill, T.D. *Measured Data for the Sandia 34-Meter Vertical Axis Wind Turbine*; SAND91-2228; Sandia National Laboratories: Albuquerque, NM, USA, 1992.
40. Shires, A. Development and Evaluation of an Aerodynamic Model for a Novel Vertical Axis Wind Turbine Concept. *Energies* **2013**, *6*, 2501–2520. [CrossRef]
41. Jacobs, E.N.; Sherman, A. *Airfoil Section Characteristics as Affected by Variations of the Reynolds Number*; Technical Report; National Advisory Committee for Aeronautics: Langley Field, VA, USA, 1937. Available online: https://ntrs.nasa.gov/api/citations/19930091662/downloads/19930091662.pdf (accessed on 15 April 2022).
42. Abbott, H.; Doenhoff, E.; Lous, S.; Stivers, J. National Advisory Commitee for Aeronautics Report No. 824: Summary of Airfoil Data. 1945. Available online: https://ntrs.nasa.gov/api/citations/19930090976/downloads/19930090976.pdf (accessed on 15 April 2022).
43. Sheldahl, R.E.; Klimas, P.C. *Aerodynamic Characteristics of Seven Symmetrical Airfoil Sections through 180-Degree Angle of Attack for Use in Aerodynamic Analysis of Vertical Axis Wind Turbines*; Technical Report; Sandia National Laboratories: Albuquerque, NM, USA, 1981. [CrossRef]
44. Bastankhah, M.; Porté-Agel, F. A New Miniature Wind Turbine for Wind Tunnel Experiments. Part I: Design and Performance. *Energies* **2017**, *10*, 908. [CrossRef]

45. Hezaveh, S.H.; Bou-Zeid, E.; Lohry, M.W.; Martinelli, L. Simulation and wake analysis of a single vertical axis wind turbine. *Wind Energy* **2017**, *20*, 713–730. [CrossRef]
46. Bedon, G.; Schmidt Paulsen, U.; Aagaard Madsen, H.; Belloni, F.; Raciti Castelli, M.; Benini, E. Computational assessment of the DeepWind aerodynamic performance with different blade and airfoil configurations. *Appl. Energy* **2017**, *185*, 1100–1108. [CrossRef]
47. Rossander, M.; Dyachuk, E.; Apelfröjd, S.; Trolin, K.; Goude, A.; Bernhoff, H.; Eriksson, S. Evaluation of a Blade Force Measurement System for a Vertical Axis Wind Turbine Using Load Cells. *Energies* **2015**, *8*, 5973–5996. [CrossRef]
48. Shires, A.; Kourkoulis, V. Application of Circulation Controlled Blades for Vertical Axis Wind Turbines. *Energies* **2013**, *6*, 3744–3763. [CrossRef]
49. Nakano, T.; Fujisawa, N.; Oguma, Y.; Takagi, Y.; Lee, S. Experimental study on flow and noise characteristics of NACA0018 airfoil. *J. Wind. Eng. Ind. Aerodyn.* **2007**, *95*, 511–531. [CrossRef]
50. Bianchini, A.; Balduzzi, F.; Rainbird, J.M.; Peiro, J.; Graham, J.M.R.; Ferrara, G.; Ferrari, L. An Experimental and Numerical Assessment of Airfoil Polars for Use in Darrieus Wind Turbines—Part I: Flow Curvature Effects. *J. Eng. Gas Turbine Power* **2016**, *138*, 032602. [CrossRef]
51. Bianchini, A.; Balduzzi, F.; Rainbird, J.M.; Peiro, J.; Graham, J.M.R.; Ferrara, G.; Ferrari, L. An Experimental and Numerical Assessment of Airfoil Polars for Use in Darrieus Wind Turbines—Part II: Post-stall Data Extrapolation Methods. *J. Eng. Gas. Turbine Power* **2016**, *138*, 032603. [CrossRef]
52. Istvan, M. Turbulence intensity effects on laminar separation bubbles formed over an airfoil. *AIAA J.* **2018**, *56*, 335–1347. [CrossRef]
53. Istvan, M.S.; Yarusevych, S. Effects of free-stream turbulence intensity on transition in a laminar separation bubble formed over an airfoil. *Exp. Fluids* **2018**, *59*, 52. [CrossRef]
54. Claessens, M.C. The Design and Testing of Airfoils in Small Vertical Axis Wind Turbines. Master's Thesis, Delft University of Technology, Delft, The Netherlands, 2006. Available online: https://repository.tudelft.nl/islandora/object/uuid%3Afe4a7ae3-103e-40f3-a1f1-ae6d910d8c71 (accessed on 10 April 2022).
55. Du, L. Numerical and Experimental Investigations of Darrieus Wind Turbine Start-up and Operation. Ph.D. Thesis, Durham University, Durham, UK, 2016. Available online: http://etheses.dur.ac.uk/11384/ (accessed on 10 April 2022).
56. Müller-Vahl, H.F.; Strangfeld, C.; Nayeri, C.; Paschereit, C.O.; Greenblatt, D. Control of Thick Airfoil, Deep Dynamic Stall Using Steady Blowing. *AIAA J.* **2015**, *53*, 277–295. [CrossRef]
57. Melani, P.F.; Balduzzi, F.; Ferrara, G.; Bianchini, A. An Annotated Database of Low Reynolds Aerodynamic Coefficients for the NACA0018 Airfoil. *AIP Conf. Proc.* **2019**, *2191*, 020110. [CrossRef]
58. Belabes, B.; Paraschivoiu, M. Numerical study of the effect of turbulence intensity on VAWT performance. *Energy* **2021**, *233*, 121139. [CrossRef]
59. Tangermann, E.; Klein, M. Numerical simulation of laminar separation on a NACA0018 airfoil in freestream turbulence. In Proceedings of the AIAA Scitech 2020 Forum, Orlando, FL, USA, 6–10 January 2020; pp. 1–10. [CrossRef]
60. Marxen, O.; Rist, U.; Wagner, S. Effect of spanwise-modulated disturbances on transition in a separated boundary layer. *AIAA J.* **2004**, *42*, 937–944. [CrossRef]
61. Galbraith, M.C.; Visbal, M.R. Implicit Large Eddy Simulation of Low-Reynolds-Number Transitional Flow Past the SD7003 Airfoil. In Proceedings of the 40th Fluid Dynamics Conference and Exhibit, Chicago, IL, USA, 28 June–1 July 2010. [CrossRef]
62. Zhiyin, Y. Large-eddy simulation: Past, present and the future. *Chin. J. Aeronaut.* **2015**, *28*, 11–24. [CrossRef]
63. Kim, J.-H.; Ahn, J. Large Eddy Simulation of Leakage Flow in a Stepped Labyrinth Seal. *Processes* **2021**, *9*, 2179. [CrossRef]
64. Huang, Z.; Shi, G.; Liu, X.; Wen, H. Effect of Flow Rate on Turbulence Dissipation Rate Distribution in a Multiphase Pump. *Processes* **2021**, *9*, 886. [CrossRef]
65. Walters, D.K.; Cokljat, D. A three-equation eddy-viscosity model for Reynolds-averaged Navier-Stokes simulations of transitional flow. *J. Fluids Eng.* **2008**, *130*, 121401. [CrossRef]
66. Dick, E.; Kubacki, S. Transition Models for Turbomachinery Boundary Layer Flows: A Review. *Int. J. Turbomach. Propuls. Power* **2017**, *2*, 4. [CrossRef]
67. Menter, F.R.; Langtry, R.B.; Likki, S.R.; Suzen, Y.B.; Huang, P.G.; Völker, S. A Correlation-Based Transition Model Using Local Variables: Part I—Model Formulation. *J. Turbomach.* **2006**, *128*, 413–422. [CrossRef]
68. Turner, C. Laminar Kinetic Energy Modelling for Improved Laminar-Turbulent Transition Prediction. Ph.D. Thesis, School of Mechanical, Aerospace and Civil Engineering, The University of Manchester, Manchester, UK, 2012. Available online: https://www.proquest.com/pagepdf/1774233482 (accessed on 10 April 2022).
69. Suluksna, K.; Juntasaro, E. Assessment of intermittency transport equations for modeling transition in boundary layers subjected to freestream turbulence. *Int. J. Heat Fluid Flow* **2008**, *29*, 48–61. [CrossRef]
70. Choudhry, A.; Arjomandi, M.; Kelso, R. A study of long separation bubble on thick airfoils and its consequent effects. *Int. J. Heat Fluid Flow* **2015**, *52*, 84–96. [CrossRef]
71. Aftab, S.M.A.; Mohd Rafie, A.S.; Razak, N.A.; Ahmad, K.A. Turbulence Model Selection for Low Reynolds Number Flows. *PLoS ONE* **2016**, *11*, e0153755. [CrossRef] [PubMed]
72. Michna, J.; Rogowski, K.; Bangga, G.; Hansen, M.O.L. Accuracy of the Gamma Re-Theta Transition Model for Simulating the DU-91-W2-250 Airfoil at High Reynolds Numbers. *Energies* **2021**, *14*, 8224. [CrossRef]

73. Tescione, G.; Ragni, D.; He, C.; Ferreira, C.J.S.; van Bussel, G.J.W. Near wake flow analysis of a vertical axis wind turbine by stereoscopic particle image velocimetry. Renew. *Energy* **2014**, *70*, 47–61. [CrossRef]
74. Guo, Z.; Fletcher, D.F.; Haynes, B.S. Implementation of a height function method to alleviate spurious currents in CFD modelling of annular flow in microchannels. *Appl. Math. Model.* **2015**, *39*, 4665–4686. [CrossRef]
75. Kapsalis, P.C.S.; Voutsinas, S.; Vlachos, N.S. Comparing the effect of three transition models on the CFD predictions of a NACA0012 airfoil aerodynamics. *J. Wind. Eng. Ind.* **2016**, *157*, 158–170. [CrossRef]
76. Morgado, J.; Vizinho, R.; Silvestre, M.A.R.; Páscoa, J.C. XFOIL vs. CFD performance predictions for high lift low Reynolds number airfoils. *Aerosp. Sci. Technol.* **2016**, *52*, 207–214. [CrossRef]
77. Günel, O.; Koç, E.; Yavuz, T. CFD vs. XFOIL of airfoil analysis at low reynolds numbers. In Proceedings of the 2016 IEEE International Conference on Renewable Energy Research and Applications (ICRERA), Birmingham, UK, 20–23 November 2016; pp. 628–632. [CrossRef]
78. Cakmakcioglu, S.C.; Sert, I.O.; Tugluk, O.; Sezer-Uzol, N. 2-D and 3-D CFD Investigation of NREL S826 Airfoil at Low Reynolds Numbers. *J. Phys. Conf. Ser.* **2014**, *524*, 012028. [CrossRef]
79. Gerakopulos, R.; Boutilier, M.S.H.; Yarusevych, S. Aerodynamic Characterization of a NACA 0018 Airfoil at Low Reynolds Numbers. In Proceedings of the AIAA 2010-4629, 40th Fluid Dynamics Conference and Exhibit, Chicago, IL, USA, 28 June–1 July 2010. [CrossRef]

Advances in Science and Technology Research Journal

Advances in Science and Technology Research Journal, 2025, 19(2), 136–150
https://doi.org/10.12913/22998624/195556
ISSN 2299-8624, License CC-BY 4.0

Received: 2024.08.28
Accepted: 2024.12.15
Published: 2025.01.01

Aerodynamic performance analysis of NACA 0018 airfoil at low Reynolds numbers in a low-turbulence wind tunnel

Krzysztof Rogowski[1*], Robert Flemming Mikkelsen[2], Jan Michna[1], Jan Wiśniewski[1]

[1] Institute of Aeronautics and Applied Mechanics, Warsaw University of Technology, Nowowiejska 24, 00-665 Warsaw, Poland
[2] DTU Wind & Energy Systems, Technical University of Denmark, Roskilde, Denmark
* Corresponding author's e-mail: krzysztof.rogowski@pw.edu.pl

ABSTRACT

The objective of this study was to measure the aerodynamic characteristics of the NACA 0018 airfoil across a range of low Reynolds numbers, with a particular focus on the unique behaviours observed in this regime. The experiments were conducted primarily in a low-turbulence wind tunnel using wall pressure taps, a pressure rake, and a force gauge. The Reynolds numbers investigated ranged from 30.000 to 160.000, with angles of attack spanning from -190 to +20 degrees. A major achievement of this research was the successful acquisition of data at Re = 30.000, where the lift behaviour significantly deviated from that observed at higher Reynolds numbers. The results demonstrated a strong dependency of aerodynamic characteristics on Reynolds number, with the drag coefficient at zero angle of attack decreasing by over 700 percent when Re increased from 30.000 to 160.000. Additionally, two independent techniques for measuring lift force were employed, both yielding consistent results despite the low Reynolds number. The experimental results were also compared with XFOIL and 2-D CFD simulations, which, although not perfectly accurate, provided reasonably good predictions.

Keywords: NACA 0018 airfoil, Lift and drag characteristics, low Reynolds number, wind tunnel, XFOIL, Small-scale wind turbine design.

INTRODUCTION

As awareness of the consequences of fossil fuel exploitation continues to rise globally, there has been a significant expansion in the development of renewable energy sources. Since the fuel crisis of the 1970s, the wind energy sector has predominantly focused on horizontal-axis wind turbines (HAWT). This type of turbine has been extensively studied, and enhancing the rotor power coefficient characteristics across a broad range of tip speed ratios presents a significant challenge. Increasing attention is now being directed toward improving the aerodynamic performance of vertical-axis wind turbines (VAWT) to narrow the efficiency gap between these two turbine types [1, 2].

Currently, many researchers propose solutions based on the so-called upscaling. This approach aims to study the aerodynamic characteristics of a turbine rotor at a small scale, calibrate more or less reduced aerodynamic models based on these results, and then simulate wind turbines, often several hundred meters in scale [3]. However, the problem lies in the vastly different conditions present in modern wind tunnels compared to those in Earth's atmosphere [4–6]. This paper does not address the topic of upscaling but instead focuses on issues within the scale of the wind tunnel itself, where the flow should be minimally disturbed. It turns out, however, that calibrating numerical models is a challenging task, and even the most advanced contemporary numerical models struggle to handle such conditions effectively [7]. Most importantly, there is still an insufficient amount of experimental data in the literature to even begin calibrating the turbulence models used in CFD. Currently, the only numerical techniques capable of providing reliable data are Large Eddy Simulation (LES) or even Direct Numerical Simulation (DNS) [8]. However, these techniques are still too computationally expensive to be used across a wide range of angles of attack and under different flow conditions.

The main problem with simulations using Reynolds-Averaged Navier-Stokes (RANS) techniques is the occurrence of laminar separation near the surface of the airfoil. RANS models do not simulate such phenomena based on the solution of the N-S equations but instead rely on correlations. This means that the position of the laminar-turbulent transition is determined based on local flow conditions (such as local turbulence intensity), which is tracked by one of the transport equations in the Transition SST model and compared with an appropriate database developed experimentally. However, this approach is insufficient and often lacks accuracy [9].

In recent years, there have even been studies on wind turbines at a laboratory scale, where the chord-based Reynolds number reaches values in the range of 20.000–30.000 [3]. These are extremely small ranges. Moreover, in such cases, airfoils from the four-digit NACA series are quite often used. However, these airfoils perform poorly under such flow conditions. The reason why many contemporary engineers and researchers continue to use them is due to several factors. One of these is the aforementioned lack of airfoil characteristics across a wide range of Reynolds numbers and, more importantly, over a broad spectrum of angles of attack. As a result, up until almost 2011, the only available database of airfoils was the one created by Sheldahl and Klimas [10], which mainly contained characteristics of airfoils from the four-digit NACA series. For low Reynolds numbers, the results published in this report differ significantly from those found in more recent studies [11].

In recent years, several modern wind tunnel studies have been conducted on the NACA 0018 airfoil at low Reynolds numbers [12–16]. The first modern experimental studies of the NACA 0018 airfoil at such low Reynolds numbers were conducted by Timmer [12]. The author emphasizes that at low Reynolds numbers, the NACA 0018 airfoil is predominantly affected by laminar separation on the lower surface, which significantly influences its aerodynamic characteristics and the noise it generates. The application of zigzag tape effectively reduces this noise. Timmer also observed large post-stall hysteresis loops, which increase in size with rising Reynolds numbers. Timmer's research covered a range of Reynolds numbers from 150.000 to 1,000.000. However, Timmer noted that at the lowest Reynolds number of 150.000, the pressures were insufficient for wake measurements. Consequently, the drag curve at this Reynolds number was inferred using data for parasitic drag and aspect ratio from tests conducted at Re 300.000. Unique studies using the PIV technique were conducted by Nakano et al. [13]. The main accomplishments of this research include a thorough experimental investigation of the flow and noise characteristics of the NACA 0018 airfoil at a moderate Reynolds number of 160.000. The research effectively uncovered the connection between flow separation, reattachment, and the generation of tonal noise, offering significant insights into the aerodynamic performance of the airfoil under these specific conditions. Significant advancements in measurement techniques for the NACA 0018 airfoil and other airfoils from the four-digit NACA series have been made by the University of Waterloo. A prime example is the publication by Gerakopulos et al. [14]. Their study made notable contributions through the experimental analysis of the NACA 0018 airfoil at low Reynolds numbers, specifically within the range of 80.000 to 200.000. The researchers effectively characterized the airfoil's lift and separation bubble behaviour, uncovering two distinct regions in the lift curve associated with varying angles of attack. Additionally, their work highlighted how the separation bubble's position and length adjust with changes in Reynolds numbers and angles of attack, offering essential insights into the aerodynamic performance of the airfoil in low Reynolds number conditions. Following the work of Gerakopulos et al., another significant study in this research area was conducted by Longhuan Du in 2016 [15]. Du's study involved an in-depth experimental and numerical analysis of the NACA 0018 airfoil, focusing on its aerodynamic characteristics at low Reynolds numbers, specifically ranging from 60.000 to 140,000. The research utilized sophisticated measurement techniques, including Particle Image Velocimetry (PIV) for detailed flow visualization and pressure distribution analysis, to explore flow separation, reattachment, and the airfoil's overall aerodynamic behaviour. This work provided additional insights into low Reynolds number aerodynamics, contributing significantly to the existing knowledge in the field. Other independent measurements were conducted at Imperial College in a low-turbulence wind tunnel [16]. Pressure distribution measurements were employed to capture the aerodynamic characteristics of the airfoils. The experimental studies were carried out within a Reynolds number range of 60.000 to 300.000 and angles of attack from 0° to 180°. The results provided empirical data that validated the hypothesis of virtual camber effects, showing significant differences in performance between the standard and transformed airfoils.

Against the backdrop of the existing state of knowledge, our research provides an additional contribution. Specifically, we extended the study to even lower Reynolds numbers, down to 30.000, where the lift coefficient (C_L) exhibits a completely different behaviour compared to higher Reynolds number values. Moreover, to accurately measure the lift coefficient, we successfully employed two techniques: force gauge and wall pressure taps, which were not utilized by the previously mentioned authors.

In recent years, the use of composite materials has gained prominence across various engineering applications, including aerospace, automotive, and energy industries. This trend reflects a broader shift toward materials that offer high strength-to-weight ratios, thermal stability, and resistance to environmental factors. Such advancements have enhanced the performance and durability of structures, as seen in both civil and military aviation applications. For instance, Setlak et al. highlight the substantial benefits of composite materials in reducing weight and increasing the structural integrity of military aircraft, such as the F-35, where composite components contribute to improved durability and reduced radar detectability due to their unique mechanical and electromagnetic properties [17]. Our study builds on this foundation by examining the aerodynamic performance of the NACA 0018 airfoil at low Reynolds numbers, with a focus on its behaviour in low-turbulence environments. By comparing experimental data with computational predictions, we aim to contribute valuable insights into the optimization of airfoil designs for both small-scale wind turbines and low-speed aircraft, where composite airfoils have shown potential in enhancing efficiency and reducing structural loads. The findings provide further data critical for advancing turbulence models and adapting composite airfoils in applications demanding reliable performance in varied operational conditions.

EXPERIMENTAL SETUP AND METHODOLOGY FOR AERODYNAMIC LOAD MEASUREMENT IN A LOW-TURBULENCE WIND TUNNEL

The experimental investigations were conducted in a low-turbulence wind tunnel at the Technical University of Denmark (DTU) in Lyngby. This is the so-called Red Wind Tunnel (Fig. 1), belonging to the DTU Wind Energy Department. The open-loop wind tunnel is equipped with a test section measuring H×W = 0.5×0.75 m, with a total length of L = 2 m. The tunnel is capable of reaching a maximum flow velocity of 40 m/s while maintaining a turbulence intensity of less than 0.1%. The reference pressure is determined using a standard Pitot tube. Aerodynamic loads were assessed using wall-mounted pressure taps (Fig. 2b) to determine lift coefficients, and a wake rake setup was employed to measure drag coefficients. The pressure measurements were

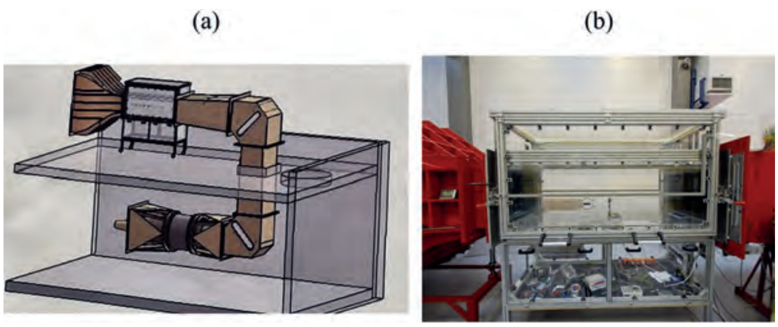

Figure 1. (a) Schematic diagram of the DTU Red Wind Tunnel configuration, (b) photograph of the measurement section of the DTU Red Wind Tunnel

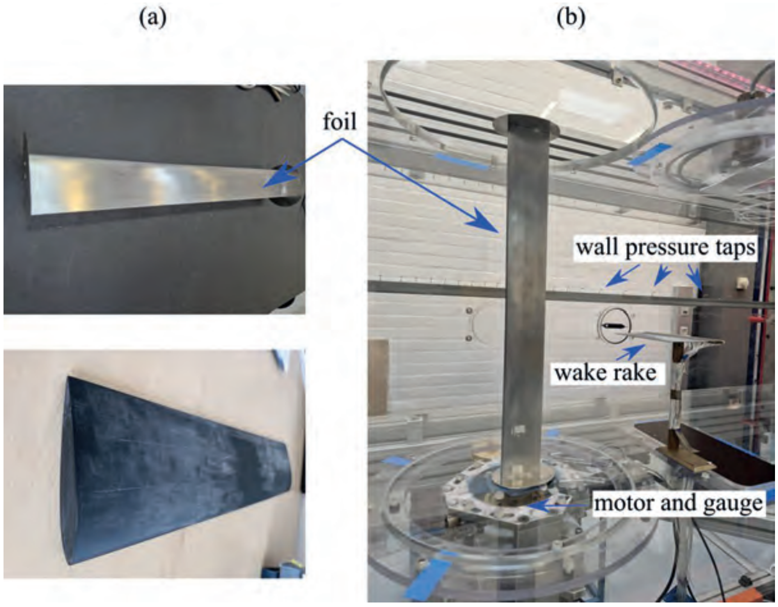

Figure 2. (a) Two foils used in the experimental study: the upper foil is made of aluminium, while the lower one is 3D printed using PLA; (b) the experimental setup inside the DTU Red Wind Tunnel shows the mounted foil, wall pressure taps, wake rake, and motor and gauge used for measurements

conducted using Pressure Systems scanners, with a total range of ± 2.5 kPa for wall pressures and ± 7 kPa for wake pressures. Data acquisition was performed at a sampling rate of 125 Hz, with measurements taken for 10 seconds at each angle of attack. In addition, a load cell was used to measure the lift force.

The experimental study utilized two rectangular foils (Fig. 2a) with a symmetrical NACA0018 airfoil. Most of the wind tunnel tests were conducted using a foil with a chord length of 60 mm, which was extruded from aluminium – shown in the top illustration in Figure 2a. The aluminium foil was made from an actual blade of the TU Delft VAWT rotor [18]. The rotor blade was cut to a length of 500 mm, matching the height of the wind tunnel's test section, and was sanded down with very fine sandpaper.

The second wing (bottom image in Fig. 2a) had a chord length of 106 mm and was produced on a 3D printer using PLA RE from Smartfill – a slightly stiffer material than standard PLA made from recycled PLA. The NACA 0018 blade featured one cylindrical inner spar and three shear webs with 3 mm edge blends and a middle section thickness of 5 mm each. The total length of the blade was 500 mm, divided into three sections. The final model chord was 106 mm after blunting the trailing edge by 3 mm. The final surface roughness of the blade was achieved by wet sanding with P800 sandpaper.

EXPERIMENTAL ANALYSIS OF AERODYNAMIC CHARACTERISTICS UNDER VARYING REYNOLDS NUMBERS AND ANGLES OF ATTACK

This paper presents the results of several measurement series. Most of the tests were conducted on the aluminium foil due to its lower chord length (resulting in lower blockage effects) and larger stiffness, which allowed for force measurements over a wide range of angles of attack. The following measurement series were conducted for this foil. For Reynolds numbers of 100.000 and 160.000, both components of the aerodynamic force were measured over an angle of attack range of ± 17 degrees. Two measurement techniques were used in these cases: wall pressure taps and a force gauge. The drag coefficient was determined based on wake velocity measurements. For Reynolds numbers of 30 k, 50 k, 80 k, 100 k, and 160 k, the lift component was measured over a wide range of angles of attack, from -190 degrees to +20 degrees. Since the wake rake used in our studies was not sufficiently wide, we present results for the drag coefficient only within the ± 20-degree range. For the 3D-printed wing, we present data only for a Reynolds number of Re = 100 k as an additional validation of the results presented here. Wall interference correction was considered [20] and being proportional to chord/width ratio c/w = 60 mm/750 mm and 106 mm/750 mm, which for both foils is very small, correction on aoa, lift and drag coefficients are less than 0.5% for attack range of ± 17 degrees. Blockage ratio for the attack range of 30 to 150 deg is at max 8% which is considered acceptable for separated flow.

Figure 3 compares the aerodynamic characteristics of the NACA0018 airfoil for a Reynolds number of 100 k, obtained using three independent measurement systems. The measurements indicate significant hysteresis in both the lift and drag coefficients in the region of the critical angle of attack. Such behaviour of the aerodynamic characteristics is typical for these flow conditions. Both measurement techniques confirm a high level of agreement in the lift force results. In addition to the hysteresis, a certain asymmetry in the lift force relative to the zero angle of attack is also noticeable. Similar phenomena were observed in the famous report [19] when investigating various airfoils at low Reynolds numbers. Timmer's research [12] also confirms this kind of behaviour, particularly at the lowest Reynolds number he studied – 150 k. The strong agreement between both measurements is further confirmed by comparing the same results as a C_L versus C_D relationship, as shown in the graph in Figure 4.

During the lift force measurements while increasing the angle of attack, a maximum lift coefficient of 0.948 was recorded (Fig. 3). On the return path (while decreasing the angle of attack), this value decreased by approximately 12%.

The zero angle of attack and its close vicinity proved to be extremely challenging to measure. While passing through this region, noticeable aerodynamic noise was observed, resulting from the shedding of vortex structures from both the suction and pressure sides. These structures are a consequence of laminar boundary layer separation and the formation of bubbles, which then evolve into the flow in the aerodynamic wake. The existence of such bubbles has also been documented in studies by other authors [13]. The presence of laminar separation bubbles results in significant nonlinearities in the lift force characteristics up to the critical angle of attack. The drop in lift force observed in the obtained characteristics after exceeding this critical angle of attack appears to be substantial. The loss of lift in the considered case is approximately 58.4%.

Up to this point, the lift force has been measured using two techniques: a force gauge measurement and a pressure measurement. The purpose of the next figure (Fig. 5) is to examine how both techniques perform when measuring over a much wider range of angles of attack at a Reynolds number of 100.000. The measurements were conducted starting from an angle of attack of -190 degrees and then

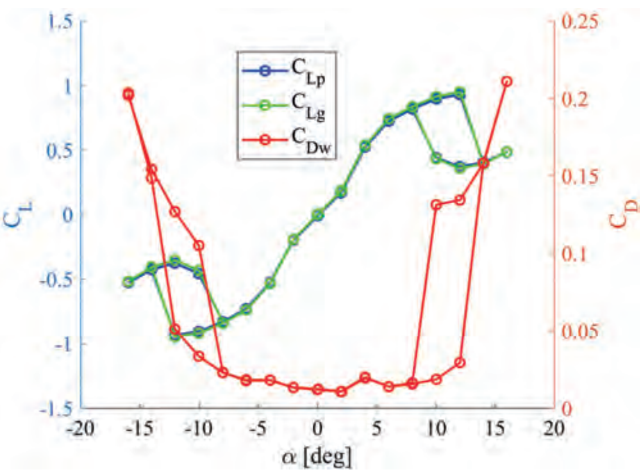

Figure 3. Comparison of the lift coefficient obtained using wall pressure taps (C_{Lp}) and a force gauge (C_{Lg}), along with the drag coefficient (C_{Dw}) measured using a wake rake. These results are for a Reynolds number of Re = 100 k

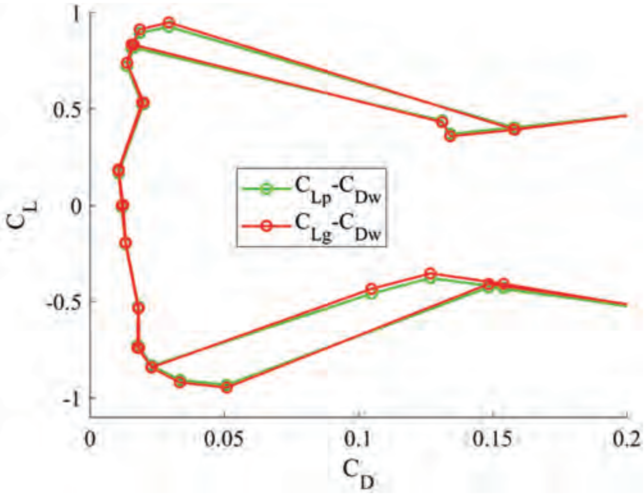

Figure 4. Polar plots of the lift coefficient (C_L) versus the drag coefficient (C_D) for a Reynolds number of Re = 100 k. The plot compares the results obtained from pressure taps (C_{Lp}), a force gauge (C_{Lg}), and a wake rake (C_{Dw})

increasing the angle up to 20 degrees. In this case, the measurements were performed in only one direction, so hysteresis is not observed.

As can be observed from Figure 5, there is strong agreement between the two measurement techniques, except in the range from -149 to -25 degrees. These differences are attributed to the limited number of pressure taps. In our case, the number of pressure taps was 64–32 on each side wall of the tunnel. When the angles of attack are low, the sensors 'see' a larger area of the wing. It should also be noted that at large angles of attack, the wing, supported at a single point, experiences increasing vibrations. With a small wing chord of 6 cm, the undisturbed flow velocity must be sufficiently high. For the highest Reynolds number we tested, 160 k, we used nearly the maximum achievable flow velocity in our wind tunnel

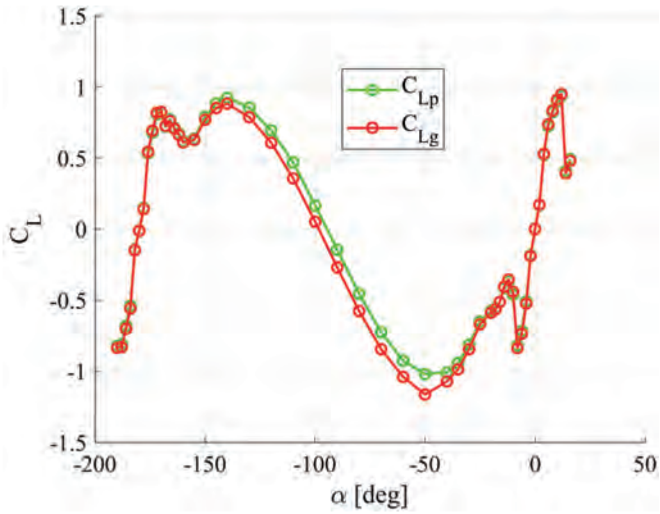

Figure 5. Comparison of the lift coefficient (C_L) over a wide range of angles of attack (α) for Re = 100 k, using two different measurement techniques. The green line (C_{Lp}) represents the results obtained from wall pressure taps, while the red line (C_{Lg}) represents the results from the force gauge

(approximately 40 m/s). In the case of the highest Reynolds number we examined, 160 k, to avoid vibrations, the wing was additionally supported with a pin attached to the ceiling of the wind tunnel's test section. Therefore, in this case (Re = 160 k), only the results obtained using the pressure measurement technique could be used. Conducting this test at Re = 100 k to verify the lift force measurement using both the force gauge and wall pressure taps was therefore necessary. Despite the differences in the C_L results visible in the angle of attack range from -149 to -25 degrees (Fig. 5), both curves are acceptable. The largest discrepancy is observed at an angle of attack around -50 degrees. The pressure sensors recorded a lift coefficient of -1.021 in this case, with the lift force prediction from the second measurement system differing by approximately 12.3%.

Figures 6, 7, and 8 present the results of the aerodynamic force coefficients for five different Reynolds numbers over a wide range of angles of attack, from -190 to 20 degrees. Figure 7 shows

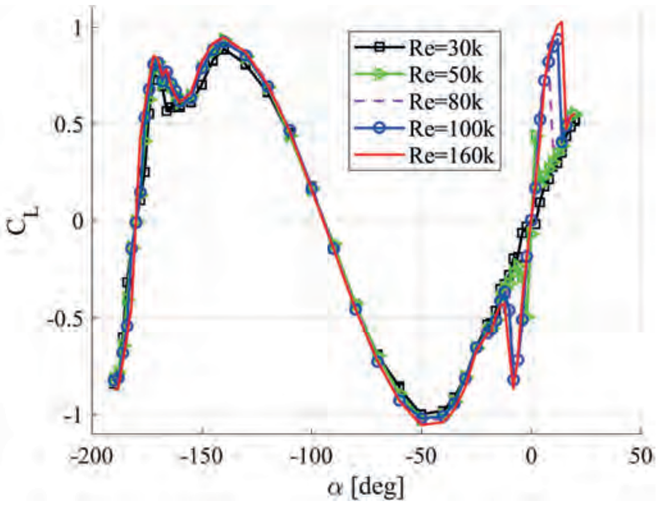

Figure 6. The lift coefficient (C_L) as a function of angle of attack (α) for different Reynolds numbers shows the significant impact of Reynolds number on the aerodynamic characteristics

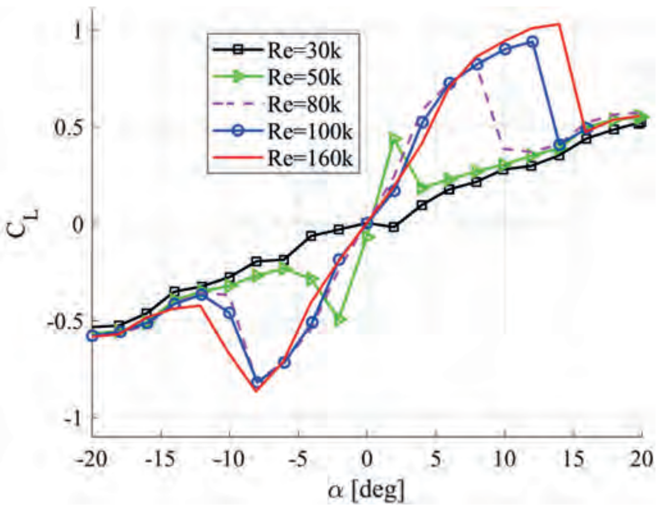

Figure 7. The lift coefficient (CL) as a function of angle of attack (α) for different Reynolds numbers shows the significant impact of Reynolds number on the aerodynamic characteristics

the same lift coefficient results as in Figure 6 but within a narrower range of angles of attack, from -20 to 20 degrees. The characteristics displayed in Figures 6 and 7 were obtained solely from pressure measurements for reasons discussed in the previous paragraph. Figure 8, on the other hand, presents the drag coefficient characteristics only within the angle of attack range from -20 to 20 degrees. The wake rake used had too short a span to capture all the details in the wide aerodynamic wake and integrate them. The presented results indicate that the largest discrepancies are observed at the lowest Reynolds numbers tested in this measurement campaign, specifically for Re 30 k and 50 k. At the lowest Reynolds number, the lift force is practically negligible, while at 50 k, it is tiny, with a maximum lift coefficient, C_{Lmax}, of only 0.435 at an angle of attack of just 3 degrees. The results indicate that the most significant discrepancies are observed at the lowest Reynolds numbers tested in this measurement campaign, specifically for Re 30 k and 50 k. Even a slight increase in the Reynolds number from 80k to 100k leads to a 14% increase in lift from 0.803. Similarly, an increase from Re = 100 k to 160 k results in a further 9.6% increase. A similar strong dependence on the Reynolds number is observed for the drag coefficient. For Re = 160 k, the drag coefficient at a zero angle of attack is 0.0084. In contrast, at Re = 30 k, this coefficient is as much as 586% higher at the same zero angle of attack. In this paper, two types of measurement series were conducted for the aluminum foil. The tests primarily differed in that, in one case, the range of angles of attack varied within a shorter range of ± 20 degrees (in both directions), while in the other case, it ranged from -190 degrees to 20 degrees (in only one direction). To demonstrate that in both tests, the results are generated similarly for the ± 20 degree range, a separate graph was prepared (Fig. 9). This figure shows the comparison of results for Test A corresponding to the shorter range of angles of attack and Test B corresponding to the longer range. The figure clearly shows that for the angle of attack range from -20 to 20 degrees, the results are the same when the angle of attack increases.

Figure 10 compares the lift force results for a Reynolds number of 100k for two foils: an aluminium foil and a printed foil. Both foils are made from different materials, and their roughness slightly differs. Despite these minor imperfections in both wings, the obtained lift force results are surprisingly almost identical. This suggests a high reliability of the measurement system used. Figures 11 and 12 illustrate the dependence of the aerodynamic characteristics of the airfoil on the Reynolds number. Two Reynolds numbers, 100 k and 160 k, are compared in these figures. In this case, we focused primarily on the quantitative and qualitative comparison of the hysteresis loops. As previously indicated, the loss of lift force after exceeding the critical angle of attack

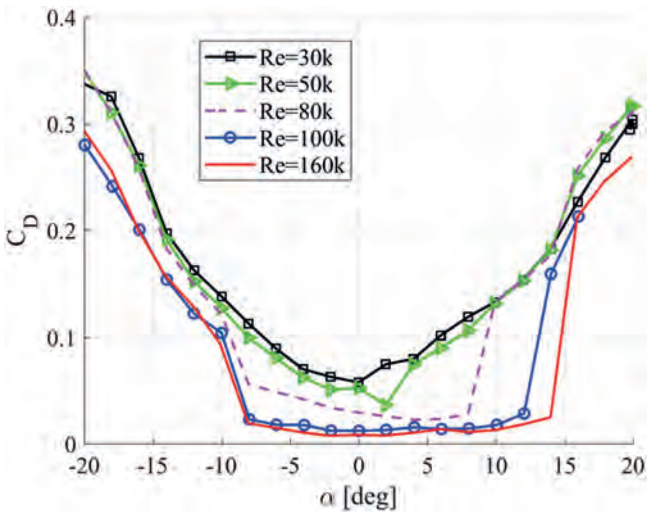

Figure 8. The drag coefficient (CD) as a function of angle of attack (α) for different Reynolds numbers shows the significant impact of Reynolds number on the aerodynamic characteristics

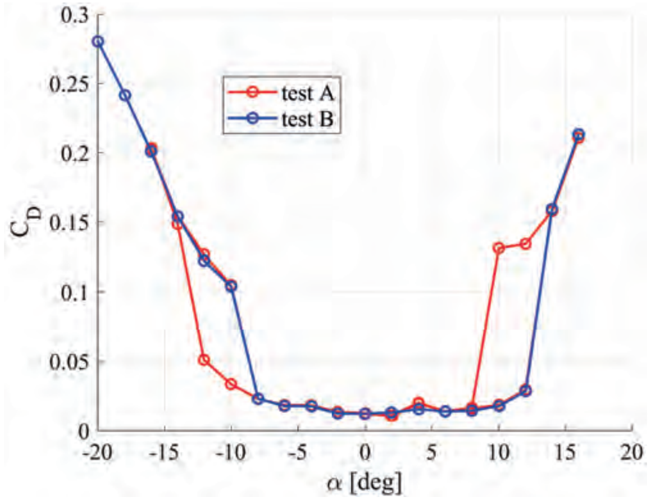

Figure 9. Comparison of the drag coefficient C_D as a function of the angle of attack α for two types of tests at a Reynolds number of 100 000. Test A (red curve) corresponds to a shorter range of angles of attack (± 20 degrees), whereas Test B (blue curve) corresponds to a wider range (-190 degrees to 20 degrees). The results show the consistency of drag coefficient behaviour in the overlapping range of angles

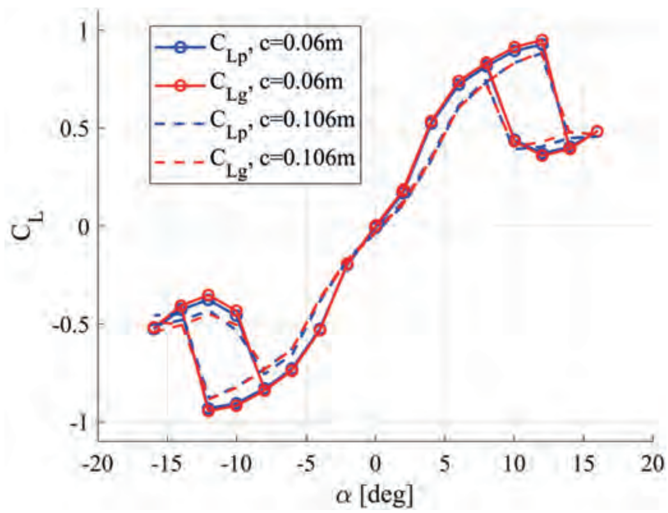

Figure 10. Lift coefficient (C_L) as a function of the angle of attack (α) for two airfoils with different chord lengths and materials at a Reynolds number of 100.000. The solid lines with markers represent measurements for the aluminium foil with a shorter chord length (c = 0.06 m), while the dashed lines represent measurements for the 3D-printed foil with a longer chord length (c = 0.106 m)

is rapid and occurs for both Reynolds numbers presented in Figure 11. For Re = 160 k, the maximum lift coefficient C_{Lmax} was recorded as 1.012 at an angle of attack of 14.02 degrees. During the wing's movement in the opposite direction (decreasing angle of attack), the lift coefficient C_L was 0.421 at the same angle of attack, indicating a decrease in lift force by approximately 58.4%. In the case of Re = 100 k, the maximum lift coefficient C_{Lmax} was 0.926 at an angle of attack of 12.04 degrees, with a corresponding drop in lift force of about 60%. Visually, the lift force hysteresis loops for both Reynolds numbers are similar and almost linearly shifted.

The shape of the drag coefficient hysteresis (Fig. 12) is also similar and shifted; however, the

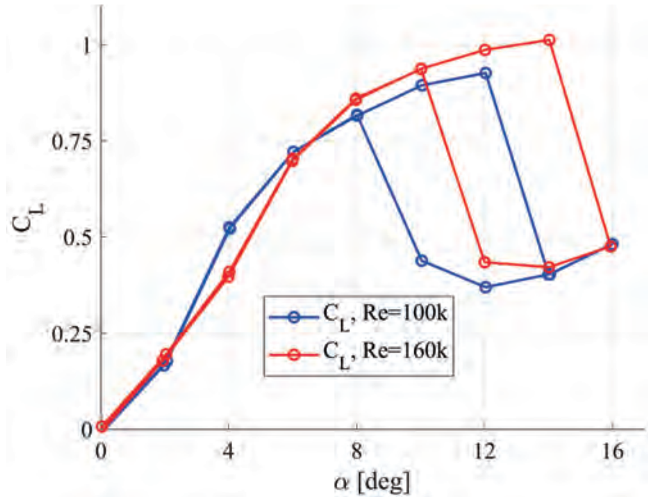

Figure 11. Comparison of lift coefficient hysteresis loops for the NACA 0018 airfoil at two Reynolds numbers (Re = 100 k and Re = 160 k)

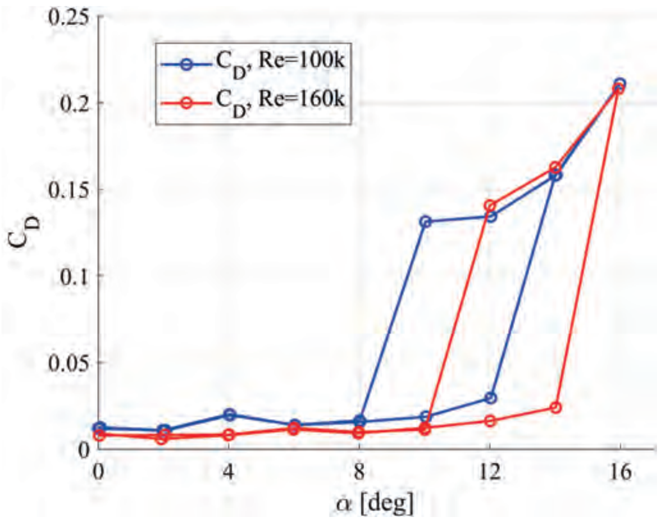

Figure 12. Comparison of drag coefficient hysteresis loops for the NACA 0018 airfoil at two Reynolds numbers (Re = 100 k and Re = 160 k)

differences in value increments are much larger than for the lift force and are strongly dependent on the Reynolds number. During the increase in the angle of attack for Re = 100 k, there is a sharp rise in drag starting from an angle of attack of 12.04 degrees. At this angle, the drag coefficient is 0.0294. An increase in the angle of attack by two degrees results in a rise in the drag coefficient by about 453%. In the case of Re = 160 k, the sharp increase in lift force begins slightly later, at an angle of attack of 14.03 degrees. An increase in the angle of attack by two degrees (from 14.03 to 15.95 degrees) generates an increase in the drag coefficient by approximately 769.5%. The sudden drop in the lift coefficient during the wing's movement in the opposite direction (from positive to negative angles of attack) is similar: 92% for Re = 160 k (for angles between 12.01 and 10.02 degrees) and 87.5% for Re = 100 k (for angles between 10.04 and 8.02 degrees).

ASSESSMENT OF AERODYNAMIC PERFORMANCE USING EXPERIMENTAL AND NUMERICAL METHODS

Figures 13 and 14 compare the lift and drag characteristics obtained experimentally with the results from XFOIL. The calculations with this tool were performed using the parameter N = 9. Despite the low Reynolds numbers, a strong similarity was observed between the experimental and computational results. For the lowest Reynolds number examined, XFOIL confirmed an almost linear lift characteristic. The difference in drag between Re = 30 k and Re = 160 k calculated using this tool is also similar. For the two highest Reynolds numbers investigated in the measurement campaign, the XFOIL results show a significant increase in drag for similar angles of attack. The maximum lift coefficient values obtained with XFOIL are overestimated compared to the experimental results, which is an expected outcome. The lift characteristics obtained with this numerical tool are also strongly nonlinear within the range of angles of attack up to the critical angle of attack.

Figure 15 compares the aerodynamic characteristics of the airfoil at Re = 160 k obtained using the 2-D CFD approach. The numerical calculations were performed using the model discussed and described in [4]. This referenced publication contains a detailed description of the model,

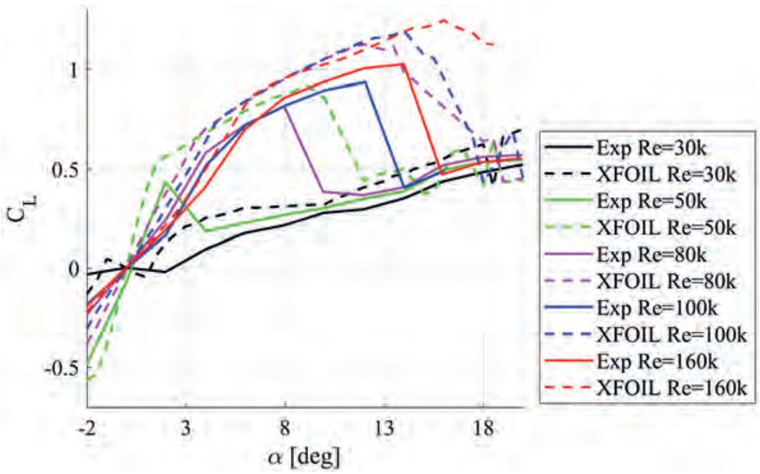

Figure 13. Lift coefficient as a function of the angle of attack. Comparison of experimental results with XFOIL

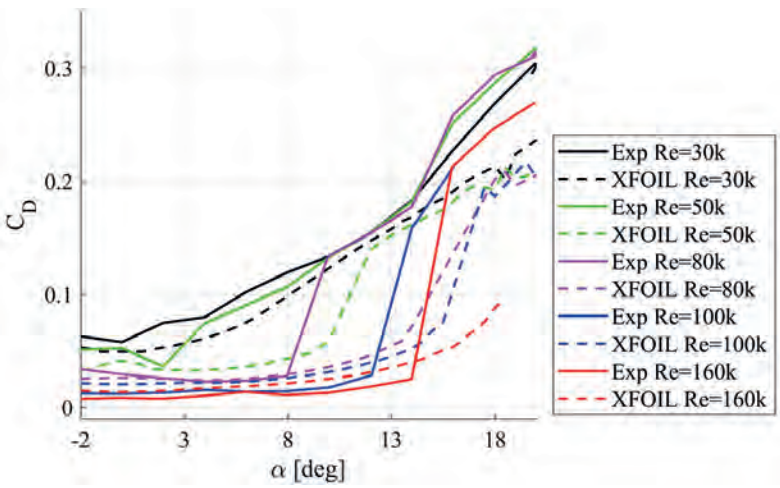

Figure 14. Drag coefficient as a function of the angle of attack. Comparison of experimental results with XFOIL

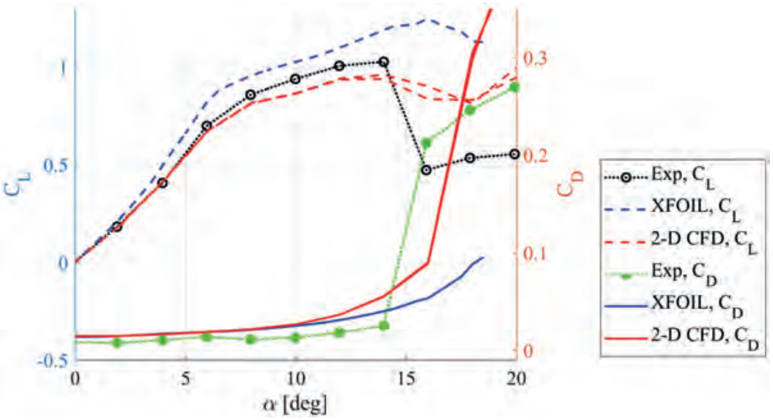

Figure 15. Comparison of airfoil characteristics at Re = 160 k obtained from experiments and 2-D CFD using the Transition SST model

methodology, as well as a mesh sensitivity test. In this study, the range of angles of attack was extended to 20 degrees. Figure 15 clearly shows that the 2-D CFD approach underestimates the lift force. In contrast to XFOIL, the Transition SST model more accurately predicts the significant increase in drag.

A reliable scientific paper should also refer to the results of experimental studies by other authors if such exist. Contemporary measurement results for the NACA0018 profile at Re approximately 150 k, starting from Timmer's publication, do not differ significantly from each other. All of them show a nonlinear range of C_L characteristics as a function of the angle of attack. Most of the existing experimental studies have been compared in previous publications by the first author of this paper. The differences between the existing studies were also pointed out by Melani et al. [11]. Therefore, in this publication, we compare only the results of three contemporary experimental studies available in the literature. To the best of our knowledge, only Timmer has published the characteristics of the NACA0018 profile considering hysteresis. However, it should be noted that this author mentioned that for this Reynolds

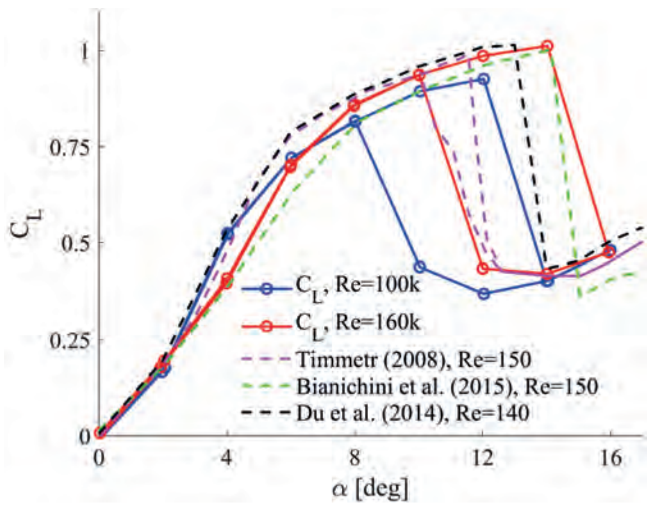

Figure 16. Comparison of lift coefficients obtained in our study with experimental results from other authors. The data shows results for Reynolds numbers Re = 100 k and Re = 160 k compared to the experimental findings of Timmer [12] at Re = 150 k, Bianchini et al. [16] at Re = 150 k, and Du et al. [15] at Re = 140 k

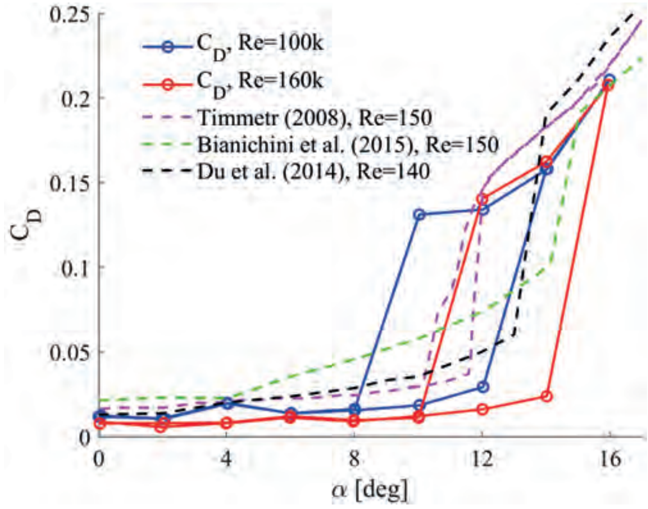

Figure 17. Comparison of drag coefficients obtained in our study with experimental results from other authors

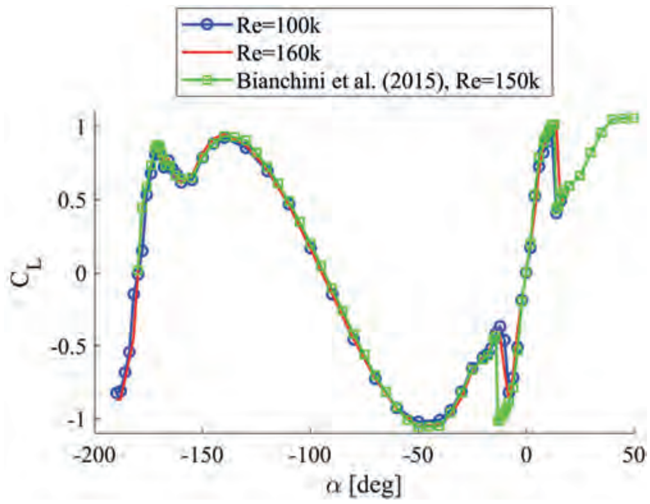

Figure 18. Comparison of drag coefficients obtained in our study with experimental results from Bianchini et al. [16] at Re = 150 k

number (150k), he was only able to measure the lift force reliably. Therefore, the drag force results are extrapolated in this case. The results shown in Figures 16 and 17 indicate that Timmer's hysteresis is smaller than in our case. This, of course, does not imply an error in our measurements. We have already informed the reader that measuring aerodynamic loads at such low Reynolds numbers can be subject to various errors primarily related to the measurement technique used and the flow conditions in the wind tunnel. Figure 17 also illustrates the significant differences in drag coefficients obtained by various independent authors. It is also worth emphasizing that two independent tests, ours and the one published by Bianchini et al. [16], show a high degree of consistency in the lift coefficient results for a wide range of angles of attack (Fig. 18).

CONCLUSIONS

This study focused on investigating the aerodynamic characteristics of the NACA 0018 airfoil across a range of low Reynolds numbers, emphasizing the distinct behaviours observed within this flow regime. The experiments were primarily conducted in a low-turbulence wind tunnel, utilizing wall pressure taps, a pressure rake, and a force gauge to gather data. The Reynolds numbers examined spanned from 30.000 to 160.000, with angles of attack ranging from -190 to +20 degrees. Based on the conducted research, the following conclusions can be drawn:

The comparison of the two measurement techniques (pressure taps and force gauge) for lift force at Re = 100 000 shows strong agreement across most of the tested angle of attack range, despite some discrepancies in specific regions, confirming the reliability of both methods under varying conditions. In the study, tests were also conducted using two different foils. These tests demonstrated the proper functioning of two independent systems for measuring lift force, confirming the reliability and accuracy of the measurement methodologies employed. The comparison of the three measurement systems for the NACA 0018 airfoil at Re = 100 k demonstrates significant hysteresis and asymmetry in the aerodynamic coefficients, with a strong agreement in the lift and drag measurements, confirming the reliability of the methods used for determining the lift coefficient. A decrease of approximately 12% in the maximum lift coefficient was observed when reducing the angle of attack.

Challenges in measuring around the zero angle of attack were noted, with significant aerodynamic noise associated with vortex shedding from both sides of the airfoil, highlighting the complexity of laminar boundary layer separation and bubble formation in this region.

The formation of laminar separation bubbles leads to considerable nonlinearities in lift force behaviour, with a significant loss of lift – around 58.4% at Re = 100 k – occurring after surpassing the critical angle of attack.

In the case of such low Reynolds numbers, both lift and drag characteristics are highly dependent on the Reynolds number. This dependency is particularly evident in the drag coefficient, which shows significant variation, increasing substantially as the Reynolds number decreases.

This paper also investigated the effect of the Reynolds number on the geometry of the stationary hysteresis loop. The comparison was conducted for Reynolds numbers 100 k and 160 k. Our study showed that an increase in Reynolds number causes almost a linear shift of the entire loop towards higher angles of attack and slightly higher lift coefficients. The shape of the drag coefficient loop is also similar with the increase in Reynolds number. However, a two-degree increase in the angle of attack results in a significant rise in drag.

The comparison between experimental results and XFOIL simulations reveals a strong agreement in both lift and drag characteristics, even at low Reynolds numbers. While XFOIL tends to overestimate the maximum lift coefficient, it accurately captures the overall trends, including the linear lift behaviour at the lowest Reynolds number and the significant drag increase at higher Reynolds numbers. These findings validate the reliability of XFOIL as a predictive tool for aerodynamic analysis within the tested parameter range.

The 2-D CFD approach, utilizing the Transition SST model, provides a more accurate prediction of drag increase compared to XFOIL but tends to underestimate lift values. This highlights the importance of selecting appropriate models for accurate aerodynamic simulations, especially at higher angles of attack.

Acknowledgements

This work was supported by the POB Energy program of Warsaw University of Technology, under the Excellence Initiative: Research University (IDUB) scheme (Grant No. 1820/355/Z01/POB7/2021). Additionally, the research benefited from resources provided by the Interdisciplinary Centre for Mathematical and Computational Modelling (ICM) at the University of Warsaw, through computational grants no. G93-1588 and G92-1487. I would also like to extend my sincere thanks to Mr. Eng. Tomasz Szuster, a retired academic from Warsaw University of Technology, for his invaluable support and mentorship.

REFERENCES

1. Kumar R., Raahemifar K., Fung A.S. A critical review of vertical axis wind turbines for urban applications. Renewable and Sustainable Energy Reviews. 2018, 89, 281–91. https://doi.org/10.1016/j.rser.2018.03.033
2. Bianchini A., Ferrara G., Ferrari L. Pitch optimization in small-size Darrieus wind turbines. Energy Procedia. 2015, 81, 122–32. https://doi.org/10.1016/j.egypro.2015.12.067

3. Huang M. Wake and wind farm aerodynamics of vertical axis wind turbines. Doctoral dissertation, Technische Universiteit Delft, 2023. https://doi.org/10.4233/uuid:14619578-e44f-45bb-a213-a9d179a54264
4. Michna J, Rogowski K. Numerical study of the effect of the reynolds number and the turbulence intensity on the performance of the NACA 0018 Airfoil at the low Reynolds Number Regime: Processes. 2022, 10(5), 1004. https://doi.org/10.3390/pr10051004
5. Rogowski K, Królak G, Bangga G. Numerical Study on the Aerodynamic Characteristics of the NACA 0018 Airfoil at Low Reynolds Number for Darrieus Wind Turbines Using the Transition SST Model. Processes. 2021, 9(3), 477. https://doi.org/10.3390/pr9030477
6. Bangga G., Dessoky A., Wu Z., Rogowski K., Hansen M.O.L. Accuracy and consistency of CFD and engineering models for simulating vertical axis wind turbine loads. Energy. 2020, 206. https://doi.org/10.1016/j.energy.2020.118087
7. Carreño Ruiz M., D'ambrosio D. Validation of the γ-Re θ transition model for airfoils operating in the very low Reynolds number regime. Flow, Turbulence and Combustion. 2022, 109(2), 279–308. https://doi.org/10.1007/s10494-022-00331-z
8. Zhang W., Samtaney R. Assessment of spanwise domain size effect on the transitional flow past an airfoil. Computers & Fluids. 2016, 124, 39–53. https://doi.org/10.1016/j.compfluid.2015.10.008
9. Langtry R. B., Menter, F. R. Correlation-based transition modeling for unstructured parallelized computational fluid dynamics codes. AIAA journal. 2009, 47(12), 2894–2906. https://doi.org/10.2514/1.42362
10. Sheldahl R.E., Klimas P.C. Aerodynamic characteristics of seven symmetrical airfoil sections through 180-Degree Angle of Attack for Use in Aerodynamic Analysis of Vertical Axis Wind Turbines. Technical Report; Sandia National Laboratories: Albuquerque, NM, USA, 1981. https://doi.org/10.2172/6548367
11. Melani P. F., Balduzzi F., Ferrara, G., Bianchini A. An annotated database of low Reynolds aerodynamic coefficients for the NACA0018 airfoil. In AIP Conference Proceedings. 2019, 2191(1), AIP Publishing. https://doi.org/10.1063/1.5138843
12. Timmer W.A. Two-Dimensional Low-Reynolds Number Wind Tunnel Results for Airfoil NACA 0018. Wind engineering. 2008, 32, 525–537. https://doi.org/10.1260/030952408787548848
13. Nakano T., Fujisawa N., Oguma Y., Takagi Y., Lee S. Experimental study on flow and noise characteristics of NACA0018 airfoil. Journal of Wind Engineering and Industrial Aerodynamics. 2007, 95, 511–531. https://doi.org/10.1016/j.jweia.2006.11.002
14. Gerakopulos R., Boutilier M.S.H., Yarusevych S. Aerodynamic Characterization of a NACA 0018 Airfoil at Low Reynolds Numbers. In Proceedings of the AIAA 2010-4629, 40th Fluid Dynamics Conference and Exhibit, Chicago, IL, USA, 28 June–1 July 2010. https://doi.org/10.2514/6.2010-4629
15. Du L. Numerical and Experimental Investigations of Darrieus Wind Turbine Start-up and Operation [doctoral thesis]. Durham, UK: Durham University; 2016. Available at: http://etheses.dur.ac.uk/11384/
16. Bianchini A., Balduzzi F., Rainbird J. M., Peiro J., Graham, J. M. R., Ferrara, G., Ferrari, L. An experimental and numerical assessment of airfoil polars for use in Darrieus wind turbines: Part 1—Flow curvature effects. In Turbo Expo: Power for Land, Sea, and Air 56802, V009T46A006. American Society of Mechanical Engineers. 2015. https://doi.org/10.1115/GT2015-42284
17. Setlak L., Kowalik R., Lusiak T. Practical use of composite materials used in military aircraft. Materials, 2021, 14, 4812. https://doi.org/10.3390/ma14174812
18. Tescione G., Ragni D., He C., Ferreira C. S., Van Bussel, G. J. W. Near wake flow analysis of a vertical axis wind turbine by stereoscopic particle image velocimetry. Renewable Energy. 2014, 70, 47-61. https://doi.org/10.1016/j.renene.2014.02.042
19. Althaus D. Profilpolaren für den Modellflung, Band 1. Necktar-Verlag, Vs-Villingen. Institut für Aerodynamik und Gasdynamik der Universität Stuttgart, 1980. (in German).
20. Allen H.J., Vincenti W.G. Wall interference in a two-dimensional-flow wind tunnel, with consideration of the effect of compressibility. NACA report no. 782. 1944.

energies

Article

The Harmonic Pitching NACA 0018 Airfoil in Low Reynolds Number Flow

Jan Michna , Maciej Śledziewski and Krzysztof Rogowski *

Institute of Aeronautics and Applied Mechanics, Warsaw University of Technology, Nowowiejska 24, 00-665 Warsaw, Poland; jan.michna.dokt@pw.edu.pl (J.M.); maciej.sledziewski.stud@pw.edu.pl (M.Ś.)
* Correspondence: krzysztof.rogowski@pw.edu.pl

Abstract: This study investigates the aerodynamic performance of a symmetric NACA 0018 airfoil under harmonic pitching motions at low Reynolds numbers, a regime characterized by the presence of laminar separation bubbles and their impact on aerodynamic forces. The analysis encompasses oscillation frequencies of 1 Hz, 2 Hz, and 13.3 Hz, with amplitudes of 4° and 8°, along with steady-state simulations conducted for angles of attack up to 20° to validate the numerical model. The results reveal that the γ-Re_θ turbulence model provides improved predictions of aerodynamic forces at higher Reynolds numbers but struggles at lower Reynolds numbers, where laminar flow effects dominate. The inclusion of the 13.3 Hz frequency, relevant to Darrieus vertical-axis wind turbines, demonstrates the effectiveness of the model in capturing dynamic hysteresis loops and reduced oscillations, in contrast to the k-ω SST model. Comparisons with XFOIL further highlight the challenges in accurately modeling laminar-to-turbulent transitions and dynamic flow phenomena. These findings offer valuable insights into the aerodynamic behavior of thick airfoils under low Reynolds number conditions and contribute to the advancement of turbulence modeling, particularly in applications involving vertical-axis wind turbines.

Keywords: NACA 0018; airfoil; low reynolds number; Transition SST; turbulence models; wind turbines

check for updates

Academic Editor: Francesco Castellani

Received: 30 April 2025
Revised: 14 May 2025
Accepted: 28 May 2025
Published: 30 May 2025

Citation: Michna, J.; Śledziewski, M.; Rogowski, K. The Harmonic Pitching NACA 0018 Airfoil in Low Reynolds Number Flow. *Energies* **2025**, *18*, 2884. https://doi.org/10.3390/en18112884

1. Introduction

In recent years, there has been a growing interest in micro air vehicles (MAVs) driven by advancements in electronics and energy storage technologies. MAVs hold significant potential for military applications, particularly in environments where the risk to human life is high. Recently, a Japanese research group proposed aircraft-like devices specifically designed for Mars exploration. The low weight and small size of these devices, combined with the need for low-speed cruising, require them to operate in environments characterized by very low Reynolds numbers, typically ranging from 10^3 to 10^5 [1–4], and thus their dynamics differ significantly from those of conventional UAVs [5].

Another category of devices operating within a similar Reynolds number range includes small-scale wind turbines used in wind tunnel experiments. These turbines often have rotor diameters of one meter or smaller [6,7]. The results obtained from such experiments are frequently scaled up to predict the performance of full-scale wind turbines, which can reach diameters of several hundred meters [8,9]. Propeller and wind turbine blades operating under unsteady inflow conditions are subject to oscillating loads and fluctuating angles of attack. For vertical-axis wind turbines (VAWTs), these oscillations are inherent and occur continuously during their operation [10].

In low-Reynolds-number flows, laminar boundary layer separation occurs, which leads to the formation of laminar separation bubbles through transition to turbulence. The size of these bubbles can vary depending on the angle of attack and Reynolds number, both of which influence the characteristics of flow separation [11,12].

Generally, laminar separation bubbles can be classified into two types: short and long. Short bubbles decrease in length with increasing angle of attack and can cause significant flow instability. However, the study of these phenomena is time-consuming and computationally demanding, as it often requires advanced numerical approaches such as Direct Numerical Simulation (DNS) or Large-Eddy Simulation (LES), which are typically performed on supercomputers [1,13]. In recent years, several studies have employed both Large-Eddy Simulation (LES) and Direct Numerical Simulation (DNS). Due to the significant computational costs, these studies have primarily focused on thin airfoils. The results confirmed the formation of short laminar separation bubbles at low Reynolds numbers and their impact on the nonlinearity of the lift forces. However, the current state of knowledge still does not fully explain the causes of these nonlinearities.

One alternative method for studying transition phenomena in low Reynolds number flows involves the use of modern models designed to capture the laminar-to-turbulent transition. Prior to the introduction of transition turbulence models, engineers primarily relied on turbulence models that treated the entire boundary layer as fully turbulent. Traditional turbulence models, such as those from the k-ω or k-ε families, fail to predict the nonlinear behavior of the C_L below the critical angle of attack [14]. For applications in aeronautics, where the Reynolds numbers typically reach several million or higher, neglecting the transition effects is often sufficient due to the dominance of turbulent boundary layers. One reason for the omission of transition effects in traditional turbulence models is the complexity and variability of the transition mechanisms. Another key limitation is the absence of appropriate methods to describe transition flows, including both linear and nonlinear effects, within the framework of Reynolds-averaged Navier–Stokes (RANS) equations.

Among the more recent advancements in modeling transition phenomena is the correlation-based γ-Re_θ model, also known as the Transition SST turbulence model [15,16]. This model predicts the transition based on local flow conditions by solving transport equations that account for these conditions. In contrast, earlier transition models, such as the e^N method proposed by Smith and Gamberoni [17], relied on global flow parameters and were challenging to implement in modern general-purpose CFD software. While these older models could yield reasonable transition predictions for airfoil analysis in homogeneous flows, they were less effective for more complex cases.

Several studies have validated the effectiveness of the Transition SST turbulence model in capturing transition phenomena at low Reynolds numbers. Melani et al. [14] compiled a wide range of experimental and numerical data on the aerodynamic performance of the NACA 0018 airfoil at low and moderate Reynolds numbers. Their findings reveal that as the Reynolds number decreases, the discrepancies in aerodynamic force predictions increase, particularly in the range of Reynolds numbers from 40,000 to 160,000. Melani et al. [14] also provided lift force characteristics for a Reynolds number of 150,000, obtained using the Transition SST model. These results, which are also available in [18], show excellent agreement with experimental data for angles of attack up to 6 degrees.

A significant challenge for the Transition SST model is accurately estimating the dynamic characteristics of the pitching NACA 0018 airfoil under very low Reynolds number conditions.

Theodorsen and Glauert made groundbreaking contributions to the understanding of unsteady aerodynamics, particularly with respect to pitching airfoils [19–21]. They provided foundational insights into the behavior of two-dimensional harmonically oscillating airfoils in inviscid and incompressible flows that were subjected to small disturbances. Theodorsen's analytical framework remains a key reference for the performance analysis of both fixed-wing and rotating-wing systems, serving as a basis for further advancements in unsteady aerodynamics.

Theodorsen's theory has several important limitations: it does not account for flow viscosity, is tailored specifically for thin airfoils, and lacks the capability to predict drag forces. Furthermore, at low Reynolds numbers, flows tend to separate prematurely, even at modest angles of attack, which further restricts the applicability of the theory under such conditions. Despite these limitations, Theodorsen's framework has been adapted to address various aerodynamic challenges, including sudden changes in the angle of attack, sinusoidal gust responses, and the dynamics of returning wakes [22].

A key parameter for characterizing the behavior of an airfoil undergoing harmonic oscillations is the reduced frequency, k, defined as $k = \omega c / 2V_0$, where c represents the chord length, V_0 is the free-stream velocity, and ω denotes the angular frequency of oscillation. When $k = 0$, the flow is considered to be steady. For cases where unsteady effects are minimal, the reduced frequency lies in the range $0 < k \leq 0.05$. As k increases beyond 0.05, the flow transitions into the unsteady regime, and when $k \geq 0.2$, the flow is classified as highly unsteady, exhibiting significant deviations from quasi-steady behavior [21,23]. In this study, the oscillation frequencies are reported in physical units (Hz) to align with the operating characteristics of a real Darrieus-type wind turbine rotor. However, the corresponding reduced frequencies k are also calculated and discussed throughout the manuscript to ensure compatibility with the non-dimensional analyses.

Theoretical studies similar to those presented in this paper, focusing on a two-dimensional flat plate undergoing harmonic pitching oscillations (without plunging motion) about the quarter-chord within a Reynolds number range of 10^4–10^5 and reduced frequencies between 0.001 and 0.3, were conducted by Badrya et al. [19] The authors aimed to analyze the influence of viscosity on flow behavior and the generation of aerodynamic forces and moments. Additionally, they compared the results obtained for a flat plate with those obtained for a thin NACA 0012 airfoil. Badrya et al. [19] also employed Theodorsen's theory and observed significant discrepancies between its predictions and numerical results. These differences were particularly pronounced at low Reynolds numbers and were attributed to the inability of the theory to account for viscous effects. Furthermore, for the NACA 0012 airfoil, it was found that this airfoil failed to generate sufficient pressure differences between the upper and lower surfaces, resulting in very low maximum lift coefficients.

Another notable study on pitching motions at low Reynolds numbers was conducted by Stevens and Babinsky [24]. They investigated the behavior of a flat plate undergoing harmonic pitching oscillations with a high reduced frequency of 0.394 at a Reynolds number of 20,000. Their work combined experimental measurements with a reduced-order model that incorporated both circulation and vortex advection velocities, as informed by the experimental data. This approach highlights the significance of including unsteady aerodynamic effects when modeling such flows.

Moreover, Brunton and Rowley [25] demonstrated the applicability of Theodorsen's classical theory [19] in predicting the lift for attached flows during pure pitching motion. They concluded that for scenarios dominated by non-circulatory and circulatory effects, Theodorsen's model provides a reasonable approximation despite its limitations in capturing vortex dynamics. These studies collectively underscore the complexity of flow behavior at low Reynolds numbers and the challenges in bridging the theoretical predictions with experimental results.

The interplay between geometry, kinematics, Reynolds numbers, and three-dimensional effects significantly influences the aerodynamic forces and flow structures around pitching and plunging flat plates at low Reynolds numbers, as demonstrated by Kang et al. [26]. Shallow- and deep-stall motions reveal dominant geometric effects, such as massive leading-edge separation on sharp-edged flat plates that overshadow viscosity-related influences. Compared to blunter airfoils like the SD7003, flat plates exhibit earlier and stronger leading-edge vortex formation, resulting in enhanced lift and drag characteristics under similar conditions.

Moriche et al. [27] analyzed the stability of a plunging and pitching wing with an infinite aspect ratio at low Reynolds numbers. By varying the mean pitch angle and phase shift between pitching and plunging, they identified cases that produced different aerodynamic forces and wake structures. Notably, one configuration exhibited a period-doubling phenomenon and was linearly unstable, leading to a fully three-dimensional wake downstream. Despite this, the aerodynamic forces in the three-dimensional simulations remained consistent with those in the two-dimensional simulations.

The current study aims to bridge the knowledge gap in understanding the aerodynamic performance of thick airfoils, such as NACA 0018, under low Reynolds number regimes with harmonic pitching motions. Specifically, the research focuses on a pitching motion frequency of 13.3 Hz, motivated by the operational characteristics of Darrieus vertical-axis wind turbines (VAWTs). These turbines, including the rotor tested in the TU Delft wind tunnel [6], provide a unique context in which laminar separation bubbles and oscillatory aerodynamic forces significantly influence performance. By employing advanced turbulence modeling techniques, such as the γ-Re_θ transition and k-ω SST models, and comparing the numerical predictions with experimental data, this study aims to unravel the dynamics of hysteresis loops, laminar separation bubbles, and turbulence effects. These findings contribute to a deeper understanding of aerodynamic force oscillations and their dependence on Reynolds numbers, thereby supporting the optimization of thick airfoils for a wide range of engineering applications.

2. The Harmonic Pitching NACA 0018 Airfoil

The concept of pure pitching motion for the NACA 0018 airfoil is illustrated in Figure 1. The symmetric NACA 0018 airfoil oscillates harmonically according to a sinusoidal function (also shown in the figure) about a pivot point located on the chord at a distance of c/4 from the leading edge. The chord length, denoted as c, is also depicted in the sketch and is 6 cm.

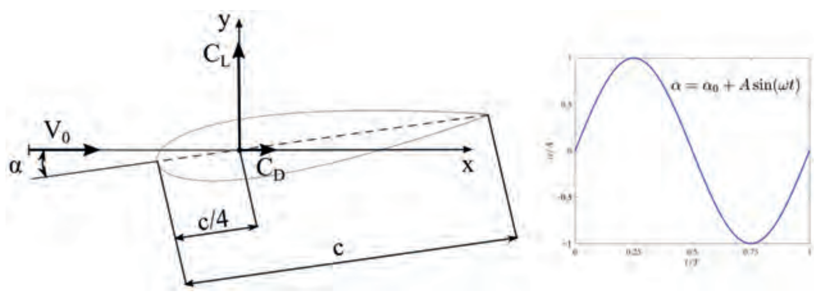

Figure 1. Pitching NACA 0018 airfoil.

The oscillation frequency is denoted by *f*, with the corresponding period T, angular frequency ω, and amplitude A. The origin of the coordinate system is defined at the quarter-chord point, measured from the leading edge. The constant pitch angle is represented as α_0. In this study, only cases with $\alpha_0 = 0^\circ$ are considered.

It is important to clarify that, in this study, the angle of attack is directly defined by the prescribed pitch angle. Since the airfoil performs pure harmonic pitching around the quarter-chord axis, with no plunging motion or flow curvature effects, the angle of attack is equal to the instantaneous pitch angle. Consequently, no separate calculation of the angle of attack is performed for the flow field.

2.1. Simulation Setup and Turbulence Modeling

The lift coefficient (CL) and drag coefficient (CD) used in this study are defined as follows:

$$C_{L,D} = L, D/\left(0.5 \cdot \rho \cdot V_0^2 c\right) \quad (1)$$

where L and D are the lift and drag forces acting on the airfoil, ρ is the fluid density, V_0 is the free-stream velocity and is the chord length of the airfoil. These non-dimensional coefficients were evaluated at each time step based on the instantaneous aerodynamic forces computed from the surface pressure and shear stress distributions.

All numerical simulations summarized in this paper were conducted using the unsteady Reynolds-averaged Navier–Stokes (URANS) approach. The computational domain was developed based on the working section of the Red Wind Tunnel (RWT) at the TU Delft.

The test section of the wind tunnel measures 2000 mm in length and 500 mm in height. Its width gradually increases from 750 mm at the inlet to 770 mm at the outlet. This slight expansion compensates for the boundary layer growth along the walls and ensures an almost zero pressure gradient in the empty tunnel. The turntable center is positioned 750 mm from the inlet. Additional details regarding the experimental setup and settings can be found in [28].

The URANS approach employed in these simulations required one of two methods: a dynamic or sliding mesh. Although the sliding mesh method is less computationally demanding, it necessitates the definition of an additional domain surrounding the oscillating foil. In our model, a circular domain with a diameter of two chord lengths was considered around the airfoil, with its center coinciding with the origin of the defined coordinate system [29]. This moving subdomain, surrounding the pitching airfoil, was embedded within the stationary outer domain using the sliding mesh technique. As a result, the grid around the airfoil dynamically adjusted its position at each time step in accordance with the airfoil's motion.

The solver used was pressure-based and transient, with air as the working fluid. Air was modeled with a constant density of ρ = 1.225 kg/m^3 and a constant viscosity of μ = 1.7895 $\times$ 10^{-5} kg/(ms). The boundary conditions were specified as follows: a velocity inlet at the left vertical edge of the domain, a pressure outlet at the right edge of the tunnel, and no-slip walls along both the tunnel walls and airfoil surface [30].

As noted earlier, the sliding mesh approach was utilized in this study. This method requires the creation of two regions: a stationary region and a moving region that oscillates with the airfoil. An interface was defined at the boundary between the two regions to facilitate their interaction.

For the numerical solution of the momentum equations and turbulence model equations, a second-order upwind discretization scheme was employed, along with a least-squares cell-based gradient evaluation. Pressure-velocity coupling was achieved using the SIMPLE algorithm. The residuals for all the equations were maintained at a level of 10^{-7}. In the transient simulations, the maximum number of iterations per time step was set to 20. The time step size corresponded to an angular step size of 0.5°, which was sufficient to achieve a satisfactory azimuthal resolution within the prescribed iteration limit per time step [30]. The turbulence intensity at the domain inlet was set to 0.1%, corresponding to the free-stream conditions observed in the TU Delft Red Wind Tunnel. This value was chosen to represent a low-turbulence environment suitable for studying laminar-to-turbulent transition phenomena.

All simulations were performed using 24 parallel computing cores (Intel Haswell, Cray XC40 supercomputer Okeanos in ICM Warsaw). For the Transition SST model, the solver achieved a speed of approximately 40 time steps per minute. The k-ω SST model converged slightly faster due to its simpler formulation with only two transport equations.

This study focuses on the flow over a thick airfoil at low Reynolds numbers, where the formation of laminar separation bubbles plays a significant role in determining the aerodynamic characteristics. These bubbles can notably impact lift and drag, making their accurate prediction essential for understanding flow behavior.

To accurately capture the complex flow phenomena associated with laminar separation bubbles, the Transition SST turbulence model, also known as the γ-Re_θ model, is employed in this study. Developed by Langtry [15] and Menter et al. [31], this model builds upon the widely used k-ω Shear Stress Transport (SST) framework by introducing two additional transport equations: one for the momentum-thickness Reynolds number, Re_θ, and another for intermittency, γ. These enhancements enable precise prediction of the laminar-to-turbulent transition, which is crucial for flows influenced by separation bubbles.

Implemented in the ANSYS Fluent 2024 R1 solver, the Transition SST model employs a correlation-based approach reliant on local flow variables, making it suitable for a wide range of engineering applications. By simultaneously resolving the turbulent kinetic energy, its dissipation rate, and transition-specific parameters, this model provides a more accurate representation of the flow physics. Comprehensive details of the model formulation can be found in the works of Langtry [15] and Menter et al. [31]. The following equations summarize the transport models used in this study. For the k-ω SST turbulence model:

$$\begin{gathered}\frac{\partial(\rho k)}{\partial t}+\frac{\partial\left(\rho u_j k\right)}{\partial x_j}=P_k-\beta^*\rho k\omega+\frac{\partial}{\partial x_j}\left[\left(\mu+\sigma_k\mu_t\right)\frac{\partial k}{\partial x_j}\right]\\ \frac{\partial(\rho\omega)}{\partial t}+\frac{\partial\left(\rho u_j\omega\right)}{\partial x_j}=\alpha\frac{\omega}{k}P_k-\beta\rho\omega^2+\frac{\partial}{\partial x_j}\left[\left(\mu+\sigma_\omega\mu_t\right)\frac{\partial\omega}{\partial x_j}\right]+2(1-F_1)\frac{\rho\sigma_{\omega 2}}{\omega}\frac{\partial k}{\partial x_j}\frac{\partial\omega}{\partial x_j}\end{gathered} \tag{2}$$

and for the γ-Re_θ turbulence model:

$$\begin{gathered}\frac{\partial(\rho\gamma)}{\partial t}+\frac{\partial\left(\rho u_j\gamma\right)}{\partial x_j}=P_\gamma-E_\gamma+\frac{\partial}{\partial x_j}\left[\left(\mu+\sigma_\gamma\mu_t\right)\frac{\partial\gamma}{\partial x_j}\right]\\ \frac{\partial(\rho Re_\theta)}{\partial t}+\frac{\partial\left(\rho u_j Re_\theta\right)}{\partial x_j}=P_{\theta t}+\frac{\partial}{\partial x_j}\left[\left(\mu+\sigma_{\theta t}\mu_t\right)\frac{\partial Re_\theta}{\partial x_j}\right]\end{gathered} \tag{3}$$

In addition to the γ-Re_θ approach, for comparison purposes, certain cases were also computed using the well-known two-equation k-ω Shear Stress Transport (SST) turbulence model to highlight the differences between the two modeling approaches.

2.2. Numerical Mesh

The computational domain, shown in Figure 2, was discretized using a hybrid mesh comprising a structured mesh near the airfoil edges and tunnel walls and an unstructured mesh in the remaining regions. The application of a structured mesh is essential for accurately resolving the flow in the boundary layer near the wall surfaces. The mesh on the airfoil surface consists of a total of 1669 nodes: 830 nodes along the upper edge, 830 along the lower edge, and nine nodes at the trailing edge. A uniform element distribution was employed. A structured mesh near the airfoil edges was constructed with 37 layers and a growth rate of 1.13 in the direction normal to the surface. The thickness of the first wall-adjacent element was set to 5×10^{-6} m. This resolution was validated by the authors and adhered to the recommendations of ANSYS Fluent v2024. The thickness of the first element ensures that the wall y^+ criterion $y^+ \leq 1.0$ is satisfied for all cases considered in this study. At the interfaces, a uniform element size of 5×10^{-4} m was used. For the tunnel walls, a structured mesh was applied with the following parameters: thickness of the first element of 5×10^{-6} m, 40 layers in the normal direction, and an element growth rate of 1.2. Similar to the structured mesh around the airfoil edges, these parameters are consistent with ANSYS Fluent guidelines and meet the wall y^+ criterion [30]. In the unstructured mesh, the moving domain surrounding the airfoil employed elements with a size of 5×10^{-4} m. In the stationary domain, the element size was 4×10^{-3} m. Additionally, a smaller region within the stationary domain, extending 1 chord length (1c) from the interface to the outlet edge of the tunnel, was defined. This modification was performed to better resolve the flow in the wake region. In this additional region, the element size was 2×10^{-3} m. The chosen element sizes were sufficient, even for the LES simulations [32,33]. The nominal mesh designed in this manner comprises a total of 285,016 nodes and 282,934 elements.

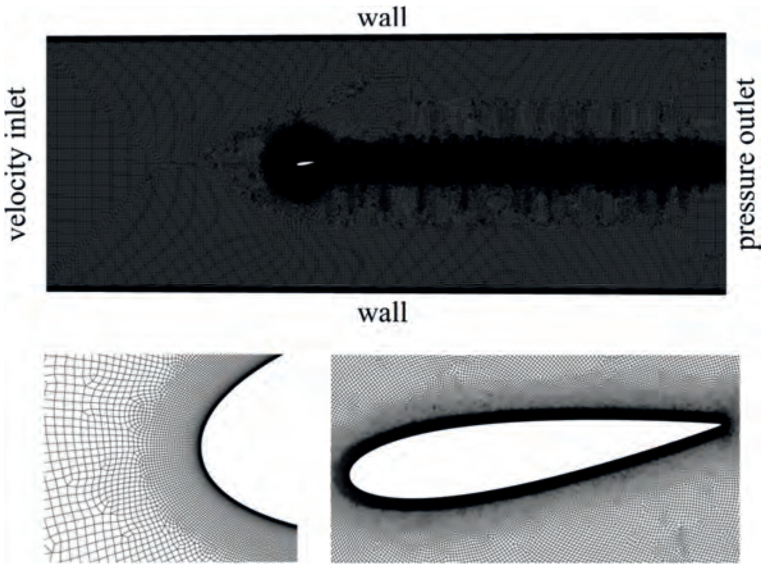

Figure 2. Numerical mesh: entire domain (**top** image) and zoomed-in mesh around the airfoil (**bottom** images). Additionally, boundary conditions are shown in the top image.

A mesh sensitivity analysis was conducted to evaluate the influence of the grid resolution on the numerical solution. This test was performed for a stationary case, where the frequency of the pitching motion of the NACA 0018 airfoil was set as zero.

The analysis was carried out at a fixed angle of attack of 8° and at the highest Reynolds number considered in this study, that is, Re = 160,000. Four different meshes were used: two coarser meshes with the number of nodes reduced by factors of $\sqrt{2}$ and 2 compared with the nominal mesh, and one finer mesh with the number of nodes on the airfoil surface increased by a factor of $\sqrt{2}$ relative to the nominal configuration.

The lift and drag coefficients as functions of the number of nodes on the airfoil surface are shown in Figure 3. The results clearly indicate that the lift coefficient is independent of the grid resolution, while the drag coefficient exhibits minimal sensitivity to the number of nodes. In other words, increasing the number of nodes beyond the nominal mesh resolution does not enhance the accuracy of the computed aerodynamic loads but merely increases the computational cost.

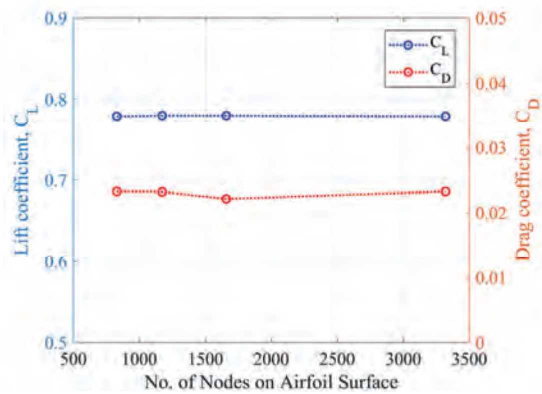

Figure 3. Mesh sensitivity analysis: Lift coefficient C_L and drag coefficient C_D as functions of the number of nodes on an airfoil surface. The results indicate that C_L is independent of the grid resolution, while C_D exhibits minimal sensitivity to the number of nodes. Increasing the grid resolution beyond the nominal mesh does not significantly enhance the accuracy but increases the computational cost.

The flow simulations around the NACA 0018 airfoil, even for the "no pitch" case and at low angles of attack, required the use of the unsteady Reynolds-averaged Navier-Stokes (URANS) approach with the advanced γ-Re_θ transition model. This is due to the high temporal variability of the physical phenomena occurring within the boundary layer near the airfoil surface. The application of the URANS approach necessitates the definition of a time step [11].

In this work, the SIMPLE (Semi-Implicit Method for Pressure-Linked Equations) algorithm was utilized. In SIMPLE, there is no need to set the Courant–Friedrichs–Lewy (CFL) condition because SIMPLE is an iterative method that is not directly dependent on the time-step size. Instead, SIMPLE operates based on quasi-static computations, where the pressure and velocity equations are solved iteratively until convergence is achieved. As a result, the stability of the solution is not directly affected by the time step size or the CFL number. This makes the SIMPLE method "unconditionally stable" in a numerical sense [30].

The time step applied for the "no pitch" case was 0.001 s. For cases in which the pitch motion was greater than zero, the time step was set to 1/720 of the period. Specifically, for a frequency of 1 Hz, the time step was 0.001388 s, whereas for a frequency of 2 Hz, the time step was 0.0006944 s.

3. Aerodynamic Load Analysis for the Pitching NACA 0018 Airfoil

3.1. Aerodynamic Load Analysis for 0 Hz Pitching Motion

Figure 4 presents the aerodynamic characteristics C_L and C_D as functions of the angle of attack α for the NACA 0018 airfoil. The analysis was conducted for two Reynolds numbers, Re = 80k and Re = 160k. Numerical simulations were performed over an angle of attack range of 0° to 20° to capture the stall point. Although the results represent steady aerodynamic characteristics, they were obtained using the URANS approach and averaged over the last second of the simulation.

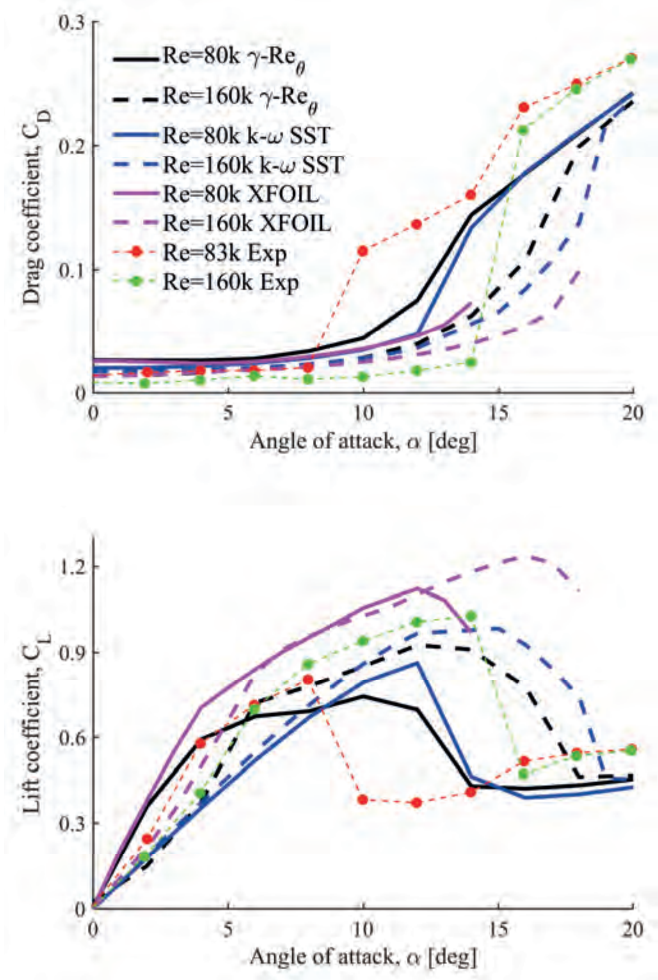

Figure 4. Comparison of drag coefficient (C_D, top subplot) and lift coefficient (C_L, bottom subplot) as functions of the angle of attack, α, for different Reynolds numbers (Re = 80k and Re = 160k) and modeling approaches. Experimental data from [28].

The primary turbulence model used in this study was a four-equation γ-Re$_\theta$ transition model. For comparison, a two-equation k-ω SST turbulence model was employed. Additionally, experimental data obtained by the authors in a low-turbulence wind tunnel at the Technical University of Denmark were included. The experimental results, along with data from the well-known XFOIL tool, were summarized by Rogowski et al. [28].

The figure highlights the strong sensitivity of the aerodynamic forces to the Reynolds number. Notably, the experimental lift coefficient C_L exhibits nonlinear behavior below the critical angle of attack. As proposed by Rogowski et al. [28], this nonlinearity arises from the presence and evolution of the laminar separation bubbles. These bubbles increase the lift at low angles of attack but also significantly increase the drag. A decrease in the Reynolds number by half reduces C_{Lmax} from 1.027 at α = 13.99° to 0.803 at α = 7.95°. Interestingly, at α = 3.96°, the lift coefficient is higher at the lower Reynolds number, with values of 0.406 for Re = 160k and 0.578 for Re = 80k.

These physical phenomena are challenging to model numerically. The least accurate results were obtained with the fully turbulent k-ω SST model, which produces linear lift characteristics up to the critical angle. However, at Re = 160k and low angles of attack (up to 3°–4°) as well as near the critical angle (12°–14°), the discrepancies in lift and drag are less significant. Despite overestimating the drag coefficients at Re = 160k, the drag coefficient for the SST model converged more closely to the experimental values at lower Reynolds numbers, with a deviation of only 15.6% at Re = 80k. This can be attributed to the increased boundary layer interactions at lower Reynolds numbers, leading to a higher form drag.

XFOIL demonstrates a similar trend for lift, with higher coefficients at lower angles of attack for lower Reynolds numbers. However, the C_{Lmax} predicted by XFOIL is overestimated compared to the experimental results across the entire angle of attack range. This overprediction may stem from the lack of calibration of XFOIL for thick airfoils, as the model was initially developed for flat plates. Additionally, this study did not examine the effect of the transition parameter N, which was set to a default value of 9. While appropriate for low-turbulence wind tunnels, even slight changes in turbulence intensity at low Reynolds numbers can significantly affect aerodynamic characteristics. Interestingly, XFOIL predicts a minimum drag coefficient at a nonzero angle of attack, with the drag decreasing slightly (by about 8%) as α increased from 0° to 4° at Re = 80k.

As mentioned in Section 2.2, when analyzing the flow around a clean airfoil under low Reynolds number conditions, even in the "no pitch" scenario, a transient approach must be considered due to the unsteady phenomena occurring within the boundary layer.

As discussed in the Introduction, the magnitude and frequency of these unsteady phenomena depend on the Reynolds number and the angle of attack. In practice, the magnitude of these unsteady effects manifests as oscillations in the aerodynamic forces, both in terms of their amplitude and frequency. As shown in Figure 5, the largest oscillations in the lift coefficient (C_L) are observed at a Reynolds number of 160k, particularly at angles of attack up to 8°. These oscillations decrease around the stall angle but begin to grow again at higher angles of attack. A similar behavior is observed for the drag coefficient (C_D), although its oscillation amplitudes are significantly smaller. In contrast, for a Reynolds number of 80k, the oscillations in the aerodynamic forces are much smaller. The aerodynamic characteristics C_L and C_D shown in Figure 4 represent the time-averaged values of C_L (time) and C_D (time) (Figure 5) over the last second of the simulation.

Figure 6 compares the pressure coefficient (C_p), and *x*-wall shear stress distributions along the chordwise coordinate (x/c) for the two examined Reynolds numbers and three representative angles of attack (2°, 4°, and 8°). These plots confirm that, for a Reynolds number of 160k, the intensity of the laminar separation bubbles is significantly higher than that at Re = 80k. Furthermore, at lower angles of attack, the bubbles shift closer to the airfoil leading edge.

3.2. Aerodynamic Load Analysis for 1 Hz Pitching Motion

This section presents the results of the aerodynamic load analysis of the pitching NACA 0018 airfoil. The influence of the Reynolds number on the aerodynamic force coefficients was investigated by considering two pitching amplitudes: 4° and 8°. The frequency of the 1 Hz pitching motion corresponds to a reduced frequency of approximately 0.01 for Re = 80k and around 0.005 for Re = 160k, highlighting the influence of the Reynolds number on the normalized temporal scaling of the motion. The corresponding amplitude-to-chord ratios are approximately 0.067 for A = 4° and 0.133 for A = 8°, assuming a chord length of 6 cm.

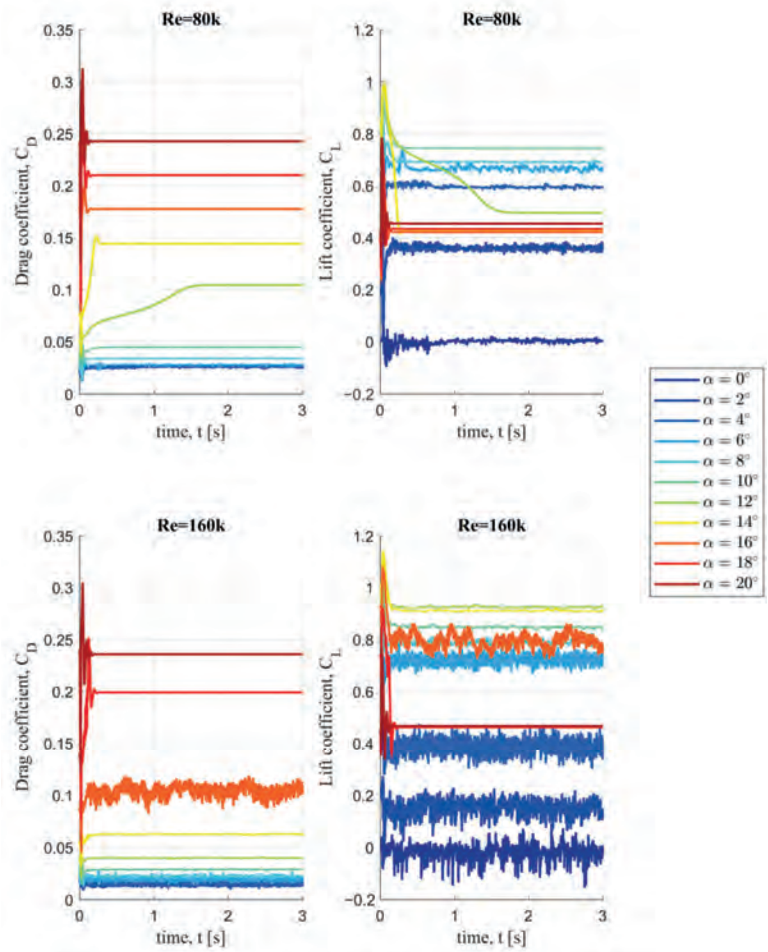

Figure 5. Comparison of drag (C_D) and lift (C_D) coefficients over time for different angles of attack (α) at Reynolds numbers of 80k (top row) and 160k (bottom row). The left column shows C_D and the right column shows C_L.

It was observed that the drag coefficient component is the most sensitive to both the Reynolds number and the amplitude of pitching (Figure 7). To confirm the influence of the Reynolds number on the drag coefficient, the values were averaged over the last computed cycle of motion.

For amplitude A = 4°, the drag coefficient for Re = 80k was approximately 67% higher than that for Re = 160k. For A = 8°, the drag coefficient is about 51% higher under the same comparison.

Our observations further revealed that the maximum values of the lift coefficient for the amplitude A = 4° were higher at lower Reynolds numbers. The maximum drag coefficient in this case was about 44% higher than that at Re = 160k at the same amplitude. Interestingly, for amplitude A = 8°, the opposite is true: the lift maxima for Re = 160k are greater, although the difference in these maxima is significantly smaller. This reversal in lift coefficient trends between A = 4° and A = 8° can be explained by the nonlinear characteristics of the laminar-to-turbulent transition and their sensitivity to the Reynolds number. At lower amplitudes (A = 4°), the airfoil operates primarily in a regime in which the transition location is delayed, especially at lower Reynolds numbers, resulting in more extensive laminar flow and higher lift. At larger amplitudes (A = 8°), the pitching motion enters a more dynamic regime with stronger flow separation. In this case, a higher Reynolds number (Re = 160k) promotes an earlier transition and reattachment, yielding a higher maximum lift. Similar effects were observed in [11], where the lift behavior at low Re was shown to depend on the position and strength of the laminar separation bubbles. The transition model struggles to resolve these effects purely from first principles due to its reliance on empirical correlations rather than the direct resolution of boundary layer physics.

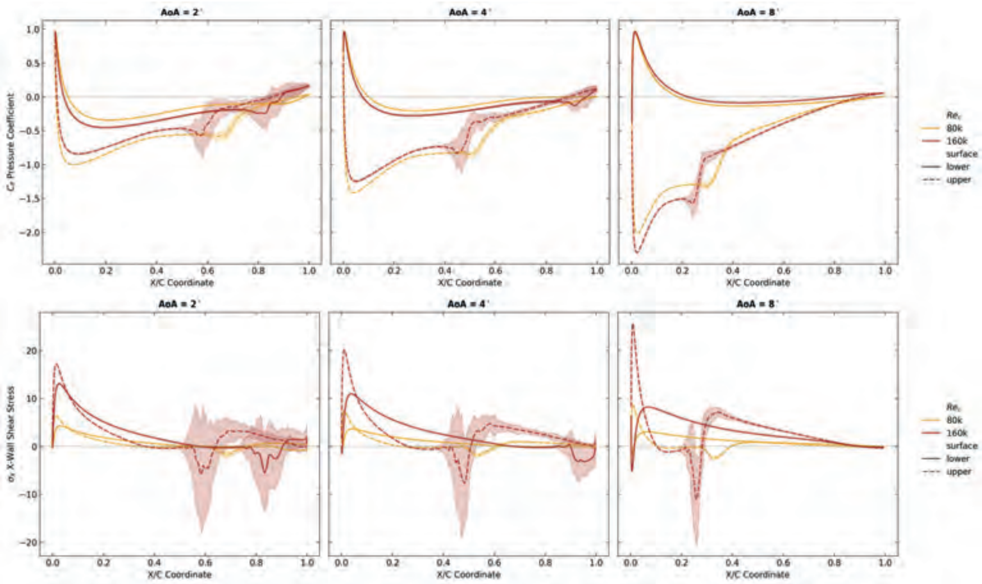

Figure 6. Comparison of pressure coefficient (C_p) and wall shear stress (τ_x) distributions along the airfoil chord (x/c)) at different angles of attack (2°, 4°, and 8°) for Reynolds numbers of 80k and 160k. The top row presents the C_p distributions, while the bottom row shows σ_x. The solid lines correspond to the lower surface and the dashed lines to the upper surface.

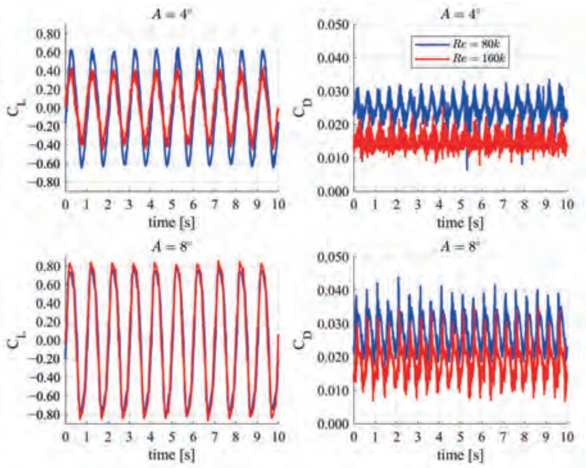

Figure 7. Time histories of the lift coefficient (C_L) and drag coefficient (C_D) for pitching amplitudes A = 4° and A = 8° at Reynolds numbers Re = 80k and Re = 160k—γ-Re_θ model used with 1 Hz frequency motion. The top row corresponds to A = 4°, while the bottom row corresponds to A = 8°.

For both the analyzed amplitudes and Reynolds numbers, the mean values of the normal force coefficient are, as expected, very close to zero.

Figure 7 illustrates the influence of the Reynolds number on the aerodynamic loads as a function of time. For a better comparison, the same results for the aerodynamic force coefficients are also presented in a different format, plotted against the angle of attack α. Figure 8 shows a comparison of the hysteresis loops of the aerodynamic force coefficients under the investigated wing motion parameters. In the case of the lift coefficient, the hysteresis loop is the widest at an angle of attack of $\alpha = 0°$. An increase in the Reynolds number from 80k to 160k reduces the loop width for both the lift and drag coefficients. The relatively low oscillations of the drag coefficient at small angles of attack can be attributed to the stable nature of the boundary layer and the weak influence of laminar separation. At higher angles, the laminar separation bubble becomes larger and less stable, and reattachment behavior becomes more sensitive to the phase of the oscillation, leading to more pronounced and nonlinear drag oscillations.

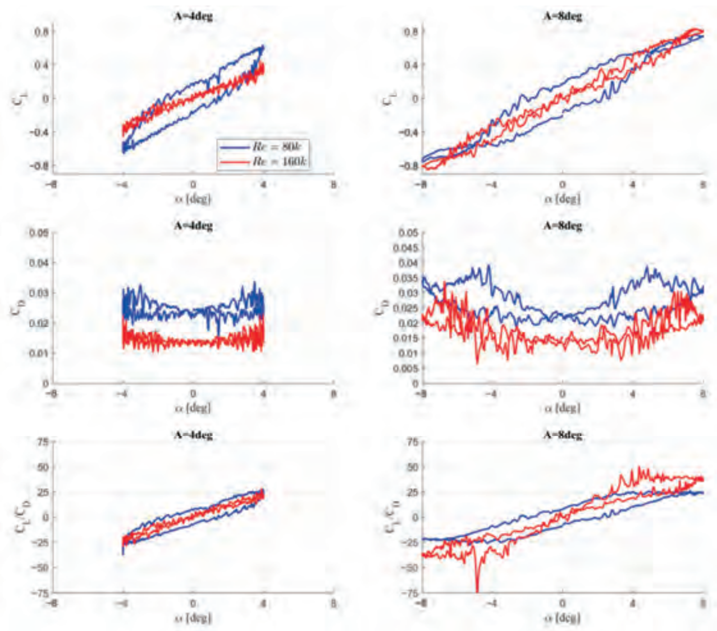

Figure 8. Hysteresis loops of the lift coefficient (C_L), drag coefficient (C_D), and lift-to-drag ratio (C_L/C_D) as a function of the angle of attack (α) for pitching amplitudes A = 4° and A = 8° at Reynolds numbers Re = 80k and Re = 160k—γ-Re_θ model used with 1 Hz frequency motion. The left column corresponds to A = 4°, and the right column corresponds to A = 8°.

The top-left panel of Figure 8 highlights the significant impact of the Reynolds number on the shape and slope of the lift coefficient as a function of the angle of attack. Furthermore, Figure 8 compares the relationship between the lift-to-drag ratio (C_L/C_D) and the angle of attack for two Reynolds numbers, 80k and 160k.

This comparison reveals a considerably smaller influence of the Reynolds number on the aerodynamic efficiency, particularly for the smaller amplitude of 4. This indicates that the higher drag associated with, the lower Reynolds number offsets the potential benefits of higher lift coefficient values.

For the larger amplitude under investigation, a higher Reynolds number results in greater values of the C_L/C_D ratio, especially at higher angles of attack.

Figure 9 illustrates the influence of the amplitude on the hysteresis loops at a given Reynolds number. To compare the aerodynamic force coefficients for different amplitudes, the values of the coefficients were normalized by their respective maximum values. A similar normalization was applied to the angle of attack.

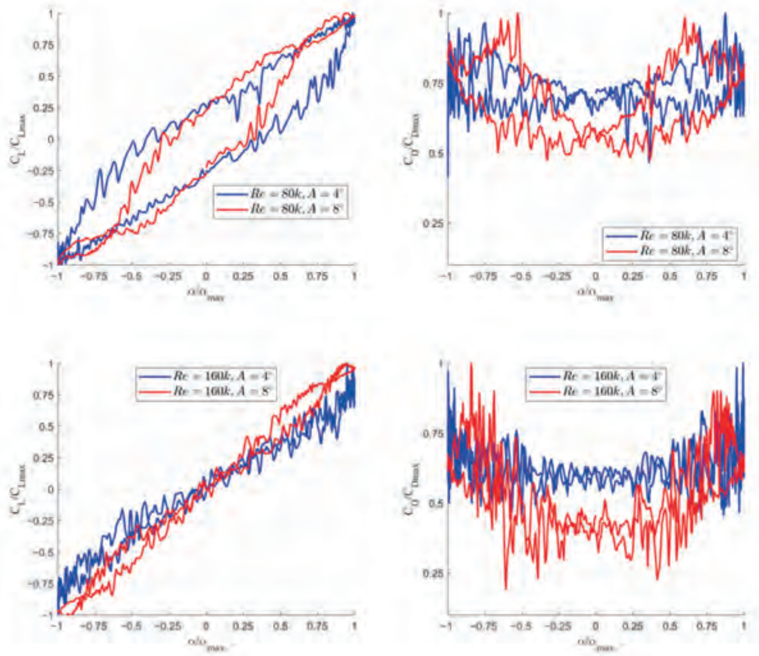

Figure 9. Normalized lift coefficient (C_L/C_{Lmax}) and drag coefficient (C_D/C_{Dmax}) as a function of normalized angle of attack (α/α_{max}) for Reynolds numbers Re = 80k and Re = 160k and pitching amplitudes A = 4° and A = 8°—γ-Re_θ model used with 1 Hz frequency motion. The top row compares Re = 80k, while the bottom row compares Re = 160k.

The plots presented in this figure reveal that the amplitude has the greatest impact on the drag coefficient at low values of the angle of attack. For both Reynolds numbers, the minimum drag coefficient for the amplitude A = 8° was lower than that for A = 4°. This is most likely associated with the higher linear velocity at the leading edge.

As shown in the top-left panel, the Reynolds number also significantly affects the lift coefficient. The largest differences are observed for α/α_{max} in the range from 0.5 to 1.0.

3.3. Aerodynamic Forces Predicted by the k-ω SST Model for Pitching Motion

This section presents the dynamic characteristics of the harmonically oscillating NACA0018 airfoil using the classical 2-equation k-ω turbulence model. Figure 10 compares the aerodynamic force components in the time domain for the two cases.

The aerodynamic forces generated on the surface of the oscillating airfoil are, as expected, nearly harmonic functions. Due to the wall-layer modeling approach, no irregularities associated with laminar separation bubbles are visible in the characteristics. In contrast to the γ-Re_θ model, the k-ω SST turbulence model showed that the maximum lift coefficient values calculated for case A = 4° and Re = 160,000 were slightly higher than those for Re = 80,000.

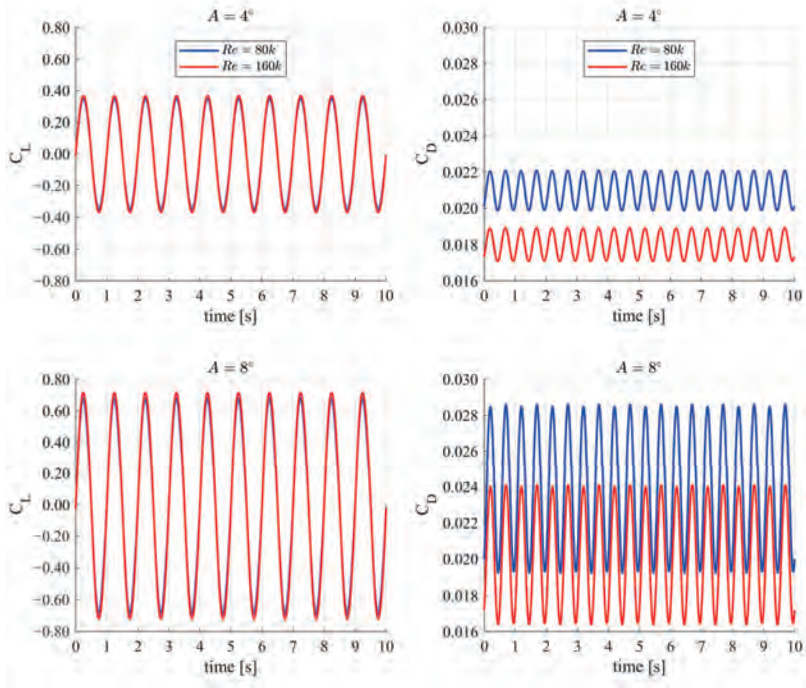

Figure 10. Time histories of the lift coefficient (CL) and drag coefficient (CD) for pitching amplitudes A = 4° and A = 8° at Reynolds numbers Re = 80k and Re = 160k—k-ω model used with 1 Hz frequency motion. The top row corresponds to A = 4°, while the bottom row corresponds to A = 8°.

An increase in the amplitude to 8° resulted in a slight increase in the difference between the amplitudes. Despite minor differences in lift force estimation, drag is much more dependent on the Reynolds number, as shown in the right-hand column of the plots in Figure 10.

The drag coefficient at the lower amplitude (A = 4°) exhibits an almost entirely periodic nature, repeating in each cycle of airfoil oscillation. This indicates the establishment of a steady dynamic regime in which the aerodynamic response is cyclically repeatable.

For an oscillation amplitude of 8° and Reynolds number Re = 80,000, very small differences in successive drag force amplitudes were observed. This may have resulted from the proximity to the critical static angle of attack, which affects the flow characteristics around the airfoil and stabilizes the aerodynamic forces.

The characteristics of the aerodynamic force coefficients and aerodynamic efficiency as a function of the angle of attack are shown in Figure 11. All plots reveal the absence of effects associated with the laminar separation bubbles.

The hysteresis loops of the C_L were nearly identical for A = 4° and A = 8°, showing only a scaling effect. For the C_D hysteresis, a practically uniform shift dependent only on the Reynolds number was observed. The characteristics are symmetrical about alpha = 0°.

Additionally, the Reynolds number is reflected in the slightly different slopes of the C_L/C_D ratios. This highlights the role of the Reynolds number in determining the aerodynamic efficiency under dynamic conditions.

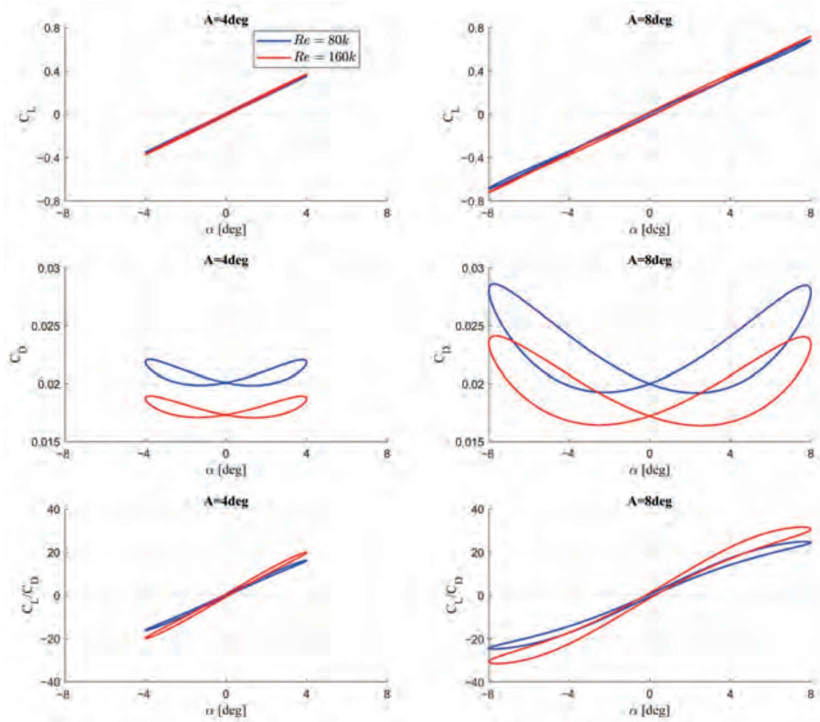

Figure 11. Hysteresis loops of the lift coefficient (C_L), drag coefficient (C_D), and lift-to-drag ratio (C_L/C_D) as a function of the angle of attack (α) for pitching amplitudes A = 4° and A = 8° at Reynolds numbers Re = 80k and Re = 160k—k-ω model used with 1 Hz frequency motion. The left column corresponds to A = 4°, and the right column corresponds to A = 8°.

This comparison also serves to explain a surprising result observed in our recent VAWT simulations [32], where both models predicted similar rotor loads despite fundamentally differing in how they handled the transition. The present simplified configuration highlights the underlying differences more clearly and will help guide further refinement of turbulence modeling in practical applications.

Figure 12 illustrates the greater influence of the Reynolds number on the ratio C_L/C_{Lmax} as a function of the normalized angle of attack. An increase in Re causes a broader hysteresis at small angles of attack.

Interestingly, the shape of the CL/C_{Lmax} curve is more dependent on the Reynolds number than on the amplitude. Similarly, the Reynolds number has a more significant impact on the drag coefficient, although in this case, the amplitude plays a key role.

As with the turbulence model accounting for the laminar-to-turbulent transition, a significant drop in α/α_{max} is observed for the higher amplitude case.

3.4. Aerodynamic Load Analysis for 2 Hz Pitching Motion

The reduced frequencies for the 2 Hz pitching motion are approximately 0.02 for Re = 80k and 0.01 for Re = 160k. The amplitude-to-chord ratios remain the same as in the 1 Hz case, i.e., 0.067 for 4° and 0.133 for 8°. The time histories of the aerodynamic force coefficients, shown in Figure 13, exhibit a similar qualitative trend as that observed for the 1 Hz pitching motion. For the lower Reynolds number of Re = 80k, the maximum values of C_L are higher than those for Re = 160k. However, for amplitude A = 8°, the differences in the maximum C_L values between the two Reynolds numbers are significantly smaller, similar to the 1 Hz case. Both the Reynolds number and amplitude primarily influence the drag coefficient, which is consistently lower at higher Reynolds numbers.

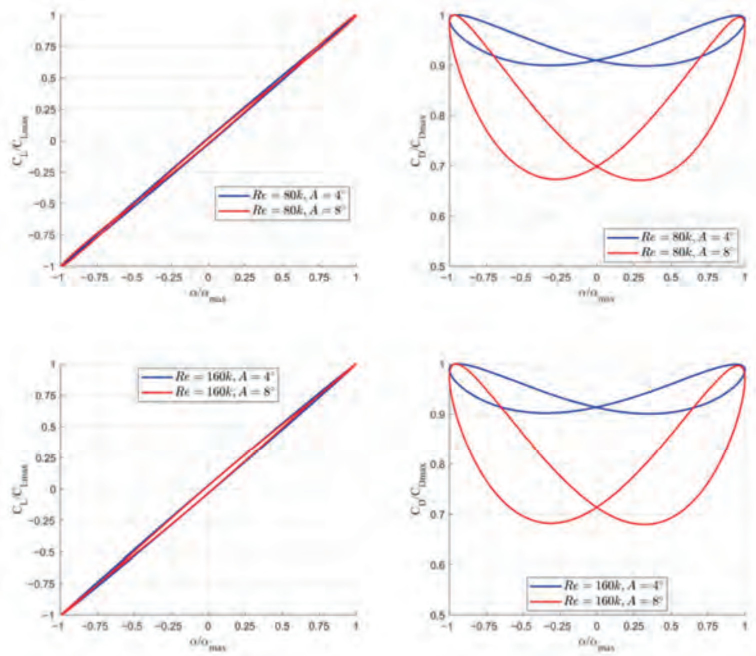

Figure 12. Normalized lift coefficient (C_L/C_{Lmax}) and drag coefficient (C_D/C_{Dmax}) as a function of normalized angle of attack (α/α_{max}) for Reynolds numbers Re = 80k and Re = 160k and pitching amplitudes A = 4° and A = 8°—k-ω model used with 1 Hz frequency motion. The top row compares Re = 80k, while the bottom row compares Re = 160k.

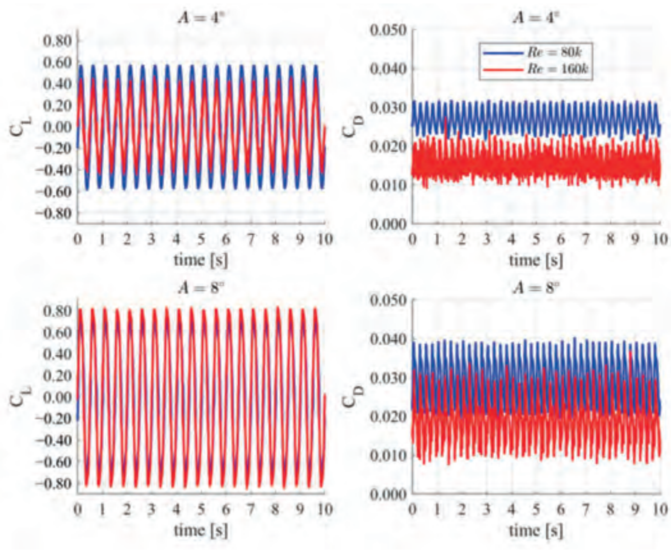

Figure 13. Time histories of the lift coefficient (C_L) and drag coefficient (C_D) for pitching amplitudes A = 4° and A = 8° at Reynolds numbers Re = 80k and Re = 160k—γ-Re_θ model used with 2 Hz frequency motion. The top row corresponds to A = 4°, while the bottom row corresponds to A = 8°.

An interesting observation, as shown in Figure 13 and even more clearly in Figure 14, which depicts the aerodynamic force coefficients as a function of the angle of attack, is the less oscillatory nature of the coefficients for the Reynolds number Re = 80k. For Re = 160k, oscillations are more pronounced but remain smaller than those in the 1 Hz case.

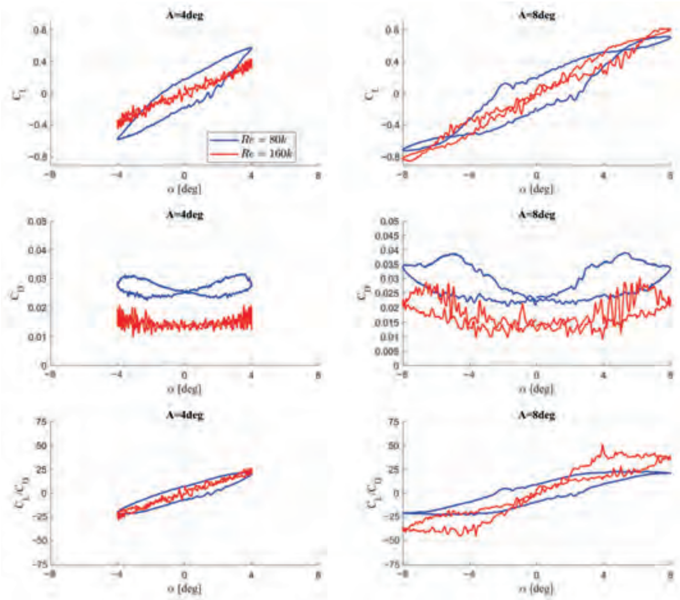

Figure 14. Hysteresis loops of the lift coefficient (C_L), drag coefficient (C_D), and lift-to-drag ratio (C_L/C_D) as a function of the angle of attack (α) for pitching amplitudes A = 4° and A = 8° at Reynolds numbers Re = 80k and Re = 160k—γ-Re_θ model used with 2 Hz frequency motion. The left column corresponds to A = 4°, and the right column corresponds to A = 8°.

The remaining qualitative effects for both Reynolds numbers, including the aerodynamic force coefficients and lift-to-drag ratio (C_L/C_D), are consistent with the trends discussed in Section 3.2 of this paper.

Figure 15 compares the normalized lift and drag coefficients as a function of the normalized angle of attack. This comparison clearly shows that, for the Reynolds number of Re = 80k, the effect of laminar separation bubbles is significantly smaller than that for Re = 160k. Similar to the 1 Hz frequency case, a notable reduction in the minimum drag coefficient is observed for the higher amplitude.

3.5. Hysteresis Loop Analysis for the Pitching Airfoil

In Section 3.4, the aerodynamic load characteristics, including the lift and drag components on the surface of the pitching airfoil, were analyzed as functions of the Reynolds number and amplitude. Both factors significantly influence the characteristics and shape of the hysteresis loop.

The wide loop observed at low angles of attack is primarily attributed to phenomena occurring in the boundary layer, particularly the detachment of the laminar boundary layer. Figure 16 illustrates the detachment location as a function of the dimensionless time t/T, where t is the time and T is the motion period.

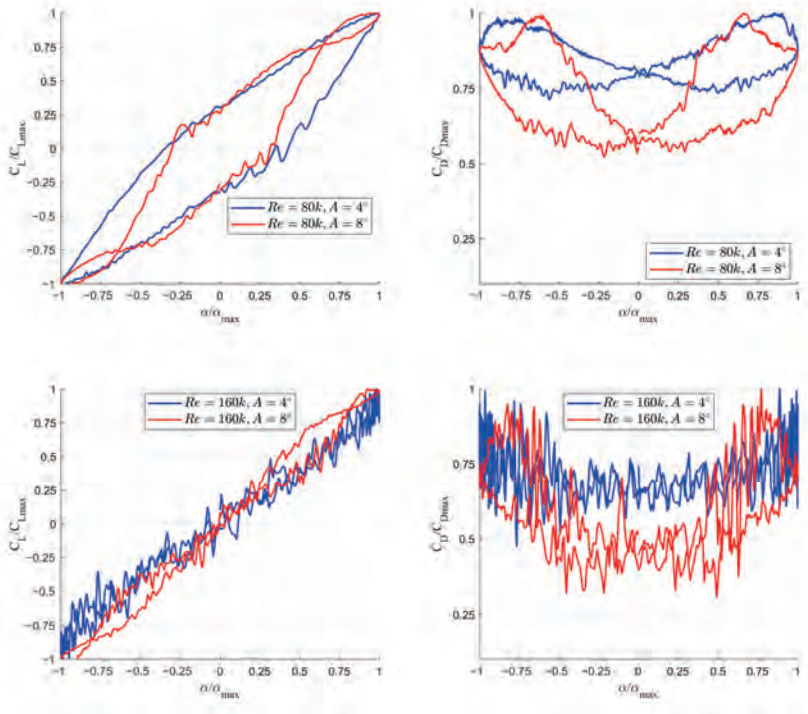

Figure 15. Normalized lift coefficient (C_L/C_{Lmax}) and drag coefficient (C_D/C_{Dmax}) as a function of normalized angle of attack (α/α_{max}) for Reynolds numbers Re = 80k and Re = 160k and pitching amplitudes A = 4° and A = 8°—γ-Re_θ model used with 2 Hz frequency motion. The top row compares Re = 80k, while the bottom row compares Re = 160k.

This figure shows the evolution of the pressure coefficient (C_p) and *x*-wall shear stress for a pitch angle varying from 0 to its maximum value. The analysis considers an amplitude A = 4° and Re = 80k. Based on the x-wall shear stress characteristics, the local position of the laminar boundary layer separation can be identified, which is marked by a change in the x-wall shear stress from positive to negative.

In the C_p plots, the separation is reflected by a stagnation region (the flat part of the curve). Figure 16c depicts the "migration" of the transition location, x_{tr}/c, normalized by airfoil chord c. Different colors represent the transition characteristics of the suction and pressure sides of the airfoil.

The figure demonstrates that as the pitch angle increases, separation occurs later on the suction side and earlier on the pressure side. The contour map of the vorticity vector parallel to the *z*-axis, shown in Figure 16b, visualizes the aerodynamic wake around the airfoil.

Both panels illustrate the same pitch angle of 2° during the increasing (upper plot) and decreasing (lower plot) pitch angles. The figure clearly reveals the large vortex structures generated at the trailing edge on both sides of the airfoil. It also highlights their dependence on the direction of the airfoil motion. Additionally, a slight curvature of the wake is observed during the decreasing pitch angle phase.

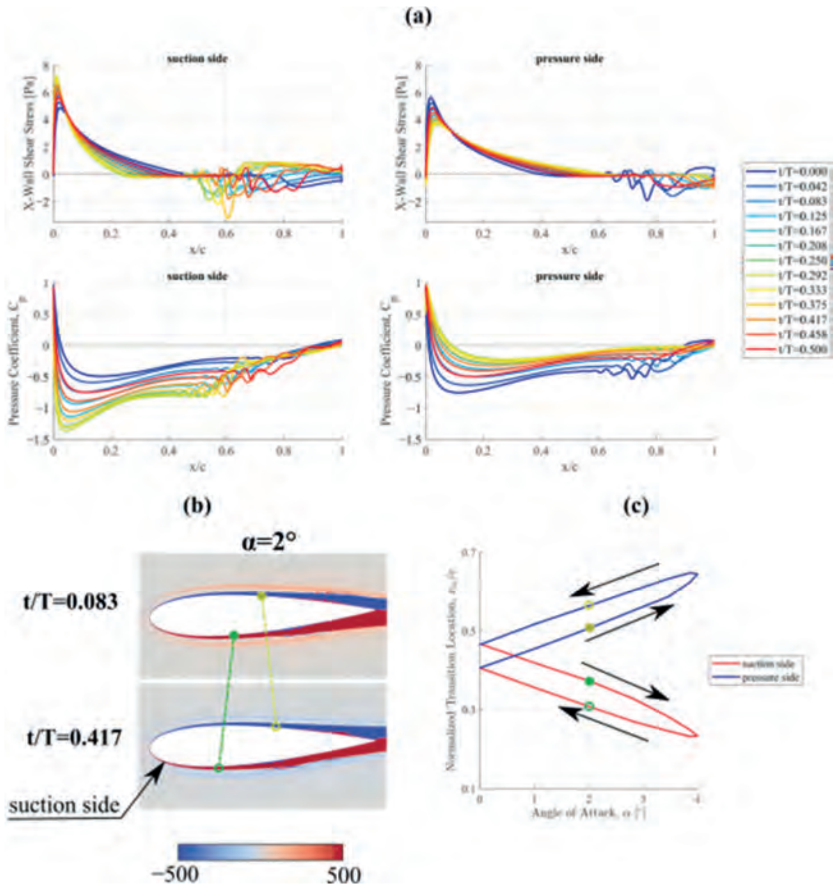

Figure 16. Normalized lift coefficient (C_L/C_{Lmax}) and drag coefficient (**a**) Pressure coefficient, C_p, and *x*-wall shear stresses; (**b**) *z*-vorticity contours; (**c**) normalized transition location, x_{tr}/c.

3.6. Aerodynamic Load Analysis for 13 Hz Pitching Motion

This section discusses the case in which the pitching motion frequency is 13.3(3) Hz. The reduced frequencies were 0.129 for Re = 80k and 0.065 for Re = 160k. For this case as well, the amplitude-to-chord ratios are 0.067 (4°) and 0.133 (8°), based on a 6 cm chord. The aerodynamic loads of a pitching NACA 0018 foil were analyzed at this "unusual" frequency because of the rotational speed of a Darrieus vertical-axis wind turbine (VAWT). This rotor was tested in the TU Delft wind tunnel, and the results of these tests can be found in [6]. Since the publication of these tests, numerous scientific papers have been devoted to this rotor.

Some authors have utilized the experimental data of this turbine to validate numerical methods, including the γ-Re_θ transition model. Additionally, studies comparing turbine performance using various turbulence models, such as the k-ω SST model, have emerged. The results published by various authors confirm that both models generate similar results for aerodynamic loads, namely, the tangential and normal components, as shown, for example, in [10,34,35]. These minor discrepancies are puzzling because both models exhibit significant differences in the stationary lift force characteristics. Furthermore, as sections of this article discussing the force dynamics for a foil oscillating at 1 Hz and 2 Hz have shown, laminar separation bubbles play a substantial role in the oscillations of aerodynamic forces. Consequently, the lack of significant differences between the aerodynamic load characteristics obtained using the γ-Re_θ transition and k-ω SST models was partially attributed to turbulence intensity. The effect of bubbles diminishes with increasing turbulence intensity [36]. However, in the case of this particular rotor, this does not appear to be the main reason, as it was tested in a low turbulence intensity wind tunnel [6].

The results presented in this section partially resolve the puzzle of the significant similarities in loads obtained using both approaches-γ-Re_θ and k-ω SST. Figures 17 and 18 illustrate the hysteresis loops of the aerodynamic coefficients at the two examined Reynolds numbers and two amplitudes. Both figures compare the results of the two turbulence models, with the dashed lines representing the k-ω SST approach. As can be seen, the k-ω SST model results improved with increasing the Reynolds number. Interestingly, the hysteresis of the C_L coefficient obtained using this model is broader for Re = 160k and A = 8°, whereas the agreement between the two approaches for A = 4° is very high. Additionally, the drag coefficients for both amplitudes at high Reynolds numbers are surprisingly consistent.

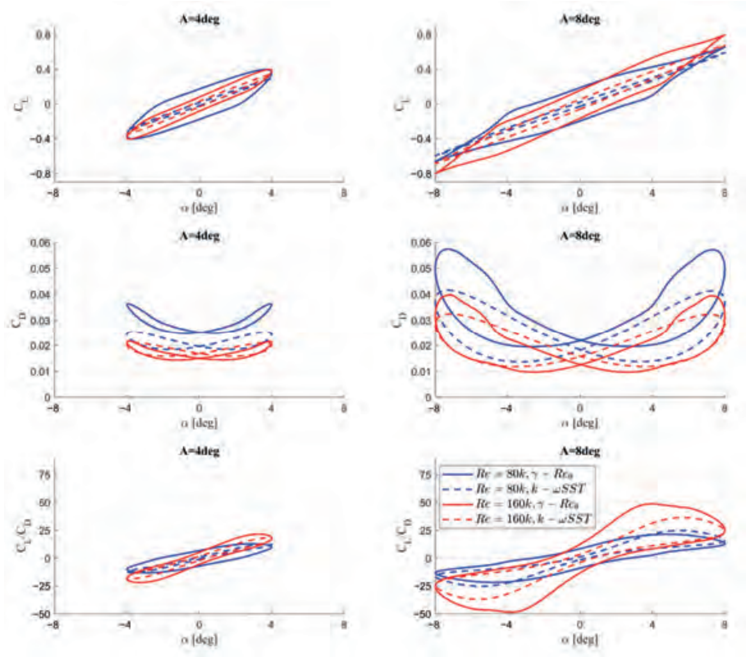

Figure 17. Hysteresis loops of the lift coefficient (C_L), drag coefficient (C_D), and lift-to-drag ratio (C_L/C_D) as a function of the angle of attack (α) for pitching amplitudes A = 4° and A = 8° at Reynolds numbers Re = 80k and Re = 160k—13.3 Hz frequency motion. The left column corresponds to A = 4°, and the right column corresponds to A = 8°.

Another critical observation from these figures is the absence of aerodynamic load oscillations obtained using the γ-Re_θ transition model, indicating the reduced impact of laminar separation bubbles. Comparing the results shown in this section with those in Section 3.4 further reveals that at lower oscillation frequencies, the bubble effect weakens at lower Reynolds numbers.

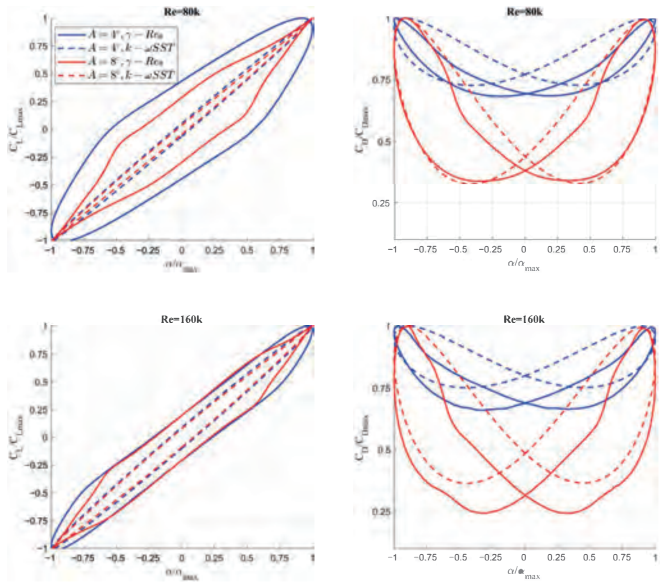

Figure 18. Normalized lift coefficient (C_L/C_{Lmax}) and drag coefficient (C_D/C_{Dmax}) as a function of normalized angle of attack (α/α_{max}) for Reynolds numbers Re = 80k and Re = 160k and pitching amplitudes A = 4° and A = 8°—13.3 Hz frequency motion. The top row compares Re = 80k, while the bottom row compares Re = 160k.

4. Conclusions

The primary objective of this study was to analyze the aerodynamic loads on a symmetric, thick NACA 0018 airfoil under pitching motion at low Reynolds numbers. The oscillation frequencies were set to 1 and 2 Hz, and the amplitudes were set to 4 and 8 degrees. Additionally, steady-state simulations for a clean airfoil were conducted for angles of attack of up to 20 degrees to validate the numerical model. The main observations of this study are as follows:

1. The four-equation γ-Re_θ turbulence model performed significantly better in predicting the steady aerodynamic characteristics at higher Reynolds numbers. At lower Reynolds numbers, as the flow becomes laminar, the model struggles to accurately capture the C_L curve, even at small angles of attack. For a more accurate representation under these conditions, three-dimensional modeling and at least LES approaches are required. Nevertheless, the results from the Transition SST model are more physical than those from classical turbulence models.

2. The classical two-equation k-ω SST turbulence model, which assumes a fully turbulent boundary layer, does not produce any nonlinearities in the lift force characteristics for angles of attack below the critical angle. Consequently, the laminar boundary layer separation effects are absent. Interestingly, the difference between the drag coefficient predicted by this model and the experimental results decreases as the Reynolds number decreases.

3. The XFOIL approach, which also models the laminar-to-turbulent transition, overestimates the lift coefficients, although the drag coefficients are acceptable for moderate angles of attack. Calibration is required when using XFOIL for thick airfoils.

4. The dynamic characteristics of an airfoil are strongly influenced by both the oscillation amplitude and reduced frequency. At lower Reynolds numbers, earlier boundary layer separation leads to an increase in the amplitude of the lift coefficient for small oscillation amplitudes.

5. Laminar separation bubbles cause significant hysteresis in the lift coefficient at low angles of attack and lead to notable oscillations in the aerodynamic forces. For the C_L characteristics obtained using the k-ω SST model, oscillations are nearly absent, and the hysteresis in the C_L is minimal.

6. Both the Reynolds number and the oscillation amplitude and frequency significantly affect the drag coefficient, as shown by both turbulence models used in this study. Specifically, when the Reynolds number is halved from 160k, the drag coefficient decreases substantially. Furthermore, increasing the amplitude at the same Reynolds number significantly reduced the ratio of the minimum to maximum drag coefficients (C_D/C_{Dmax}).

7. An increase in the oscillation frequency from 1 Hz to 2 Hz results in a significant reduction in the oscillations of the aerodynamic force components at a Reynolds number of 80k.

8. The pitching motion of the NACA 0018 airfoil induced notable hysteresis at the transition location, even at small amplitudes.

9. This study demonstrates that the similarity in the aerodynamic loads obtained from the γ-Re_θ and k-ω SST models can be partially explained by the reduced impact of laminar separation bubbles under the tested conditions. The results highlight that the γ-Re_θ model provides consistent performance with negligible oscillations, particularly at lower frequencies and Reynolds numbers, while the k-ω SST model shows improved agreement with the γ-Re_θ model at higher Reynolds numbers. These findings emphasize the importance of considering the laminar separation bubble dynamics and Reynolds number effects when selecting turbulence models for simulating pitching airfoils, especially in applications involving vertical-axis wind turbines.

10. While this study is limited to 2D URANS simulations, the authors recognize the importance of extending the analysis to 3D LES or DNS approaches. However, such simulations are currently beyond the available computational capacity, especially for Reynolds numbers exceeding 100,000 and under unsteady conditions. Preliminary estimates suggest that a 3D mesh resolution of at least 60 to 160 million elements is required, along with high-order discretization schemes and long simulation times. Therefore, the present study provides a foundational step toward more advanced and higher-fidelity investigations.

These findings provide new insights into the aerodynamic performance of thick airfoils at low Reynolds numbers and demonstrate the importance of turbulence modeling for accurately capturing flow physics.

Although the Transition SST model significantly improves the predictions compared with the standard k-ω SST model by incorporating transition physics, discrepancies with the experimental data persist, especially at higher angles of attack. These deviations stem from the model's correlation-based formulation, which relies on local flow parameters rather than directly resolving the transition mechanisms from the Navier–Stokes equations. Our previous attempts to calibrate the model by adjusting the transition onset parameter s_1 [37] yielded limited improvements. This highlights the need for more robust transition modeling or 3-D high-fidelity simulations in future studies to improve the accuracy in the stall region.

Author Contributions: Conceptualization, J.M., M.Ś. and K.R.; methodology, J.M., M.Ś. and K.R.; software, J.M., M.Ś. and K.R.; validation, J.M., M.Ś. and K.R.; formal analysis, J.M., M.Ś. and K.R.; investigation, J.M., M.Ś. and K.R.; resources, J.M., M.Ś. and K.R.; data curation, J.M., M.Ś. and K.R.; writing—original draft preparation, J.M., M.Ś. and K.R.; writing—review and editing, J.M., M.Ś. and K.R.; visualization, J.M., M.Ś. and K.R.; supervision, J.M., M.Ś. and K.R.; project administration, J.M., M.Ś. and K.R.; funding acquisition, K.R. All authors have read and agreed to the published version of the manuscript.

Funding: This research received no external funding. The APC was funded by the authors.

Data Availability Statement: The data presented in this study are available upon request from the corresponding author.

Acknowledgments: This research was conducted with the assistance of the Interdisciplinary Centre for Mathematical and Computational Modelling (ICM) at the University of Warsaw under computational allocations no. GB83-33. The author would like to express heartfelt gratitude to Tomasz Szuster, a retired academic teacher from the Warsaw University of Technology, for his invaluable support and guidance during the study. No generative AI tools were used in the preparation of this manuscript.

Conflicts of Interest: The authors declare no conflicts of interest.

References

1. Kojima, R.; Nonomura, T.; Oyama, A.; Fujii, K. Large-eddy simulation of low-Reynolds-number flow over thick and thin NACA airfoils. *J. Aircr.* **2013**, *50*, 187–196. [CrossRef]
2. Anyoji, M.; Nonomura, T.; Aono, H.; Oyama, A.; Fujii, K.; Nagai, H.; Asai, K. Computational and experimental analysis of a high-performance airfoil under low-Reynolds-number flow condition. *J. Aircr.* **2014**, *51*, 1864–1872. [CrossRef]
3. Fujino, K.; Suzuki, K. Mechanism of periodic oscillation in low-Reynolds-number buffet around an airfoil at angle of attack. *Phys. Fluids* **2024**, *36*, 046126. [CrossRef]
4. Li, J.; Nagata, K.; Watanabe, T. Aerodynamic characteristics of airfoils with fractal structures in low-Reynolds-number regime. *CEAS Aeronaut. J.* **2025**, *16*, 17–32. [CrossRef]
5. Jimenez-Soler, P.; Lichota, P. Mitigating sensor quality issues in UAV system identification through wavelet decomposition. *Bull. Pol. Acad. Sci. Tech. Sci.* **2025**, *73*, e152216. [CrossRef]
6. Rogowski, K.; Michna, J.; Ferreira, C. Numerical Analysis of Aerodynamic Performance of a Fixed-Pitch Vertical Axis Wind Turbine Rotor. *Adv. Sci. Technol. Res. J.* **2024**, *18*, 97–109. [CrossRef]
7. Tescione, G.; Ragni, D.; He, C.; Simão Ferreira, C.J.; van Bussel, G.J.W. Near wake flow analysis of a vertical axis wind turbine by stereoscopic particle image velocimetry. *J. Renew. Energy* **2014**, *70*, 47–61. [CrossRef]
8. Huang, M.; Sciacchitano, A.; Ferreira, C. On the wake deflection of vertical axis wind turbines by pitched blades. *Wind Energy* **2023**, *26*, 365–387. [CrossRef]
9. Huang, M. Wake and Wind Farm Aerodynamics of Vertical Axis Wind Turbines. Ph.D. Thesis, Delft University of Technology, Delft, The Netherlands, 2023. [CrossRef]
10. Rogowski, K. CFD Computation of the H-Darrieus wind turbine—The impact of the rotating shaft on the rotor performance. *Energies* **2019**, *12*, 2506. [CrossRef]
11. Michna, J.; Rogowski, K. Numerical study of the effect of the Reynolds number and the turbulence intensity on the performance of the NACA 0018 airfoil at the low Reynolds number regime. *Processes* **2022**, *10*, 1004. [CrossRef]
12. Istvan, M.S.; Yarusevych, S. Effects of free-stream turbulence intensity on transition in a laminar separation bubble formed over an airfoil. *Exp. Fluids* **2018**, *59*, 52. [CrossRef]
13. Kawai, S.; Asada, K.; Oyama, A. Freestream Turbulence Effects in Large-Eddy Simulations of Laminar Separation Bubble. *J. Aircr.* **2023**, *60*, 1721–1727. [CrossRef]
14. Casteleim, D.; Tescione, G.; Ragni, D.; Simao Ferreira, C.; Gaunaa, M. Creating a benchmark of Vertical Axis Wind Turbines in Dynamic Stall for validating numerical models. In Proceedings of the 33rd Wind Energy Symposium, Kissimmee, FL, USA, 5–9 January 2015; AIP Publishing: New York, NY, USA, 2015. [CrossRef]
15. Langtry, R.B. A Correlation-Based Transition Model Using Local Variables for Unstructured Parallelized CFD Codes. Ph.D. Thesis, Universitaet Stuttgart, Stuttgart, Germany, 2006. [CrossRef]
16. Divakaran, U.; Ramesh, A.; Mohammad, A.; Velamati, R.K. Effect of Helix Angle on the Performance of Helical Vertical Axis Wind Turbine. *Energies* **2021**, *14*, 393. [CrossRef]
17. Smith, A.M.O.; Gamberoni, N. *Transition, Pressure Gradient and Stability Theory*; Douglas Aircraft Company, El Segundo Division: Los Angeles, CA, USA, 1956.
18. Bianchini, A.; Balduzzi, F.; Rainbird, J.M.; Peiro, J.; Graham, J.M.R.; Ferrara, G.; Ferrari, L. An Experimental and Numerical Assessment of Airfoil Polars for Use in Darrieus Wind Turbines—Part I: Flow Curvature Effects. *J. Eng. Gas Turbine Power* **2016**, *138*, 032602. [CrossRef]
19. Badrya, C.; Govindarajan, B.; Chopra, I. Basic Understanding of Unsteady Airfoil Aerodynamics at Low Reynolds Numbers. In Proceedings of the 2018 AIAA Aerospace Sciences Meeting, Astronautics, Kissimmee, FL, USA, 8–12 January 2018. [CrossRef]
20. Theodorsen, T. *General Theory of Aerodynamic Instability and The Mechanism of Flutter*; NASA Reference Publication; NASA Ames Research Center Classical Aerodynamics Theory: Washington, DC, USA, 1979.
21. Glauert, H. The Force and Moment on an Oscillating Airfoil. In *Vorträge aus Dem Gebiete der Aerodynamik und Verw Andter Gebiete*; Gilles, A., Hopf, L.V., Kármán, T., Eds.; Springer: Berlin, Heidelberg, Germany, 1930.

22. Leishman, J.G. *Principles of Helicopter Aerodynamics*, 2nd ed.; Cambridge University Press: New York, NY, USA, 2006.
23. Mikkelsen, R.; Bak, C.; Gaunaa, M.; Fischer, A.; Olsen, A.S.; Ildvedsen, S.; Beckerlee, J. Dynamic stall measurements of a harmonic pitching NACA63-018 airfoil at high Reynolds numbers. *J. Phys. Conf. Ser.* **2024**, *2767*, 022067. [CrossRef]
24. Stevens, P.R.R.J.; Babinsky, H. Experiments to investigate lift production mechanisms on pitching flat plates. *Exp. Fluids* **2017**, *58*, 7. [CrossRef]
25. Brunton, S.; Rowley, C. Modeling the unsteady aerodynamic forces on small-scale wings. In Proceedings of the 47th AIAA Aerospace Sciences Meeting Including the New Horizons Forum and Aerospace Exposition, Orlando, FL, USA, 5–8 January 2009. [CrossRef]
26. Kang, C.K.; Aono, H.; Baik, Y.S.; Bernal, L.P.; Shyy, W. Fluid dynamics of pitching and plunging flat plate at intermediate Reynolds numbers. *AIAA J.* **2013**, *51*, 315–329. [CrossRef]
27. Moriche, M.; Flores, O.; García-Villalba, M. Three-dimensional instabilities in the wake of a flapping wing at low Reynolds number. *Int. J. Heat Fluid Flow* **2016**, *62*, 44–55. [CrossRef]
28. Rogowski, K.; Mikkelsen, R.F.; Michna, J.; Wiśniewski, J. Aerodynamic performance analysis of NACA 0018 airfoil at low Reynolds numbers in a low-turbulence wind tunnel. *Adv. Sci. Technol. Res. J.* **2025**, *19*, 136–150. [CrossRef]
29. Vitagliano, P.L.; Minervino, M.; Quagliarella, D.; Catalano, P. A conservative sliding mesh coupling procedure for U-RANS flow simulations. *Aircr. Eng. Aerosp. Technol.* **2016**, *88*, 151–158. [CrossRef]
30. Fluent, A. *ANSYS Fluent User's Guide, 2020R2*; ANSYS: Canonsburg, PA, USA, 2020.
31. Menter, F.R.; Langtry, R.B.; Likki, S.R.; Suzen, Y.B.; Huang, P.G.; Völker, S. A correlation-based transition model using local variables—Part 1: Model formulation. *J. Turbomach.* **2006**, *128*, 413–422. [CrossRef]
32. Rogowski, K.; Michna, J.; Mikkelsen, R.F.; Ferreira, C.S. Impact of zigzag tape on blade loads and aerodynamic wake in a vertical axis wind turbine: A Delft VAWT case study. *Energy* **2025**, *321*, 135344. [CrossRef]
33. Mendoza, V.; Bachant, P.; Ferreira, C.; Goude, A. Near-wake flow simulation of a vertical axis turbine using an actuator line model. *Wind Energy* **2018**, *22*, 171–188. [CrossRef]
34. Rezaeiha, A.; Kalkman, I.; Blocken, B. CFD simulation of a vertical axis wind turbine operating at a moderate tip speed ratio: Guidelines for minimum domain size and azimuthal increment. Renew. *Energy* **2017**, *107*, 373–385. [CrossRef]
35. Rezaeiha, A.; Montazeri, H.; Blocken, B. On the accuracy of turbulence models for CFD simulations of vertical axis wind turbines. *Energy* **2019**, *180*, 838–857. [CrossRef]
36. Damiola, L.; Siddiqui, M.F.; Runacres, M.C.; De Troyer, T. Influence of free-stream turbulence intensity on static and dynamic stall of a NACA 0018 aerofoil. *J. Wind Eng.* **2023**, *232*, 105270. [CrossRef]
37. Michna, J.; Rogowski, K.; Kubacki, S. Investigation of Aerodynamic Performance of the NACA 0018 Airfoil at Low Reynolds Numbers: A Comparative Study of 2-D and 3-D Models Using Transition SST and k-ω SST Approaches. In Proceedings of the 2024 Research & Education in Aircraft Design (READ 2024), Warsaw, Poland, 15–17 May 2024. Available online: https://read.meil.pw.edu.pl/wp-content/uploads/Program/2024/READ_2024.html (accessed on 15 May 2025).

Advances in Science and Technology Research Journal

Advances in Science and Technology Research Journal, 18(6), 97–109
https://doi.org/10.12913/22998624/191128
ISSN 2299-8624, License CC-BY 4.0

Received: 2024.06.10
Accepted: 2024.08.15
Published: 2024.09.08

Numerical Analysis of Aerodynamic Performance of a Fixed-Pitch Vertical Axis Wind Turbine Rotor

Krzysztof Rogowski[1*], Jan Michna[1], Carlos Ferreira[2]

[1] Institute of Aeronautics and Applied Mechanics, Warsaw University of Technology, Nowowiejska 24, 00-665 Warsaw, Poland

[2] Faculty of Aerospace Engineering, Delft University of Technology, Kluyverweg 1, 2629 HS Delft, The Netherlands

* Corresponding author's e-mail: krzysztof.rogowski@pw.edu.pl

ABSTRACT

The aim of this study was to assess the accuracy of predicting the aerodynamic loads and investigate the aerodynamic wake characteristics of a vertical axis wind turbine (VAWT) rotor using a simplified two-dimensional numerical rotor model and an advanced numerical approach – the Scale Adaptive Simulation (SAS) coupled with the four-equation $\gamma - Re_\theta$ turbulence model. The challenge for this approach lies in the operating conditions of the rotor, the blade pitch angles, and the very small geometric dimensions of the rotor. The rotor, with a diameter of 0.3 m, operates at a low tip speed ratio of 2.5 and an extremely low blade Reynolds number of approximately 22.000, whereas the pitch angles, β, are: -10, 0, and 10 degrees. Validation was conducted based on high-fidelity measurements obtained using the PIV technique at TU Delft. The obtained results of rotor loads and velocity profiles are surprisingly reliable for cases of $\beta = 0°$ and $\beta = -10°$. However, the 2-D model is too imprecise to estimate both aerodynamic loads and velocity fields accurately.

Keywords: wind turbine, VAWT, Darrieus, aerodynamics, RANS, scale adaptive simulation, turbulence.

INTRODUCTION

As the global discussion about the consequences of exploiting fossil fuels grows, the development of green energy sources has increased widely. In the wind energy industry, the concerns have been focused mainly on horizontal-axis wind turbines (HAWTs) since the 1970s and the fuel crisis. This type of turbine is well-investigated, and improving its aerodynamic performance is challenging. More and more efforts are concentrated on vertical-axis wind turbines (VAWTs), especially to bridge the aerodynamic performance gap between these two types [1, 2].

VAWT has many advantages over the horizontal-axis type. It does not need any yaw mechanics, a smaller wake area behind the rotor, and low installation and maintenance costs because of easy access to the generator lying on the ground [3]. However, the vertical-axis type poses some challenges, e.g., complex turbine aerodynamics, a demanding self-starting process (low self-start torque), and generally lower current efficiency than HAWTs.

The most critical challenge is rotor aerodynamic performance estimation because of the phenomena which are complicated to model, such as dynamic stall and blade-wake interaction [4]. The power performance of VAWTs depends on various operational parameters, among others, an airfoil (shape, chord length), blade pitch angle, the solidity of a turbine, Reynolds numbers, tip speed ratio, shaft diameter, and turbulence intensity [1, 5].

To study blade pitch angle, one of the operational parameters, many researchers investigated the power performance of fixed- and variable-pitch angle VAWT. Fiedler and Tullis [6] found that toe-in fixed pitch angle can significantly lower the wind turbine performance. Using large eddy simulations (LES) with experimental measurements, Elkhoury et al. [7] demonstrated that variable-pitch mechanisms can give higher power coefficients than fixed-pitch ones. Rezaieha et al. [8] showed a large hysteresis of dynamic loads on the blades and boundary layer events (such as laminar-to-turbulent transition). Meanwhile, Huang et al. [9] proved that pitch angle configuration significantly influences wake deflection and deformation. Szczerba et al. [10] noticed that achieving the best performance requires high blade setting precision with less than 1 degree tolerance. Elsakka et al. [11] demonstrated that pitch angle has a lower influence on power performance than tip speed ratio and solidity, but switching angle improves turbine aerodynamic performance.

In the presented research, the well-known γ–Re_θ transition turbulence model was utulized [12]. This four-equation model includes the intermittency and transition momentum thickness transport equations, combined with the two-equation k-ω SST turbulence model. This correlation-based approach was designed for general-purpose use across a broad range of flow classes, but as a correlation model, it requires validation against experimental data or high-fidelity simulations such as LES or detached eddy simulation (DES) [13]. The complex flow at the very low Reynolds number of approximately 22.000 considered in this study presents significant validation challenges due to the scarcity of experimental data. ANSYS Fluent provides two transition models, γ–Re_θ and κ–κ_L–ω, both of which necessitate validation and calibration based on experimental studies to ensure accurate predictions.

VERTICAL AXIS WIND TURBINE AND ITS OPERATIONAL CONDITIONS

This study analyzed a simplified two-dimensional model of a vertical-axis wind turbine (VAWT) rotor. The rotor consists of only two symmetrical NACA0012 airfoils representing blades of infinite length. Additional simplifications of the model include the lack of a rotating shaft and blade supports (e.g., struts). The geometric dimensions of the rotor, such as the rotor diameter (D = 0.3 m) and the airfoil chord length (c = 0.03 m), correspond to the dimensions of a wind turbine developed by TU Delft for laboratory-scale research. The attachment point of the blade was located at one-quarter of the chord length measured from the airfoil leading edge. The study analyzed the rotor performance for three fixed blade pitch angles, β, (the blade pitch angle remained constant during rotor's movement). Figure 1 shows the simplified wind turbine model and the convention for indicating the sign of blade pitch angles. Positive pitch angles mean the blade is turned inward.

The operational parameters of the rotor are as follows: the undisturbed flow velocity, V_0, is 5 m/s; rotor rotational velocity is assumed to be 800 rpm; tip speed ratio, *TSR*, is equal to 2.5. The tip speed ratio is a dimensionless quantity that relates the angular velocity ω of the rotor, its radius, R, and the velocity of the undisturbed flow: $TSR = \omega \cdot R/V_0$. Figure 1 depicts the velocity vectors and illustrates the method of measuring rotor position using the azimuthal angle θ. A schematic of the laboratory-scale VAWT model is additionally presented in Figure 1. During the wind tunnel tests, two components of the aerodynamic force were measured using three load cells mounted on the bottom of the standing frame. Details of the experiment can be found in [14].

GRID AND COMPUTATIONAL METHODOLOGY

This paper section first describes the computational domain and the numerical grid used for the calculations. The numerical model settings are described in the subsequent part of this section.

The two-bladed wind turbine rotor was surrounded by a rectangular domain with dimensions of 7.5 × 6 m, corresponding to 25 × 20 D, where D represents the rotor diameter (Fig. 2). These dimensions were selected based on the numerical study by Rezaeiha et al. [15], who analyzed the impact of domain size and the distance of the rotor axis from the inlet on the aerodynamic performance of the wind turbine. The domain dimensions adopted in the conducted simulations allow for the aerodynamic blade loads to be obtained with negligible error resulting from the assumed boundary conditions. In the case of VAWTs, the fluctuations in aerodynamic loads during each rotation are very significant. Hence, unsteady simulations are necessary, utilising the unsteady Reynolds-averaged Navier-Stokes (URANS) approach. The performed analyses used the ANSYS Fluent 2022 code and the well-known sliding

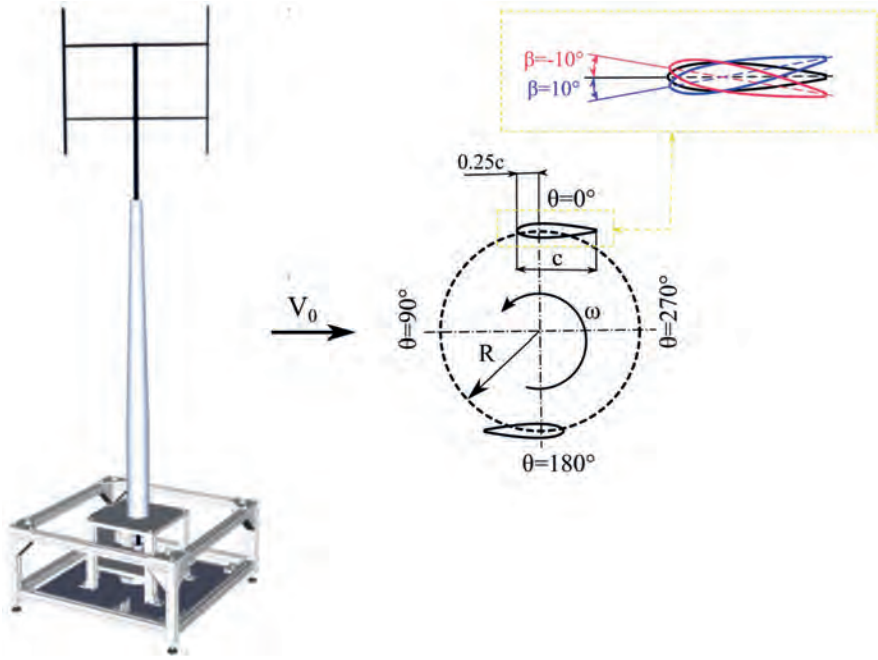

Figure 1. Schematic of the investigated VAWT model. On the left is a conceptual drawing of the laboratory-scale rotor. The figure is taken from [9] with permission. On the right is a 2-D schematic used in numerical computations and the pitch angle convention

mesh technique. However, this technique requires separating the area around the rotor, which will move during the simulation. In the analyzed model, the moving area around the rotor is a circle with a diameter of 1.5 D. Data between both regions is exchanged during calculations via the interface. Applying this condition (interface) may result in a small numerical error at the boundary between areas. However, Bangga et al. [16] demonstrated that the diameter adopted in these studies (1.5 D) is sufficient to minimize numerical error. Figure 2 illustrates the computational domain along with the prescribed boundary conditions. At the domain boundaries, the following boundary conditions are applied: velocity inlet, pressure outlet, and wall (no slip), respectively, at the inlet, outlet, and airfoil edges. In addition, the "symmetry" boundary condition is used on the side edges of the domain, which allows for the same effect as the wall (slip) boundary condition.

The geometric model of the rotor described above was discretized with a control volume mesh. The numerical mesh consists of a structured mesh near the edges of the airfoils and an unstructured mesh in the remaining area. The number of grid points on each airfoil edge was equal to 2400. Rezaeiha et al. [8], who analyzed the sensitivity of the solution to grid density for steady-state calculations of the NACA0015 airfoil at a low Reynolds number, obtained sufficiently accurate results for grid nodes equal to 1600 along the entire airfoil edge. This grid density analyzed by Rezaeiha et al. was subsequently used by them for VAWT simulations. The mesh was not additionally refined near the leading and trailing edges; in other words, the element size along the airfoil edge was uniform. In the normal direction to the airfoil edge, 25 layers of structural mesh were applied. The first layer thickness was 0.00001 m, which ensured a maximum value of the wall y+ parameter < 1.2. However, the average value of this parameter for various rotor angles was approximately 0.8. Maintaining the value of this parameter at the recommended level ≈ 1 is practically impossible in the case of a VAWT rotor calculated using the sliding mesh technique. Moreover, according to the ANSYS Fluent documentation [17], wall y+ < 1.2 values do not produce significant numerical error. Each subsequent layer of the structural mesh was thicker than the previous one, and the growth rate of subsequent layers was 1.1. This value is also consistent with the recommendations of the ANSYS Fluent documentation. Such a mesh should be sufficient to model all phenomena occurring in the boundary layer during the rotation, such as the laminar-to-turbulent transition and stall effects. At the interface, the same number of grid points was assumed and established to equal 150 in the fixed and moving domains to minimize the numerical error. Therefore, the mesh element size at the interface is 100 times lower than the rotor diameter. The maximum size of unstructured mesh elements in the rotor area (in a circular domain) is 3e-3m. This size is also 100 times lower compared to the rotor diameter. The area in the aerodynamic wake downstream behind the rotor has also been refined. The maximum element size in this area was 60 times lower than the rotor diameter. The area covered by this refined mesh extends 20 D behind the rotor and has a width of 2 D. The modeled mesh effectively captures a broad spectrum of vortex structures present in the rotor and wake regions [18]. The final mesh is depicted in Figure 2, comprising 510.271 elements.

The description above pertains to the geometric and discretized model. The numerical model settings are outlined below. The numerical calculations of the flow around the rotating rotor were conducted using the 2-D URANS approach. The adopted closure model was the 4-equation $\gamma\text{-}Re_\theta$ model, known as the Transition SST turbulence model in ANSYS Fluent. To represent the velocity field more accurately in the rotor region and the rotor aerodynamic wake, the Scale Adaptive Simulation (SAS) approach was utilized [19, 20]. The simulations considered air with a constant density of 1.225 kg/m^3 and viscosity of 1.7894e-05 kg/(m·s). A turbulence intensity of 2% was assumed at the inlet [9]. The turbulence scale value at the inlet was not measured; therefore, following Rezaeiha et al. [15], the scale length was assumed to equal the rotor diameter. The coupled scheme was employed for the Pressure-Velocity Coupling method in these investigations. The least squares cell based was also used for spatial discretization and second-order schemes for all computed equations except for the momentum equations, where

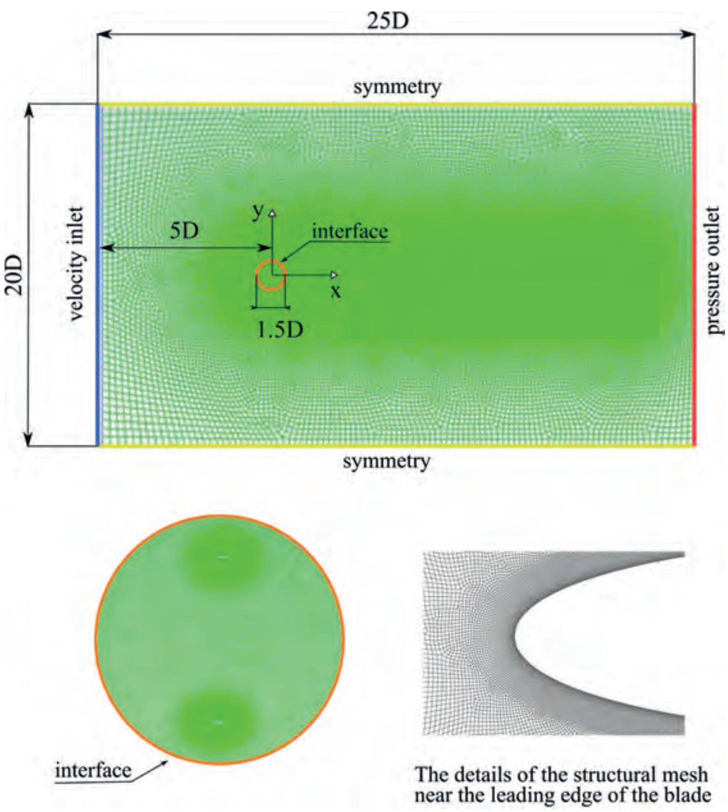

Figure 2. Numerical domain; boundary conditions; mesh

the bounded central differencing was utilized. The convergence criterion for all equations was set to 1e-7. The Courant Number value was left as default, equal to 200. According to [17], in the case of the pressure-based solver and the Coupled scheme, the Courant Number stabilizes the convergence behavior. In these studies, the influence of time step size on the calculated aerodynamic characteristics of the rotor was not analysed. This is, of course, a very significant parameter affecting the accuracy of simulations. However, several credible, independent scientific works have examined this effect depending on various operational parameters of the rotor. Therefore, in this work, the time step size was selected based on the guidelines of Rezaeiha et al. [15] and own experiences [21]. The time step size, Δt, was set in this work to 2.09e-05 seconds, equivalent to an azimuth increment of Δθ = 0.1 deg.

RESULTS AND DISCUSSION

This section presents the characteristics of two components of the aerodynamic force acting on the entire wind turbine rotor: the component parallel to the flow direction, known as thrust, and the lateral force. The obtained loads are then validated against experimental measurements to assess the reliability of the adopted simplified 2-D numerical rotor model. In the next part of this section, aerodynamic loads on the rotor blade are analyzed. The Reynolds-averaged Navier-Stokes simulation was compared with high-fidelity experimental data in this next section of the paper.

Aerodynamic load components

The two components of aerodynamic force, the streamwise (T_x) and lateral (T_y), are given as dimensionless coefficients:

$$C_{T_{x,y}} = \frac{T_{x,y}}{0.5\rho V_0^2 A} \tag{1}$$

where: ρ – air density, V_0 – undisturbed flow velocity, A – the frontal area of the turbine. In the considered rotor $A = D \cdot H$, where H is the rotor height.

Figure 3a depicts the dependence of both components, thrust and lateral, of the aerodynamic force on the number of rotor revolutions. For clarity, only the results for a zero-pitch angle (β = 0 deg) are shown in this graph. In the case of the remaining analyzed pitch angles, the nature of the aerodynamic forces follows a similar pattern. Figure 3a also shows that the influence of initial conditions on these rotor operational parameters (TSR = 2.5) is noticeable only in the first few rotations. Initial conditions, i.e., flow parameters at each control volume at t = 0 s, were assumed to be the same as at the inlet. This effect is visible in the aerodynamic loads corresponding to the first few revolutions in numerical simulations. To eliminate this effect, the number of rotations required to calculate depends on the rotor's operating parameters and geometry. Rogowski [21] also studied the rotor in laboratory-size scale but operating at TSR = 4.5. Rogowski determined that the minimum number of rotations necessary to achieve a power coefficient independent of initial conditions is 15. This result is consistent with the numerical research conducted independently by Rezaeiha [22], who additionally demonstrated that in the case of a rotor with higher solidity, σ, the number of rotations required for simulation slightly increases. The rotor solidity is defined in the case of Darrieus-type rotors as:

$$\sigma = c \cdot N/D \tag{2}$$

where: c – chord length, N – number of turbine blades and D – rotor diameter.

Rezaeiha et al. [22] investigated rotors with solidities of 0.12 and 0.24. In the conducted investigations, this parameter was equal to 0.2. Additionally, Rezaeiha et al. also demonstrated that for a more heavily loaded rotor operating at TSR = 2.5, the influence of initial conditions is significantly reduced. The average power coefficient of the rotor becomes independent of initial conditions after about ten full revolutions. As it can be seen in (Figure 3a), the results of both components of the aerodynamic force differ slightly from each other in each rotor revolution. However, this is the proper behavior of the numerical model and has several reasons. Primarily, the wind turbine rotor operates under significant geometric angles of attack of the rotor blades. The geometric angle of attack, α_g, is determined based on the velocity triangle (Figure 3b) as [23]:

$$\alpha_g = \tan^{-1}\left(\frac{\sin\theta}{\cos\theta + TSR}\right) \tag{3}$$

This model of the geometric angle of attack is, of course, highly simplified. Determining the actual angle of attack is quite challenging. However, there are analytical methods allowing for estimation of the actual angle of attack based on the velocity field, e.g. [24], indicate that in the upwind part of the rotor (for θ from 0 to 180 deg, see Figure 1), such an approximation is sufficient and enables understanding of certain phenomena. The actual angle of attack differs mainly in the downwind part (for θ from 180 to 360 deg) compared to the geometric angle. It is known that due to the deceleration of the flow velocity by the blades traveling in the upwind part, there can be a significant decrease in the magnitude of the angle of attack depending on the tip speed ratio [9]. Figure 3b shows that at TSR = 2.5, the angle of attack amplitude is significant; in this case, it is as much as 30 degrees.

The second reason for the irregularity of the aerodynamic forces shown in (Figure 3a) is the local blade Reynolds number. The Reynolds number can be approximately estimated using the local geometric angle of attack introduced earlier and the local relative velocity, V_R, given as:

$$V_R = V_0\sqrt{(TSR + \cos\theta)^2 + (\sin\theta)^2} \quad (4)$$

The local Reynolds number is equal to:

$$Re = \frac{V_R \cdot c}{\mu} \quad (5)$$

where: μ – dynamic viscosity of air, c – chord length.

The local Reynolds number is given by equation 3, while its average value is only 21.860. The rotor of the investigated turbine operates in the range of subcritical Reynolds numbers and very large angles of attack.

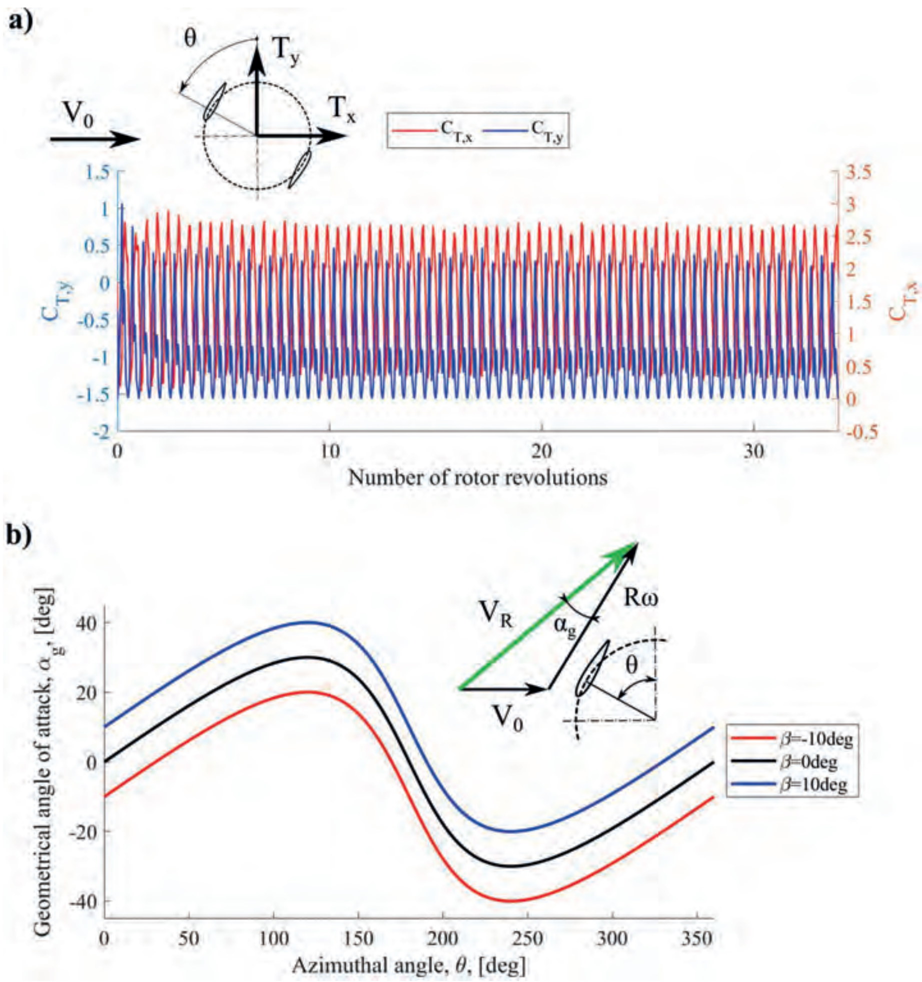

Figure 3. (a) Trust and lateral coefficient, (b) geometric angle of attack for zero-pitch angle configuration

The irregularities shown in (Figure 3a) are also attributed to the turbulence model employed in this study. Using classical one- or two-equation turbulence models such as k-ω or k-ε leads to unrealistic averaging of flow disturbances. Consequently, the wake generated by the blades traveling in the upwind part of the rotor rapidly dissipates, resulting in a regular and repeatable aerodynamic force distribution for individual blades and the entire rotor. Rogowski et al., in their work [20], demonstrated a comparison of aerodynamic loads obtained using classical turbulence models and the Scale Adaptive Simulation approach for a one-bladed Darrieus rotor. Applying this technique allows for capturing much more flow detail and, consequently, a more irregular nature of aerodynamic loads on the blades, which is more physically realistic. This action, however, involves the necessity of averaging the loads over a larger number of rotations than different approaches. Figure 4 shows the dependencies of $C_{T,x}$ and $C_{T,y}$ averaged over one full rotor revolution. These values are presented as a function of the number of revolutions for the last ten calculated rotor revolutions. As it seen in this figure, the average values of the loads differ in each subsequent revolution. However, it should be emphasized that the fluctuations of these average values are small. In the conducted investigation, it was also examined how the components of the aerodynamic force differ when the averaging time is increased. To achieve this, the times corresponding to the averaged rotations ranging from 1 to 10 full rotations of the rotor were investigated. The conducted research has shown that the relative difference of different averaging times compared to the averaging time corresponding to 10 complete rotations is relatively small, not exceeding 3.2% for $C_{T,y}$ and 1% for $C_{T,x}$. Additionally, it was found that an averaging time equal to 5 full rotations is sufficient. The relative errors of $C_{T,y}$ and $C_{T,x}$ components are 1.1% and 0.4%, respectively. Therefore, in all analyses conducted in this paper, the average values of the aerodynamic force components were calculated using the data from the last five rotations of the rotor.

Validation

Table 1 compares the calculated average values of the rotor aerodynamic loads with the values measured by Huang [9]. The obtained results of the $C_{T,x}$ component are slightly overestimated compared to the experimental values, but the nature of the changes for cases $\beta = 0°$ and $\beta = -10°$ is similar. The agreement between the calculated and measured lateral aerodynamic force component is even better. Significant differences were only observed for the case $\beta = 10°$, especially for the $C_{T,x}$ component. These differences can be explained based on the aerodynamic wake patterns behind the wind turbine rotor measured in the

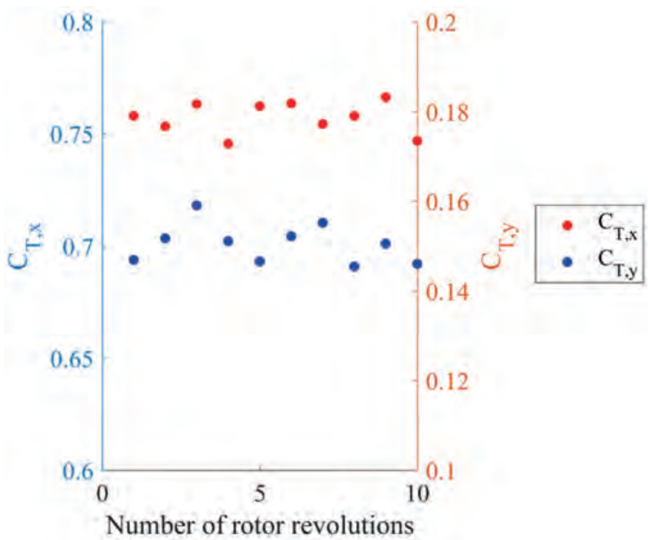

Figure 4. The mean coefficients of the aerodynamic force components for each of the last ten calculated rotations of the rotor

Table 1. Calculated and measured $C_{T,x}$ and $C_{T,y}$

Test case	Trust, $C_{T,x}$			Lateral, $C_{T,y}$		
	Experiment	CFD	Δ%	Experiment	CFD	Δ%
β = –10°	0.60	0.73	21.67	0.09	0.09	0.00
β = 0°	0.65	0.76	16.92	0.14	0.15	7.14
β = 10°	0.81	0.64	-20.99	0.39	0.51	30.17

experiment using the PIV method. In cases β = 0° and β = –10°, the aerodynamic wake is more "filled" in the equatorial plane compared to the case β = 10°. This is due to 3-D effects, which are strongest in this particular case. These effects are impossible to determine using a 2-D numerical approach. Despite the limitations of the applied approach, the largest absolute relative error Δ% is 30% for $C_{T,y}$ and 21% for $C_{T,x}$.

Aerodynamic loads on the rotor blade

The analyses above concerned averaged rotor aerodynamic loads. This part of the paper aimed to determine the aerodynamic load distribution along a single blade. Figures 5a and 5b depict the aerodynamic force components acting on a single rotor blade for the last calculated rotation of the rotor. The aerodynamic loads are presented as dimensionless coefficients for three pitch angles. The coefficients of tangential (C_T) and normal (C_N) aerodynamic forces are given by:

$$C_{T,N} = \frac{T,N}{0.5\rho V_0^2 A} \tag{6}$$

The tangential component of the aerodynamic load is responsible for generating torque, which is the product of the tangential force and the distance from its point of application to the rotor axis. As it is shown in Figure 5b, this force is an order of magnitude smaller than the normal component. Moreover, as it can be seen from this figure, a large portion of all displayed C_T characteristics has a negative value. The average C_T values for all analyzed pitch angles are negative and close to zero. Negative values of the tangential force indicate that a rotor with such a configuration must be powered to maintain the desired operational conditions. The normal component (Figure 5a) is slightly shifted for angles β = –10° and β = 10° compared to the β = 0°. This is due to the shift of the local attack angle at the introduced pitch angles. Therefore, such behavior of the characteristics proves the correct qualitative functioning of the simplified numerical model. Numerous fluctuations of the components, on the other hand, indicate a very complex nature of the flow in the regime of deep dynamic stall.

Velocity deficit profiles

In this part of the paper, the Reynolds-averaged Navier-Stokes simulation was compared

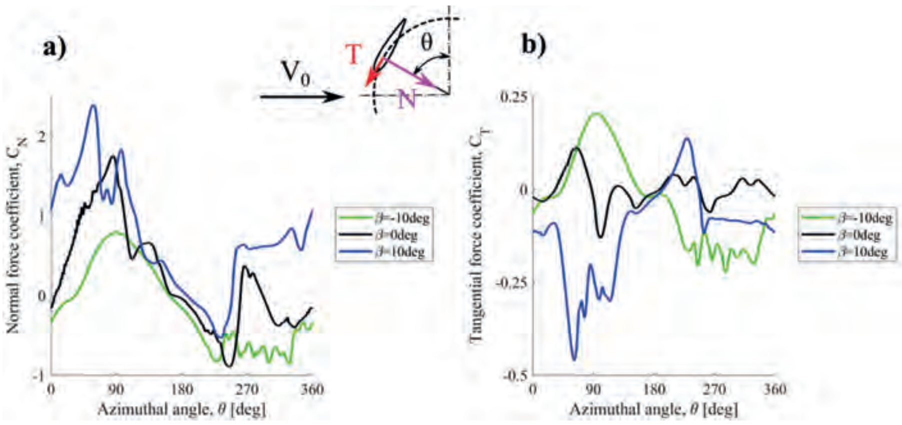

Figure 5. Aerodynamic blade load coefficients at three pitch angles: (a) normal components, (b) tangential components

with high-fidelity experimental data and with the actuator line model (ALM) results by Huang [9]. Figure 6 compares the velocity deficit profiles for two cases: β = 0° and β = 10°, where $\Delta u/V_0 = 1 - u/V_0$, where u represents a local air velocity component parallel to the undisturbed flow velocity. The results presented in this figure have been averaged over one full rotor revolution. In this case, the additional influence of averaging time on wake velocity characteristics was not tested. However, as it can be observed in (Fig. 6), the simplified 2-D model with the SAS approach reasonably covers the velocity profiles for the β = 0° case even at a distance of 10D downstream from the rotor. It can be further seen from Fig. 6 that the SAS approach provides more details about the flow itself. Unfortunately, the wake predictions for the most heavily loaded rotor (β = 10°) are significantly worse up to 5D behind the rotor. In this case, the reduced 2-D model shows significant differences in velocity deficit profiles.

As it is shown in (Figure 6), the ALM + RANS approach provides significantly higher fidelity compared to the CFD approach for the β = 10° case. The ALM approach incorporates a

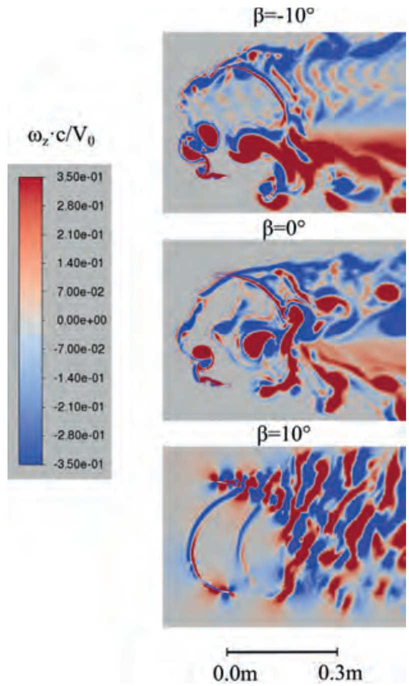

Figure 7. Contours of normalized z-vorticity in the rotor area at three pitch angles

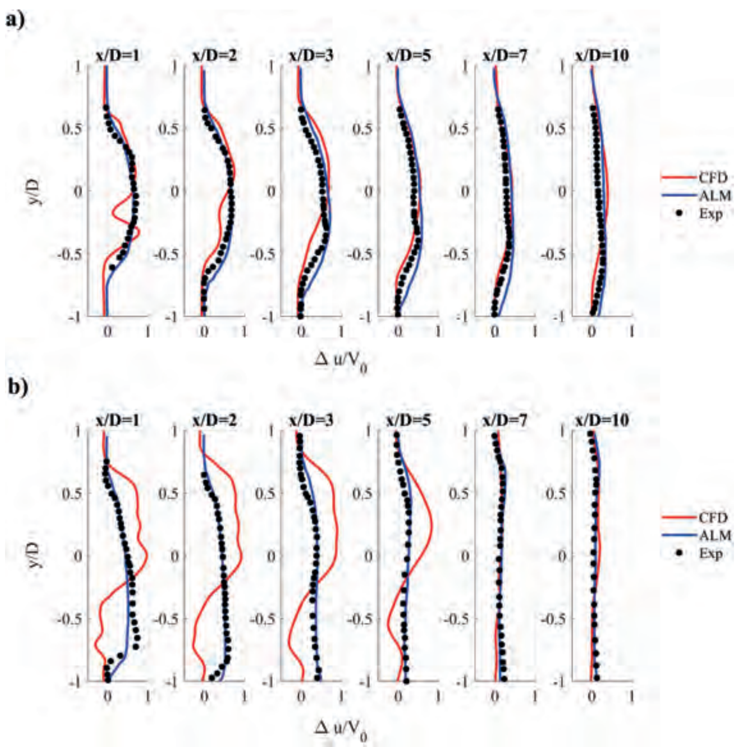

Figure 6. Velocity deficit profiles for (a) β = 0°, (b) β = 10°

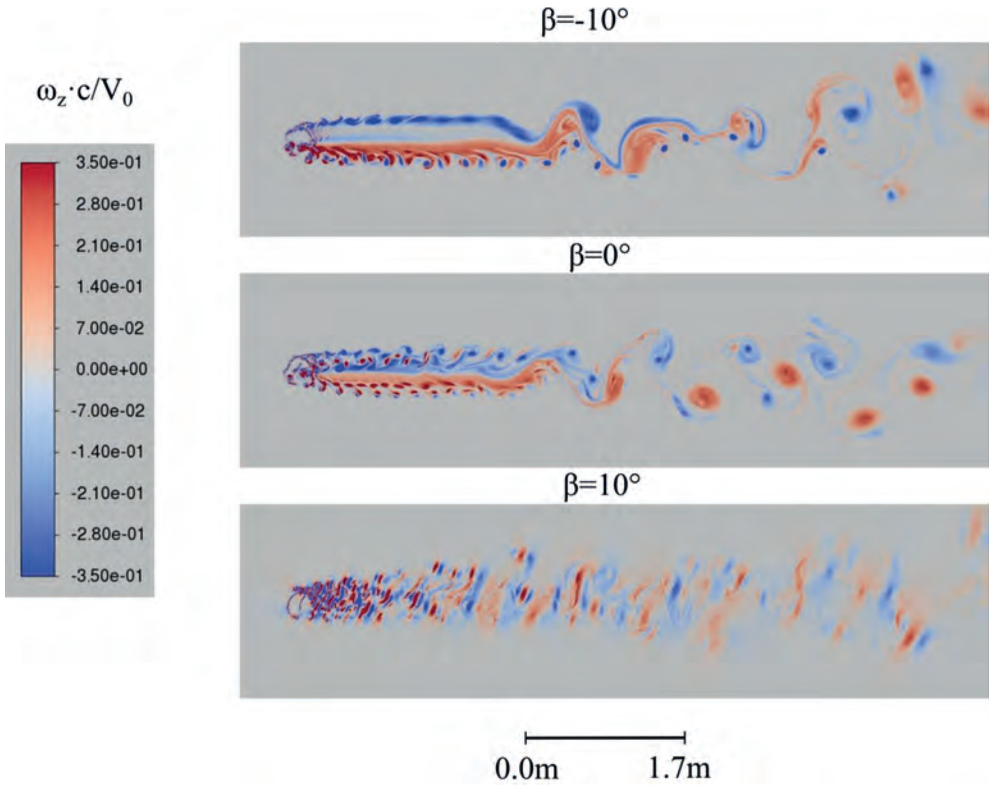

Figure 8. Contours of normalized z-vorticity in the wake of the rotor at three pitch angles

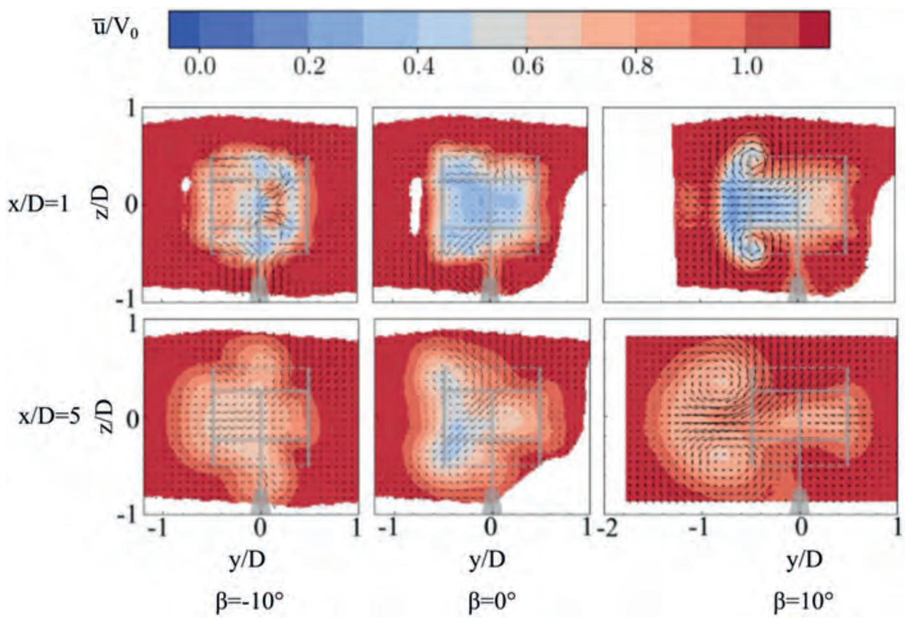

Figure 9. Contours of streamwise velocity with in-plane velocity vectors for the VAWT at three pitch angles and at two positions behind the rotor. The photos come from Huang's doctoral dissertation [25]. The authors of this paper have the permission to publish them

three-dimensional rotor model, while to determine the velocity field in the rotor region, the URANS approach with the k-ε turbulence model was employed [9].

Figures 7 and 8 depict contours of normalized vorticity ω_z for three analyzed pitch angles. In 2-D flow, the velocity lacks a z-component, and the vorticity vector is parallel to the rotor axis. The red and blue colors correspond to opposite directions of the vorticity vector. Contour maps were prepared on two scales to illustrate differences in flow structure around the rotor and far downstream. Both figures compare instantaneous vorticity fields for the same azimuthal position. Calculations were performed for 40 complete rotor revolutions to ensure fully developed vorticity fields. The results clearly demonstrate a similar flow character for cases of β = 0° and β = –10°, and a completely different character for the case of β = 10°.

CONCLUSIONS

The main aim of this paper was to validate a reduced numerical model of a vertical-axis wind turbine based on high-fidelity experimental data developed at TU Delft [9]. The model was simplified by replacing the three-dimensional rotor with a two-dimensional model. The primary numerical tool employed was the Scale Adaptive Simulation approach with the Transition SST turbulence model. The results obtained allowed drawing the following conclusions:

The operating conditions and geometry of the rotor are extreme. Flow in the rotor region is highly complex, and the blades operate under conditions of deep dynamic detachment.

Significant differences in the aerodynamic wake compared to the experiment, especially for the case of β = 10°, are mainly due to 3-D phenomena. The 2-D model cannot account for changes in velocity and pressure in the axial direction, as well as the interactions between the blades and the blade tips.

Introducing a significant positive pitch angle increases the local angle of attack and normal blade loading, resulting in the formation of strong trailing edge vortices that significantly modify the two-dimensional flow. Figure 9 depicts the time-averaged streamwise velocity contours and in-plane velocity vectors of the laboratory-scale VAWT operating at various pitch angles and in different positions behind the rotor. These findings were obtained through stereo-PIV measurements.

As long as the trailing edge vortices are small to moderate, the aerodynamic wake is more “filled” and uniform. Under such conditions, the reduced approach yields significantly better results. A pitch angle of 10 degrees significantly alters the lateral force and, therefore, modifies the wake geometry. A positive pitch angle results in significant blade work under conditions of dramatic detachment but also significantly modifies the flow in the rotor wake. This effect can be utilized in designing a wind farm with such rotors for passive control of wake geometry. Deterioration of the aerodynamic properties of the upstream rotor may enhance the performance of the wind turbine array.

As it is shown in this paper, the 2-D CFD approach fails in the case of the most heavily loaded rotor. However, the 2-D model is attractive due to its low computational cost, even with the current level of computerization. Therefore, to completely rule out this approach in studies of such cases, it is necessary to examine one more significant aspect. Specifically, the impact of the rotor aspect ratio (AR), which is the ratio of the rotor height to its diameter, on the geometry of the aerodynamic wake needs to be analyzed. Huang studied this effect using a two-bladed VAWT configuration based on experimental research from Delft. The examined rotor had a diameter of 1 m and a blade chord length of 0.06 m. The aerodynamics of this rotor were analyzed at TSR = 4.5. Studies conducted using the ALM technique for ARs ranging from 1 to 10 showed that the thrust coefficient of this rotor increased from 0.75 for AR = 1 to 0.91 for AR = 10. This suggests that the width of the aerodynamic wake should increase with AR. However, Huang’s studies focused only on the case of β = 0°. Therefore, a hypothesis can be proposed: in the case where β > 0° (or even $\beta \gg 0°$) and AR is sufficiently large, the 2-D CFD model will provide more physical results. This hypothesis, however, requires appropriate experimental and numerical analyses.

Acknowledgements

Research was funded by POB Energy of Warsaw University of Technology within the Excellence Initiative: Research University (IDUB) programme (Grant No. 1820/355/Z01/POB7/2021). This research was also conducted with the assistance of the Interdisciplinary Centre for Mathematical and Computational Modelling (ICM) at the University of Warsaw under computational allocations no. G93-1588 and G92-1487. I would like to express my heartfelt gratitude to Mr. Eng. Tomasz Szuster, a retired academic teacher from the Warsaw University of Technology, for his invaluable support and guidance.

REFERENCES

1. Kumar R., Raahemifar K., Fung A.S. A critical review of vertical axis wind turbines for urban applications. Renewable and Sustainable Energy Reviews. 2018, 89, 281–91. DOI: 10.1016/j.rser.2018.03.033.
2. Bianchini A., Ferrara G., Ferrari L. Pitch optimization in small-size darrieus wind turbines. Energy Procedia. 2015, 81, 122–32. DOI: 10.1016/j.egypro.2015.12.067.
3. Du L., Ingram G., Dominy R.G. A review of H-Darrieus wind turbine aerodynamic research. Proceedings of the Institution of Mechanical Engineers, Part C: Journal of Mechanical Engineering Science. 2019, 233(23–24), 7590–616. DOI: 10.1177/0954406219885962.
4. Amet E., Maître T., Pellone C., Achard J.L. 2D Numerical simulations of blade-vortex interaction in a darrieus turbine. Journal of Fluids Engineering. 2009, 131(111103). DOI: 10.1115/1.4000258.
5. Rezaeiha A., Montazeri H., Blocken B. Characterization of aerodynamic performance of vertical axis wind turbines: Impact of operational parameters. Energy Conversion and Management. 2018, 169, 45–77. DOI: 10.1016/j.enconman.2018.05.042.
6. Fiedler A.J., Tullis S. Blade offset and pitch effects on a high solidity vertical axis wind turbine. Wind Engineering. 2009, 33(3), 237–46. DOI: 10.1260/030952409789140955.
7. Elkhoury M., Kiwata T., Aoun E. Experimental and numerical investigation of a three-dimensional vertical-axis wind turbine with variable-pitch. Journal of Wind Engineering and Industrial Aerodynamics. 2015, 139, 111–23. DOI: 10.1016/j.jweia.2015.01.004.
8. Rezaeiha A., Kalkman I., Blocken B. Effect of pitch angle on power performance and aerodynamics of a vertical axis wind turbine. Applied Energy. 2017, 197, 132–50. DOI: 10.1016/j.apenergy.2017.03.128.
9. Huang M., Sciacchitano A., Ferreira C. On the wake deflection of vertical axis wind turbines by pitched blades. Wind Energy. 2023, 26(4), 365–87. DOI: 10.1002/we.2803.
10. Szczerba Z., Szczerba P., Szczerba K., Szumski M., Pytel K. Wind tunnel experimental study on the efficiency of vertical-axis wind turbines via analysis of blade pitch angle influence. Energies. 2023, 16(13), 4903. DOI: 10.3390/en16134903.
11. Elsakka M.M., Ingham D.B., Ma L., Pourkashanian M., Moustafa G.H., Elhenawy Y. Response surface optimisation of vertical axis wind turbine at low wind speeds. Energy Reports. 2022, 8, 10868–80. DOI: 10.1016/j.egyr.2022.08.222.
12. Menter F.R., Langtry, R.B., Likki, S.R., Suzen, Y.B., Huang, P.G., Völker, S.A. Correlation-based transition model using local variables: Part I—model formulation. J. Turbomach. 2006, 128, 413–422. DOI: 10.1115/1.2184352.
13. Michna J., Rogowski K. Numerical study of the effect of the reynolds number and the turbulence intensity on the performance of the NACA 0018 airfoil at the low reynolds number regime. Processes. 2022, 10, 1004. DOI: 10.3390/pr10051004.
14. Huang M., Ferreira C., Sciacchitano A., Scarano F. Experimental comparison of the wake of a vertical axis wind turbine and planar actuator surfaces. J. Phys. Conf. Ser. 2020, 1618, 052063. DOI: 10.1088/1742-6596/1618/5/052063.
15. Rezaeiha A., Kalkman I., Blocken B. CFD simulation of a vertical axis wind turbine operating at a moderate tip speed ratio: Guidelines for minimum domain size and azimuthal increment. Renew. Energy 2017. 107, 373–385. DOI: 10.1016/j.renene.2017.02.006.
16. Bangga G., Hutomo G., Wiranegara R., Sasongko H. Numerical study on a single bladed vertical axis wind turbine under dynamic stall. J. Mech. Sci. Technol. 2017. 31(1), 261–267. DOI: 10.1007/s12206-016-1228-9.
17. Ansys® Fluent Release 2022, ANSYS, Inc.
18. Mendoza V., Bachant P., Ferreira C., Goude A. Near-wake flow simulation of a vertical axis turbine using an actuator line model. Wind Energy 2019. 22, 171–188. DOI: 10.1002/we.2277.
19. Rezaeiha A., Montazeri H., Blocken B. CFD analysis of dynamic stall on vertical axis wind turbines using Scale-Adaptive Simulation (SAS): Comparison against URANS and hybrid RANS/LES. Energy Convers. Manag. 2019. 196, 1282–1298. DOI: 10.1016/j.enconman.2019.06.081.
20. Rogowski K., Hansen M., Maroński., Lichota P. Scale adaptive simulation model for the darrieus wind turbine. J. Phys. Conf. Ser. 2016, 753, 022050. DOI: 10.1088/1742-6596/753/2/022050.
21. Rogowski K. CFD computation of the H-Darrieus wind turbine—The impact of the rotating shaft on the rotor performance. Energies 2019. 12(13), 2506. DOI: 10.3390/en12132506.
22. Rezaeiha A., Montazeri H., Blocken B. Towards accurate CFD simulations of vertical axis wind

turbines at different tip speed ratios and solidities: Guidelines for azimuthal increment, domain size and convergence. Energy Convers. Manag. 2018. 156, 301–316. DOI: 10.1016/j.enconman.2017.11.026.

23. Rogowski K., Maroński R., Piechna J. Numerical analysis of a small-size vertical-axis wind turbine performance and averaged flow parameters around the rotor. Arch. Mech. Eng. 2017, 64(2), 205–218. DOI: 10.1515/meceng-2017-0013.
24. Mendoza V., Bachant P., Wosnik M., Goude A. Validation of an Actuator line model coupled to a dynamic stall model for pitching motions characteristic to vertical axis turbines. J. Phys. Conf. Ser. 2016, 753, 022043. DOI: 0.1088/1742-6596/753/2/022043.
25. Huang M. Wake and wind farm aerodynamics of vertical axis wind turbines. Doctoral dissertation, Technische Universiteit Delft, 2023. DOI: 10.4233/uuid:14619578-e44f-45bb-a213-a9d179a54264.

energies

Article

A Refined Approach for Angle of Attack Estimation and Dynamic Force Hysteresis in H-Type Darrieus Wind Turbines

Jan Michna and Krzysztof Rogowski *

Institute of Aeronautics and Applied Mechanics, Warsaw University of Technology, Nowowiejska 24, 00-665 Warsaw, Poland; jan.michna.dokt@pw.edu.pl
* Correspondence: krzysztof.rogowski@pw.edu.pl

Abstract: This study investigates the aerodynamic performance and flow dynamics of an H-type Darrieus vertical axis wind turbine (VAWT) using combined numerical and experimental methods. The analysis examines the effects of operational parameters, such as rotor solidity and pitch angle, on aerodynamic loads and flow characteristics, using a 2-D URANS simulation with the Transition SST model to capture transient effects. Validation was conducted in a low-turbulence wind tunnel to observe the impact of variable flow conditions. The LineAverage method for determining the angle of attack demonstrated strong correlations between rotor configuration and load variations, particularly highlighting the influence of blade number and pitch angle on aerodynamic efficiency. This research supports optimization strategies for Darrieus VAWTs in urban environments, where turbulent, low-speed conditions challenge conventional wind turbine designs.

Keywords: vertical axis wind turbine; pitch angle; URANS; angle of attack; turbulence modeling; aerodynamic load analysis; urban wind energy

check for updates

Citation: Michna, J.; Rogowski, K. A Refined Approach for Angle of Attack Estimation and Dynamic Force Hysteresis in H-Type Darrieus Wind Turbines. *Energies* **2024**, *17*, 6264. https://doi.org/10.3390/en17246264

Academic Editor: Antonio Segalini

Received: 19 November 2024
Revised: 9 December 2024
Accepted: 10 December 2024
Published: 12 December 2024

1. Introduction

The 2021 special report by the International Energy Agency (Net Zero by 2050) [1] highlights the critical role of renewable energy sources in achieving global carbon neutrality by mid-century. Among these, wind energy is projected to supply a significant portion of future electricity demand. While offshore wind turbines have garnered attention for their capacity to harness high-quality winds, they face substantial challenges related to installation, maintenance, and scalability [2,3].

In contrast, vertical axis wind turbines (VAWTs), particularly the H-type Darrieus design, offer unique advantages for deployment in urban and low-wind-speed environments [4]. Their ability to operate efficiently without a yaw system makes them highly adaptable to the turbulent and unpredictable wind conditions typical of urban areas [5]. Moreover, their smaller physical footprint and lower noise emissions render them suitable for residential and distributed energy systems. However, these turbines face notable challenges, including limited self-starting capability and reduced aerodynamic efficiency at lower Reynolds numbers, which hinder their broader adoption [6,7].

This study aims to address these challenges by analyzing the aerodynamic characteristics of H-type Darrieus VAWTs across various geometrical configurations. A novel methodology is introduced, combining advanced numerical modeling with experimental validation, with a focus on improving turbulence modeling accuracy at low Reynolds numbers. The key contributions of this work include an in-depth analysis of the angle of attack and dynamic aerodynamic loads, which are critical for understanding the complex physical phenomena associated with the intricate flow around this type of turbine. These findings also play a vital role in efforts to improve engineering aerodynamic models for VAWTs, enhancing their performance and applicability in diverse operational conditions.

The airflow around the blades of a working wind turbine rotor is complex and highly unsteady. This complexity arises from the continuous shift in the tangential velocity direction of the blade, leading to constant changes in the angle of attack and relative velocity. Additionally, as the blades alternate between the upwind and downwind sections of the rotor, they interact with the rotor's aerodynamic wake and operate in conditions of varying turbulence intensity [8,9]. Due to these complexities, computational fluid dynamics (CFD) methods utilizing the Reynolds-averaged Navier–Stokes (RANS) equations, paired with various turbulence models, have become essential tools in recent years for numerically analyzing aerodynamic characteristics [10–12].

Due to the necessity of employing dense computational meshes, simulation methods such as large eddy simulation (LES) and even 3-D unsteady Reynolds-averaged Navier–Stokes (URANS) are significantly constrained [13,14]. Additionally, RANS methods are often combined with turbulence models, typically employing one- or two-equation approaches such as the Spalart–Allmaras [15,16] model or the k-ω and k-ε families [12,17]. In recent years, transition models have gained increasing popularity, primarily due to the need for more accurate representations of transitional phenomena, such as laminar–turbulent bubbles and other forms of flow transition [18–21]. Although the accuracy of these models can be limited for certain flow conditions [9,22–24], and the application of URANS to 3-D problems remains restricted by computational resources and sometimes licensing costs [25,26], CFD methods remain invaluable for analyzing rotors with complex geometries. These methods also serve as powerful tools to gain insights into unsteady physical phenomena associated with Darrieus rotor flows [27–29]. Understanding these phenomena is essential for the aerodynamic optimization of the rotor [27] and can further contribute to the development of methods based on blade element theory, such as blade element momentum (BEM) [30], lifting-line methods [31], and actuator line methods [32].

When modifying blade element-based methods, it is essential to accurately estimate the local angle of attack, which changes with the azimuth during each rotor revolution. To leverage CFD results in improving such methods, it is necessary to extract the angle of attack from the velocity field around the blade. Unfortunately, this task is complicated by additional effects such as virtual camber [33] and dynamic stall [34]. Moreover, depending on the tip-speed ratio, the amplitude of the angle of attack variations can be huge.

Some of the popular methods for extracting the local angle of attack in horizontal-axis wind turbines are the inverse BEM method and the averaging technique. The first method uses the load distribution as input data but is limited to one-dimensional assumptions. The second method, averaging, provides good results in the middle section of the blade, though it requires many measurement points and is more challenging to apply under complex flow conditions [35]. In the approach utilizing a priori imposed forces, the angle of attack is calculated by predefined forces based on either experimental measurements or computed values. This method is widely recognized for providing reasonably reliable results, which can subsequently be used in BEM codes for further predictions. However, a primary limitation of this approach is its reliance on 1-D theory. Notably, the direction of the incoming wind is assumed not to be influenced by blade-flow interactions, leading to significant errors in cases of high deflection. Additionally, BEM models require tip correction, where accuracy is crucial for a reliable evaluation of airfoil data [36]. Another technique developed for horizontal-axis wind turbines (HAWTs) is the "averaging technique", as applied by Hansen and Johansen [37] and further explored by Johansen et al. [38]. In this approach, the local angle of attack is calculated by reconstructing the velocity triangle on the blade: the peripheral speed is known in both magnitude and direction, while the relative speed is derived from CFD calculations by analyzing the flow in the rotor plane. However, as noted by Zhong Shen et al. [35], this method requires analyzing many points in the computational domain to capture local flow features due to its reliance on averaged data. Additionally, it is challenging to apply this approach under more general flow conditions, such as yawed flow.

Guntur and Sørensen [39] examined several methods of determining the angles of attack on wind turbine blades. One approach utilized computational fluid dynamics (CFD) to compute the local induced velocities at the rotor plane. By analyzing the velocity field from a full rotor 3-D CFD simulation, they could extract axial velocity profiles at different radial and azimuthal positions around the rotor. This data was processed by averaging velocities in specific annular sections or by obtaining pointwise values across the azimuth. Interpolating these velocities allowed them to estimate the induced axial flow at the rotor plane, providing a basis for determining the effective α at various blade sections and enhancing the accuracy of aerodynamic performance assessments [39,40]. Recent advances in input design and power spectrum optimization for aerodynamic analysis provide valuable methodologies that could enhance the precision of computational fluid dynamics (CFD) models, especially in capturing unsteady phenomena in rotor flows [41,42].

In Darrieus-type wind turbines, describing the flow field around the rotor is particularly challenging due to the variable angle of attack encountered during blade rotation, often exceeding the static stall angle. Balduzzi et al. [33] proposed an approach to estimate the angle of attack in such turbines based on an averaging technique and an inverse BEM method, which allowed for preliminary studies on flow curvature effects. While this approach yielded promising results, its application is limited to situations where the flow remains attached to the blades, and its accuracy is constrained by inherent limitations that require further analysis.

Saverin and Frank [43] introduced a method for improving the numerical prediction of the blade angle of attack (α). In their research, a method was employed to monitor the blade α within the simulation. The authors argued that using too few sampling points or a too-limited area around the blade leads to unreliable results. To obtain a credible estimation of the flow velocity components around the blade, a broader area or a greater number of sampling points is required, which allows for a more accurate capture of flow variations. Consequently, the researchers defined a finite control volume around the rotor blade, within which the velocity components of each finite volume element were averaged. Saverin and Frank emphasized that the control volume must not be too small. If the volume were too small, the averaged velocity components might not adequately reflect the actual flow experienced by the blade. It is crucial that the control volume encompasses a sufficient area around the blade to account for the flow's impact on it. At the same time, the volume should not be excessively large, as regions outside the rotor's direct influence might contribute to the averaged value, thereby distorting the results.

Bianchini et al. [36] proposed a new method for determining the angle of attack on an airfoil rotating around an axis orthogonal to the flow direction using CFD analysis. This approach incorporates the "virtual camber" effect, allowing the real airfoil to be treated as a virtual, straight-flow equivalent with a similar pressure distribution, which simplifies the assessment of aerodynamic performance. Pressure coefficient distributions for the virtual airfoil are normalized and compared with CFD results for the rotating airfoil, enabling accurate angle of attack estimation at various azimuthal positions. The method eliminates the need for user-selected variables, enhancing its robustness compared to previous BEM-based methods. Tests on a NACA0018 airfoil with different chord-to-radius ratios confirmed strong alignment with theoretical predictions, demonstrating the method's effectiveness. This approach shows potential as a versatile tool for analyzing complex flow phenomena around vertical-axis wind turbines, particularly in dynamic stall effects and other unsteady flow conditions.

Delafin et al. [44] proposed a method for determining the angle of attack based on analyzing the position of the stagnation point on the blade, which allows for calculating an equivalent angle of attack depending on the azimuthal angle. The developed method uses the location of the stagnation point on the blade as an indicator of the angle of attack, enabling the consideration of unsteady phenomena, such as the wake of another blade or a tower. By comparing the stagnation point position at fixed angles of attack, it is possible to interpolate and determine the equivalent angle of attack for the turbine. Although the method does not account for the pitching motion of the blades, its local approach makes it well suited for aerodynamic analysis under variable flow conditions.

Melani et al. [45] mention three additional methods for estimating angles of attack on airfoils in cycloidal motion: the 3-Points method, the Trajectory method, and the Area Averaging Technique (AAT). The 3-Points method uses three sampling points on each side of the airfoil, allowing for angle of attack estimation that accounts for local velocity variations. The Trajectory method employs a single sampling point along the blade's trajectory, simplifying calculations but offering less accuracy under dynamic conditions. The Area Averaging Technique (AAT), in turn, is based on analyzing the velocity field in the area around the turbine, enabling a more precise capture of the induced flow's impact on the angle of attack. In this paper, the LineAverage method is used to determine the angle of attack for an airfoil rotating around an axis perpendicular to the flow direction. The choice of this method is due to its high accuracy, which has been validated in other studies, and its ability to account for circulation effects and flow distortions, which is particularly important in Darrieus turbine analysis. Additionally, the LineAverage method enables a more precise representation of unsteady aerodynamic phenomena, such as dynamic stall hysteresis cycles, making it a suitable tool for this type of analysis.

2. Materials and Methods

2.1. Numerical Reference Model of the Rotor, Analyzed Rotor Configurations, and Operating Parameters

A simplified numerical model of the wind turbine rotor (Figure 1) was developed based on the experimental studies presented in [46]. The rotor model consists of only two blades, represented by symmetric NACA0018 airfoils. In the present study, the rotating tower and struts were omitted for simplicity. The rotor's diameter is 0.5 m, with a chord length of 0.06 m. The blades are attached at a distance of 0.4c from the leading edge. The pitch angle is set to 0 degrees, meaning the blade's chord is tangential to its path. The developed model is two-dimensional, meaning that blade edge vortex effects are not considered. However, it is worth noting that for the reference rotor model, the blade aspect ratio, defined as the ratio of blade length to chord length, is 16.67. As documented by studies such as [9,27], the contribution of 3-D effects to the overall rotor torque is minimal in the case of moderately loaded rotors. The solidity, σ, of the reference rotor is 0.24, defined as:

$$\sigma = B \cdot c / R, \tag{1}$$

where B is the number of blades, c is the chord length, and R is the rotor radius.

The above description refers to the reference rotor. In this study, several additional rotor configurations were also investigated. Two additional series of tests were conducted. In the first series, the number of rotor blades was varied, and rotors with 1, 2, 3, and 4 blades were analyzed. The blade chord remained constant. In the second series, the effect of fixed pitch angles was studied, considering three angles: $-10°$, $0°$, and $10°$ (for positive values, the leading edge is pitched inwards).

The rotor described in [46] operated at a tip speed ratio (TSR) of 4.5, defined as the ratio of the blade's tangential speed to the undisturbed flow velocity. The undisturbed flow velocity V_0 was 9.3 m/s, and the angular velocity ω was 83.7 rad/s. It was assumed that the turbulence intensity of the undisturbed flow was 1%, with a turbulence scale of 0.001 m. The impact of these parameters on the aerodynamic characteristics of the rotor was not investigated in this study.

2.2. Numerical Model Setup for the Vertical Axis Wind Turbine Simulation

Due to significant fluctuations in the aerodynamic loads on the rotor blades during a single rotation, the calculations must be performed in an unsteady mode. In this study, the unsteady Reynolds-averaged Navier–Stokes (URANS) equations were used to account for these transient effects. One implementation of this approach is the sliding mesh technique, which requires the development of an appropriate computational domain. This technique allows the independent mesh in the vicinity of the rotor path to rotate relative to the non-rotating mesh. An interface is defined between these areas to enable data exchange between the rotating and stationary meshes. It is critical that the distance between the surface of the blade profile and the interface is sufficient to avoid errors in the estimation of vorticity distributions. In this study, a circular region surrounding the rotor with a diameter slightly larger (1.5D) than the rotor itself was defined, with the radius of the rotating part of the mesh being 0.5 m. This radius is 50% larger than the turbine rotor to ensure adequate computational accuracy and stability. Figure 2 shows the rectangular computational domain within which the rotor is placed. The scale of both the rotor and the domain was maintained. This circular region can rotate with constant angular velocity ω during the simulation while the rectangular domain remains stationary. Both the rectangular and circular domains are meshed separately, and the data exchange between them is handled by an interface. Boundary conditions such as velocity inlet, pressure outlet, and symmetry were applied at the outer edges of the rectangular domain (Figure 2).

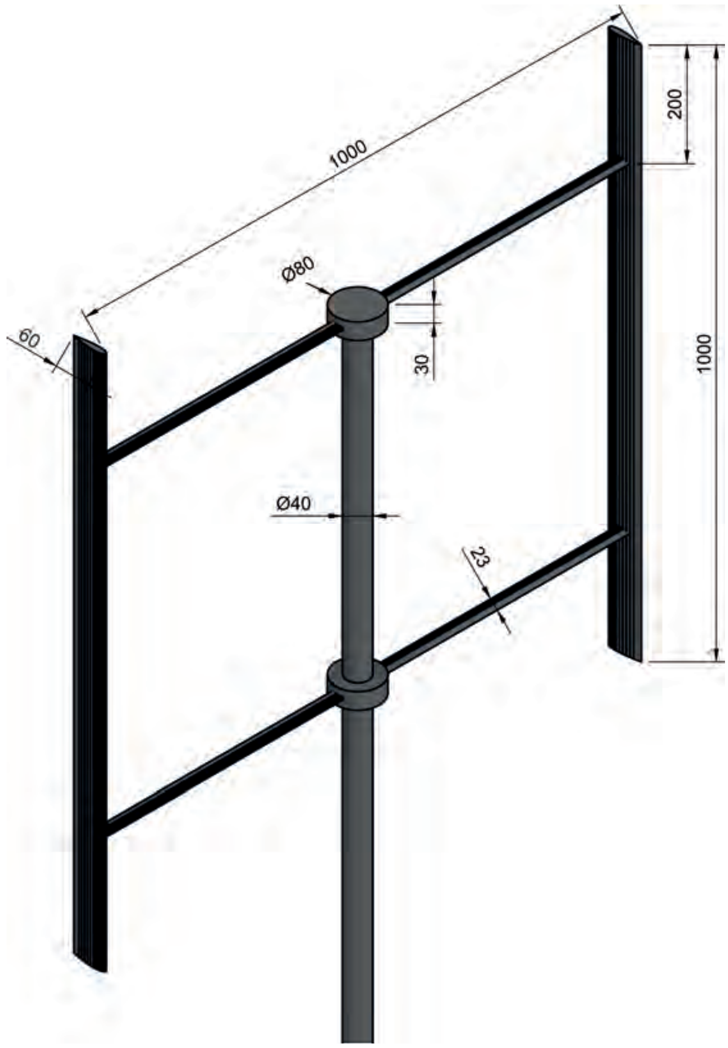

Figure 1. Diagram of an H-type vertical axis wind turbine structure with dimensions.

Due to the low Mach number, the flow was treated as incompressible. Air with a constant density of 1.225 kg/m^3 and a viscosity of 1.7894 $\times$ 10^{-5} kg/(ms) was used as the working medium.

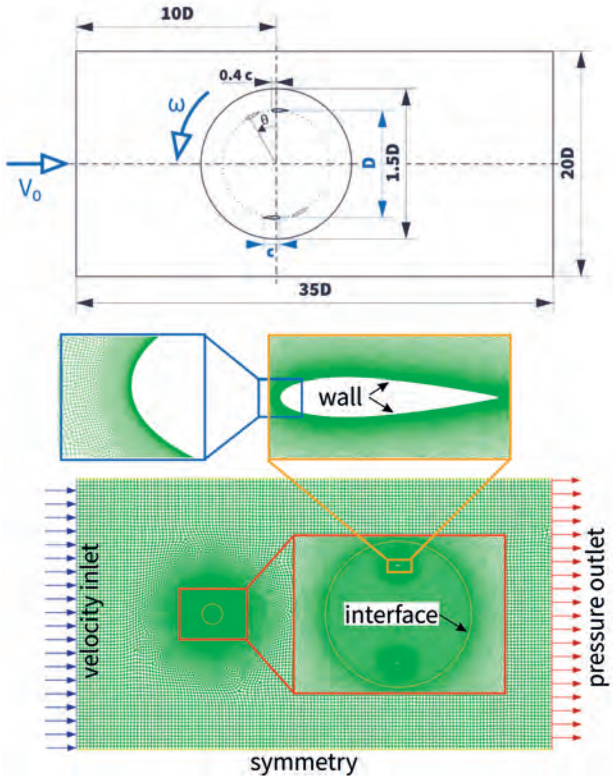

Figure 2. Domain schema with dimensions (**upper**) and mesh layout with boundary conditions for the CFD simulation (**bottom**). The diagram shows the defined boundary conditions: velocity inlet on the left, pressure outlet on the right, symmetry on the top and bottom, wall on the airfoil surface, and interface region connecting different mesh zones. Enlarged sections illustrate the mesh refinement around the airfoil and interface areas.

The numerical simulations were conducted using ANSYS Fluent 2023. The SIMPLE scheme was employed for pressure–velocity coupling. The spatial discretization of the equations was achieved using the least squares cell-based method for gradients, bounded central differencing for the momentum equation, and second-order upwind for all other equations. The residuals convergence criterion was set to 1×10^{-9} for all equations. At the beginning of the iterative process, constant initial conditions equal to the inlet values were applied.

The 2-D CFD simulations were conducted for 40 full rotor revolutions, with a time step size equivalent to an azimuth increment $\Delta\theta$ of 0.5 degrees. As demonstrated in our previous studies [9], this number of rotations is sufficient to obtain results independent of initial conditions for the considered tip-speed ratio of 4.5. In Rezaeiha et al. [47], the authors conducted several analyses for azimuth increments between 0.5 and 0.05 degrees, showing that within this range, the difference in the rotor power coefficient is negligible for a tip-speed ratio of 4.5. Moreover, simulating at least 25 full rotor revolutions ensures that the effect of initial conditions is negligible after 10 revolutions. The instantaneous blade load results presented in this work correspond to the final calculated rotation.

In this study, the Reynolds number was not explicitly analyzed. However, it can be estimated based on the chord length (c) of the blade using the following formula:

$$Re_c = \omega R c \rho / \mu, \quad (2)$$

where ω is the angular velocity of the rotor, R is the rotor radius, ρ is the air density, and μ is the dynamic viscosity of air. For the considered rotor, with an air density of 1.225 kg/m^3 and viscosity of 1.7894×10^{-5} kg/(ms), the Reynolds number is approximately 160,000 [8]. While this value is an approximation, it provides a sufficiently accurate representation of the flow regime.

2.3. Advanced Turbulence Modeling Using Scale-Adaptive Simulation (SAS) for VAWT Analysis

While most computational fluid dynamics (CFD) simulations rely on Reynolds-averaged Navier–Stokes (RANS) turbulence models, certain flow scenarios exceed their capabilities. Scale-resolving simulation (SRS) models, which resolve part or all of the turbulence spectrum in specific regions, have emerged as a solution to address these limitations [48].

The use of SRS models is motivated by the need for greater detail and accuracy. For instance, the complex flow around a vertical axis wind turbine (VAWT) rotor involves dynamic interactions between unsteady airflow, rotor blades, and varying turbulence intensities—challenges that RANS struggles to capture. While RANS is effective for wall-bounded flows due to calibration with the law of the wall, its accuracy declines for free shear flows with larger turbulence scales [49].

Large eddy simulation (LES) can resolve these scales but remains computationally prohibitive, especially for industrial applications. Hybrid approaches, such as detached eddy simulation (DES) and scale-adaptive simulation (SAS), combine the strengths of RANS near walls with the scale-resolving capabilities of LES in free shear regions. SAS, in particular, is well-suited for capturing unsteady flow structures, making it an effective tool for simulating complex aerodynamic phenomena like those encountered in wind turbine rotors [50].

This chapter highlights the advantages of the SAS approach and demonstrates its application in analyzing intricate and dynamic flows.

The scale-adaptive simulation (SAS) model adjusts the turbulence length scale dynamically in response to local flow conditions. This enables it to capture a wider range of turbulence structures in unstable flow regions. Its methodology is based on von Karman's length scale theory and Rotta's theoretical developments from 1972. By including an additional source term in the governing equations, the model transitions naturally between RANS-like behavior in stable flows and LES-like performance in more complex, unsteady flow situations [51]. The SAS approach introduces a significant improvement over traditional RANS models by reformulating the scale-defining equation to include the second derivative of the velocity field, allowing for more accurate adaptation to varying flow conditions. This innovation builds on Rotta's original transport equation for turbulence length scale and was further refined by Menter and Egorov [51] to overcome the limitations of earlier models. The SAS model introduces the von Karman length scale, a key term absent in standard RANS models, enabling it to dynamically adapt its length scale based on resolved flow structures. This adjustment, driven by the second velocity derivative, significantly improves the model's ability to replicate experimental observations in flows with large separation zones or instabilities. Furthermore, the von Karman length scale can be integrated into different scale-defining equations, extending SAS functionality to various turbulence models, as demonstrated in the SAS-SST model. Importantly, the additional term in the ω -equation of the SAS-SST model has been carefully designed to maintain standard RANS behavior for wall-bounded flows while enabling a switch to SRS (scale-resolving simulation) mode in cases of unstable flow separations.

Detailed explanations of the SAS methodology and its derivation can be found in the referenced works, particularly Menter and Egorov [51], which provide comprehensive insights into the development and implementation of the model.

Despite the refinement of the computational mesh and the use of a fine azimuth increment, certain limitations persist in the numerical model. The 2-D simulations inherently neglect three-dimensional effects, such as tip vortices and spanwise flow. Additionally, the Reynolds-averaged Navier–Stokes (RANS) approach, while effective for steady and mildly unsteady flows, may struggle to fully capture transient phenomena, particularly in regions of high turbulence intensity and dynamic stall. Future studies could employ more advanced turbulence models, such as scale-resolving simulations (e.g., LES or DES), to address these challenges.

2.4. Mesh Sensitivity Test

An essential part of validating the developed numerical model is conducting a mesh sensitivity test. The purpose of this test is, of course, to demonstrate how changes in mesh density affect the final results. In this study, a two-bladed rotor model was analyzed using four different mesh densities. The nominal mesh (Figure 2) used had 1689 divisions along the edge of a single airfoil: 840 elements on the suction side, 840 elements on the pressure side, and 9 elements at the trailing edge. Volume statistics of the mesh reveal that the minimum cell volume is 1.05×10^{-10} m^3, while the maximum cell volume is 9.5×10^{-2} m^3. The generated mesh was refined in the rotor region to ensure accurate resolution of the blade wake and flow structures, while coarser cells were used further away from the rotor to reduce computational cost. The distribution of mesh elements was uniform. This mesh had already been employed in previous analyses of the clean airfoil's performance [22,23]. For the present work, the mesh was subjected to similar sensitivity tests.

To analyze the sensitivity of the numerical solution to mesh density, four different meshes were used, each differing in the number of divisions along the airfoil's edge. The number of mesh elements was either decreased or increased using a factor of the square root of two, which is a common practice in mesh sensitivity tests [52]. No other mesh parameters were examined in this study. As shown in Figure 3, the number of divisions used in the nominal mesh is sufficient. The size of the mesh used for further investigations is approximately 270,000 cells.

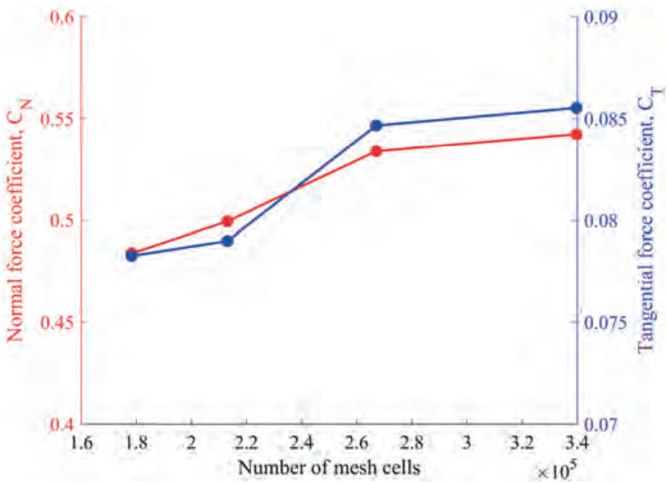

Figure 3. Variation of the mesh sensitivity test results: The plot shows the normal force coefficient C_N (red) and the tangential force coefficient C_T (blue) as a function of the number of mesh cells. C_N is plotted on the left axis and C_T on the right axis. The results indicate that both coefficients stabilize as the mesh density increases from 180,000 to 340,000 cells.

2.5. Aerodynamic Load Consistency Analysis Across Rotor Revolutions

Unlike the classical URANS approach, simulations using the SAS model capture more vortex structures in the flow [8]. As a result, the aerodynamic loads for each subsequent revolution are less repeatable than in typical URANS simulations, especially when a 2-bladed rotor operates, as in this case, at a tip speed ratio of 4.5, where moderate local angles of attack are expected. In Figure 4, the average tangential force coefficient is shown as a function of the number of revolutions from the 30th to the 40th. The black dots represent the average values for each individual rotor revolution, while the red dashed line indicates the average over the last ten revolutions. The vertical axis of the graph has been scaled to highlight the differences; however, as can be seen, the variations in force values between revolutions are minimal compared to the overall average. Moreover, as shown in Figure 5, the difference in the tangential force coefficient C_T as a function of the azimuth between the last computed revolution and the average of all ten revolutions is also very small. Therefore, in the results section, only the aerodynamic load components for the last rotor revolution are compared.

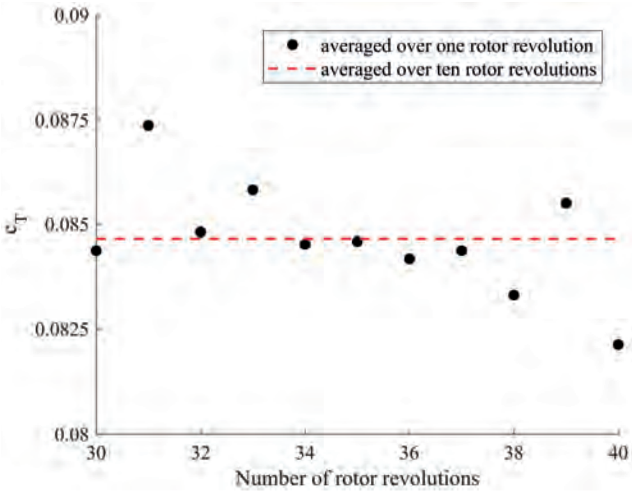

Figure 4. Variation of the tangential force coefficient C_T as a function of the number of rotor revolutions. Black dots represent values averaged over individual rotor revolutions, while the red dashed line shows the average C_T over the last ten rotor revolutions. The figure illustrates the consistency of the aerodynamic loads over the examined revolutions, with minimal variation observed between individual revolutions and the overall average.

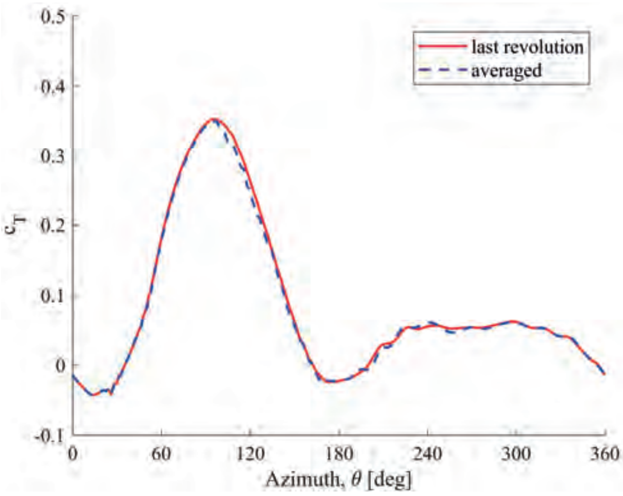

Figure 5. Comparison of the tangential force coefficient C_T as a function of azimuth angle θ. The red solid line represents the tangential load component calculated for the last rotor revolution, while the blue dashed line shows the same component, averaged over ten revolutions, both plotted as a function of the azimuth angle.

3. Validation of the Reference Case: Velocities and Analysis of Loads

3.1. Velocity Profiles in the Rotor Wake

This section of the paper focuses on the validation of the 2-D SAS (scale-adaptive simulation) approach, addressing both the velocity field behind the rotor and the instantaneous sectional loads on the rotor blades.

Figure 6 compares the computed velocity profiles of the V_x component in the rotor wake for several positions downstream of the rotor, denoted by the coordinate x. The velocity profiles were collected using rakes, each two rotor diameters in length and positioned perpendicular to the rotor axis. Each rake consisted of 1000 checkpoints. The distances of the rakes, shown on the graph, are referenced to the rotor diameter D. For better visualization of the results, a color palette was used where the farther the rake is from the rotor, the colors transition from cool blue tones to warm orange for the most distant rake studied in this work.

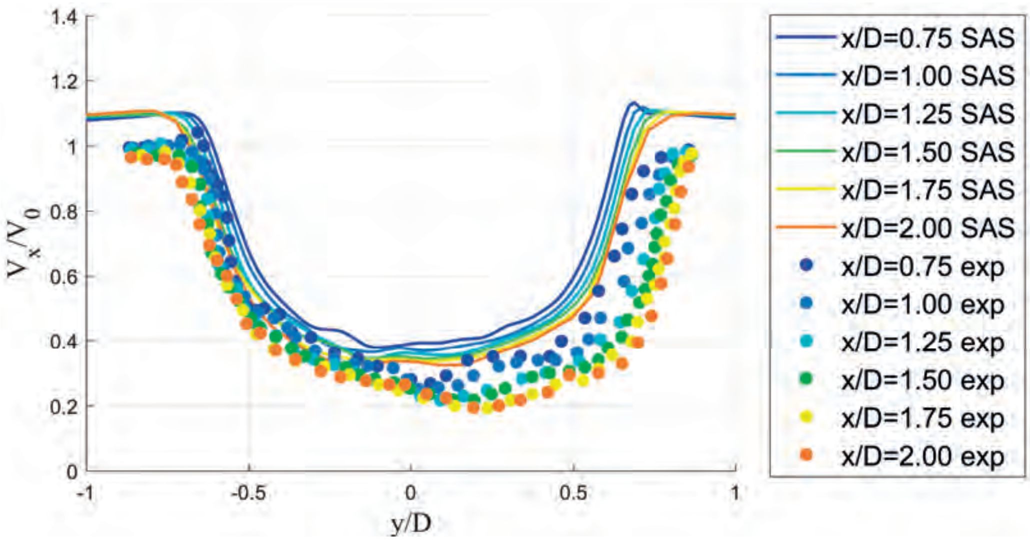

Figure 6. Comparison of the V_x/V_0 velocity component in the rotor wake for various downstream positions x/D, calculated using the SAS approach and validated against experimental data [46].

The results presented in this figure highlight several important observations. First, the 2-D CFD results tend to underestimate compared to the experimental data. The computed velocities are slightly higher, particularly in the positive y/D range, which corresponds to the blade moving "upwind." The second key observation is that the general trend of both the experimental and numerical results is similar: as the x-coordinate increases, the velocity V_x decreases more significantly. Lastly, there is a noticeable asymmetry in the experimental velocity profiles compared to the CFD results, with the experimental data showing greater asymmetry.

One of the likely reasons for the differences in velocity profiles is the absence of the rotating tower in our model, which was neglected. Another factor could be 3-D effects, which were also not accounted for. Additionally, it is possible that even with the SAS approach, the numerical dissipation is too high to predict the numerous structures in the aerodynamic wake accurately. In this study, the mesh density in the wake region was not analyzed. Another potential cause could be the aerodynamic characteristics of the airfoil. In this case, the airfoil moves through an environment with varying turbulence intensity, transitioning from high to low turbulence regions. As shown by Michna and Rogowski [23], turbulence intensity has a significant impact on the aerodynamic characteristics of clean airfoils.

The plot shows a noticeable deviation between the SAS simulation and the experimental data for the V_y velocity component in the rotor wake (Figure 7). The agreement between the CFD results and the experiment is better within the y/D range from −0.5 to 0.5. Although the differences between the SAS and experimental results appear significant, the absolute values of the V_y velocity component are relatively small. The likely causes for these discrepancies stem from certain assumptions made in the model, such as the 2-D approach, the absence of a rotating shaft, and the lack of struts. Nevertheless, the computed results preserve the correct trend, capturing not only the tilt but also the expected behavior as the x-coordinate increases.

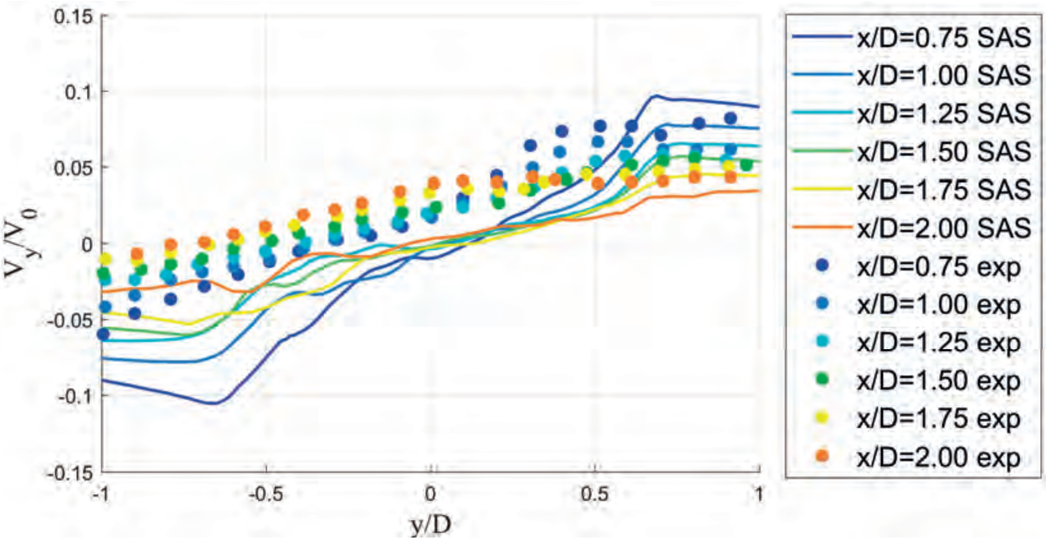

Figure 7. Comparison of the V_y/V_0 velocity component in the rotor wake for various downstream positions x/D, calculated using the SAS approach and validated against experimental data [46].

3.2. Aerodynamic Loads Validation

In their study, Castelein et al. [53] measured the normal and tangential force coefficients for an H-type vertical axis wind turbine (VAWT) operating at various azimuthal positions using velocity fields obtained through Particle Image Velocimetry (PIV). By employing the Noca method [54], which relies on these PIV-derived velocity fields, they calculated the aerodynamic forces around the blade without direct force measurements. This indirect approach allowed them to observe force trends associated with different flow characteristics [53].

At a tip-speed ratio (TSR) of 4.5, the authors found that the normal force generally followed expected trends for VAWTs, while the tangential force showed minimal positive values, indicating limited power production between the leeward and upwind positions. The authors noted that a high deviation in tangential force was observed at the azimuthal position 270°, which they attributed to interactions with the wake from the turbine mast. Given the observed uncertainties, especially in the tangential force measurements, the authors recommended further research to reduce these uncertainties, suggesting an improvement in post-processing methods to enhance the accuracy of tangential force estimations [53].

Due to the high uncertainty in the tangential load component obtained in the experimental studies, only the normal blade load component was used for validation in this work. The loads presented in Figure 8 are expressed in the dimensionless form $C_N = F_N/\left(0.5 \cdot \rho \cdot V_0^2 \cdot R\right)$, where ρ is the air density, assumed to be 1.225 kg/m^3 in the calculations, V_0 is the undisturbed flow velocity, and R is the rotor radius. The results obtained using the SAS approach, shown in Figure 8, in the upstream part of the rotor, up to the maximum values of the normal force, are in reasonably good agreement with the experiment. In the remaining azimuthal range, larger differences are observed, most likely due to 3-D effects and secondary effects, such as struts or the rotating shaft, that are not taken into account in this investigation.

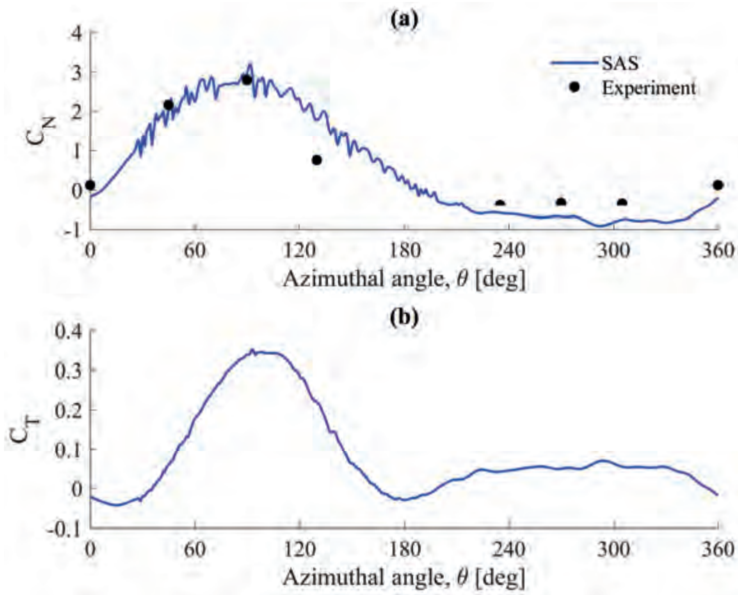

Figure 8. Comparison of simulated and experimental force coefficients [53] as a function of azimuthal angle, θ. (**a**) Normal force coefficient C_N, shows a general agreement between the SAS simulation and experimental data. (**b**) Tangential force coefficient, C.

4. Reference Case: Local Angle of Attack, Relative Velocity, and Dynamic Lift and Drag Coefficients Assessment

4.1. Methodology for Determining Local Angle of Attack and Relative Velocity

The previous section discussed both the methodology used in this paper and the accuracy of the approach in determining the velocity field. A reliable description of the velocity field is essential for estimating the local angle of attack and relative velocity, which are critical parameters for blade element theory-based methods, such as the actuator line approach. While comparing velocities or loads obtained from different methods is relatively straightforward, extracting the angle of attack, especially for vertical axis wind turbines (VAWTs), poses a greater challenge.

One of the primary contributions of this paper is the analysis of the angle of attack and relative velocity for a blade profile in a Darrieus-type VAWT. The aim of this study is not to compare various existing methods for determining this parameter but rather to adopt one of the approaches proposed by Melani et al. [45] for calculating the angle of attack. Before delving into the method used to determine the local angle of attack, we will briefly introduce the basic definitions of velocity and angle of attack.

The angle of attack is defined as the angle between the chord line of the blade profile and the direction of the relative velocity (Figure 9). For the reference rotor, the chord is tangential to the path (pitch angle β is equal to 0°). The relative velocity vector, V_{rel}, results from the vector sum of the blade's tangential velocity $V_{BT} = \omega R$ (taken with a negative sign) and the airflow velocity V acting on the blade. The airflow velocity at the turbine rotor is lower than the undisturbed wind speed far upstream as the rotor decelerates the air passing through it. In the one-dimensional stream-tube theory used in the classical blade element momentum (BEM) method, only one component of the flow velocity in the undisturbed flow direction, V_x, is considered. In this study, however, the airflow velocity component V_y, perpendicular to the undisturbed flow direction, is also taken into account, as shown in Figure 9.

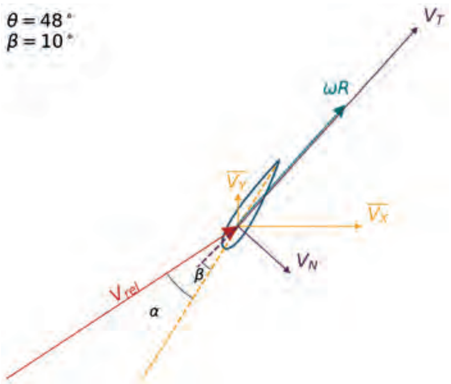

Figure 9. Illustration of the angle of attack (α) and relative velocity (V_{rel}) for a blade in a vertical-axis wind turbine. The pitch angle (β = 10°) and the azimuthal position angle (θ = 48°) are indicated.

Based on the figure above and considering the pitch angle β, with its sign convention illustrated in this figure, the angle of attack can be calculated using the normal and tangential components, V_n and V_t, of the relative velocity vector according to the following mathematical formula:

$$\alpha = \tan^{-1}(-V_n/V_t) + \beta \quad (3)$$

where

$$V_t = V_x \cos\theta + V_y \sin\theta + \omega R \quad (4)$$

$$V_n = -V_x \sin\theta + V_y \cos\theta \quad (5)$$

where ω is the angular velocity of the rotor, and R is the rotor radius.

In this study, only one method for extracting the local angle of attack was used: the so-called Line Average method, which was introduced by Jost et al. [55] and successfully implemented by Melani et al. [47]. The goal of Jost et al. [55] was to achieve greater accuracy compared to previously existing approaches in accounting for the effects of shed and trailing vorticity on the measured angle of attack. According to Melani et al. [45], a circular sampling line with a radius of r = 1c was defined around the airfoil profile, centered at the aerodynamic center located at 1/4 of the chord length from the leading edge (Figure 10). Along this line, a series of points were evenly distributed. The authors of this method tested different sampling resolutions, ranging from six to eighty points. The contribution of this study is to test this method further for a larger range of control point counts. Figure 11 presents a sensitivity analysis of the angle of attack based on the number of sampling points used. In these analyses, a maximum of 2000 points was considered. For each tested number of points, the process of picking control points on the circular line was performed 100 times with a random shift but with the same even distribution. The mean and standard deviation of difference relative to the maximum points case were calculated. As shown in Figure 11, the highest sensitivity was observed for the lowest number of control points (five points) and for azimuth angles between 80° and 180°. The distribution of velocity components V_x and V_y as a function of the angle of attack for various azimuth angles reveals a local peak in these components within a narrow range of azimuths, resulting from the presence of the wake behind the profile. For instance, at an azimuth of 0°, the average component is 7.94 m/s, while its extreme value reaches −8.81 m/s. Moreover, the area of the line where this peak occurs constitutes 1.63% of the total. Thus, evenly but sparsely distributed control points may lead to significant errors in estimating the flow velocity. The desired flow velocity V is the integral average of the flow velocity field along a closed line around the airfoil. In conclusion, the figures above demonstrate that 200 sampling points provide sufficient accuracy for determining the true angle of attack. This resolution ensures that the local flow characteristics are captured effectively, minimizing errors and enhancing the reliability of the angle of attack estimation.

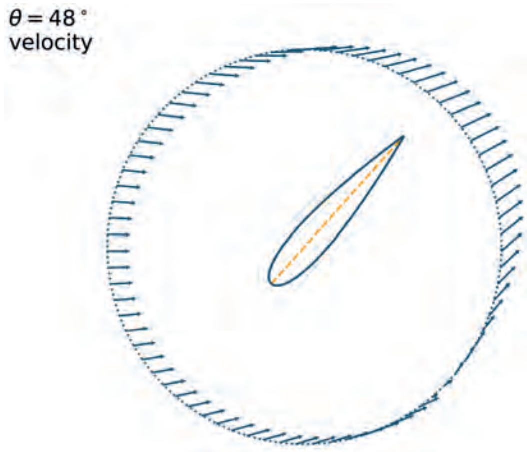

Figure 10. Velocity distribution around the airfoil at an azimuthal angle θ = 48°. The circular sampling line with evenly distributed points surrounds the airfoil, with arrows representing the local flow velocities at each point.

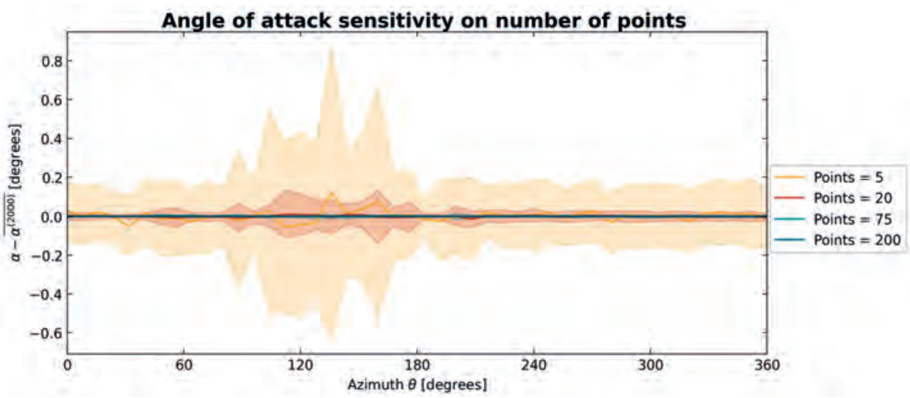

Figure 11. Sensitivity analysis of the angle of attack ($\alpha - \overline{\alpha^{(2000)}}$) based on the number of sampling points along the circular line surrounding the airfoil as a function of the azimuth angle θ. Standard deviation is chosen as an error measure.

In the previous paragraph, we discussed the methodology for estimating the local angle of attack. This angle is essential for determining the local flow velocity at the rotor, specifically on the rotor blade. Based on this velocity and the blade's tangential velocity, the relative airflow velocity vector can be estimated. Using the previously determined tangential and normal components of this velocity, we can express it as follows:

$$\vec{V}_{rel} = \vec{V}_n + \vec{V}_t \tag{6}$$

The sensitivity analysis for relative velocity was also performed in this case (Figure 12), using the mean and the standard deviation approach as previously applied for the angle of attack. As shown in the figure above, 200 sampling points are sufficient to achieve an accurate estimation of the relative velocity. This resolution minimizes fluctuations and ensures a reliable measurement across the azimuth range, demonstrating that higher sampling densities provide better stability and precision in capturing the true relative velocity profile.

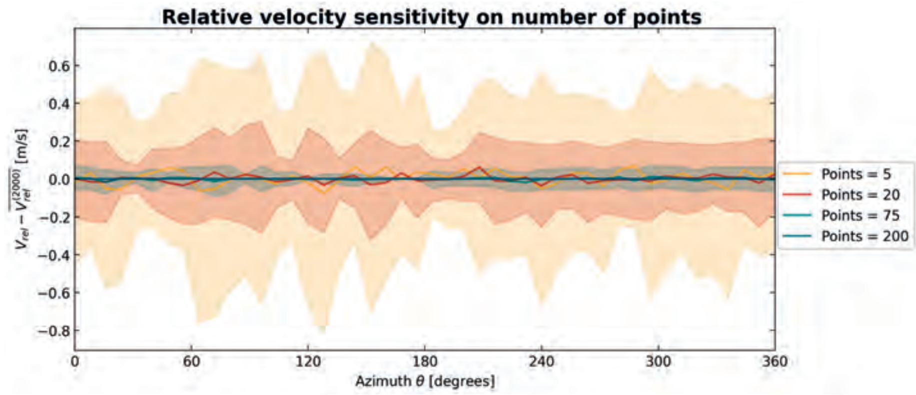

Figure 12. The mean relative velocity is represented by lines. Standard deviation is chosen as an error measure.

4.2. Angle of Attack and Relative Velocity Analysis

Figure 13 presents the results of the local angle of attack and relative velocity obtained using the scale-adaptive simulation (SAS) approach with the Transition SST model and the angle of attack estimation method described in the previous subsection of this paper. In this study, the local angle of attack was calculated based on the velocity field around the blade, derived from 2-D CFD simulations with a resolution of $\Delta\theta = 5°$. The $\alpha(\theta)$ and $V_{rel}(\theta)$ curves shown in this figure are thus developed from 200 points evenly distributed around the blade trajectory. Due to fluctuations in the normal component of the aerodynamic load, our local angle of attack predictions do not capture all the details of angle variations at $\Delta\theta$ resolutions smaller than 5°. Despite these limitations, Figure 13 shows that the maximum local angle of attack in the upwind part of the rotor reaches 9.65°, which closely matches the independent result obtained by Melani et al. [45].

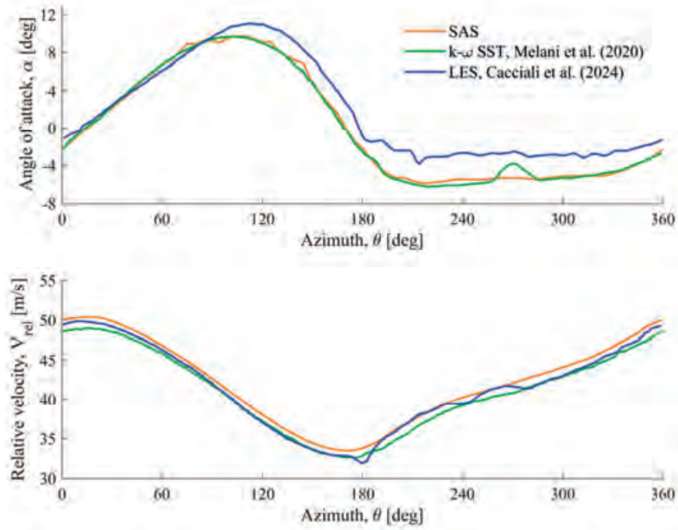

Figure 13. Validation of angle of attack (α) and relative velocity (V_{rel}) results obtained using the SAS approach, compared with literature data from Melani et al. [45] and Cacciali et al. [8].

Our analysis does not account for the rotating rotor shaft in the downwind region, which explains the absence of an additional peak in $\alpha(\theta)$ around an azimuth of 270°. Nevertheless, it is noteworthy that the local angle of attack in this part of the rotor also aligns well with the results from [45]. The local angle of attack in the downwind part remains relatively constant over most azimuths, ranging between −5.8° and −5.3°. For the second independent dataset from Cacciali et al. [8], angles of attack starting from an azimuth of approximately 92° are larger than those presented in this study and those reported by Melani et al. [45]. This discrepancy arises from a different sampling approach for the velocity used to calculate the angle of attack. Additionally, Cacciali et al. [8] incorporated extra submodels in their ALM approach along with the Smagorinsky–Lilly model. In Cacciali et al.'s study [8], the maximum local angle of attack reaches around 11°. Further differences are due to the use of external experimental airfoil data by the cited researchers. As demonstrated in [22], the Transition SST approach used in this paper and the k-ω SST model applied in Melani et al. [45] yield significant differences in lift coefficient characteristics (C_L) for angles below the critical angle, which is also documented in recent independent experimental research by Rogowski et al. [56].

The relative velocity derived from the calculated local velocity field around the blade is shown in the lower part of Figure 13. Despite the greater discrepancies in angle of attack estimates compared to Cacciali et al. [8], the differences in relative velocity values are minimal. The maximum local relative velocity calculated using the SAS approach is 50.36 m/s, occurring at an azimuth of 15°. The minimum value of this velocity is still observed in the upwind part of the rotor, at an azimuth of 175°, and is approximately 35 m/s.

4.3. Dynamic Lift and Drag Coefficients Analysis

Figure 14 presents a comparison of dynamic lift (C_L) and drag (C_D) coefficients with static data based on different turbulence models: Transition SST (γ-Re_θ) and k-ω SST [23]. The same coefficients are shown in two ways: as a function of azimuth (top plots) and as a function of angle of attack (bottom plots). In each plot, the red open circles represent results for the azimuth range from 0 to 180 degrees (SAS), the red filled circles represent results for the range from 180 to 360 degrees (SAS), and the black open circles indicate reference data from Melani et al. [45]. Presenting the results in this way allows for an understanding of the differences in aerodynamic characteristics at various stages of the azimuthal cycle and provides an assessment of the SAS-based results compared to established literature data. The results obtained using the scale-adaptive simulation (SAS) approach exhibit significantly more chaotic behavior, particularly in the upwind part of the rotor, starting at an azimuth of approximately 50–60 degrees. This effect coincides with frequent changes in the normal force, as shown in Figure 8. Since these fluctuations occur more frequently than the sampling points for the angle of attack, we opted to display only the points on these plots to capture the local values of the coefficients better.

It is notable that the slope of the static C_L curve corresponds closely to that of the dynamic curve despite the fact that the latter does not pass through zero angle of attack. As noted by Bianchini et al. [36], this is due to the "virtual camber" effect, which can influence results for the dynamic angle of attack. The k-ω SST model, used in the study by Melani et al. [45], appears to yield better results for more turbulent regions of the flow, whereas the Transition SST model seems more suitable for regions with lower turbulence intensity, such as the downwind part of the rotor. Presenting both dynamic and static results provides valuable insight into how different turbulence models impact the accuracy of aerodynamic calculations in various phases of the turbine's operating cycle.

Rezaeiha et al. [57], who also considered the reference rotor presented in this study, obtained fairly similar hysteresis loops for both lift and drag forces. In their research, a slightly different method of sampling the velocity components was used to determine the local angle of attack. Specifically, they applied velocity sampling at monitoring points on a circular path with a fixed distance of 0.2d upstream of the turbine. Additionally, these researchers determined the aerodynamic force components using the geometric angle of attack. The differences, particularly in the drag coefficient, are highly dependent on both sides of the rotor. This suggests that our use of the SAS approach does not significantly impact aerodynamic force predictions; rather, the primary influence comes from the turbulence model.

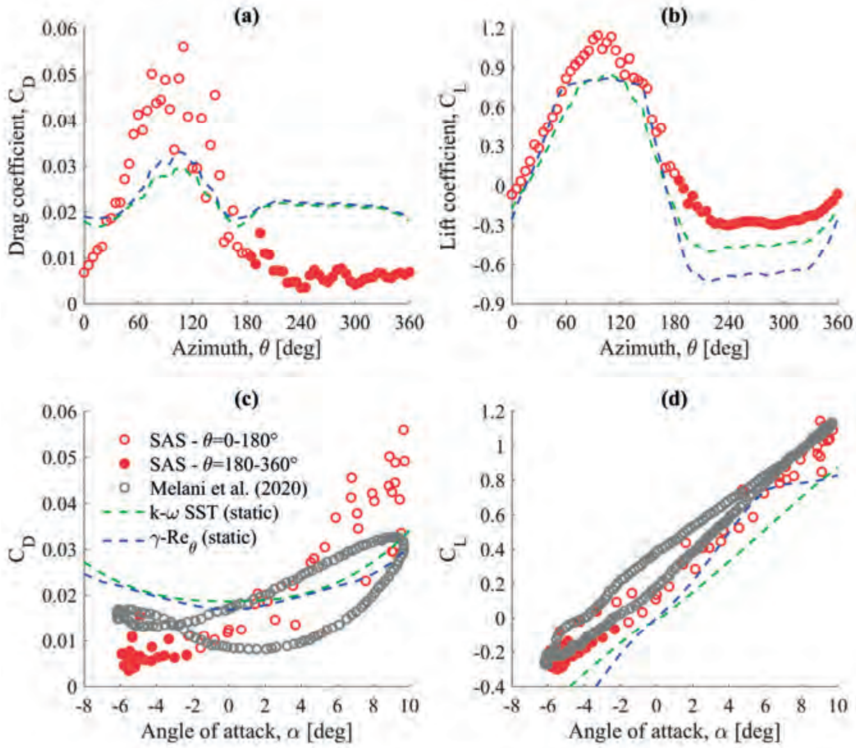

Figure 14. The upper subfigures illustrate the drag coefficient C_D (**a**) and lift coefficient C_L (**b**) as functions of the azimuthal angle θ. The lower subfigures depict the same coefficients—drag (**c**) and lift (**d**)—analyzed for varying angles of attack α. The presented data include results obtained using the SAS approach, static results reported by Rogowski et al. [22], and reference data from Melani et al. [45].

5. Impact of Rotor Configuration on Aerodynamic Force Components and Local Angle of Attack

5.1. Number of Blade Effects

Figure 15 shows the coefficients of the aerodynamic blade load components, tangential and normal. The results presented in these figures correspond to a rotor operating at a tip speed ratio of 4.5. The colors, ranging from red to blue, represent four rotor configurations based on the number of blades: red for the single-bladed rotor and blue for the four-bladed rotor. The results displayed in these graphs suggest a significant influence of the blade number on turbine performance. The primary consequence of a reduced blade count is notably higher loads, especially tangential loads, in the downwind part of the rotor. For the two- and three-bladed rotors, the tangential force is zero or even negative, indicating a low or negative contribution of this component to energy production. In the case of the normal components, the differences in load are less pronounced. However, for both the tangential and normal components, the largest discrepancies are observed for the single-bladed configuration.

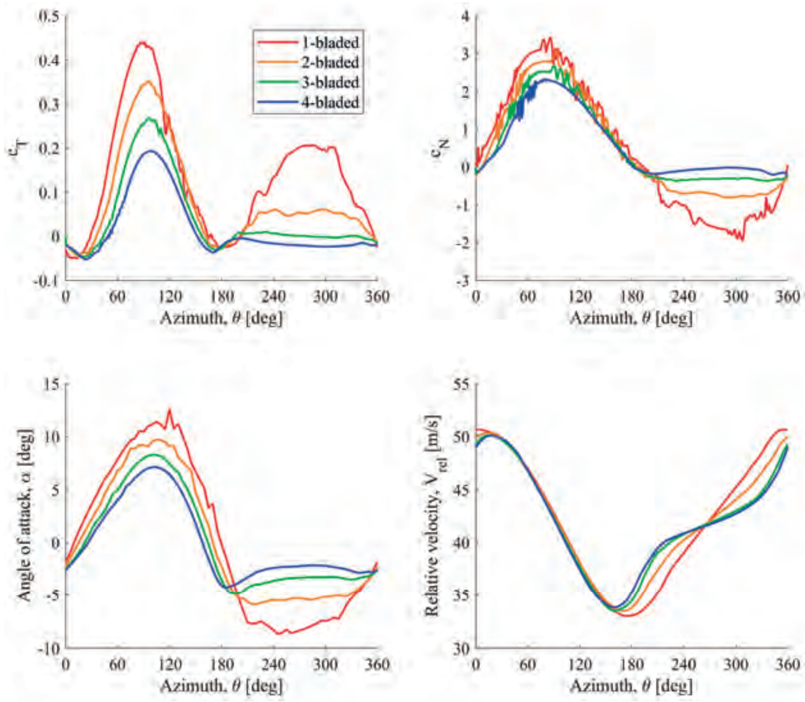

Figure 15. Effect of the number of blades on the normal and tangential force coefficients, as well as on the local angle of attack and relative velocity, as a function of azimuth θ at a tip-speed ratio of 4.5.

Figure 15, bottom-left and bottom-right plots, compare the local angle of attack, α, and relative velocity, V_{rel}, respectively, for a rotor operating at a tip speed ratio of 4.5, as a function of the number of blades. The most significant differences in local angle of attack are observed across the entire rotor, while for relative velocity, the differences are mainly present in the downwind part of the rotor. The large variations in the angle of attack correlate with significant differences in tangential force, as shown in this figure. The maximum local angle of attack is observed at an azimuth angle of approximately 100–105 degrees and decreases linearly from 10.16 degrees for a single-bladed rotor to 6.34 degrees for a four-bladed rotor. As the number of blades decreases, the shape of the angle of attack curve becomes more sinusoidal and approaches the geometric angle of attack, as the angle of attack in the downwind region of the rotor increases. Increasing the number of blades causes the local angles of attack in the downwind part to decrease, and their distribution becomes almost flat, similar to the tangential force characteristics.

A reduction in the number of blades also causes the maximum local angle of attack to approach or even slightly exceed the critical static angle of attack. This explains the local peaks in the angle of attack, as well as the characteristic wavy pattern of the tangential and normal force distributions in the azimuth range of approximately 70 to 210 degrees, which results from the numerous vortices generated on the airfoil.

Figure 15 also shows that at zero azimuth, the local angle of attack is non-zero and slightly increases with the number of blades, from -1.67 degrees for the single-bladed rotor to -2.38 degrees for the four-bladed rotor.

Despite the significant influence of rotor solidity on the local angle of attack in both the upstream and downstream regions, notable differences in relative velocity are only observed in the downstream part of the rotor, starting around an azimuth angle of 155 degrees, still within the wake region. A higher number of blades causes a greater deflection of the relative velocity curve. Interestingly, all curves intersect at the same point, approximately 265 degrees. In the azimuth range from 155 to 265 degrees, the relative velocity decreases as the number of blades increases, while beyond this characteristic azimuth, the trend is reversed.

Figure 16 presents a comparison of aerodynamic coefficients for different rotor configurations with one to four blades. The plots of drag coefficient C_D and lift coefficient C_L as a function of azimuth angle θ (Figure 16a,b) illustrate how the number of blades influences the distribution of aerodynamic forces during the last rotation of the rotor. The same coefficients are also shown as a function of the angle of attack α (Figure 16c,d), allowing the observation of hysteresis loops. It is evident that as the number of blades increases, and consequently the solidity increases (Equation (1)), the range of angles of attack decreases. This, in turn, leads to a reduction in tangential force, as discussed in detail in the previous paragraph. Additionally, the aerodynamic force characteristics acting on the rotor blade elements exhibit fewer oscillations with an increasing number of blades, indicating more stable aerodynamic properties.

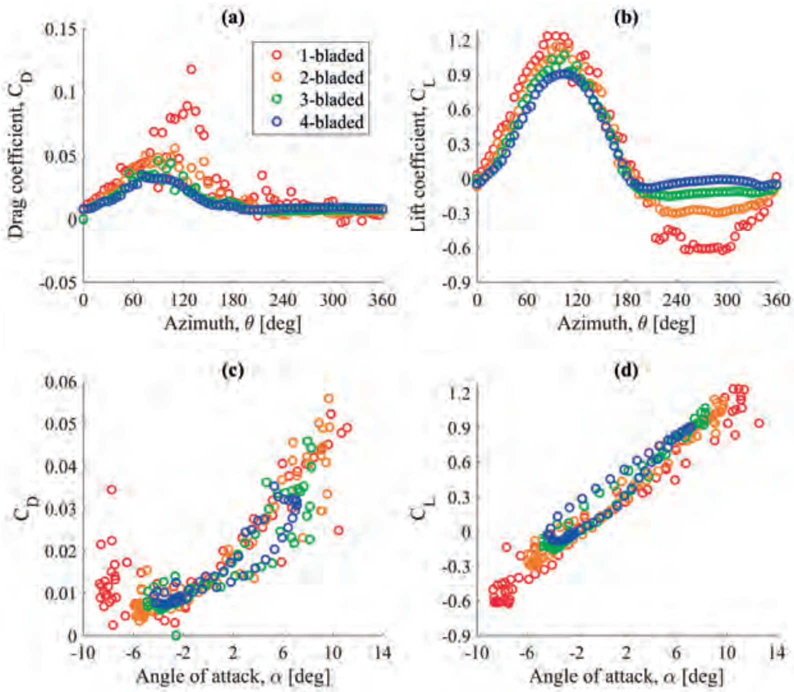

Figure 16. The subfigures show the drag coefficient C_D (**a**,**c**) and lift coefficient C_L (**b**,**d**) for different azimuthal angles (**a**,**b**) and angles of attack (**c**,**d**). The presented data shows comparison of aerodynamic coefficients for 1-bladed, 2-bladed, 3-bladed, and 4-bladed configurations.

5.2. Pitch Angle Effects

Figure 17, top-left and top-right plots, compare the load characteristics of a two-bladed rotor with three different pitch angles: −10, 0, and 10 degrees. As shown in the first figure, both large positive and negative pitch angles result in a significant deterioration of the rotor's aerodynamic performance. However, current research trends in Darrieus wind turbines are focused on evaluating the aerodynamic wake for different rotor configurations and the potential for active and passive control of this wake. Therefore, in this comparison, the more critical load component is the normal force. The figure illustrates the expected trend in estimated loads and highlights the significant impact of dynamic effects, which generate vortex structures manifesting as oscillations in the curves.

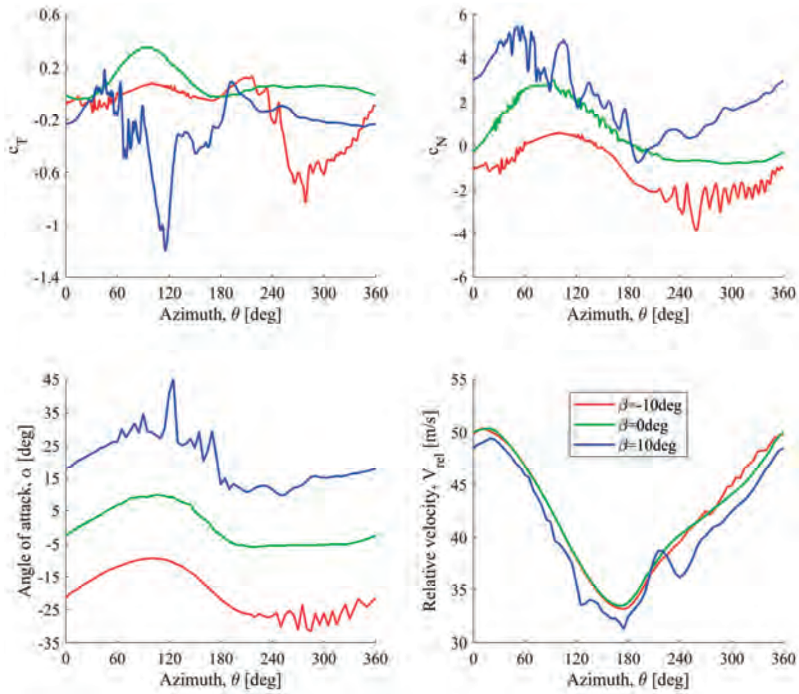

Figure 17. Effect of the pitch angle on the normal and tangential force coefficients, as well as on the local angle of attack and relative velocity, as a function of azimuth θ for a 2-bladed rotor configuration at a tip-speed ratio of 4.5.

Figure 17's bottom-left and bottom-right plots illustrate the effect of pitch angles on the local angle of attack and relative velocity, respectively. As observed in both figures, regarding the shape of the curves, the pitch angle does not significantly influence the characteristics of the relative velocity compared to the number of rotor blades. For the angle of attack, however, the pitch angle generally causes a shift in the curve by about 10 degrees. The most notable differences are seen with a pitch angle of 10 degrees. The angle of attack curve (Figure 17) displays several sharp peaks. This curve could be smoother, and the number of peaks could increase if the angle of attack were sampled with a much smaller azimuthal increment. Additionally, the case with a 10-degree pitch angle represents the rotor under the heaviest load compared to the 0-degree and −10-degree cases. However, this does not apply to the tangential load component, where the average tangential force coefficients are −0.24, 0.08, and −0.14 for pitch angles of 10 degrees, 0 degrees, and −10 degrees, respectively. For the normal load, the average force coefficients are 2.2, 0.5, and −1.16 for the same pitch angles, respectively. The maximum magnitudes of the normal force coefficients are 5.45, 3.05, and 3.85, respectively.

As demonstrated in their work by Melani et al. [45], the static critical angle of attack for the NACA0018 airfoil, as predicted by the four-equation transition turbulence model, is approximately 12 degrees. As shown in Figure 17, this angle is reached at an azimuth of about 30 degrees. In the case of a 10-degree pitch angle, the absence of oscillations in the normal force component is observed from around 28–30 degrees azimuth. Significant oscillations in both aerodynamic load components and a sudden loss of tangential force begin to appear around an azimuth of approximately 55 degrees. Therefore, it can be inferred that in the azimuth range of approximately 30 to 55 degrees, dynamic effects occur that do not cause a loss of lift. In the case of the downstream part of the rotor, the obtained angle of attack values for a pitch angle of −10 degrees may indicate that the rotor is operating within the range of maximum dynamic lift coefficients.

As demonstrated in [9], due to significant 3-D effects in this case resulting from large tip losses near the blade ends, the results obtained using the 2-D CFD approach should be interpreted more qualitatively than quantitatively. For a more accurate quantitative comparison, a rotor with a much higher blade aspect ratio would need to be constructed than the reference rotor used in this study. However, in the same study [9], we showed that for a pitch angle of −10 degrees, the impact of these tip losses is not as significant. The oscillations in both the angle of attack and aerodynamic loads visible in the downstream part of the rotor indicate high turbulence intensity and numerous vortices.

Figure 18 illustrates the effect of blade pitch angle on the aerodynamic coefficients of the rotor. In plot (a), the drag coefficient C_D is shown as a function of azimuth angle θ. For non-zero pitch angles, the drag coefficient is generally higher, which can be attributed to the exceeding of critical static angles of attack in both cases. It is clearly visible that for $\beta = 10°$, a sharp increase in drag occurs in the windward region of the rotor, whereas for the negative pitch angle ($\beta = -10°$), a similar increase is observed in the leeward region. In plot (d), a noticeable shift in the C_L characteristic can be seen, depending on the pitch angle. The highest values of the lift coefficient C_L are observed for $\beta = 10°$ in the windward section of the rotor, reaching values close to 2. This analysis clearly shows that increasing the pitch angle intensifies the lift force while significantly affecting the distribution of aerodynamic forces as a function of rotor azimuth.

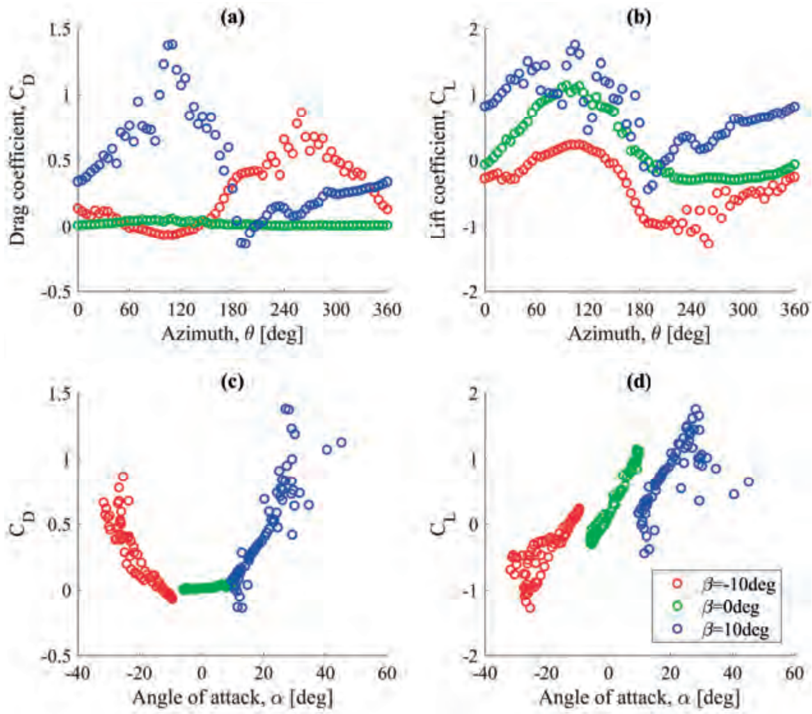

Figure 18. The subfigures show the drag coefficient C_D (**a**,**c**) and lift coefficient C_L (**b**,**d**) for different azimuthal angles (**a**,**b**) and angles of attack (**c**,**d**). The data presented above shows aerodynamic coefficient comparison for varying blade pitch angles ($\beta = -10°, 0°, 10°$).

6. Conclusions

This paper analyzes the aerodynamics of a reference VAWT rotor using the well-established Transition SST turbulence model combined with the scale-adaptive simulation (SAS) approach to enhance the accuracy of velocity field representation in the rotor area. Here are some key conclusions drawn from our study:

1. The study demonstrates that the Line Average method is an effective approach for accurately determining the local angle of attack, as it considers the effects of shed and trailing vorticity around the airfoil. By averaging velocity components along a circular line centered at the aerodynamic center, this method minimizes errors from wake effects, particularly when using a sufficient number of sampling points. Our analysis shows that 200 sampling points offer a reliable resolution, capturing essential flow characteristics while minimizing sensitivity to the azimuth angle, especially in regions prone to high variability. This method was validated for different rotor configurations, and the trend in resulting values appears consistent and accurate across configurations, supporting the robustness of this approach.
2. Furthermore, the findings of this work hold significant potential for advancing engineering methodologies tailored to the aerodynamic analysis of vertical axis wind turbines (VAWTs). Accurate determination of the local angle of attack is a crucial step in aerodynamic modeling, as it enables precise estimation of aerodynamic loads acting on the blades. These loads directly influence the design, performance optimization, and operational stability of wind turbines. The methodology developed and validated in this study could be instrumental in improving predictive capabilities for aerodynamic performance and dynamic loading in future studies. We believe the results presented here provide a strong foundation for the continued development of engineering models aimed at enhancing the design and efficiency of wind turbines with vertical axes.
3. The comparison of turbulence models highlights their varying performance in capturing aerodynamic and dynamic characteristics within the rotor region. While the SAS approach with the Transition SST model allows for more precise velocity field mapping and captures oscillations in normal forces, the overall aerodynamic loads remain similar to those obtained using the standard Transition SST model or even the classical URANS approach reported by Rezaeiha et al. [57]. Additionally, the k-ω SST model yields results comparable to the Transition SST model for aerodynamic load components, local angle of attack, and relative velocity. However, it differs in capturing the dynamic characteristics of drag and lift coefficients as functions of the local angle of attack. Furthermore, the Transition SST model shows better performance in the upwind region of the rotor due to transitional phenomena, while the k-ω SST model is more effective in handling the higher turbulence levels in the downwind region.
4. The analysis demonstrates that the number of blades has a significant impact on the aerodynamic performance of the rotor. Fewer blades lead to notably higher aerodynamic loads, especially tangential loads, in the downwind region, with single-bladed configurations often showing minimal or even negative contributions to energy production. Variations in the local angle of attack and relative velocity are also strongly influenced by blade count, with fewer blades causing larger fluctuations in the angle of attack, which approaches a sinusoidal pattern and even exceeds the critical static angle at times. Higher blade counts stabilize the angle of attack and in the downwind region, resulting in a flatter distribution of loads. This highlights the crucial role of blade count in shaping the aerodynamic forces and flow stability around the rotor.
5. The analysis showed that large positive and negative pitch angles significantly impact the rotor's aerodynamic performance, especially by increasing loads on the normal force component. Dynamic effects, including vortex formations, cause oscillations, especially pronounced at a 10-degree pitch angle. While pitch angle has minimal effect on relative velocity, it shifts the angle of attack curve, with the most considerable differences observed for a 10-degree pitch. Notably, high turbulence intensity and vortex shedding are evident in the downstream region, especially for a -10-degree pitch angle. Varying the blade pitch angle alters the aerodynamic force characteristics, with positive pitch angles ($\beta > 0^\circ$) enhancing lift generation but also increasing drag, particularly in the windward region. Negative pitch angles ($\beta < 0^\circ$) reduce drag in

the upwind section but lead to higher drag in the downwind region, highlighting the trade-off between aerodynamic efficiency and force distribution. Overall, these results indicate that extreme pitch angles lead to performance fluctuations, which are further amplified by 3-D effects and tip losses, suggesting the need for higher blade aspect ratios for quantitative accuracy.

The next step of this work will be employing the Line Average method in the pitching airfoil model. This model can be a simplified model of VAWT's blade during rotation. Determining the angle of attack during that airfoil pitch motion is crucial to investigating dynamic phenomena influencing the airfoil aerodynamic loads. That will be the next important step in analyzing the modeling of the aerodynamic performance of vertical axis wind turbines methods.

Author Contributions: Conceptualization, K.R. and J.M.; methodology, K.R. and J.M.; software, K.R. and J.M.; validation, K.R. and J.M.; formal analysis, K.R. and J.M.; investigation, K.R. and J.M.; resources, K.R. and J.M.; data curation, K.R. and J.M.; writing—original draft preparation, K.R. and J.M.; writing—review and editing, K.R. and J.M.; visualization, K.R. and J.M.; supervision, K.R.; project administration, K.R.; funding acquisition, K.R. All authors have read and agreed to the published version of the manuscript.

Funding: This work was supported by the POB Energy program at Warsaw University of Technology, under the Excellence Initiative: Research University (IDUB) (Grant No. 1820/355/Z01/POB7/2021). Computational resources were provided by the Interdisciplinary Centre for Mathematical and Computational Modelling at the University of Warsaw (ICM UW) through computational allocations no. G93-1588 and G94-1718.

Data Availability Statement: The original contributions presented in this study are included in the article. Further inquiries can be directed to the corresponding author.

Conflicts of Interest: The authors declare no conflicts of interest.

References

1. Bouckaert, S.; Pales, A.F.; McGlade, C.; Remme, U.; Wanner, B.; Varro, L.; D'Ambrosio, D.; Spencer, T. *Net Zero by 2050: A Roadmap for the Global Energy Sector*; OECD: Paris, France, 2021.
2. Al Mowafy, A.; Lotfian, S.; Brennan, F. Decommissioning Offshore Wind Fixed Steel Pile Foundations: A Critical Review. *Energies* **2024**, *17*, 5460. [CrossRef]
3. Gwec. Global Wind Report 2024. Available online: https://gwec.net/global-wind-report-2024/ (accessed on 13 November 2024).
4. Durakovic, A. GE Haliade-X Offshore Wind Turbine Reaches 14 MW Output. 2021. Available online: https://www.offshorewind.biz/2021/10/05/ge-haliade-x-offshore-wind-turbine-reaches-14-mw-output/ (accessed on 13 November 2022).
5. Alam, F.; Jin, Y. The Utilisation of Small Wind Turbines in Built-Up Areas: Prospects and Challenges. *Wind* **2023**, *3*, 418–438. [CrossRef]
6. Kumar, R.; Raahemifar, K.; Fung, A.S. A critical review of vertical axis wind turbines for urban applications. *Renew. Sustain. Energy Rev.* **2018**, *89*, 281–291. [CrossRef]
7. Abdolahifar, A.; Zanj, A. Addressing VAWT Aerodynamic Challenges as the Key to Unlocking Their Potential in the Wind Energy Sector. *Energies* **2024**, *17*, 5052. [CrossRef]
8. Cacciali, L.; Hansen, M.O.L.; Rogowski, K. Highly Stable Lattice Boltzmann Method with a 2-D Actuator Line Model for Vertical Axis Wind Turbines. *Energies* **2024**, *17*, 4847. [CrossRef]
9. Rogowski, K.; Michna, J.; Ferreira, C.S. Numerical analysis of Aerodynamic Performance of a Fixed-Pitch Vertical Axis Wind Turbine Rotor. *Adv. Sci. Technol. Res. J.* **2024**, *18*, 97–109. [CrossRef]
10. Chen, W.-H.; Lam, T.T.; Chang, M.-H.; Jin, L.; Chueh, C.-C.; Augusto, G.L. Optimizing H-Darrieus Wind Turbine Performance with Double-Deflector Design. *Energies* **2024**, *17*, 503. [CrossRef]
11. Srinivasan, L.; Ram, N.; Rengarajan, S.B.; Divakaran, U.; Mohammad, A.; Velamati, R.K. Effect of Macroscopic Turbulent Gust on the Aerodynamic Performance of Vertical Axis Wind Turbine. *Energies* **2023**, *16*, 2250. [CrossRef]
12. Rogowski, K. CFD Computation of the H-Darrieus Wind Turbine—The Impact of the Rotating Shaft on the Rotor Performance. *Energies* **2019**, *12*, 2506. [CrossRef]
13. Shamsoddin, S.; Porté-Agel, F. A Large-Eddy Simulation Study of Vertical Axis Wind Turbine Wakes in the Atmospheric Boundary Layer. *Energies* **2016**, *9*, 366. [CrossRef]
14. Belabes, B.; Paraschivoiu, M. Numerical study of the effect of turbulence intensity on VAWT performance. *Energy* **2021**, *233*, 121139. [CrossRef]

15. Redchyts, D.; Portal-Porras, K.; Tarasov, S.; Moiseienko, S.; Tuchyna, U.; Starun, N.; Fernandez-Gamiz, U. Aerodynamic Performance of Vertical-Axis Wind Turbines. *J. Mar. Sci. Eng.* **2023**, *11*, 1367. [CrossRef]
16. Shukla, V.; Kaviti, A.K. Performance evaluation of profile modifications on straight-bladed vertical axis wind turbine by energy and Spalart Allmaras models. *Energy* **2017**, *126*, 766–795. [CrossRef]
17. Yang, Y.; Cao, Y.; Qian, Z.; Wang, J.; Zhu, Y.; Chen, X.; Zhang, W.; Wang, Y.; Wu, G.; Chen, S. A Study on the Effect of Turbulence Intensity on Dual Vertical-Axis Wind Turbine Aerodynamic Performance. *Energies* **2024**, *17*, 4124. [CrossRef]
18. Menter, F.R.; Langtry, R.B.; Likki, S.R.; Suzen, Y.B.; Huang, P.G.; Völker, S. A correlation-based transition model using local variables—Part 1: Model formulation. *J. Turbomach.* **2006**, *128*, 413–422. [CrossRef]
19. Langtry, R.B.; Menter, F.R.; Likki, S.R.; Suzen, Y.B.; Huang, P.G.; Völker, S. A correlation-based transition model using local variables—Part 2: Test cases and industrial applications. *J. Turbomach.* **2006**, *128*, 423–434. [CrossRef]
20. Dick, E.; Kubacki, S. Transition Models for Turbomachinery Boundary Layer Flows: A Review. *Int. J. Turbomach. Propuls. Power* **2017**, *2*, 4. [CrossRef]
21. Rezaeiha, A.; Kalkman, I.; Montazeri, H.; Blocken, B. Effect of the shaft on the aerodynamic performance of urban vertical axis wind turbines. *Energy Convers. Manag.* **2017**, *149*, 616–630. [CrossRef]
22. Rogowski, K.; Królak, G.; Bangga, G. Numerical Study on the Aerodynamic Characteristics of the NACA 0018 Airfoil at Low Reynolds Number for Darrieus Wind Turbines Using the Transition SST Model. *Processes* **2021**, *9*, 477. [CrossRef]
23. Michna, J.; Rogowski, K. Numerical Study of the Effect of the Reynolds Number and the Turbulence Intensity on the Performance of the NACA 0018 Airfoil at the Low Reynolds Number Regime. *Processes* **2022**, *10*, 1004. [CrossRef]
24. Choudhry, A.; Arjomandi, M.; Kelso, R. A study of long separation bubble on thick airfoils and its consequent effects. *Int. J. Heat Fluid Flow* **2015**, *52*, 84–96. [CrossRef]
25. Mălăel, I.; Strătilă, S. High-Precision Numerical Investigation of a VAWT Starting Process. *Processes* **2024**, *12*, 2263. [CrossRef]
26. Escudero Romero, A.; Blasetti, A.P.; Acosta-López, J.G.; Gómez-García, M.-Á.; de Lasa, H. Vorticity and Its Relationship to Vortex Separation, Dynamic Stall, and Performance, in an H-Darrieus Vertical-Axis Wind Turbine Using CFD Simulations. *Processes* **2024**, *12*, 1556. [CrossRef]
27. Rezaeiha, A.; Montazeri, H.; Blocken, B. Towards optimal aerodynamic design of vertical axis wind turbines: Impact of solidity and number of blades. *Energy* **2018**, *165*, 1129–1148. [CrossRef]
28. Santamaría, L.; Galdo Vega, M.; Pandal, A.; González Pérez, J.; Velarde-Suárez, S.; Fernández Oro, J.M. Aerodynamic Performance of VAWT Airfoils: Comparison between Wind Tunnel Testing Using a New Three-Component Strain Gauge Balance and CFD Modelling. *Energies* **2022**, *15*, 9351. [CrossRef]
29. Luo, W.; Liu, W.; Yang, M.; Chen, S.; Song, X.; Wu, W. Load Characteristics and Extreme Response of Straight-Bladed Floating VAWT Using a Fully Coupled Model. *J. Mar. Sci. Eng.* **2023**, *11*, 185. [CrossRef]
30. Ferreira, C.S.; Madsen, H.A.; Barone, M.; Roscher, B.; Deglaire, P.; Arduin, I. Comparison of aerodynamic models for Vertical Axis Wind Turbines. *J. Phys. Conf. Ser.* **2014**, *524*, 012125. [CrossRef]
31. Balduzzi, F.; Bianchini, A.; Ferrara, G.; Marten, D.; Pechlivanoglou, G.; Nayeri, C.N.; Paschereit, C.O.; Drofelnik, J.; Campobasso, M.S.; Ferrari, L. Three-Dimensional Aerodynamic Analysis of a Darrieus Wind Turbine Blade Using Computational Fluid Dynamics and Lifting Line Theory. In *Volume 2A: Turbomachinery*; ASME International: New York, NY, USA, 2017. [CrossRef]
32. Mendoza, V.; Bachant, P.; Ferreira, C.; Goude, A. Near-wake flow simulation of a vertical axis turbine using an actuator line model. *Wind Energy* **2019**, *22*, 171–188. [CrossRef]
33. Balduzzi, F.; Bianchini, A.; Maleci, R.; Ferrara, G.; Ferrari, L. Blade design criteria to compensate the flow curvature effects in H-Darrieus wind turbines. *J. Turbomach.* **2015**, *137*, 011006. [CrossRef]
34. Simão Ferreira, C.; Van Kuik, G.; Van Bussel, G.; Scarano, F. Visualization by PIV of dynamic stall on a vertical axis wind turbine. *Exp. Fluids* **2009**, *46*, 97–108. [CrossRef]
35. Shen, W.Z.; Hansen, M.O.; Sørensen, J.N. Determination of angle of attack (AOA) for rotating blades. In *Wind Energy*; Springer: New York, NY, USA, 2007; pp. 205–209.
36. Bianchini, A.; Balduzzi, F.; Ferrara, G.; Ferrari, L. A computational procedure to define the incidence angle on airfoils rotating around an axis orthogonal to flow direction. *Energy Convers. Manag.* **2016**, *126*, 790–798. [CrossRef]
37. Hansen, M.O.L.; Johansen, J. Tip studies using CFD and comparison with tip loss models. *Wind Energy* **2004**, *7*, 343–356. [CrossRef]
38. Johansen, J.; Sørensen, N. Aerofoil Characteristics from 3D CFD Rotor Computations. *Wind Energy* **2004**, *7*, 283–294. [CrossRef]
39. Guntur, S.; Sørensen, N.N. An evaluation of several methods of determining the local angle of attack on wind turbine blades. *J. Phys. Conf. Ser.* **2014**, *555*, 012045. [CrossRef]
40. Syed Ahmed Kabir, I.F.; Gajendran, M.K.; Ng, E.Y.K.; Mehdizadeh, A.; Berrouk, A.S. Novel Machine-Learning-Based Stall Delay Correction Model for Improving Blade Element Momentum Analysis in Wind Turbine Performance Prediction. *Wind* **2022**, *2*, 636–658. [CrossRef]
41. Lichota, P.; Norena, D.A. A Priori Model Inclusion in the Multisine Maneuver Design. In Proceedings of the 17th International Carpathian Control Conference, High Tatras, Slovakia, 29 May–1 June 2016; Petras, I., Podlubny, I., Kacur, J., Eds.; IEEE: Tatranská Lomnica, Slovakia, 2016; pp. 440–445. [CrossRef]
42. Lichota, P.; Szulczyk, J.; Noreña, D.A.; Vallejo Monsalve, F.A. Power spectrum optimization in the design of multisine manoeuvre for identification purposes. *J. Theor. Appl. Mech.* **2017**, *55*, 1193–1203. [CrossRef]

43. Saverin, J.; Frank, S. The Loading Cycle of a H-Blade Type Vertical Axis Wind Turbine. In Proceedings of the ASME Turbo Expo 2015: Turbine Technical Conference and Exposition, Montreal, QC, Canada, 15–19 June 2015; V009T46A002. ASME: New York, NY, USA, 2015; Volume 9. [CrossRef]
44. Delafin, P.-L.; Deniset, F.; Astolfi, J.A.; Hauville, F. Performance Improvement of a Darrieus Tidal Turbine with Active Variable Pitch. *Energies* **2021**, *14*, 667. [CrossRef]
45. Melani, P.F.; Balduzzi, F.; Ferrara, G.; Bianchini, A. How to extract the angle attack on airfoils in cycloidal motion from a flow field solved with computational fluid dynamics? Development and verification of a robust computational procedure. *Energy Convers. Manag.* **2020**, *223*, 113284. [CrossRef]
46. Tescione, G.; Ragni, D.; He, C.; Simão Ferreira, C.J.; van Bussel, G.J.W. Near wake flow analysis of a vertical axis wind turbine by stereoscopic particle image velocimetry. *Renew. Energy* **2014**, *70*, 47–61. [CrossRef]
47. Rezaeiha, A.; Kalkman, I.; Blocken, B. CFD Simulation of a Vertical Axis Wind Turbine Operating at a Moderate Tip Speed Ratio: Guidelines for Minimum Domain Size and Azimuthal Increment. *Renew. Energy* **2017**, *107*, 373–385. [CrossRef]
48. Menter, F.R. *Best Practice: Scale-Resolving Simulations in ANSYS CFD*; ANSYS Report; ANSYS Inc.: Canonsburg, PA, USA, 2015.
49. Durbin, P.A.; Pettersson Reif, B.A. *Statistical Theory and Modeling for Turbulent Flows*; John Wiley & Sons, Ltd.: Hoboken, NJ, USA, 2011.
50. Spalart, P.R.; Jou, W.H.; Strelets, M.; Allmaras, S.R. Comments on the feasibility of LES for wings, and on a hybrid RANS/LES approach. *Adv. DNS/LES* **1997**, *1*, 4–8.
51. Menter, F.R.; Egorov, Y. The Scale-Adaptive Simulation Method for Unsteady Turbulent Flow Predictions. Part 1: Theory and Model Description. *Flow Turbul. Combust.* **2010**, *85*, 113–138. [CrossRef]
52. Rezaeiha, A.; Kalkman, I.; Blocken, B. Effect of pitch angle on power performance and aerodynamics of a vertical axis wind turbine. *Appl. Energy* **2017**, *197*, 132–150. [CrossRef]
53. Castelein, D.; Ragni, D.; Tescione, G.; Ferreira, C.J.S.; Gaunaa, M. Creating a benchmark of Vertical Axis Wind Turbines in Dynamic Stall for validating numerical models. In Proceedings of the 33rd Wind Energy Symposium, AIAA SciTech, AIAA 2015-0723, Kissimmee, FL, USA, 5–9 January 2015. [CrossRef]
54. Noca, F.; Shiels, D.; Jeon, D. A comparison of methods for evaluating time-dependent fluid dynamic forces on bodies, using only velocity fields and their derivatives. *J. Fluids Struct.* **1999**, *13*, 551–578. [CrossRef]
55. Jost, E.; Klein, L.; Leipprand, H.; Lutz, T.; Krämer, E. Extracting the angle of attack on rotor blades from CFD simulations. *Wind Energy* **2018**, *21*, 807–822. [CrossRef]
56. Rogowski, K.; Mikkelsen, R.F.; Michna, J.; Wiśniewski, J. Aerodynamic performance analysis of NACA 0018 airfoil at low Reynolds numbers in a low-turbulence wind tunnel. *Adv. Sci. Technol. Res. J.* **2025**, *accepted for publication*. Available online: https://www.astrj.com/Aerodynamic-performance-analysis-of-NACA-0018-airfoil-at-low-Reynolds-numbers-in,195556,0,2.html (accessed on 9 December 2024).
57. Rezaeiha, A.; Montazeri, H.; Blocken, B. Characterization of aerodynamic performance of vertical axis wind turbines: Impact of operational parameters. *Energy Convers. Manag.* **2018**, *169*, 45–77. [CrossRef]

Energy 321 (2025) 135344

Contents lists available at ScienceDirect

Energy

journal homepage: www.elsevier.com/locate/energy

Impact of zigzag tape on blade loads and aerodynamic wake in a vertical axis wind turbine: A Delft VAWT case study

Krzysztof Rogowski [a],*, Jan Michna [a], Robert Flemming Mikkelsen [b], Carlos Simao Ferreira [c]

[a] Institute of Aeronautics and Applied Mechanics, Warsaw University of Technology, Nowowiejska 24, Warsaw, 00-665, Poland
[b] Department of Wind and Energy Systems, Technical University of Denmark, Kgs. Lyngby, DK-2800, Denmark
[c] Faculty of Aerospace Engineering, Delft University of Technology, Kluyverweg 1, 2629 HS Delft, The Netherlands

ARTICLE INFO

Keywords:
Zigzag tape
VAWT
Actuator line model
URANS
Aerodynamic wake

ABSTRACT

This study investigates the impact of zigzag tape on the aerodynamic performance and wake characteristics of the Delft Vertical Axis Wind Turbine (VAWT). The primary aim is to understand how the zigzag tape affects blade loads and the resulting aerodynamic wake. A comprehensive analysis was conducted using the Actuator Line Model (ALM) with airfoil characteristics measured in the wind tunnel at the Technical University of Denmark (DTU). Additionally, a 2-D CFD analysis with k-ω SST and γ-Re_θ turbulence models were employed to evaluate the influence of laminar transition phenomena on rotor characteristics. Results indicate that while the zigzag tape linearizes the lift coefficient characteristic, it leads to a notable reduction in aerodynamic efficiency due to increased drag and decreased lift below the critical angle of attack. The simulations were performed at a tip-speed ratio (TSR) of 4.5 to avoid a dynamic stall, as this operating condition ensures that the rotor blades remain below the static stall threshold and large offshore VAWTs are designed to operate near their maximum aerodynamic efficiency (C_P) for the majority of their operational time. The aerodynamic wake behind the rotor also shows significant changes, with the zigzag tape promoting asymmetry and affecting the wake recovery distance. The study's findings highlight the importance of considering surface contamination effects, represented by zigzag tape, in evaluating VAWT performance and wake behavior, offering valuable insights for wind turbine design and optimization.

1. Introduction

In 2015, Tescione et al. [1] conducted extensive experimental studies on a 2-bladed H-shaped VAWT at Delft University of Technology, using Particle Image Velocimetry (PIV) in the Open Jet Facility (OJF). The turbine, featuring NACA0018 aluminum blades, had a height and rotor diameter of 1 m, with a chord length of 0.06 m. The blades were mounted at a point 0.4c from the leading edge. Operating at a free stream velocity of 9.3 m/s, it achieved a tip speed ratio of 4.5.

Since 2015, numerous numerical analyses of this rotor have been conducted. Rotors based on this geometry have been studied using the classical 2-D CFD approach with various boundary layer modeling methods [2–5] and more advanced three-dimensional unsteady Reynolds-averaged Navier–Stokes (URANS) equations [6]. While 3-D CFD, particularly URANS, provides valuable insights into complex flow phenomena such as tip vortices and dynamic stall, its high computational cost remains a limitation. Therefore, lower-order models such as blade element momentum (BEM) and actuator line model (ALM) remain popular alternatives [7]. These methods rely on airfoil aerodynamic characteristics and additional corrections (e.g., flow curvature, dynamic stall models) and can incorporate finite blade and added mass effects [8].

The aerodynamics of a VAWT rotor are complex and challenging to estimate, leading to significant differences in the aerodynamic characteristics estimated by various researchers [9]. This variability arises from the different modeling approaches employed, including numerical methods such as computational fluid dynamics (CFD), as well as lower-order models such as blade element momentum (BEM) and vortex models, in addition to the inherent sensitivity of the NACA0018 airfoil to operating conditions. For this turbine, the chord-based Reynolds number Re_c at a TSR of 4.5 is approximately 1.7×10^5 [10]. In the "low Reynolds number" range (10^3 to 10^5), viscous effects, laminar separation bubbles, and turbulence play a significant role [11]. According to Winslow et al. [12], at low Reynolds numbers, the boundary layer remains laminar over a larger portion of the airfoil surface, making it more susceptible to separation due to an adverse pressure gradient. The separated shear layer may transition to turbulence and reattach, forming a laminar separation bubble (LSB). However, as the Reynolds

* Corresponding author.
E-mail address: krzysztof.rogowski@pw.edu.pl (K. Rogowski).

https://doi.org/10.1016/j.energy.2025.135344
Received 2 October 2024; Received in revised form 4 February 2025; Accepted 28 February 2025
Available online 18 March 2025
0360-5442/

number decreases, the reattachment point moves further downstream, increasing bubble size and drag while reducing lift efficiency. In the range of $10^4 < Re < 5 \times 10^4$, the shear layer often does not reattach, leading to trailing edge stall and significantly degraded aerodynamic performance. The NACA0018 profile, common in VAWT design, was not examined under low Reynolds number conditions in a wind tunnel until recently. Early studies, such as those of Jacobs and Sherman (J&S) [13], were limited and influenced by high levels of wind tunnel turbulence. The widely used database by Sheldahl and Klimas (S&K) published in 1971 [14,15] was dominant for a long time, but recent wind tunnel studies and numerical tools such as XFOIL and CFD have provided more accurate data [16–18]. Modern measurements of C_L and C_D at around $Re = 150k$ differ significantly from the S&K and J&S data, showing that flow around a clean profile at sub-critical angles is dominated by laminar bubbles. This causes the $C_L(\alpha)$ curve to follow two different derivatives rather than one. Gerakopulos et al. [19] identified the point that separates these two regions. Contemporary studies indicate that advanced transition models, such as $\gamma - Re_\theta$ and e^N methods, often misestimate this region without calibration [20]. The aerodynamic characteristics of the NACA0018 profile, as in most airfoils, are sensitive to variations in the Reynolds number. However, in the case of the NACA0018 airfoil, which is often used in VAWT applications, this sensitivity becomes particularly critical due to the low Reynolds number regime in which these turbines are typically operated [20,21].

An effective method to influence the behavior of the boundary layer in experimental aerodynamics is the use of zigzag tape. In the TU Delft VAWT experiment (Fig. 1), zigzag tape was applied at the length of the 8% chord on both sides of the blades to mitigate laminar separation bubbles. The tape, a 3D-turbulator by Glasfaser Flugzeug, had a point distance of 6 mm, was 0.20 mm thick, 12 mm wide, and followed a zigzag pattern of 60° [1]. In addition to promoting transition, zigzag tape is commonly used in experiments to improve control over the aerodynamic characteristics of an airfoil by modifying the behavior of the boundary layer and reducing the influence of laminar separation bubbles [22], as well as mitigating aerodynamic noise [23].

The primary tool used to investigate the impact of zigzag tape on VAWT aerodynamics in this paper is the Actuator Line Model (ALM). To further verify these results and understand the impact of transition phenomena, such as laminar separation bubbles, a 2-D CFD analysis was also performed using the k-ω SST and γ-Re$_\theta$ models. These models have been shown to predict rotor loads accurately [4,24]. The k-ω SST model is a turbulence model that assumes a fully turbulent flow throughout the boundary layer, providing robust and reliable predictions, particularly in regions with strong adverse pressure gradients. It has also been used successfully to approximate the effect of zigzag tape by enforcing the early transition [22]. In contrast, the γ-Re$_\theta$ model is a transition model that explicitly accounts for the laminar-to-turbulent transition, making it more suitable for capturing transitional effects such as laminar separation bubbles and their influence on aerodynamic loads. This distinction is particularly relevant when analyzing flow conditions at low Reynolds numbers, where transition plays a critical role. Similarly, Kruse et al. [25] studied the aerodynamic characteristics of the NACA 63_3-418 airfoil, demonstrating the significance of surface roughness and transition modeling. Therefore, verifying whether the k-ω SST model's rotor blade loads match the zigzag tape trend provides further justification for its use in our simulations.

Our analyses revealed several important issues for understanding the relationship between airfoil aerodynamic characteristics and rotor wake. Firstly, in addition to the significant impact on aerodynamic blade loads, the zigzag tape also affects the wake downstream of the rotor–an effect not previously considered for VAWTs but crucial for analyzing the influence of dirty blades on wake geometry. Additionally, using the S&K database results in notable differences in velocity profiles compared to clean airfoils.

This paper has two main parts. The first part presents the aerodynamic characteristics of the clean NACA0018 airfoil and the zigzag tape airfoil, measured at the Technical University of Denmark (DTU). Comparison of the obtained C_L and C_D with XFOIL and the complete 2-D CFD results. The second part discusses VAWT aerodynamic characteristics using the 3-D ALM approach, including a 2-D CFD analysis to understand the impact of laminar transition effects on aerodynamic loads and wake.

2. Experimental setup and wind tunnel testing

The blade model used for wind tunnel tests to determine aerodynamic characteristics C_L and C_D was crafted from a section of a wind turbine blade, as shown in Fig. 2. The blade is an extruded aluminum wing with a NACA0018 airfoil profile. The chord and length of the rectangular wing section were 60 mm and 500 mm, respectively. The airfoil surface was smooth and polished using 800-grit sandpaper to ensure minimal surface roughness.

The dimensions of the wind tunnel test section are $H \times W \times L = 0.5\,\mathrm{m} \times 0.75\,\mathrm{m} \times 2.0\,\mathrm{m}$ with a contraction ratio of 8.5, which provides a very low turbulence intensity ($TI < 0.1\%$) of the mean flow, ensuring that natural transition processes can develop. The maximum velocity achievable in the tunnel is 40 m/s. Measurements were conducted with a sampling rate of 125 Hz for 10 s at each angle of attack (α). Pressure scanners from Pressure Systems were used, having a full range of

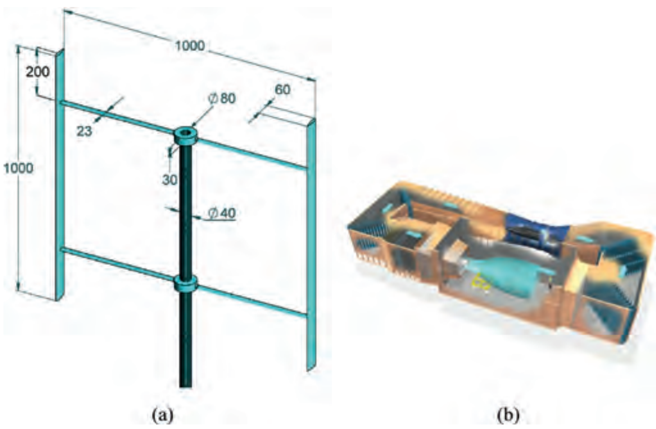

Fig. 1. The VAWT model (dimensions in mm) (a); Schematics of the Open Jet Facility (OJF) [1] (b).

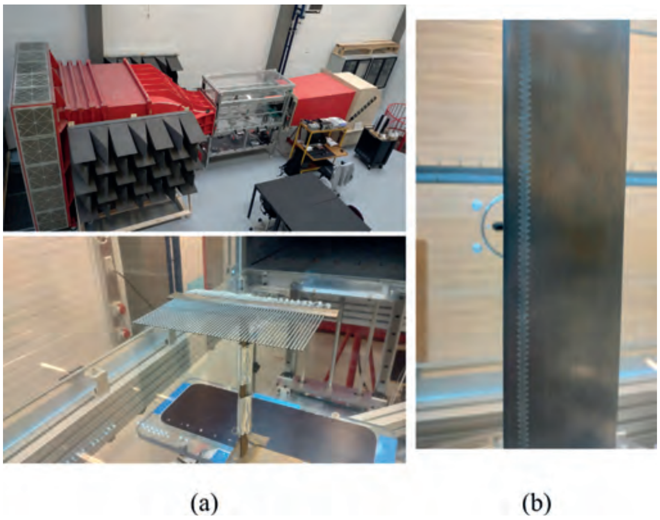

Fig. 2. Experiment equipment and blade configuration.

±2.5 kPa for wall pressures and ±7 kPa for wake pressures. Aerodynamic forces were measured using force gauges, wall pressure measurements, and wake pressure readings for the drag. The lift measurements from the force gauge and wall pressures showed good agreement. However, wake measurements are reliable only for $\alpha < \pm 20$ degrees; at higher angles of attack, the wake becomes too wide for the rake used. Also, the airfoil exhibited tonal noise around an angle of attack of 0 degrees.

The baseline aerodynamic characteristics of the clean NACA0018 airfoil were presented in detail in [26], where the discussion of the experimental setup and fundamental data was provided. Due to space limitations, this article does not repeat those details. Instead, it focuses on entirely new results concerning the influence of zigzag tape on the aerodynamic performance of the airfoil.

2.1. Impact of Zigzag tape on NACA0018 airfoil performance

The main goal of the experimental part was to obtain the $C_L(\alpha)$ and $C_D(\alpha)$ characteristics of the NACA0018 airfoil for a Reynolds number as close as possible to the chord-based value, which for the considered 1-m VAWT at TSR=4.5 is 1.7×10^5. Taking into account the chord length of the airfoil (6 cm) and the maximum flow speed in the wind tunnel (40 m/s), we obtained a Reynolds number of 1.6×10^5. In our previous work [26], we presented the characteristics of the NACA0018 airfoil for a range of Reynolds numbers from 0.3×10^5 to 1.6×10^5. The aerodynamic forces that were obtained were validated based on experimental studies by other authors and compared with the predictions of the XFOIL approach. This work discusses the impact of zigzag tape on the airfoil polars.

Fig. 3 shows the performance of the NACA0018 airfoil with zigzag tape; the lift and drag coefficients, C_{Lg}, C_L, and C_D, were estimated using a gauge, wall pressure taps, and a wake rake, respectively. These aerodynamic force characteristics as a function of the angle of attack, shown in this figure, were obtained for $Re = 1.6\times10^5$ in the range from −20° to 20°, and then back to −20° to obtain a complete aerodynamic hysteresis loop. Two independent measurement techniques, pressure taps, and force gauge, showed very similar lift coefficients. During the "upward" measurement, the maximum lift coefficient, C_{Lmax}, reached 1.02 at a critical angle of attack of 14°. The lift for the same angle of attack during the "downward" measurement decreased by 58.3%. The C_{Lmax} during the "downward" measurement was 0.88 at an angle of attack of 10°. A relatively large hysteresis loop is also visible in the drag coefficient. The minimum drag coefficient, C_{Dmin}, was 0.019. The tape causes the lift coefficient to grow almost linearly for angles of attack up to α_{crit} at such low Reynolds numbers, with the derivative $dC_L/d\alpha$ equal to 4.87 rad^{-1}.

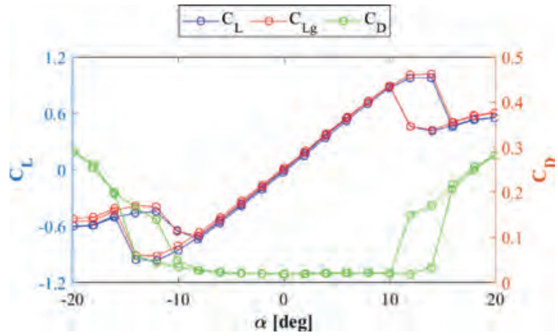

Fig. 3. Experimental Lift Coefficient (C_L) using wall pressure taps and a force gauge (C_{L_g}) as well as Drag Coefficient (C_D) Variation with Angle of Attack (α) for zigzag Configuration.

A comparison of the obtained characteristics for the airfoil with zigzag tape (Fig. 3) and the clean airfoil configuration is presented in Fig. 4. The $C_L(\alpha)$ characteristics of the clean airfoil are nonlinear below α_{crit}, which is due to the presence of laminar bubbles that form on both sides of the airfoil up to the transition angle α_t of approximately 6°–7°, or only on the pressure side beyond α_t [19,20]. Applying the zigzag tape induces turbulence in the boundary layer, eliminating this effect. Interestingly, despite removing laminar bubbles, the hysteresis loops

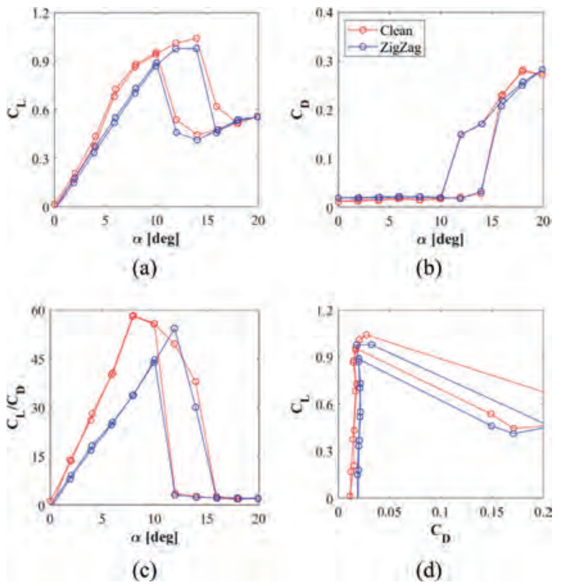

Fig. 4. Comparison of aerodynamic performance for the NACA0018 airfoil: (a) lift coefficient C_L vs. angle of attack α, (b) drag coefficient C_D, (c) lift-to-drag ratio C_L/C_D, and (d) C_L vs. C_D. Results are shown for both clean [26] and zigzag tape configurations.

for both the clean airfoil and the airfoil with zigzag tape remain quite similar in terms of value and shape. However, the presence of the tape increases the minimum drag by approximately 73.4%. The nonlinearity of the $C_L(\alpha)$ curve leads to a significant improvement in aerodynamic efficiency (Fig. 4c).

2.2. The effect of Reynolds number on the performance of NACA0018 airfoil with zigzag tape

The results given in Fig. 5 are compared for Reynolds numbers 0.83×10^5 and 1.60×10^5. This comparison aims to highlight the zigzag tape's significant impact on the airfoil characteristics, especially within the range of such low Reynolds numbers. As shown in Fig. 5a, the zigzag tape linearizes the C_L characteristics, resulting in very similar $dC_L/d\alpha$ derivatives for both Reynolds numbers. The derivatives of both characteristics, calculated in the range from 0° to 10°, have an average value of 4.87 rad^{-1}. This value is 22.5% lower compared to the theoretical derivative of 2π of a thin airfoil as predicted by Thin Airfoil Theory [18]. As mentioned earlier in the previous subsection, two regions can be distinguished for the clean airfoil characteristics: in the first region, laminar separation bubbles occur on both sides of the airfoil, while in the second, they appear only on the suction side. Gerakopulos et al. [19] demonstrated that for $Re = 0.8 \times 10^5$, the derivative in the angle of attack range $0° \leq \alpha \leq 6°$ is 0.14, while in the range $6° \leq \alpha \leq 10°$, it is 0.03. In our measurements, the transition angle α_t occurred slightly earlier, at approximately 4°, with aerodynamic derivatives for the first and second regions being 0.145 and 0.056, respectively. For $Re = 1.6 \times 10^5$, Gerakopulos et al. [19] obtained derivatives for the first region ($0° \leq \alpha \leq 8°$) of 0.11 and for the second region ($8° \leq \alpha \leq 14°$) of 0.02. Our predictions are 0.108 for the first region ($0° \leq \alpha \leq 8°$) and 0.027 for the second region ($8° \leq \alpha \leq 14°$).

Moreover, the Reynolds number significantly affects C_{Lmax}, with the observed differences becoming more pronounced as the Reynolds number decreases. This effect is particularly evident in the case of the clean configuration, where the lack of surface modifications leads to

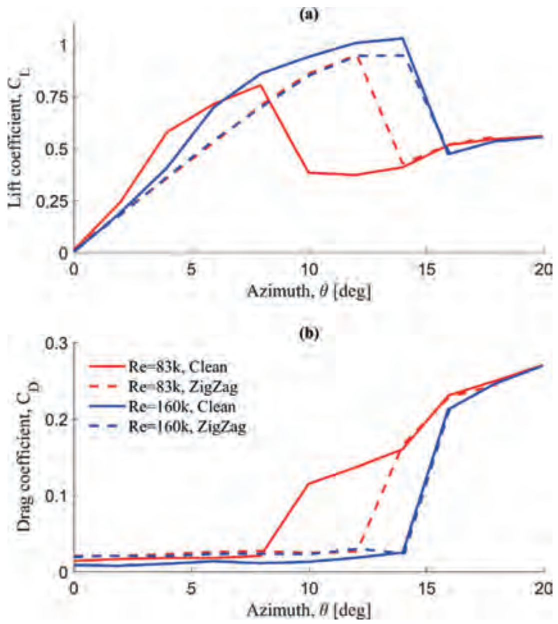

Fig. 5. Comparison of the lift coefficient C_L (a) and drag coefficient C_D (b) for the zigzag configuration of the NACA0018 airfoil, with clean airfoil data from [26], across three Reynolds numbers ($Re = 83k$ and $Re = 160k$) for angles of attack ranging from 0° to 20°.

greater sensitivity to flow separation and boundary layer behavior at lower Reynolds numbers. The C_{Lmax} for the lowest examined Re is 0.8 at $\alpha = 8°$ for the clean airfoil and 0.94 at $\alpha = 12°$ for the zigzag configuration. When comparing these results to other studies, specifically for the clean airfoil case, as no similar investigations involving zigzag tape are known to the authors of this paper, Gerakopulos et al. [19] reported a C_{Lmax} of 0.88 at $\alpha = 10°$ for $Re = 0.8 \times 10^5$, and 1.02 at $\alpha = 14°$ for $Re = 1.6 \times 10^5$. For the higher Reynolds number of $Re = 1.6 \times 10^5$, the differences in C_{Lmax} between the clean and zigzag configurations are relatively small. The C_{Lmax} for the clean configuration is 1.027, which is 8% lower compared to the zigzag configuration. For $Re = 1.6 \times 10^5$, the critical angle of attack α_{crit} is 14°. This analysis demonstrates that the measurement results presented in this paper are acceptable. The differences between our results and those taken from the literature increase as the Reynolds number decreases, and these differences are influenced by the conditions in the wind tunnel and the measurement tools used.

The Reynolds number also significantly affects the drag coefficient (Fig. 5b). The clean airfoil's minimum drag coefficient strongly depends on the Reynolds number. As shown in [26], C_{Dmin} increased from 0.0084 for $Re = 1.6 \times 10^5$ to 0.014 for $Re = 0.83 \times 10^5$, that is, by 65. 5%. The zigzag tape, however, causes the drag coefficient to increase more slowly, from 0.0195 for $Re = 1.6 \times 10^5$ to 0.0196 for $Re = 0.83 \times 10^5$. The increase in the angle of attack first causes a slight increase in drag, followed by a sharp increase. Both the Reynolds number and the zigzag tape significantly affect the angle of attack at which this sharp increase in drag occurs. For $Re = 0.83 \times 10^5$, this sharp increase appears in $\alpha = 7.95°$ for clean airfoil and 12.04° for zigzag tape. For the highest Reynolds number studied in this work, a sharp increase in drag is observed at the same angle of attack.

3. Methodology

3.1. Actuator line approach

The three-dimensional Actuator Line Model (ALM), developed by Sørensen and Shen [27], combines classical blade element theory with Navier–Stokes-based flow models. This study uses the turbinesFoam library by Bachant et al. [28] within the OpenFOAM CFD framework, significantly reducing computational costs compared to RANS simulations solved with 3D blades.

The ALM represents wind turbine blades as lines of actuator elements at their quarter-chord position, using 2-D airfoil lift and drag coefficients. Blade forces are calculated from local velocities using the angle of attack and relative velocity for each blade element. The blade element method couples with a modified Leishman–Beddoes dynamic stall model [29–31] to determine dynamic blade force coefficients. The calculated body forces are reintroduced into the Navier–Stokes solver as momentum equation terms.

The relative flow velocity and angle of attack for each blade element are computed using the vector sum of the tangential velocity V_t and the local inflow velocity U_{in}. The tangential velocity $V_t = -\omega R$ is determined by the rotor angular velocity ω and the rotor radius R, while U_{in} is obtained from the surrounding flow field at the position of the quarter-chord of the blade element. In OpenFOAM, the `interpolationCellPoint` class is used for linearly weighted interpolation of cell values, ensuring smooth sampling of U_{in}. According to Mendoza et al. [32], this approach mitigates abrupt velocity variations caused by mesh resolution, particularly when the mesh size is comparable to the chord length and blade elements traverse approximately one cell per time step.

Prandtl's lifting line theory is applied in the ALM to account for the blade's end effects. The geometric angle of attack is expressed as a function of the non-dimensional span position, allowing for the determination of unknown Fourier coefficients that describe the circulation distribution along the span. These coefficients are then used to adjust the lift coefficient distribution, ensuring consistency with the physical effects of blade-tip vortices. Based on the normalized spanwise lift coefficient distribution, the correction function is incorporated into the ALM to model the lift force variations near the blade tips accurately.

In this study, dynamic effects on lift and drag are taken into account using the Dynamic Stall Model (DSM), which ensures proper aerodynamic modeling in different operating conditions. These effects are characterized by the reduced frequency $k = \frac{\mathrm{TSR}\cdot c}{2R}$, where k depends on the tip speed ratio (TSR), the length of the blade chord c, and the radius of the rotor R. For the turbine examined in this manuscript, at TSR = 4.5, the reduced frequency is 0.27, matching the conditions of an experimental turbine studied by Bachant et al. [33]. Although the range of attack angles experienced by the turbine blades in this study did not exceed critical static stall angles, rendering the dynamic stall effects negligible [7], the DSM was still implemented consistently [32] to ensure robustness and accuracy in aerodynamic modeling.

Based on Mendoza et al. [7], who investigated various Large Eddy Simulation (LES) approaches (including Smagorinsky, dynamic k-equation, and dynamic Lagrangian turbulence models) and found minimal differences, the Smagorinsky LES approach was used in this study to calculate the velocity field. A detailed description of the ALM methodology and additional models is available in Bachant et al. [33]. The Navier–Stokes equations for incompressible flow are solved using the Pressure-Implicit with Splitting of Operators (PISO) algorithm [34].

The TU Delft VAWT (Fig. 1) simulated in this study is based on the geometry of Tescione et al. [1], with the struts and supporting towers excluded for simplicity. The simulation domain (Fig. 6) was set to 20D to examine the wake at a greater distance behind the rotor.

The uniform distribution of hexahedral cells was used near the turbine rotor, with a local refinement level of $n = 4$, gradually transitioning to a coarser mesh further from the rotor to accurately capture the details of the wake (Fig. 7). This topology remained consistent and was globally refined, with the mesh scaled proportionally in all directions. The finest refinement region extends $1D$ upwind and $11D$ downwind from the central shaft, covering $1D$ horizontally and vertically from the equatorial blade section.

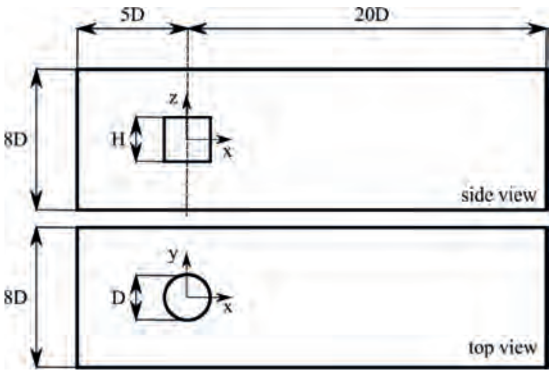

Fig. 6. Schematic of the numerical simulation domain for the TU Delft VAWT for the ALM approach.

Fig. 8 compares the power coefficient c_P for the entire rotor at three mesh resolutions: $D/60$, $D/80$, and $D/96$. Although small differences in the curves can be observed, particularly for finer mesh resolutions, these differences remain minor and are natural in the case of the applied LES approach, where finer meshes capture more detailed flow structures. This observation is consistent with the findings of Mendoza et al. [7], who showed that increasing mesh density within the range of $D/40$ to $D/96$ leads to minor changes in aerodynamic wake profiles. However, these changes remain at the flow details level and do not significantly impact the velocity profiles behind the rotor, which could influence the power characteristics of a downstream turbine.

Similar conclusions were drawn by Huang [35], who validated the ALM approach for a similar but slightly smaller rotor with a diameter of 0.3 m. Huang's work, which involved PIV measurements of a significantly longer aerodynamic wake, demonstrated that using the k-epsilon turbulence model provides sufficiently accurate results to estimate the wake deficit, even with less dense computational meshes.

Given the scope of our study, the reference mesh resolution for this work is $D/80$. This resolution offers a practical balance between computational efficiency and accuracy, ensuring reliable predictions of flow characteristics within the rotor aerodynamic wake, which are crucial for assessing the potential placement of downstream wind turbines in a wind farm.

As recommended by Mendoza et al. [7], the maximum Courant number (Co) should be kept below 0.25. In this study, it remained below 0.15.

3.2. 2-D CFD modeling

The 2-D computational domain (Fig. 9) represents the equatorial plane of the TU Delft VAWT with a high blade aspect ratio (H/c) of 16.7 and a zero-pitch angle; therefore, the 3-D tip effects are insignificant [2,36]. The domain width is $W = 25D$, providing a blockage ratio, defined as the ratio of turbine diameter D to domain width W, of 4%. Rezaeiha et al. [37] showed that for CFD simulations of VAWTs, a blockage ratio of less than 5% is necessary to minimize the effect of boundary conditions on the results. The distance from the inlet to the rotor axis was set to $10D$, while the total domain length was $35D$. In the rotor area, a moving ring with an outer diameter of $2D$ and an inner diameter of $0.5D$ was used. The dimensions of our domain meet the

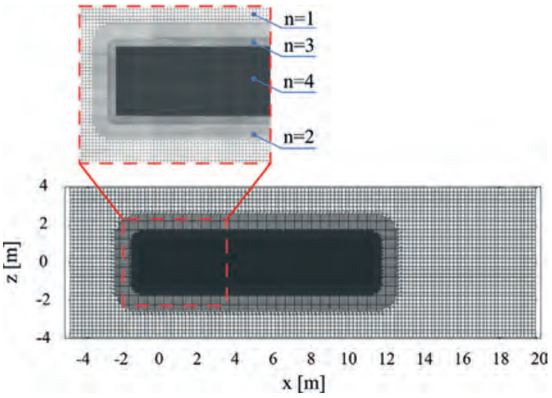

Fig. 7. Mesh for VAWT simulations using the ALM approach. The figure shows the full view of the mesh in the x–z plane with a zoomed-in section illustrating different levels of local refinement: $n = 1$, $n = 2$, $n = 3$, and $n = 4$.

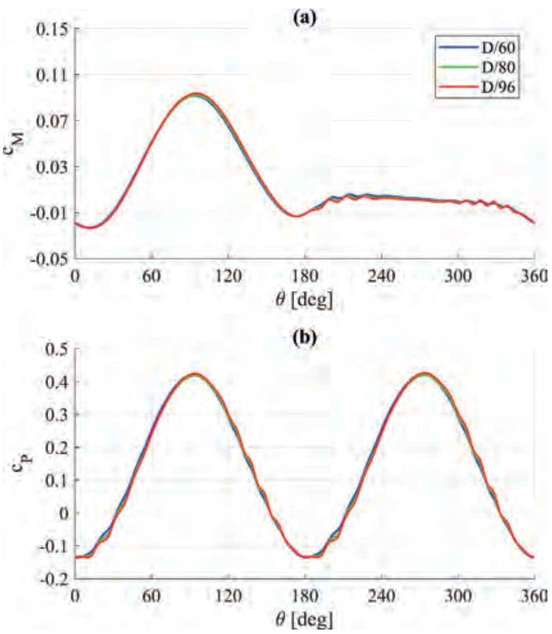

Fig. 8. Comparison of the moment coefficient c_M for a single rotor blade (top) and the power coefficient c_P for the entire rotor (bottom) at three mesh resolutions: $D/60$, $D/80$, and $D/96$.

minimum criteria specified in Rezaeiha et al. [37] for small VAWTs of low solidity that operate at moderate tip speed ratios.

Fig. 9 presents the mesh for the TU Delft VAWT, consisting of quadrilateral mapped elements. Following a grid independence study (Fig. 10) conducted on meshes ranging from 1000 to 2000 nodes on the airfoil edges, a mesh with 1460 nodes and a total of approximately 1,276,000 elements was selected for use. The grid convergence study was conducted using a refinement factor of $\sqrt{2}$. The coarser mesh contained approximately 1,033,000 elements, while the finest mesh comprised 2,104,000 cells.

The boundary conditions applied include a uniform velocity at the inlet, zero gauge pressure at the outlet, no-slip conditions on the airfoils, and symmetry along the domain sides. The rotating ring is connected to the stationary surrounding domain via a sliding mesh interface. The turbulence intensity (TI) at the inlet was set to 5%, while the turbulence length scale was assumed to be 0.004 m. The turbulence decay is observed, and TI levels before the rotor become 0.25–0.35%, consistent with the estimation formula proposed in the ANSYS Fluent Theory Guide [38]. The turbulence intensity level is consistent with the experiment [1] where the maximum available values of TI are 0.5%.

Fig. 10 presents the results of the instantaneous moment coefficient at the 20th rotor revolution for the three investigated mesh distributions. As can be seen from the figure, the differences between the curves are minimal. Furthermore, the coefficient of determination R^2 of the curves compared to the finest mesh result is greater than 0.9999 for both $N = 1460$ and $N = 1000$ cases.

4. Results and discussion

4.1. Aerodynamic blade loads

Fig. 11 presents the local angle of attack of the TU Delft VAWT blade calculated using the 3-D ALM approach based on the lift and drag characteristics of the NACA0018 airfoil measured in the DTU wind tunnel. The blue curve represents the data for the clean airfoil, while the red curve shows the zigzag tape configuration. For comparison, the figure also displays the angle of attack obtained using the airfoil characteristics from Sheldahl and Klimas [14] (black curve). The blade's angle of attack calculated using this database is almost perfectly in line with the results of Mendoza et al. [7], who also used polars from the S&K database in their work. This confirms that the ALM approach implemented in this study is accurate and reliable.

Figs. 12 and 13 compare the components of the sectional aerodynamic blade load, namely the normal and tangential components, calculated using the 3-D ALM and 2-D full CFD approaches. The angle of attack of the blade and the sectional forces differ slightly from each other. It is essential to clarify that the "sectional angle of attack" refers to the angle of attack calculated locally for the blade element in the equatorial plane based on the velocity components and airfoil characteristics specific to that section. This term differs from the "blade angle of attack", which represents the angle calculated for the entire blade, assuming uniform flow conditions. In Fig. 11, the local blade angle of attack is compared with the sectional blade angle of attack for the blade element in the equatorial plane. The color scheme of the curves corresponding to the various airfoil characteristics has been preserved, but dashed lines have been used for differentiation. Fig. 11 shows that, particularly in the upwind part of the rotor, the differences between the $\alpha(\theta)$ curves are small enough that an additional zoomed-in plot Fig. 11b was prepared to capture them. Higher angles of attack are achieved for the S&K database and for the zigzag configuration, which corresponds to linear $C_L(\alpha)$ characteristics. For the zigzag case, the maximum sectional angle of attack is 13.48° at an azimuth of 106°, while for the S&K database, it is 13.46° at an azimuth of 103.3°. In the case of the clean airfoil, the maximum angle of attack is 12.9° at an azimuth of 104.3°. The average sectional maximum angle of attack is 3.22% lower compared to the blade angle of attack.

For the S&K database, the maximum static lift coefficient of the NACA0018 at $Re = 1.6 \times 10^5$ is reached at $\alpha_{\text{crit}} = 12°$, meaning that dynamic stall effects are not significant, as also confirmed by Mendoza et al. [7]. For the VAWT blade angle of attack with the measured airfoil characteristics, the static $C_{L\max}$ is never reached for both the clean airfoil and the zigzag configuration, $\alpha_{\text{crit}} = 13.92°$ (Fig. 5).

The differences between all curves are also insignificant in the downwind part, although they are slightly larger than in the upwind part. For the azimuth range of $\theta \approx 260° - 280°$, there is a slight deviation in the angle of attack characteristics calculated for the S&K case compared to the results of Mendoza et al. [7]. This discrepancy arises only because the effect of the rotating tower is not considered in our simulations. However, even without accounting for this effect, the

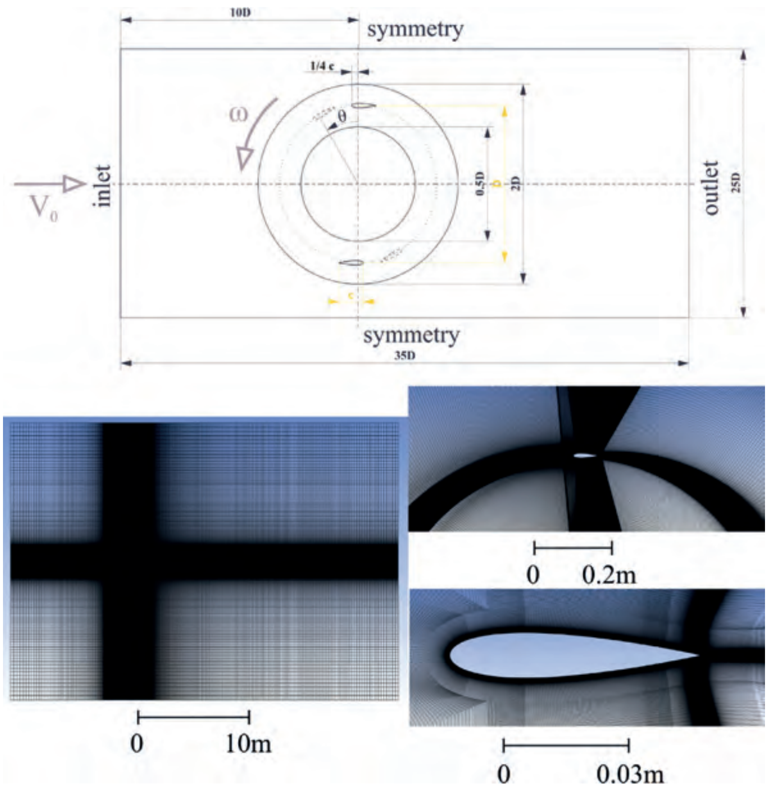

Fig. 9. Computational domain and numerical grid for 2-D CFD simulations. The top scheme illustrates the overall computational domain with boundary conditions and key dimensions. The bottom left image shows a cross-sectional view of the mesh, while the bottom right images provide detailed views of the mesh refinement around the blade.

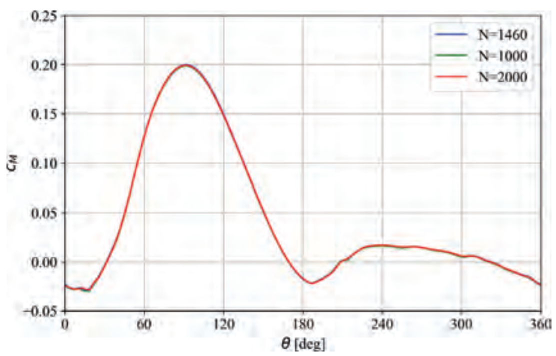

Fig. 10. Instantaneous moment coefficient from 2-D CFD simulations. Mesh sensitivity test. N is the number of nodes on the airfoil edges.

differences between our calculated results and those from the literature are minimal.

The azimuth range corresponding to the largest differences in the angle of attack estimation is $\theta \approx 197° - 300°$. These differences are caused by the velocity field affected by the blade moving in the upwind part of the rotor and by the airfoil characteristics. The velocity field behind the clean airfoil is more disturbed due to laminar separation bubbles that form on the airfoil surfaces, shed vortices, and evolve in the wake, as also shown in Section 4.2. The differences between the blade and the sectional angle of attack are also more significant than in the upwind part of the rotor.

Since the rotor of the considered TU Delft VAWT operates at a TSR = 4.5, dynamic stall effects are not particularly significant. Therefore, the primary influence on the aerodynamic blade loads, namely the normal and tangential components shown in the non-dimensional form in Figs. 12 and 13, is exerted by the local angle of attack and static airfoil characteristics. The instantaneous sectional loads obtained using the 3-D ALM method and presented in these figures are additionally compared with the 2-D CFD predictions.

It is worth noting that the differences between the 2-D CFD results for the two turbulence models, the k-ω SST and the γ-Re_θ, are minimal, despite the noticeable differences in the static $C_L(\alpha)$ and $C_D(\alpha)$ characteristics generated by both models, as shown in studies by [16,20]. Similar conclusions regarding aerodynamic loads for this 2-D VAWT at TSR = 4.5 examined using SST-based turbulence models can be found in [10]. Determining the local angle of attack using the full 2-D CFD approach is quite challenging. Melani et al. [39], who attempted to determine the local angle of attack for the considered VAWT, concluded that the resulting angle of attack trends showed significant sensitivity to the chosen method, especially in the range of azimuths where the

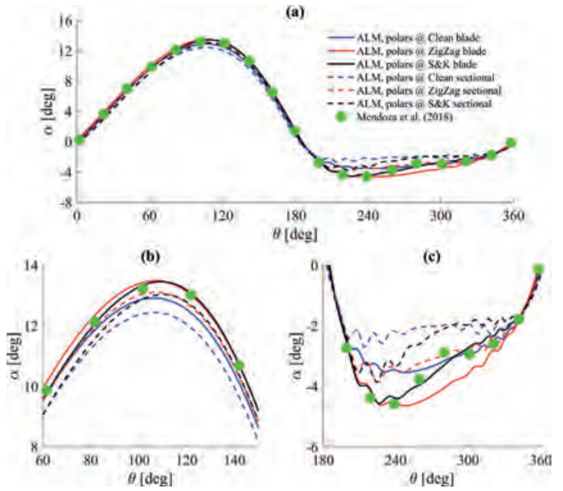

Fig. 11. Local angle of attack characteristics for the TU Delft VAWT. The results obtained by Mendoza et al. [7] using the LES approach are included for comparison.

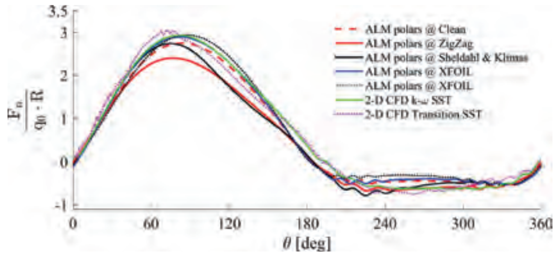

Fig. 12. Comparison of the normal force characteristics for the TU Delft VAWT using different airfoil polars and a 2-D CFD approach.

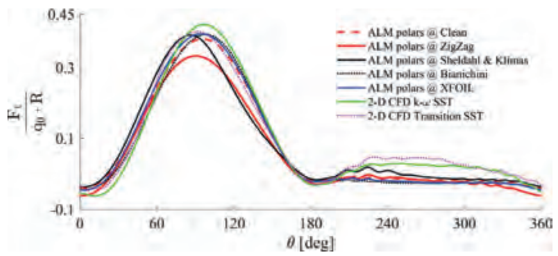

Fig. 13. Comparison of the tangential force characteristics for the TU Delft VAWT using different airfoil polars and a 2-D CFD approach.

blade angles of attack reach their maxima. Nevertheless, these authors demonstrated that, depending on the method used, the maximum local blade angle of attack ranges between 8 and 11 degrees. Therefore, the flow should be considered as mostly attached. Furthermore, within the angle of attack range of 8 to 11 degrees, the $C_L(\alpha)$ results obtained with the k-ω SST model are slightly higher compared to the γ-Re$_\theta$ approach, which explains the slight excess in tangential blade loads (Fig. 13). Laminar separation bubble effects captured by the γ-Re$_\theta$ model are evident in the aerodynamic load coefficients up to approximately $\theta \approx 80°$. It can be observed that the loads generated by the transition model are slightly greater, with small vortex structures appearing.

It should be emphasized that the differences between the results from the ALM with polars of the clean airfoil (excluding the S&K database) and 2-D CFD are minimal in the upwind part of the rotor, while they are somewhat larger in the downwind part. This results from the two different ways of modeling rotor flow: 3-D ALM and full 2-D CFD. In the downwind part, the 2-D CFD approach has the advantage of determining aerodynamic characteristics by considering local flow conditions. On the other hand, in the ALM approach, airfoil characteristics measured or calculated under low-turbulence conditions are used for the entire rotor revolution. However, the full 2-D CFD does not account for the influence of the third dimension. Huang [35] analyzed the TU Delft VAWT for various aspect ratios (AR) ranging from 1 to 10 (where $AR = H/D$) using the ALM approach. He showed that for AR = 10, the 3-D effects are much less significant. Therefore, it can be assumed that the aerodynamic loads in the downwind part of a 3-D rotor will be smaller than suggested by the 2-D CFD model, as also demonstrated by Lam and Peng [6].

The aerodynamic blade loads obtained for airfoil characteristics with zigzag tape differ the most from the others but are qualitatively the closest to the blade loads computed using the S&K database. The differences arise from the balance between the lift and drag coefficients. As shown in the experimental section, the airfoil with the zigzag tape maintains the maximum lift coefficient at the level of the clean airfoil's C_{Lmax}. Still, the lift is significantly lower below the critical angle of attack. Since, as discussed in the paragraph on the local angle of attack, the static critical angle of attack is not exceeded, the rotor blade at TSR = 4.5 operates at much lower C_L and simultaneously at higher C_D than the clean blade. This finding explains the much lower maximum values of the tangential and normal force coefficients than the other characteristics. Due to the similar linear behavior of the lift coefficient in the case of the S&K database, the nature of the aerodynamic loads is similar to that of the zigzag configuration. However, the very low drag coefficients in the case of this database mean that the maximum aerodynamic loads are higher than the zigzag.

There are publications [25] showing that the k-ω SST turbulence model, treating the entire boundary layer as turbulent, can approximate the effect of zigzag tape or profile contamination to some extent. This particular example shows that the impact of the applied zigzag tape on airfoil performance is significant enough that attempting to model the effect of the tape using the 2-D CFD approach with the k-ω SST turbulence model yields results that are more similar to those of the clean airfoil.

To contextualize these findings further, it is worth noting that similar observations have been made in previous studies. For example, Mendoza [40] analyzed a 3-bladed 12 kW turbine operating at an optimal TSR of 3.44, comparing results obtained using two independent sources for airfoil polars: XFOIL and the S&K database. Their findings indicated that the C_P curve was significantly underestimated when using S&K data, while XFOIL results led to a slight overestimation. Despite the fact that the rotor diameter in Mendoza's study was more than six times larger than that of the TU Delft VAWT, the normal force results obtained for both polar sources showed qualitative agreement with our findings.

Furthermore, Mendoza [40] noted that the dynamic stall model (DMS) they applied tended to overestimate drag, which consequently led to an underestimation of the tangential force and thus lower C_P values. This aligns with our findings regarding the impact of different polar sources on aerodynamic loads, particularly for the zigzag configuration. These results reinforce the need for further refinements in dynamic stall modeling within the ALM framework to improve simulation accuracy.

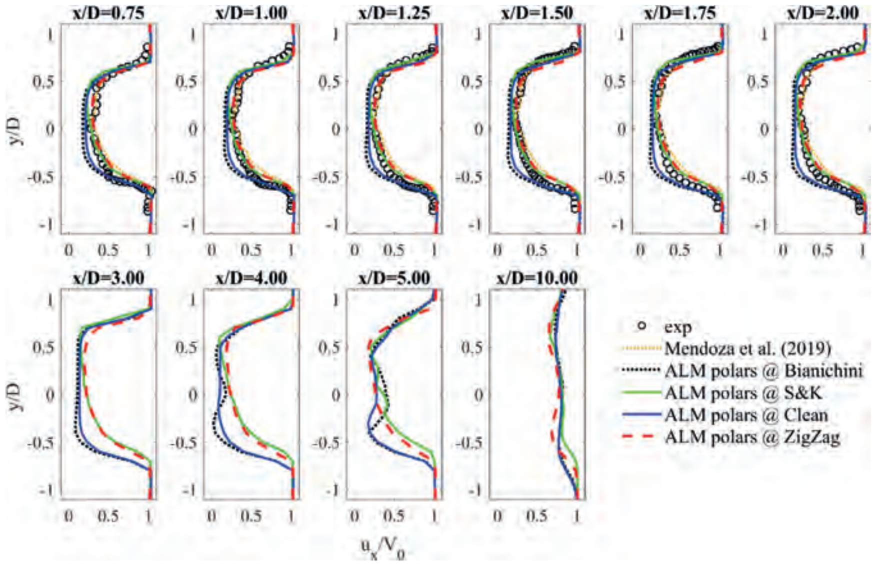

Fig. 14. Comparison of the normalized u_x velocity profiles at various distances x/D downstream of the rotor, obtained using the ALM with experimental results from [1] and velocity profiles from [7].

4.2. Velocity profiles in the aerodynamic wake

Fig. 14 compares the profiles of the average u_x velocity component normalized by the undisturbed flow velocity V_0 at various distances x/D downstream behind the rotor, obtained by the Actuator Line Model. In the experiment, the velocity profiles were recorded up to $x/D = 2.0$. Our paper extends this range to $x/D = 10$ to demonstrate the effect of the zigzag tape on the aerodynamic wake at a distance suitable for installing another wind turbine. For this comparison, we used two sets of polars from our experiment and two from the literature: Bianchini et al. [41] and Sheldahl and Klimas [14]. The velocity profiles from Mendoza et al. [7] were also used for comparison. The figure shows that the velocity profiles using S&K polars, calculated by both this study (green curve) and Mendoza et al. (orange dashed curve), are similar. The minor differences in these profiles are likely due to the influence of the rotating shaft and struts, which were not included in our simulations. This conclusion is supported by Huang et al. [42], who also neglected the struts and supporting towers in their simulations of the TU Delft VAWT. The velocity results show the asymmetry of u_x profiles around $y/D = 0$ for the S&K polars and zigzag tape, compared to the clean profile, which is due to vortex structures generated on the profile with the free transition. Fig. 14 shows that, for a turbine operating in the wake of another, this effect can be significant at $x/D > 1.75$. As shown in Fig. 15, the profile's surface condition has little impact on the lateral velocity component u_y in the wake. However, effects related to laminar bubbles remain noticeable at $x/D = 4$.

Fig. 16 shows the u_x velocity component distributed along lines parallel to the turbine shaft at several x/D positions. The ALM approach with S&K characteristics yields results similar to Mendoza et al. [7]. Up to $x/D = 1.0$, the ALM with both S&K and zigzag tape characteristics closely matches the experimental data. However, accuracy declines as x/D increases, likely due to modeling issues, such as boundary conditions and empirical relationships for a finite-length blade.

4.3. Velocity fields in the wake of a rotor

The previous subsection discussed velocity distributions along selected lines behind the rotor, showing that the zigzag tape increases wake asymmetry. This section presents instantaneous and averaged velocity fields in the rotor area to highlight further this asymmetry caused by the absence of laminar bubbles. The experiment by Tescione et al. [1] included PIV measurements of the velocity field in the rotor area, with an example of the instantaneous velocity u_x/V_0 shown in Fig. 17. The results of the ALM approach from Mendoza et al. [7] are presented alongside. Fig. 17 compares our ALM-derived velocity field distributions for the clean and zigzag tape configurations. Compared to Mendoza et al. [7], the slightly coarser grid reveals fewer details. For the clean profile, a wide, more symmetrical low-velocity region is visible compared to the zigzag tape results. Fig. 18 essentially shows the same results as Fig. 17, but it covers a much longer area behind the rotor, extending ten rotor diameters. The figure compares the instantaneous velocity u_x/V_0 for the clean profile and zigzag tape. From this perspective, two features are apparent: the aerodynamic wake is wider for the clean profile, and wake recovery occurs later for the zigzag tape profile.

Fig. 17 shows that both turbulence models in our 2-D CFD simulations yield similar results, closely matching those from the zigzag tape and the ALM approach by Mendoza et al. [7] using S&K data.

Fig. 19 provides another view of the velocity field behind the rotor, showing time-averaged streamwise velocity contours at various x/D locations. At $x/D = 10$, the wake recovers faster with S&K data and zigzag tape than with the clean airfoil. Closer positions, up to $x/D \approx 4.0$, reveal a higher velocity region for negative y/D.

5. Conclusions

The research presented in this paper focuses on investigating the impact of zigzag tape on the performance of the TU Delft VAWT and the aerodynamic wake downstream behind it. Numerical studies were conducted using the actuator line model and airfoil characteristics measured in the DTU wind tunnel. The conclusions drawn from this study are as follows:

- The measured aerodynamic characteristics of a rectangular wing with a NACA0018 airfoil, without the use of turbulators, show a strong nonlinearity in the $C_L(\alpha)$ characteristic, resulting from the formation of laminar bubbles on both the suction and pressure

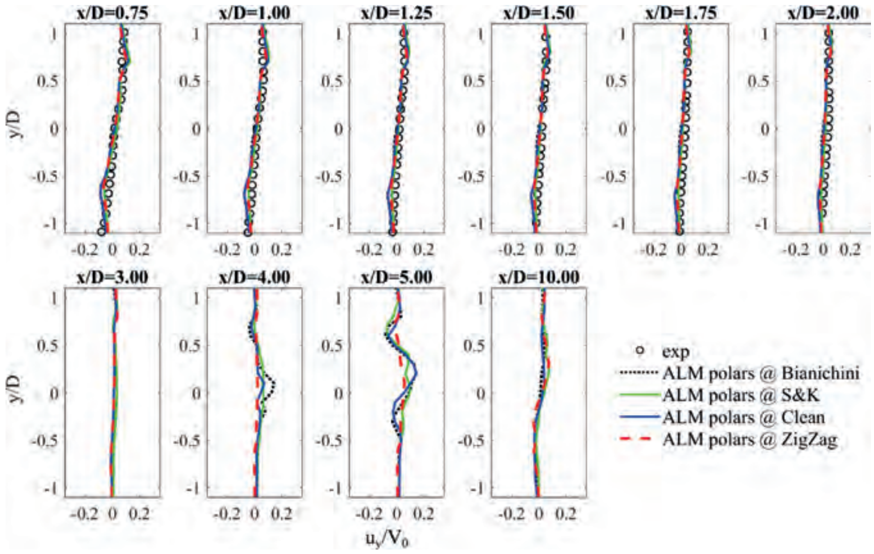

Fig. 15. Comparison of the normalized u_y velocity profiles at various distances x/D downstream of the rotor, obtained using the ALM, with experimental results from [1].

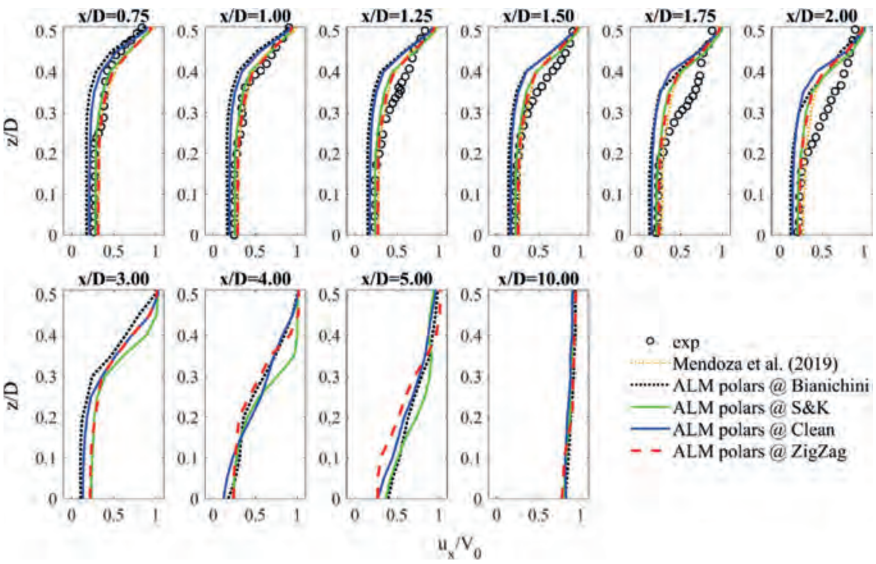

Fig. 16. Comparison of the normalized u_x velocity profiles at various distances x/D downstream of the rotor, obtained using the ALM, with experimental results from [1] and velocity profiles from [7].

sides of the airfoil. This indicates that the selected airfoil performs poorly under these flow conditions, especially at such a low Reynolds number. The application of turbulators allows for the linearization of the lift coefficient characteristic without a significant loss in the maximum C_L value. However, this procedure ultimately leads to a deterioration of the overall aerodynamic characteristics of the rotor, as the lift coefficient values below α_{crit} degrade significantly, and the presence of turbulators generates substantial additional drag.

- The zigzag tape, despite "linearizing" the static lift coefficient characteristic without reducing the maximum lift, significantly lowers the aerodynamic loads on the rotor blades operating at a tip-speed ratio where high aerodynamic efficiency, i.e., a high power coefficient, is expected. It also leads to a substantial change in the wake velocity field behind the rotor.
- The zigzag tape, in addition to controlling flow separation on the airfoil, can also be used to emulate surface contamination caused by factors such as insects, dust, etc. A tape of such a large

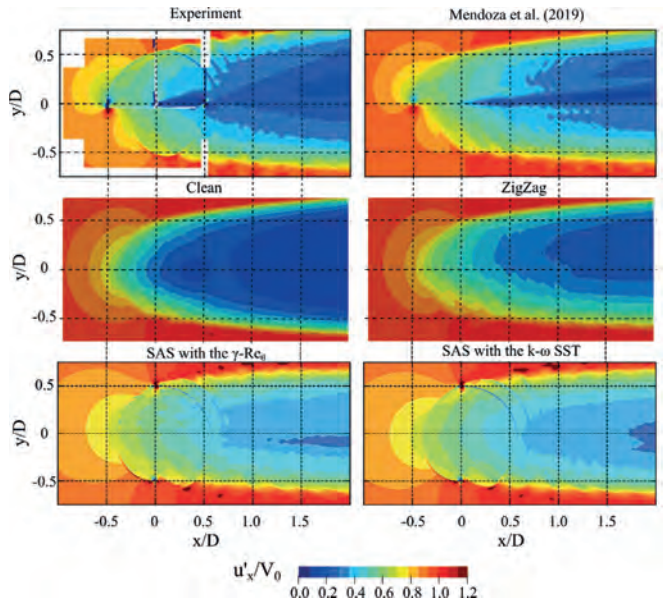

Fig. 17. Contour plots of the normalized instantaneous u'_x/V_0 velocity component in the turbine wake for clean and zigzag tape configurations. The top row compares PIV measurements with the ALM model from [7], the middle row shows velocity distributions for both configurations, and the bottom row presents 2-D CFD results.

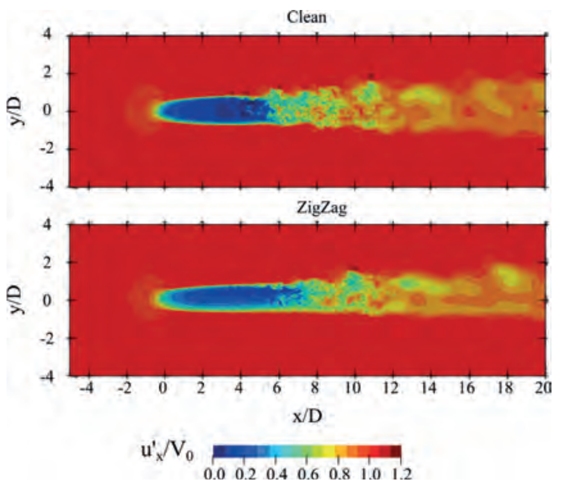

Fig. 18. Contour plots of the normalized instantaneous u'_x/V_0 velocity component in the far wake downstream behind the rotor.

size relative to the blade's chord length can simulate a case of rather extreme surface contamination. Therefore, the results of this study can be considered as a test for such situations.

- The analysis shows that the differences in the angle of attack estimation are generally small, especially in the upwind section of the rotor. Higher angles of attack are observed for the S&K database and zigzag configurations, while the clean airfoil has a slightly lower maximum angle of attack. The static maximum lift coefficient is not reached for the measured airfoil characteristics, regardless of the clean or zigzag configurations. The most significant differences in estimating the angle of attack occur in the downwind azimuth range, which is influenced by the velocity field and airfoil characteristics. These differences are primarily caused by the more disturbed velocity field in the clean airfoil case due to the laminar separation bubbles.
- The 2-D CFD results indicate little difference between the turbulence models used, even though the static airfoil characteristics vary between them. The *k*-*ω* SST model produces slightly higher lift coefficients compared to the γ-Re$_\theta$ model within the relevant angle of attack range, which explains the minor increase in tangential blade loads. Overall, the flow around the blade should be considered mostly attached, and the laminar separation bubble effects are visible only in the early stages of the rotor cycle.
- The comparison between ALM and 2-D CFD shows that the aerodynamic blade loads are very similar in the upwind part of the rotor but differ more in the downwind section. This difference arises from the 3-D ALM approach considering blade characteristics under low turbulence, whereas the 2-D CFD accounts for local flow conditions. Although 2-D CFD does not capture 3-D effects, existing studies suggest that the actual 3-D aerodynamic loads in the downwind section may be lower than predicted by the 2-D model.
- The nonlinear lift characteristic results from the formation of laminar separation bubbles on the airfoil surface. This leads to a "fuller" and more symmetric aerodynamic wake compared to the case with a linear lift characteristic. The turbulization of the boundary layer also causes the appearance of a small side force acting on the rotor.

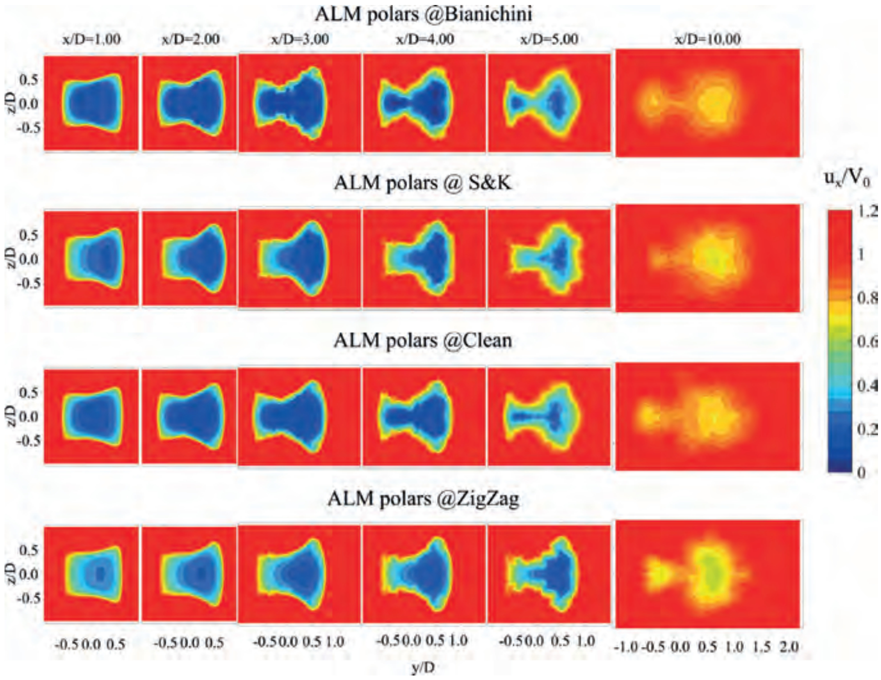

Fig. 19. Contours of normalized streamwise velocity and in-plane velocity fields from 1 to 10 *D* downstream of the VAWT velocity downstream behind the rotor.

CRediT authorship contribution statement

Krzysztof Rogowski: Writing – review & editing, Writing – original draft, Visualization, Validation, Supervision, Software, Resources, Project administration, Methodology, Investigation, Funding acquisition, Formal analysis, Data curation, Conceptualization. **Jan Michna:** Writing – review & editing, Writing – original draft, Visualization, Validation, Software, Methodology, Formal analysis, Data curation, Conceptualization. **Robert Flemming Mikkelsen:** Writing – review & editing, Writing – original draft, Validation, Methodology, Investigation, Data curation, Conceptualization. **Carlos Simao Ferreira:** Writing – review & editing, Writing – original draft, Supervision, Conceptualization.

Declaration of competing interest

The authors declare that they have no known competing financial interests or personal relationships that could have appeared to influence the work reported in this paper.

Acknowledgments

This research was also conducted with the assistance of the Interdisciplinary Centre for Mathematical and Computational Modeling (ICM) at the University of Warsaw under computational allocations no. G93-1588 and G92-1487.

Data availability

No data was used for the research described in the article.

References

[1] Tescione G, Ragni D, He C, Simão Ferreira CJ, van Bussel GJW. Near wake flow analysis of a vertical axis wind turbine by stereoscopic particle image velocimetry. Renew Energy 2014;70:47–61. http://dx.doi.org/10.1016/j.renene.2014.02.042.

[2] Rezaeiha A, Montazeri H, Blocken B. Towards optimal aerodynamic design of vertical axis wind turbines: Impact of solidity and number of blades. Energy 2018;165:1129–48. http://dx.doi.org/10.1016/j.energy.2018.09.192.

[3] Rezaeiha A, Montazeri H, Blocken B. Active flow control for power enhancement of vertical axis wind turbines: Leading-edge slot suction. Energy 2019;189:116131. http://dx.doi.org/10.1016/j.energy.2019.116131.

[4] Rogowski K. CFD computation of the H-Darrieus wind turbine—The impact of the rotating shaft on the rotor performance. Energies 2019;12(13):2506. http://dx.doi.org/10.3390/en12132506.

[5] Cacciali L, Hansen MOL, Rogowski K. Highly stable lattice Boltzmann method with a 2-D Actuator Line Model for Vertical Axis Wind Turbines. Energies 2024;17(19):4847. http://dx.doi.org/10.3390/en17194847.

[6] Lam H, Peng H. Study of wake characteristics of a vertical axis wind turbine by two- and three-dimensional computational fluid dynamics simulations. Renew Energy 2016;90:386–98. http://dx.doi.org/10.1016/j.renene.2016.01.011.

[7] Mendoza V, Bachant P, Ferreira C, Goude A. Near-wake flow simulation of a vertical axis turbine using an actuator line model. Wind Energy 2019;22(2):171–88. http://dx.doi.org/10.1002/we.2277.

[8] Melani PF, Balduzzi F, Ferrara G, Bianchini A. Tailoring the actuator line theory to the simulation of vertical-axis wind turbines. Energy Convers Manage 2021;243:114422. http://dx.doi.org/10.1016/j.enconman.2021.114422.

[9] Castelein D, Tescione G, Ragni D, Simao Ferreira C, Gaunaa M. Creating a benchmark of vertical axis wind turbines in dynamic stall for validating numerical models. In: 33rd Wind energy symposium. AIAA sciTech forum, American Institute of Aeronautics and Astronautics; 2015, http://dx.doi.org/10.2514/6.2015-0723.

[10] Rezaeiha A, Montazeri H, Blocken B. On the accuracy of turbulence models for CFD simulations of vertical axis wind turbines. Energy 2019;180:838–57. http://dx.doi.org/10.1016/j.energy.2019.05.053.

[11] Mueller TJ. Fixed and flapping wing aerodynamics for micro air vehicle applications. Reston ,VA: American Institute of Aeronautics and Astronautics; 2001, http://dx.doi.org/10.2514/4.866654.

[12] Winslow J, Otsuka H, Govindarajan B, Chopra I. Basic understanding of airfoil characteristics at low Reynolds numbers (104–105). J Aircr 2018;55(3):1050–61. http://dx.doi.org/10.2514/1.C034415.

[13] Jacobs EN, Sherman A. Airfoil section characteristics as affected by variations of the reynolds number. Technical report NACA-TR-586, Langley Field, VA, USA: National Advisory Committee for Aeronautics; 1937, p. 227–67.
[14] Sheldahl RE, Klimas PC. Aerodynamic characteristics of seven symmetrical airfoil sections through 180-degree angle of attack for use in aerodynamic analysis of vertical axis wind turbines. Technical report SAND-80-2114, Sandia National Lab.(SNL-NM), Albuquerque, NM (United States); 1981, http://dx.doi.org/10.2172/6548367.
[15] Paraschivoiu I. Wind turbine design: with emphasis on Darrieus concept. Presses inter Polytechnique; 2002.
[16] Rogowski K, Królak G, Bangga G. Numerical study on the aerodynamic characteristics of the NACA 0018 airfoil at low reynolds number for darrieus wind turbines using the transition SST model. Processes 2021;9(3):477. http://dx.doi.org/10.3390/pr9030477.
[17] Bianchini A, Balduzzi F, Rainbird JM, Peiro J, Graham JMR, Ferrara G, et al. An experimental and numerical assessment of airfoil polars for use in darrieus wind turbines—Part I: Flow curvature effects. J Eng Gas Turbines Power 2015;138(3):032602. http://dx.doi.org/10.1115/1.4031269.
[18] Melani PF, Balduzzi F, Ferrara G, Bianchini A. An annotated database of low Reynolds aerodynamic coefficients for the NACA0018 airfoil. In: AIP conference proceedings, vol. 2191. Erode, India: American Institute of Physics; 2019, 020110. http://dx.doi.org/10.1063/1.5138843.
[19] Gerakopulos R, Boutilier M, Yarusevych S. Aerodynamic characterization of a NACA 0018 airfoil at low Reynolds numbers. In: 40th Fluid dynamics conference and exhibit. Fluid dynamics and co-located conferences, Chicago, Illinois: American Institute of Aeronautics and Astronautics; 2010, p. 4629. http://dx.doi.org/10.2514/6.2010-4629.
[20] Michna J, Rogowski K. Numerical study of the effect of the Reynolds number and the turbulence intensity on the performance of the NACA 0018 Airfoil at the low Reynolds number regime. Processes 2022;10(5):1004. http://dx.doi.org/10.3390/pr10051004.
[21] Boutilier MS, Yarusevych S. Parametric study of separation and transition characteristics over an airfoil at low Reynolds numbers. Exp Fluids 2012;52:1491–506. http://dx.doi.org/10.1007/s00348-012-1270-z.
[22] Zhang Y, Van Zuijlen A, Van Bussel G. The MEXICO rotor aerodynamic loads prediction: ZigZag tape effects and laminar-turbulent transition modeling in CFD. J Wind Eng Ind Aerodyn 2017;168:152–63. http://dx.doi.org/10.1016/j.jweia.2017.06.002.
[23] Timmer W. Two-dimensional low-Reynolds number wind tunnel results for airfoil NACA 0018. Wind Eng 2008;32(6):525–37. http://dx.doi.org/10.1260/030952408787548848.
[24] Rezaeiha A, Montazeri H, Blocken B. On the accuracy of turbulence models for CFD simulations of vertical axis wind turbines. Energy 2019;180:838–57. http://dx.doi.org/10.1016/j.energy.2019.05.053.
[25] Kruse EK, Sørensen NN, Bak C. Predicting the influence of surface protuberance on the aerodynamic characteristics of a NACA 63_3 -418. J Phys: Conf Series 2018;1037:022008. http://dx.doi.org/10.1088/1742-6596/1037/2/022008.
[26] Rogowski K, Mikkelsen RF, Michna J, Wiśniewski J. Aerodynamic performance analysis of NACA 0018 airfoil at low Reynolds numbers in a low-turbulence wind tunnel. Adv Sci Technol Res J 2025;19:136–50. http://dx.doi.org/10.12913/22998624/195556.
[27] Sørensen JN, Shen WZ. Computation of wind turbine wakes using combined Navier-Stokes/actuator-line methodology. In: Proceedings of the 1999 European wind energy conference and exhibition. Nice, France: Routledge; 1999, p. 156–9.
[28] Bachant P, Goude A, daa-mec, Wosnik M. Turbinesfoam/turbinesfoam: v0.1.1. 2019, http://dx.doi.org/10.5281/zenodo.3542301, Version v0.1.1.
[29] Leishman JG, Beddoes TS. A semi-empirical model for dynamic stall. J Am Helicopter Soc 1989;34(3):3–17. http://dx.doi.org/10.4050/JAHS.34.3.3.
[30] Sheng W, Galbraith RA, Coton FN. Improved Dynamic-Stall-Onset criterion at low Mach numbers. J Aircr 2007;44(3):1049–52. http://dx.doi.org/10.2514/1.29163.
[31] Dyachuk E, Goude A, Bernhoff H. Dynamic stall modeling for the conditions of vertical axis wind turbines. AIAA J 2014;52(1):72–81. http://dx.doi.org/10.2514/1.J052633.
[32] Mendoza V, Bachant P, Wosnik M, Goude A. Validation of an actuator line model coupled to a dynamic stall model for pitching motions characteristic to vertical axis turbines. J Phys Conf Ser 2016;753(2):022043. http://dx.doi.org/10.1088/1742-6596/753/2/022043.
[33] Bachant P, Goude A, Wosnik M. Actuator line modeling of vertical-axis turbines. 2018, http://dx.doi.org/10.48550/arXiv.1605.01449, arXiv, URL https://arxiv.org/abs/1605.01449, arXiv:1605.01449.
[34] Nordlund M, Stanic M, Kuczaj A, Frederix E, Geurts B. Improved PISO algorithms for modeling density varying flow in conjugate fluid–porous domains. J Comput Phys 2016;306:199–215. http://dx.doi.org/10.1016/j.jcp.2015.11.035.
[35] Huang M. Wake and wind farm aerodynamics of vertical axis wind turbines [Ph.D. thesis], Delft University of Technology; 2023, http://dx.doi.org/10.4233/uuid:14619578-e44f-45bb-a213-a9d179a54264.
[36] Rogowski K, Michna J, Ferreira CS. Numerical analysis of aerodynamic performance of a fixed-pitch Vertical Axis Wind Turbine rotor. Adv Sci Technol Res J 2024;18(6):97–109. http://dx.doi.org/10.12913/22998624/191128.
[37] Rezaeiha A, Kalkman I, Blocken B. CFD simulation of a vertical axis wind turbine operating at a moderate tip speed ratio: Guidelines for minimum domain size and azimuthal increment. Renew Energy 2017;107:373–85. http://dx.doi.org/10.1016/j.renene.2017.02.006.
[38] ANSYS fluent theory guide, release 2023 R2. ANSYS Inc.; 2023.
[39] Melani PF, Balduzzi F, Brandetti L, Ferreira CS, Bianchini A. An experimental and numerical analysis of the dynamic variation of the angle of attack in a vertical-axis wind turbine. J Phys Conf Ser 2020;1618(5):052064. http://dx.doi.org/10.1088/1742-6596/1618/5/052064.
[40] Mendoza V. Aerodynamic studies of vertical axis wind turbines using the actuator line model. [Ph.D. thesis], Uppsala, Sweden: Uppsala: Acta Universitatis Upsaliensis; 2018.
[41] Bianchini A, Balduzzi F, Rainbird JM, Peiro J, Graham JMR, Ferrara G, et al. An experimental and numerical assessment of airfoil polars for use in darrieus wind turbines—Part II: Post-stall data extrapolation methods. J Eng Gas Turbines Power 2015;138(3):032602. http://dx.doi.org/10.1115/1.4031269.
[42] Huang M, Ferreira C, Sciacchitano A, Scarano F. Wake scaling of actuator discs in different aspect ratios. Renew Energy 2022;183:866–76. http://dx.doi.org/10.1016/j.renene.2021.11.045.

B Co-Authors' statements

In the next pages, all co-authors' statements describing detailed contributions are attached.

September 25, 2025

Declaration

I hereby declare that the contribution to the following paper:

Michna, J., Rogowski, K., Bangga, G., & Hansen, M. O. L. (2021). Accuracy of the Gamma Re-Theta Transition Model for Simulating the DU-91-W2-250 Airfoil at High Reynolds Numbers. *Energies*, *14*(24), Article 24. https://doi.org/10.3390/en14248224

is correctly characterized below:

KR prepared a concept of the paper. JM prepared and processed the CFD ANSYS analysis with KR supervising. GB prepared and processed the CFD STAR-CCM+ analysis. MOLH prepared and processed the CFD FLOWer analysis. KR prepared and processed the XFOIL analysis. JM and KR processed and validated the results with the preparation of visualizations. KR prepared the original draft. KR, JM, GB and MOLH reviewed and made text adjustments. GB and MOLH supervised the study. All authors read and approved the final manuscript.

Name	Abbreviation	Signature
Jan Michna	JM	Jan Michna
Krzysztof Rogowski	KR	Krzysztof Rogowski
Galih Bangga	GB	
Martin O. L. Hansen	MOLH	[illegible]

September 25, 2025

Declaration

I hereby declare that the contribution to the following paper:

Michna, J., & Rogowski, K. (2022). Numerical Study of the Effect of the Reynolds Number and the Turbulence Intensity on the Performance of the NACA 0018 Airfoil at the Low Reynolds Number Regime. *Processes*, *10*(5), Article 5. https://doi.org/10.3390/pr10051004

is correctly characterized below:

KR prepared a concept of the paper. JM prepared and processed the CFD ANSYS analysis with KR supervising. JM and KR processed and validated the results with the preparation of visualizations. KR prepared the original draft. KR and JM reviewed and made text adjustments. KR supervised the study. All authors read and approved the final manuscript.

Name	Abbreviation	Signature
Jan Michna	JM	
Krzysztof Rogowski	KR	

September 25, 2025

Declaration

I hereby declare that the contribution to the following paper:

Rogowski, K., Mikkelsen, R. F., Michna, J., & Wiśniewski, J. (2025). Aerodynamic performance analysis of NACA 0018 airfoil at low Reynolds numbers in a low-turbulence wind tunnel. *Advances in Science and Technology. Research Journal*, *19*(2), 136–150. https://doi.org/10.12913/22998624/195556

is correctly characterized below:

KR prepared the concept of this paper. JW prepared the airfoil model for the experiment. KR and RFM run the experiments in the wind tunnel. JM prepared and processed CFD simulations. KR and JM processed and validated the results. KR, JM and RFM prepared the original draft. KR, JM, RFM and JW reviewed and made text adjustments. All authors read and approved the final manuscript.

Name	Abbreviation	Signature
Krzysztof Rogowski	KR	Krzysztof Rogowski
Robert Mikkelsen	RFM	Robert Mikkelsen
Jan Michna	JM	Jan Michna
Jan Wiśniewski	JW	Jan Wiśniewski

September 25, 2025

Declaration

I hereby declare that the contribution to the following paper:

Michna, J., Śledziewski, M., & Rogowski, K. (2025). The Harmonic Pitching NACA 0018 Airfoil in Low Reynolds Number Flow. *Energies*, *18*(11), Article 11. https://doi.org/10.3390/en18112884

is correctly characterized below:

KR, JM and MS prepared the concept of the paper. MS prepared and processed the CFD ANSYS analysis with KR and JM supervising. MS, JM and KR processed and validated the results with the preparation of visualizations. KR, JM and MS prepared the original draft. KR, JM, and MS reviewed and made text adjustments. KR and JM supervised the study. All authors read and approved the final manuscript.

Name	Abbreviation	Signature
Jan Michna	JM	Jan Michna
Maciej Śledziewski	MS	Maciej Śledziewski
Krzysztof Rogowski	KR	Krzysztof Rogowski

September 25, 2025

Declaration

I hereby declare that the contribution to the following paper:

Rogowski, K., Michna, J., & Ferreira, C. S. (2024). Numerical Analysis of Aerodynamic Performance of a Fixed-Pitch Vertical Axis Wind Turbine Rotor. *Advances in Science and Technology Research Journal*, *18*(6), 97–109. https://doi.org/10.12913/22998624/191128

is correctly characterized below:

KR, JM, and CSF prepared the concept of the paper. KR prepared and processed the CFD ANSYS analysis. KR and JM processed and validated the results with the preparation of visualizations. KR and JM prepared the original draft. KR, JM and CSF reviewed and made text adjustments. CSF supervised the study. All authors read and approved the final manuscript.

Name	Abbreviation	Signature
Krzysztof Rogowski	KR	Krzysztof Rogowski
Jan Michna	JM	Jan Michna
Carlos Ferreira	CSF	

September 25, 2025

Declaration

I hereby declare that the contribution to the following paper:

Michna, J., & Rogowski, K. (2024). A Refined Approach for Angle of Attack Estimation and Dynamic Force Hysteresis in H-Type Darrieus Wind Turbines. *Energies*, *17*(24), Article 24. https://doi.org/10.3390/en17246264

is correctly characterized below:

KR and JM prepared a concept of the paper. KR and JM prepared and processed the CFD ANSYS analysis. JM prepared scripts for the Angle of Attack Estimation Algorithm. JM and KR processed and validated the results with the preparation of visualizations. KR and JM prepared the original draft. KR and JM reviewed and made text adjustments. KR supervised the study. All authors read and approved the final manuscript.

Name	Abbreviation	Signature
Jan Michna	JM	
Krzysztof Rogowski	KR	

September 25, 2025

Declaration

I hereby declare that the contribution to the following paper:

Rogowski, K., Michna, J., Mikkelsen, R. F., & Ferreira, C. S. (2025). Impact of zigzag tape on blade loads and aerodynamic wake in a vertical axis wind turbine: A Delft VAWT case study. *Energy*, *321*, 135344. https://doi.org/10.1016/j.energy.2025.135344

is correctly characterized below:

KR, JM, RFM and CSF prepared a concept of the paper. KR and RFM run the experiments in the wind tunnel. JM prepared and processed the CFD ANSYS analysis. KR prepared and processed the ALM CFD ANSYS analysis. KR, RFM and JM analyzed and validated the results. JM and KR processed the results and prepared visualizations. KR, JM, RFM and CSF prepared the original draft. KR, JM, RFM and CSF reviewed and made text adjustments. KR and CSF supervised the study. All authors read and approved the final manuscript.

Name	Abbreviation	Signature
Krzysztof Rogowski	KR	Krzysztof Rogowski
Jan Michna	JM	Jan Michna
Robert Mikkelsen	RFM	Robert Mikkelsen
Carlos Ferreira	CSF	

C Copies of the publications not included in the dissertation

At the end, the copies of the author's publications not included in the dissertation are attached.

Michna and Rogowski (2023)

Title: "CFD Calculations of Average Flow Parameters around the Rotor of a Savonius Wind Turbine"

Authors: Jan Michna, Krzysztof Rogowski

Journal: Energies *16*,281 **Date:** January 2023 **MNiSW:** 140 pts

DOI: https://doi.org/10.3390/en16010281

Michna et al. (2024)

Title: "Investigation of aerodynamic performance of the NACA 0018 airfoil at low Reynolds numbers: A comparative study of 2-D and 3-D models using Transition SST and K- ω SST approaches"

Authors: Jan Michna, Krzysztof Rogowski, Sławomir Kubacki

Conference: *READ 2024* **Date:** November 2024 **MNiSW:** — pts

URL: https://psaa.meil.pw.edu.pl/READ2024/Papers/paperID80.pdf

Rogowski et al. (2026)

Title: "DNS Dataset of a Thick Symmetric Airfoil at Low Reynolds Number"

Authors: Krzysztof Rogowski, Sławomir Kubacki, **Jan Michna**

Journal: *JAFM 19*,29–44 **Date:** February 2026 **MNiSW:** 70 pts

DOI: https://doi.org/10.47176/jafm.19.2.3738

energies

Article

CFD Calculations of Average Flow Parameters around the Rotor of a Savonius Wind Turbine

Jan Michna and Krzysztof Rogowski *

Institute of Aeronautics and Applied Mechanics, Warsaw University of Technology, 00-665 Warsaw, Poland
* Correspondence: krzysztof.rogowski@pw.edu.pl; Tel.: +48-506-19-39-19

Abstract: The geometry of a conventional two-bladed Savonius rotor was used in this study based on a report available in the literature. A two-dimensional rotor model consisting of two buckets and an overlap ratio of 0.1 was prepared. The unsteady Reynolds averaged Navier-Stokes (URANS) equations and the eddy-viscosity turbulence model SST k-ω were employed in order to solve the fluid motion equations numerically. Instantaneous velocities and pressures were calculated at defined points around the rotor and then averaged. The research shows that the operating rotor significantly modifies the flow on the downwind part of the rotor and in the wake, but the impact of the tip speed ratio on the average velocity distribution is small. This parameter has a much greater influence on the characteristics of the aerodynamic moment and the distribution of static pressure in the wake. In the upwind part of the rotor, the average velocity parallel to the direction of undisturbed flow is 29% lower than in the downwind part.

Keywords: Savonius; wind turbine; VAWT; CFD; RANS; turbulence

check for updates

Citation: Michna, J.; Rogowski, K. CFD Calculations of Average Flow Parameters around the Rotor of a Savonius Wind Turbine. *Energies* **2023**, *16*, 281. https://doi.org/10.3390/en16010281

Academic Editor: Davide Astolfi

Received: 1 December 2022
Revised: 23 December 2022
Accepted: 24 December 2022
Published: 27 December 2022

1. Introduction

In recent years, global concern about the consequences of exploiting fossil fuel resources has increased. Some of the effects of this exploitation include global warming and environmental pollution. One of the ways to protect the environment is to invest in renewable energy sources and decentralize energy sources. The Savonius wind turbine can be an alternative for distributed power generation.

The Savonius wind turbine rotor (Figure 1) is a fluid-mechanical device that many researchers have investigated since 1931 [1,2]. There are many different applications of this device, such as driving an electrical generator, providing ventilation, or due to high torque, pumping water. The Savonius rotor is also used to measure the velocity of ocean currents.

Due to the relatively low aerodynamic efficiency at tip speed ratios larger than one, they cannot compete with either a Darrieus or a propeller-type wind turbine. However, it has several advantages compared to typical horizontal axis wind turbines, such as high starting torque [3], low noise emission [4], the ability to operate under complex turbulent flows [5,6], and relatively simple construction at low cost [7,8]. The great interest in Savonius wind turbines is also due to their potential as hydrokinetic devices [9].

The aerodynamic performance of a conventional Savonius turbine depends, among other things, on the aspect ratio, the tips speed ratio, airflow parameters, the number of blades, the overlap, the turbine shaft, the number of steps, end plates, and, to a lesser extent, the Reynolds number [9–11]. Depending on these geometric, flow, and operational parameters, the aerodynamic efficiency of the device, the rotor power coefficient, may reach maximum values in the range of around 0.05–0.30 [12]. Generally, the Savonius wind turbine is a device whose axis of rotation is perpendicular to the direction of undisturbed flow (to the direction of the wind). The rotor uses drag to generate torque, although lift is also created on its blades as the rotor rotates. During the operation of the device, the aerodynamic forces acting on its buckets change cyclically during each full rotation of the rotor. Therefore, the torque created by the rotor, at a constant angular velocity, cyclically varies during the device's rotation [11].

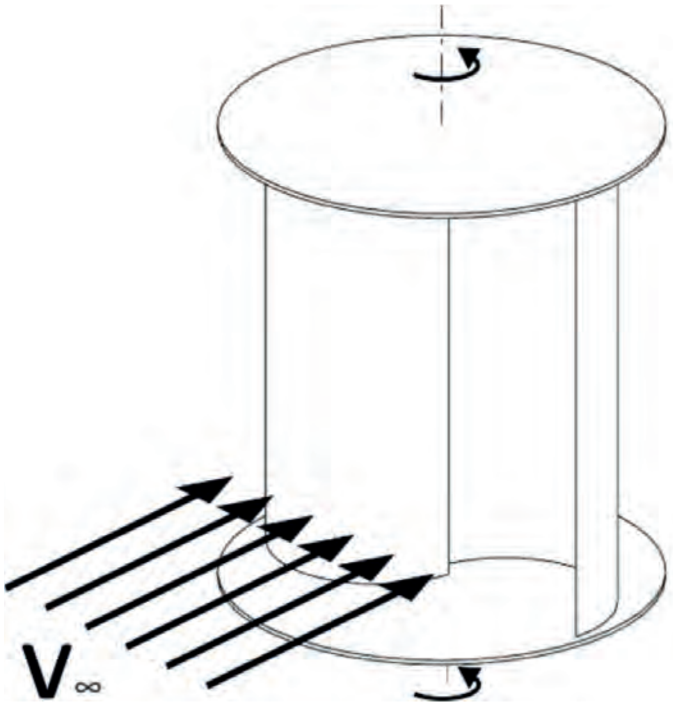

Figure 1. Silhouette of the Savonius wind turbine.

In recent years, thanks to the development of computational fluid dynamics techniques, researchers have devoted much attention to the analysis of the influence of the rotor geometric parameters on its performance. Among other things, the influence of the gap length, 3D effects, blade shapes, shaft, and stages were analyzed [12–14].

Zhou and Rempfer compared the aerodynamic performance of Bach and Savonius rotors using a two-dimensional unsteady numerical model [15]. Roy and Ducoin [16] analyzed the instantaneous lateral lift and longitudinal drag forces acting on each of the blades of the conventional and modified Savonius rotor. These authors also performed a time-dependent analysis of the flat flow around the rotors.

Unfortunately, a detailed analysis of the Savonius rotor flow around requires the use of three-dimensional numerical models. In recent years, such studies have been conducted, among others, by Jaohindy et al. [17], Mendoza et al. [18] or recently, Marinić-Kragić [19]. Jaohindy et al. [17] studied the transient aerodynamic loads acting on rotors with different aspect ratios. Mendoza et al. [18] studied the flow around Savonius wind turbines with twisted blades using OpenFOAM. Marinić-Kragić et al. [19] optimized the performance of the multi-blade rotor based on circular arc segments.

In the literature, there are also numerical–experimental studies of the performance of the Savonius wind turbine. Ferrari et al. [14] studied 2D and 3D models using the CFD code—OpenFOAM. These authors provided a tool for the geometric optimization of the rotor. In their work, these researchers analyzed, among other things, the influence of geometric parameters, such as rotor height, on the flow around the wind turbine rotor and its power coefficient. They also studied the influence of the tip speed ratio. Talukdar et al. [9] analyzed both numerically and experimentally the effect of the number of rotor blades on the performance of the Savonius hydrokinetic turbine. These researchers compared the aerodynamic efficiency of both two- and three-bladed rotors. They also investigated the performance of the elliptical blade rotor, confirming its inferior aerodynamic properties compared to a two-bladed Savonius hydrokinetic turbine with conventional semicircular blades. Nasef et al. [20], however, conducted experimental and numerical studies of the influence of the overlap ratio on the aerodynamic characteristics of Savonius. The authors of these studies managed to present, in addition to static and dynamic loads, pressure distributions along the walls. The influence of the buckets overlap ratio of a Savonius wind rotor was also analyzed numerically by Akwa et al. [12].

In recent years, there have also been many CFD studies aimed at improving the aerodynamic performance of Savonius by using various types of aerodynamic devices, such as, for example, deflectors [21] or a system of ducted nozzle [22]. El-Askary et al. [23] proposed three methods of controlling the wind direction around the area of the conventional Savonius wind turbine.

Other contemporary trends in the study of various types of wind turbines, including the Savonius wind turbine, are the investigation of their efficiency in the vicinity of various types of terrain obstacles that may occur, for example, in urbanized areas [24,25] and in wind farms [26,27].

The results obtained using CFD techniques may be sensitive due to the computational grid used and the choice of the turbulence model [28]. However, the ability to solve momentum equations on finite-volume grids makes it possible to analyze the performance of these devices with almost any rotor configuration operating in rugged terrain, for example, in urbanized areas [29,30].

The review of the literature presented above shows that many researchers in their work focus mainly on the analysis of the aerodynamic performance of the Savonius wind turbine—the torque coefficient and the power coefficient of the rotor. The causes of some physical transient phenomena, such as vortex structures flowing off the rotor blades, are explained in these works using instantaneous distributions of flow parameters such as velocity and pressure. Understanding the nature of the flow of such a complicated device as the Savonius wind turbine, however, requires an in-depth study of the fields of both instantaneous and time-averaged flow parameters. To the best of the authors' knowledge, this paper is the first attempt to estimate the two velocity components, axial and lateral, in the vicinity of a Savonius wind turbine rotor. This work aims to determine what influence both velocity components have on flow deflection and how these values depend on the tip speed ratio. This work is extremely important for several reasons. Firstly, the results of the presented research allow for a deeper understanding of the impact of the two velocity components on the nature of the flow around the working rotor. Secondly, knowledge of the averaged values of velocities and pressures in the rotor area can significantly help in the design of additional devices that improve the efficiency of the rotor, such as deflectors. Third, this article proposes a new method for obtaining these averaged flow parameters. It is possible to use the same procedure for a Darrieus wind turbine and a classical horizontal axis wind turbine. This method, therefore, makes it possible to compare wind turbines of various types in terms of the distribution of averaged flow parameters in the rotor area.

2. Numerical Model of the Savonius Wind Turbine

2.1. Description of the Rotor

Two-dimensional modeling for the geometry of the vertical-axis Savonius turbine in operation is performed in Figure 2. The rotor consists of two semicircular blades, whereas the dimensionless overlap ratio of this turbine, s/d, is equal to 0.10. The reason for choosing this overlap is the need to conduct a validation study based on the experimental results published in the report [10]. The dimensions of the vertical-axis Savonius turbine are given in Table 1.

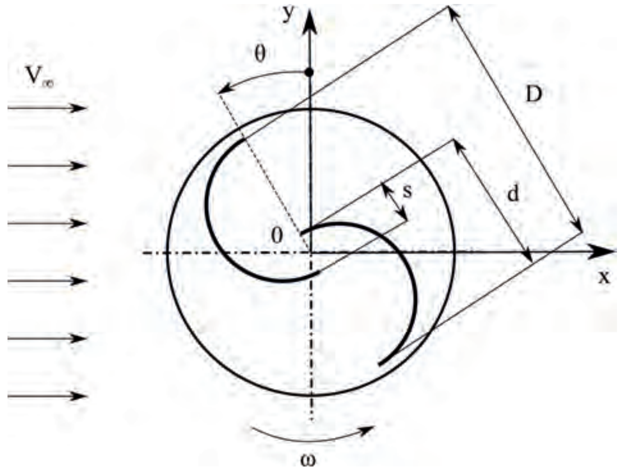

Figure 2. Conventional two-bladed Savonius wind turbine.

Table 1. Turbine dimensions.

Parameter	Value
blade/bucket diameter, d [m]	0.5
number of buckets, N	2
diameter of the turbine, D [m]	0.95
overlap ratio, OR	0.1
sheet thickness, δ [m]	0.0005

2.2. Benchmark

In order to validate the CFD results, measurement data from the Sandia Laboratories report by Blackwell et al. were used [10,31]. The report by Blackwell et al. [10] is one of the older works on the aerodynamics of the Savonius wind turbine. However, the authors of this report put in a lot of effort to measure fifteen different rotor configurations in the wind tunnel. The aerodynamic performance of two- and three-bladed rotors was compared for different rotor heights, and different overlap ratios, for one- and two-stages and for two Reynolds numbers. The results of these measurements are a benchmark for many researchers [12–14,32–37]. Roy and Ducoin [16] compared the results of the average torque coefficient for three experiments by D'Alessandro et al. [38], Roy and Saha [39], and Blackwell et al. [10]. Although the experimental conditions for each reference were different, these compared characteristics are very similar. In the studies of Mereu et al. [27], C_P and C_Q coefficients were compared for 2D and 3D rotor models. It also turns out that the comparison of the results of numerical research using CFD methods with experimental results from different periods gives similar conclusions. That is, if the numerical model of the rotor is two-dimensional, then the obtained C_P values are overestimated in comparison with these experiments [9].

Research by Blackwell et al. was carried out for two Reynolds numbers 4.32×10^5 and 8.67×10^5. As this larger Reynolds number was much less often taken into account by researchers, all simulations presented in this paper have been performed for the larger Reynolds number. The Reynolds number is based on the rotor diameter and the bulk velocity:

$$Re = \frac{D \cdot V_\infty}{\nu} \quad (1)$$

where ν is the kinematic viscosity of air. The validation process is based on dynamic experimental data [10].

2.3. Rotor Aerodynamic Performance

The torque, Q, generated by the rotor at a constant angular velocity, ω, cyclically varies during the rotation of the rotor. The rotor power, P, which is directly related to the torque, is used to evaluate the efficiency of the device. In order to calculate the aerodynamic efficiency of the device, called the power factor C_P, the power, P, produced by the rotor should be divided by the power, $P_{available}$, available in the air stream flowing through the rotor cross-sectional area at the wind velocity V_∞:

$$C_P = \frac{P}{P_{available}} = \frac{Q\omega}{(1/2)\rho A V_\infty^3} = C_Q \cdot TSR \tag{2}$$

where: A is the area of the rotor projected at the flow direction, C_Q is the torque coefficient and TSR is the tip speed ratio. The last two values are defined, respectively, as follows:

$$C_Q = \frac{Q}{(1/2)\rho A R V_\infty^2} \tag{3}$$

$$TSR = \frac{\omega R}{V_\infty} \tag{4}$$

where R is the rotor radius. In this paper, the area A in Equations (2) and (3) is equal to:

$$A = (2d - s) \cdot H = (2d - s) \cdot 1 = 0.95 \text{ m}^2 \tag{5}$$

where: rotor high H in the present paper equals 1 m.

2.4. Computational Domain and Boundary Conditions

The computational domain consists of two parts: a rectangular fixed domain, and a circular rotating domain containing the wind turbine rotor, that rotates with the same angular velocity as the Savonius wind turbine. Too small a computational domain may affect the obtained aerodynamic characteristics. If the domain is not large enough and its boundaries are too close to the rotor, then air is artificially forced into the rotor because there is not enough room to flow around the turbine. This in turn causes an overestimation of the torque and aerodynamic efficiency of the device. Mohamed proved that the minimum distance from the rotor in each direction should be at least ten rotor diameters [40,41]. On this basis, in this study, a square computational domain, Figure 3, with a length of 12 m was selected for the simulation; therefore, the distance from the axis of rotation of the rotor to the boundaries of the domain is D/L = 12.63.

As shown in Figure 3, the velocity inlet boundary condition was assumed on the left vertical edge of the square domain, and on the right edge, the pressure outlet condition. On the other hand, the symmetry condition was defined on the upper and lower edges. The boundary condition "symmetry" can be employed to model zero-shear slip walls in viscous flows [42]. A circular sliding interface was used between the two parts of the domain, fixed and circular [11,12]. The distance between the rotor surfaces and the interface should be large enough that there are no errors in estimating distributions of vorticity [43,44]. To avoid numerical errors on the interface and their impact on the results of the velocity and pressure fields, the diameter of the circular part of the domain was set to 2 m. In Figure 4, the distributions of static pressure and velocity magnitude on the interfaces for the fixed and moving parts of the mesh are shown. This figure clearly shows that both the velocity and pressure profiles are the same on each mesh in the interface zone.

2.5. Solver Settings and Turbulence Model

For all 2D simulations presented in this paper, the time step size is equivalent to 1000 time steps per one complete revolution of the rotor, corresponding to 0.36° per time step. For unsteady Reynolds-averaged Navier-Stokes (URANS) simulations, the well-known SIMPLE algorithm was employed for pressure–velocity coupling. The gradients are computed employing the least-square cell-based method. All variables were calculated using second-order upwind schemes.

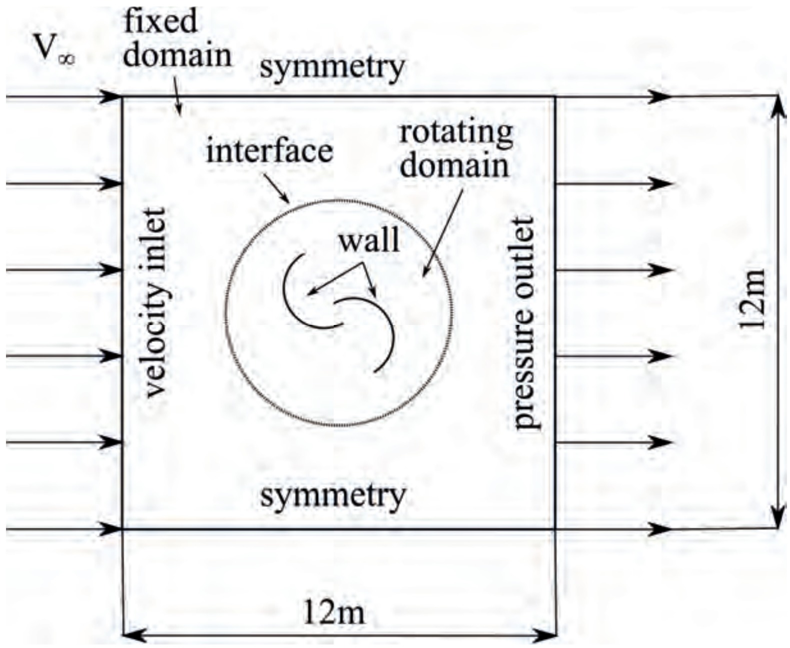

Figure 3. Computational domain and boundary conditions.

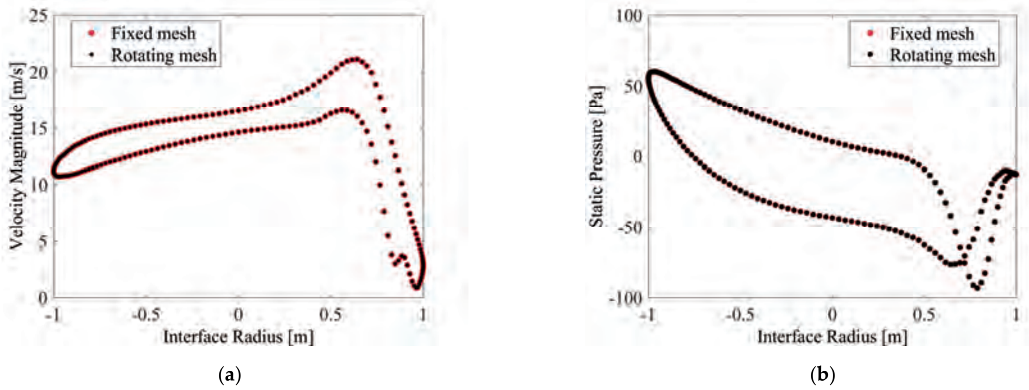

Figure 4. Flow parameters across the two sides of the interface zone: (**a**) Velocity profiles; (**b**) static pressure profiles.

In this paper, the average fields of flow parameters in the rotor area are analyzed for three tip speed ratios: 0.75, 1.00, and 1.25. Each of these tip speed ratios corresponds to a different angular velocity of the rotor; the angular velocities for individual tip speed ratios are, respectively, equal to 22.10, 29.47, and 36.84 rad/s. For all the analyses shown in this paper, fifteen full rotations of the rotor were simulated in order to avoid the effect of initial conditions.

Popular CFD solvers such as ANSYS Fluent offer their users a wide choice of different turbulence models. The most popular and most frequently chosen models are the k-ε and k-ω models. These are, of course, the basic variants of these models. In applications with rotating blades and when using unstructured meshes, modified variants of these models are highly recommended, e.g., the realizable k-ε model or the SST k-ω model that blends both k-ε and k-ω turbulence models. The SST k-ω approach was used in this work due to its stability and high accuracy in solving the boundary layer [29]. The governing equations of these turbulence models are not presented in this paper because they are clearly described in the documentation of CFD solvers offering this turbulence model.

2.6. Mesh Convergence Study

In order to determine an efficient mesh and to prevent divergence generated by an unsuitable mesh refinement strategy, a grid convergence study must be performed. In this paper, the computational domain was discretized using a hybrid mesh that consists of a quadrilateral structured mesh near the blades and a triangular unstructured mesh in the rest of the domain, as it is shown in Figure 5. The growth rate of the unstructured mesh was managed as 1.06; therefore, the grid density changed gradually, starting from the rotating domain. The structured part of the mesh was applied in order to capture the boundary layer viscous effects near the blades. The mesh first layer thickness from the blades was equal to 26 μm, which fulfills condition y+<1 required by turbulence models [40,45]. The number of structural mesh layers was 75, while the bias factor was 50. For a structured mesh, this bias factor corresponds to a growth rate of 1.06. We intended to provide a numerical grid that satisfies three assumptions at once: it will ensure small numerical dissipation of turbulence parameters between the inlet and the rotor; provides a smooth transition between structural and unstructured mesh elements; gives better numerical results of the wake behind the rotor. A grid independence study was performed for the three cases, as shown in Table 2. The three meshes used in the mesh sensitivity test differed in the number of nodes, N, on the edges of the rotor blades. The following three cases were investigated: $N = 500$, $N = 750$, and $N = 1000$. As can be seen from Table 2, the torque and power coefficients obtained for the coarse mesh are not significantly different from those for the fine mesh. Also, two publications proved that the number of nodes on the edges equal to 620 is sufficient for the solution to be independent of mesh density [46,47].

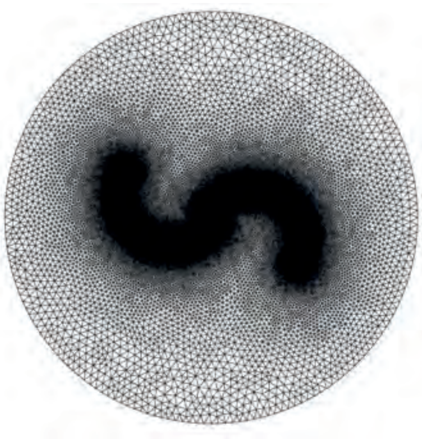

(**a**)

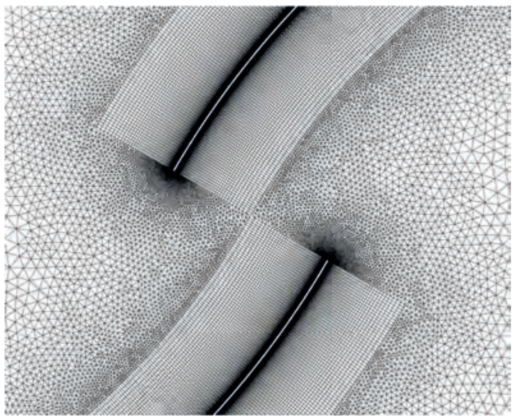

(**b**)

Figure 5. 2D mesh for two-bladed rotor: (**a**) Mesh of the rotating domain; (**b**) the zoom view on mesh details around the blade.

Table 2. Grid analysis.

Name	TSR	Cells	C_Q	C_P	Err
Fine	1	498,766	0.2815	0.2815	-
Medium	1	388,328	0.2810	0.2810	−0.16%
Coarse	1	277,898	0.2818	0.2818	0.11%

2.7. Validation

In these studies, the validation process was performed based on two data sources. The first source is the experiment [10] (Figure 6a,b), while the second is the numerical results from the publication [12] (Figure 7a,b). However, this second comparison is not direct because the results for a different value of the overlap ratio and a different value of the Reynolds number were compared. The second comparison makes sense, however, for two reasons. Firstly, Blackwell et al. [10] proved in their experiment that the differences in rotor aerodynamic performance are minimal for both Reynolds numbers 4.32 and 8.64. In Figure 6a,b, two sets of experimental data are summarized for these two Reynolds numbers. Second, the CFD results presented in this study were compared with two sets of numerical results by Akwa et al. [12]. These two datasets represent two overlap ratios of 0.0 and 0.15. These values are relatively close to those used in this study. As can be seen from Figure 6a,b, the nature of the numerical results is close to experimental. The obtained CFD values are also slightly different from the numerical results obtained by Akwa et al. [12], in particular, to those with an overlap ratio of 0.15.

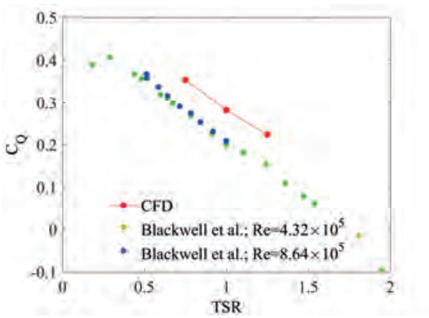

(**a**)

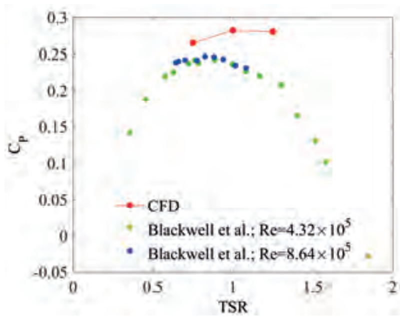

(**b**)

Figure 6. Comparison of CFD results with the experiment [10]: (**a**) Torque coefficient; (**b**) power coefficient.

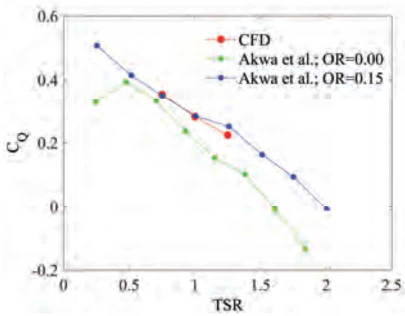

(**a**)

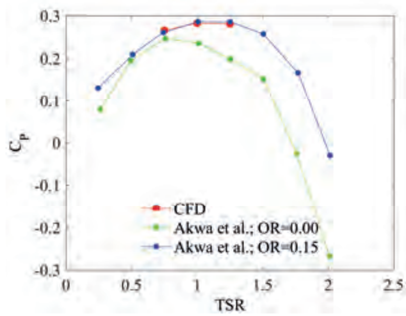

(**b**)

Figure 7. Comparison of CFD results with numerical results from [12]: (**a**) Torque coefficient; (**b**) power coefficient.

Also, significant differences in the CFD (2D model) and experimental results were also observed by, among others, Talukdar et al. [9]. These authors concluded that the dimensionality effect excluded during the CFD simulations may be responsible for this minor discrimination. Ferrari et al. [14] conducted CFD studies of one of the Blackwell et al. [10] configurations (overlap ratio of 0.2 and $Re = 4.32{\cdot}10^5$). Ferrari et al. [14] obtained similar accuracy of the numerical results for the 2D model compared to the experiment as the authors of this paper. Ferrari et al. proved that only the 3D model significantly improves the results.

2.8. Flow Parameters Averaging Method

The primary purpose of this paper is to examine the averaged fields of flow parameters in the rotor area and the wake downstream behind the rotor, depending on the tip speed ratio. The averaged flow parameters analyzed in this work are two components of air velocity and static pressure. In order to study these values, two series of points were defined, where these instantaneous flow parameters were calculated, which were then saved to a file and then averaged. One series of checkpoints was typically arranged behind the rotor, as shown in Figure 8a. The second one was located around the rotor every 10 degrees at the distance D/2+d (according to the dimensions given in Table 1) from the axis of rotation of the rotor—Figure 8b. The sampling rate, f, was:

$$f = \frac{18{\cdot}\omega}{\pi} \tag{6}$$

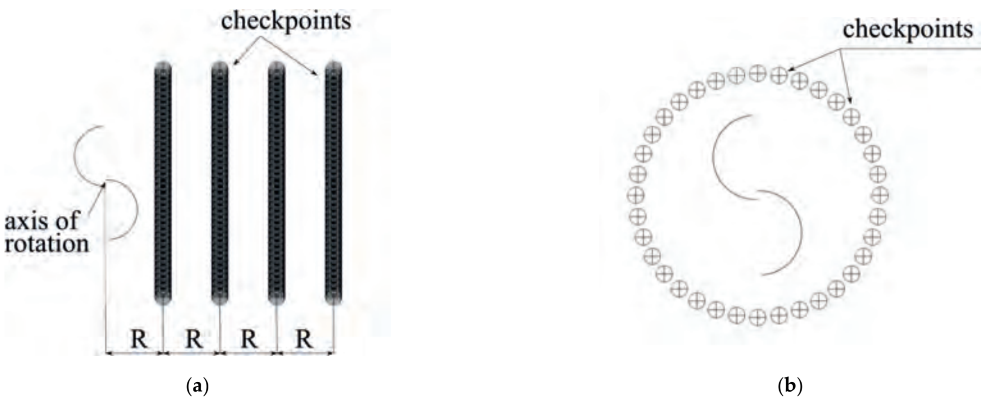

Figure 8. Checkpoints for recording speeds and pressures: (**a**) Points in the wake; (**b**) points around the rotor.

3. Results

3.1. Torque Coefficient and Forces Acting on the Rotor

The dimensionless torque and power coefficients shown in Figures 6 and 7 are, of course, the result of integrating the aerodynamic torque for one complete revolution of the rotor. Unlike conventional horizontal-axis wind turbines, the Savonius rotor's aerodynamic moment significantly changes with azimuth. The lower the number of rotor blades, the larger the difference between the minimum and maximum torque. At the same time, the larger the number of rotor blades, the larger the number of torque changes per rotor revolution. Figure 9 shows the rotor aerodynamic moment as a dimensionless coefficient, according to Equation (3). The torque coefficient is also compared for three different values of the tip speed ratio. As can be seen in Figure 9, relatively small changes in the tip speed ratio provide significant differences in the amplitude of changes, i.e., in the difference between changes in the maximum and minimum value of the torque coefficient. The differences of these changes for TSR = 0.75, 1.00, and 1.25 are equal to 5, 10, and 15 respectively. It is also worth noting that at a constant angular velocity, the changes in the power coefficient for the first and second halves of the rotation are the same. Moreover, as can be seen in Figure 9, the maximum values of the torque coefficient are the highest for the optimal tip speed ratio. On the other hand, the modules of the minimum values of this coefficient increase with the increase of the tip speed ratio. It is also clear that the tip speed ratio significantly affects these lower values of the torque coefficient. The last thing worth observing is the faster occurrence of the minimum values of the torque coefficient for higher and higher tip speed ratios.

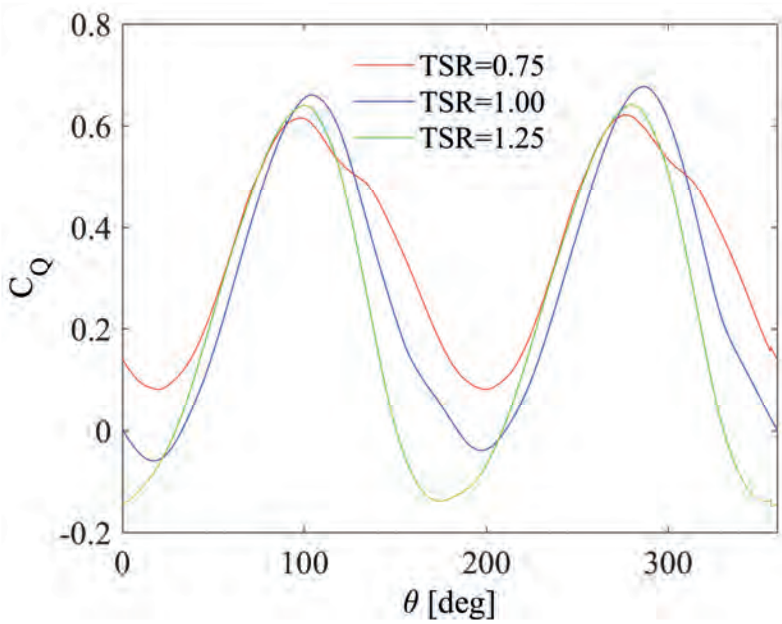

Figure 9. Torque coefficient as a function of azimuth.

In addition to the total torque acting on the entire rotor (Figure 9), it is also interesting how the individual blades contribute to this torque. Figure 10 compares the torque characteristics for one blade for three tip speed ratios. In addition, for TSR = 1.0, the torque characteristics were compared separately for the first and second blades. As it turns out, the torque characteristics for each of the blades are not as different from each other as the total torque acting on the rotor. The maximum values of the torque coefficient for the two largest tip speed ratios investigated in this work reach almost the same value. The largest differences between the three curves are visible in the results for the downstream part of the rotor. The most important observation, however, is that each blade produces a positive torque in the azimuth range from 34–38 to 222–245 degrees, depending on the tip speed ratio. That means, as the tip speed increases, the aerodynamic drag acting on the blade in the downstream part of the rotor increases.

3.2. Averaged Flow Parameters

Figures 11 and 12 show the average flow parameters around the rotor. Figure 11a,b shows the two components of the flow velocity, a component, V_x, parallel to the wind direction, and a component, V_y, perpendicular, respectively. In contrast, Figure 12a,b shows the flow angle and the static pressure distribution around the rotor, respectively. The velocities in Figure 11 have been normalized by the undisturbed flow velocity V_∞. This flow angle is defined as $tan^{-1}(V_y/V_x)$ [48] and expressed in degrees. All results are compared for three tip speed ratios.

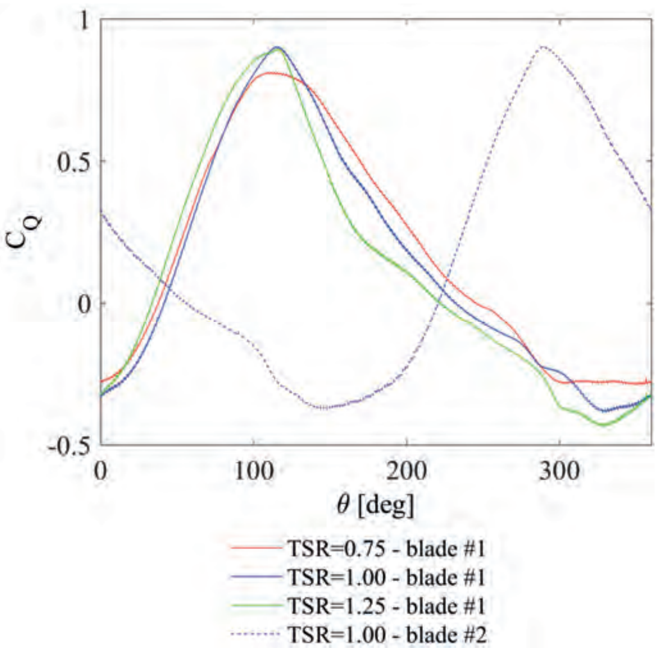

Figure 10. Torque coefficient acting on individual blades.

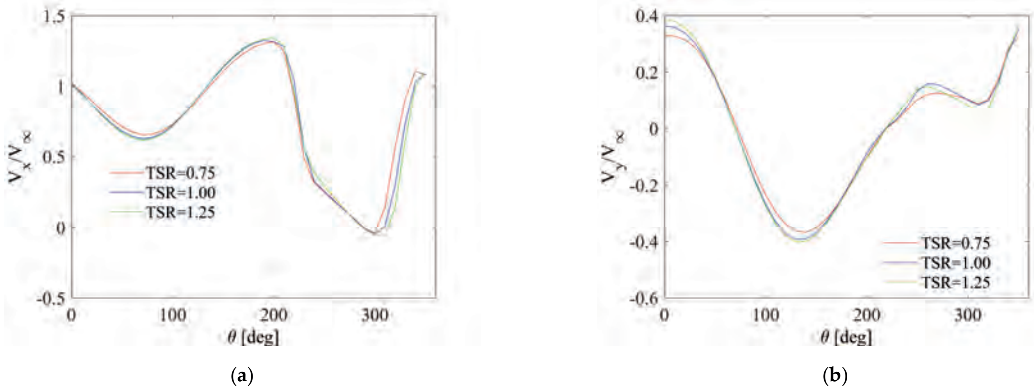

Figure 11. Average flow parameters around the rotor: (**a**) V_x velocity component; (**b**) V_y velocity component.

Analyzing the distribution of the V_x component of the flow velocity (Figure 11a), two characteristic decreases in this velocity can be seen. The first is for the windward part of the rotor, for azimuth in the range of 0 to 180 degrees, and the second is for the leeward part, for azimuth in the range of 180 to 360 degrees. Of course, the velocity drop in this second part of the rotor is greater compared to the velocity drop in the windward part. What is evident from these results, however, is that the velocity distribution is not significantly TSR-dependent. The average velocity for all tip speed ratios for the windward part of the rotor is 12.49 m/s and for the leeward part, it is equal to 8.79 m/s. It is worth emphasizing that with increasing tip speed ratio, average V_x decrease, but these differences are negligible. The difference in average velocity V_x for TSR = 0.75 and 1.25 is 0.08 m/s for the windward part and 0.48 for the leeward part. This is therefore a difference of less than one meter per second. This is a different tendency than in the case of the Darrieus wind turbine, for which the distribution of the average velocity V_x depends quite significantly on the tip speed ratio [49,50]. In addition, unlike the Darrieus wind turbine, a significant increase in the average velocity V_x can be seen near the azimuth of 180 degrees. In the case of the Darrieus wind turbine, for this azimuth and for optimal TSR, it can be seen that the local flow velocity V_x reaches or slightly exceeds the wind velocity V_∞ [50]. In contrast, in the case of the Savonius wind turbine, the local velocity V_x can increase by up to 32% on average compared to the undisturbed flow velocity V_∞. It is also interesting that the maximum value of this velocity is localized for the azimuth of 190–200 degrees. Thus, it appears already in the downwind part of the rotor. On the other hand, the area for which the velocity ratio V_x/V_∞ is greater than one and extends in the azimuth range from 140 to 220 degrees. This local increase in the average speed V_x up to the azimuth of about 200 degrees entails a decrease in the rotor torque coefficient (Figure 9), which for the azimuth of 172–200 degrees, depending on the tip speed ratio, reaches a minimum value.

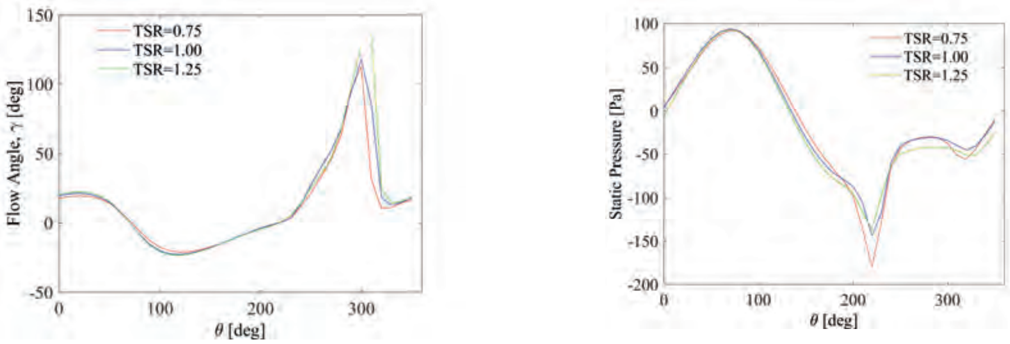

(**a**) (**b**)

Figure 12. Average flow parameters around the rotor: (**a**) Flow angle; (**b**) static pressure.

In the downwind part of the rotor, a significant decrease in V_x velocity down to a negative value is visible, which means that locally, the flow velocity is opposite to the direction of the wind (In the leeward part of the rotor, a significant decrease in V_x velocity down to a negative value is visible, which means that locally the flow velocity is opposite to the direction of the wind). This local velocity V_x drop also significantly modifies the velocity component field V_y (Figure 11b), and the static pressure field (Figure 12b). The minimum value of the velocity V_x was obtained with an average of -0.73 m/s, which corresponds to an azimuth of 300 degrees and a maximum flow angle of 122 degrees on average (Figure 11b).

The pressure reaches a local minimum value at the azimuth of 220 degrees, which is shown in Figure 12a. At this azimuth, both blades simultaneously achieve a very similar torque value close to zero, which can be seen in Figure 10. This pressure peak seen in the graph is also directly related to the presence of a vortex structure that is formed at the tip of the blade from an azimuth of about 136 degrees (Figure 13).

Figures 14–16 illustrate the distribution of pressure and velocity components in the wake downstream behind the rotor. These results shown in the graphs were calculated on defined rakes located behind the rotor as shown in Figure 8. The instantaneous values were then averaged, as discussed in Section 2.8 of this paper. In contrast to the velocity distributions, the characteristics of the pressures behind the rotor differ significantly more depending on the tip speed ratio. Therefore, in Figures 14 and 15, these relationships are shown separately for each of the rakes. It is clear from these graphs that these results are a function of both the tip speed ratio and the x and y coordinates. The largest pressure drop is visible for the location x/R = 1 and the case TSR = 0.75. However, this research has shown that the greatest impact on the velocity distribution, especially the component parallel to the direction of undisturbed flow, has the distance from the rotor axis. Therefore, in order to save space, only the results for the case TSR = 1.00 are presented in this article in Figure 16. These studies have shown that as the x coordinate increases, the velocity distribution V_x becomes more and more symmetric concerning the y = 0 coordinate. This is due to the weakening of the vortex flowing down from the lower blade.

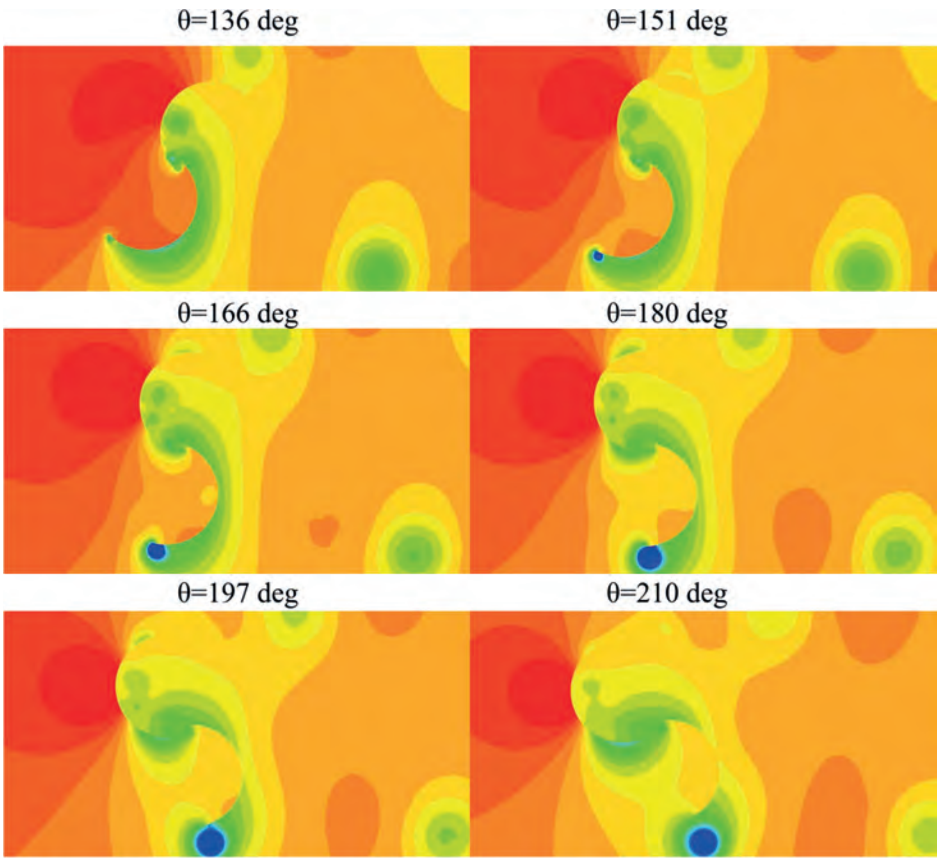

Figure 13. Instantaneous static pressure distributions for the tip speed ratio of 1.00.

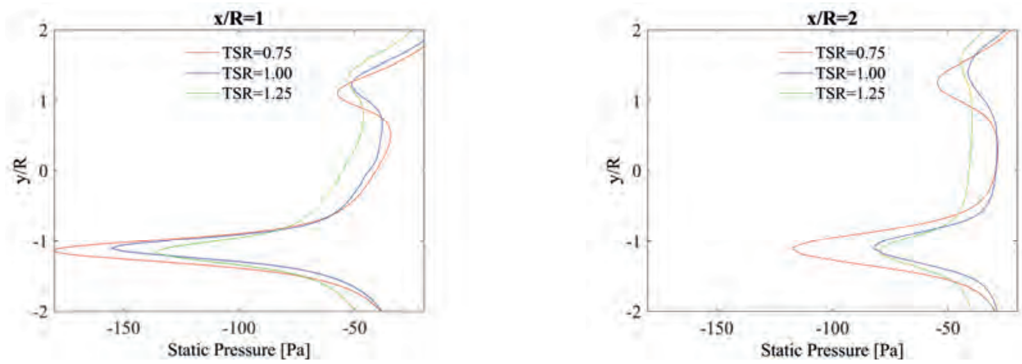

(**a**) (**b**)

Figure 14. Static pressure in the wake: (**a**) Location x/R = 1 behind the rotor axis; (**b**) location x/R = 2 behind the rotor axis.

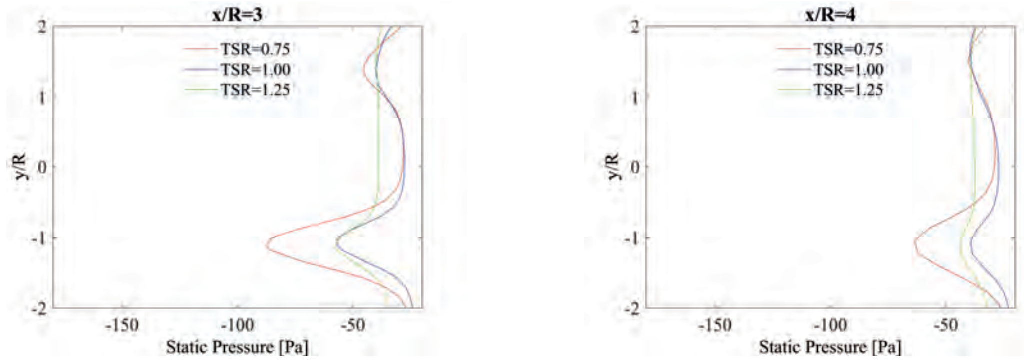

(**a**) (**b**)

Figure 15. Static pressure in the wake: (**a**) Location x/R = 3 behind the rotor axis; (**b**) location x/R = 4 behind the rotor axis.

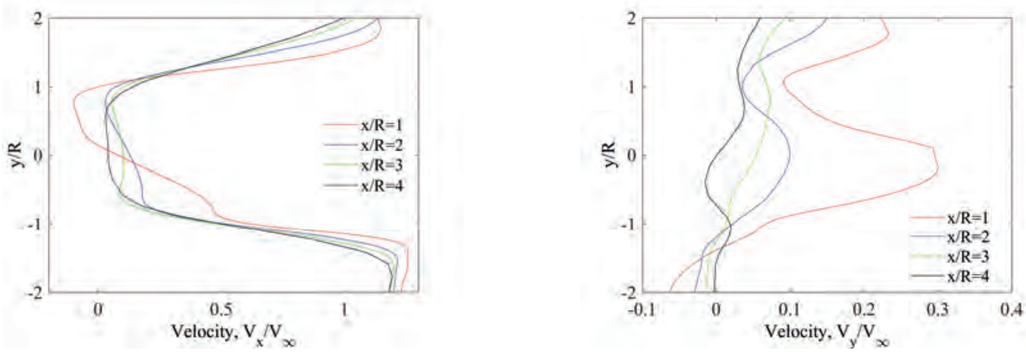

(**a**) (**b**)

Figure 16. Velocity components in the wake at TSR = 1.00 for four x/R locations: (**a**) Velocity component V_x; (**b**) velocity component V_y.

4. Conclusions

In this paper, the average values of static pressure and velocity components around the rotor were studied. The purpose of this analysis is to examine the effect of the tip speed ratio on the average velocity field and the pressure field around the rotor and to compare the flow parameters for two rotor halves: windward and leeward. Based on the conducted research, the following conclusions were obtained:

- Aerodynamic performance, rotor power coefficient, directly depends on aerodynamic torque. The aerodynamic torque of the two-bladed rotor changes significantly with azimuth. The operation of the rotor at these tip speed ratios requires, of course, the use of a second additional rotor section with blades rotated 90 degrees relative to the first section;
- Each blade produces a positive torque in the azimuth range from 34–38 to 222–245 degrees, depending on the tip speed ratio. As the tip speed increases, the aerodynamic drag acting on the blade in the downstream part of the rotor increases;
- Contrary to the Darrieus rotor, in the case of the Savonius rotor, the tip speed ratio has little influence on the average speed distribution around the rotor. This applies to both the velocity component parallel to the direction of undisturbed flow and the perpendicular component. In the upwind part of the rotor, the average velocity parallel to the direction of undisturbed flow is on average 29% lower than in the downwind part;

- In the case of the Savonius wind turbine, an increase in the V_x velocity can be observed locally in relation to the undisturbed flow velocity. Locally, the velocity component V_x may be as much as 32% higher when compared to the velocity V_∞. In addition, the maximum of the velocity component V_x is observed already in the leeward part of the rotor;
- In the downwind part of the rotor, the flow is much more complex. Both the pressure and the flow angle reach their extreme values. On the other hand, the velocity component V_x reaches a locally negative value. This is directly influenced by the geometry of the rotor and the aerodynamic performance of the rotor blades;
- Negative static pressure is visible throughout the area on the downwind part of the rotor. This is another significant difference compared to Darrieus wind turbine rotor with high solidity and operating at low tip speed ratios [49];
- The influence of the tip speed ratio on the pressure distribution in the wake downstream behind the rotor is much larger than in the case of the pressure distribution around the rotor;
- As in the case of the distribution of velocity components around the rotor, the impact of the tip speed ratio on the velocity distributions in wake is definitely much smaller;
- Both the static pressure and the tip speed ratio are a function of the distance from the axis of the rotor;
- As the distance from the rotor axis increases, the velocity V_x distribution becomes more symmetrical with respect to the y = 0 coordinate; and
- Moving away from the rotor axis has a much greater effect on the pressure distribution than on the velocity distribution.

Author Contributions: Conceptualization, J.M. and K.R.; methodology, J.M. and K.R.; software, J.M. and K.R.; validation, J.M.; formal analysis, J.M. and K.R.; investigation, J.M. and K.R.; data curation, J.M. and K.R.; writing—original draft preparation, K.R.; writing—review and editing, J.M.; visualization, J.M. and K.R.; supervision, K.R.; project administration, K.R.; funding acquisition, K.R. All authors have read and agreed to the published version of the manuscript.

Funding: Research was funded by POB Energy of Warsaw University of Technology within the Excellence Initiative: Research University (IDUB) programme (Grant No. 1820/355/Z01/POB7/2021). This research was supported in part by PL-Grid Infrastructure.

Institutional Review Board Statement: Not applicable.

Informed Consent Statement: Not applicable.

Data Availability Statement: The data presented in this study are available upon request from the corresponding author.

Acknowledgments: The authors would like to thank the editors and reviewers for their valuable comments on this research.

Conflicts of Interest: The authors declare no conflict of interest.

References

1. Yao, J.; Li, F.; Chen, J.; Yuan, Z.; Mai, W. Parameter Analysis of Savonius Hydraulic Turbine Considering the Effect of Reducing Flow Velocity. *Energies* **2020**, *13*, 24. [CrossRef]
2. Savonius, S. The S-Roter and Its Applications. *Mech. Eng.* **1931**, *53*, 333–338.
3. Sivasegaram, S. Design parameters affecting the performance of resistance-type, vertical-axis windrotors—An experimental investigation. *Wind Energy* **1977**, *1*, 207–217.
4. Shigetomi, A.; Murai, Y.; Tasaka, Y.; Tasaka, Y. Interactive flow field around two Savonius turbines. *Renew. Energy* **2011**, *36*, 536–545. [CrossRef]
5. Pope, K.; Dincer, I.; Naterer, G. Energy and energy efficiency comparison of horizontal and vertical axis wind turbines. *Renew. Energy* **2010**, *35*, 2102–2113. [CrossRef]
6. Tian, W.; Song, B.; Van Zwieten, J.H.; Pyakurel, P. Computational Fluid Dynamics Prediction of a Modified Savonius Wind Turbine with Novel Blade Shapes. *Energies* **2015**, *8*, 7915–7929. [CrossRef]

7. Menet, J.-L. A double-step Savonius rotor for local production of electricity: A design study. *Renew. Energy* **2004**, *29*, 1843–1862. [CrossRef]
8. Olabi, A.G.; Wilberforce, T.; Elsaid, K.; Salameh, T.; Sayed, E.T.; Husain, K.S.; Abdelkareem, M.A. Selection Guidelines for Wind Energy Technologies. *Energies* **2021**, *14*, 3244. [CrossRef]
9. Talukdar, P.K.; Sardar, A.; Kulkarni, V.; Saha, U.K. Parametric analysis of model Savonius hydrokinetic turbines through experimental and computational investigations. *Energy Convers. Manag.* **2018**, *158*, 36–49. [CrossRef]
10. Blackwell, B.; Sheldahl, R.; Feltz, L. *Wind Tunnel Performance Data for Two-and-Three-Bucket Savonius Rotors*; US Sandia Laboratories Report SAND76-0131; Sandia Laboratories: Springfield, VA, USA, 1977.
11. Nakajima, M.; Iio, S.; Ikeda, T. Performance of double-step Savonius rotor for environmentally friendly hydraulic turbine. *J. Fluid Sci. Tech.* **2008**, *3*, 410–419. [CrossRef]
12. Akwa, J.; Junior, G.; Petry, A. Discussion on the verification of the overlap ratio influence on performance coefficients of a Savonius wind rotor using computational fluid dynamics. *Renew. Energy* **2012**, *38*, 141–149. [CrossRef]
13. Meziane, M.; Faqir, M.; Essadiqi, E.; Ghanameh, M.F. CFD analysis of the effects of multiple semicircular blades on Savonius wind turbine performance. *Int. J. Renew. Energy Res.* **2020**, *10*, 1316–1326. [CrossRef]
14. Ferrari, G.; Federici, D.; Schito, P.; Inzoli, F.; Mereu, R. CFD study of Savonius wind turbine: 3D model validation and parametric analysis. *Renew. Energy* **2017**, *105*, 722–734. [CrossRef]
15. Zhou, T.; Rempfer, D. Numerical study of detailed flow field and performance of Savonius wind turbines. *Renew. Energy* **2013**, *51*, 373–381. [CrossRef]
16. Roy, S.; Ducoin, A. Unsteady analysis on the instantaneous forces and moment arms acting on a novel Savonius-style wind turbine. *Energy Convers. Manag.* **2016**, *121*, 281–296. [CrossRef]
17. Fernando, M.S.U.K.; Modi, V. A numerical analysis of the unsteady flow past a Savonius wind turbine. *J. Wind Eng. Ind. Aerodyn.* **1989**, *32*, 302–327. [CrossRef]
18. Mendoza, V.; Katsidoniotaki, E.; Bernhoff, H. Numerical Study of a Novel Concept for Manufacturing SAVONIUS Turbines with Twisted Blades. *Energies* **2020**, *13*, 1874. [CrossRef]
19. Marinić-Kragić, I.; Vučina, D.; Milas, Z. Global optimization of Savonius-type vertical axis wind turbine with multiple circular-arc blades using validated 3D CFD model. *Energy* **2022**, *241*, 122841. [CrossRef]
20. Nasef, M.H.; El-Askary, W.A.; AbdEL-hamid, A.A.; Gad, H.E. Evaluation of Savonius rotor performance: Static and dynamic studies. *J. Wind Eng. Ind. Aerodyn.* **2013**, *123*, 1–11. [CrossRef]
21. Aboujaoude, H.; Beaumont, F.; Murer, S.; Polidori, G.; Bogard, F. Aerodynamic performance enhancement of a Savonius wind turbine using an axisymmetric deflector. *J. Wind. Eng. Ind. Aerodyn.* **2022**, *220*, 104882. [CrossRef]
22. Elbatran, A.H.; Elbatran, Y.M.; Shehata, A.S. Shehata. Performance study of ducted nozzle Savonius water turbine, comparison with conventional Savonius turbine. *Energy* **2017**, *134*, 566–584. [CrossRef]
23. El-Askary, W.A.; Nasef, M.H.; Abdel-Hamid, A.A.; Gad, H.E. Harvesting wind energy for improving performance of Savonius rotor. *J. Wind Eng. Ind. Aerodyn.* **2015**, *139*, 8–15. [CrossRef]
24. Ramarajan, J.; Jayavel, S. Numerical study on the effect of out-of-phase wavy confining walls on the performance of Savonius rotor. *J. Wind Eng. Ind. Aerodyn.* **2022**, *226*, 105023. [CrossRef]
25. Longo, R.; Nicastro, P.; Natalini, M.; Schito, P.; Mereu, R.; Parente, A. Impact of urban environment on Savonius wind turbine performance: A numerical perspective. *Renew. Energy* **2020**, *156*, 407–422. [CrossRef]
26. Shaheen, M.; El-Sayed, M.; Abdallah, S. Numerical study of two-bucket Savonius wind turbine cluster. *J. Wind Eng. Ind. Aerod* **2015**, *137*, 78–89. [CrossRef]
27. Mereu, R.; Federici, D.; Ferrari, G.; Schito, P.; Inzoli, F. Parametric numerical study of Savonius wind turbine interaction in a linear array. *Renew. Energy* **2017**, *113*, 1320–1332. [CrossRef]
28. Rogowski, K.; Maroński, R. CFD computation of the Savonius rotor. *J. Theor. Appl. Mech.* **2015**, *53*, 37–45. [CrossRef]
29. Larin, P.; Paraschivoiu, M.; Aygun, C. CFD based synergistic analysis of wind turbines for roof mounted integration. *J. Wind Eng. Ind. Aerodyn.* **2016**, *156*, 1–13. [CrossRef]
30. Mao, Z.; Yang, G.; Zhang, T.; Tian, W. Aerodynamic Performance Analysis of a Building-Integrated Savonius Turbine. *Energies* **2020**, *13*, 2636. [CrossRef]
31. Sheldahl, R.E.; Feltz, L.V.; Blackwell, B.F. Wind tunnel performance data for two-and three-bucket Savonius rotors. *J. Energy* **1978**, *2*, 160–164. [CrossRef]
32. Zhang, B.; Song, B.; Mao, Z.; Tian, W.; Li, B.; Li, B. A Novel Parametric Modeling Method and Optimal Design for Savonius Wind Turbines. *Energies* **2017**, *10*, 301. [CrossRef]
33. Sun, X.; Luo, D.; Huang, D.; Wu, G. Numerical study on coupling effects among multiple Savonius turbines. *J. Renew. Sustain. Energy* **2012**, *4*, 053107. [CrossRef]
34. Alaimo, A.; Esposito, A.; Milazzo, A.; Orlando, C.; Trentacosti, F. Slotted Blades Savonius Wind Turbine Analysis by CFD. *Energies* **2013**, *6*, 6335–6351. [CrossRef]
35. Kim, S.; Cheong, C. Development of low-noise drag-type vertical wind turbines. *Renew. Energy* **2015**, *79*, 199–208. [CrossRef]
36. Blanco Damota, J.; Rodríguez García, J.d.D.; Couce Casanova, A.; Telmo Miranda, J.; Caccia, C.G.; Galdo, M.I.L. Optimization of a Nature-Inspired Shape for a Vertical Axis Wind Turbine through a Numerical Model and an Artificial Neural Network. *Appl. Sci.* **2022**, *12*, 8037. [CrossRef]

37. dos Santos, A.L.; Fragassa, C.; Santos, A.L.G.; Vieira, R.S.; Rocha, L.A.O.; Conde, J.M.P.; Isoldi, L.A.; dos Santos, E.D. Development of a Computational Model for Investigation of and Oscillating Water Column Device with a Savonius Turbine. *J. Mar. Sci. Eng.* **2022**, *10*, 79. [CrossRef]
38. Alessandro, D.; Montelpare, S.; Ricci, R.; Secchiaroli, A. Unsteady Aerodynamics of a Savonius wind rotor: A new computational approach for the simulation of energy performance. *Energy* **2010**, *35*, 3349–3363. [CrossRef]
39. Roy, S.; Saha, U.K. Wind tunnel experiments of a newly developed two-bladed Savonius-style wind turbine. *Appl. Energy* **2015**, *137*, 117–125. [CrossRef]
40. Mohamed, M.H.; Thevenin, D. Performance optimization of a Savonius turbine considering different shapes for frontal guiding plates. In Proceedings of the 10th International Conference of Fluid Dynamics ICFD, Cairo, Egypt, 16–19 December 2010.
41. Mohamed, M.H.; Janiga, G.; Pap, E.; Thévenin, D. Optimal blade shape of a modified Savonius turbine using an obstacle shielding the returning blade. *Energy Convers. Manag.* **2011**, *52*, 236–242. [CrossRef]
42. ANSYS, Inc. *ANSYS Fluent Theory Guide, Release 19.1.*; ANSYS, Inc.: Canonsburg, PA, USA, 2019.
43. Bangga, G.; Hutomo, G.; Wiranegara, R.; Sasongko, H. Numerical study on a single bladed vertical axis wind turbine under dynamic stall. *J. Mech. Sci. Technol.* **2017**, *31*, 261–267. [CrossRef]
44. Rogowski, K. Numerical studies on two turbulence models and a laminar model for aerodynamics of a vertical-axis wind turbine. *J. Mech. Sci. Technol.* **2018**, *32*, 2079–2088. [CrossRef]
45. Kacprzak, K.; Liskiewicz, G.; Sobczak, K. Numerical investigation of conventional and modified Savonius wind turbines. *Renew. Energy* **2013**, *60*, 578–585. [CrossRef]
46. Bouzaher, M.T.; Guerira, B. Impact of Flexible Blades on the Performance of Savonius Wind Turbine. *Arab J. Sci. Eng.* **2022**, *47*, 15365–15377. [CrossRef]
47. Mari, M.; Venturini, M.; Beyene, A. Performance Evaluation of Novel Spline-Curved Blades of a Vertical Axis Wind Turbine Based on the Savonius Concept. In Proceedings of the ASME 2016 International Mechanical Engineering Congress and Exposition, Phoenix, AZ, USA, 11–17 November 2016. [CrossRef]
48. Hansen, M.O.L. *Aerodynamics of Wind Turbines*; Earthscan: London, UK, 2008.
49. Rogowski, K.; Maroński, R.; Piechna, J. Numerical analysis of a small-size vertical-axis wind turbine performance and averaged flow parameters around the rotor. *Arch. Mech. Eng.* **2017**, *64*, 205–218. [CrossRef]
50. Madsen, H.; Larsen, T.; Vita, L.; Paulsen, U. Implementation of the Actuator Cylinder flow model in the HAWC2 code for aeroelastic simulations on Vertical Axis Wind Turbines. In Proceedings of the 51st AIAA Aerospace Sciences Meeting Including the New Horizons Forum and Aerospace Exposition, Grapevine, TX, USA, 7–10 January 2013. [CrossRef]

READ 2024
RESEARCH & EDUCATION IN AIRCRAFT DESIGN
WARSAW, POLAND | 6-8 NOVEMBER 2024

INVESTIGATION OF AERODYNAMIC PERFORMANCE OF THE NACA 0018 AIRFOIL AT LOW REYNOLDS NUMBERS: A COMPARATIVE STUDY OF 2-D AND 3-D MODELS USING TRANSITION SST AND K- ω SST APPROACHES

Jan Michna[1], Krzysztof Rogowski[1] & Sławomir Kubacki[1]

[1] Institute of Aeronautics and Applied Mechanics, Warsaw University of Technology, 00-665 Warsaw, Poland

Abstract

This paper presents an in-depth analysis of the aerodynamic performance of the NACA 0018 airfoil at low Reynolds numbers, focusing on the behaviour of laminar separation bubbles and the predictive capabilities of various turbulence models. Conducted at a Reynolds number of 160,000 and for angles of attack of 4° and 8°, this study employs both 2-D and 3-D models using the Transition SST and k-ω SST approaches to capture the nuanced aerodynamic behaviour of the airfoil in wind energy applications. Comparative simulations using the 2-D γ-Re_θ transition model with calibrated transition onset parameters, alongside the 3-D Scale Adaptive Simulation (SAS) methodology, allow for an assessment of how model dimensionality and transition calibration influence the accuracy of C_p distributions and laminar bubble prediction. Results are validated against experimental data to evaluate model precision, particularly in regions associated with pressure recovery. The study confirms that increasing the angle of attack shifts the laminar separation point closer to the leading edge, with the 3-D SAS approach aligning closely with the 2-D URANS results for pressure distribution. However, the k-ω SST model, which lacks transitional prediction capabilities, significantly deviates from experimental observations, underscoring the importance of transition-aware models for accurate low Reynolds number simulations. This work offers valuable insights into turbulence model selection for low-turbulence environments, particularly relevant to wind turbine design and optimization, where sustained efficiency and model fidelity are crucial for performance prediction and reliability.

Keywords: airfoil, laminar separation bubble, Transition SST, URANS

1. Introduction

In recent years, the famous series of four-digit NACA airfoil profiles has gained considerable interest, particularly in the context of wind energy [1-4]. Although these profiles were not originally designed for operation at low or very high Reynolds numbers, they are now being intensively studied within these ranges [5,6]. In both cases, they are typically not optimal solutions; however, they continue to be utilized, especially in vertical-axis wind turbines, for two main reasons. First, these profiles are among the most extensively studied, both experimentally and numerically, and serve as valuable references for validation and as a starting point for optimizing airfoils for specific conditions. Second, a significant amount of research, especially on the aerodynamics of vertical-axis wind turbines, has been conducted using these profiles [7].

Experimental studies show that these profiles, particularly the NACA 0018 profile considered here, perform poorly in low Reynolds number flows, and calculating their characteristics is challenging for modern analytical tools such as the Transition SST turbulence model [8]. Our previous experiences with turbulence modelling using this tool have shown significant difficulties in accurately determining the geometry of the laminar separation bubble, especially within the angle of attack range below the critical angle [1].

Our research presented in this paper concerns the characteristics of the NACA 0018 profile at a Reynolds number of 160,000. The necessity of studying this profile at such a low Reynolds number arises from the flow conditions encountered in wind turbine studies conducted in wind tunnels [9]. Reynolds numbers based on the blade's chord often reach values below 200,000 and in some cases, even as low as 20,000–30,000. Such studies are essential for subsequent upscaling and for validating numerical methods [6].

At such low Reynolds numbers, the lift characteristic is usually nonlinear due to the presence of the laminar separation bubble. The Transition SST turbulence model is a so-called general-purpose model based on correlations derived from flat plate experimental results [10]. It can be calibrated by adjusting constants related to specific physical phenomena in the wall boundary layer associated with the laminar-turbulent transition. One of the aims of this work is to examine the impact of the s_1 constant (Cs1), which affects the point of laminar separation. As Ruiz and D'Ambrosio [11] demonstrated with the SD7003 airfoil at Re=60,000, changing this parameter can significantly influence the drag coefficient characteristics by shifting the position of the laminar separation.

Additionally, traditional two-equation turbulence models, such as the k-ω SST model, generate an unrealistic lift curve that is linear up to the critical angle of attack, as bubble-related effects are entirely omitted [8]. This is due to the model's treatment of the entire boundary layer as turbulent, thus increasing drag. In contrast, the Transition SST model provides a more accurate representation by accounting for laminar regions.

An additional aim of this paper is to determine whether modelling the flow around the airfoil in three dimensions significantly alters the laminar bubble characteristics. To the best of our knowledge, the results of such a test have not yet been published. Within the angle range below the critical angle of attack, two regions exist: one below an angle of attack of 6.5°, and the other above. In the first range, laminar bubbles appear on both sides of the airfoil, while in the second, they only occur on the suction side. Therefore, the results presented in this study were compared for two angles of attack: 4° and 8°.

2. Methodology

2.1 URANS Model Description

The numerical model of the virtual wind tunnel, developed in both 2-D and 3-D configurations, was based on the experimental setup. All geometric dimensions of the working section in the actual wind tunnel were carefully preserved, including the tunnel width and the distance from the inlet to the airfoil mounting point. The simulations were conducted for two angles of attack, 4° and 8°. The 4° angle represents a region where laminar separation bubbles may form on both the suction and pressure sides of the airfoil. For an angle of attack of 8°, experimental studies indicate the presence of laminar separation bubbles only on the suction side [12].

To ensure consistent mesh topology for both angles of attack, a circular domain with a diameter of 3 times the chord len gth was defined around the airfoil (Fig. 1). This approach facilitated accurate comparison and alignment of numerical and experimental data across the chosen angles.

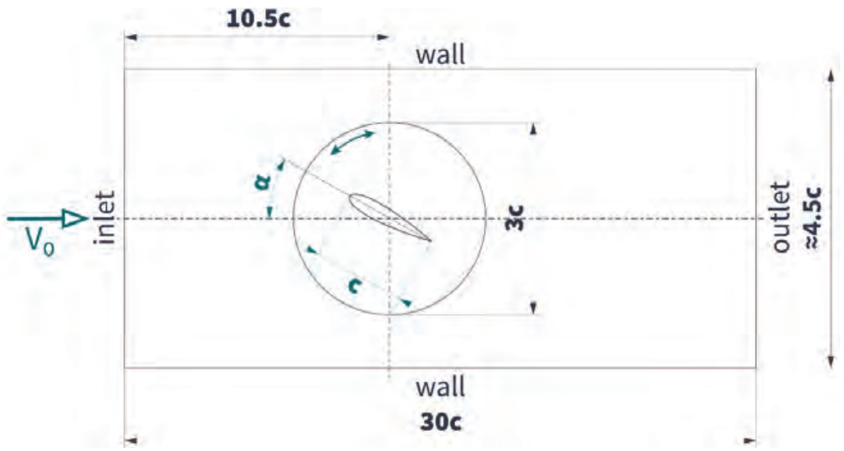

Figure 1 – Schematic of the computational domain for the virtual wind tunnel

In this study, the Unsteady Reynolds-Averaged Navier-Stokes (URANS) model was employed to analyze the flow around a NACA 0018 airfoil at low Reynolds numbers. The analysis was conducted at a Reynolds number of Re=160,000, which corresponds to a freestream velocity V_0=11,7m/s and and a chord length c=0,2m. The air properties were defined with a density ρ=1,225kg/m^3 and a dynamic viscosity μ=1,7894×10^{-5}kg/(ms).

The URANS simulations were carried out with a time step Δt=10^{-4}s to accurately capture unsteady flow phenomena, with a total of 50,000 time steps for adequate temporal resolution. To replicate realistic conditions, an inlet turbulence intensity TI_{inlet}=0.3% was set, along with an inlet turbulence length scale l_t=0,02m. These values were chosen to approximate the low-turbulence environments typically encountered in wind tunnel testing for aerodynamic profiles like the NACA 0018.

The NACA 0018 airfoil, known for its symmetrical shape and extensive use in wind turbine studies, provided a well-documented profile suitable for examining the effects of low Reynolds numbers on laminar separation and the performance of turbulence models, particularly the Transition SST model applied in this URANS framework. The model setup in this study aimed to capture both the aerodynamic forces and the onset of laminar separation bubbles at specific angles of attack, contributing valuable insights for validating turbulence models under these conditions.

The 2-D and 3-D model meshes, as shown in Figure 2, were designed based on our prior experience with simulating the NACA 0018 airfoil at similar Reynolds numbers. For the 2-D model, both edges of the airfoil were divided into 800 equal segments. Around the airfoil edges, a structured mesh was applied, with the first layer having a thickness of 1.29E-05 to satisfy the wall y+ < 1 condition. This structured mesh consists of 40 layers with a growth rate of 1.1.

In the 3-D model, the spanwise direction of the wing was divided into 40 uniform sections, with the cross-sectional cell distribution matching that of the 2-D mesh. Boundary conditions were set as follows: velocity inlet at the domain inlet, pressure outlet at the domain outlet, and wall (no-slip) on the airfoil surfaces. To simplify the model and avoid calculating the boundary layer on the tunnel walls, slip wall boundary conditions were applied to the side walls of the computational domain.

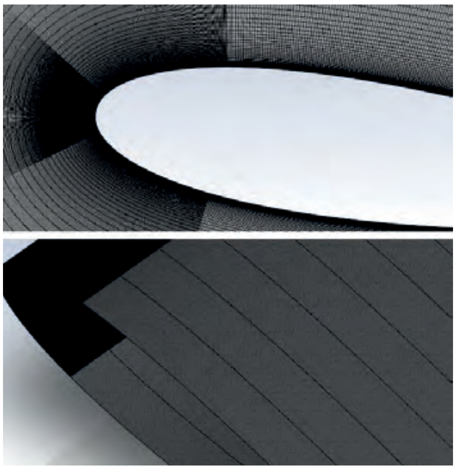

Figure 2 – Mesh around the NACA 0018 airfoil. The top view shows the structured mesh near the airfoil surface, focusing on the boundary layer, while the bottom view highlights the uniform spanwise cell distribution for 3-D simulations.

2.2 Turbulence Modeling Approaches for Transition Prediction

In this paper, the primary approach utilized is the Transition SST (Shear Stress Transport) turbulence model, which is specifically designed to handle the transition from laminar to turbulent flow. This model's ability to account for intermittency and transition onset Reynolds numbers makes it particularly suitable for applications involving low Reynolds number flows, such as those around airfoils in vertical-axis wind turbines (VAWTs). Additionally, the Transition SST model is compared with the algebraic turbulence model and the two-dimensional k−ω SST model. These comparisons provide insights into the relative performance of each model in accurately predicting transition phenomena and capturing the effects of boundary layer development, turbulence intensity, and laminar separation bubbles.

The Transition SST model is a widely-used turbulence model in computational fluid dynamics (CFD) that addresses the transition from laminar to turbulent flow, which is particularly relevant for airfoils at low Reynolds numbers, such as the NACA 0018. This model, built upon the traditional SST k−ω turbulence model, includes additional equations to predict laminar-turbulent transition, focusing on both the onset and length of transition zones. Unlike conventional models, which often assume fully turbulent flow, the Transition SST model incorporates intermittency and transition onset Reynolds numbers as variables, allowing for a more accurate representation of boundary layer development and laminar separation bubbles. This model employs local flow properties, allowing it to adapt to changes in turbulence intensity and Reynolds number within the flow, which is especially useful for modeling the unstable flow regimes typical of low-turbulence wind tunnels and the environments VAWTs encounter [1].

The algebraic turbulence model presented in this study focuses on simulating the transition from laminar to turbulent flow in boundary layers under various conditions, including bypass, separation-induced, and wake-induced transitions. This model employs the concept of intermittency, where intermittency (denoted as γ) represents the fraction of time during which the flow is turbulent at a given point. The model modifies production terms in the k−ω turbulence framework by Wilcox, incorporating mechanisms for handling high-frequency disturbances in laminar flows and providing a breakdown pathway for laminar shear layers under free-stream turbulence. Calibration and validation were performed using flat plate flows and turbomachinery cascades, showing effective performance across different turbulence levels and flow regime [13].

The Scale-Adaptive Simulation (SAS) model is an advanced turbulence model used to capture unsteady turbulent structures by dynamically adjusting the turbulence length scale to the resolved flow scales. Unlike traditional URANS models, which can only simulate large-scale unsteadiness in unstable flows, the SAS model adapts to smaller turbulent eddies, providing results comparable to Large Eddy Simulation (LES) while being less computationally intensive. This is achieved by introducing a source term in the turbulence frequency equation, which allows the model to respond to flow instabilities more effectively [14].

In this study, the URANS approach was applied to determine the aerodynamic characteristics of a 2-D airfoil profile. The primary objective was to evaluate how adjustments to the s_1 constant in the Transition SST model could enhance prediction accuracy. For the 3-D model, the SAS approach was additionally employed to achieve a more precise velocity field behind the airfoil.

3. Results

3.1 Pressure Distributions on the Airfoil

The results of static pressure coefficients from 3-D SAS k-ω SST and γ-Re_θ simulations, as well as from 2-D γ-Re_θ simulations with different transition onset values (s_1=2.0 and s_1=3.0), are presented in Figure 3. Experimental data from [2] are included for validation, highlighting differences in Cp predictions among the models, especially in the pressure recovery region. This figure clearly demonstrates the expected trend that an increase in angle of attack shifts the laminar separation point of the boundary layer toward the leading edge. The 3-D SAS approach shows very similar pressure distribution results to the 2-D URANS model. As anticipated, the predictions from the two-equation k-ω SST model deviate the most from the experimental data.

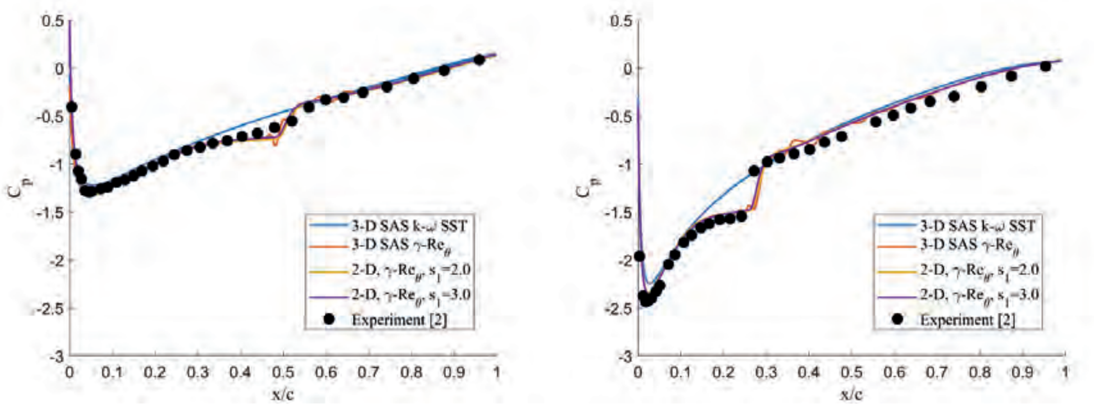

Figure 3 – Pressure coefficient distributions Cp along the NACA 0018 airfoil surface for angles of attack AoA=4deg (left) and AoA=8deg (right).

3.2 Analysis of Laminar Separation Bubble Geometry Using Transition SST Model

Figure 4 shows the geometry of the laminar separation bubble calculated using a 2-D CFD approach with the Transition SST turbulence model. The locations of the separation, transition, and reattachment points were determined based on the skin friction coefficient (C_f) distribution in the final computed time step, following the method outlined in studies [8] and [15]. The separation and reattachment points of the laminar boundary layer are identified at the two extreme points of the C_f function. The laminar-turbulent transition location was found between the separation and reattachment points, specifically at the point where the C_f curve shows a sharp rise.

The position of the separation location can be adjusted by tuning the constant s1, which accounts for the influence of Kelvin-Helmholtz instabilities on the flow within a detached boundary layer exposed to low turbulence levels outside the layer. The default value of this constant is set to 2. Figure 4 illustrates the dependency of the s_1 constant on position relative to the airfoil chord. An increase in s_1 generally causes a delay in the separation location on both the suction and pressure sides, except for the case at AoA=8deg on the pressure side, where an inverse trend is observed, albeit with minor differences.

Currently, we lack experimental data to validate the accuracy of the s_1(x/c) distribution obtained in this study. More precise experimental studies of pressure distributions on the pressure side are needed. Additionally, it is notable that reattachment on the pressure side is absent, and for AoA=8deg, the Transition SST model does not detect a transition location either. Comparison with experimental results suggests that as the angle of attack increases, the required s_1 value also needs to be higher to improve the prediction accuracy.

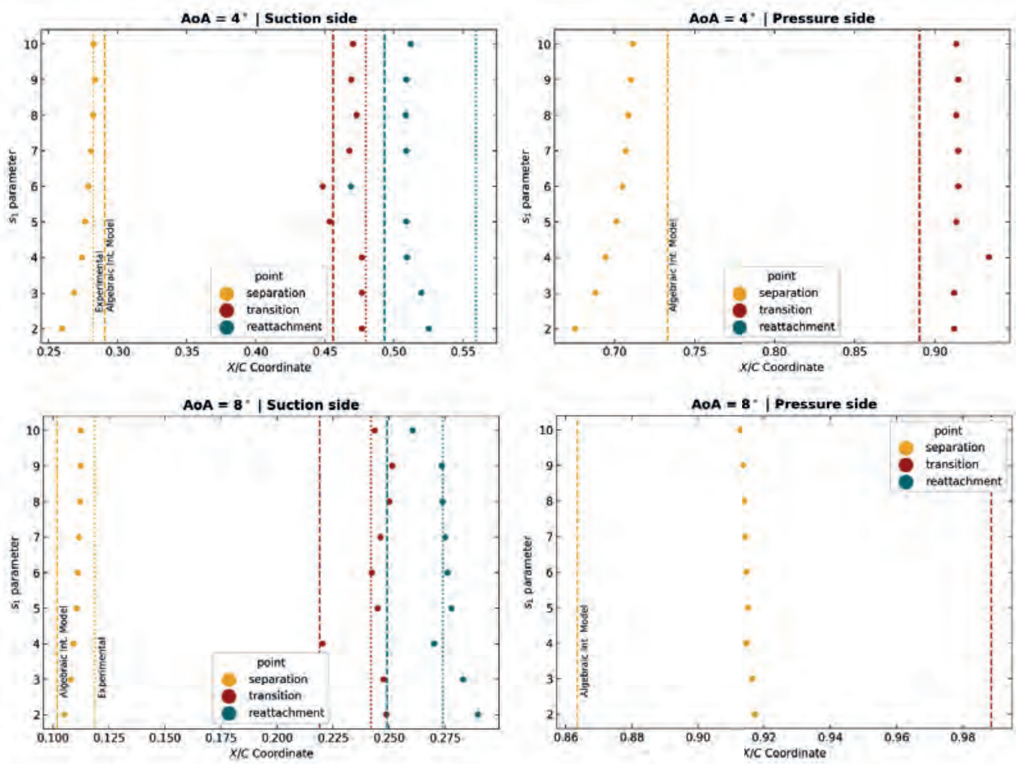

Figure 4 – Distributions of the s1 parameter as a function of the x/c coordinate for both the suction and pressure sides of the airfoil at angles of attack (AoA) of 4° and 8°.

3.3 Turbulence Modeling Approaches for Transition Prediction

Figure 5 presents normalized iso-surfaces of the Q-criterion, colored by velocity magnitude, to illustrate the vortex structures behind the airfoils at an angle of attack (AoA) of 8°, obtained using the Transition SST and k-ω SST models. The Transition SST model reveals prominent, irregular vortex structures in the wake, suggesting a more detailed capture of turbulent flow dynamics. In contrast, the k-ω SST model, even with the application of the SAS model, does not display large vortex structures, indicating a smoother, more streamlined wake pattern. This difference implies that the k-ω SST model could serve as a suitable surrogate for simulating "dirty wing" flow conditions, where large-scale vortex dynamics may be less critical. The velocity magnitude color scale further aids in distinguishing flow speeds within these vortex structures, offering insights into the intensity and distribution of turbulent regions around the airfoils.

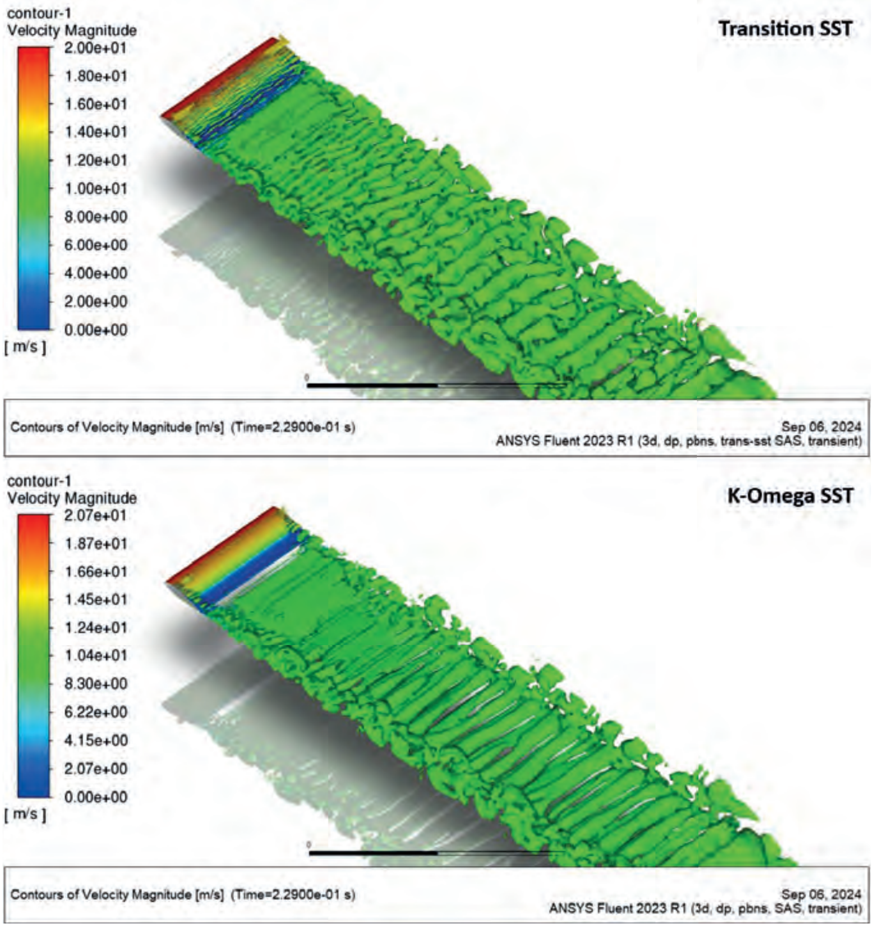

Figure 5 – Comparison of wake structures behind an object simulated using two turbulence models: Transition SST (top) and K-Omega SST (bottom).

4. Conclusions

The flow around a NACA0018 airfoil is complex due to the physical phenomena occurring in the boundary layer, and its accurate simulation requires advanced numerical tools. For a more precise prediction of the geometry of laminar-turbulent bubbles, the original formulation of the Transition SST approach requires calibration. This study also investigates whether the use of a 3-D model combined with the advanced Scale Adaptive Simulation (SAS) technique can improve the results generated by a 2-D model.

The comparison of static pressure coefficient predictions from 3-D SAS k-ω SST and γ-Re_θ simulations, along with 2-D γ-Re_θ models at different transition onset values, reveals distinct model behaviors. As angle of attack increases, the laminar separation point of the boundary layer moves closer to the leading edge, a trend consistent across simulations. The 3-D SAS model shows good alignment with the 2-D URANS approach, while the k-ω SST model demonstrates the greatest deviation from experimental trends.

The findings indicate that the geometry of the laminar separation bubble and the locations of separation, transition, and reattachment points can be effectively determined using a 2-D CFD approach with the Transition SST turbulence model, based on skin friction coefficient distribution. The study highlights the influence of the s_1 constant on the separation position along the airfoil chord, suggesting that tuning this parameter can adjust separation to improve prediction accuracy.

However, the lack of experimental data limits validation. Further experimental research, particularly on the pressure side at higher angles of attack, is recommended to refine the model and improve the predictive accuracy of laminar-to-turbulent transition locations.

The use of a 3-D model combined with the uncalibrated Transition SST turbulence model does not improve the accuracy of the laminar transition location compared to the 2-D model.

The results indicate that while the Transition SST model captures detailed and complex vortex structures in the wake, the k-ω SST model provides a smoother representation, even when using the SAS approach. This suggests that the k-ω SST model could be effectively utilized as a surrogate for simulating conditions with less pronounced vortex dynamics, such as those found in "dirty wing" flows, where large-scale turbulence structures are less critical.

5. Contact Author Email Address

For any further question, please be free to contact authors of this work via email address: jan.michna@pw.edu.pl.

6. Copyright Statement

References

[1] Michna J, Rogowski K. Numerical Study of the Effect of the Reynolds Number and the Turbulence Intensity on the Performance of the NACA 0018 Airfoil at the Low Reynolds Number Regime. *Processes*. 10(5):1004, 2022. doi: 10.3390/pr10051004

[2] Gerakopulos R, Boutilier M, Yarusevych S. Aerodynamic Characterization of a NACA 0018 Airfoil at Low Reynolds Numbers. *40th Fluid Dynamics Conference and Exhibit*. Chicago, Illinois: American Institute of Aeronautics and Astronautics; 2010 https://arc.aiaa.org/doi/10.2514/6.2010-4629

[3] Timmer WA. Two-Dimensional Low-Reynolds Number Wind Tunnel Results for Airfoil NACA 0018. *Wind engineering*. Vol 32, No 6, pp 525–537, 2008. DOI: 10.1260/030952408787548848

[4] Boutilier MS, Yarusevych S. Parametric study of separation and transition characteristics over an airfoil at low Reynolds numbers. *Experiments in fluids*. Vol 52, pp. 1491-1506, 2012. DOI: 10.1007/s00348-012-1270-z

[5] Rogowski K, Michna J, Ferreira C. Numerical Analysis of Aerodynamic Performance of a Fixed-Pitch Vertical Axis Wind Turbine Rotor. *Advances in Science and Technology Research Journal*. Vol 18, No 6, pp. 97–109, 2024. DOI: https://doi.org/10.12913/22998624/191128

[6] Huang M, Sciacchitano A, Ferreira C. On the wake deflection of vertical axis wind turbines by pitched blades. *Wind Energy*. Vol 26, No 4, pp. 365–87. 2023. DOI: 10.1002/we.2803.

[7] Paraschivoiu I. *Wind Turbine Design with Emphasis on Darrieus Concept*. Presses Internationales Polytechnique: Montréal, QC, Canada, 2009.

[8] Rogowski K, Królak G, Bangga G. Numerical Study on the Aerodynamic Characteristics of the NACA 0018 Airfoil at Low Reynolds Number for Darrieus Wind Turbines Using the Transition SST Model. *Processes*. Vol 9, No 3, 2021. https://doi.org/10.3390/pr9030477

[9] Rogowski K. CFD Computation of the H-Darrieus Wind Turbine—The Impact of the Rotating Shaft on the Rotor Performance. *Energies*. Vol. 12, No 13, 2019. https://doi.org/10.3390/en12132506

[10] Langtry RB, Menter FR. Correlation-based transition modeling for unstructured parallelized computational fluid dynamics codes. *AIAA journal*. Vol. 47, No 12, pp. 2894-2906, 2009. DOI: 10.2514/1.42362

[11] Carreño Ruiz M, D'ambrosio D. Validation of the γ-Reθ transition model for airfoils operating in the very low Reynolds number regime. Flow, Turbulence and Combustion, Vol. 109, No 2, pp. 279-308, 2022. https://doi.org/10.1007/s10494-022-00331-z

[12] Rogowski K, Mikkelsen R, Michna J, Wisniewski J. Aerodynamic Performance Analysis of NACA 0018 Airfoil at Low Reynolds Numbers in a Low-Turbulence Wind Tunnel. *Advances in Science and*

Technology Research Journal. Accepted for publication.

[13] Kubacki S, Dick E. An algebraic intermittency model for bypass, separation-induced and wake-induced transition. *International Journal of Heat and Fluid Flow*. 62:344–61, 2016. Doi: 10.1016/j.ijheatfluidflow.2016.09.013

[14] Rogowski K, Hansen MOL, Maroński R, Lichota P. Scale Adaptive Simulation Model for the Darrieus Wind Turbine. Journal of Physics: Conference Series. Vol. 753, No 022050, 2016. doi:10.1088/1742-6596/753/2/022050

[15] Choudhry A, Arjomandi M, Kelso R. A study of long separation bubble on thick airfoils and its consequent effects. International Journal of Heat and Fluid Flow, Vol. 52, pp. 84-96, 2015. https://doi.org/10.1016/j.ijheatfluidflow.2014.12.001

Journal of Applied Fluid Mechanics, Vol. 19, No. 2, pp. 29-44, 2026.
Available online at www.jafmonline.net, ISSN 1735-3572, EISSN 1735-3645.
https://doi.org/10.47176/jafm.19.2.3738

DNS Dataset of a Thick Symmetric Airfoil at Low Reynolds Number: NACA 0018 with LES Comparison

K. Rogowski†, S. Kubacki , and J. Michna

Institute of Aeronautics and Applied Mechanics, Warsaw University of Technology, Nowowiejska 24, 00-665 Warsaw, Poland

†*Corresponding Author Email:* Krzysztof.Rogowski@pw.edu.pl

ABSTRACT

This study examines the aerodynamic behavior of the symmetric National Advisory Committee for Aeronautics (NACA) 0018 airfoil at a chord-based Reynolds number of 30,000, utilizing Direct Numerical Simulation (DNS) as the primary tool, supplemented by selected Large Eddy Simulation (LES) cases. DNS covers a full sweep of angles of attack from 0° to 10°, while LES was conducted at α = 4° and 8° to verify consistency between the two approaches. Despite the limited LES dataset-restricted by computational cost, the results showed nearly identical aerodynamic loads and surface pressure distributions, thereby reinforcing confidence in the DNS database. To further assess robustness, two additional DNS cases were performed for the NACA 0012 airfoil at α = 3° and 6° under identical grid resolution and flow conditions. These simulations demonstrated very good agreement with published experiments, extending validation beyond a single geometry. In both DNS and LES, clean inflow conditions were imposed, ensuring that the domain inlet did not introduce resolved turbulence. The results captured laminar boundary-layer separation on the suction side without reattachment, producing bluff-body-like wake dynamics dominated by periodic vortex shedding, while classical Kelvin–Helmholtz instabilities were not significant. Computed aerodynamic coefficients, including time-averaged lift, showed good agreement with measurements. The novelty of this work lies in providing the first DNS dataset for a thick symmetric airfoil (NACA 0018) at Re = 30,000, further validated through NACA 0012 comparisons. The findings establish a benchmark for future investigations of unsteady aerodynamics, particularly dynamic stall in pitching motions, and are directly relevant for the design of low-Reynolds-number devices such as micro air vehicles, unmanned aerial vehicles, and vertical-axis wind turbines.

Article History

Received July 15, 2025
Revised October 1, 2025
Accepted October 4, 2025
Available online December 6, 2025

Keywords:

NACA 0018 airfoil
Low Reynolds number flow
Direct Numerical Simulation (DNS)
Large Eddy Simulation (LES)
Boundary layer separation

1. INTRODUCTION

In recent years, there has been a substantial increase in interest regarding the aerodynamics of flows at very low Reynolds numbers. Winslow et al. (2018) narrowed the range of small chord-based Reynolds numbers from 10^5-10^6 to 10^4-10^5, a shift of particular significance for the design of micro air vehicles (MAVs), unmanned aerial vehicles (UAVs), small vertical-axis wind turbines, and low-speed flight systems. Research into low chord-based Reynolds number flows is crucial due to the growing interest in MAVs, which are driven by advancements in compact electronics and the need for situational awareness in environments where conventional aircraft and larger UAVs face significant challenges. These vehicles hold potential for military, civilian, and scientific applications, including reconnaissance in hostile territories, scouting dangerous environments, and even Mars exploration as a mobile alternative. Numerous studies have been conducted in this area, including both experimental studies, such as those by Ohtake et al. (2007), and numerical studies, such as those by Winslow et al. (2018).

Research on airfoils at low Reynolds numbers remains highly relevant, as comparable flow regimes are frequently encountered in wind tunnel experiments involving wind turbines. These conditions are significant for upscaling, where the velocity field data obtained in the wake of small-scale turbines is applied to large-scale rotors, enabling more accurate predictions and optimization of wind farm performance (Huang et al., 2023). Recent experimental investigations by Verma and Sarkar (2024) using high-speed particle image velocimetry (PIV) have further highlighted the complexity of wake dynamics behind low-Reynolds-number airfoils, underlining the need for temporally resolved flow measurements to complement numerical predictions. Even though thick airfoils from the four-digit NACA series are not optimal for use in low-Reynolds-number applications (McMasters and Henderson, 1979; Winslow et al., 2018), their utilization becomes necessary due to the requirements of upscaling (Bensason et al. 2024). In studies conducted by leading research teams, the chord-based Reynolds numbers of rotating blades are typically in the range of 30,000 to 200,000 (see Molina et al. 2019; Huang et al. 2023; or Tescione et al. 2014).

A significant challenge in analyzing aerodynamic characteristics at low Reynolds numbers is the limited predictive capability of turbulence models available in commercial CFD solvers, such as, e.g., the k-ε family or the k-ω family, which are generally unsuitable for accurately capturing transitional flows. To address this, transition models have been developed specifically for simulating such flow regimes. In the literature, examples can be found comparing experimental results with numerical simulations, showing varying degrees of agreement. Generally, the lower the Reynolds number, the greater the discrepancies are observed. Based on available comparisons, such as those by Melani et al. (2019a, 2019b), it can be noted that the γ-Re_θ transition model generates relatively acceptable aerodynamic force predictions for airfoils at Reynolds numbers of 100,000 or higher, even for thick symmetric profiles like the NACA 0021, as demonstrated by Balduzzi et al. (2018). A similar agreement is confirmed by independent experimental and numerical studies of the NACA 0018 airfoil at a Reynolds number of 160,000 (Rogowski et al., 2025a). Lee et al. (2015) analyzed the aerodynamic performance of the NACA 0012 airfoil at Reynolds numbers of 10,000, 30,000, and 50,000, utilizing, among other methods, the Baldwin-Lomax turbulence model. They demonstrated that this approach predicts the separation point closer to the trailing edge than the two-dimensional laminar simulations and three-dimensional implicit large-eddy simulations. However, as the boundary layer flow on the airfoil's surface is assumed to be fully turbulent when using the Baldwin–Lomax model, the separation bubble was not captured. Furthermore, the study revealed that no nonlinearity in the lift curve is observed below the critical angle of attack, underscoring the intrinsic limitations of RANS-based turbulence models in accurately capturing transitional low-Reynolds flows. This underlines the necessity for further development of advanced modelling approaches, which must be supported by detailed experimental investigations and high-fidelity LES/DNS data.

A fundamental conclusion from the work of Lee et al. (2015) is that only eddy-resolving techniques, such as LES or DNS, are capable of providing quantitative results for both aerodynamic loads and the detailed characteristics of phenomena occurring within the boundary layer. Similar evidence supporting the effectiveness of the LES approach in studying the aerodynamic characteristics of thin airfoils at low Reynolds numbers has also been presented by other authors, including Anyoji et al. (2014) and Kojima et al. (2013). Accurately capturing the intricate flow dynamics and transition phenomena, which lie beyond the capabilities of RANS-based turbulence models, necessitates the use of eddy-resolving methods. The two-dimensional laminar model and the implicit LES (iLES) approach, as outlined in the work of Lee et al. (2015), effectively captured the nonlinear behaviour of the lift coefficient (C_L), including its negative values at low angles of attack. Additionally, the impact of the angle of attack on the location of the laminar separation bubble was also examined. This work provides a foundation for further research utilizing DNS and LES approaches. None of the previously cited studies have analyzed the NACA 0018 airfoil at a Reynolds number of 30,000 using LES or DNS. The application of these eddy-resolving approaches enables the evaluation of the aerodynamic performance and flow characteristics of a thick, symmetric airfoil under challenging low-Reynolds-number conditions.

While thin airfoils such as NACA 0012 have been extensively studied at low Reynolds numbers using DNS and LES, there is still a clear lack of high-fidelity data for thick symmetric airfoils in this regime. To the best of our knowledge, the present study provides the first DNS/LES dataset for the NACA 0018 airfoil at $Re \approx 3 \times 10^4$. This gap is significant because, although thick four-digit NACA sections are not optimal for practical low-Re applications (McMasters & Henderson, 1979; Winslow et al., 2018), their use becomes essential in laboratory-scale wind tunnel studies of vertical-axis wind turbines (VAWTs). In such scaled experiments, blockage effects constrain the chord-based Reynolds number to values as low as 30,000, while maintaining realistic rotor solidity.

Recent experimental research confirms the increasing importance of thick airfoil data in this context. For instance, Bensason et al. (2024, 2025) demonstrated that the aerodynamic interaction between closely spaced VAWTs strongly depends on the underlying blade aerodynamics at low Reynolds numbers, which directly motivates the need for accurate reference datasets on thick symmetric profiles. Moreover, comparative studies of symmetric airfoils at high Reynolds numbers ($Re \sim 3 \times 10^6$) showed that differences between NACA 0012, 0015, and 0018 are relatively minor up to the stall angle and can be reliably predicted with classical turbulence models such as k–ω SST (Rogowski et al., 2020). Substantial differences emerge only in the post-stall regime, where thicker sections exhibit a more gradual loss of lift. In contrast, at $Re \sim 3 \times 10^4$ the aerodynamic force characteristics of these airfoils diverge dramatically, with strong implications for rotor performance and wake development. The limited availability of aerodynamic data for thick profiles at very low Reynolds numbers is further illustrated by the well-known *Profilpolaren für den Modellflug* report by Althaus (1980). While polar data for the NACA 0012 are available down to Re = 40,000, the corresponding dataset for the NACA 0033 begins only at Re = 80,000, leaving a clear gap at lower values. Notably, even at Re = 80,000, the comparison between NACA 0012 and NACA 0033 reveals substantial differences in lift and drag characteristics, highlighting the importance of systematically documenting the performance of thick airfoils in this regime.

In this sense, the novelty of the present work lies in delivering the first high-fidelity DNS/LES dataset for a thick symmetric airfoil (NACA 0018) at *Re* = 30,000. The results not only provide new benchmark data for the community but also address a pressing need arising from scaled VAWT experiments and wind farm wake studies. By bridging this gap, the present study establishes a solid foundation for both validating transition/turbulence models and accurately analyzing turbine wake interactions at low Reynolds numbers.

2. Aerodynamic Analysis of the NACA 0018 Airfoil at Low Reynolds Numbers

This study analyzes the symmetric NACA 0018 airfoil (Fig. 1). The four-digit NACA airfoil series, developed by the National Advisory Committee for Aeronautics (NACA), is widely used in aerodynamics as classical airfoil shapes. These airfoils are described by simple parameters that define their maximum thickness, camber, and position of the maximum camber, making them easily adaptable for various aerodynamic applications. Furthermore, these airfoils are commonly employed in theoretical and experimental analyses as benchmarks, serving as baseline models for more complex aerodynamic designs (Jacobs and Sherman, 1937; Abbott and Von Doenhoff, 1959) and flight mechanics studies (Lichota et al., 2020; Lichota, 2023). This study examines the aerodynamic performance of an airfoil with a 6 cm chord length at a Reynolds number of 30,000. Tests were conducted under steady flow conditions to provide reliable aerodynamic data essential for the reduced-order modelling of wind turbine aerodynamics. The results are particularly relevant to aviation, where accurately characterizing airfoils at low Reynolds numbers remains a major challenge and a limiting factor in designing efficient flight systems.

This paper examines the aerodynamic characteristics of an airfoil at low Reynolds numbers through numerical simulations, which are validated against existing experimental measurements. Experimental data for the NACA 0018 airfoil at low Reynolds numbers were obtained in the Red Wind Tunnel (RWT) at the Technical University of Denmark. The tunnel configuration and measurement techniques are described in Rogowski et al. (2025). For the numerical simulations presented here, both the airfoil geometry and the actual test-section dimensions of the wind tunnel were faithfully reproduced. The working section of the tunnel has an approximately rectangular shape, and the airfoil was mounted at the quarter-chord position, i.e., 25% of the chord length from the leading edge.

3. Numerical Approach

The eddy-resolving strategies employed in this study used a 3D model to predict the aerodynamic performance of the NACA 0018 airfoil in a low Reynolds number regime. The model was implemented using the ANSYS Fluent solver, configured with a pressure-based transient solver to capture the time-dependent characteristics of the flow field. The working fluid was air, treated as an

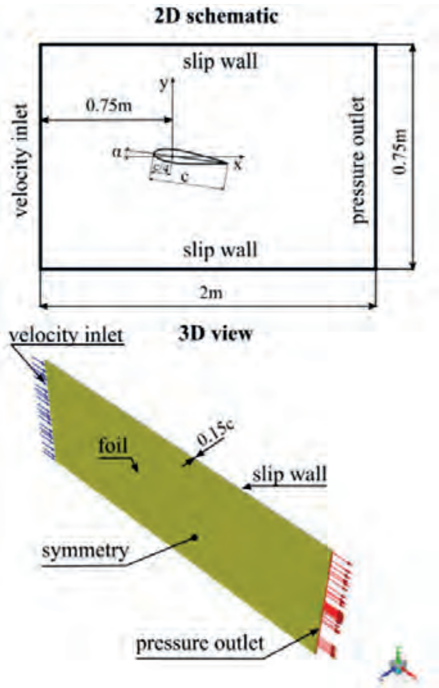

Fig. 1 2D schematic (top) and 3D view (bottom) of the computational domain, including the coordinate system and boundary conditions

incompressible fluid with constant properties: a density of 1.225 kg/m^3, a viscosity of 1.7894×10^{-5} $kg/(ms)$.

The solution method employed the SIMPLE (Semi-Implicit Method for Pressure-Linked Equations) algorithm for pressure-velocity coupling. Spatial discretization used least-squares cell-based gradients and a bounded central differencing scheme for the convective terms in the momentum equations. The unsteady integration consisted of 20,000 time steps, each 0.0001 s in size, with up to 20 inner iterations per step. At each time step, convergence was enforced by driving the residuals of all governing equations below 10^{-6}. Although SIMPLE was originally introduced for segregated RANS solvers, its application in eddy-resolving simulations is well established: for example, LES of the canonical circular cylinder at *Re* = 3900 has been successfully performed with a pressure-based finite-volume code based on SIMPLE, with results validated against detailed measurements Rajani at al. (2016). Similarly, recent LES in ANSYS Fluent continue to employ SIMPLE-family schemes (e.g., SIMPLEC) for unsteady external flows, including LES of turbulent flow over staggered tube clusters (circular cylinders), which reported good agreement with experiments Bedrouni at al. (2020). More recently, wall-resolved LES at comparable Reynolds numbers have explicitly solved the pressure–velocity coupling with SIMPLE, further underscoring the method's suitability for unsteady, separated flows Zöschg (2024). In our setup, the combination of a small time step and strict per-step convergence (residuals $\leqslant 10^{-6}$ with ~20 inner iterations) minimizes splitting errors and yields a time-accurate solution; in line with established best-practice guidelines for scale-resolving simulations, the overall sensitivity to the pressure scheme is typically moderate on high-quality meshes, provided consistent spatial/temporal resolution is ensured (Menter, 2015).

The computational domain was defined with specific boundary conditions to accurately replicate the flow environment. A constant velocity was specified at the inlet, and the outlet was set to a static pressure equal to atmospheric pressure to permit flow discharge at ambient conditions (Fig. 1). Symmetry boundaries were set on the sides of the domain in a spanwise *z*-direction to minimize computational costs and simulate an unbounded flow environment. An interface was defined between the circular and rectangular domains to ensure smooth data transfer between zones. A no-slip wall condition was applied to the airfoil surface to accurately model boundary layer development. The upper and lower walls of the domain were treated as slip walls to mimic free-stream conditions. On the lateral (spanwise) boundaries, we imposed symmetry rather than periodic conditions. For low to moderate incidence angles ($\alpha \leqslant 10°$) of an isolated section, published studies suggest that this choice does not affect near-wall quantities. For example, Venkatachari, et al. (2024) compared C_f maps of the Pazy wing at $Re_c \approx 3.4\times10^5$ and $\alpha = 6°$ using periodic and symmetry boundaries, and reported "virtually no discernible difference" between the two. Moreover, several fully three-dimensional airfoil simulations at comparable Reynolds numbers have employed spanwise symmetry and achieved excellent agreement with experimental data. For example, Solís-Gallego et al. (2020) carried out a wall-resolved LES of the FX 63-137 airfoil using symmetry on the spanwise boundaries with a modest spanwise extent (L_z/c = 0.164) and matched both aerodynamic force coefficients and the normal-to-airfoil distribution of streamwise velocity. Likewise, Chen et al. (2021) employed LES/DDES for a NACA 65(12)-10 section with symmetry in the spanwise direction, accurately reproducing the measured Sound Pressure Level (SPL) spectra. Taken together, these studies support the use of spanwise symmetry for pre-stall angles investigated here, provided that the spanwise extent is sufficient.

In the LES approach, the dynamic Smagorinsky–Lilly model, as proposed by Germano et al. (1991), was employed to represent the subgrid-scale shear stresses. A clean inlet condition, without unresolved perturbations at the domain inlet, was imposed. The experiments were conducted in a low-turbulence wind tunnel, where the turbulence intensity at the inlet was less than 0.1%. In the present DNS/LES we intentionally prescribe a clean uniform inflow (0% resolved turbulence) to establish a controlled baseline for low-Reynolds-number separated airfoil flow. This approach is common in high-fidelity studies at comparable Re to isolate intrinsic shear-layer and wake dynamics from externally imposed fluctuations; e.g., Rodríguez et al. (2013) imposed a uniform inlet for DNS of a symmetric airfoil (NACA 0012) at *Re* = 50,000, focusing on fully stalled conditions, while Trias et al. (2015) prescribed a constant-velocity inlet in DNS of a bluff body (square cylinder) at *Re* = 22,000, explicitly targeting reference data rather than reproducing tunnel freestream turbulence intensity.

For DNS, the continuity and momentum equations are formulated as:

$$\nabla \cdot \boldsymbol{u} = 0 \tag{1}$$

$$\frac{\partial \boldsymbol{u}}{\partial t} + (\boldsymbol{u} \cdot \nabla)\boldsymbol{u} = -\frac{1}{\rho}\nabla p + \nu\nabla^2\boldsymbol{u} \tag{2}$$

where: $\boldsymbol{u}$ is the velocity vector, p is the pressure, ρ is the density, and ν is the kinematic viscosity.

3.1 Grid Generation and Quality Assessment

In this study, a 3D numerical hybrid grid was employed (Fig. 2). The computational grid was developed based on the 2D mesh model previously analyzed by Rogowski et al. (2021). The key features include a hybrid mesh, consisting of a structured grid near the airfoil surface and an unstructured grid in the remaining regions. The structured mesh comprises 37 layers with a growth rate of 1.13 and an initial wall-adjacent element thickness of 5×10^{-6} meters, ensuring a wall y^+ value of less than 1.

Although a purely structured mesh (e.g., an O-grid or C-grid) is commonly used for steady airfoil simulations, we opted for a hybrid unstructured mesh in this study to better accommodate the problem setup and future needs. First, our computational domain directly replicates a rectangular wind tunnel test section (Rogowski et al., 2025); forcing a single-block structured O- or C-grid to fill this rectangular domain would introduce distortions or require complex multi-block interfaces. In contrast, the chosen hybrid mesh (structured prism layers near the airfoil and unstructured elements in the far field) naturally conforms to the rectangular boundaries, thereby preserving fidelity to the experimental geometry. Second, while the present case is static, this mesh strategy provides flexibility for planned dynamic simulations (e.g., pitching or oscillating airfoils), where unstructured grids adapt more readily to moving boundaries or localized refinement. Third, extensive literature shows that unstructured meshes can achieve accuracy on par with structured meshes for Large-Eddy Simulations, provided that near-wall regions are sufficiently resolved Cao and Tamura (2016) or Lloyd and James (2016). For example, Cao and Tamura (2016) compared LES results on structured vs. unstructured grids for flow over a bluff body and found both approaches produced similarly accurate time-averaged and RMS flow quantities. Likewise, Lloyd and James (2016) reported that an unstructured grid can even resolve wake flow features better than a structured grid of comparable size, given equivalent boundary-layer resolution. These findings demonstrate that a hybrid mesh does not compromise solution fidelity. In our case, the use of 37 high-quality prism layers (growth ratio 1.13, first-layer y^+<1) around the airfoil ensures the viscous sublayer is well-resolved, satisfying the same criteria a structured mesh would. Therefore, our hybrid mesh choice is well-justified by the rectangular domain requirements, future dynamic applications, and evidence from prior studies confirming the accuracy of unstructured LES meshes.

The spanwise extent of the computational domain was set to $L_z = 0.15c$ (with $c = 0.06c$). Near the airfoil, the surface mesh was constrained to a nominal surface element size of $6 \cdot 10^{-5}$ m, which yields $\sim$150 cells across the span at the airfoil and ensures adequate spanwise resolution; the airfoil edge itself was discretized with 830 divisions in the streamwise direction. In the outer tunnel block, the structured grid was extruded with 25 layers in the *z*-direction. Historically anchored and moving to unconfined cases, we note that Zhang & Samtaney (2016) surveyed airfoil DNS/LES practice and documented that spanwise aspect ratios used in numerical simulations are most commonly in the range $AR = L_z/c \approx 0.1 - 0.2$. In the present study ($\alpha \leq 10°, Re \approx 3 \cdot 10^4$), our choice $L_z = 0.15c$ lies within this documented band for unconfined low-to-moderate-AoA airfoils. Each static angle-of-attack case required on the order of 10^2 wall-clock hours on 960 Cray XC40 cores.

To evaluate the quality of the computational grid and its suitability for resolving near-wall turbulence in LES simulations, the dimensionless wall distance (y^+) and the grid resolutions in the streamwise (Δx^+) and spanwise (Δz^+) directions were analyzed. These parameters were assessed for the unstructured triangular grid, with particular attention given to the case of a Reynolds number of 30,000 and an angle of attack (α) of 4 degrees.

For the suction side of the airfoil, the average y^+ was approximately 0.052, with a minimum of 0.0023 and a maximum of 0.21. On the pressure side, the averaged y^+ value was 0.081, with a minimum of 0.017 and a maximum of 0.19. These results confirm that the near-wall grid resolution was sufficiently fine, maintaining $y+$ value within the recommended range for accurate capture of near-wall turbulence effects.

Regarding grid resolution, on the suction side-where the element size was relatively uniform, the average Δx^+ and Δz^+ were approximately 1.36. On the pressure side, the averaged Δx^+ and Δz^+ values were slightly higher at 2.09. These results suggest that the grid was adequately refined in both directions to capture key flow features around the airfoil. The grid resolution achieved in this study is entirely sufficient to accurately resolve the physical phenomena within the boundary layer, particularly at the low Reynolds number considered (Kojima et al., 2013).

A final grid resolution assessment was performed by evaluating the ratio of the local grid spacing (Δ) to the Kolmogorov length scale, $\eta = (\nu^3/\varepsilon)^{1/4}$. The dissipation, ε, was derived under a local equilibrium condition, $\varepsilon \cong \langle \nu_{SGS} \bar{S}^2 \rangle$ following You et al. (2007). In the formula, ν_{SGS} and $\bar{S}$ denote the subgrid-scale viscosity and the time-averaged magnitude of the strain-rate tensor, respectively. Figure 3 presents the distribution of the Δ/η parameter in the vicinity of the airfoil. As demonstrated by Pope (2000) the scales Δ/η sized between 8 and 60 are responsible for the bulk of dissipation. The results show that the maximum value of Δ/η does not exceed 3.5. Following the recommendations by Pope and the results by Kubacki et al. (2013) and Kubacki at al. (2014), it was concluded that a sufficient grid resolution was achieved to capture the relevant flow structures in LES, but also in DNS (Pope, 2000).

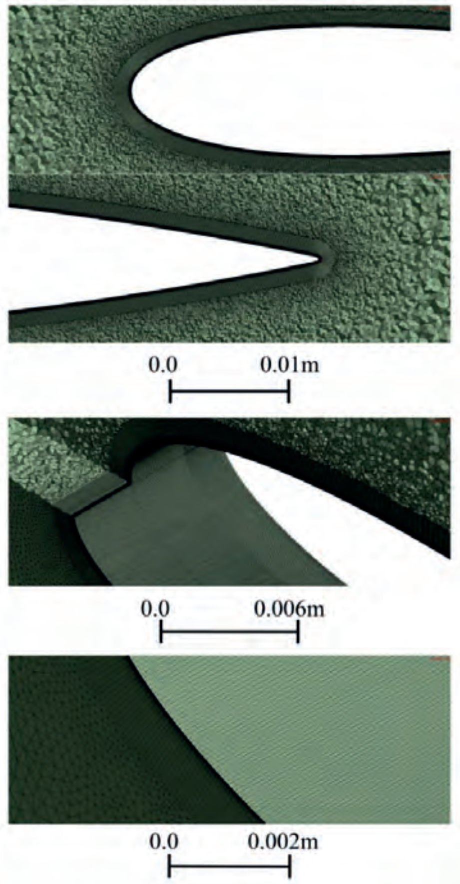

Fig. 2 Computational mesh used for DNS and LES simulations

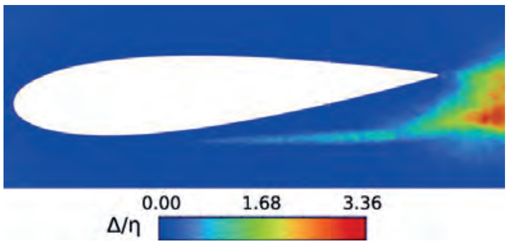

Fig. 3 Distribution of the grid resolution parameter *Δ/η* around the airfoil at α=4°

3.2 Mesh Sensitivity Test

The mesh sensitivity study was performed for an angle of attack of 8°. Specifically, we investigated how changes in mesh density affect the accuracy of the computed aerodynamic force coefficients and the surface distribution of flow quantities. In particular, the influence of mesh resolution on the lift (C_L) and drag (C_D) coefficients was examined, alongside its effect on the pressure coefficient (C_p) and skin friction coefficient (C_f) distributions.

The main mesh parameter varied in this study was the surface element size. For the nominal mesh, this size was

0.00006 m (as described earlier), resulting in approximately 52 million elements. A coarser mesh was generated by increasing the element size to 0.000085 m, which produced about 40 million elements. In contrast, the finest mesh used a smaller element size of 0.00005 m, yielding roughly 62 million elements. In other words, reducing the surface element size by about 17% (from 0.00006 m to 0.00005 m) increased the mesh by nearly 10 million elements.

Table 1 presents the resulting aerodynamic force coefficients computed using the three grids. For clarity, the coarse mesh is labeled CG (Coarse Grid), the nominal mesh NG (Nominal Grid), and the fine mesh FG (Fine Grid). As shown, the differences in the force coefficients across the grids are very small. In fact, the lift coefficient values differ only in the fifth decimal place, indicating excellent consistency between the meshes. Slightly larger differences are observed for the drag coefficient—for example, refining the mesh by 17% (reducing the element size) changes the predicted drag by less than 5%. This level of variation is acceptable, suggesting that the solution is essentially mesh-independent for the quantities of interest (Zöschg, 2024).

Table 1 Mesh sensitivity test results for the three considered grids (CG = Coarse Grid, NG = Nominal Grid, FG = Fine Grid)

Case	C_L	C_D
CG	0.10073	0.18759
NG	0.10051	0.19270
FG	0.10173	0.20189

Additionally, Fig. 4 compares the pressure coefficient and skin friction coefficient distributions obtained using the coarse, nominal, and fine meshes. These results have been time-averaged and also averaged along the spanwise direction for a representative comparison. It can be seen that the C_p and C_f profiles for all three cases are practically identical. This further confirms that the solution shows very little sensitivity to the mesh density in the examined scenario.

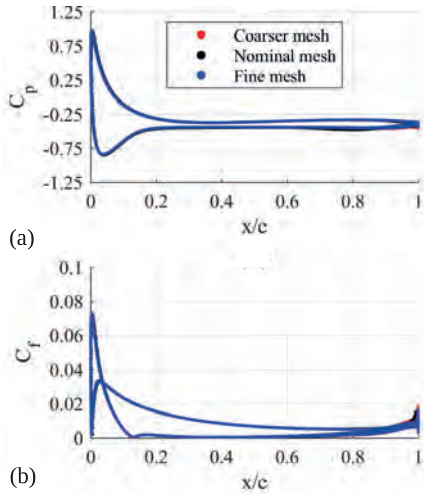

Fig. 4 Mesh sensitivity test at α = 8°: (a) static pressure coefficient and (b) skin friction coefficient

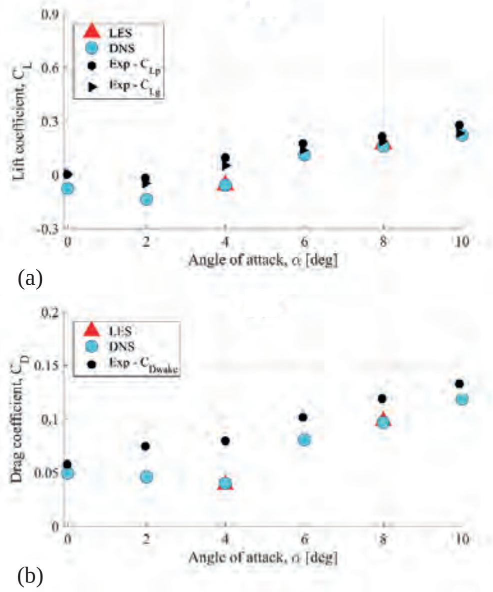

Fig. 5 Comparison of lift (a) and drag (b) versus angle of attack for the NACA 0018 airfoil. DNS and LES are compared with the experiments of Rogowski et al. (2025): C_{Lp} from wall-pressure taps, C_{Lg} from a force balance, and C_{Dwake} from a wake-rake survey

4. RESULTS

4.1 Aerodynamic Force Predictions from DNS and LES at Low Reynolds Numbers

Figure 5 presents the aerodynamic characteristics, specifically the lift coefficients, as functions of the angle of attack for a Reynolds number of 30,000, obtained using LES and DNS simulations. For completeness, we note that DNS covers α = 0°-10°, whereas LES is shown at α = 4° and 8° to provide direct cross-validation with DNS at representative low-AoA conditions. These results are compared with experimental data acquired in the Red Wind Tunnel (RWT) at the Technical University of Denmark (DTU), as reported by Rogowski et al. (2025). Previous studies by Kojima et al. (2013) indicated good agreement of the 3D LES approach over a wide range of angles of attack and satisfactory performance of the 2D DNS approach at low angles of attack. As observed from the experimental data obtained using both wall pressure measurements and force gauges, identifying the critical angle of attack, α_{crit}, for this relatively thick airfoil is challenging. The critical angle of attack is typically associated with a sharp drop in lift, resulting in a distinct bending of the $C_L(\alpha)$ curve. At low Reynolds numbers, viscous forces dominate, leading to an extended laminar boundary layer and severe flow separation. The separation point can be highly sensitive to minute flow disturbances or surface roughness, making accurate prediction difficult. The critical angle of attack is also influenced by airfoil geometry, including airfoil thickness and leading-edge shape, as discussed by Kurtulus (2022).

The negative lift value was accurately reproduced using DNS at an angle of attack equal to 2°. The LES simulations were performed only for two angles of attack, 4 ° and 8°, yielding aerodynamic force coefficients nearly identical to those obtained from the DNS. Experimental results from other researchers, such as Ohtake et al. (2007), and numerical studies by Kojima et al. (2013), also confirmed the occurrence of this effect, caused by strong inverse pressure gradients. A similar phenomenon was observed by Yarusevych (2006), who analyzed the aerodynamic performance of a NACA 0025 airfoil. In his experimental study, negative lift coefficients were reported at Reynolds numbers as low as 55,000 and 100,000, even for positive angles of attack up to 5°, due to the formation of large separation regions on the suction side without flow reattachment. The asymmetry of pressure distributions at low Reynolds numbers resulted in a net downward force, which is atypical for symmetric airfoils.

Comparable observations were made by Ohtake et al. (2007), who investigated the NACA 0012 airfoil at Reynolds numbers ranging from 10,000 under low turbulence intensity conditions (≈approximately 0.1%). However, a comparison between the present study and the findings by Yarusevych (2006) and Ohtake et al. (2007) reveals that the extent of the negative-lift region increases with airfoil thickness. For the NACA 0012 airfoil, negative lift is typically confined to the range of 1°–2°. In our analysis of the thicker NACA 0018, this range extends to approximately 2° in experiments and up to 4° in DNS simulations. In contrast, Yarusevych (2006) reported negative lift values at α = 5° for the even thicker NACA 0025 profile.

It is also noteworthy that this phenomenon becomes negligible or even absent when the turbulence intensity increases. For instance, studies by Tsuchiya et al. (2013) and Albrecht et al. (2022) demonstrated that at higher freestream turbulence levels, the lift curve regains its expected monotonic and symmetric shape, with minimal deviation from classical thin-airfoil theory.

Table 2 reports the error metrics between the numerical predictions and the experiments for both lift and drag. Errors are evaluated at the DNS angles of attack after interpolating the experimental series onto the same α-grid. For a quantity q, the pointwise error is $\Delta q(\alpha_i) = q_{DNS}(\alpha_i) - q_{Exp}(\alpha_i)$. We list: $RMSE = \sqrt{1/N \sum_i \Delta q_i^2}$, $MAE = 1/N \sum_i |\Delta q_i|$, $max|\Delta| = max_i |\Delta q_i|$ and $NRMSE = RMSE/\left(q_{Exp,max} - q_{exp,min}\right)$.

As shown, DNS accurately reproduces the experimental lift trends. Overall, the magnitudes of RMSE/MAE and the modest NRMSE confirm good predictive skill in the $\alpha = 0° - 10°$ range. Although the absolute drag errors (RMSE/MAE) are small, the normalized error (NRMSE) can be comparable to or larger than that for lift because the experimental C_D variation over this narrow α-interval is itself small. Residual differences are expected at low Reynolds numbers, where C_D is highly sensitive to near-separation losses and to wake-based measurements (here C_{Dwake} from the rake). Taken together, the metrics substantiate the visual agreement in the figure and provide a concise, quantitative validation beyond lift alone.

Table 2 Error metrics between DNS and the experiments of Rogowski et al. (2025)

	RMSE	MAE	$max\|\Delta\|$	NRMSE
C_D	0.02456	0.0224	0.0396	0.324078
C_{Lp}	0.09516	0.0882	0.1526	0.319445
C_{Lg}	0.06832	0.0578	0.1086	0.242585

The skin friction coefficient (C_f and σ_x) and pressure coefficient C_p for angles of attack α = 4° and 8° are presented in Figure 6. Here, $C_\mathrm{f} \equiv \tau_\mathrm{w}/(0.5\rho V_0^2)$ is defined as the skin-friction coefficient, representing the total wall shear stress, σ_x is the x-component of the wall shear stress in pascals (Pa), while $C_\mathrm{p} \equiv (p - p_\infty)/(0.5\rho V_0^2)$ is the static pressure coefficient, representing the pressure relative to freestream conditions.

Figure 6 presents a comparison between the surface pressure coefficient distributions obtained from the present DNS simulations at α = 10° and the experimental measurements reported by Yarusevych and Boutilier (2010). To the best of our knowledge, these are the only pressure distributions available in the literature for the NACA 0018 airfoil at Reynolds numbers close to those considered in the present study. Although the DNS was performed at *Re* = 30,000 and the experimental data correspond to *Re* = 40,000, the overall agreement is encouraging. Both datasets show the characteristic sharp suction peak near the leading edge, followed by a gradual recovery toward the trailing edge. The most noticeable differences appear at the leading edge, where the DNS predicts a stronger suction peak, which can be attributed to the lower Reynolds number used in the simulation and the clean inflow condition (*TI* = 0%) compared with the finite turbulence level in the wind tunnel. Downstream of x/c ≈ 0.2, the correspondence between the DNS and the measurements improves significantly, with the predicted C_p profiles closely following the experimental trend. Some discrepancies in the mid-chord region may also reflect the limited readability of the experimental curves, as Yarusevych and Boutilier (2011) plotted multiple Reynolds numbers (40,000–70,000) on the same figure, leading to partial overlap. It should also be noted that Yarusevych and Boutilier (2011) distinguished two qualitatively different regimes of C_p distributions: one for Reynolds numbers between 40,000 and 70,000 and another for Reynolds numbers above 100,000, where the flow characteristics change markedly. Within these limitations, the present comparison demonstrates that the DNS captures the essential features of the low-Reynolds-number pressure distribution on the NACA 0018 airfoil, further supporting the reliability of the simulations as a reference dataset.

Both LES and DNS predict the separation of the laminar boundary layer on the airfoil's suction side at x/c ≈ 0.25 and x/c ≈ 0.13 for α = 4° and 8°, respectively. For α = 4°, the flow experiences near-zero shear stress in the region between x/c = 0.7 and 0.9 (see also Figure 7) prior

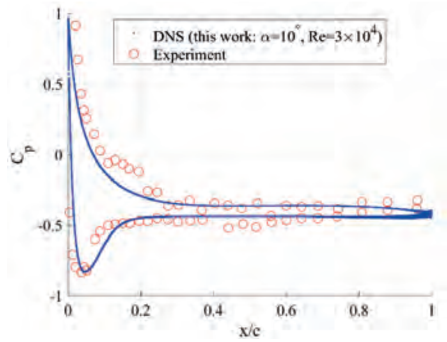

Fig. 6 Comparison of static pressure coefficient (C_p) distributions at α = 10° for the NACA 0018 airfoil. The present DNS results at Re = 30,000 are shown alongside the experimental measurements of Yarusevych and Boutilier (2010) at *Re* = 40,000

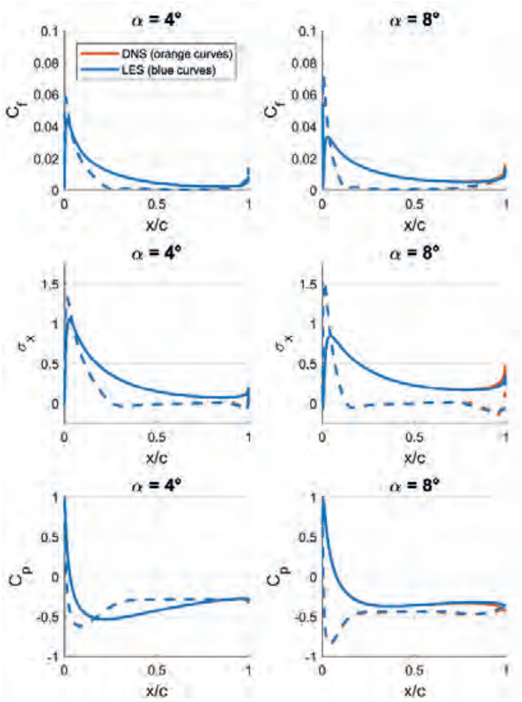

Fig. 7 Skin friction coefficient (C_f), X-wall shear stress (σ_x), and static pressure coefficient (C_p) at two angles of attack, computed using DNS (orange curves) and LES (blue curves). Solid lines represent the pressure side, while dashed lines represent the suction side

to re-separating more abruptly near the trailing edge, while for α = 8°, an earlier onset of near-zero shear stress is observed along the streamwise extent from *x/c* = 0.4 to 0.7. The results show that no transition to turbulence is observed on the suction side for either case.

4.2 High Angle-of-Attack Flow and Stall Characteristics

Figure 8 presents the flow visualization around the NACA 0018 airfoil for angles of attack from 0° to 10°

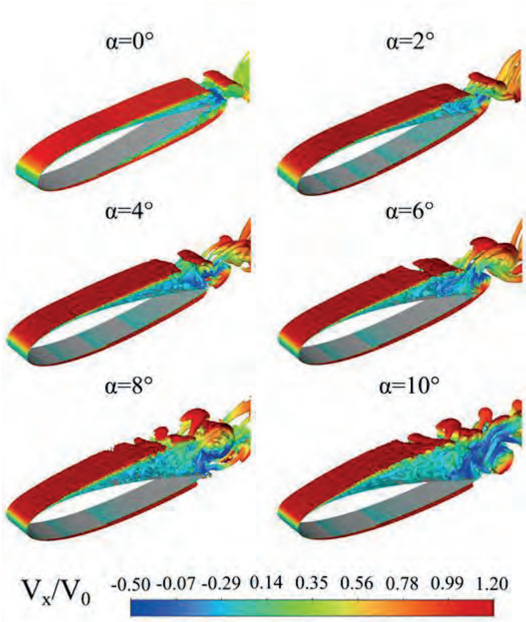

Fig. 8 Flow visualization around the NACA 0018 airfoil at 0°–10° angles of attack from DNS. Q-criterion isosurfaces colored by normalized *x*-velocity

based on DNS simulations. The visualizations use Q-criterion iso-surfaces colored by normalized streamwise velocity V_x/V_0, which clearly reveal the evolution of vortex structures in the wake.

At low angles of attack ($\alpha \leq 4°$), the flow remains largely attached over the suction side, with only minor separation near the trailing edge. As the angle of attack increases to 6°–8°, flow separation moves progressively upstream, and spanwise vortices begin to develop more prominently in the wake. At α = 10°, which exceeds the stall angle for this airfoil under the present Reynolds number and inflow conditions, the laminar boundary layer separates around mid-chord (*x/c* ≈ 0.5) and does not reattach, resulting in a large separated wake region. This wake is characterized by strong, coherent vortices shed from the separated shear layer, as well as a highly unsteady flow pattern.

These results illustrate how increasing the angle of attack leads to earlier separation, more complex wake dynamics, and eventually massive separation at post-stall conditions, demonstrating the capability of the present numerical approach to capture key features of the flow across a wide range of α.

4.3 Flow Separation and Wake Dynamics at Low Reynolds Numbers

In the context of low-Reynolds-number aerodynamics, the flow over the symmetric NACA 0018 airfoil at angles of attack (8° and 4°) exhibits the prominent emergence of coherent vortex structures on the suction side. The vortical formations initiated in the vicinity of the leading edge exert a decisive influence on the downstream evolution of the boundary layer, mediating the onset of complex flow phenomena observed further along the airfoil surface, particularly in the proximity of the trailing edge. The immediate neighborhood of the leading edge is characterized by early separation of the laminar boundary layer, while the trailing-edge region reveals the development of large-scale, organized vortical structures indicative of intricate interactions between shear layer instabilities and the outer flow.

Figure 9a shows the mean streamwise velocity profiles at mid-span along the airfoil surface covering the streamwise distances from x/c=0.4 to 0.99 for Re=30,000 and α = 4°. The figure indicates that the boundary layer remains separated over a large portion of the suction side, from approximately x/c=0.4. The boundary layer separation is significant, with a thickness corresponding to 15% of the chord at the trailing edge. Importantly, the suction side shows neither shear layer reattachment nor the presence of a separation bubble. Such a separation bubble is only expected to form at significantly higher Reynolds numbers, around 100,000 (Yarusevych and Boutilier, 2011).

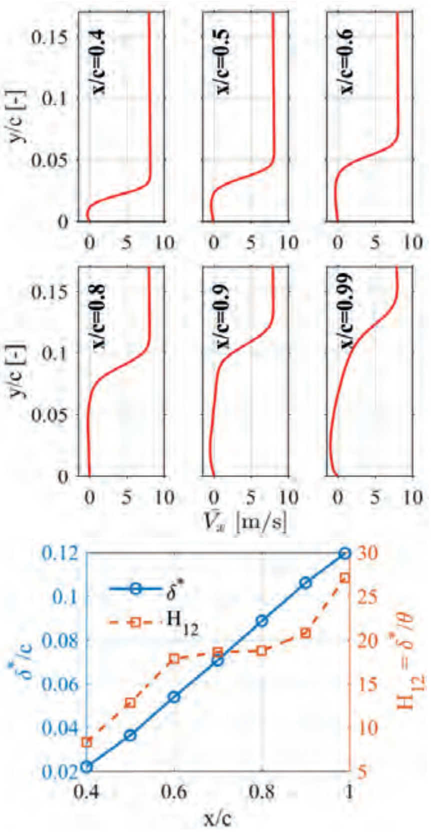

Fig. 9 (a) Mean streamwise velocity profiles at selected chordwise locations on the suction side of the NACA 0018 airfoil at *Re* = 30,000 and *α* = 4°. (b) Streamwise evolution of the displacement thickness δ* and shape factor H_{12} = δ*/θ extracted from the velocity profiles shown in (a)

Further analyses were undertaken to determine if the Kelvin–Helmholtz instability develops in the flow over the NACA0018 profile. We evaluated the displacement thickness, δ^*, and the shape factor, $H_{12} = \delta^*/\theta$, from the DNS data. The resulting values are shown in Fig. 9b. The elevated magnitudes of $\delta^*$and H_{12} are primarily due to the large separated region extending over 60% of the profile. To corroborate these findings, we also performed XFOIL calculations (the force-coefficient results from XFOIL are discussed in Rogowski et al., 2025). A direct comparison confirmed large shape-factor values, with H_{12} reaching approximately 25. XFOIL reproduced the initial growth of H_{12} on the fore part of the chord, but farther downstream its empirical transition correlations (e.g e^N -based triggering) attempted to enforce transition under conditions of massive separation, which makes those predictions unreliable for the present case. In contrast, the DNS exhibit no evidence of a laminar–to-turbulent transition driven by the Kelvin–Helmholtz instability and subsequent boundary layer reattachment.

Figure 10 presents the energy spectra of the streamwise fluctuating velocity component (Fig. 10a) and the static pressure fluctuations (Fig. 10b) obtained at several locations along the airfoil surface, starting from x/c=0.35. The velocity and pressure signals were acquired at a wall-normal location corresponding to the recirculation region near the airfoil surface. The dominant frequency, f_s, corresponding to the peak of E_{uu}, is measured at 219 Hz. This peak is attributed to vortex shedding. Additionally, a subharmonic peak is observed at approximately 95 Hz, along with a higher harmonic at 438 Hz, which is typical of periodic flow phenomena. The presence of these peaks indicates complex flow interactions, such as dynamic boundary layer separation and breakdown of the vortex structures. Aligned with the observations by Yarusevych (2006) and Yarusevych and Boutilier (2011), the dominant frequency identified herein can be linked to the effects of vortex shedding behind the airfoil in the absence of boundary layer reattachment. The pressure fluctuations induced by vortex shedding have a significant impact on the flow dynamics near the airfoil surface. As illustrated in Fig. 8a, the energy spectra imply that the flow is predominantly in a separated and transitional state, with the $f^{-5/3}$ slope, characteristic of small-scale turbulence, observed only in a small fraction of vortex structures at frequencies exceeding 500-600 Hz (x/c=0.45-0.8).

To further characterise the dominant frequency (f_s = 219 Hz) identified in Fig. 10, two definitions of the Strouhal number were adopted. The first Strouhal number, $St_{K-H} = f_s \cdot \theta / V_s$, is defined using the momentum thickness, θ, and the mean velocity, V_s, at the separation point. The Strouhal number characterizes the receptivity mechanism of the Kelvin–Helmholtz (K-H) instability, which results in the roll-up of the separated shear layer. Yang and Voke (2001) state that the Kelvin–Helmholtz instability occurs when the St_{K-H} falls within 0.005–0.011 range, whereas Talan and Hourmouziadis (2002) propose a slightly different range (0.008–0.012). In our work, the Strouhal number based on the momentum thickness falls within the 0.25-0.29 range, which lies outside the mentioned ranges. Thus, the present results indicate that

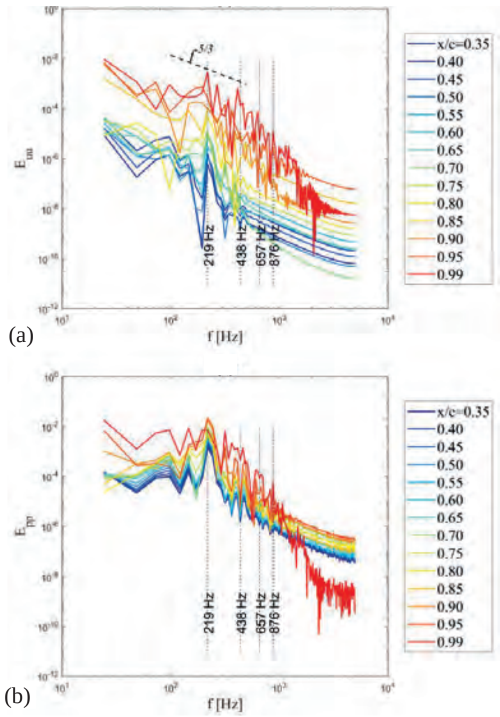

Fig. 10 Energy spectra of streamwise velocity fluctuations (a) and static pressure fluctuations (b) measured along the airfoil at *Re* = 30,000 and angle of attack AoA = 4°. *x/c* denotes the normalized streamwise distances

the observed flow unsteadiness does not support the presence of the K–H instability. The second definition given by $St_0 = f_s \cdot d/V_0$, where *d* is the projected height of the airfoil in the *y*-direction and V_0 is the freestream velocity, follows the approach previously adopted by Yarusevych (2006) and Yarusevych and Boutilier (2011). Based on the present simulations, the estimated value of St_0 is 0.3366. This result is in strong agreement with the experimental data reported by Yarusevych and Boutilier (2011) for Re_c = 30,000–60,000, concerning flow over a NACA0018 airfoil at a 10° angle of attack (see their Fig. 5b). This indicates a common origin of fluctuations near the airfoil surface, namely the vortex shedding process in flow without boundary layer reattachment.

Previous results did not indicate the presence of classical Kelvin–Helmholtz (K–H) instability. However, based on the hypothesis proposed by Yarusevych and Boutilier (2011), it is expected that in the absence of shear-layer reattachment, transition to turbulence occurs within the separated free shear layer, resulting in the formation of large-scale vortex structures. Figure 11a illustrates the streamlines shaded by instantaneous velocity magnitude, while Figure 11b depicts the instantaneous velocity vectors, coloured by the instantaneous *z*-direction vorticity, for the flow at *Re* = 30,000 and α = 4°. In Figure 11, the vorticity contours are colored by the *z*-component of vorticity (ω_z), which corresponds to the out-of-plane vorticity in this configuration. This component is used because it highlights the spanwise (transverse) vortex structures shed

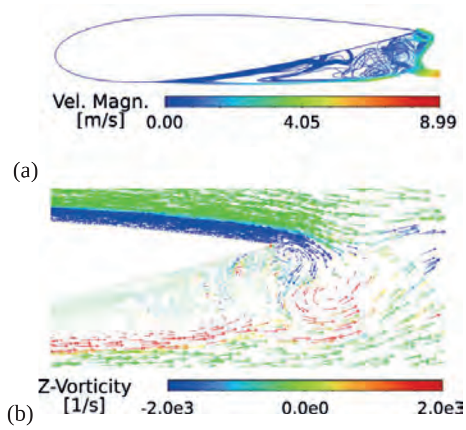

Fig. 11 Flow at *Re* = 30,000 and α = 4°. (a) Flow streamlines colored by instantaneous velocity magnitude. (b) Close-up view of the separated shear layer and vortex shedding near the trailing edge, colored by vorticity in *z*-direction

in the wake of the airfoil, making it easier to visualize the flow pattern. The wake development resembles that of a bluff body without reattachment, characterized by a wider wake compared to flows at higher Reynolds numbers (Yarusevych and Boutilier, 2011). To further investigate the nature of flow unsteadiness close to the airfoil surface, additional spectral analysis was performed in the wake region. Informed by the velocity vector distribution depicted in Fig. 11b, monitoring points were placed at *y/c* = 0.07 downstream of the airfoil trailing edge (see Fig. 1 for the coordinate system), with their streamwise positions extending from *x/c* = 1.0 to *x/c* = 2.75. Figure 12 presents the energy spectra of the *y*-velocity component, wherein the spectral peak corresponding to a wake vortex shedding frequency of 230 Hz is closely aligned with the previously determined shedding frequency of f_s = 219 Hz in the vicinity of the airfoil surface (Fig. 10).

The Strouhal number, calculated using the height of the airfoil projection on a plane normal to the flow and the measured shedding frequency, was determined to be 0.36. Yarusevych and Boutilier (2011) reported a Strouhal number of approximately 0.25 in their studies; however, their experiments were conducted at an angle of attack of 10˚. The results obtained by Huang and Lin (1995) for a NACA 0012 airfoil further confirm that the Strouhal number decreases with a reduction in angle of attack. Additionally, their values for a similar Reynolds number range and an angle of attack of 5˚ are very close to those obtained in the present work. A similar flow behavior has been experimentally observed by Yarusevych and Boutilier (2010), who studied the NACA 0018 airfoil at α = 10° and *Re* = 30,000. Although our simulations were carried out at α = 4°, the qualitative agreement is notable. Both studies report a wide wake, absence of boundary layer reattachment, and coherent vortex shedding under low-turbulence inflow conditions. Yarusevych and Boutilier (2010) identified a shedding frequency of approximately 12 Hz, corresponding to a Strouhal number around 0.2, based on projected airfoil height. In the present

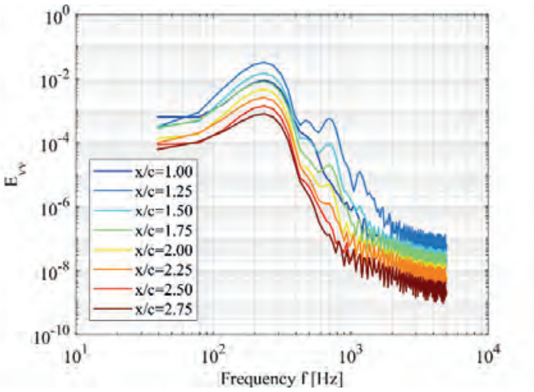

Fig. 12 Energy spectra of the y-fluctuating velocity component gathered at various streamwise positions x/c behind the airfoil trailing edge

work, the dominant shedding frequency is higher ($f_s \approx$ 219 Hz), but the resulting Strouhal number ($St \approx 0.3366$) remains within the expected range for bluff-body-type flows at low Reynolds numbers. These observations further support the conclusion that, for thick, symmetric airfoils like the NACA 0018, flow separation without reattachment can persist over a range of angles of attack, and the associated unsteadiness is not driven by the classical Kelvin–Helmholtz instability.

Figure 13 illustrates the mean *x*-velocity, V_x/V_0, and the root mean square (RMS) of the fluctuating *x*-velocity component, v'/V_0, as obtained from LES computations, in the wake downstream of the airfoil trailing edge over the range of x/c = 1.25 to 3.0. The mean velocity profiles indicate a velocity deficit of 0.43 at x/c = 1.25 and y/c = 0. This value is consistent with the experimental measurements of Yarusevych and Boutilier (2011), showing V_x/V_0=0.45-0.50, at a Reynolds number of 30,000, although their profiles were obtained at an angle of attack of 10°. As the flow develops downstream, a steady recovery of the symmetric wake velocity is observed. The velocity deficit increases from 0.43 at x/c=1.25 to 0.755 at x/c=1.75 and further to 0.8345 at x/c=2.0, indicating rapid initial growth. Beyond x/c=2.0, the more gradual spreading of the wake region is observed, suggesting a stabilization of the wake characteristics. The v'/V_0 profiles (Fig. 13b) reveal a distinct double-peak distribution, corresponding to the shear layer cores generated by flow separation from the upper and lower surfaces of the airfoil (Yarusevych and Boutilier, 2011).

4.4 Comparison of NACA 0012 and NACA 0018 Airfoils

This subsection compares the aerodynamic performance of two symmetric NACA four-digit airfoils with different relative thicknesses, namely 18% (NACA 0018) and 12% (NACA 0012). The NACA 0012 airfoil has been investigated more extensively in the literature, both experimentally and numerically, which provides a broader reference database for comparison. Figures 14 and 15 present the lift and drag characteristics, respectively. For NACA 0012, two independent experimental datasets

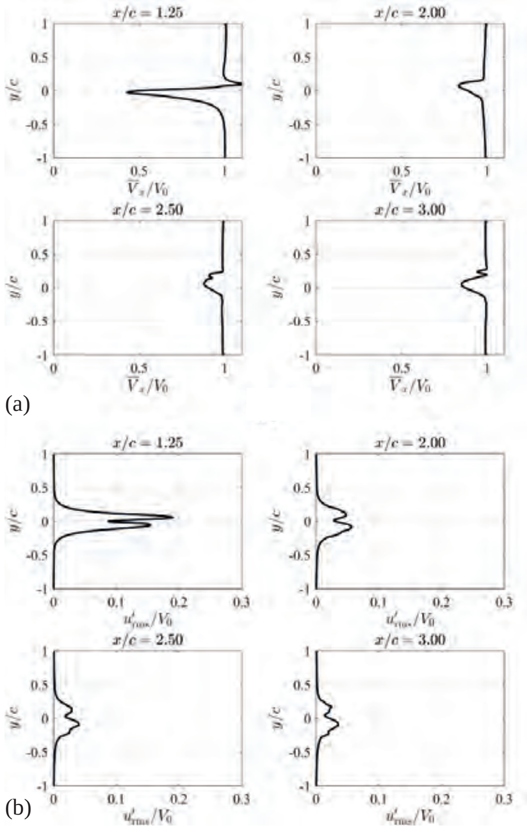

Fig. 13 (a) Mean wake velocity profiles and (b) RMS wake velocity profiles

are considered: Ohtake et al. (2007) and Althaus (1980). In addition, results from two independent LES studies are included: Kojima et al. (2013) at Re=23,000 and Lee et al. (2015) at Re=30,000, both assuming zero free-stream turbulence intensity.

To further validate the DNS approach described in Subsection 3, two additional DNS simulations were performed for the NACA 0012 airfoil at angles of attack of 3° and 6°. These simulations employed the same grid distribution and identical flow conditions (Re=30,000, TI=0%) as in the case of the NACA 0018 computations. The DNS results are shown in Figures 14 and 15 using red markers. The agreement between LES and DNS is very good, providing additional confirmation of the reliability of the DNS methodology used in this study.

The lift and drag coefficients of NACA 0012 were also compared directly with those of NACA 0018 presented earlier in Section 4. Both DNS data and experimental curves from Rogowski et al. (2025) were employed for this purpose. Figures 14 and 15 clearly demonstrate the influence of airfoil thickness on the aerodynamic loads.

A comparison of drag coefficients between the experiments of Rogowski et al. (2025) and Ohtake et al. (2007) reveals similar trends and a distinct upward shift in

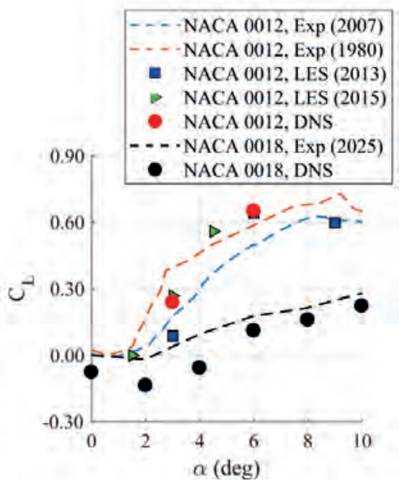

Fig. 14 Lift coefficient (C_L) versus angle of attack for NACA 0012 and NACA 0018 airfoils. Experimental data for NACA 0012 are taken from Ohtake et al. (2007) and Althaus (1980), while LES results are from Kojima et al. (2013) and Lee et al. (2015). Additional DNS simulations for NACA 0012 at α= 3˚ and 6˚ are shown with red markers. Experimental and DNS results for NACA 0018 are taken from Rogowski et al. (2025)

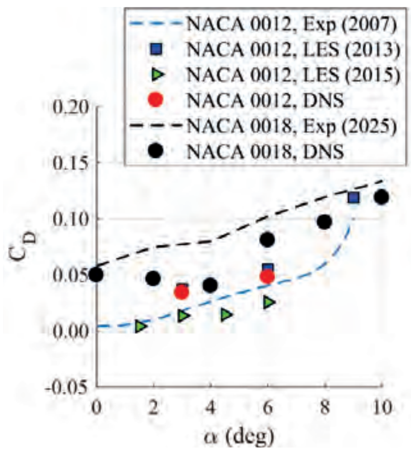

Fig. 15 Drag coefficient (C_L) versus angle of attack for NACA 0012 and NACA 0018 airfoils

the range of angles of attack from 0° to 8°. In this interval, the mean drag coefficient equals 0.026659 for the NACA 0012 and 0.085880 for the NACA 0018. The average increase in drag, defined as the difference between the mean drag of the thicker and thinner airfoil, amounts to 0.059221. The relative increase, calculated with respect to the thinner airfoil, reaches 222.14%. In other words, increasing the relative thickness from 12% to 18% results in more than a threefold increase in drag in the low-angle range of 0–8°.

Equally pronounced differences are observed in the characteristics of the lift. In this case, the comparison was performed using the experimental datasets of Rogowski et al. (2025) and Ohtake et al. (2007) over the angle of attack range 0–9°. The mean lift coefficient is 0.324018 for the NACA 0012 and 0.105225 for the NACA 0018. This corresponds to a relative decrease of −67.53%. In other words, the thicker airfoil loses approximately two-thirds of its lift in this angle-of-attack range.

Figure 16 compares the Q-criterion isosurfaces for the NACA 0018 and NACA 0012 airfoils. The isosurface threshold values are identical in both visualizations. In both cases, the angle of attack is 6° and the chord-based Reynolds number is 30,000. The flow structures obtained for the NACA 0012 airfoil closely resemble those photographed by Kim et al. (2009) for the same airfoil at an angle of attack of 6° and Reynolds numbers of 2.3×10^4 and 3.3×10^4. In addition, Kojima et al. (2013), using implicit LES to analyze the velocity field around NACA 0012, reported very similar flow structures at $Re = 23{,}000$ and α=6˚ Figure 16 clearly demonstrates that, despite the relatively small difference in thickness ratio between the two airfoils, the nature of the boundary-layer development and subsequent flow structures is entirely different. For the thicker NACA 0018 section, the separated shear layer rolls up into large, more coherent vortical structures, producing a bluff-body-like wake, whereas for the thinner NACA 0012 the flow rapidly transitions into smaller, irregular vortices, yielding a more turbulent and disordered wake. Consistent with this picture, the Q-criterion fields in Figure 16 further corroborate the presence of Kelvin-Helmholtz (K-H) instability in the separated shear layer over NACA 0012 at α=6˚: spanwise-coherent rollers form and subsequently break down into hairpin-like structures. This behavior mirrors the iLES observations of Kojima et al. (2013), who explicitly link the periodic 2-D vortices to K-H instability arising from a hyperbolic-tangent-like shear-layer profile.

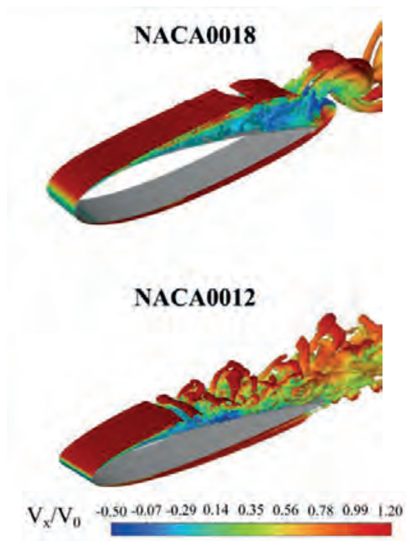

Fig. 16 Q-criterion isosurfaces for the NACA 0018 and NACA 0012 airfoils at α = 6° and Re = 30,000

As already shown in Figure 14, the lift coefficients of NACA 0012 and NACA 0018 differ markedly across the entire angle-of-attack range considered. These differences stem from the underlying pressure distributions. Figure 17 compares DNS static-pressure coefficients $C_p(x/c)$ at α=6˚, $Re = 3.0 \times 10^4$, for the two airfoils. NACA 0012 exhibits a sharper leading-edge suction peak and a faster recovery toward the trailing edge—features consistent with stronger bound circulation and higher lift—whereas NACA 0018 shows an attenuated suction peak and a broad, gently recovering plateau on the suction side, indicative of earlier separation/longer laminar-bubble behavior at this low Reynolds number. For reference, the figure also includes NACA 0012 iLES at $Re = 2.3 \times 10^4$ from Kojima et al. (2013), which agrees closely near the leading edge and follows the overall trend, with modest mid-/aft-chord deviations attributable to the lower Reynolds number and methodological differences.

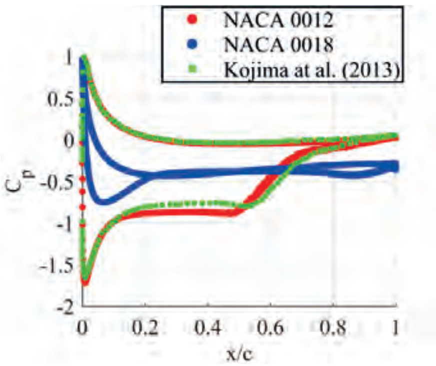

Fig. 17 DNS static-pressure coefficient, $C_p(x/c)$, at α=6˚: NACA 0012 vs NACA 0018; includes NACA 0012 iLES at Re=23,000 (Kojima et al., 2013)

5. CONCLUSION

This study evaluated the aerodynamic performance and flow dynamics of the NACA 0018 airfoil at a chord-based Reynolds number of 30,000 using Direct Numerical Simulation (DNS) as the primary methodology, complemented by a limited set of Large Eddy Simulation (LES) cases at α = 4° and 8°. The LES results closely matched DNS predictions, thereby reinforcing the reliability of the DNS dataset. Both methods successfully captured the key aerodynamic features, including laminar boundary layer separation, vortex shedding, and wake development under clean inflow conditions.

The simulations revealed an early separation of the laminar boundary layer past the leading edge, with no reattachment occurring along the suction side, resulting in a bluff-body-like wake structure. The energy spectra of the fluctuating velocity and pressure measured near the airfoil surface revealed a dominant vortex shedding frequency, aligning with previously reported experimental findings (Yarusevych and Boutilier, 2011). The estimated Strouhal numbers confirmed the absence of classical Kelvin–Helmholtz instabilities, further supporting the bluff-body shedding mechanism.

Comparison with experimental data demonstrated very good agreement in terms of aerodynamic forces, skin friction distribution, and wake characteristics, validating the accuracy of the LES and DNS approaches. The mean wake velocity profiles indicated steady wake recovery downstream, in line with established low-Reynolds-number flow behavior.

Overall, the results underscore the importance of employing eddy-resolving methods, such as DNS and LES, for predicting complex flow phenomena at low Reynolds numbers, thereby providing valuable benchmarks for future studies on small UAVs, rotorcraft, and microwind turbines.

This study provides a reference for future work on analyzing pitching motion and the influence of inlet turbulence intensity on airfoil characteristics.

In the present work, a clean inflow (0% resolved turbulence) was prescribed instead of the ≈0.1% measured in the wind tunnel. This choice was intentional, as it isolates the effect of wake flow on the separated boundary layer in the absence of freestream turbulence. Introducing resolved inlet fluctuations would have required a substantially finer mesh upstream of the airfoil, which was beyond the available computational resources.

Although LES was restricted to two representative angles of attack due to computational cost, its excellent agreement with DNS indicates that future LES studies can be confidently extended to broader parameter ranges. In this way, LES provides a supporting role in validating DNS and highlights the robustness of both eddy-resolving strategies for low-Reynolds-number separated flows.

While the present LES dataset was restricted to α = 4° and 8° due to computational cost, we are extending the simulations to additional angles to further populate the low-Re map. These forthcoming results will be reported together with studies on pitching motion and on the sensitivity to freestream turbulence intensity.

Finally, we note that the spanwise symmetry boundary condition, supported by published URANS and LES results for isolated wings and airfoils, is appropriate for the present $\alpha \leq 10°$ cases; for strongly three-dimensional post-stall flows or for configurations exhibiting spanwise-coherent shedding at long wavelengths, a periodic treatment and/or increased L_z may be preferable.

The NACA 0012 airfoil proves to be significantly more aerodynamically efficient than the NACA 0018 in the low-angle-of-attack regime at *Re* = 30,000. In contrast, the thicker NACA 0018 airfoil should only be considered in applications where structural strength and resistance to torsional loads are prioritized, such as in *H*-type VAWTs, and this comes at the expense of aerodynamic efficiency.

ACKNOWLEDGEMENTS

This research was funded by the POB Energy program at Warsaw University of Technology as part of the Excellence Initiative: Research University (IDUB) under Grant No. 1820/355/Z01/POB7/2021. The computational work was supported by the Interdisciplinary Centre for Mathematical and Computational Modelling at the University of Warsaw (ICM UW), with resources allocated under project numbers G93-1588, G94-1718 and G98-2095.

CONFLICT OF INTEREST

The authors declare that they have no conflicts of interest to disclose.

AUTHORS CONTRIBUTION

Krzysztof Rogowski: Conceptualization, Methodology, Formal analysis, Investigation, Writing – original draft. **Sławomir Kubacki:** Supervision, Writing – review & editing, Validation. **Jan Michna:** Data curation, Writing – review & editing, Visualization.

REFERENCES

Abbott, I. H., & Von Doenhoff, A. E. (1959). *Theory of wing sections: including a summary of airfoil data*. Dover Publications, Inc., New York.

Albrecht, M. B., Olson, D. A., Naguib, A. M., & Koochesfahani, M. (2022). Reynolds number and freestream shear effects on a NACA 0012 airfoil in the Reynolds number Range 10,000-30,000. In *AIAA SCITECH 2022 Forum* (p. 1055). https://doi.org/10.2514/6.2022-1055

Althaus, D. (1980). Profilpolaren für den Modellflug: Windkanalmessungen an Profilen im kritischen Reynoldszahlbereich. Band 1. Necktar-Verlag, Vs-Villingen. Institut für Aerodynamik und Gasdynamik der Universität Stuttgart (in German).

Anyoji, M., Nonomura, T., Aono, H., Oyama, A., Fujii, K., Nagai, H., & Asai, K. (2014). Computational and experimental analysis of a high-performance airfoil under low-Reynolds-number flow condition. *Journal of Aircraft, 51*(6) 1864-1872. https://doi.org/10.2514/1.C032553

Balduzzi, F., Bianchini, A., Ferrara, G., Holst, D., Church, B., Wegner, F., Pechlivanoglou, G., Nayeri C.N., Paschereit C.O., & Ferrari, L. (2018). *Static and dynamic analysis of a NACA 0021 airfoil section at low Reynolds numbers based on experiments and CFD*. In Turbo Expo: Power for Land, Sea & Air (51180, p. V009T48A004). American Society of Mechanical Engineers. https://doi.org/10.1115/GT2018-75426

Bedrouni, M., Khelil, A., Braikia, M., & Naji, H. (2020). Large Eddy simulation of a turbulent flow over circular and mixed staggered tubes' cluster. *Journal of Applied Fluid Mechanics*, *13*(5), 1471-1486. https://doi.org/10.36884/jafm.13.05.31119

Bensason, D., Mulay, J., Sciacchitano, A., & Ferreira, C. (2025). Experimental demonstration of regenerative wind farming using a high-density layout of vertical-axis wind turbines. *Wind Energy Science*, *10*(7), 1499-1528. https://doi.org/10.5194/wes-10-1499-2025

Bensason, D., Sciacchitano, A., Giri Ajay, A., & Simao Ferreira, C. (2024). A Study of the Near Wake Deformation of the X‐Rotor Vertical‐Axis Wind Turbine With Pitched Blades. *Wind Energy*, *27*(11), 1388-1411. https://doi.org/10.1002/we.2863

Cao, Y., & Tamura, T. (2016). Large-eddy simulations of flow past a square cylinder using structured and unstructured grids. *Computers & Fluids*, *137*, 36-54. https://doi.org/10.1016/j.compfluid.2016.07.013

Chen, N., Liu, H., Liu, Q., Zhao, X., & Wang, Y. (2021). Effects and mechanisms of LES and DDES method on airfoil self-noise prediction at low to moderate Reynolds numbers. *AIP Advances*, *11*(2). https://doi.org/10.1063/5.0038183

Germano, M., Piomelli, U., Moin, P., & Cabot, W. H. (1991). A dynamic subgrid-scale eddy viscosity model. *Physics of Fluids A: Fluid Dynamics*, *3*(7), 1760–1765. https://doi.org/10.1063/1.857955

Huang, M., Sciacchitano, A., & Ferreira, C. (2023). On the wake deflection of vertical axis wind turbines by pitched blades. *Wind Energy*, *26*(4), 365-387. https://doi.org/10.1002/we.2803

Huang, R. F., & Lin, C. L. (1995). Vortex shedding and shear-layer instability of wing at low-Reynolds numbers. *AIAA Journal*, *33*(8), 1398-1403. https://doi.org/10.2514/3.12561

Jacobs, E. N., & Sherman, A. (1937). Airfoil section characteristics as affected by variations of the Reynolds number. *NACA Technical Report, 586*(1), 227-267. https://ntrs.nasa.gov/citations/19930091662

Kim, D. H., Yang, J. H., Chang, J. W., & Chung, J. (2009, January). Boundary layer and near-wake measurements of NACA 0012 airfoil at low Reynolds numbers. In 47th AIAA Aerospace Sciences Meeting Including the New Horizons Forum and Aerospace Exposition (p. 1472). https://doi.org/10.2514/6.2009-1472

Kojima, R., Nonomura, T., Oyama, A., & Fujii, K. (2013). Large-eddy simulation of low-Reynolds-number flow over thick and thin NACA airfoils. *Journal of Aircraft*, *50*(1), 187-196. https://doi.org/10.2514/1.C031849

Kubacki, S., Rokicki, J., & Dick, E. (2013). Predictions of round impinging jet heat transfer with two k‐ω hybrid RANS/LES models. *International Journal of Numerical Methods for Heat & Fluid Flow*, *23*(6), 1023-1048. https://doi.org/10.1108/HFF-07-2011-0149

Kubacki, S., Rokicki, J., & Dick, E. (2014). *Hybrid RANS/LES of flow in a rib-roughened rotating channel.* In Turbo Expo: Power for Land, Sea & Air, 45714, (p. V05AT12A033). American Society of Mechanical Engineers. https://doi.org/10.1115/GT2014-26194

Kurtulus, D. F. (2022). Critical Angle and Fundamental Frequency of Symmetric Airfoils at Low Reynolds Numbers. *Journal of Applied Fluid Mechanics*, *15*(3), 723-735. https://doi.org/10.47176/jafm.15.03.33099

Lee, D., Nonomura, T., Oyama, A., & Fujii, K. (2015). Comparison of numerical methods evaluating airfoil aerodynamic characteristics at low Reynolds number. *Journal of Aircraft*, *52*(1), 296-306. https://doi.org/10.2514/1.C032721

Lichota, P. (2023). Wavelet Transform-Based Aircraft System Identification, *Journal of Guidance, Control & Dynamics*, *46*(2), 350–361. https://doi.org/10.2514/1.G006654

Lichota, P., Dul F., & Karbowski A. (2020). System identification and LQR controller design with incomplete state observation for aircraft trajectory tracking. *Energies* *13*(20), 5354. https://doi.org/10.3390/en13205354

Lloyd, T. P., & James, M. (2016). Large eddy simulations of a circular cylinder at Reynolds numbers surrounding the drag crisis. *Applied Ocean Research*, *59*, 676-686. https://doi.org/10.1016/j.apor.2015.11.009

McMasters, J., & Henderson, M. (1979). *Low-speed single-element airfoil synthesis*. Technical Soaring, 6(2), 1-21.

Melani, P. F., Balduzzi, F., Ferrara, G., & Bianchini, A. (2019a). An annotated database of low Reynolds aerodynamic coefficients for the NACA0018 airfoil. In *AIP Conference Proceedings, 2191(020110)*. AIP Publishing. https://doi.org/10.1063/1.5138843

Melani, P. F., Balduzzi, F., Ferrara, G., & Bianchini, A. (2019b). An annotated database of low Reynolds aerodynamic coefficients for the NACA0018 airfoil. In *AIP Conference Proceedings, 2191(020111)*. AIP Publishing. https://doi.org/10.1063/1.5138844

Menter, F. R. (2015) Best Practice: Scale-Resolving Simulations in ANSYS CFD; ANSYS Report; ANSYS Inc.: Canonsburg, PA, USA.

Molina, A. C., De Troyer, T., Massai, T., Vergaerde, A., Runacres, M. C., & Bartoli, G. (2019). Effect of turbulence on the performance of VAWTs: An experimental study in two different wind tunnels. *Journal of Wind Engineering and Industrial Aerodynamics*, *193*, 103969. https://doi.org/10.1016/j.jweia.2019.103969

Ohtake, T., Nakae, Y., & Motohashi, T. (2007). Nonlinearity of the aerodynamic characteristics of NACA0012 aerofoil at low Reynolds numbers. *Japan Society of Aeronautical Space Sciences*, *55*(644), 439-445. https://doi.org/10.2322/jjsass.55.439

Pope, S. B. (2000). *Turbulent Flows*. Cambridge University Press.

Rajani, B. N., Kandasamy, A., & Majumdar, S. (2016). LES of flow past circular cylinder at Re= 3900. *Journal of Applied Fluid Mechanics*, *9*(3), 1421-1435. https://doi.org/10.18869/acadpub.jafm.68.228.24178

Rodríguez, I., Lehmkuhl, O., Borrell, R., & Oliva, A. (2013). Direct numerical simulation of a NACA0012 in full stall. *International Journal of Heat and Fluid Flow*, *43*, 194-203. https://doi.org/10.1016/j.ijheatfluidflow.2013.05.002

Rogowski, K., Hansen, M. O. L., & Bangga, G. (2020). Performance analysis of a H-Darrieus wind turbine for a series of 4-digit NACA airfoils. *Energies*, *13*(12), 3196. https://doi.org/10.3390/en13123196

Rogowski, K., Królak, G., & Bangga, G. (2021). Numerical Study on the Aerodynamic Characteristics of the NACA 0018 Airfoil at Low Reynolds Number for Darrieus Wind Turbines Using the Transition SST Model. *Processes*, *9*(3), 477. https://doi.org/10.3390/pr9030477

Rogowski, K., Mikkelsen, R. F., Michna, J., & Wiśniewski, J. (2025a). Aerodynamic performance analysis of NACA 0018 airfoil at low Reynolds numbers in a low-turbulence wind tunnel. *Advances in Science and Technology Research Journal*, *19*(2), 136-150. https://doi.org/10.12913/22998624/195556

Solís-Gallego, I., Argüelles Díaz, K. M., Fernández Oro, J. M., & Velarde-Suárez, S. (2020). Wall-resolved LES modeling of a wind turbine airfoil at different angles of attack. *Journal of Marine Science and Engineering*, *8*(3), 212. https://doi.org/10.3390/jmse8030212

Talan, M., & Hourmouziadis, J. (2002). Characteristic regimes of transitional separation bubbles in unsteady flow. *Flow, Turbulence and Combustion*, *69*(3), 207-227. https://doi.org/10.1023/A:1027355105017

Tescione, G., Ragni, D., He, C., Ferreira, C. S., & Van Bussel, G. J. W., (2014), Near wake flow analysis of a vertical axis wind turbine by stereoscopic particle image velocimetry. *Renewable Energy*, *70*, 47-61. https://doi.org/10.1016/j.renene.2014.02.042

Trias, F. X., Gorobets, A., & Oliva, A. (2015). Turbulent flow around a square cylinder at Reynolds number 22,000: A DNS study. *Computers & Fluids*, *123*, 87-98. https://doi.org/10.1016/j.compfluid.2015.09.013

Tsuchiya, T., Numata, D., Suwa, T., & Asai, K. (2013, January). *Influence of turbulence intensity on aerodynamic characteristics of an NACA 0012 at low Reynolds numbers*. In 51st AIAA aerospace sciences meeting including the new horizons forum and aerospace exposition (p. 65). https://doi.org/10.2514/6.2013-65

Venkatachari, B. S., Hildebrand, N. J., Choudhari, M. M., & Chwalowski, P. (2024). Transition Analysis for the Pazy Wing. In AIAA SCITECH 2024 Forum (p. 2685). https://doi.org/10.2514/6.2024-2685

Verma, A., & Kulkarni, V. (2024). Monitoring the Wake of Low Reynolds Number Airfoils for Their

Aerodynamic Loads Assessment. *Journal of Applied Fluid Mechanics*, *17*(11), 2481-2498. https://doi.org/10.47176/jafm.17.11.2607

Winslow, J., Otsuka, H., Govindarajan, B., & Chopra, I. (2018). Basic understanding of airfoil characteristics at low Reynolds numbers (10 4–10 5). *Journal of Aircraft*, *55*(3), 1050-1061. https://doi.org/10.2514/1.C034415

Yang, Z., & Voke, P. R. (2001). Large-eddy simulation of boundary-layer separation and transition at a change of surface curvature. *Journal of Fluid Mechanics*, *439*, 305-333. https://doi.org/10.1017/S0022112001004633

Yarusevych, S. (2006). *Investigation of Airfoil Boundary Layer and Turbulent Wake Development at Low Reynolds.* PhD Thesis, University of Toronto.

Yarusevych, S., & Boutilier, M. (2010, June). *Vortex shedding characteristics of a NACA 0018 Airfoil at low Reynolds numbers.* In 40th Fluid Dynamics Conference and Exhibit (p. 4628). https://doi.org/10.2514/6.2010-4628

Yarusevych, S., & Boutilier, M. S. (2011). Vortex shedding of an airfoil at low Reynolds numbers. *AIAA Journal*, *49*(10), 2221-2227. https://doi.org/10.2514/1.J051028

You, D., Wang, M., Moin, P., & Mittal, R. (2007). Large-eddy simulation analysis of mechanisms for viscous losses in a turbomachinery tip-clearance flow. *Journal of Fluid Mechanics*, *586*, 177-204. https://doi.org/10.1017/S0022112007006842

Zhang, W., & Samtaney, R. (2016). Assessment of spanwise domain size effect on the transitional flow past an airfoil. *Computers & Fluids*, *124*, 39-53. https://doi.org/10.1016/j.compfluid.2015.10.008

Zöschg, H. (2024). Large Eddy Simulations of Flow Past Circular Cylinders to Determine Head Loss Coefficients of Circular Bar Trash Racks with Perpendicular Inflow Conditions. *Water*, *16*(2), 347. https://doi.org/10.3390/w16020347